Hydrothermal fluxes in the mantle lithosphere : An experimental study of the serpentinization process

Sofia Escario Perez

THÈSE POUR OBTENIR LE GRADE DE DOCTEUR DE L'UNIVERSITÉ DE MONTPELLIER

En sciences de la Terre

École doctorale GAIA

Unité de recherche Géosciences Montpellier

Flux hydrothermaux dans le manteau lithosphérique : étude expérimentale des processus de serpentinisation et de carbonatation

Présentée par Sofia ESCARIO

Le 21 Septembre 2018

Sous la direction de Marguerite GODARD et Philippe GOUZE

Devant le jury composé de

Dr. Muriel ANDREANI, Maître de conférences, Université Claude Bernard Lyon 1	Rapporteur
Dr. Isabelle MARTINEZ, Maître de conférences, Université Paris Diderot	Rapporteur
Dr. Pascale BENEZETH, Directeur de Recherche, CNRS, Université de Toulouse	Examinateur
Dr. Manuel MUÑOZ, Professeur, Université de Montpellier	Président
Dr. Marguerite GODARD, Directeur de Recherche, CNRS, Université de Montpellier	Directrice de Thèse
Dr. Philippe GOUZE, Directeur de Recherche, CNRS, Université de Montpellier	Co-directeur de Thèse

The research leading to these results has received funding from the People Programme (Marie Curie Actions) of the European Union's Seventh Framework Programme FP7/2007-2013/ under REA - Grant Agreement n°608001

THESIS FOR THE DEGREE OF DOCTOR OF PHILOSOPHY FROM THE UNIVERSITY OF MONTPELLIER

In Earth Science

GAIA Doctoral School

Research Laboratory Géosciences Montpellier

Hydrothermal fluxes in the mantle lithosphere: An experimental study of the serpentinization and carbonation processes

Defended by Sofia ESCARIO

The 21th September 2018

Under the supervision of Marguerite GODARD and Philippe GOUZE

In front of the thesis jury composed of

Dr. Muriel ANDREANI, Maître de conférences, Université Claude Bernard Lyon 1	Reviewer
Dr. Isabelle MARTINEZ, Maître de conférences, Université Paris Diderot	Reviewer
Dr. Pascale BENEZETH, Directeur de Recherche, CNRS, Université de Toulouse	Examiner
Dr. Manuel MUÑOZ, Professeur, Université de Montpellier	President
Dr. Marguerite GODARD, Directeur de Recherche, CNRS, Université de Montpellier	Supervisor
Dr. Philippe GOUZE, Directeur de Recherche, CNRS, Université de Montpellier	Co-supervisor

The research leading to these results has received funding from the People Programme (Marie Curie Actions) of the European Union's Seventh Framework Programme FP7/2007-2013/ under REA - Grant Agreement n°608001

A mis padres

Acknowledgments

For beging, I would like to acknowledge the European Commission for funding the ABYSS Initial Training Network under the Seventh Framework Programme for Research and Technological Development (FP7).

I first would like to acknowledge the members of my thesis committee, Muriel Andreani and Isabelle Martinez for agreeing to evaluate my manuscript and Pascale Bénézeth and Manuel Muñoz for accepting to read the manuscript and to participate in the defense of my thesis.

I sincerely thank my supervisors, Margot Godard and Philippe Gouze, for making this work possible. In particular, I thank Margot for her continous support of my reasearch, for her patience, motivation, encouragements and always useful advices she had provided me throughout my thesis. You have helpme to improve every day. I thank my co-supervisor Philippe Gouze for his constructive advices on reactive transport and the development of the experiments. Thank you both, I will always be very grateful to you!

I specially thank to Richard Leprovost for his help during the reactive percolation experiments. For all the hours spent to making possible to run the experiments and all your constructive advices. Muchas gracias!!!

I would like to thank all Géosciences Montpellier. Jose Alberto Padron Navarta, thank you for your discussions and encouragements during all my thesis they were always very helpful. All the equipe manteau et interface. Maria Garcia-Rios thank you for guidance in the lab and answer all my questions! Christophe Nevado and Doriane Delmas for the preparation of the polished sections. Fréderic Fernandez for analytical assistance during SEM-EDS analyses and Chantal Douchet and Lea Causse for analytical assistance during ICP-OES/MS. Thank you Anne for your graphic designer service.

I can forget Hydrosciences Montpellier! Thanks Sandra Van Exter for her guidance in the alkalinity and chromatography analysis and Remi Freydier for his assistance during ICP-MS. Linda Luquot thanks for all your encourage and pacience for all my questions in reactive transport and been there for everything!

I would like to thank all the people from Statoil for their host during my stay at Trondheim, Jens Emil, Keshvad, Bente Cecile, Carsten, Sturla and Kathin. It was a pleasure to work with you.

Specially thanks for all the Voxaya group, Olivier, Vanessa and Thierry for their help during post-processing of the X-ray tomography images.

I would like to thank to the local contacts at the ESRF, Elodie Boller and Alexander Rack for their assistance during the X-ray tomography analysis.

Special thanks to all the ABYSS group and network. All the meetings have been important opportunities to exchange and discuss about our scientific subjects. Many thanks to, Carlotta, Barbara, Zeudia, Karin, Rachael, Kristina, Adriana, Justine, Tom, Manuel, Manolis, Aurélien, Val and Pavel. Special thanks to Chloe and Alida for your hard work to organize all ABYSS activities, whithout you have not been possible.

I would also like to thanks all the doctorants at Géosciences Montpellier and Hydrosciences Montpellier for their support and good moments shared during this four years! Thank you, Ben, Romain, Manon, Audrey, Sev, Annita, Anaïs, Laure, Max, Sam, Alizia, Lucan, Manuel, Carol, Céline, Julie, Asma, Camille, Alex, Enora, Alex, Justine, Barbara, Vanessa, Arianna, Elenora, Sonia, Arnold, Lidia, Camille, Antoine, Alec, hope not forget someone! Many thanks for you, Carlotta who share the office with me during this four years, thanks for your support since the first day of the thesis and all your good humor.

I would like to thank all the spanish community in Montpellier! Thank you Javi, Cynthia, Alvaro, Marta, Alvarito, Gloria, Manu, Nico, Pedro, Ana, Irene and Thomas! For all the good moments shared during this four years.

Quiero agradecer a María y Benjamin y a los pequeños Noa y Satya por acogerme en Montpellier desde el primer día y por todo vuestro apoyo durante estos cuatro años. Nunca me olvidaré de vosotros.

Unas gracias enormes a mi familia. Muchas gracias Mamá y Papá por motivarme a hacer este doctorado y por todo el apoyo que me habéis ofrecido siempre que he querido hacer algo. Muchas gracias a mis hermanos Miguel, Juan y Félix por su sentido del humor y apoyo cuando dije que comenzaba esta aventura! Gracias a Cris por todos sus animos en los momentos difíciles y por todos los momentos compartidos. Muchas gracias a Tita que siempre se interesó por mis andanzas en la geología! Gracias a mis abuelos, a mis tíos Margari, Teruca, Pepe, Fede, Carlos y Maite y a mis primos Gonzalo, Jorge, Jaime, Almudena, Carlos, Natalia, Alvaro, Iñigo, no me olvido de vosotros !!!

Je tiens enfin à remercier à Aurélien pour ton aide, ta pacience, ton affection et ta présence près de moi.

Muchas gracias a todos !

Sofía

Abstract

The hydrothermal alteration of the mantle lithosphere at mid-ocean ridges provides a mechanism for transferring heat and mass between the deep Earth and the overlaying ocean. The mantle lithosphere is constituted by ultramafic rocks, also called *Peridotites*. They comprise more than 70% of olivine, associated pyroxenes and minor mineral phases. The percolation of seawater into the ultramafic basement produces the alteration of olivine and pyroxenes to serpentine through the so-called *serpentinization process* and its associated oxidation and carbonation reactions, the later when CO_2 is present. The serpentinization process has special interest on H_2 production, CO_2 storage, development of life, and the production of economically valuable ore-deposits concentrated at hydrothermal vents. The sustainability and efficiency of the reactions requires penetration and renewal of fluids at the mineral-fluid interface. Oceanic detachment faults and fractures are highly permeable zones allowing seawater derived fluids to penetrate deeply into the mantle lithosphere. However, the serpentinization process lead to the precipitation of low density minerals that can fill the porous network, clogging flow paths efficiently that may in turn modify the hydrodynamic properties and the reactivity of the reacted rocks.

This PhD thesis aims at better understanding the feedback effects of chemical reactions on the hydrodynamic rock properties that occurred on highly permeable zones during the earliest stages of alteration of the ultramafic basement. It focuses in particular on the changes in texture of the ultramafic rocks and on chemical reaction paths during serpentinization and carbonation processes by assessing the effects of (i) flow rate and (ii) CO_2-rich saline fluids. Two suite of reactive percolation experiments were performed at T=170-190°C and P=25MPa. The first suite of experiments consisted in injecting artificial seawater into porous compressed olivine powder cores over a wide range of constant flow rates. X-Ray μ-tomography of high resolution was acquired before and after the experiment run with high flow rates; in order to evaluate the micro-structural changes of the rock occurred during the serpentinization reaction. The second suite of experiments consisted in injecting CO_2-rich saline fluids into serpentinized peridotite cores mechanically fractured. X-Ray microtomography was performed in the cores after the experiments.

The results of this research project allowed us to put in light the control of: (1) the fluid flow velocity on the solute transport and on the resulted reaction paths during serpentinization and carbonation, (2) the concentration of CO_2 dissolved in the fluid on the reaction paths and the rock textural change. This results also confirm that the formation of carbonate minerals ($(Ca,Mg)CO_3$) during the hydrothermal alteration of ultramafic rock can store CO_2 in a form of stable mineral at long-term. The efficiency of CO_2-storage in peridotite fractured reservoirs can be enhanced or limited by the degree of silicate dissolution that increase the porosity of the reacted rock and by the formation of secondary minerals that could clog the porosity and therefore the fluid flow path.

These new supporting data suggest a complex control of the structure of the ultramafic rocks during serpentinization and carbonation process and provides new insights for the potential CO_2-storage in peridotite fractured reservoirs.

Résumé

L'altération hydrothermale du manteau lithosphérique dans les dorsales médio-océaniques fournit un mécanisme de transfert de chaleur et de masse entre la terre profonde et l'océan en surface. Le manteau lithosphérique est constituée de roches ultramafiques, également appelées *péridotites*. Ils comprennent plus de 70% d'olivine, des pyroxènes associés et des phases minérales mineures. La percolation de l'eau de mer dans les roches ultramafiques produit l'altération de l'olivine et des pyroxènes en serpentine par le processus de *serpentinisation* et il est associé à des réactions d'oxydation et de carbonatation (lorsque le CO_2 est présent dans le fluide). Le processus de serpentinisation présente un intérêt particulier pour la production de H_2, le stockage du CO_2, le développement de la vie et la production de gisements de minerai économiquement intéressants concentrés dans les fumeroles hydrothermales. La durabilité et l'efficacité des réactions nécessitent la pénétration et le renouvellement des fluides à l'interface fluide-minéral. Les failles et les fractures de détachement océanique sont les zones hautement perméables qui permettent à l'eau de mer de pénétrer profondément dans le manteau lithosphérique. Cependant, le processus de serpentinisation conduit à la précipitation de minéraux de faible densité qui peuvent remplir le réseau poreux, colmatant les chemins d'écoulement qui peuvent modifier les propriétés hydrodynamiques et la réactivité des roches réagies.

Ces travaux de thèse visent à améliorer la compréhension des effets en retour des réactions chimiques sur les propriétés hydrodynamique du milieu dans les zones hautement perméables au cours des premières étapes de l'altération des roches ultramafiques. Ils se concentrent en particulier sur les changements de texture et les réactions chimiques des roches ultramafiques en évaluant les effets du (i) débit et (ii) des fluides salins riches en CO_2. Deux séries d'expériences de percolation réactive ont été réalisées à T = 170-190°C et P = 25MPa. La première série d'expériences consistait à injecter de l'eau de mer dans des échantillons de poudre d'olivine compressée couvrant une large gamme de débits constants. La tomographie par rayons X de haute résolution a été acquise avant et après les expériences avec des débits élevés, afin d'évaluer les changements dans la microstructure de la roche lors de la réaction de serpentinisation. La deuxième série d'expériences consistait à injecter des fluides salins riches en CO_2 dans des échantillons de péridotite serpentinisée fracturés

mécaniquement. La tomographie par rayons X a été acquise dans les échantillons de péridotite après les expériences.

Les résultats de ce projet de recherche ont permis de mettre en lumière le contrôle : (1) de la vitesse du fluide sur le transport des solutés et sur la séquence réactionnelle résultante au cours des processus de serpentinisation et de carbonatation, (2) de la concentration du CO_2 dissout dans le fluide sur la séquence réactionnelle et sur la texture de la roche. Ces résultats confirment également que la formation des carbonates ($(Ca,Mg)CO_3$) au cours de l'altération hydrothermale des roches ultramafiques permet de stocker du CO_2 sous la forme de minéraux stables à long terme. L'efficacité du stockage du CO_2 dans des reservoirs de peridotite fracture peut être augmentée ou diminuée par le degré de dissolution des silicates, qui tend à augmenter la porosité de la roche qui a réagi et par le degré de formation de minéraux secondaires qui peuvent colmater le milieu poreux et donc l'apport de fluide.

Ces nouvelles données suggèrent un contrôle complexe de la structure des roches ultramafiques dans le processus de serpentinisation et fournissent de nouvelles perspectives pour le stockage potentiel du CO_2 dans les réservoirs fracturés de péridotite.

Table of contents

Chapter I

Introduction

The hydrothermal alteration of the mantle lithosphere is one of the most important processes controlling energy and chemical exchanges between the deep earth and its outer envelopes. The mantle lithosphere is constituted of ultramafic rocks (peridotites) that mostly contain silicate minerals (olivine and pyroxene). The exposure of the ultramafic rocks to circulating aqueous fluids at temperatures lower than ~400°C triggers the *serpentinization process* that encompasses a suite of complex chemical reactions that modifies the circulating aqueous fluids and the ultramafic rock. This suite of reactions led to the formation of serpentine phases (lizardite and chrysotile) ± brucite ± talc ± magnetite, and carbonates when CO_2 is dissolved in the aqueous fluids.

Serpentinization can modify the rheological, geophysical and chemical properties of the lithosphere and thus the Earth's dynamics along tectonic plate boundaries (Escartin et al., 2001; Maffione et al., 2014; Oufi et al., 2002; Paulick et al., 2006). Serpentinization also impacts the deep marine environment through H_2 production, deep carbon cycling and the production of economically valuable ore-deposits concentrated at hydrothermal vents (Charlou et al., 2002,2013; Früh-Green et al., 2004; Tivey, 2007). Fluids emanating from ultramafic-hosted hydrothermal systems exhibit a range of pH from 3 at high-temperatures vents to 12 at low-temperature vent (review in Humphris et al., 2018). They are characterized by exceeding high H_2 and CH_4 concentrations that provide chemical energy to support unique microbial communities (e.g., Brazelton et al., 2012; Douville et al., 2002; Kelley et al., 2005).

Moreover serpentinization in ultramafic hydrothermal systems led to the formation of carbonated deposits when CO_2 is present in the fluid. At the deep sea hydrothermal fields, e.g., Lost City, the mixing of the discharging high-pH and Ca-rich hydrothermal fluids with seawater results in the precipitation of mixtures of aragonite and brucite that form carbonates towers (up to 60 m) (Kelley et al., 2001). However, massive carbonate deposits have been found in the form of travertine or ophicarbonates in Oman and New Caledonia (e.g., Barnes et al., 1978). The high content of silicate minerals in divalent cations (Ca^{+2}, Mg^{+2} and Fe^{+2}) confers peridotites highly potential to trap CO_2 as carbonates (e.g., Garcia et al., 2010; Kelemen et al., 2011; Xu et al., 2004). Thus, the serpentinization process plays a major role on CO_2-storage (Kelemen et al., 2011). The injection of CO_2-rich fluids into ultramafic reservoir would allow to store CO_2 as carbonates, for example magnesite ($MgCO_3$) (e.g., Oelkers et al., 2008; Kelemen and Matter, 2008; Matter and Kelemen, 2009), and could

contribute to reduce the anthropogenic CO_2. Likewise, the production of H_2 as substitute of conventional energy fuel (petroleum) could contribute also to reduce the generation of anthropogenic CO_2.

The conditions that control the serpentinization and carbonation reactions have been experimentally studied over a wide range of physical-chemical parameters (e.g. temperature, pressure, pH, water/rock ratios, fluid composition and rock composition) mostly under closed conditions (e.g., Andreani et al., 2013; Grozeva et al., 2017; Janecky and Seyfried, 1986; Lafay et al, 2012a,2014; Martin and Fyfe, 1970; Marcaillou et al., 2011; Malvoisin et al., 2012; Pens et al., 2016; Seyfried et al, 2003; Wegner and Ernst, 1983). However, circulation of fluid through ultramafic rocks is characterized by complex physical and chemical feedback processes that change rock properties such as porosity and permeability (Godard et al., 2013; Farough et al., 2016). Chemical reactions, such as mineral dissolution and/or precipitation can often modify flow path geometries and permeability (e.g., Luquot et al., 2009; Luhmann et al., 2017b). This can significantly affect the subsequent solute transport in a porous and/or fractured medium, closing the feedback loop of flow and chemical reactions (e.g., Andreani et al., 2009).The sustainability of serpentinization and carbonation reaction requires the access for the fluid to mineral surfaces. Thus, the study of solute transport in the rock becomes an important parameter to understand the serpentinization process.

This thesis aims to better understand the effects of solute transport and injected fluid composition (e.g.,$CO_{2(g)}$) on incipient serpentinization and carbonation reaction paths. A suite of reactive percolation experiments were conducted at T=170-190°C and P=25MPa using the Icare 3 bench (Géosciences Montpellier) after the percolation of seawater ($\pm CO_{2(g)}$) into: *(i)* highly porous olivine samples and *(ii)* serpentinized peridotite cores mechanically fissured. After these experiments I evaluate:

- The effects of solute transport on reaction paths during incipient serpentinization (*Chapter IV*)

- The effect of CO_2-rich solutions on carbonation into fractured serpentinized peridotite reservoirs (*Chapter V*)

Thesis outline

This thesis is organized in six chapters: *Chapter I* describes the motivation and objective of this study. *Chapter II* presents an overview of the serpentinization process in the lithospheric mantle. It describes the natural places where serpentinization and carbonation reaction takes place and detail review of the physico-chemical parameters that controls the serpentinization and carbonation reactions studied after experimental conditions. *Chapter III* presents firstly a detailed description of the experimental methodology, the reactive percolation bench (Icare 3) and the protocol developed to perform the reactive percolation experiments, followed by the analytical techniques used to characterize the fluids and rock before and after the experiments. Also the chapter contains a description of the geochemical codes used to perform solubility-speciation calculations and reaction path calculations. *Chapter IV* describes the flow rate effect on reaction paths during incipient serpentinization and X-Ray μ-tomography study of the physical changes produced on the rock by the percolation of very high flow rates. *Chapter V* describes the effect of CO_2-rich solutions on carbonation of serpentinized peridotite mechanically fractured. *Chapter VI* provides a summary of the main contributions of this thesis and future research directions.

Introduction (Français)

L'altération hydrothermale du manteau lithosphérique est l'un des processus les plus importants contrôlant les échanges énergétiques et chimiques entre la terre profonde et ses enveloppes extérieures. Le manteau lithospherique est constituée de roches ultramafiques (péridotites) qui contiennent principalement des minéraux silicatés (olivine et pyroxène). L'exposition des roches ultramafiques à des fluides aqueux circulants à des températures inférieures à ~ 400°C déclenche le processus de serpentinisation qui englobe une série de réactions chimiques complexes qui modifient les fluides et la roche. Cette suite de réactions conduit à la formation de phases secondaires incluant la serpentine (lizardite et chrysotile) ± brucite ± talc ± magnétite, et ± carbonates lorsque le CO_2 est dissous dans les fluides aqueux.

La serpentinisation peut modifier les propriétés rhéologiques, géophysiques et chimiques de la lithosphère et donc la dynamique de la Terre le long des limites des plaques tectoniques (Escartin et al., 2001 ; Maffione et al., 2014 ; Oufi et al., 2002 ; Paulick et al., 2006 ;). La serpentinisation a également un impact sur l'environnement de l'océan profond par la production de H_2, le cycle profond du carbone et la production de gisements de minéraux économiquement intéressants concentrés dans les sources hydrothermales (Charlou et al., 2002,2013; Früh-Green et al., 2004 ; Tivey, 2007). Les fluides émanant de systèmes ultramafique hydrothermaux présentent une gamme de pH allant de 3 à des évents à haute température à 12 à des évents à basse température (voir Humphris et al., 2018). Ils sont caractérisés par un excès de concentrations élevées de H_2 et de CH_4 qui fournissent de l'énergie chimique pour soutenir des communautés microbiennes uniques (par exemple, Brazelton et al., 2012 ; Douville et al., 2002 ; Kelley et al., 2005).

De plus, la serpentinisation dans les systèmes hydrothermaux ultramafiques a conduit à la formation de dépôts carbonatés lorsque du CO_2 est présent dans le fluide. Dans les champs hydrothermaux profonds, par exemple Lost City, le mélange des fluides hydrothermaux aux pH élevés et riches en calcium avec l'eau de mer entraîne la précipitation d'un mélange d'aragonite et de brucite, formant des tours spectaculaires de carbonates (jusqu'à 60 m) (Kelley et al., 2001). Cependant, des dépôts carbonatés massifs ont été trouvés sous la forme de travertin ou d'ophicarbonates en Oman et en Nouvelle-Calédonie (par exemple, Barnes et

al., 1978). La teneur élevée des cations divalents dans les minéraux silicatés (Ca^{+2}, Mg^{+2} et Fe^{+2}) confère aux péridotites un potentiel élevé de piégeage du CO_2 sous forme de carbonates (Garcia et al., 2010 ; Kelemen et al., 2011; Xu et al., 2004). Ainsi, le processus de serpentinisation joue un rôle majeur sur le stockage du CO_2 (Kelemen et al., 2011). L'injection de fluides riches en CO_2 dans un réservoir ultramafique permettrait de stocker le CO_2 sous forme de carbonates, par exemple de magnésite ($MgCO_3$) (par exemple, Kelemen et Matter, 2008 ; Matter et Kelemen, 2009 ; Oelkers et al., 2008) et pourrait contribuer à réduire le CO_2 anthropique. De même, la production de H_2 en tant que substitut du combustible énergétique classique (pétrole) pourrait contribuer également à réduire la production de CO_2 anthropique.

Cette thèse vise à mieux comprendre les effets du transport des solutés et de la composition du fluide injecté (par exemple, $CO_{2(g)}$) sur les séquences réactionnelles au cours de la serpentinisation et de la carbonatation. Une série d'expériences de percolation réactive a été réalisée à *T*=170-190 ° C et *P*=25MPa en utilisant le banc Icare 3 (Géosciences Montpellier) après percolation de l'eau de mer (± $CO_{2(g)}$) dans: (i) des échantillons d'olivine hautement poreux et (ii) des péridotites serpentinisées fissurés mécaniquement. D'après ces expériences, j'évalue:

- Les effets du transport des solutés sur la séquence de réactions au cours du processus de serpentinization (Chapitre IV)

- L'effet des solutions riches en CO_2 sur le processus de carbonatation dans les réservoirs fracturés de péridotite serpentinizes (Chapitre V)

Organisation de la thèse

Cette thèse est organisée en six chapitres: le *chapitre I* décrit la motivation et l'objectif de cette étude. Le *chapitre II* présente un aperçu du processus de serpentinisation dans le manteau lithosphérique. Il décrit les lieux naturels où se déroule la réaction de serpentinisation et de carbonatation et examine en détail les paramètres physico-chimiques qui contrôlent les réactions de serpentinisation et de carbonatation étudiées après les conditions expérimentales. Le *chapitre III* présente tout d'abord une description détaillée de la méthode expérimentale, du banc de percolation réactive (Icare 3) et du protocole mis au

point pour réaliser les expériences d'altération hydrothermales, puis une description détaillée des techniques d'analyse utilisées pour caractériser les fluides et la roche avant et après les essais de percolation. Le *chapitre III* contient également une description des codes géochimiques utilisés pour effectuer des calculs de solubilité-spéciation et des calculs de la séquence réactionnelle. Le *chapitre IV* décrit l'effet du débit sur la séquence réactionnelle au cours de la serpentinisation et l'étude des changements physiques produits sur la roche pendant la percolation de très hauts débits après une étude de micro-tomographie des rayons X. Le *chapitre V* décrit l'effet des solutions riches en CO_2 sur la carbonatation de la péridotite serpentinizé et fracturée mécaniquement. Le *chapitre VI* fournit un résumé des principales contributions de cette thèse et des futures orientations de recherche.

Chapter II

Overview of the serpentinization process in the lithospheric mantle

1. Serpentinization

The interior of Earth is divided into layers of different compositions (crust, mantle and core). The mantle is located between the crust (oceanic and continental) and the outer core. The uppermost part of the mantle and the crust constitute the lithosphere, a rigid superficial envelop, fragmented into about twenty mobile tectonic plates. The mantle is composed of ultramafic rocks also named *peridotites*. The major silicate minerals that constitute the ultramafic are predominantly olivine ($(Mg,Fe)_2SiO_4$), clinopyroxene $(Mg,Fe,Ca)_2Si_2O_6$, orthopyroxenes $(Mg,Fe)_2Si_2O_6$ and in a lesser extent spinel ($MgAl_2O_4$). Nevertheless, olivine is the main mineral in ultramafic rocks and represent more than >70% of the minerals of these rocks (Bodinier and Godard, 2003). Peridotites are classified according to their respective proportions of olivine, clinopyroxene and orthopyroxene (Fig.2.1). Thermodynamic studies show that mantle minerals, olivine and pyroxene, are unstable below 450°C and 5 kbar, and therefore are highly reactive when water is present (e.g., Klein and Garrido., 2011; O'Hanley et al., 1996; Palandri and Reed., 2004). The hydration of ultramafic rocks triggers a complex set of chemical reactions called *serpentinization* (e.g., Evans et al., 1976, Moody, 1976, Mével, 2003, O'Hanley, 1996). During serpentinization olivine and pyroxene are replaced by hydrous minerals (e.g., serpentine, brucite and talc), accessory minerals such as Fe-oxides (magnetite) and carbonate minerals when CO_2 is present in the water. The reaction pathways for the serpentinization of olivine can be written as:

$$3\ \mathbf{(Mg,Fe)_2SiO_4} + 4.1\ H_2O \rightarrow 1.5\ \mathbf{(Mg,Fe)_3Si_2O_5(OH)_4} + 0.9\ \mathbf{(Mg,Fe)(OH)_2} + 0.2\ \mathbf{Fe_3O_4} + 0.2\ \mathbf{H_2}$$

Olivine *Serpentine* *Brucite* *Magnetite* (R1)

Serpentinization process and associated reactions can modify the rheological (e.g., Escartin et al., 2001), geophysical (e.g., Maffione et al., 2014) and chemical (e.g., Paulick et al., 2006) properties of the ocean mantle lithosphere. It is also an important vector of energy and chemical exchanges between the ocean and the deep lithosphere at ridges through the development of mantle hosted hydrothermal vents characterized by their unique fluid chemistry rich in H_2, CH_4 and abiotic hydrocarbons (e.g., Charlou et al., 2013).

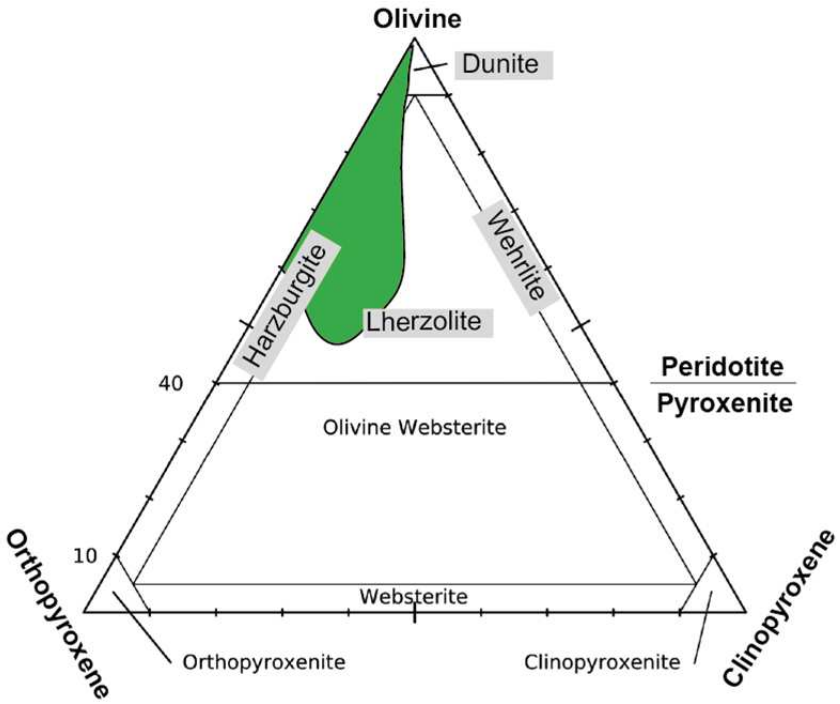

Fig.2.1. Modal composition of peridotite and pyroxenite plotted on the olivine-orthopyroxene-clinopyroxene diagram. The green area encompasses the most common compositions of orogenic, ophiolitic and abyssal peridotites on the mantle lithosphere (modified from Bodinier and Godard (2004).

1.1 Serpentine minerals and their stability

Serpentine minerals are the hydrated form of olivine (and also in a lesser extent both pyroxenes). They are trioctahedral 1:1 layer silicates. They consist of alternating infinite sheets of 4-coordinated Si and 6-coordinated Mg. The three dominated species are lizardite, chrysotile and antigorite (Fig.2.2). The general formula of serpentines is $Mg_3Si_2O_5(OH)_4$. Substitution of Al and Fe^{3+} for Si may occur in tetrahedral sites, and that of Fe^{2+},Fe^{3+},Cr, Al, Ni and Mn for Mg in octahedral sites. The main serpentine minerals are distinguished by their crystal structure. Lizardite consists of planar layers while chrysotile consists of scrolled layers which tend to form cylinder (Fig.2.2a-b). However, antigorite possesses a modulated structure in which the 1:1 layer could reverse itself (O'Hanley, 1996) (Fig.2.2c).

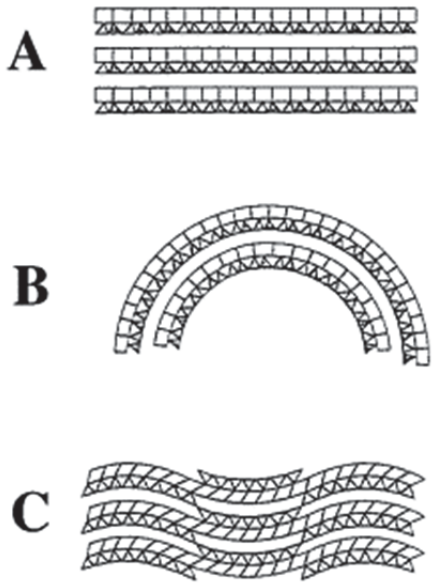

Fig.2.2. Sketch of crystallographic structures of serpentine minerals: (A) lizardite (B) chrysotile (C) antigorite (From Mével, 2003).

Serpentine minerals are stable over a wide range of temperatures (25 to 700°C). Chrysotile and lizardite are stable at temperatures lower than antigorite (Evans et al., 1976; Moody, 1976) (Fig.2.3). Antigorite is the serpentine species stable at high temperatures (up to 500°C) (Evans et al., 1976). O'Hanley (1996) constructed on the basis of thermodynamic data a phase diagram that shows the sequence antigorite>chrysotile>lizardite with decreasing temperature (Fig.2.3). Forsterite, the Mg-endmember of olivine (Mg_2SiO_4), is stable down to 350°C (Fig.2.3).

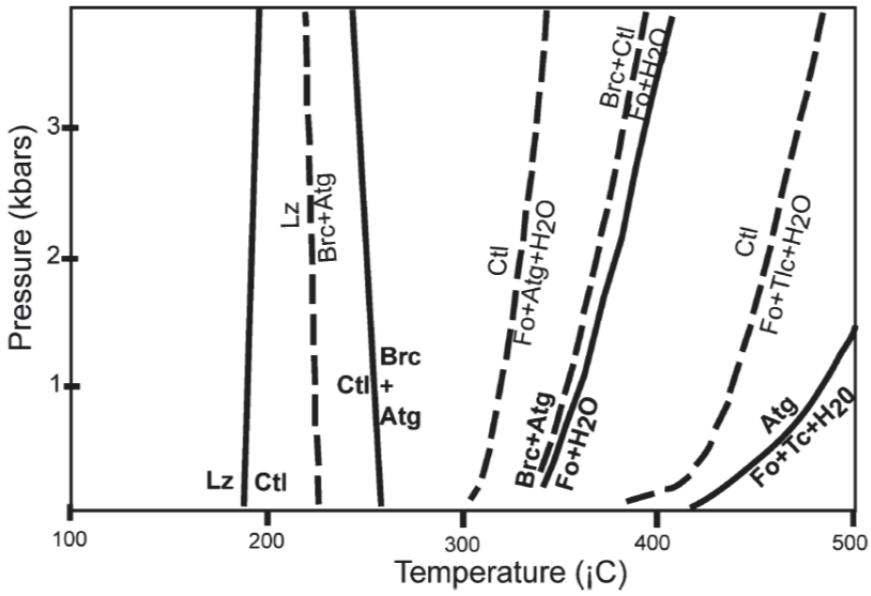

Fig.2.3. Temperature-pressure diagram of the MgO-SiO_2-H_2O system from Mével (2003). The phase diagram shows the phase relationships of serpentine species and related minerals. The continuous lines represent stable reaction curves and dashed lines represent metastable reaction curves. Atg: Antigorite; Ctl: Chrysotile; Lz : Lizardite ; Brc: Brucite; Fo: Forsterite; Tlc: Talc.

Serpentine replacing olivine is typically devoid of aluminium and chromium but contains some nickel, matching the composition of olivine (Mével et al., 2003). The amount of Fe in the serpentine is controlled by the degree of serpentinization (Andreani et al., 2013, Stamoudi,2002). Fe in serpentine globally decreases when the local degree of serpentinization increases and Fe is incorporated into the magnetite (Andreani et al., 2013). Thus the amount of Fe in serpentinites varies with the abundance of associated magnetite which reflects oxidizing conditions.

1.2 Serpentine formation and associated chemical reactions

The hydration of the ultramafic rocks encompasses a suite of reactions that are related to the mineralogical composition of the initial rock (olivine, orthopyroxene and clinopyroxene). These reactions may take place over a wide-range of temperatures and are slightly dependent on pressure. Serpentinization takes place when water reacts with the peridotite minerals. However, when the water contains dissolved CO_2 carbonates can be produced and carbonation reactions are produced. This section describes the chemical reactions produced by the reaction of olivine and pyroxenes with pure water and CO_2-rich solutions.

Serpentinization reactions

Serpentine and ***brucite*** result from the hydration of olivine at low temperatures (<400°C) (Mével, 2002) (R2). Brucite ($Mg(OH)_2$) is an Mg-hydroxide occasionally found in natural serpentinites (Bach et al., 2004) and commonly observed in the endproduct of serpentinization experiments (e.g., Lafay et al., 2012). When iron is present in the olivine, Fe can substantially incorporate in serpentine and brucite resulting in ferroan serpentine and brucite as is described in reaction (R1).

$$2\ Mg_2SiO_4 + 3\ H_2O \rightarrow Mg_3Si_2O_5(OH)_4 + Mg(OH)_2 \quad \text{(R2)}$$

Olivine + water = serpentine + brucite

Talc ($Mg_3SiO_2O_5(OH)_4$) is commonly associated with the alteration of orthopyroxene (Mével, 2003). Its formation is mainly controlled by silica activity in the fluid phase (Tutolo et al., 2018; Syverson et al., 2017). Orthopyroxene will completely react with excess fluids to form talc and olivine at temperatures less than 650°C at 1 kbar (Iyer et al., 2008) (R3).

$$5\ MgSiO_3 + H_2O \rightarrow Mg_2SiO_4 + Mg_3Si_2O_5(OH)_4 \quad \text{(R3)}$$

Orthopyroxene + water = olivine + talc

Magnetite *(Fe_3O_4)* is another accessory mineral commonly formed during serpentinization of ultramafic minerals (R1). A common characteristic of natural serpentinites is the exponential increase of modal magnetite content as a function of serpentinization degree in bulk rock (Bach et al., 2006; Oufi et al., 2002; Toft et al., 1990). Magnetite is associated to redox (reduction-oxidation) reactions and hydrogen production (H_2) (Bach et al., 2004; Evans, 2008). A redox reaction is a type of chemical reaction that involves a transfer of electrons between two species. Oxidation reactions involve the loss of an electron, whereas reduction reactions involve the gain of an electron. Redox reactions leads to the generation of hydrogen during serpentinization from the oxidation of ferrous iron (Fe^{2+}) present in olivine and pyroxenes to ferric iron (Fe^{3+}) in magnetite through reaction with water, thus the hydrogen of the water is reduced into (H_2), as shown in equation (R4):

$$2FeO + H_2O \rightarrow Fe_2O_3 + H_{2(aq)} \quad \text{(R4)}$$

Iron + water = magnetite + hydrogen

The precipitation of magnetite confers highly reducing conditions that native metals (Cu) and alloys (e.g., Ni-Fe alloys (Frost, 1985)) to be stable (e.g., Horita and Berndt. 1999; Foustoukos and Seyfried. 2004; Klein and Bach. 2009; Klein et al., 2015b; McCollom and Seewald. 2001).

Magnetite was thought to be the sole Fe^{3+}-bearer during H_2 production notably because the valence of iron in serpentine minerals and its relationship with both magnetite abundance and serpentinization degree are usually not determined. However, the generation of H_2 is not exclusively related to the production of magnetite. Experiments and thermodynamics models show that serpentine can accommodate both divalent and trivalent iron in their structure (Beard et al., 2009; Klein et al., 2009; Seyfried et al., 2007; Wicks and Whittaker, 1975), which contributes to the generation of hydrogen (Andreani et al., 2013; Marcaillou et al., 2011; Seyfried et al., 2007). Fe^{3+} in serpentine can account for the entire production of H_2 at low temperatures, where magnetite formation is limited (Klein et al., 2014; Mayhew et al., 2013). The typical reaction to produce H_2 after Fe-olivine hydrolysis is (Klein et al., 2014):

$$(Mg,Fe)_2SiO_4 + aH_2O \rightarrow 0.5(Mg,Fe^{2+},Fe^{3+})(Si,Fe^{3+})_2O_5(OH)_4 + b(Mg,Fe)(OH)_2 + cFe_3O_4 + dH_2 \quad (R5)$$

Olivine + water = Serpentine + Brucite + Magnetite

The mineral composition of the peridotite has an influence on the H_2 generation. Therefore, serpentinization of olivine-rich lithologies produces more ferric iron in secondary minerals (mainly magnetite) and thus more $H_{2(aq)}$ compared to serpentinization of pyroxene-rich lithologies where the generation of $H_{2(aq)}$ comes from the incorporation of ferric iron in serpentine rather than magnetite (Klein et al., 2013).

Carbonation reactions

Carbonates are associated to serpentines only when CO_2 is dissolved in the fluid. The hydration of peridotites bring out high amounts of divalent cations (Mg^{2+}, Ca^{2+} and Fe^{2+}) in solution. The interaction of divalent cations and carbonate ions induce the precipitation of carbonates such as magnesite ($MgCO_3$), calcite ($CaCO_3$) and dolomite $(Ca,Mg)CO_3$ that provide a long term storage for CO_2 (Garcia et al., 2010; Kelemen et al., 2011; Matter and Kelemen, 2009; Oelkers et al., 2008; Seifritz, 1990; Xu et al., 2004).

In a pure magnesian system, Mg-olivine reacts with water and the dissolved CO_2 to produce serpentine and magnesite (R6). However, when the stoichiometric relation of CO_2/H_2O is 5 for 4 moles of forsterite, talc is formed instead of serpentine (R7) (Kelemen et al., 2011). In an anhydrous system, forsterite react with CO_2 to produce quartz and magnesite (R8) (Kelemen et al., 2011). The reaction of olivine and (Ca-Mg) pyroxene with water and CO_2 produces serpentine, calcite and magnesite (R9) (Kelemen et al., 2011).

$$4\ Mg_2SiO_4 + 4\ H_2O + 2\ CO_2 = 2\ Mg_3Si_2O_5(OH)_4 + 2\ MgCO_3 \quad (R6)$$

Forsterite + water = Serpentine + Magnesite

$$4\ Mg_2SiO_4 + H_2O + 5\ CO_2 = Mg_3Si_4O_{10}(OH)_2 + 5\ MgCO_3 \quad (R7)$$

Forsterite + water = Talc + Magnesite

$$4\ Mg_2SiO_4 + 8\ CO_2 = 4\ SiO_2 + 8\ MgCO_3 \quad (R8)$$

Forsterite = Quartz + Magnesite

$$Mg_2SiO_4 + CaMgSi_2O_6 + 2\ CO_2 + 2\ H_2O = Mg_3Si_2O_5(OH)_4 + CaCO_3 + MgCO_3 \quad (R9)$$

Mg-olivine + CaMg-pyroxene = Serpentine + Calcite + Magnesite

Finally, in a later stage the hydrated phases (serpentine and talc) could also react with CO_2 to form carbonates (magnesite) and quartz (R10) and (R11) (Kelemen et al., 2011).

$$Mg_3Si_2O_5(OH)_4 + 3\ CO_2 = 2\ SiO_2 + 2\ H_2O + 3\ MgCO_3 \quad (R10)$$

Serpentine = Quartz + Magnesite

$$Mg_3Si_4O_{10}(OH)_2 + 3\ CO_2 = 4\ SiO_2 + H_2O + 3\ MgCO_3 \quad (R11)$$

Talc = Quartz + Magnesite

All the reactions describe above are thermodynamic stable until 400°C and 30 MPa. Thermodynamic calculations show the stability field of magnesite increases when the CO_2 fraction increases (Fig.2.4). Under a pressure of 30 MPa carbonates such as magnesite could form until 400°C when the CO_2 fraction is high enough ($XCO_2 > 10^{-2}$) (Kelemen et al, 2011).

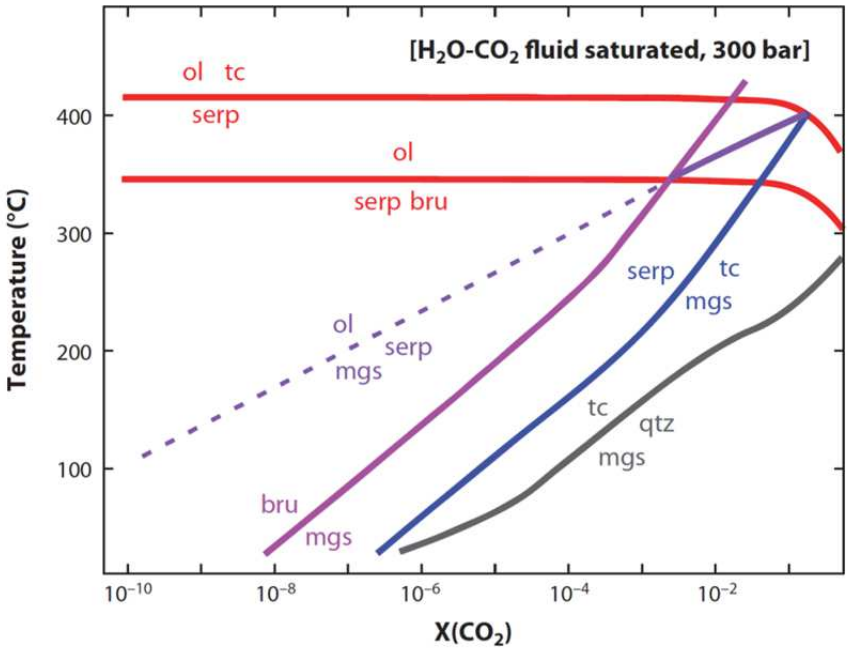

Fig.2.4. Phase diagram (Temperature versus CO_2 fraction) on the system H_2O-CO_2 at 30 MPa, for the hydration and carbonation reactions with olivine (ol), chrysotile (serp) , talc (tc), quartz (qtz), brucite (bru) and magnesite (mgs) on the system MgO-SiO_2-H_2O-CO_2 (Kelemen et al, 2011).

1.3 Consequences of serpentinization on physical properties of peridotites

Serpentinization is an exothermic process (e.g., MacDonald and Fyfe, 1985; Lowell and Rona, 2002) which means that heat is produced during the replacement of olivine and pyroxenes into serpentine. The amount of heat released from complete serpentinization of 1 kg of peridotite is 250 Joules, this means an increase of 50°C of 1 L of water. In addition to the release of heat and the modification of the rock and the fluid composition another important effects of serpentinization is the ***change in density*** of the pristine ultramafic rocks. The average densities of unaltered peridotite and serpentine are approximately 3.3 g/cm^3 and 2.5 g/cm^3 respectively Mével (2003). The density of serpentinized rock is inversely proportional to the amount of serpentinization (Fig.2.5a). The decrease in density of serpentinized ultramafic rocks also influences the ***seismic velocity*** (Fig.2.5b). Seismic velocities measured in serpentinites show a strong inverse dependence on the amount of serpentinization (Miller and Christensen, 1997). The replacement of olivine grains by an isotropic network of serpentine (i.e., increase the serpentinization degree) results in the

decrease of anisotropy of P- and S-waves, as shown in the figure 2.5 (Horen et al., 1996; Mével, 2003).

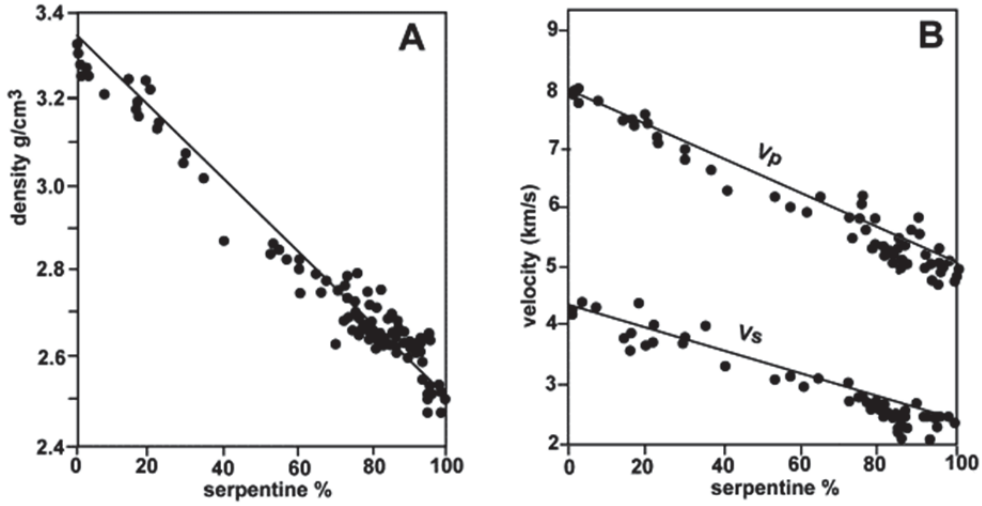

Fig.2.5. (A) compilation of densities and (B) seismic velocities measured on ocean floor serpentinites as a function of the degree of serpentinization (Mével, 2003).

Complete serpentinization of olivine results in a water uptake of 13% by weight and a ***volume increase*** of around 40% (e.g., Coleman, 1971; Schroeder et al., 2002; Shervais et al., 2005). Thus, serpentinization tends to reduce porosity and permeability and inhibit fluid circulation. Serpentinization reactions will tend to be a self-limiting process; however, ocean hydrothermal systems hosted in extensively serpentinized ultramafic rocks remains active for thousands of years (Früh-Green et al., 2003). This suggests accessibility of water to unreacted olivine and pyroxenes grains is required to maintain the serpentinization reaction (e.g., Malvoisin and Brunet, 2014; Farough et al., 2016). Several studies has been done in this direction and suggest that the precipitation of low density serpentine minerals creates local gradients in pressure around growing crystals, and thus a differential stress that generates cracks which provides fluid access to unreacted olivine and pyroxene grains, this is the so called *reaction-driven cracking theory* (Kelemen and Hirth, 2012). Therefore, a connected network of cracks with apertures exceeding that of the olivine grain boundary appears as a way to enhance water transport within oceanic peridotites bodies (e.g., Plümper et al., 2012). Hence, hydrodynamic conditions in these systems are of special relevance to understand the progression of the serpentinization reaction.

Changes on porosity and permeability also influence the ***rheology*** of the rock. This has important implications for tectonic activity occurring within oceanic lithosphere. The presence of small amounts of serpentine reduces the strength of un-altered peridotite (Escartin et al., 1997a,b; Escartin et al., 2001). Serpentine carries nondilatant brittle deformation while olivine remains undeformed (Escartin et al., 2001). A transition from brittle to ductile deformation occurs as the confining pressure increase from ~200 to ~400 MPa and corresponds to change in deformation mechanism from brittle faulting to ductile (Escartín et al., 1997a). Deformation in both regimes is accommodated by shear microcracks. In the brittle regime, the strain localizes on a single fault formed at high angles (30-45°) to the shortening direction while in the ductile regime, numerous shear zones that are homogeneously distributed throughout the sample accommodate small amounts of strain (Escartín et al., 1997a). The low internal friction coefficient of serpentine (μ~0.3, dimensionless scalar) can significantly reduce the optimal fault angle of large-displacement faults and increase the displacement along low-angle detachment faults providing paths for fluid infiltration at the end segments of slow- spreading ridges (Escartín et al., 1997b). Formation of serpentine along these fault planes would also enhance strain localization (Escartín et al., 1997b; Escartín et al., 2001). The changes in rheology accompanying serpentinization can thus influence the tectonics of the oceanic lithosphere due to weakening and promote formation of fault structures and strain localization within them.

Serpentinization of ultramafic rocks produces magnetite due to the oxidation of the iron component present in olivine and pyroxene (see R1). This strongly affects the ***magnetic properties*** of the rocks (e.g., Oufi et al., 2002). The magnetic susceptibility and ferromagnetic behavior of peridotites increase with increasing amounts of serpentinization due to production of magnetite and is linearly related to the amount of magnetite (Oufi et al., 2002). High degrees of serpentinization also result in an increase in natural remnant magnetization which can contribute to oceanic magnetic anomalies (Dyment et al., 1997). Study of Bach et al.(2006) shows that the increase in magnetic susceptibility with the degree of serpentinization is not linear. During incipient stages of serpentinization (<60-70% conversion), the iron partioning from the breakdown of olivine and orthopyroxene into Fe-rich serpentine (up to 6% FeO) and Fe-rich brucite results in a lower magnetite proportion in the serpentinized rock (Bach et al., 2006). However, during progressive stages of reaction (>70%) Fe-rich serpentine and Fe-rich brucite are destabilized, and forms Fe-poor serpentine and Fe-poor brucite (2-3% FeO; Oufi et al., 2002) and so magnetite become enriched in Fe.

In some environments, the breakdown of orthopyroxene, during the later stages of serpentinization, strongly affects the composition of the reacting fluid (Bach et al., 2006). The high silica activities results in the breakdown of ferroan brucite to form serpentine and magnetite (Tutolo et al., 2018). Serpentinized peridotites could attain high values of natural remnant magnetization due to the presence of small magnetite grains associated with mesh-textured serpentine (Oufi et al., 2002).

2. Serpentinization in natural systems

Serpentinization processes are often observed in a variety of tectonic environments where the mantle peridotite is exposed to the interaction with fluids. Serpentinization occurs mainly along mid-ocean ridges where circulating hydrothermal fluids interact with ultramafic rocks exposed by seafloor spreading (Cannat et al., 2010; Mével et al., 2003); and along broad areas along subduction zones (e.g., Deschamps et al., 2013). Additionally, ongoing serpentinization has been observed on continental settings hosted by ophiolite complex (e.g., Barnes and O'Neil, 1969; Neal and Stanger, 1985). The various settings in which serpentinites occur are briefly detailed below.

2.1 Ocean floor serpentinization

Over the last four decades, more than 500 sites of seafloor hydrothermal venting have been identified in a range of tectonic settings; in divergent margins such as: mid-ocean ridge detachment faults and convergent margins such as: subduction zones (back-arc basins and island arc volcanoes) (e.g., German and Seyfried, 2003; Humphris and Klein, 2018). The hydrothermal vents represent the seafloor manifestation of seawater circulation through the oceanic basement (e.g., Schroeder et al., 2002) and are generated in regions of high heat flow. As seawater penetrates into and flows through hot and permeable rocks, a variety of chemical reactions take place that alter the composition of both the circulating seawater and surrounding rock. The seawater can reach maximum temperatures of 400°C (German and Seyfried, 2003). At these temperatures, the fluids become buoyant and rise rapidly back to the seafloor where they are expelled into the overlying water column. Seafloor hydrothermal circulation plays a significant role in the cycling of energy and mass between the solid earth and the oceans (e.g., Humphris and Thompson 1978a,b; Mottl, 1983, Alt, 1995, Elderfield

and Schultz, 1996, Mottl, 2003, Jarrard, 2003, Kodolanyi et al. 2012). Furthermore, the interaction of seawater with the oceanic basement triggers complex reactions (i.e., *serpentinization*) that generate volatiles such as H_2, CO_2, and CH_4. The release of those volatiles in the vent fluids can serve as energy sources for microbial ecosystems that develop around the hydrothermal vents (e.g., Charlou et al., 2002, Früh-Green et al., 2004).

Divergent margins: Mid-ocean ridges

Hydrothermal circulation occurs predominantly along the global mid-ocean ridge (MOR) crest, a near-continuous volcanic chain that extends over ~60,000 km (German and Seyfried, 2003). The MOR accounts for 73% of Earth's volcanic activity (Perfit and Davidson, 2000) (Fig.2.6). The first sites of hydrothermal venting to be discovered were located along intermediate to fast spreading ridges (e.g., at the Galapagos spreading centre in the eastern equatorial Pacific in 1977 (Edmond et al., 1979)). Several authors propose that the faster the spreading rate the more abundant the hydrothermal activity (Charlou et al., 1996; Von Damm et al., 2003). The incidence of hydrothermal venting along the ridge crest should be correlated positively with spreading rate because the latter is intrinsically linked to the magmatic heat flux (Baker et al., 1996).

However, along some of the slow (e.g., Mid-Atlantic ridge) and ultraslow (e.g., Southwest Indian ridge) spreading sections of the global ridge crest (Früh-Green et al., 2003; Kelley et al., 2001) (Bach et al., 2002; German et al., 1998) hydrothermal vents has also been found providing support for models of hydrothermal activity involving more than just magmatic activity (German and Lin, 2004). Hence, the influence of tectonic effects imposed by detachment faulting plays and important role, providing permeability that allows seawater-derived hydrothermal fluids to penetrate deeply and mine heat from the lower crust and upper mantle before venting at sites distant from the heat source. Consequences of these low-angle detachment fault zones are the formation of corrugated massifs (commonly called oceanic core-complex), resulting from the uplift and exposure of lower crustal and upper mantle rocks on the ocean floor. The extensive faulting and fracturing associated with this uplift as well as the latent heat of the rock promotes fluid circulation that can result in extensive *serpentinization* of the mafic and ultramafic rocks (Schroeder et al., 2002; Mével, 2003).

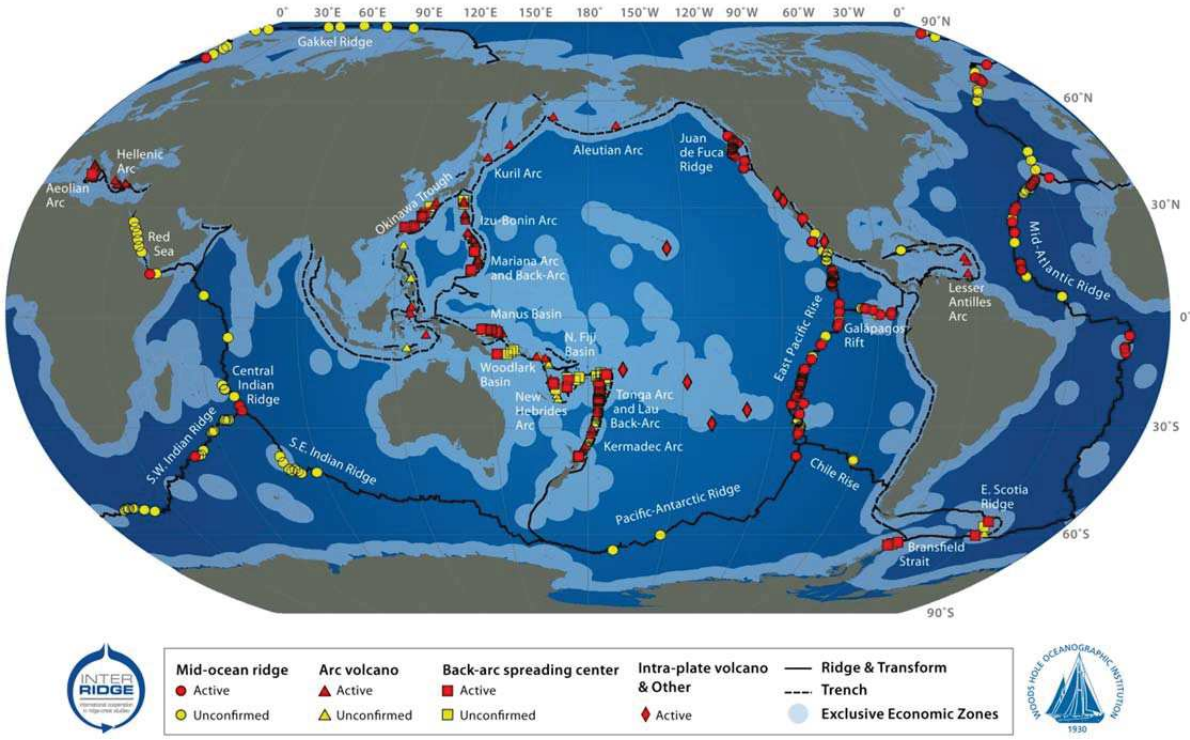

Fig.2.6. Global distribution of hydrothermal vent fields along mid-ocean ridges. Active hydrothermal vents (red symbols) and unconfirmed (yellow symbols). (http://www.interridge.org/irvents/).

The hydrothermal vents have been exhaustively studied depending on the hosted rock (mafic or ultramafic). They show that the composition of the emanating fluids is different depending on the hosted rock; this indicates different reaction paths during fluid-rock interactions. The composition of hydrothermal vent fluids are of interest because: (1) it influences and controls ocean chemistry (Elderfield and Schultz, 1996, Mottl, 2003), (2) it provides an integrated record of the reactions and the pressure and temperature conditions that these fluids have experienced during their transit through the oceanic floor (Von Damm, 1995; Seyfried et al., 2015) (3) it suggests information on the residence time of fluids within the oceanic rocks at certain temperatures and (4) it provide energy sources for microbial communities (Charlou et al., 2002; Früh-Green et al., 2004).

In this chapter the high and low temperature hydrothermal systems hosted on ultramafic rocks are described, but for studies performed on hydrothermal systems hosted on mafic rocks, the reader could be addressed to: e.g., Charlou et al. (1996), Chiba et al. (2001), Butterfield et al. (1994), Von Damm et al. (2005).

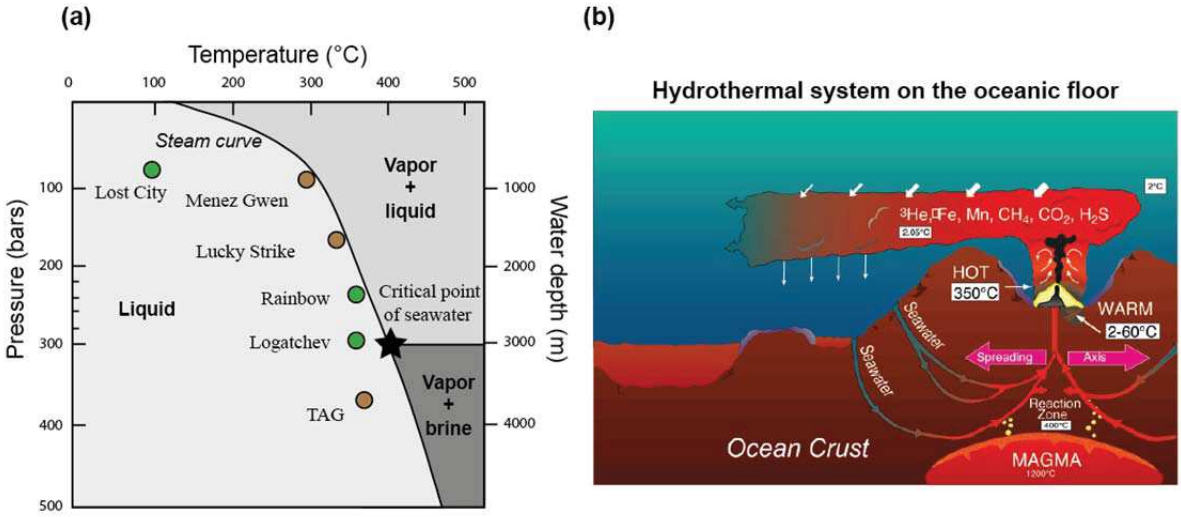

Fig.2.7. (a) Hydrothermal systems hosted on ultramafic rocks (green circle) and hosted on mafic rocks (brown circle) plot on the liquid phase region (redrawn from Kelley and Shank, 2010). (b) Sketch of hydrothermal system on the oceanic floor (from Schmidt ocean institute). Circulation of seawater occurs within the oceanic crust at a mid-ocean ridge. The seawater percolate on the ocean crust by permeable zones (e.g., fractures) then is heated as it undergoes chemical modification due to their interaction with the adjacent rocks. When the fluids reach temperatures of 400°C, they become buoyant, rise until the surface and exit the seafloor, forming a hydrothermal vent. These plumes are a sink for gases and metals.

Rainbow hydrothermal vent field on the Mid-Atlantic Ridge is an example of high temperature ultramafic hosted hydrothermal systems. It is located at a water depth of 2300 m on the western flank of the Rainbow Massif (Douville et al., 2002). Chimneys vents at high temperatures (up to 367°C) are hosted in serpentinized peridotites; however there are proximal basaltic rocks at 1 km of the vent field (Fouquet et al., 1997). Fluids emanating from the discharged vents are slightly acid, phase separated, depleted in dissolved Mg and SO_4 but enriched in Ca (Fig.2.8). Seyfried et al. (2015) suggest the highest amount of Ca in the fluid came from the dissolution of tremolite from the hosted rocks. Vent fluids display very high concentrations of dissolved H_2, CH_4 and other organic species (Charlou et al., 2002). They contain the highest dissolved Fe concentrations of any vent fluid yet studied in the ocean (German and Seyfried, 2014). However, $SiO_{2(aq)}$ concentrations are significantly lower than those in mafic-hosted hydrothermal systems (e.g., ~6 mM compared to ~16 mM in Lucky Strike a mafic-hosted vent) (Fig.2.8). The high temperature of the venting fluids triggers phase separation of the fluids that led high Cl contents of the brine. This evidence

together with the high temperatures and the acidity of the fluids, enhance the solubility of transition metals and rare earth elements leached from the predominantly peridotite host rock (Douville et al., 2002).

Other examples of high temperature hydrothermal vents hosted on ultramafic basements are Logatchev and Nibelungen fields located also at the Mid-Atlantic Ridge (Schmidt et al., 2007; Schmidt et al., 2011). They are characterized by high temperature venting fluids at ~350-372°C. They display similar fluid elemental concentrations like Rainbow but a mafic-hosted hydrothermal signature related to their respective B and Li concentrations.

*The **Lost City hydrothermal vent field*** is located at 15 km west of the Mid-Atlantic Ridge axis and represents a different type of hydrothermal activity related to moderately low fluid temperatures associated to an ultramafic hosted hydrothermal system. The hydrothermal field is emplaced in a tectonically uplift section where detachment faults exhumed oceanic rocks characterized by >70% peridotite and <30% gabbro (Kelley et al., 2001). The peridotites are highly serpentinized (70-100%) with primary olivine and orthopyroxene replaced by serpentine and magnetite with minor chlorite, amphibole, and talc (Boschi et al., 2008).

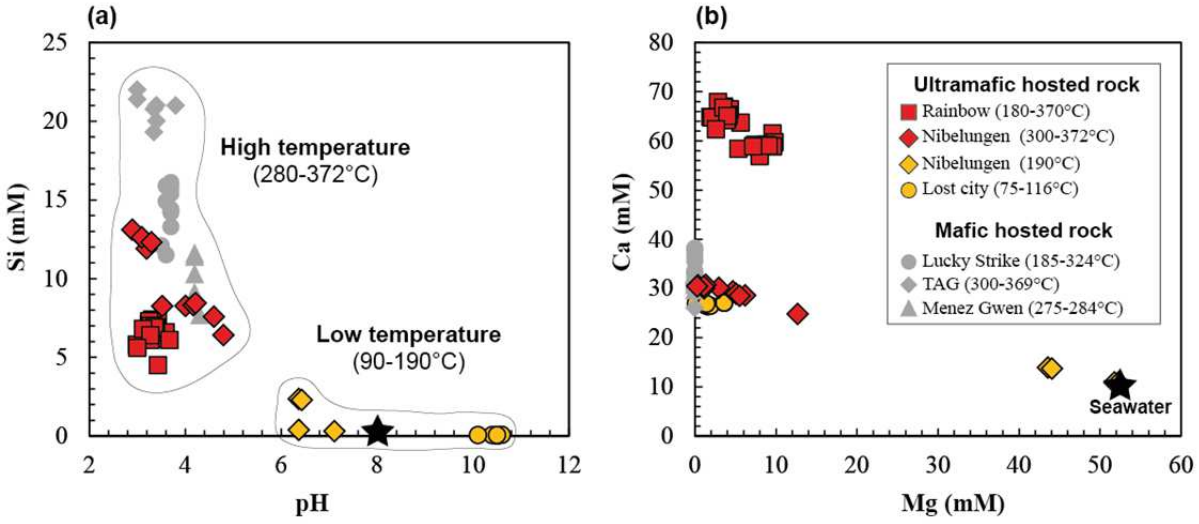

Fig.2.8. Compilation of the chemistry composition of hydrothermal vent fluids from ultramafic hosted rock and mafic hosted rock. (a) Si vs pH. High temperature venting fluids shows an increase on the Si concentrations and a decrease on the pH. (b) Ca vs Mg. All fluids show depletion on Mg and increase on Ca compared to seawater concentrations. Rainbow show the highest concentration in Ca compared

to the other hydrothermal vent fluids. The concentrations are in mili-mols (mM).Ultramafic hosted rock: Rainbow (Seyfried et al., 2011); Nibelungen (Schmidt et al (2011); Lost City (Seyfried et al (2015). Mafic hosted rock: Lucky Strike (Charlou et al (2000)); TAG (Chiba et al (2001)); Menez Gwen (Charlou et al (2000)).

Table.2.1. Fluid compositions of vent fluid from mid-ocean ridge hydrothermal systems host on ultramafic-hosted and mafic-hosted rocks. Seawater was compiled from Seyfried et al (2015). The fluid composition from ultramafic hosted systems correspond to: Rainbow vent (Stylo 1 – 354-CGT-B) (Seyfried et al., 2011); Logatchev from Schmidt et al (2007); Nibelungen vent Drachenschlund (314-ROV-2) from Schmidt et al (2011). Lost city vent BH (J2-360-IGT2) from Seyfried et al (2015). The composition from mafic hosted systems correspond to: Lucky Strike vent MrK US 4 from Charlou et al (2000); Menez Gwen vent Mogued Gwen from Charlou et al (2000); TAG from Chiba et al (2001). Values are in mM (mmol/L) and µM (µmol/L).

	Seawater	**Ultramafic hosted**				**Mafic hosted**		
		Rainbow	Logatchev	Nibelungen	Lost City	Lucky Strike	Menez Gwen	TAG
Depth (m)		2300	3000	3000	750	1700	850	3600
Max. T (°C)	2	367	350	372	116	310	281	360
pH (25°C)	8	3.39	3.9	3.1	10.4	3.7	4.2	3.35
Cl (mM)	554	750	551	567	542	433	381	636
SO_4 (mM)	28.7	2.01	1.3	(-)	4.12	(-)	(-)	(-)
Na (mM)	475	560	455	448	491	357	317	557
Si (mM)	0.025	6.8	8.6	12.6	0.068	16.1	11.6	20.75
Mg (mM)	53.3	3.92	0	4.69	1.9	0	0	0
K (mM)	10.3	(-)	24	17.9	10.5	21.9	23.8	(-)
Ca (mM)	10.4	64.2	29	29.4	26.5	33.2	30.8	30.8
Fe (µM)	0	20200	2410	4750	1.2	282	24.1	5590
Al (µm)	(-)	6.14	12	(-)	(-)	(-)	(-)	(-)
Sr (µM)	92	174	127	84.8	101	77	101	(-)
Li (µM)	24	(-)	252	313	44	287	270	(-)
Rb (µM)	1.4	35.8	27	17.7	2.8	22.7	26.4	(-)
Cs (µM)	<0.01	(-)	343	0.2	0.2	0.167	0.285	(-)
Mn (µM)	<0.001	0.017	338	(-)	(-)	303	64	(-)
Cu (µM)	<0.1	182	44	47	(-)	7.6	2.9	(-)
Zn (µM)	<0.01	123	36	(-)	(-)	30	5.1	(-)
Pb (nM)	<0.01	(-)	0.13	(-)	(-)	(-)	(-)	(-)
CH_4 (mM)	0	(-)	3.5	(-)	1.32	0.3	1.35	(-)
H_2 (mM)	0	14.8	19	(-)	11.5	0.725	0.462	(-)
CO_2 (mM)	2.3	26	(-)	(-)	(-)	21.1	22.5	(-)
H_2S (mM)	(-)	2.3	2.5	0.1	(-)	3	1.5	2.5

The measured temperature venting fluids range from 28-116°C (Seyfried et al., 2015). The heat source required to drive hydrothermal circulation at Lost City is likely derived from cooling of the rocks and lesser contributions from exothermic serpentinization reactions (Früh-Green et al., 2003; Kelley et al., 2005). The isotopic composition of fluids venting at

this location is consistent with formation from exothermic serpentinization at temperatures 110-150°C (Früh-Green et al., 2003). The fluids exhibit very high pH, high Ca content relative to seawater and low dissolved metals H_2S contents (Früh-Green et al., 2003; Seyfried et al., 2015) (Fig.2.8, Table 2.1). The vent fluids are characterized by low concentrations in Mg relative to seawater concentrations (Table 2.1).

The Lost City fluids are also highly enriched in CH_4 and H_2, similarly to the Rainbow high-temperature fluids, but they are depleted in CO_2 compared to Rainbow fluids (Kelley et al., 2001; Proskurowski et al., 2006). The high H_2 contents result from olivine hydrolysis, with buffering provided by Fe-bearing serpentine and magnetite (e.g., Frost and Beard 2007;; Klein et al., 2009, 2013; Seyfried et al., 2007, 2015). The high CH_4 concentrations show evidence of an abiogenic origin in the deep subsurface (Proskurowski et al., 2008). A particularity of this environments is the carbonate towers (up to 60 m) constituted by aragonite and brucite that results from the mixing of the discharging high-pH and Ca-rich hydrothermal fluids with seawater.

Convergent margins: Subduction zones

Serpentinization of the mantle wedge at active convergent margins could occur due to the reaction with fluids released by the subducting slab (e.g., Deschamps et al., 2013 and references therein) (Fig.2.9). The fluid is liberated by metamorphic devolatilization in subducting lithosphere and carries solutes as it migrates into the overlying mantle wedge, resulting in chemical modification or metasomatism of both slab and mantle wedge (Manning et al., 2004). Water released from the slab percolate upward by buoyancy and induces the hydration of the mantle wedge and its serpentinization when its temperature is lower than 600 °C which corresponds to the stability field of antigorite (high-T serpentine). Evidences of this process are well recognized today in the Mariana subduction zone with the formation of serpentinite seamounts in fore-arc position (Fryer, 2002). The seamounts are described as mud volcanoes (<10 to 30 km wide) consisting of serpentine fragments in a serpentine mud (O'Hanley, 1996).

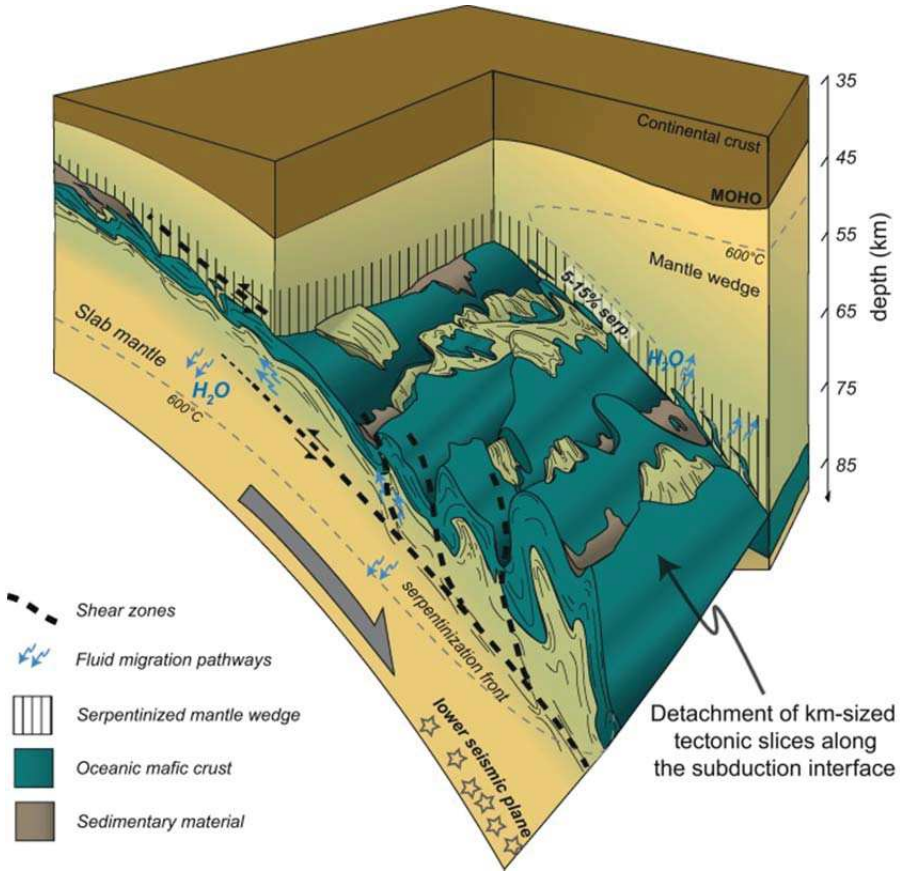

Fig.2.9. Ongoing serpentinization on the mantle wedge in subduction zones (Angiboust et al., 2012).

2.2 On land serpentinization

Ophiolites

Ophiolites represent sections of ocean crust and upper mantle that have been thrusted onto the continents by tectonic forces (Bodinier and Godard, 2003). More than 70 ophiolitic complexes have been described throughout the world; few examples correspond to: Internal Ligurides (northern Italy), Troodos (Cyprus), Semail (Sultanate of Oman), Xigaze (Tibet), Klamath Mountains (Trinity, CA) and bay of Islands (Newfoundland, Canada).

The ultramafic rocks (harzburgite, lherzolite and dunite) are overlain by a gabbroic complex, a mafic sheeted-dyke complex and a mafic-volcanic complex with pillow lava flow towards shallower levels (Penrose Field Conference, 1972). Sedimentary rocks are found at the uppermost levels of an ophiolite complex. The generally accepted mechanisms of ophiolite emplacement is thrusting of the fore-arc mantle over the accretionary wedge in a

forearc setting or thrusting over the passive margin or the arc in a back-arc setting (e.g. Laurent, 1980, Wirth and Bird, 1994, Nicolas and Boudier, 2003).

Serpentinization in ophiolites could have been already produced in the paleo-oceanic setting; for example formed from seawater as it is the case for Austro-alpine ophiolites and Oman complex (Früh-Green et al., 1990; Kelemen et al., 2011). But the actual ongoing serpentinization could be produced nowadays when ultramafic rocks are exposed to circulating groundwater for example in the Oman ophiolitic complex (Miller et al., 2016). Actual ongoing serpentinization in Oman is produced at low temperatures ~60°C (Barnes et al., 1978; Miller et al., 2016). Evidences are coming from the identification of hydrothermal settings with emanating gases (H_2, CH_4) abiogenic hydrocarbons and the presence of alkaline pH fluids (Monnin et al., 2014). Carbonate veins has also been observed as the result from the interaction of water and ultramafic rocks (Kelemen et al., 2011).

3. Serpentinization in experimental systems

Several experimental studies were interested on the serpentinization reaction over more than 30 years. They were focused on different aspects that establish the reaction. A first focus was on the rate and mechanism that trigger the ***dissolution of silicate minerals*** (e.g., Chen and Brantley, 2000; Giammar et al., 2005; Hänchen et al., 2006; Pokrovsky and Schott, 2000; Prigiobbe et al., 2009; Rosso and Rimstidt, 2000). A second focus was on the ***rate and the extent of the reaction*** (e.g., Martin and Fyfe, 1970; Okamoto et al, 2011; Lafay et al, 2012; Malvoisin et al, 2012a; Ogasawara et al, 2013). A third focus was on the ***evolution of the fluid chemistry*** during the reaction (e.g., Allen and Seyfried, 2003; Godard et al., 2013; Janecky and Seyfried, 1986; Luhmann et al., 2017; Normand et al, 2002; Seyfried and Dibble, 1980; Seyfried et al., 2007; Syverson et al., 2017; Tutolo et al., 2018). A fourth focus was on the ***production of H_2 and hydrocarbons*** which has revealed a peculiar attention since the 90' for their economic value and life production (e.g., Andreani et al., 2009; Berndt et al., 1996; Hövelmann et al., 2012; Huang et al., 2015; Huang et al., 2017; Jones et al., 2010; McCollom and Seewald., 2001; McCollom et al., 2016; Marcaillou et al., 2011). A fifth focus was on the ***CO_2-mineralization*** during the reaction due to their applicability on CO_2-storage (e.g., Andreani et al., 2009; King et al., 2010; Paukert, 2014; Peuble et al., 2015a,b). A sixth focus was on the ***permeability*** of serpentine-bearing rocks and its evolution during

serpentinization (e.g., Andreani et al., 2009; Farough et al., 2015; Godard et al., 2013; Hirose and Hayman., 2008; Luhmann et al., 2017).

All these aspects related to the serpentinization reaction mentioned above has been studied in close and open conditions using different experimental apparatus adapted for each individual study. The study of the different aspects leads to the identification of different parameters that control the serpentinization reaction such as: temperature, pressure, water/rock ratios, grain size, fluid-rock composition, alkaline and pH conditions and water supply.

In this section, I describe firstly the different experimental apparatus used for serpentinization experiments and then the parameters that control the serpentinization reaction studied in closed and open conditions.

3.1. Experimental apparatus

Batch reactors

Batch reactors are reaction vessels that are used to measure the rates of chemical reactions as a function of time or of species concentration (e.g., Chou and Wollast, 1985; Rimstidt and Dove, 1986) (Fig.2.10). Batch reactors are agitated or stirred tanks which are set up with all reactants either close or open to the atmosphere. These types of reactors follow the progress of reactions in which the chemistry changes with time due to the accumulation of reaction products. Measurements of mineral solubility and determination of coupled dissolution-precipitation rates can then be estimated using measurements of cation and anion concentrations. Batch reactor monitors the chemical reactions of small mineral volumes in large fluid volumes. The chemical reactions proceed until a chemical equilibrium is reached between the fluid and the rock. The chemical equilibrium indicates the net reaction rate is zero (products transform into reactants at the same rate as reactants transform into products).

A limitation related to the use of a batch reactor is that the progressive sampling of solution in the course of the experiment changes the proportion of mineral to fluid (i.e., water:rock ratio) so that the amount of mineral dissolution needed to produce a given change

in fluid composition gradually decreases as the experiment proceeds. Another limitation is that solid samples can only be recovered from batch apparatus at the end of the experiments. Only stacked-vessel autoclaves (Cole et al, 1992) allow time sampling of solids during the progression of the reaction. Different types of reactors have been produced such as, regular autoclave batch reactors, batch reactors with flexible reaction cell, batch micro-reactor and mixed flow-through reactors (Kaszuba et al, 2013 and references therein) (Fig.2.10). They all can proceed at elevated temperature (~400°C) and at specific partial pressure of CO_2 in order to characterize the reaction paths and equilibrium assemblages using single or polymineralic reactants in which dissolution and precipitation occurs simultaneously.

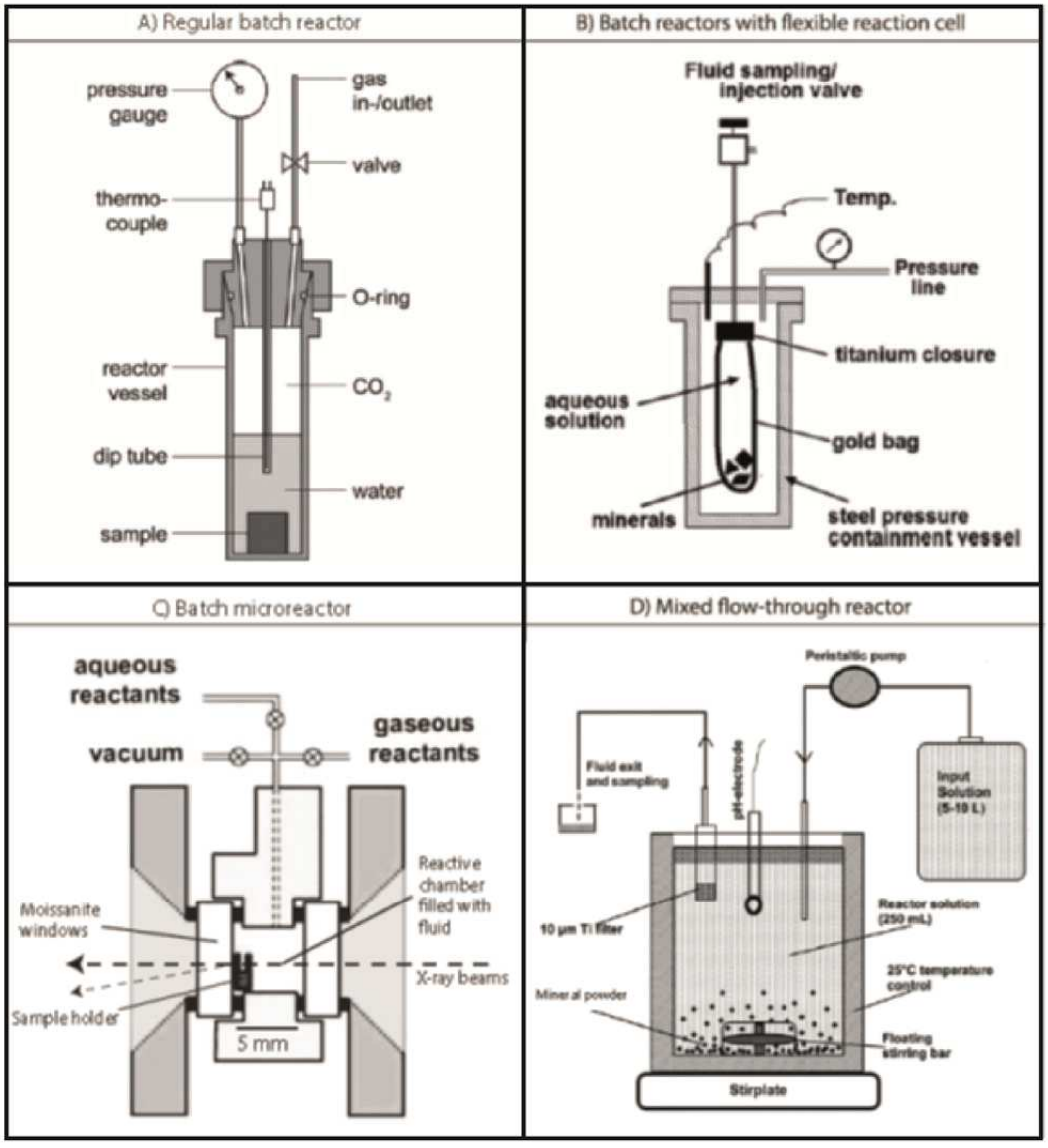

Fig.2.10. Batch reactors (Kaszuba et al., 2013). (a) Regular batch reactor (b)Batch reactor with flexible reaction cell (c) Batch microreactor (d) Mixed flow-through reactor.

Flow-through reactors

Flows through reactors are complex apparatus where the fluid is injected into the rock sample (held in a core holder) and collected at the exit point (Fig.2.11). A rock is a chemically and physically heterogeneous media in which the fluid flows and the chemical reactions may vary at macro and micrometric scales along those heterogeneities. Flow-through reactors are adequate to study the dynamics of a natural rock reservoir where a coupling between chemical reactions and hydrodynamics properties is expected. The composition of the injected fluid remains constant during the experimental time. However, the outlet fluid concentration varies until a certain time, where it reaches a constant value, the so-called steady-state. The steady-state is a chemical situation that indicates that all the state variables which define the behaviour of the system are constant in spite of ongoing processes that strive to change them (i.e., the thermodynamic properties may vary from one point to point but will remain unchanged at a given point) (Brantley et al., 2008).

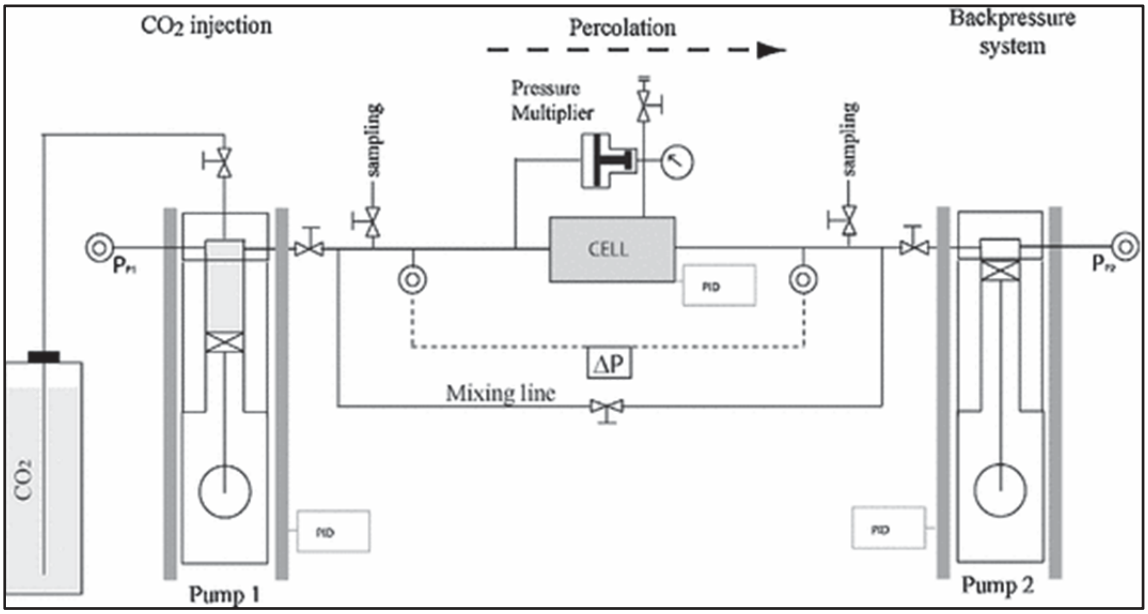

Fig.2.11. Flow through reactor ICARE 2.

This type of reactors allows to study the coupling between chemical reactions and hydrodynamic properties when fluid-rock interaction proceed in open systems (e.g., Andreani et al., 2009; Godard et al., 2013; Luquot and Gouze, 2009, Luhmann et al., 2017; Peuble et al., 2015). These reactors are a powerful tool to continuously record the permeability during the experiments using the Darcy's law. Fluid pressure at the outlet is adjusted to give pre-

determined constant flow rate, and the measured difference of pressure across the core (ΔP) is recorded during all the time-step sequences. The increases in the ΔP suggest clogging of the flow paths (e.g., mineral precipitation). The user or the reactor itself stops the experiment when the ΔP attains a certain security value.

A disadvantage of these reactors is the time that needs the reaction to proceed which is sometimes longer than the experiment time. In consequence sometimes the reaction products are very small to be measureable. This thesis will use a flow through reactor (ICARE 3 Lab) as experimental apparatus.

3.2 Serpentinization in closed systems

3.2.1 Silicate dissolution

Numerous studies dedicated to the measurement of the dissolution kinetics of olivine showed that this mineral is among the fastest dissolving silicates on Earth (Blum and Lasaga, 1988; Pokrovsky and Schott, 2000; Rosso and Rimstidt, 2000; Golubev et al., 2005; Hänchen et al., 2006; Wolff-Boenisch et al., 2011) and one of the main contributors to the release of cations (Mg, Si and Fe) in the (sea)-water (Gudbrandsson et al., 2011). The dissolution of olivine in aqueous solutions has been exhaustibly studied using the pure magnesium mineral forsterite (Mg_2SiO_4) and pure ferrous mineral fayalite (Fe_2SiO_4) to maximize the simplicity of the system (e.g., Rosso and Rimstidt, 2000; Crundwell, 2014). The overall reaction stoichiometry is given as follows (e.g., Pokrovsky and Schott, 2000):

$$Mg_2SiO_4 + 4H^+ \rightarrow 2Mg^{+2}{}_{(aq)} + Si(OH)_4{}_{(aq)} \qquad \text{(R12)}$$

Mineral dissolution involves the detachment of atoms from the mineral surface into the fluid solution. The forsterite structure consists of isolated silica tetrahedra that are branched together by magnesium octahedra chains (Birle et al., 1968) (Fig.2.12). The bonds between magnesium and oxygen are significantly weaker than the bonds between silicon and oxygen (Huggins and Sun, 1946) thus, Mg-oxygen bonds are most likely to break during the dissolution of forsterite.

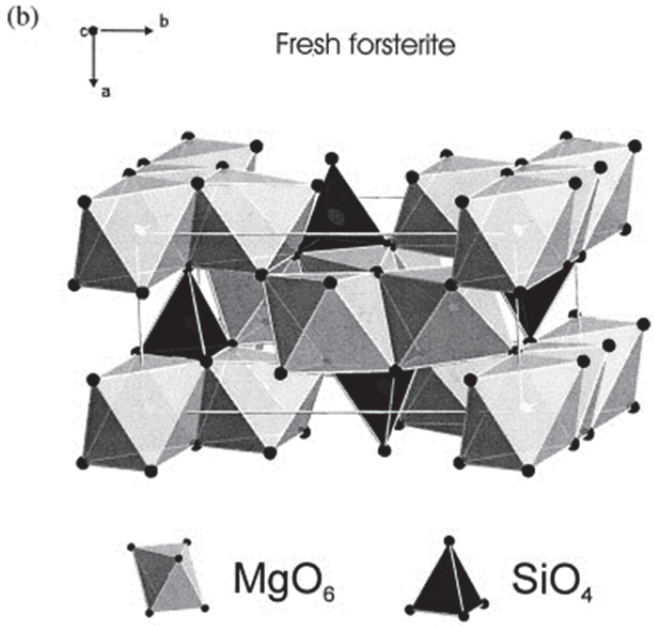

Fig.2.12. Forsterite crystallographic structure (Pokrosvsky and Schott, 2000a).

Congruent or incongruent dissolution?

Dissolution process is a response of a mineral and fluid assemblage to achieve a lower free energy state. The interaction of a mineral with water produces the dissolution of the mineral until the fluid reaches saturation, i.e. the ion activity product (IAP) in the solution is equal to the equilibrium solubility constant of the mineral (K_{sp}). One complication is that many minerals dissolve "incongruently" or non-stoichiometrically, which means that the measured elemental ion ratios in the solution are different from those in the solid phase, especially during the initial stage of dissolution process. This implies that the release of the mineral ions into the solution is produced at different rate.

Theoretical and experimental studies suggest an influence of the mineral structure on olivine dissolution rates (Eggleton, 1986; Awad et al., 2000). Experimental studies of Awad et al. (2000) revealed a preferential dissolution of olivine along the b-axis (i.e. [010]) (Fig.2.13). The b-axis ([010]) has the higher density of oxygen type $O_{(1)}$ (Birle et al., 1968). The oxygen atoms have a negative charge that confers a greater potential to become protonated. The much higher dissolution rate in the direction of the b-axis is attributed to preferential protonation of the oxygen atoms (Birle et al., 1968). The preferential adsorption of H^+ on the mineral structure generates preferential protonation of the oxygen atoms around

a tetrahedral site, which result in a higher dissolution rate of the SiO_2-tetrahedra and consequence an incongruent dissolution of olivine.

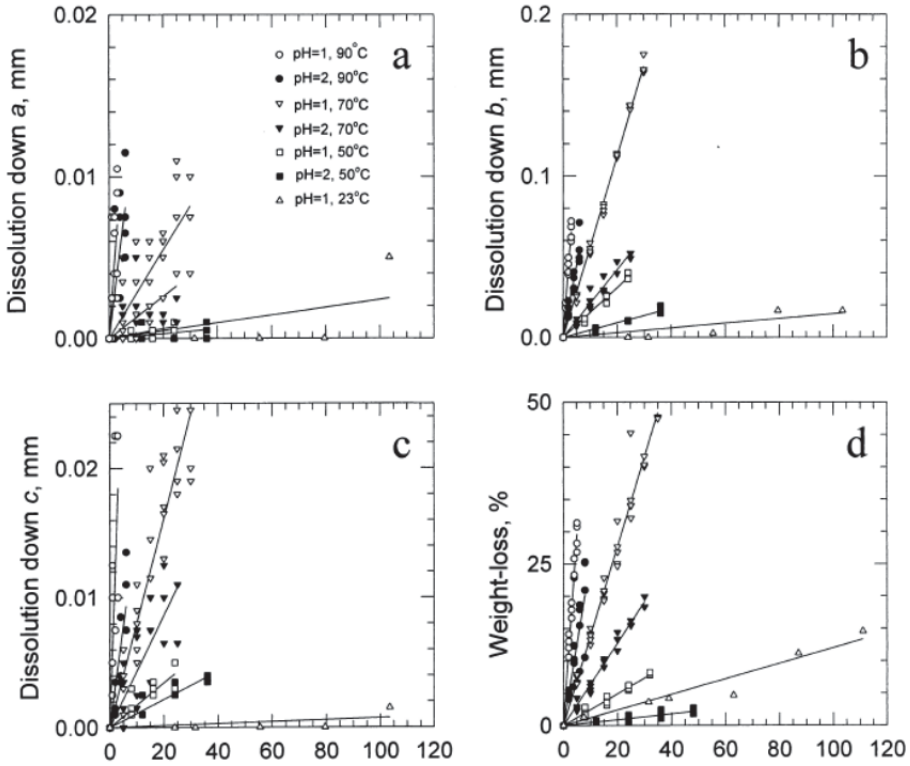

Fig.2.13. Dissolution rates in mm/h of the {100} faces for forsteritic olivine, (a) along the a-axis, (b) along the b-axis, (c) along the c-axis (d) weight loss in wt.%/h for forsteritic olivine (Awad et al., 2000).

The incongruent dissolution of olivine results in the formation of "surface altered layers" or "leached layers" enriched in one of the components of the parent phase (Mg or Si) (Ruiz-Agudo, 2014). Several authors have attributed these layers to:

(i) **Preferential leaching of cations** (Schott et al., 2012; Pokrovsky and Schott, 2000a; Daval et al., 2011) due to an exchange of H^+ and adsorption reactions occurs on the surface sites initially occupied by magnesium or silica ions. This leads to the development of Si-rich or Mg-rich layers on the olivine mineral surface. Pokrovsky and Schott (2000b) perform experiments of forsterite dissolution under acid and alkaline conditions (2<pH<12) at 25°C. They determine that the amount of H^+ consumed by the forsterite during their dissolution controls the amount of Mg and Si aqueous concentrations. They determine that at pH<9, magnesium is enriched in solution compared to silica. This indicates that the surface of

forsterite is enriched in silica. They explain this by the formation of silica-rich layer by the exchange of two hydrogen ions for a magnesium atom at the forsterite surface. This leads to the development of apparent high surface charge. At pH>10, silica is enriched in solution compared to magnesium (Fig.2.14). In contrast, the surface of forsterite is enriched in magnesium and Mg-rich layers are formed.

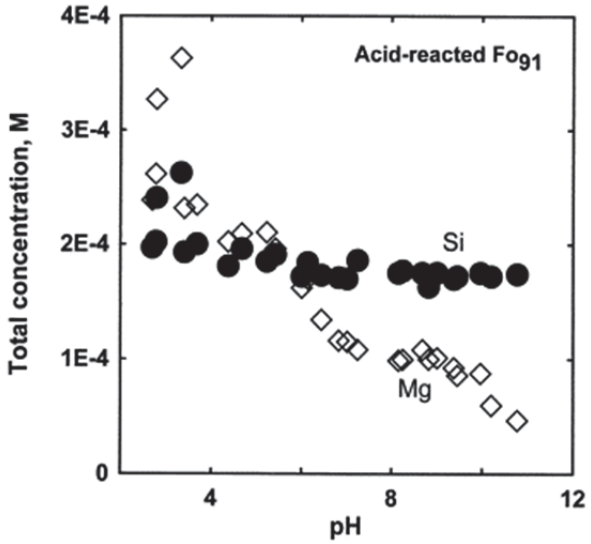

Fig.2.14. Total Mg and Si aqueous concentrations during titration of acid-reacted forsterite (Pokrovsky and Schott, 2000b). Silica increases on solution compared to Mg in alkaline conditions and Silica decreases on solution compared to Mg in acid conditions.

(ii) **Mineral-fluid equilibration process** (Ruiz-Agudo et al., 2014; O'Neil and Taylor, 1967; Hellmann et al., 2012). They suggest that when a fluid interacts with a mineral phase with which it is out of equilibrium the mineral will tend to dissolve congruently. However, depending on the fluid composition, dissolution of even a few monolayers of the parent surface may result in supersaturation of the interfacial fluid with respect to a secondary phase (e.g., silica rich phase). This produced phase may nucleate on the parent surface, within this interfacial fluid, depending on the fluid composition and the degree of epitaxy between parent and product phases. The dissolution and precipitation may be coupled in space and time (depending on the fluid composition) and result in the complete replacement of the parent mineral by the product. Nevertheless, the congruent or incongruent dissolution of olivine is still a subject of debate.

General mechanism of olivine dissolution

Assuming a congruent dissolution of solid phase, the interaction of the fluid with the mineral surface generates an aqueous boundary layer immediately adjacent to the mineral surface which has several nanometre of width (White and Brantley, 1995). Within this boundary layer a compositional gradient exists between the two phases, and elements are transported by diffusion from the mineral surface into the fluid (desorption) or vice versa (adsorption) (Fig.2.15).

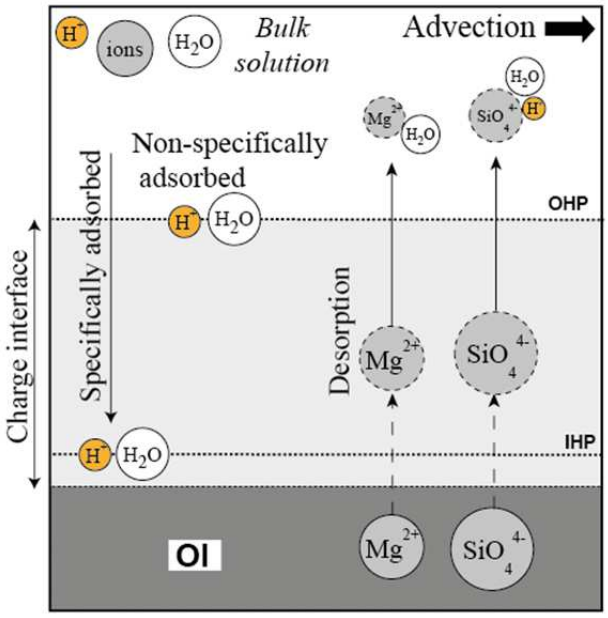

Fig.2.15. Overall mechanism of olivine dissolution (modified from Crundwell, 2014).

The surface of the olivine is charged, due to the termination of bonds at the surface and the adsorption of charged species from the solution onto the surface (Morrison, 1980). This charge is distributed across a region close to the surface in the solid and in the fluid solution. This region is called the Helmholtz layer (Crundwell, 2014). Ions absorbed from the bulk solution could interact with the mineral surface by electrostatic forces (i.e. they are called non-specific adsorbed cations) (Bard and Faulkner, 1980). However when there is a strong interaction between the surface and the adsorbed ion, the ion is specifically adsorbed and is positioned at the inner Helmholtz plane (IHP). Then, Mg-octahedra and Si-tetrahedra are detached from the olivine surface. Water molecules form a solvation sheath around the magnesium (i.e. activated complex) which transfers the magnesium to the outer Helmholtz plane. The protons absorbed (H^+) form an activated complex with the silicate groups, SiO_4^{4-},

and the silicate groups are removed intact from the surface (Crundwell, 2014). Surface magnesium and silicate species move across the charge interface at equal rates during congruent stoichiometric dissolution.

Influence on the pH on the dissolution rate

The dissolution rate of olivine exhibits a marked dependence on the solution pH. The olivine dissolution rate is faster under acid conditions rather than in alkaline to neutral solution. Previous studies suggest the rate of olivine dissolution depends on the order of reaction (Crundwell, 2014; Pokrovsky and Schott, 2000a, Rimstidt et al., 2012) (Fig.2.16). The order of reaction indicates how the rate of reaction depends on the concentration of the reactant (i.e. the amount of H^+ ions and OH^- ions in solution). The order of reaction of forsterite with respect to H^+ changes from 0.5 in the acid region to 0.25 in the alkaline region (i.e. above a value of pH of approximately 6) (Crundwell, 2014). Rimstidt et al. (2012) conclude that the change on the order of reaction is above a pH of 5.6. This change on the order of reaction precludes a different dissolution mechanism in acid and alkaline/neutral conditions.

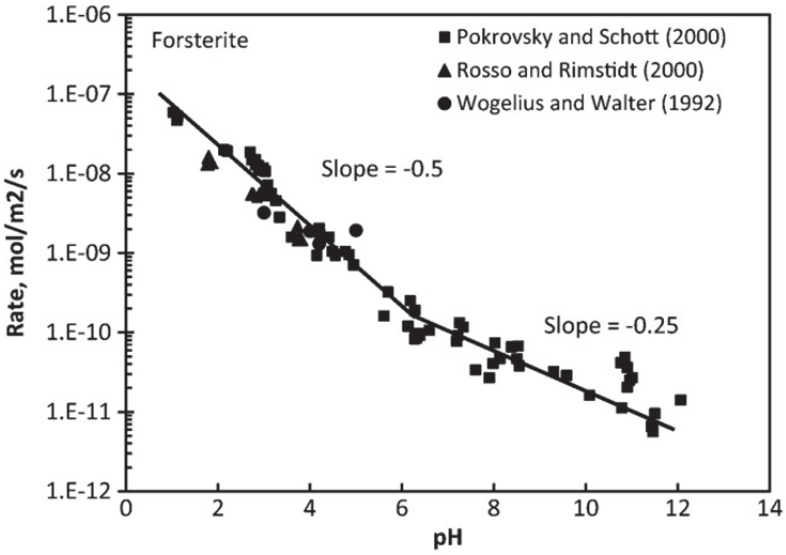

Fig.2.16. The effect of pH on the rate of dissolution of forsterite (Crundwell, 2014).

i) Acid conditions

In acid solutions, H^+ ions are present in abundance in the bulk solution (Fig.2.17a). If the rate of dissolution is slow relative to the rate of diffusion and the solution is well stirred,

the concentrations of H^+ ions at the outer Helmholtz plane is equal to the concentration of H^+ ions in the bulk (Crundwell, 2014). Thus, the charge gradient on the boundary layer is not enough to specifically adsorb the H^+ on the mineral surface (i.e. at the inner Helmoholtz plane) and the proton is positioned out of the Helmholtz plane (non-specifically absorbed). H^+ ions at the outer Helmholtz plane react with silicate tetrahedral at the surface to form $SiO_4^{-4}{}_{(aq)}$ in solution and magnesium reacts with water molecules to form $Mg^{2+}{}_{(aq)}$.

ii) Alkaline conditions

In alkaline conditions, the concentration of H^+ in solutions becomes very low, and hence its concentration at the outer Helmholtz plane becomes very low (Fig.2.17b). The charge gradient on the boundary layer is enough to specifically absorb H^+ at the inner Helmholtz plane. Thus, H^+ ions first absorb at the inner Helmholtz layer before reacting with the silicate tetrahedra to form $SiO_4^{-4}{}_{(aq)}$ in solution. This change on the position of the H^+ generates a change in the kinetics of dissolution becoming more slowly in alkaline conditions.

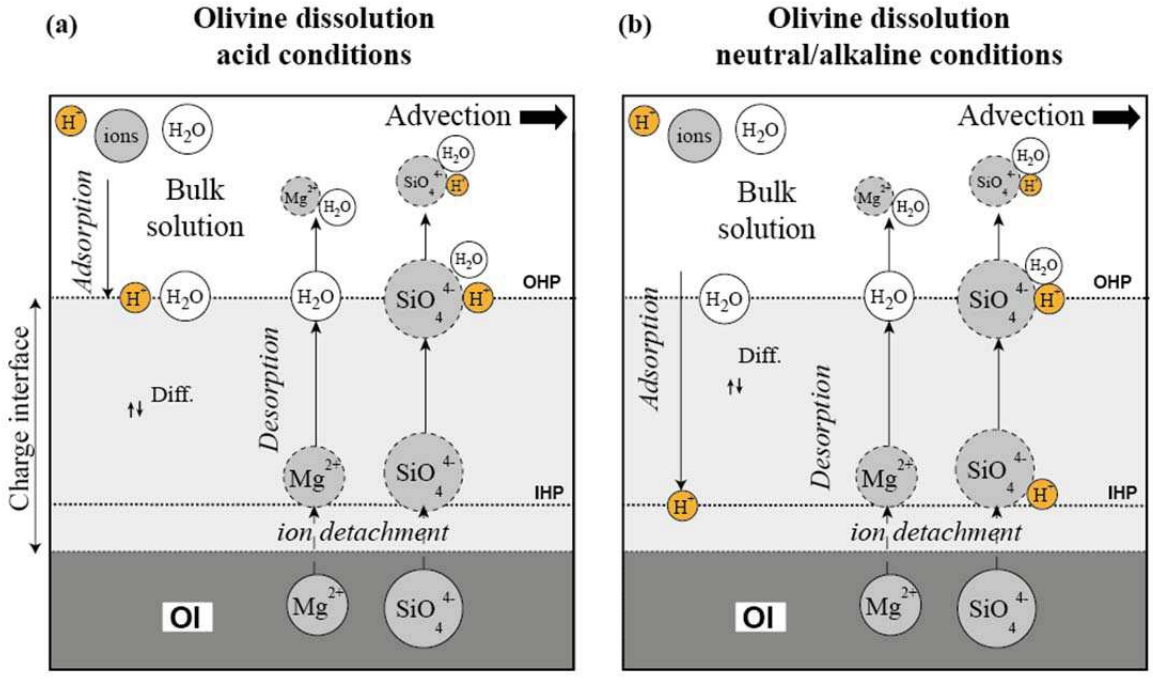

Fig.2.17. Mechanism of congruent dissolution of olivine under (a) acid conditions (b) Neutral/ alkaline conditions (modified from Crundwell, 2014. (Diff. means diffusion).

Influence of the temperature on the dissolution rate

The temperature is a fundamental parameter on silicate dissolution (Fig.2.18). The increases of temperature contribute to decrease the activation energy (E_a) required breaking the atomic bonds in the crystallographic structure (Giammar et al., 2005; Hänchen et al., 2006; Lasaga, 1984). The olivine has a activation energy of 60.2 $kJ.mol^{-1}.K^{-1}$ for 90-120°C and 43.9 $kJ.mol^{-1}.K^{-1}$ 120°C-150°C (Hänchen et al., 2006).

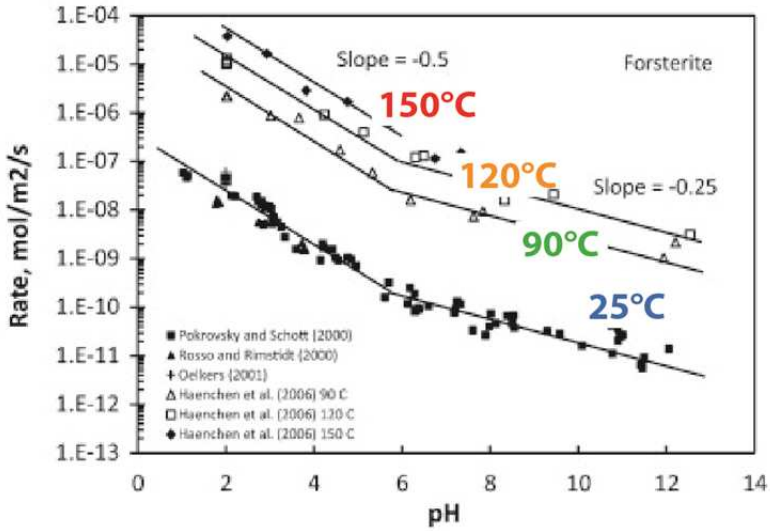

Fig.2.18. The effect of temperature on the rate of dissolution of forsterite (modified from Crundwell, 2014) vs pH. Data from Pokrovsky and Schott (2000b), Rosso and Rimstidt (2000), Oelkers (2001a,b) and Hänchen et al (2006).

3.2.2 Parameters that controls serpentinization rates

Experimental studies have been especially interested on the kinetics and mechanisms that control the serpentinization reaction over more than 30 years. The extent of the reactions as well as mineral assemblages and reaction paths depend upon a variety of factors such as: temperature, pressure, water/rock ratios, grain size, fluid-rock composition, alkaline and pH conditions and water supply. Most of the laboratory simulations were run under close conditions due to the less complexity of the experimental apparatus and measurable results in laboratory time scales. However it remains a challenging task to assess heterogeneous phase equilibria and reaction pathways in a systematic approach using hydrothermal laboratory experiments. Thermodynamic models can complement hydrothermal experiments. Here I describe the experimental and thermodynamic studies since the early's 70 until nowadays and

I focus on deciphering the effects of the parameters mentioned above on the serpentinization reaction.

i) Temperature

During the early 70's, the studies of Martin and Fyfe (1970) were the first to evaluate the effect of **temperature** on serpentinization reaction. They performed experiments during 21 days in sealed gold capsules filled with a controlled amount of pure water. The capsules were filled with olivine (forsterite) or/and pyroxene (enstatite) powder of grain size ranging 50 to 175 µm. They run experiments between 200°C and 400°C and pressure of 200 and 300 MPa. They observed that olivine shows a maximum rate of conversion into serpentine (chrysotile) between 250°C and 300°C. The hydration of enstatite reflects the formation of serpentine (chrysotile) below 400°C, and talc alone above 400°C. Later on experiments of Wegner and Ernst (1983) attribute the best effectiveness temperature of serpentinization at 310°C. They perform experiments in the MgO-SiO_2-H_2O system using cold-seal pressure vessels at temperatures from 188°C to 388°C and 1 to 300 MPa of pressure during 5 to 60 days. They fill Ag capsules with peridotite powders with selected fractions ranging from 36 to 149 µm and pure water as reagent fluid.

More recently, studies of Malvosin et al. (2012) and McCollom et al. (2016) were also interested in the effect of temperature on serpentinization. Malvoisin et al. (2012) performed experiments from 250°C to 350°C and 50 MPa. They filled Ag capsules with variable grains fractions of San Carlos olivine powder (1 to 150 µm) and pure water with a W/R of ~2.5. The capsules were welded and placed in a horizontal cold seal pressure vessel. The experiments were longer than the previous studies (up to 514 days). They determine that the highest reaction kinetics was achieved at ~300°C, in good agreement with the studies of Wegner and Ernst (1983). McCollom et al. (2016) conduct experiments from 200°C to 320°C at 35 MPa during few days to over a year. The experiments run in a flexible cell hydrothermal apparatus using a gold reaction cell with titanium fittings similar to previously proposed by Seyfried et al. (1987). They had reacted San Carlos olivine powder with a grain size of 53-212 µm with NaCl and $NaHCO_3$ bearing aqueous solutions. They show that olivine was slightly more reacted at 230°C rather than 300°C.

The estimated extent of serpentinization at the proposed effectiveness temperatures was 3.7-7.5% per day for Martin and Fyfe (1970) and 1-3% per day for Wegner and Ernst (1983) considerably higher than ~1% per day for Malvoisin et al. (2012) and ~0.1% per day for McCollom et al. (2016) (Fig.2.20). The discrepancy in estimated reaction rates between recent studies and older results could be attributed to differences in the experimental design and the lack of information on fluid compositions and detailed description of the reaction products of the older studies of Martin and Fyfe (1970) and Wegner and Ernst (1983), making difficult to assess the accuracy of the high extent of olivine conversion.

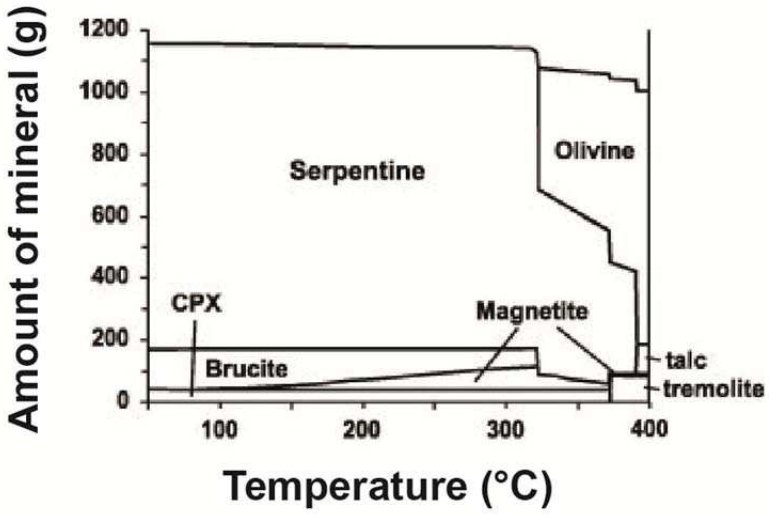

Fig.2.19. Alteration mineralogy numerically predicted using EQ3/6 during hydrothermal alteration of harzburgite for a range of temperature (25 to 400°C) at 35MPa with a water/rock ratio equal to 1 (McCollom and Bach, 2009).

Numerical simulations of McCollom and Bach (2009) determine that the reaction path during hydration of ultramafic rocks is a function of temperature (Fig.2.19). They perform thermodynamic simulations of the reaction of harzburgite with seawater at variable temperature and fixed pressure of 35 MPa. They determine the composition of minerals and coexisting fluid that would be reached at thermodynamic equilibrium for a given temperature and pressure by minimizing the Gibbs energy of the overall system. The results shows that at all temperatures below 315°C, the equilibrium mineral assemblage consists of serpentine (predominant), brucite, magnetite and minor secondary clinopyroxene (diopside). Above 315°C olivine becomes a stable member of the assemblage, and will coexist in equilibrium with the fluid and alteration minerals after it has only partially reacted. Above >390°C the amount of unaltered olivine present at equilibrium is essentially identical to that in the

original rock (i.e. a very small amount of olivine dissolves to bring the mineral into equilibrium in the fluid above 390°C). At temperatures between 370°C and 390°C the equilibrium assemblage is serpentine, tremolite, small amounts of magnetite produced from the alteration of pyroxenes and relict unreacted olivine. At temperatures >390°C, talc replaces serpentine, so the equilibrium assemblage consists of unreacted olivine, talc, tremolite and small amount of magnetite produced from the dissolution of pyroxenes.

ii) Pressure

Very little studies were interested on the effect of **pressure** on serpentinization kinetics. Wegner and Ernst (1983) were the first to consider the effect of pressure on the rate of serpentinization. They show high pressures achieve higher serpentinisation rates compared to low pressures. They determine that for a grain of 100 μm reacting with pure water at 310°C and 50 MPa is required to 1.2 years to achieve 90% of conversion. However, for 100 MPa need 0.63 years to achieve 90% and only 0.3 years under 200 MPa. They determine that the activation energy during hydration reaction decreases with pressure. At 100 MPa the activation energy is 30 kJ/mol compared to 300 MPa which is 25kJ/mol. The studies of Wegner and Ernst (1983) shows that pressure have an influence on the serpentinization rate but it should be interesting to conduct more experiments to corroborate it.

iii) Grain size

The **grain size** is another parameter important to consider in serpentinization rates. Martin and Fyfe (1970) observed than an increase of the olivine grain size from 50 μm to 150 μm produced a drop on the degree of olivine conversion to serpentine at 250°C. Similar observation was point out few years later by Wegner and Ernst (1983) which determine that grain size of 105-149 μm were less effective to achieve greater values of olivine conversion to serpentine compared to fine grains 37-62 μm at 270°C. More recently studies of Malvoisin et al. (2012) determine that serpentinization kinetics was found to be directly proportional to the olivine grain size (Fig.2.20). Small grain size has higher reactive surface area than big grains which in turn leads to achieve higher reaction rates (Brantley and Mellott, 2000). Other recent studies at different experimental conditions corroborate also this observation (e.g. McCollom et al., 2016; Lafay et al., 2012, 2014, Malvoisin and Brunet, 2014, Huang et al., 2015, Huang et al., 2017, Marcaillou et al., 2011) (Fig.2.20).

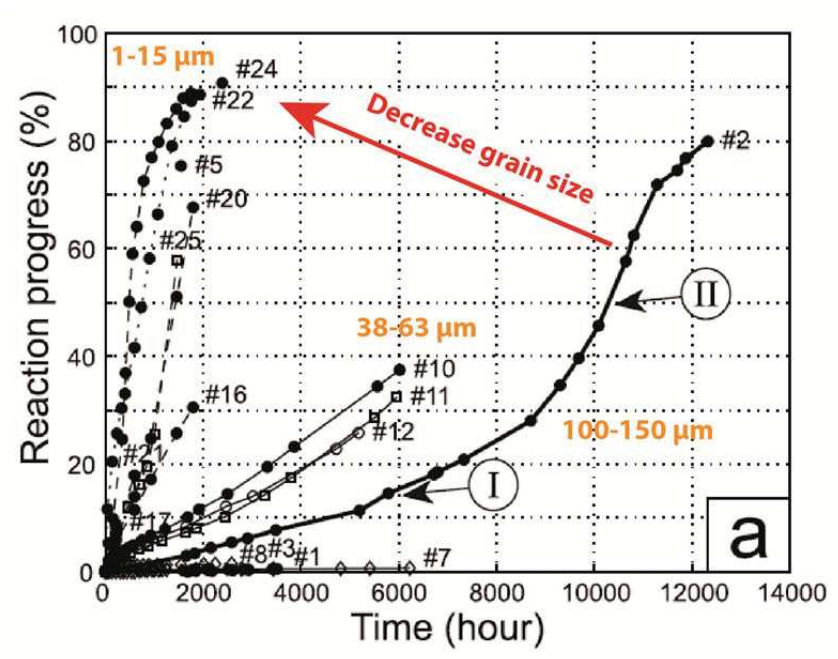

Fig.2.20. Serpentinization reaction progress using different grain size (modified from Malvoisin et al. (2012).

iv) Water/rock ratio

The effect of **water/rock weight ratios (W/R)** on serpentinization was studied since the seventies by Martin and Fyfe (1970). They determine that the rate of conversion of olivine and pyroxenes into serpentine appears to increase the greater the relative amount of water. They suggest that the removal of impurities from the reactant surface by greater solutions could explain the increase of the rate of serpentinization. Thus, Martin and Fyfe (1970) start considering that the hydration reactions were controlled by mineral surface processes. This assumption was developed in the following years (see review Ruiz-Agudo et al. (2014)).

Numerical simulations of McCollom and Bach (2009) studied the effect the water/rock ratios on the serpentinization reaction path. The models emulate reactions of harzburgite with a seawater-like fluid with different water/rock ratios (0.2 to 10) at variable temperature (100, 300 and 350°C) and fixed pressure of 35 MPa. The results show the impact of water/rock ratio on alteration mineralogy and fluid composition during serpentinization varies significantly as a function of temperature. (i) At temperatures of 100°C: the low water/rock ratios show that the fraction of magnetite in the mineral assemblage decreases

substantially throughout the reaction and the Fe content increases gradually in serpentine and brucite. At higher water/rock ratios, the amount of H_2 generated per kg of harzburgite is greater compared to W/R ratios, however the resulting concentration of $H_{2(g)}$ in the fluid decreases with increasing the W/R ratio. This is due to the fact that the H_2 generated is dissolved into a larger amount of fluid and the resulting concentrations end up to be lower. At large W/R ratios, Ca from the harzburgite is completely dissolved. (ii) At temperatures of 300°C: the H_2 generation is also favoured at high W/R ratios and it is also strongly higher at high temperature compared to low temperatures. (iii) At temperatures of 350°C: the proportion of serpentine and magnetite in the reacted rock is positively correlated with the W/R ratios. This reflects the decreasing amount of olivine that must react in order to bring the fluid into equilibrium with the mineral assemblage when the W/R ratio decreases. The proportion of Fe incorporated in the serpentine slightly increases when the W/R ratio decrease.

v) Starting fluid composition

The **salinity of the water** is important aspect to consider for serpentinization process. Pure water is the end-member with zero salinity and maximal activity (a=1). As the amount of salt increase into the solution, the activity of the water decreases, and thus brines has lower water activity compared to pure water. Experiments of Lamadrid et al. (2017) evaluate the effect that exerts the water activity on rates of serpentinization of olivine. They perform experiments during 30 to 270 days at 280°C using synthetic fluid inclusion (SFI's) as micro-reactors in olivine crystals to monitor the serpentinization reaction with time. They use $MgCl_2$-NaCl solutions with salinities of 1, 3,5, 6 to 10 wt.%. The results show that the rate of serpentinization is strongly controlled by the salinity (water activity) of the reacting fluid and demonstrate that the rate of serpentinization of olivine slows down as salinity increases and H_2O activity decreases (Fig.2.21).

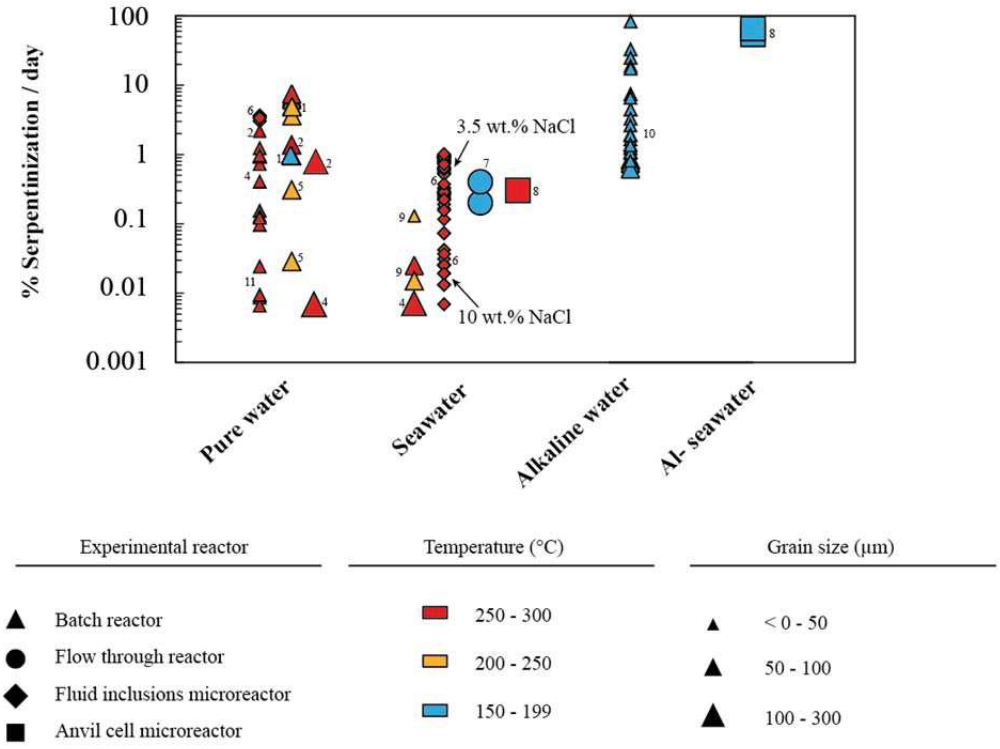

[1]Martin and Fyfe, 1973, [2]Wegner and Ernst, 1983, [3]Okamoto et al, 2011, [4]Malvoisin et al, 2012, [5]Ogasawara et al, 2013, [6]Lamadrid et al, 2017, [7]Godard et al, 2013, [8]Andreani et al, 2013, [9]McCollom et al, 2016, [10]Lafay et al,2014, [11]Malvoisin et al, 2014

Fig.2.21. Influence of fluid composition on serpentinization rates.

The presence of **aluminium in solution** was first evaluated by Andreani et al. (2013). They use low-pressure diamond-anvil cells (lp-DAC) as experimental reactors. Experiments were run for 4.5 to 7.5 days with two olivine grains reacting in saline water (0.5 mol NaCl/kg) at 200 and 300 °C, and P = 200 MPa. Aluminium was introduced either as a gel of aluminium hydroxide for experiments at 200 °C, or as Al_2O_3 ruby microspheres for experiments at 300 °C. The progress of reaction was monitored by optical microscopy and confocal Raman microspectrometry. The results show that aluminium increases the solubility of olivine and enhance the conversion of olivine into serpentine achieving rates of 53-65 % per day, definitely higher than same experiments run without aluminium (0.3 % per day) (Fig.2.21). Recent studies of Pens et al. (2016) using same experimental apparatus evaluate at 200°C and 340°C and 200 MPa the effect of alumina on serpentinization of pyroxenes. They determine that aluminium slow down the serpentinization of pyroxene compared to the speed up recorded for the serpentinization of olivine. They propose that the complexation of Al in the solution reacts differently with the different surface of olivine and pyroxene during their dissolution. The chemistry of the reacted phases during serpentinization of olivine in

presence of aluminium was also evaluated by Pens et al. (2016) at low temperature (80°C) and atmospheric pressure. They determine that in Al-rich, solutions the Al is preferably incorporated in the precipitated serpentine rather than Mg from the olivine dissolution, leading to strong amounts of Mg into the reacted solutions. However, in Al-free solutions Mg is preferentially incorporated in serpentine.

Another aspect to consider is the **alkaline conditions and pH** of the fluid solution. Lafay et al. (2012) perform experiments under high alkaline conditions. They interacts 1M of NaOH solution (pH: 13.5) with olivine at 150°C and 200°C below the vapor-saturation curve during 3 h and 90 days. The results show that olivine was replaced by chrysotile and brucite. The lack of magnetite indicates that Fe from the olivine dissolution was incorporated into brucite and chrysotile. They also show that faster serpentinization rates were achieved under alkaline conditions (0.6 to 82 %/day) compared to previous studies using seawater and pure water (Fig.2.21) but comparable to those with alumina. This suggests that alkaline conditions and the presence of alumina in solution accelerate the serpentinization reaction. Studies of Lafay et al. (2012) and Pens et al. (2016) determined that the kinetics of serpentinization is favorized under basic solutions rather than acid solutions.

The recent studies of Lafay et al. (2014) and Pens et al. (2016) were focused on the effect of **high-carbonate alkaline solutions** on the serpentinization. They perform experiments using $NaHCO_3$ solutions. They show serpentine (chrysotile), brucite and magnesite as precipitated phases. However, the rate of serpentine formation is about 3 times slower compared to magnesite formation (Lafay et al., 2014). Pens et al. (2016) determine that the reaction path is affected by the pH of the solutions. At pH of 14, the precipitation of brucite predominates compared to pH of 9 where magnesite is the major precipitated phase.

vi) Starting rock composition

The effect of the **starting rock composition** was evaluated exhaustively since the 70 and 80' after the experiments of Martin and Fyfe (1970) and Wegner and Ernst (1983). They determine different serpentinization rates for olivine and pyroxene depending on the temperature. The serpentinization rates are faster for olivine at temperatures less than <300°C and for pyroxene at temperatures more than >300°C. More recently Okamoto et al. (2011) perform experiments at 250°C under vapour-saturated pressure with pure olivine and pure

pyroxene in the starting rock reacting with pure water during 42 days. They determine olivine was more hydrated (~3.6 wt.%) than orthopyroxenite experiments (0.4 wt.%) but the produced mineral assemblage was the same for both experiments: serpentine + brucite + magnetite.

High temperature (400°C) experiments of Allen and Seyfried (2003) show reaction pathways during serpentinization of pyroxene are fundamentally different from those during serpentinization of olivine. Pyroxene minerals alter readily and produce relatively high dissolved concentrations of SiO_2, Ca and H_2. In response to the relatively high SiO_2 concentrations in solution, tremolite and talc precipitate, resulting in relatively low pH values. The low pH enhances magnetite solubility, resulting in relatively high dissolved Fe concentrations which favor the precipitation of magnetite. Increases in Si concentrations of fluids were also documented on experiments reacting artificial seawater with olivine (Allen and Seyfried, 2003; Bernt et al., 1996; Klein and McCollom, 2013) and with peridotite (Allen and Seyfried, 2003; Janecky and Seyfried, 1986; Klein et al., 2015; Seyfried and Dibble, 1980; Seyfried et al., 2007).

Thermodynamic simulations performed by Klein and Bach (2009) study the effects of the starting material on serpentinization reactions. They use two different photoliths (olivine-orthopyroxene) and (olivine-orthopyroxene-clinopyroxene). The simulations run under equilibrium conditions between 25°C and 400°C at 50 MPa. Thermodynamic predictions suggest lack of magnetite during serpentinization of orthopyroxene. They explain this by a closed loop reaction, where all Fe originally contained in orthopyroxene is partitioned into serpentine. However, Allen and Seyfried (2003) report the presence of magnetite in all their experiments including those having only pyroxene as the starting material. This points out the difficulty to reach equilibrium during experiments runs at laboratory time scales. Another observation point out during Klein and Bach (2009) simulations was the mass transfer of silica during simultaneous serpentinization of olivine and orthopyroxene. This generates Fe-poor serpentine and Fe-rich brucite and magnetite. However, when serpentinization of pyroxene and olivine are not simultaneous, then Fe-rich serpentine and talc formed. Experiments of Klein et al (2015) on uncrushed harzburgite determine that at 300°C orthopyroxene reacts significantly faster than olivine, which precludes early brucite formation during serpentinization.

vii) Water supply

The effect of the **water supply** was point out by Malvoisin and Brunet (2014). They performed experiments at 300°C on sintered aggregates of San Carlos olivine with porosities around 1 and 10% and grain size of 1-5 μm and 0-38 μm. They determine the reaction progress was very low (0.01%/day) compared to previous literature powder experiments. The low porosity conditions of their olivine aggregates (1 to 10%) limited the intergranular region accessible to water transport, thus limited olivine surface area were accessible to water and this slowed down the whole serpentinization process. Similar observation was point out one year later on experiments of Klein et al (2015) on uncrushed harzburgite at 300°C and 35MPa. They determine the rate of serpentinization was faster on the first stage of the experiments and slow down through time. They correlate the decrease of the serpentininization rate to the precipitation of serpentine inside fractures, which clogs the access of water to fresh olivine surface. Both experiments conclude that the progression of the reaction needs the continuous access of water to olivine surface to continue the reaction, thus emphasizing the central role played by water availability in the natural reaction process.

Thermodynamic models of Klein et al (2013) make reference to the impact of water renewal on H_2 generation during serpentinization. They point out that in natural systems, the generation of $H_{2(aq)}$ is actively enhanced by the renewal of fluid in the rock. The renewal of fluid in the rock produces the removal of $H_{2(aq)}$ and promotes the oxidation of ferrous to ferric iron. As a consequence, more magnetite, Fe^{+3}-serpentine and eventually hematite can form than it would be possible in a closed system where there is no renewal of fluid.

2.2.3 Parameters that controls carbonation rates

The carbonation of ultramafic rocks is a process associated to the serpentinization reaction. Carbonation process or also called *CO_2-mineralization* is the reaction of CO_2 with silicate minerals (e.g., olivine) to produce carbonate minerals (e.g., magnesite, calcite and dolomite). The parameter that controls the carbonation has been exhaustively studied numerically and experimentally. Here I describe the principal parameters that control the rate of carbonation as an associated process during serpentinization of the ultramafic rocks.

i) Temperature

The **temperature** has an effect on carbonation kinetics. Experimental studies determine optimum carbonation conditions occur at 185°C for olivine and 155°C for serpentine (Gerdermann et al., 2007; O'Connor et al., 2001; O'Connor et al., 2005,) (Fig.2.22). The carbonation process includes two distinct reactions, mineral dissolution followed by carbonate precipitation, thus temperature plays a complex role. Dissolution kinetics of ultramafic rocks is enhanced with increasing temperature (Hänchen et al., 2006) but carbonate precipitation is slower at higher temperatures due to reduced CO_2 activity (O'Connor et al., 2005).

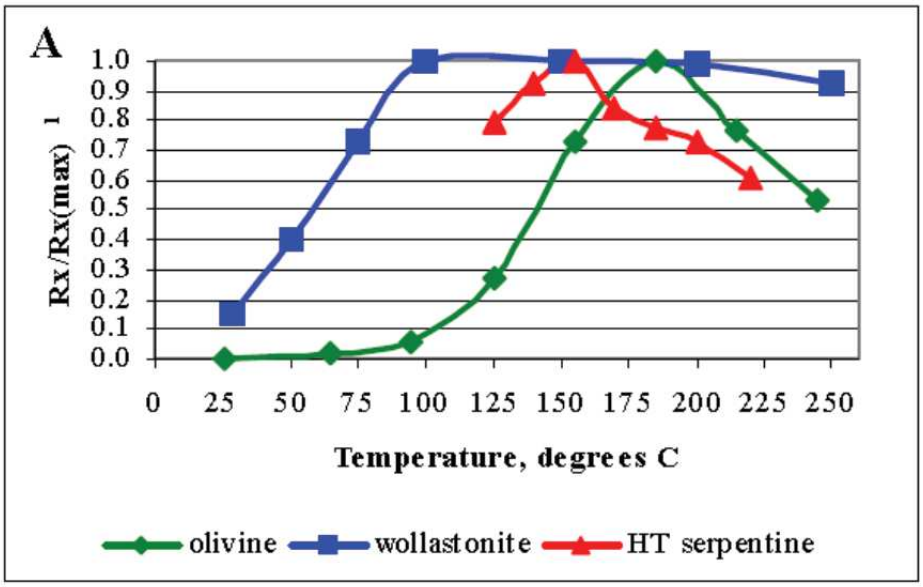

Fig.2.22. Temperature effect on the rate of silicate carbonation (O'Connor et al., 2005).

ii) Concentration of $CO_{2(aq)}$ on the fluid and pH

The **concentration of dissolved $CO_{2(aq)}$** in the fluid has an effect on carbonation rates. The concentration of dissolved CO_2 in the fluid is controlled by the Henry Law which determine the equilibrium between $CO_{2(g)}$ and $CO_{2(aq)}$:

$$CO_{2(g)} \leftrightarrows CO_{2(aq)} \qquad \text{(R13)}$$

The dissolution of CO_2 is determined by the Henry Law:

$$[CO_2](aq) = K_0 \cdot pCO_2 \qquad \text{(Eq.2.1)}$$

where $[CO_2](aq)$ is the concentration of CO_2 in the aqueous phase, pCO_2 is the partial pressure of CO_2 in the gas phase, and K_0 is the solubility coefficient of CO_2 that depends on temperature, pressure and salinity.

Studies of O'Connor et al., (2004) and Kelemen et al., (2011) revealed that Mg-silicate minerals exhibit nearly linear positive correlation between carbonation rate and the amount of dissolved CO_2. The optimum partial pressure of CO_2 (pCO_2) for olivine carbonation is 15,2 MPa, while for serpentine is 11,7 MPa (O'Connor et al., 2004) (Fig.2.23). However, very high pCO_2 could have a negative effect on carbonation. High amounts of CO_2 produce a decrease of the pH and this release H^+ in the fluid. Studies of Pokrovsky et al. (2009) determine that low pH (<5) inhibit the precipitation of carbonates. However, the addition of bicarbonate rich solutions (e.g. $NaHCO_3$) in the fluid at high pCO_2 conditions buffers the pH to basic conditions (pH ~8) and allows the carbonation to occur efficiently (Andreani et al., 2007; Chizmeshya et al., 2007; Gerderman et al., 2007; O'Connor et al., 2001; O'Connor et al., 2004; Pens et al., 2016).

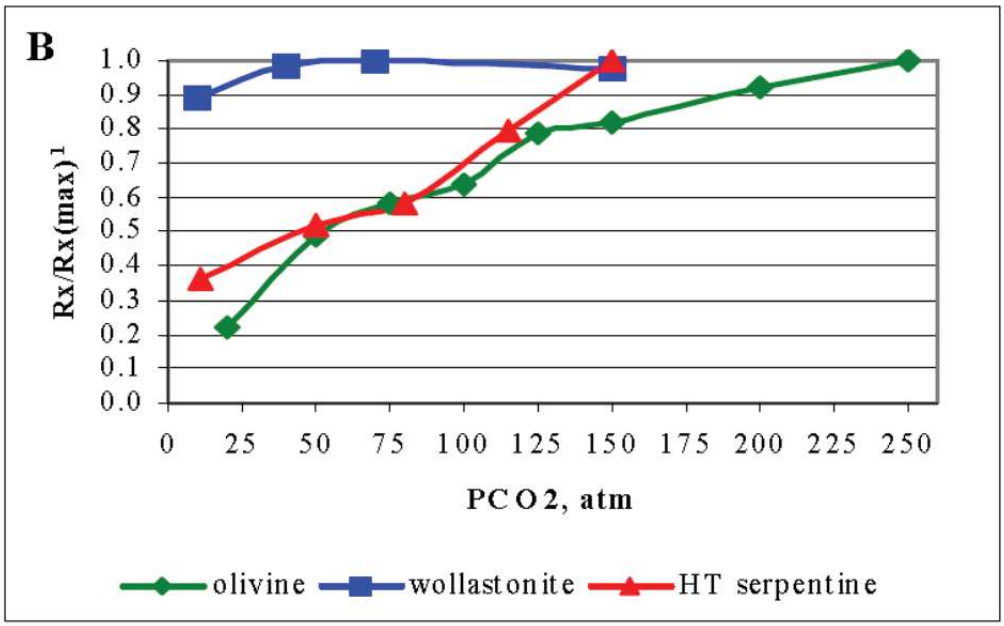

Fig.2.23. Partial pressure of CO_2 (pCO_2) effect on the rate of silicate carbonation (O'Connor et al., 2005).

iii) Starting fluid composition

As it was exposed before, the **fluid composition** exerts an effect on carbonation. Carbonation of olivine can precipitate passivating layer (e.g., Si-rich layers) on the olivine surface (Daval et al., 2011). This layer has a mitigating effect on carbonation process because it slows down the carbonation rate. Chizmeshya et al. (2007) demonstrate that the extent of olivine carbonation observed for 2.5 M $NaHCO_3$ solution was (57%). This is much higher than the one observed for 2.5M $KHCO_3$ solutions (15%). This reveals that Na^+ is substantially more effective than K^+ in mitigating passivating layer and enhancing carbonation.

Another important aspect is the role of the ionic strength of the solution on carbonation rates. The ionic strength has been demonstrated to be a positive catalysis on carbonation. The increase of the ionic strength (i.e. a reduction of the water activity) produces an increase on the rate of magnesite precipitation (Sayles and Fyfe, 1973). Saline solutions enhance magnesite reaction rates through the decrease of the activity of water and thus facilitate the dehydration of the Mg^{2+} ion. Modifying the ionic strength of the solution can alter the morphology of the precipitated carbonate phase (King et al., 2010).

iv) Reactive mineral surface

The **reactive surface** of the silicate minerals plays also a role on olivine dissolution and carbonation. As it was postulated before, during olivine carbonation Si-rich passivating layers could be form on olivine surface, decreasing their reactive surface and thus mitigating olivine dissolution and carbonation rates (Daval et al., 2011; Chizmeshya et al., 2007). The olivine surface should maintain a permeable surface to allow the diffusive transport of ions along the fluid-olivine interface to achieve effective rates of carbonation (Bearat et al., 2006; Chizmeshya et al., 2007; Daval et al., 2007, Giammar et al., 2005, Pokrovsky and Schott, 2000b). The removal of the passivating layers can be performed by physical and chemical mechanisms. Chizmeshya et al. (2007) demonstrate that the extent of carbonation is significantly enhanced from 70 to 84% when abrasive particles of quartz actively remove the passivating layers formed in the olivine surface. Also, studies of Bonfils (2012) demonstrate that the incorporation of chemical additives like magnesium oxalate (MgC_2O_4) and citrate

($C_6H_8O_7$) reduce the formation of passivating layers on the olivine surface and thus enhance olivine dissolution. However, the presence of magnesium oxalate and citrate has a negative effect on carbonate precipitation because they have a complexing effect on magnesium (Bonfils, 2012). Pokrovsky and Schott (2000) demonstrate that the generation of passivating layers are potentially formed under acid solutions. Chizmeshya et al. (2007) suggest the use of basic buffer solutions (e.g., $NaHCO_3$) can limit the polymerization of Si-rich phases on the olivine surface.

3.3 Serpentinization in open systems

3.3.1 Characteristics of the porous media

A porous media is a cohesive or non-cohesive system. It has a solid part which is formed by a solid matrix composed by grains of minerals and a fraction of volume voids accessible to fluid flow Guyon et al. (2001). This fraction of volume is composed of cavities, fractures or pores, connected to each other by channels or sometimes non-connected (see Fig.2.24). Only connected interstices can act as elementary conduits within the formation (Bear, 1972). The fraction of volume is sometimes filled by a liquid or gaseous phase or even both. This thesis focused on the study of systems filled by liquid phase.

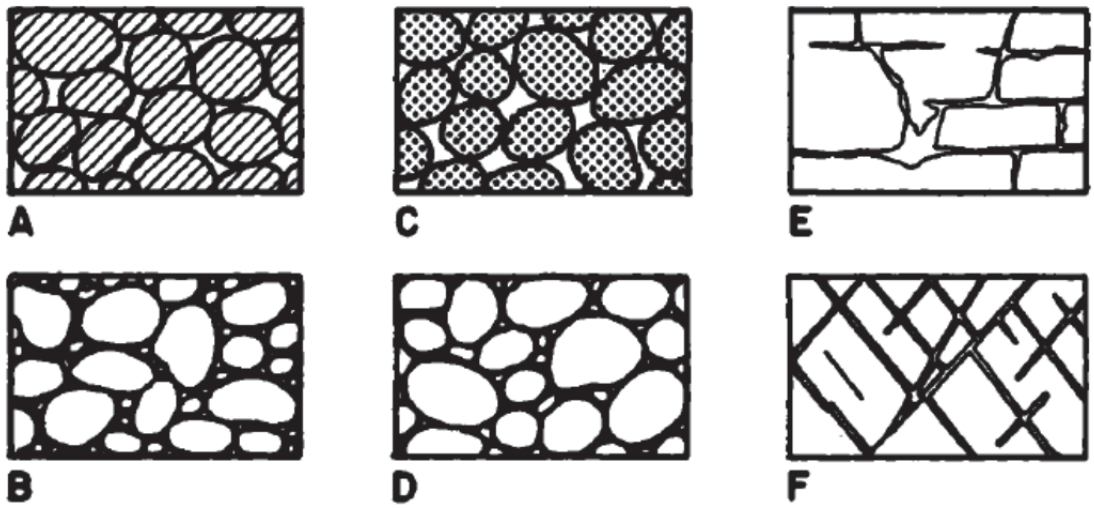

Fig.2.24. Diagram showing several types of rock interstices (from Bear (1972)). (a) Well sorted sedimentary deposit having high porosity. (b) Poorly sorted sedimentary deposit having low porosity. (c) Well-sorted sedimentary deposit consisting of pebbles that are themselves porous, so that the deposit as a whole has a very high porosity. (d) Well-sorted sedimentary deposit whose porosity has

been diminished by the deposition of mineral matter in the interstices. (e) Rock rendered porous by solution. (f) Rock rendered porous by fracturing.

Representative elementary volume

Porous media are complex structures that depend on the heterogeneous and irregular pore distribution at micrometric scale. In fact, the description of the physical properties of a system given all these heterogeneities could be a difficult task. Therefore, the system must be simplified to a homogeneous macroscopic model. Thus, the *representative elementary volume* (REV) is the smallest volume over which a measurement can be made that will yield a value representative of the whole. The REV must be small enough to take into account the microscopic structure of the system while remaining large enough to describe the overall behaviour of the rock. Therefore, the representative elemental volume is the volume beyond which an average parameter of the rock (e.g., porosity) no longer varies.

Petro-physical parameters

i) Porosity

The porosity (φ) is a geometric characteristic of the porous media. It is defined as the fraction of the volume of voids over the total volume of the rock; between 0 and 1 (i.e. is a measure of the void spaces in a rock). Commonly it is described by the ratio:

$$\varphi = \frac{Vvoid}{Vtotal} \qquad \text{(Eq.2.2)}$$

where Vv is the volume of void space and Vt is the total or bulk volume of the rock, including the solid and void components.

The fluid occupying the pores of the rock may either be mobile (flow into the rock) or immobile (remain trapped in the rock), thus it depends on the interconnection of the pores. The connected porosity is related to the connexion of the pores in the rock. During a fluid-rock interaction, the porosity evolves according to the chemical reactions between the fluid and the rock.

ii) Permeability

Permeability (k) is a measure of the ability of porous media to allow fluids (e.g., gas or liquid) to pass through it. The *intrinsic permeability* measure the ability of porous media to allow fluids to pass through it independently of the characteristics of the fluid. The intrinsic permeability is related to the shape of the grains and the connected porosity (connection between the pores in the rock). The intrinsic permeability is only defined at macro-scale or in a representative elementary volume. This thesis will use the intrinsic permeability. The permeability of a rock is calculated through the Darcy's Law which states that the fluid flow passing through a saturated porous media is: (1) proportional to the difference of the hydraulic head between the inlet and the outlet in the rock and (2) inversely proportional to the length of the porous media (de Marsily, 1986). The Darcy Law could only be applied if the fluid has a laminar flow and Newtonian behavior.

Thus, the intrinsic permeability (k) in m^2 is:

$$k = \frac{Q \cdot \mu \cdot L}{S \cdot \Delta P} \qquad \text{(Eq.2.3)}$$

with Q the injection rate (in $m^3.s^{-1}$), μ the dynamic fluid viscosity (in Pa.s), and L the length of the porous media (in m), S cross sectional area of the porous media (in m^2) and ΔP the difference in pressure between two points (Pa).

iii) Tortuosity

The tortuosity (τ) is a geometric characteristic of the porous media. The porous media is particularly complex that the fluid paths are not straight, but tortuous and meandering (Fig.2.25). The tortuosity is a parameter describing an average elongation of fluid streamlines in a porous medium as compared to free flow. The *geometric tortuosity* ($\tau_g = \langle L_g \rangle / L_s$) describes the path that follows the flow inside the rock. It is defined as the ratio of the average length, $\langle L_g \rangle$, of the geometric flow paths through the medium and the straight line length, L_s, across the medium ($\tau_g > 1$) (Adler (1992)). The definition of *hydraulic tortuosity* differs from the geometric tortuosity by the definitions of the lengths of the flow paths Carman (1937). The hydraulic tortuosity ($\tau_h = \langle L_{eh} \rangle / L_s$) takes into account the effective length of the flow path of the fluid L_{eh} and not the shortest fluid path L_g.

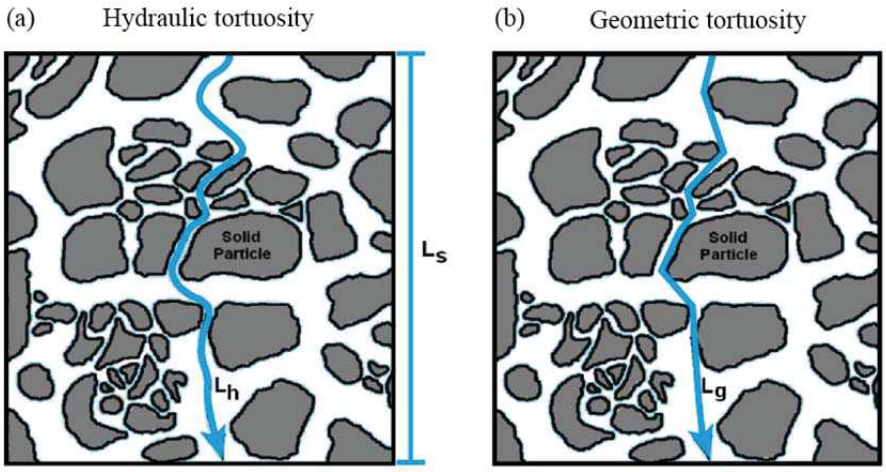

Fig.2.25. Scheme of a possible flow pathway that the fluid could follows in a porous media. (a) The flow path is represented by the hydraulic length (L_h) and (b) the flow path is represented by the geometric length (L_g). The straight path is represented by Ls. (Redrawn from Ghanbarian et al, 2013 and Gvirtzman and Gorelick, 1991).

3.3.2 Flow equations in porous media

The fluid flow in porous media is defined by the Darcy's Law (Darcy, 1856). Darcy's Law defines the ability of a fluid to flow through a porous media completely saturated. Darcy's Law is only valid for Newtonian and incompressible fluid with slow flow and with a Reynolds number less than one (Re < 1), which is in laminar conditions. The flow rate is Q ($m^3.s^{-1}$) and is proportional to the hydraulic gradient $\frac{\Delta H}{L}$:

$$Q = K \cdot S \cdot \frac{\Delta H}{L} \qquad \text{(Eq.2.4)}$$

where K is the hydraulic conductivity ($m.s^{-1}$) and S is the surface cross sectional area of the porous media (m^2).

The hydraulic conductivity (K) describes the ability which a fluid can move through pore spaces or fractures. Given the value of hydraulic conductivity for a surface system, the permeability can be calculated by $= K\frac{\mu}{\rho g}$, where k is the permeability (m^2), K is the hydraulic conductivity ($m.s^{-1}$), μ is the dynamic viscosity of the fluid (Pa.s), ρ is the density of the fluid ($kg.m^{-3}$) and g is the gravity ($m.s^{-2}$).

The hydraulic head (H) is a specific measurement of liquid pressure above a reference point and is calculated as $H = \frac{p}{\rho g} + z$ where p is the pressure (Pa), ρ the density in (kg.m^{-3}), g is the gravity (m.s^{-2}) and z s the height (m).

Darcy's Law allows estimating the velocity of the fluid between two points. Darcy velocity V_D is a fictive velocity since it assumes that flow occurs across the entire cross-section of a rock sample, porous and matrix include:

$$V_D = \frac{Q}{S} \quad \text{(Eq.2.5)}$$

where V_D is the Darcy velocity in (m.s^{-1}) , Q is the flow rate in (m^3.s^{-1}) and S is the total cross sectional area of the sample in m^2.
However, flow actually takes place only through interconnected pore channels. It is better to define the velocity V_S :

$$V_s = \frac{V_D}{\varphi} \quad \text{(Eq.2.6)}$$

where V_S is the velocity related to the interconnected pore channels, seepage velocity, in (m.s^{-1}) , V_D is the Darcy velocity in (m.s^{-1}) and φ is the porosity of the sample.

3.3.3 Reactive transport in porous media

Serpentinization in natural systems must be seen as a reaction-transport process where the kinetics of the reaction and the transport of reactive/reactants depend on each other. Thus, reactive transport in porous and fractured media consists of a series of different physical and chemical processes that can be decomposed into a sequence of steps (Fig.2.26): (1) transport of reactants from the aqueous phase to the mineral surface, (2) adsorption of the reactants on the mineral surface, (3) migration of the reactants on the mineral surface to an "active" site (e.g. mineral dislocation), (4) the chemical reaction between the absorbed reactant and the mineral, (5) migration of products away from the reaction site, (6) desorption of the reaction products to the aqueous phase, and finally (7) transport of the reaction products away from the mineral surface to the aqueous phase (Morse and Arvidson, 2002).

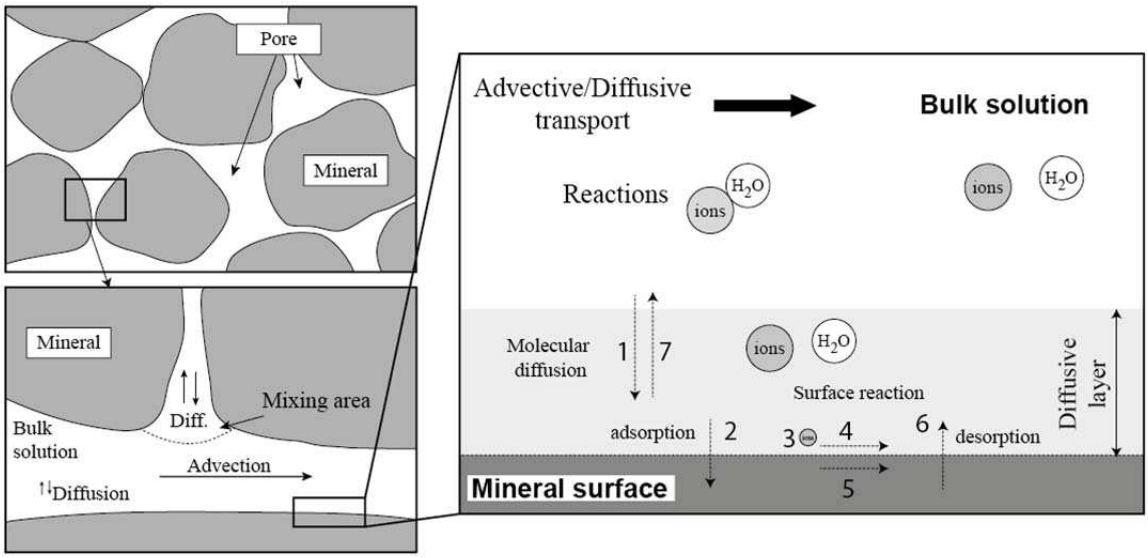

Fig.2.26. Reactive transport processes. Left image describes the localization of the different transport mechanisms (advection and diffusion) in a porous media. Advection dominates on the preferential flow paths and diffusion (Diff.) mainly dominates on the restrictive zones (small pores with low accessibility to flow). Right image describes the transport process at the mineral fluid interface (see text for explanation).

Each of these steps can potentially be rate limiting regarding the overall serpentinization process. Water availability and species transport are the likely rate limiting steps of the natural process. If the transport of the chemical elements in the fluid is relatively fast compared to the chemical reactions then the processes will be controlled by the surface reactions. On the other hand, when the reactions are relatively fast compared to the displacement of the chemical species in the solution then the processes will be governed by the transport of the fluid.

Transport equations

Transport processes are responsible for continuously introducing fluid (e.g., chemical solutes) with respect to the reactive solid phase. The transport of chemical species in the fluid is related to three transport fluxes (*J*), Advection, molecular diffusion and mechanical dispersion. Thus the **transport equation** is written by:

$$J_{\text{total}} = J_{\text{advection}} + J_{\text{diffusion}} + J_{\textit{mechanical}\ \text{dispersion}} \qquad \text{(Eq.2.7)}$$

Advection ($J_{advection}$) is the dominant mechanism when the fluid velocity is non-zero. The displacement of a particle is done according to the average displacement of the mass of water. The mass flow is then proportional to the fluid velocity. The equation in 1D is described at constant fluid velocity as follow:

$$\frac{\partial C}{\partial t} = \frac{\partial C}{\partial x}\frac{\partial x}{\partial t} = -v\frac{\partial C}{\partial x} \quad \text{(Eq.2.8)}$$

$\partial C/\partial t$ is the variation of the concentration of a certain element in (mol.L^{-1}) with time and v is the velocity of the fluid in (m/s) and x is the displacement of the particle in (m).

Molecular diffusion ($J_{diffusion}$) is a process that describes the transport of mass form one place to another in the system under the effect of random molecular motion. The process is particularly significant when the flow rate is low or zero. The diffusion equation follow the Fick's Law and allows to obtain the variation of the concentration gradient with time:

$$\frac{\partial C}{\partial t} = D_m \frac{\partial^2 C}{\partial x^2} \quad \text{(Eq.2.9)}$$

where D_m is de diffusion coefficient in (m^2.s^{-1}), x is the displacement of the particle in (m) and C is the concentration of a certain element in (mol.L^{-1}).

Mechanical dispersion ($J_{mechanical\ dispersion}$) is a mechanical process due to the different paths taken by the fluid particles to surround the grains in a porous media. The fluid particles will be moved at different velocity and will take different directions, thereby causing dispersion in the reservoir. The dispersion is defined by the longitudinal dispersion coefficient ($D_L = \alpha_L \cdot u$) and the traversal dispersion coefficient ($D_T = \alpha_T \cdot u$), where α_L is the longitudinal dispersion of the porous media and α_T is the transversal dispersion of the porous media and u the velocity of the fluid.

Actually the molecular diffusion and mechanical dispersion are hardly separable. The coupling between the molecular diffusion (D) and mechanical dispersion (D_m) is called the hydrodynamic dispersion: $D_h = D + D_m$ (Bear et al., 1972).

Thus, considering a unidirectional flux in the porous media, the transport equation of a conservative and non-reactive solute is written as:

$$\frac{\partial C}{\partial t} = -v\frac{\partial C}{\partial x} + D\frac{\partial^2 C}{\partial x^2} \quad \text{(Eq.2.10)}$$

The concentration C is a here defined as a macroscopic concentration at a scale much larger than at the pore scale. This equation is only valid on a macroscopic scale where the petro physical parameters (porosity and permeability) are defined at the sale of the VER (i.e., a minimum representative volume of the porous media on which the values do not variate by a change of scale).

Reactive transport equation

The migration of a reactive fluid through a rock implies the interaction of the fluid with the rock leading a modification of the chemical composition of the fluid and the petro-physical properties of the rock. This is a complex process because it takes into account the reaction kinetics, fluid flow and the mass transfer between the fluid and the rock. Thus, the alteration patterns will be different depending on the reaction rate and the flow regime (advective or diffusive) (Bear, 1972). The reactive transport equation follows the mass conservation law and is written as:

$$\frac{\partial C}{\partial t} = -v\frac{\partial C}{\partial x} + D\frac{\partial^2 C}{\partial x^2} - \frac{\partial q}{\partial t} \quad \text{(Eq. 2.11)}$$

where C is the concentration of the element in the solution (mol.kg^{-1}), q is the concentration of the element in the solid phase (mol.kg^{-1}) and takes into account the reaction kinetics. t is the time in s, u is the mean velocity of the fluid in m.s^{-1}, x is the displacement of the particle in m and D is the hydrodynamic dispersion in m^2.s^{-1}. $-v\frac{\partial C}{\partial x}$ is the advective transport, $D\frac{\partial^2 C}{\partial x^2}$ is the dispersive transport or diffusion transport if only diffusion is considered $D_m\frac{\partial^2 C}{\partial x^2}$ and $\frac{\partial q}{\partial t}$ is the variation of the concentration of an element in the solid phase.

Different studies have demonstrated different alteration patterns according to transport mechanisms and the kinetics of the reactions (e.g., Békri et al., 1997). Thus, two dimensionless numbers provides an estimation of the alteration patterns: the Péclet number (*Pe*) and the Damköhler (*Da*).

The relation between advection and diffusion: The Péclet number

The Péclet number (*Pe*) is a dimensionless number relevant in the study of transport phenomena in a porous/fractured media. It is define as the ratio of the advective transport over the diffusion transport.

$$Pe = \frac{v \cdot L}{D} \quad \text{(Eq.2.12)}$$

where v is the velocity of the fluid at position in $m.s^{-1}$, D the diffusion coefficient in $m^2.s^{-1}$ and L the local pore length in m.

Fluid transport is advective for $Pe >> 1$ and diffusive if $Pe << 1$. The range value of [0.1, 10] define active mechanisms of solute transport in which both diffusion and advection coexist.

The relation between chemical kinetics and fluid transport: The Damköhler number

The Damköhler number is a dimensionless number that relates the fluid transport and the chemical kinetics of a known reaction (Palciaukas and Domenico, 1976). More precisely it is the relationship between the flux of an element q and the consumption of the element q during the known reaction. This number is described by:

$$Da = \frac{\vartheta * d}{v} \quad \text{(Eq.2.13)}$$

d is the pore diameter in m, v is the mean fluid velocity in $m.s^{-1}$ and ϑ is the dissolution/precipitation rate in s^{-1}.

3.3.4 Reactive transport experimental studies of serpentinization and carbonation

The study of the serpentinization reaction has been performed in close systems using batch approaches as was described on the previous Section 3.2. However, in natural systems the characteristics of the rocks (porosity, permeability, tortuosity, etc) can modify the fluid transport and as a consequence, the chemical reaction path. Thus, several studies were interested on the feedback effects between the serpentinization and carbonation reactions on hydrodynamic properties of ultramafic rocks. This section describes the experimental studies performed in open conditions using flow through reactors.

i) Rock heterogeneity

Early studies of Andreani et al (2009) and Godard et al (2013) on sintered dunite samples suggest that the **heterogeneity of the rock** influence the dissolution-precipitation reactions on serpentinization process. Dissolution is enhanced in zones where the renewing of the fluid is large and transport is mainly advective (high peclet), and precipitation is favoured in zones where the mixing of the elements released by dissolution is the most efficient for example, in zones where diffusion becomes an important component of transport (low *Peclet*). The localization of low *Pe* zones depends primarily on the rock structure; in olivine-rich cores, they are mainly flow paths roughly perpendicular to the main fluid direction, larger pores and/or dead-ends.

More recently experiments of Peuble et al (2015) were interested on the role of the olivine **crystallographic orientation** relative to the global fluid flow direction on the mineralization of CO_2. They conducted an experiment at 180°C percolating CO_2-rich solutions (pCO_2=10 MPa) into hot pressed olivine core. The results shows that the dissolution of olivine is controlled by its crystallographic properties as shown by the development of etch-pits only on the $(010)_{ol}$ planes and with elongated shapes parallel to the $[010]_{ol}$ axes. The precipitation of carbonates is controlled by hydrodynamic properties. They are mainly located along the moderate (for dolomite) and the minor (for magnesite) flow paths, both oriented parallel to the main fluid flow direction, which allow carbonates to be supplied with divalent

cations. They suggest that CO_2-rich fluids will induce precipitation of carbonates localized along $(100)_{ol}$ planes while favouring olivine dissolution along $(010)_{ol}$ planes.

Experiments of Van Noort et al. (2012) indicate that the **microstructure** of free surface (fractures) exerts a dominant control on peridotite dissolution and carbonation rates relative to the proportion of highly reactive minerals that compose such ultramafic rocks (e.g., pyroxene, olivine and serpentine). Serpentinized veins and mineral grain boundaries allowed fluids to penetrate the rock and promote their dissolution.

ii) Permeability

Variations on the **permeability** of rock samples were monitored using (sea)-water and CO_2-rich fluids as input solutions. Experiments using sea-water or dionized water were interested on the relationships between hydration reactions and hydrodynamic properties during the onset of serpentinization. Godard et al. (2013) perform experiments at 190°C and 19MPa on sintered olivine samples of ~12% porosity during 23 days. They injected a modified seawater (pH=8.2) at 0.2 ml/h during the first 8 days and then they decrease the rate of injection at 0.06 ml/h until the end of the experiment. They show that the decrease of the flow rate produces a sharp decrease in permeability (from 0.94 x 10^{-18} m^2 to 0.08 x 10^{-18} m^2). They noticed that the rate at which permeability decreases was fastest at low flow conditions and was attributed to serpentine precipitation in the porous network. They suggested that low flow rates produce the development of low Peclet zones forming pore-scale micro-environments that controls the serpentinization reaction path. Luhmann et al. (2017) performed experiments on natural dunite samples with very low porosity (~3%) and seawater was injected solution at a flow rate of 0.6 ml/h. The results show that the permeability slightly decreases for the experiment run at 150°C and strongly decreases for the one run at 200°C, but very small physical changes were identified on the reacted samples. One goal of this study was to produce H_2 during the whole experiment, when experiments run in close conditions failed to achieve this (e.g., McCollom et al, 2016). Luhmann et al. (2017) noticed that when H2 is continuously removed from the system, the ferrous iron is continuously oxidized into ferric iron.

Another study, conducted by Farough et al. (2016), focused on the evolution of permeability, but this time on fractured rocks. They generated tensile fractures in natural ultramafic rocks and then injected dionized water into the fractured rock at 260°C and

50 MPa during ~14 days. The results show a decrease of the fracture permeability by 1-3 orders of magnitude. They observed that serpentine crystals were formed along the walls of the fracture. However, the matrix permeability was very low and the flow was essentially focused in the tensile fracture. Finally, they highlighted that the fracture network can be sealed rapidly as a result of mineral precipitation.

Another suite of experiments were interested on the modification of the hydrodynamic properties of the system during carbonation reactions. Andreani et al (2009) conducted experiments on sintered dunite samples at 160°C and flow rate of 36 ml/h and CO_2-rich solution(pCO_2=110 bars). They observed that permeability of the rock increases with time and reach a stationary regime after a short transitional period. They show that precipitations of carbonates occur during the experiments but they estimated that this proportion of carbonation of the rock didn't alter the permeability of the rock. They suggested that a competition between chemical reactions (i.e., carbonation) and elemental transport can sustain the rock permeability under favourable flow rate conditions. They demonstrate that silicate dissolution occur along the main fluid pathways, while carbonates precipitation was restricted to zones with reduced fluid flow.

Experiments performed by Peuble et al (2015) were conducted at 180°C at two different flow rates 0.1 ml/h and 1 ml/h injected CO_2-rich solution (pCO_2= 100 bars) into sintered olivine samples. Both experiments show a strong decrease of permeability at almost constant porosity. The experiment at 1 ml/h achieves faster an impermeable value (10^{-18} m^2) compared to one run at 0.1 ml/h, even if it was maintained over a longer period. The rate of permeability decrease was on average 5 x 10^{-18} m^2/h at 1 ml/h compared to 0.9 x 10^{-18} m^2/h at 0.1 ml/h. They suggest that notable changes in permeability occurred for only minor changes in porosity, which suggests a control by the geometry of the porous network. Thus, heterogeneities in the distribution of flow paths favoured the localization of secondary minerals formation, which in turn result in the closure of the flow paths. Carbonation was overall more efficient during the high flow rate experiment because permeability was maintained over a longer period.

Luhmann et al. (2017) perform experiments on basalt samples with very low porosity (~3 %) at two different flow rates (6 ml/h and 0.6 ml/h) using CO_2-rich solution (pCO_2=12.5 MPa) at 150°C and 15MPa. They show that permeability decreases slightly during the lower

flow rate experiment due to precipitation of secondary phases and increase during the higher flow rate experiment due to high dissolution rates. However, Ultra-Small-Angle Neutron Scattering Instrument (USANS) analysis determines an overall preservation of the pore structure with no change in mineral surface roughness.

All the studies describe before point out the negative feedback effect that has the permeability on the progression of the serpentinization reaction with time. The decrease of the permeability suggests the clogging of the preferential flow paths and the cessation of reaction. However, several authors suggest that a process such as reaction-driven cracking is required to maintain fluid circulation into the rock (e.g., Kelemen and Hirth, 2012; Plümper et al., 2012).

iii) Porosity

The **porosity** determines the accessibility of water into the samples and ensures the progression of reaction. As described before for the permeability, the precipitation of secondary mineral in the pores could clog the pores and stop the fluid-rock interaction. Recent studies of Peuble et al. (2017) were interested on the micro and nano-scale structures associated with peridotite carbonation. The results shows the creation of a secondary small-scale porosity at the tip of the dissolution features (etch-pits) along the (010) planes of olivine. Carbonates crystals grow within these etch-pit structures behind the dissolution front (Fig.2.26). Proto-serpentine precipitates in the smallest olivine etch pits where restricted fluid flow favours the precipitation of this hydrous mineral (Fig.2.27). The coexistence of both processes (precipitation and dissolution) was defined as *interface coupled dissolution-precipitation mechanism*. During this process, precipitation and dissolution occur at a rate that allows the secondary porosity to be maintained over the timescale of the experiment. The system self- regulates independently of the porosity change.

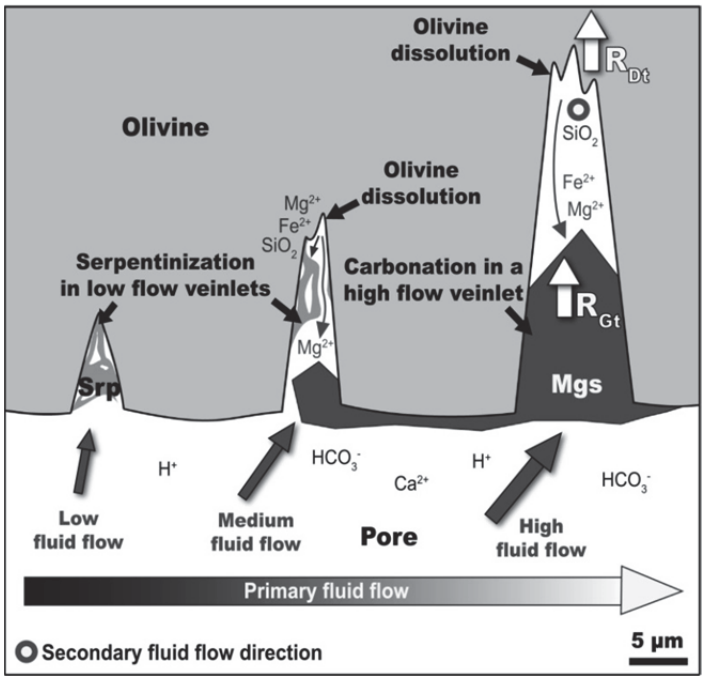

Fig.2.27. Olivine alteration process (carbonation and serpentinization) occurring in different veinlets depending on their size and flow rate (Peuble et al., 2017).

Chapter III

Methodology

1. Reactive percolation bench ICARE 3

1.1 Experimental setup and protocol

1.1.1 Set up description

Reactive percolation experiments were carried out using the percolation rig ICARE 3 (Géosciences Montpellier, France) (Fig.3.1). This experimental flow-through rig allows investigating water-rock interactions in confined permeable cylindrical samples of 9 mm diameter *(D)* and 20 mm length *(L)*. It includes an automatic system of fluid injection with three computer-controlled hydraulic pumps of, 35 mL made in Hastelloy C22 (Fig.3.1., hydraulic pump are in orange colour) that allows maintaining a constant flow rate (Q) ($10^{-6} \leq Q \leq 2$ mL.min^{-1}) and a heated confinement cell that holds the sample at constant temperature (T) (<400°C). Two pumps are dedicated to the injection of H_2O (Fig.3.1, 1 and 2) and one pump to the injection of $CO_{2(g)}$ (Fig.3.1, 3). The pressure (P < 40 MPa) is controlled by a back pressure system made of an hydraulic pump of 100 mL coupled to a pneumatic damper (Fig.3.1, 5). A confinement pressure is applied around the sample hosted into a sleeve and is controlled by a hydraulic pump of 100 mL filled with pure water (Fig.3.1, pump 4). During experiments, the difference of fluid pressure between the inlet and outlet of the sample ($0.003 < \Delta P \leq 40$ MPa) is monitored using a differential high resolution pressure sensor Rosemount 3051 (accuracy of 0.003 MPa) coupled with two pressure sensors Keller PA-33 X (accuracy of 0.035 MPa). Experimental fluid samples of volume 3 mL are collected using a pressurized computer-controlled syringe. Pump motion, valves and fluid sampling are operated by an in-house LabView-based software.

The automatic system of flow injection can operate in two modes: (i) *no mixing* and (ii) *fluid - CO_2 (g) mixing*. The first mode consists in the injection of fluid through the sample rock without gas mixed in it with CO_2 while the second one consists in the injection of the fluid mixed with CO_2 gas. The fluid mixing is operated as following: first, the H_2O-(1) pump is filled with the input solution and CO_2 pump (3) is filled with the CO_2-volume required (see *appendix A* to CO_2-volume calculation). Second, the CO_2-volume is injected into the H_2O-(1) pump. Third, the mixture between the CO_2-volume and input fluid is injected back from the H_2O-pump (1) to the empty H_2O-(2) pump. The mixture will be ready for the injection

through the sample at constant flow rate. The mixing process takes place at 25°C and at 2.5 MPa above the pressure of the experiment, to ensure all the gas is dissolved in the fluid.

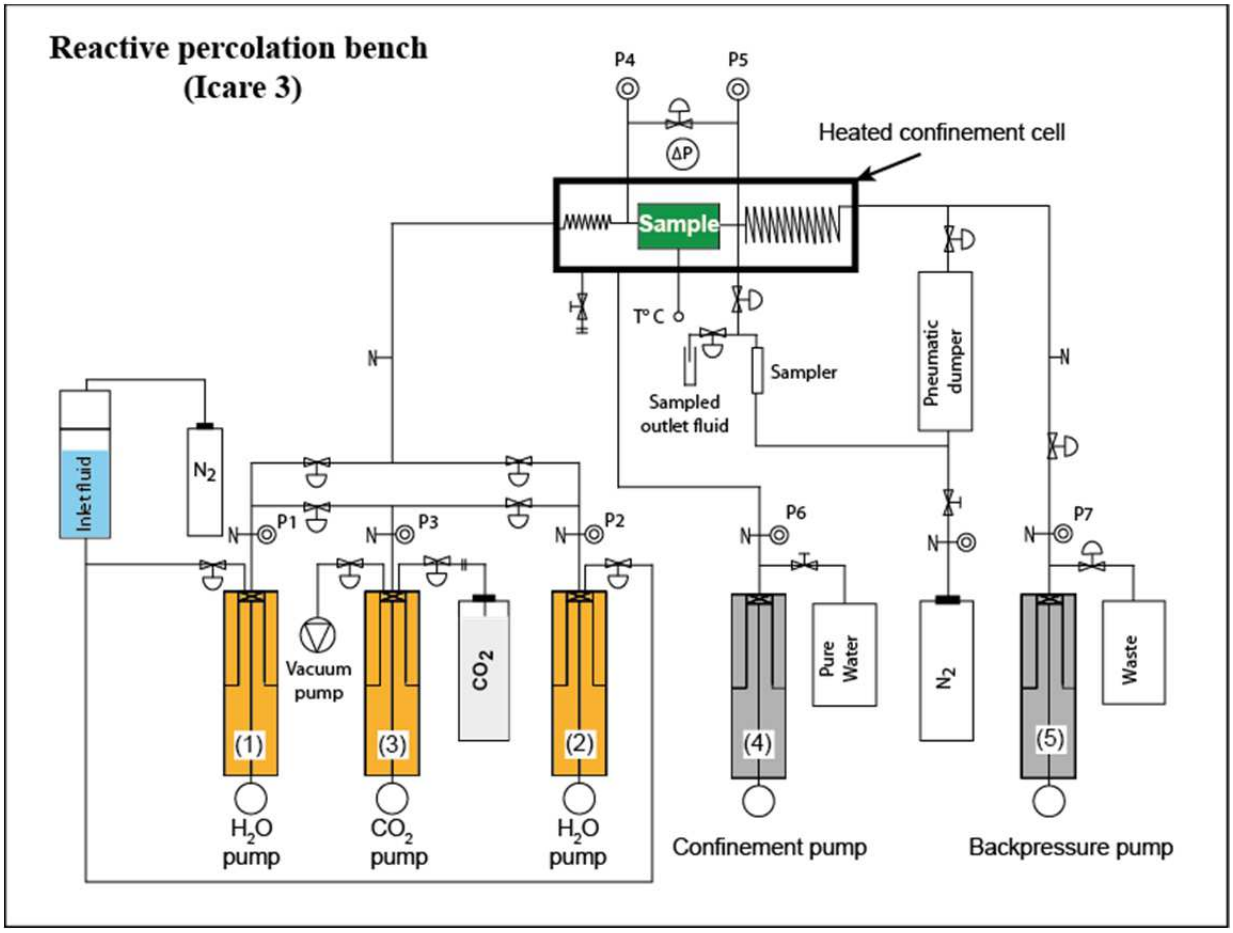

Fig.3.1. Scheme of the reactive percolation bench (ICARE -3, Géosciences Montpellier). The orange colour in the figure represents the two H_2O pumps (1 and 2) and the CO_2-pump (3) that could contain a volume of 35 mL and the grey colour represent the confinement pump (4) and backpressure (5) pumps that could contain a volume of 100 mL.

1.1.2 Experimental protocol

Before starting an experiment, the ICARE 3 needs to be rinsed with deionized water (MilliQ) during 1 to 3 days. The circulation of deionized water in the system helps to remove the remained fluid of previous experiments that could be stored in the pipelines. Once the cleaning of the bench is ensured, the sample assemblage is placed in the heated containment cell. The sample system comprises: (i) a heating coil where the injected fluid is heated, (ii) a rock sample, (iii) two fluid diffusors at the inlet and outlet of the sample, (iv) a teflon sleeve,

(v) two metallic springs above the teflon sleeve to avoid deformation and possible leaks, (vi) metallic (Au-Cu) O-ring and (vii) metallic cover that is screwed in the heating coil (Fig.3.2).

(1) First, the sample is introduced into a Teflon sleeve, made on FFKM to ensure a radial confinement pressure during the experiment (Fig.3.2c). Two types of samples were employed in this thesis, either metallic capsules filled with olivine powder (Fig.3.3) or cores of peridotite (Fig. 3.5), see *section 1.2*.

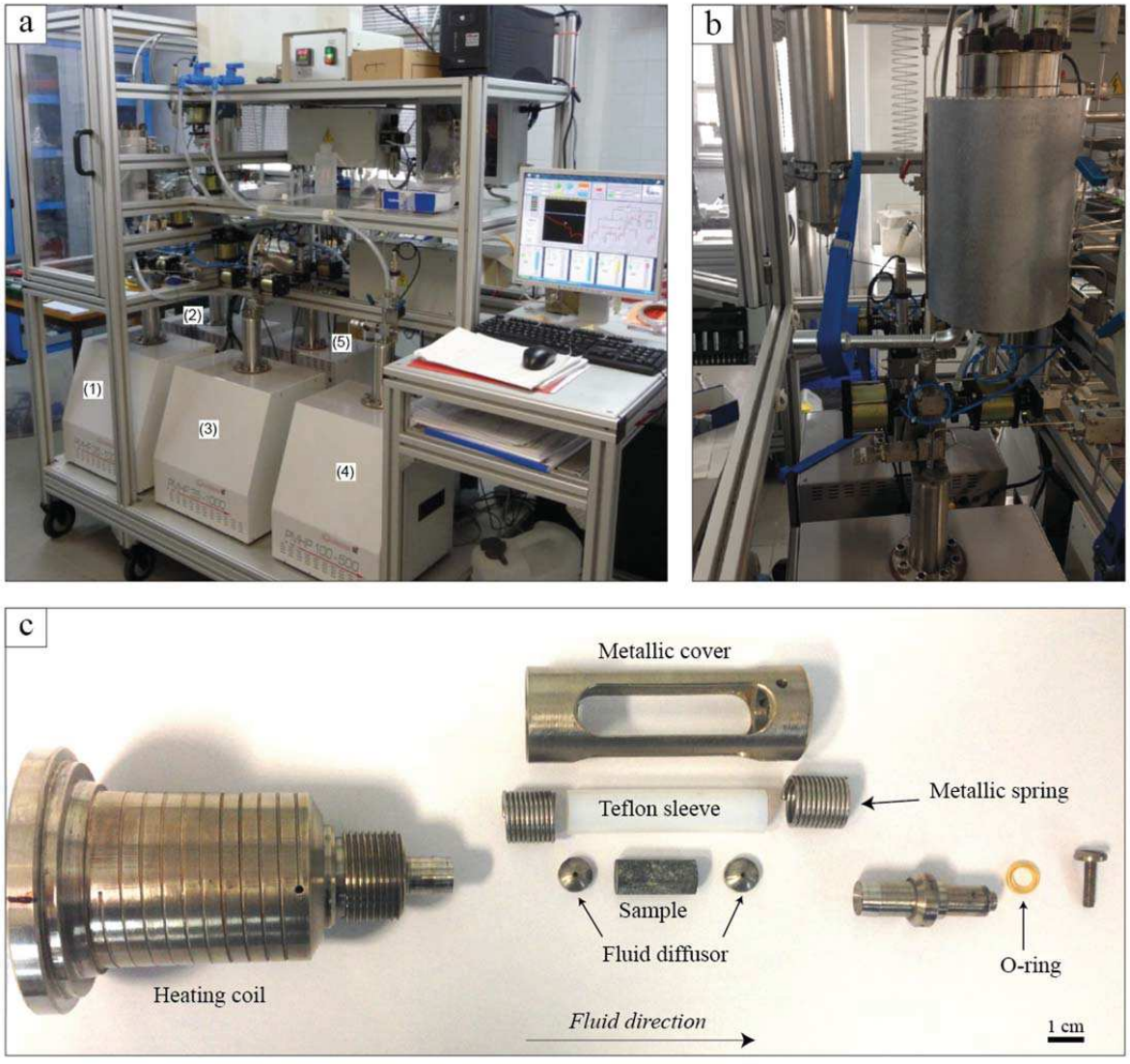

Fig.3.2. (a) Reactive percolation bench Icare 3. The numbers represents the pumps. (1) and (2) are the H2O pumps, (3) is the CO2 pump, (4) is the confinement pump and (5) is the backpressure pump.(b) Reactor cell, has a resistance of P=500 bars and T= 400°C. (c) Sampling system of Icare 3 bench. The sample assemblage consists on: (i) heating coil (ii) fluid diffusor, (iii) sample, (iv) teflon sleeve, (v) metallic cover, (vi) metallic spring and (vii) metallic O-ring.

(2) Second, two semi cylindrical diffusors were allocated in the inlet and outlet of the sample. The diffusor ensures the homogeneous distribution of the injected fluid through the sample. (3) Third, the sample assemblage is positioned inside the metallic cover (cage) and the heating coil is installed. The injected fluid flows through the heating coil before entering the sample. Two O-rings ensure the watertight in the system. The first one is set at the exit of the outlet fluids in the metallic cover and is made in Isolast j9512 FFKM. The second O-ring is set at the reactor cell and is a copper and gold Helicoflex seal (with a resistance of 600°C and 50 Mpa). (4) Fourth, the sample assemblage is positioned in the confinement cell and the injection pumps (1, 2 and 3, Fig.3.1) are isolated from the system to be filled with the input fluid. The input fluid fills the pumps H_2O-(1) and H_2O-(2) in the mode *no mixing* and if the experiments operates in the mode *fluid-*$CO_{2(g)}$ the pump 3 is filled with a volume of $CO_{2(g)}$. (5) Fifth, the confinement cell is heated at the targeted temperature for the experiment. If the pump 3 is not filled by CO_2 there is no mixing between the fluid and the CO_2 and the injection could be directly executed. Thus, the reactor is ready to be operable. (6) Sixth, once the reactor system is ready to start the experiment, a fluid sample is collected circulating through the by-pass (not circulating through the rock sample) of the reactor. It represents the initial composition of the fluid injected at the temperature and pressure chosen for the experiment. It is preferable to collect a minimum of 3 samples in order to have a more reliable value of the initial composition. (7) Seventh, the experiment is ready to start. During the experiment fluid samples can be automatically sampled recurrently.

Once the experiment is finished, the sample is removed from the reactor cell and vacuumed for 12 hours to avoid post-reaction with the fluid that could remain stored in the pores. Then the sample is dried at 25°C during almost one week (i.e. a daily measure of the sample weight is done until the weight become stable).

Fluid sampling protocol

An automatic sampling system allows collecting the fluid that has reacted with the experimental sample. Each fluid sample represents the integrated concentrations of the outlet fluids over the time required for 3mL to flow through the percolated samples. The reacted fluid is emplaced in tubes previously cleaned with HNO_3 20% (Analytika, quality for analysis) and stored at 4°C to avoid evaporation and possible precipitation. The analysis of the chemistry of the outlet fluids allows following the fluid-rock reaction. After the reacted

fluids are collected, it's necessary to clean the sampling pipelines. They are rinsed 3 times with MilliQ water and dry with air using a syringe of 10 mL volume.

1.1.3 Improvements on the experimental protocol

During this thesis analytical problems occurred related to the experimental temperature, requiring improving the experimental protocol:

A *first problem* was the deformation of the Teflon sleeve at 190°C which causes the mixing between the fluid of the confinement pump and the outlet fluids. The leaking fluid from the containment system (pure water) dilutes and potentially pollutes the outlet fluids and pollutes the rock sample. To avoid deformation of the Teflon sleeve, the sleeve was reinforced with a metallic spring (Fig.3.2). The metallic spring ensured the compression of the Teflon sleeve and thus avoided their deformation.

A *second problem* encountered was the deformation of the O-ring joint made in Isolast j9512 FFKM at 190°C. The deformation of the O-ring affects the watertight of the system and the outlet fluids were polluted and diluted by the confinement fluid. We replaced the Isolast j9512 FFKM O-ring by a metallic one (Helicoflex) which ensures a resistance of 600°C and 50 Mpa. A new teflon sleeve and O-rings were used for each of the experiments.

A total of 19 experiments and 5 tests were performed during this thesis (Table 3.1). Only 8 experiments were realized without any mechanical and protocol issue. This illustrates the complexity of the experimental work on percolation experiments.

Table 3.1. Reactive percolation experiments and tests performed during this thesis.

Experiment	Code	Date start	Date end	Duration (hours)	Type	T	P	Q	Water	pCO_2	Sample setup			Experimental issues			Conclusion
						°C	*MPa*	*mm3/min*		*MPa*	O-ring	Sleeve	Sleeve recover	Mineral plug (Stop injection)	Fluid pollution (Leak)	Mechanical problem pumps	
1	SC1	10/06/2015	17/06/2015	173	Powder	190	20	1	NSW	0.1	FFKM	Teflon	none	no	yes	no	Fail
2	SC2	22/06/2015	06/07/2015	335	Powder	190	25	5	NSW	0.1	FFKM	Teflon	none	no	yes. Small	no	Good*
3	SC3	27/10/2015	28/10/2015	29	Powder	190	25	50	NSW	0	FFKM	Teflon	none	yes	yes	no	Fail
4	SC4	30/10/2015	02/11/2015	79	Powder	190	25	60	NSW	0	FFKM	Teflon	none	yes	yes	no	Fail
5	SC5	06/11/2015	10/11/2015	103	Powder	190	25	30	NSW	0	FFKM	Teflon	none	yes	yes	no	Fail
6	SC8	15/02/2016	17/02/2016	39	Powder	190	25	8	ASW	0	FFKM	Teflon	none	no	yes	no	Fail
7	SC9	17/02/2016	22/02/2016	115	Powder	190	25	10	ASW	0	FFKM	Teflon	none	no	yes	yes	Fail
8	SC11	06/07/2016	13/07/2016	163	Powder	190	25	19	ASW	0	Metallic	Teflon	none	no	yes	yes	Fail
9	SC12	30/08/2016	06/09/2016	68	Powder	190	25	19	ASW	0	Metallic	Teflon	none	no	yes	no	Fail
10	SC15	11/10/2016	14/11/2016	814	Powder	170	25	19	ASW	0	Metallic	Teflon	Metallic spring	no	no	yes	Fail
11	SC16	16/11/2016	14/12/2016	668	Powder	170	25	8	ASW	0	Metallic	Teflon	Metallic spring	no	no	no	Good
12	SC17	05/01/2017	16/01/2017	263	Powder	170	25	19	ASW	0	Metallic	Teflon	Metallic spring	no	no	no	Good
13	SC18	05/01/2017	08/02/2017	213	Powder	170	25	4	ASW	0	Metallic	Teflon	Metallic spring	no	yes	yes	Fail
14	SC19	05/01/2017	27/02/2017	404	Powder	170	25	4	ASW	0	Metallic	Teflon	Metallic spring	no	no	no	Good
15	FP1	15/05/2017	22/05/2017	167	Fractures	170	25	100	NaCl	20	Metallic	Teflon	Metallic spring	no	no	no	Good
16	FP2	23/05/2017	29/05/2017	134	Fractures	170	25	100	NaCl	20	Metallic	Teflon	Metallic spring	no	no	no	Good
17	FP3	08/06/2017	15/06/2017	165	Fractures	170	25	50	NaCl	20	Metallic	Teflon	Metallic spring	no	no	no	Good
18	FP4	29/06/2017	10/07/2017	257	Fractures	170	25	100	NaCl	10	Metallic	Teflon	Metallic spring	no	no	no	Good
19	SC2bis	11/09/2017	09/10/2017	663	Powder	170	25	87	ASW	0	Metallic	Teflon	Metallic spring	no	no	no	Good

Test			
1	SC6	27/01/2016	Test water
2	SC7	09/02/2016	Test water
3	SC10	01/06/2016	Test Joints
4	SC13	13/09/2016	Test Joints
5	SC14	21/09/2016	Test Jackets

* only rock sample was recuperable

1.2 Starting material

1.2.1 Sample preparation

Two types of experimental samples were used for the reactive percolation experiments: (i) *San Carlos olivine (Fo90) powder* on serpentinization experiments and (ii) *fractured cores of serpentinized peridotite* on carbonation experiments.

San Carlos olivine powder samples

The rock selected for the serpentinization experiments was San Carlos olivine (Arizona, United States) (Table 3.2). The grains initially had a centimeter size. Pure grains (i.e. no associated spinel) were selected with a binocular microscope and then they were crushed and sieved in different fractions. The fraction between 100-150 μm was selected for these experiments. The selected fraction was cleaned with a solution of 2% hydrochloric acid (HCl) for 10 min in ultrasonic bath, and then the olivine grains were rinsed with MilliQ water 3 times. The cleaning cycle was repeated 3 times including a rinse step with MilliQ water. Once the olivine crystals were cleaned, they were dry at 80°C during 2 hours in a stove. Then, the metallic capsules were filled with the olivine powder, using two permeable frits at both extremities

Table 3.2. Composition of San Carlos olivine determine by electron probe micro-analyzer EPMA (Géosciences Montpellier).

(wt%)	Initial mineral composition
	Olivine
	n=3
SiO_2	41.62 ± 0.04
Al_2O_3	0.02 ± 0.01
FeO	8.63 ± 0.04
MgO	48.79 ± 0.01
MnO	0.11 ± 0.02
CaO	0.08 ± 0.002
Na_2O	< 0.01
K_2O	< 0.01
NiO	0.37 ± 0.01
Cr_2O_3	0.04 ± 0.01
TiO_2	0.02 ± 0.01
Total	99.69 ± 0.02

Two types of capsules were used on experiments: (i) Cylindrical capsule made of titanium of 2 mm of external diameter (*D*) and 20 mm length (*L*). The titanium provides low absorption for X-ray and so access into the olivine samples which is adequate for micro-tomography (XMT) analysis (*see chapter IV, section 3*). (ii) Cylindrical capsule made on stainless steel of 9 mm external diameter (*D*) and 20 mm length (*L*) (Fig.3.3).

The olivine powder was introduced in the capsules by layers; ~1 mm for the titanium capsule and ~2 mm for the steel capsule. Each olivine layer was compressed at room temperature applying pressure of ~5 MPa using an *Enerpac*® hydraulic press. The process was repeated until the capsule was completely filled. The capsules were closed with a permeable frit made on the same material of the capsules to avoid galvanic problems. Titanium frits were used for the titanium capsules and a steel frits for the steel capsules.

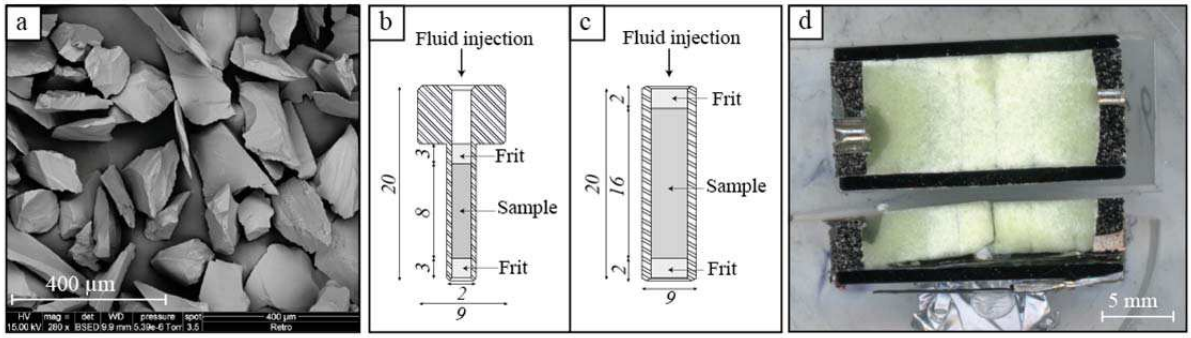

Fig.3.3. Olivine powder samples. (a) SEM image of the unreacted San Carlos Olivine powder before filling the capsules (b) Titanium capsule (c) Stainless steel capsule. Note: the dimensions of the capsules are in mm. (d) Detail of the steel capsule filled with the unreacted olivine powder. The capsule was impregnate in resin and cut in the direction of the injection fluid. The layers of olivine are visible.

Fractured cores of peridotite

Peridotite serpentinized rock samples from Oman ophiolite were used on the carbonation experiments described on *chapter V* (Fig.3.4). Two thin sections were done on the hand-picked specimen OL15, one parallel to the sample foliation (Fig.3.4.a) and the other perpendicular to the sample foliation (Fig.3.4.b). The samples were partially serpentinized (chrysotile and lizardite) with olivine, pyroxenes, magnetite and small veins of calcite identified by optical microscope. The chemical composition of the OL15 sample is described on table 3.3.

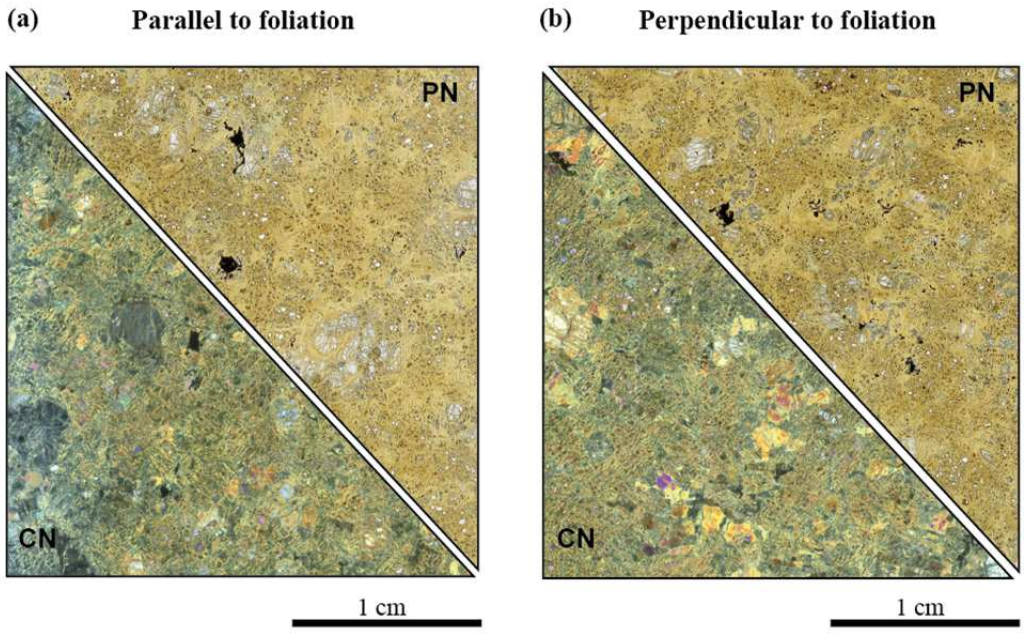

Fig.3.4. Thin section of the unreacted peridotite employed on carbonation experiments described on chapter V. The peridotite is partially serpentinized and is constituted of olivine, pyroxene, spinel, magnetite, lizardite and small veins of calcite (a) Thin section parallel to the foliation and (b) Thin section perpendicular to the foliation. PN corresponds to parallel nicols and CN crossed nicols.

Table 3.3. Chemical composition of the sample OL15 determined by XRF (X-Ray fluorescence) at Geolabs (Canada).

Oxide	wt%	**Element**	ppm
SiO_2	38.14	Co	101
Al_2O_3	0.84	Cu	<14
Fe_2O_3	7.49	Ni	2088
MnO	0.11	Pb	<12
MgO	37.61	Sr	<8
CaO	1.08	V	44
Na_2O	<0.02	Zn	43
K_2O	0.01	Zr	<10
TiO_2	0.01		
P_2O_5	<0.002		
Cr_2O_3	0.34		
BaO	<0.004		
Total	99.26		
Nitrogen 105	0.84		
Total LOI 1000	13.65		

Samples were cored from hand-sized specimen to form cylinders with 9 mm diameter (*D*) and 20 mm length (*L*) parallel to the sample foliation. After coring, samples were cut to the expected length at end surfaces.. A fracture was generated on the cores following the indirect tensile or Brazilian test (Claesson et al., 2002). The Brazilian test is a common method for determining the tensile strength of rock. It calculates the principle tensile stress, in particular at the rock core center where cracks start. Pressure was applied on the generatrix of the cylindrical cores with an *Enerpac*® hydraulic press until the first cracks appears. This avoids the core to split in two pieces and maintains the fracture inside the core. The advantage of this method is that the core maintains the rough surfaces of the walls fracture which provide more surface area for chemical reactions than if samples had been prepared by saw cutting.

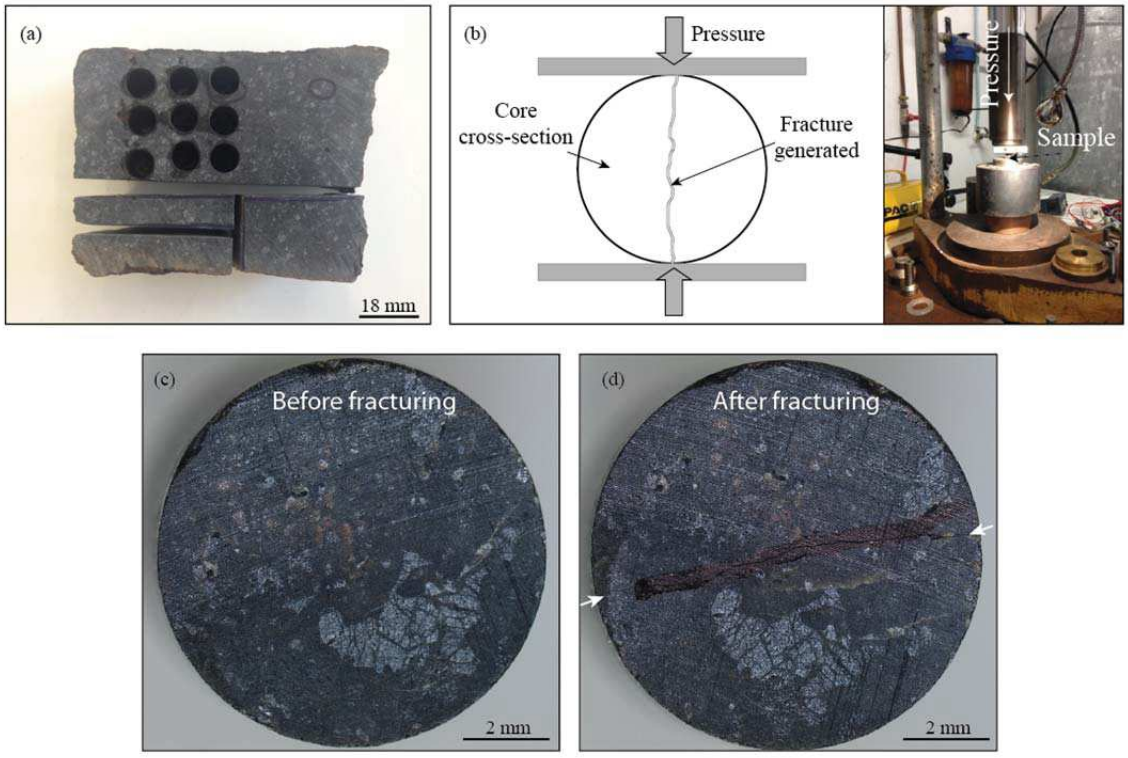

Fig.3.5. Fractured peridotites samples. (a) Peridotite slab where the cores were drilled (b) Hydraulic press employed to makes the fractures. The sample is placed horizontally and the hydraulic pressure is applied on the generatrix of the core. The pressure is distributed using a metallic square of the same dimensions of the core length. (c) Detail of the inlet of the core before fracture (d) Detail of the inlet of the core after fracturing. The white arrows indicate the fracture.

1.2.2 Injected solutions preparation

Three types of solutions were used on the percolation experiments. The first and second type was used on serpentinization experiments and the third on carbonation experiments.

The first type was *natural seawater (NSW)*. A profile of seawater from 200 m to 2000 m was collected at Villefranche sur Mer (Nice, France). To avoid biological growth seawater was treated with 0.3 ml of NaClO (Sodium hypochlorite) with 9.60% of active chlorine (Lajot) for 1L of water, then the fluids were neutralize with 0.075 ml of 2 g/dL $Na_2S_2O_3$ (sigma-aldrich) and finally seawater was filtered using a 0.22 μm filter to eliminate possible undesirable precipitates and stored in dark bottles. During the first run of experiments with natural seawater, precipitation of anhydrite ($CaSO_4$) and minor carbonates occurs at the entrance of the sample stopping the flow injection. Anhydrite has a retrograde solubility within temperature (Blount and Dickson, 1969). The high concentration of sulphate (SO_4) and calcium (Ca) in seawater at 25°C is enough to precipitate anhydrite from 150°C. This issue led us to stops using natural seawater for percolation experiments. The followed experiments were run at 170°C to ensure no mineral precipitation.

The second type was *artificial seawater (ASW)* prepared simulating theoretical composition of seawater at 200°C. Thermodynamic modelling was performed to trace the evolution of the composition of seawater with temperature using EQ3/6 geochemical code (Wolery and Jarek, 2003). The reference composition of Millero (2008) was used to compute the modelling. The solution was made using pure salts $MgCl_2 \cdot 6H_2O$, KCl, $NaHCO_3$, NaCl, Na_2SO_4, and $CaCl_2$ (Merk, Prolabo Analar normapur and Sigma Aldrich), and MilliQ water (18 MΩ·cm). The solution was stirred for 12 h to ensure complete dissolution of the salts. Then it was filtered using a 0.22 μm filter to eliminate possible undesirable precipitates. The pH measured at room temperature (25°C) was 7.56 and the conductivity was 43.5 mS/cm. The pH at 170°C was 5.8 calculated after EQ3/6 geochemical code (Wolery and Jarek, 2003) following the method of McCollom et al (2016).

The third type was a *CO_2 enriched - saline* solution. The solution was made dissolving 0.5 M of NaCl (Prolabo Analar Normapur) into MilliQ water (18M.Ω cm) at room temperature (T=25°C) and under atmospheric pressure. Industrial-grade pure $CO_{2(g)}$ was

added to the saline solution at 25 MPa of pressure and *T*=25°C, below (*S*=1.24 mol/L) which is the solubility of CO_2 (Duan et al., 2003) at the experimental conditions (*T*=170°C, *P*=25 MPa, NaCl= 0.5M) in order to ensure the complete dissolution of $CO_{2(g)}$ into the NaCl solution.. A concentration of 1 M or 0.1 M of CO_2 was added to the saline solution depending on the experiment. The initial pH of the solutions was 3.33 for the experiments with 1M and 3.83 for experiments with 0.1M. They were calculated using EQ3/6 code (Wolery and Jared, 2003) and following the method described on McCollom et al (2016).

1.3 Permeability changes

Changes on permeability of the samples *k(t)* during the experiments was calculated from the pressure difference ΔP*(t)* measured between the inlet and the outlet of the samples.

Serpentinization experiments were run with olivine powder samples i.e. a porous media. The permeability was calculated using Darcy's equation:

$$k(t) = -\frac{\mu L Q}{S \Delta P(t)} \quad \text{(Eq.3.1)}$$

with *Q* the injection rate (in $m^3.s^{-1}$), μ the dynamic fluid viscosity (0.197×10^{-3} Pa.s at 170°C and 25 MPa for a salinity of 0.5 mol/kg) (Kestin et al., 1981), Δ*P(t)* the pressure difference between the inlet and outlet of the sample in Pa and *L* and *S* the sample length (in m) and cross-sectional area (in m^2) respectively.

Carbonation experiments were run with fractured peridotites. The permeability is mainly focused on the fracture. The flow rate on fractures is calculated after the combination of Darcy law (Eq.3.2) and a cubic law for flow through two parallel plates (Huit, 1956; Witherspoon et al., 1980).

$$Q = \frac{a_h^3 \Delta P d}{12 \mu L} \quad \text{(Eq.3.2)}$$

where a_h is the hydraulic aperture of the fracture (m) and *d* is the width of the fracture (m).

The sample permeability is given by Eq. 3.1.Combining the equations, the hydraulic aperture of the fracture is:

$$a_h\,(t) = \sqrt[3]{\frac{12\mu LQ}{\Delta P(t) d}}, \qquad \text{(Eq.3.3)}$$

and the fracture permeability $k'(t)$ is:

$$k'(t) = \frac{a_h^2\,(t)}{12} \qquad \text{(Eq.3.4)}$$

Note that the ratio $k'(t)/k(t) \sim a(t)$ assuming that S/d is constant.

2. Fluid analyses

2.1 Alkalinity and pH measurements

Total alkalinity concept

Sillen (1961) argued that considering the origin of the ocean is the result of a gigantic acid-base titration in which acids such as HCl, H_2SO_4, and CO_2 that have leaked out from the interior of the earth are titrated with bases derived from the weathering of primary rock. The total alkalinity is defined as the stoichiometric sum of all bases in solution (Dickson, 1992).

$$\text{Total alkalinity (TA)} = [\text{Na}^+] + 2[\text{Mg}^{2+}] + 2[\text{Ca}^{2+}] + [\text{K}^+] + [\text{OH}^+] - [\text{Cl}^-] - 2[\text{SO}_4^{2-}] - [\text{B(OH)}_4^-] - [\text{HCO}_3^-] - 2[\text{CO}_3^{2-}] - [\text{H}^+] \pm \text{minor compounds} \qquad \text{(Eq.3.5)}$$

The charge balance in natural seawater

Alkalinity is closely related to the charge balance in seawater. The total alkalinity follows the *principle of electro-neutrality*. The sum of the charged of all anions present in seawater must equal zero. The sum of the charges of the major cations Na^+, K^+, Mg^{2+}, and Ca^{2+} are not exactly balanced by the major anions Cl^- and SO_4^{2-}. This small charge imbalance is the responsible of the total alkalinity in the ocean and is mainly compensated by the anions

of the carbonic system. The small excess of positive charge ($[Na^+] + 2[Mg^{2+}] + 2[Ca^{2+}] + [K^+]$) over negative charge ($[Cl^-] - 2[SO_4^{2-}]$) is compensated by ($[B(OH)_4^-] - [HCO_3^-] - 2[CO_3^{2-}]$). Conservative ions are ions that remain unaffected by changes of pH, pressure or temperature. The total charge concentration of the conservative cations (Na^+, Mg^{2+}, Ca^{2+}, K^+) yields 605.0 mmol/kg, while the total charge concentration of the conservative anions (Cl^- and SO_4^{2-}) yields 602.8 mmol/kg (Zeebe and Wolf-Gladrow, 2001). The small charge imbalance of 2.2 mmol/kg is equal to the total alkalinity in seawater (note: this is only correct when phosphate ammonia and bisulphate concentration are negligible).

$$\sum \text{conservative cations} - \sum \text{conservative anions} = (\text{TA}) = [\text{HCO}_3^-] + 2[\text{CO}_3^{2-}] + [\text{B(OH)}_4^-] + [\text{OH}^-] - [\text{H}^+] \quad \text{(Eq. 3.6)}$$

Conservation of total alkalinity

The total alkalinity is conservative if total alkalinity of seawater is expressed in units mol/kg, then the total alkalinity will remain exactly conserved during changes of temperature and pressure. The concentration of the conservative ions in 1 kg of seawater is unaffected by changes of temperature and pressure. However, the right hand of the Eq.3.6 triggers changes in the concentration of the chemical species due to changes on temperature and pressure. The reason for this is that the dissociation constants (*pK*) depend on temperature and pressure (Zeebe and Wolf-Gladrow, 2001). The equilibrium constant (K) is related to the standard free energy of the reaction (ΔG), thus the variation of the temperature or the pressure of the system results in a change of this energy and thus of the thermodynamic equilibrium constant.

A particularity of the total alkalinity is that the charge of the conservative ions does not change when CO_2 is exchanged between water and air. During uptake or release of CO_2, the concentrations of the individual species on the right hand of the Eq.3.6 may change dramatically because of variations in $\sum CO_2$ and pH. However, the concentrations of the conservative ions are not affected and therefore alkalinity is constant. In addition, if a strong base such as NaOH is added to the solution, the alkalinity increases because the positive charge, [Na^+], increases in solution. Thus, if a strong acid HCl is added to the solution, the alkalinity decreases because the negative charge, [Cl^-], increases in solution. Total alkalinity

is conserved during mixing with an other water because the charges of the conservative ions are additive.

However, there are several processes which lead to change the total alkalinity. One is due to changes in the charge difference between conservative cations and anions by variations with salinity. Salinity changes are due to precipitation, evaporation and formation or melting of sea ice. Another change in total alkalinity is due to precipitation of calcium carbonate ($CaCO_3$) by marine organisms (e.g., corals) and dissolution of calcareous shells or skeletons. Precipitation leads to a decrease in Ca^{2+} concentration. Thus, the charge difference between conservative cations and anions decreases and so does the total alkalinity. Minor changes of total alkalinity in the seawater are related to nitrogen assimilation by plants and release of dissolved inorganic nitrogen from organic compounds during remineralization.

Carbonate alkalinity

Carbonate (CO_3^{2-}) and bicarbonate (HCO_3^-) are the two major non conservative ions in the water, the amount of other constituents in seawater such as ammonia, silicic acid, boric acid, humic/fulvic acids and phosphates are assumed to be insignificant compared to the contributions by carbonate and bicarbonate and can be safely ignored (Hem (1985); Pankow (1991); Stumm and Morgan (1996)).

$$(CA) = [HCO_3^-] + 2[CO_3^{2-}] \qquad \text{(Eq.3.7)}$$

Thus we assume that the total alkalinity is equivalent to the *carbonate alkalinity (CA)*, which is the stoichiometric sum of $HCO_3^- + 2 \times CO_3^{2-}$. The factor 2 stems from the fact that CO_3^{2-}has to accept 2 protons in order to be converted to carbonic acid (H_2CO_3). The figure 3.6 shows that the carbonate system is described by the various proportion of carbonic acid (H_2CO_3), bicarbonate ((HCO_3^-) and carbonate (CO_3^{2-}) as a function of pH.

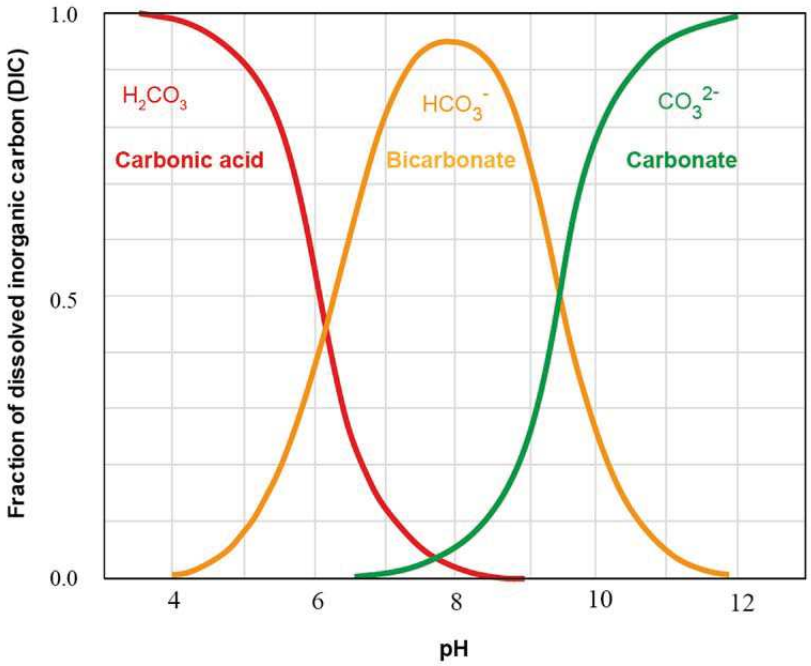

Fig.3.6. Relationship between carbon species and pH. Redrawn from Homen (1992). The relative proportions of the different carbon species depend on the alkalinity and the totaldissolved inorganic carbon (DIC); these proportions in turn determine the pH. Salinity and temperature also exert control on the proportions of carbon species. In the seawater for a pH 8.2 at 25°C, most of the carbon is in the form of HCO_3^-, with relative small amounts of CO_3^{2-} and carbonic acid $H_2CO_3^-$.

Reacted fluid sampling

The sampling of the reacted fluids from 25MPa to atmospheric pressure produces the degasification of the sample which produces the loss of the dissolved CO_2. However the alkalinity on the sample doesn't changes. The alkalinity is constant because it follows the principle of electro-neutrality described above. Thereby when CO_2 is lost from the solution by degassing, the solution consumes the H^+ to compensate the charge imbalance and thus the pH of the remained solution will increase but total alkalinity does not change (see Eq.3.9 and Eq.3.10). The carbonic system will evolve to ensure electro-neutrality on the solution. Thus, the carbonates (CO_3^{2-}) will consume the remaining protons of the solution and recombine to produce bicarbonate (HCO_3^-) (Eq.3.11) that will then combine with H^+ to generate carbonic acid ($H_2CO_3^-$) (Eq.3.10). So the net change in alkalinity is exactly zero. The pH and speciation of the fluid will change, but not carbonate alkalinity. Here are described the speciation equations of CO_2 in water:

$$CO_{2(g)} \leftrightarrows CO_{2(aq)} \quad \text{(Eq.3.8)}$$

$$CO_{2(aq)} + H_2O \leftrightarrows H_2CO_3^- \quad \text{(Eq.3.9)}$$

$$H_2CO_3^- \leftrightarrows HCO_3^- + H^+ \quad \text{(Eq.3.10)}$$

$$HCO_3^- + H^+ \leftrightarrows CO_3^{2-} + 2H^+ \quad \text{(Eq.3.11)}$$

The sum of the dissolved forms $CO_{2(aq)}$, HCO_3^- and CO_3^{2-}, is called total Dissolved Inorganic Carbon, which is denoted as DIC ($DIC = \sum CO_2 = [CO_2] + [HCO_3^-] + [CO_3^{2-}]$) (Zeebe and Wolf-Gladrow, 2001).

Measuring the alkalinity changes of the reacted fluids at 25°C provides a first estimate of the fluid-rock interactions at the experiment conditions. However, to perform the mass balance and the fluid speciation characterization at the experimental temperature (170°C) is necessary to re-calculate the pH and total carbon concentration which is done after geochemical modelling describe on section 4.

Carbonate alkalinity determination by acidimetric titration

The fluid samples were titrated by acidimetric titration at constant temperature of 25°C. The titration systems used to determine the carbonate alkalinity (CA) using a Metrohm Titrino 848 and a Metrohm LL Micro glass electrode to measure the pH. The acidimetric titration is a volumetric analysis where an acid, with a known concentration, is added to a fluid sample until is neutralized. The acidimetric titration relies on the neutralization reaction. The electro neutrality of the solution remains constant during acidimetric titration because the conservative ions are not affected by pH variation (the conservative ions don't react with H^+ in solution) (Morel and Hering, 1993; Wolf-Gladrow et al., 2006).

Hydrochloric acid is a strong acid and dissociates completely into H^+ and Cl^-. Upon addition of HCl to the fluid sample, the protons (H^+) will mainly combine with carbonate ion (CO_3^{2-}) to form bicarbonate (HCO_3^-). As the result, (CO_3^{2-}) decreases and (HCO_3^-) initially increases. The *first equivalence point (EP1)* is reached when all CO_3^{2-} is converted into HCO_3^- (Fig.3.7). Then the continuous addition of HCl into the fluid sample produce the strictly decrease of (HCO_3^-) while carbonic acid ($H_2CO_3^-$) increases because bicarbonate is converted to carbonic acid. The *second equivalence point (EP2)* is reached when all the

HCO_3^- is converted into H_2CO_3 (Fig.3.7). Thus, when all carbonate and bicarbonate ions are converted to carbonic acid means that the charge of the anions of carbonic acid has been neutralized by H^+. In seawater, the first equivalence point (EP1) is achieved at around pH of 8.3 and the second equivalence point (EP2) is achieved at around pH of 4.2 (Wolf-Gladrow, 2006):

$$CO_3^{2-} + HCl \leftrightarrows HCO_3^- + H^+ + Cl^- \quad \text{(First equivalence point EP1)} \quad \text{(Eq.3.12)}$$

$$HCO_3^- + HCl \leftrightarrows H_2CO_3^- + Cl^- \quad \text{(Second equivalence point EP2)} \quad \text{(Eq.3.13)}$$

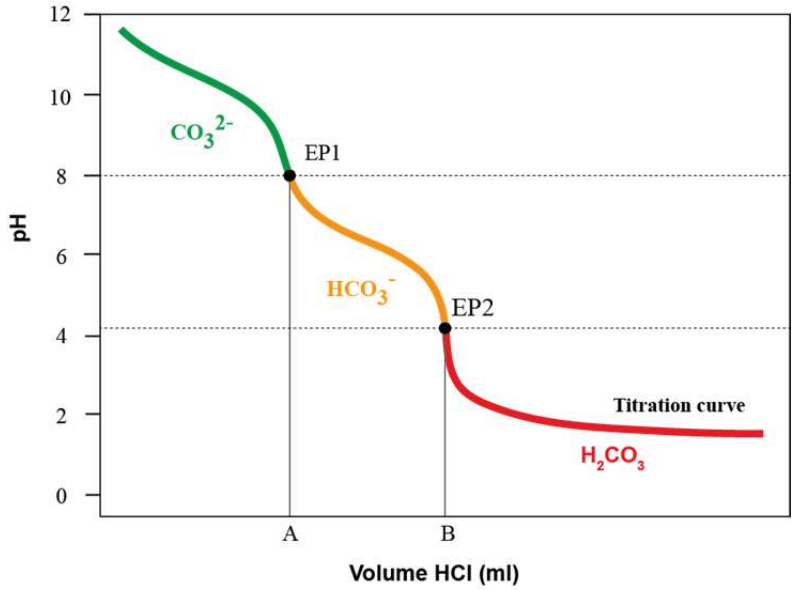

Fig.3.7. Titration curve of seawater using HCl as titration acid. EP1 is the first equivalent point which corresponds to the conversion of CO_3^{2-} to HCO_3^- and requires adding a volume A of HCl to achieve it. EP2 is the second equivalent point which corresponds to the conversion of HCO_3^- to dissolved CO_2 and requires adding a volume B of HCl to achieve it.

The *carbonate alkalinity* (Eq.3.7) of the sample is calculated with the sum of the concentrations of HCO_3^- and CO_3^{2-} in solution. To calculate the concentration of carbonate ions in solution, I use the simple specification method defined by *National Field Manual for the Collection of Water-Quality Data (NFM)* of the USGS. The method estimates the concentration of carbonate ions after the volume of acid (HCl) added to solution to achieve the EP1 and EP2 during titration. The equations to calculate $[HCO_3^-]$ and $[CO_3^{2-}]$ are reported in table 3.3.

The NFM method assumes that only carbonate (CO_3^{2-}) ions are titrated in the pH range above the carbonate equivalence point (EP1), and only bicarbonate (HCO_3^-) ions are titrated in the pH range between the carbonate equivalence point and the bicarbonate equivalence point (EP2). Also, the method assumes that the effect of OH^- and other constituents with acid/base properties are negligible. The simple NFM method could be apply to samples with pH lower than 9.3 (which is the case for the experiments performed in this thesis), because the effect of OH^- is negligible. The accuracy of the method for samples with pH less than 9.2 is less than 10% after the NFM of the USGS.

Table 3.3. Calculation of HCO_3^- and CO_3^{-2} by the titration with strong acid (HCl).

Specie	Units	Equation
HCO_3^-	meq/L	$1000*(B-2A)*C_{acid}$ (CF)/Vo
	mg/L as HCO_3^-	$61017*(B-2A)*C_{acid}*(CF)/Vo$
CO_3^{-2}	meq/L	$2000*(A)*C_{acid}*(CF)/Vo$
	mg/L as CO_3^{2-}	$60009*(A)*C_{acid}*(CF)/Vo$

where:

A is the volume of acid titrant needed to reach the carbonate equivalence point near pH 8.3, if present, in ml

B is the total volume of acid titrant needed to reach the bicarbonate equivalence point near pH 4.2, in ml

C_{acid} is the normality of the acid titrant, in equivalents per liter

CF is an acid correction factor (1.00 by default. 1.01 for many Hach digital titrator cartridge)

V_o is the initial volume of the sample being titrated, in ml.

Development of a new protocol to determine the alkalinity in small fluid sample volumes

The fluid sample collected by the ICARE 3 provides a maximal volume of ~3mL. The analysis of the cations and anions of the reacted samples lets only 1 ml available for the alkalinity measurement. Conventional titration devices required a minimum of 50 mL of fluid sample to determine alkalinity. Metrohm Titrino 848 allows measuring alkalinity of small volumes, however the minimum volume required for analysis is 2 mL because is the minimum volume required to fits the pH electrode into the vessel. However is still higher than the volume disposable (1 mL) for measurements.

During this thesis I develop a protocol to measure the alkalinity of small volumes (1 mL). I evaluate the effects that have the dilution of the reacted sample with MilliQ water on the alkalinity and pH measurements. I evaluate two dilutions: 2 and 7 and I compared with samples that are not diluted. The fluid samples were titrated with 0.01M of HCl using the alkalinity of Volvic® as reference. During this thesis the pH of the input and outlet solutions was <7, thus the contribution of ($[CO_3^{2-}]$) to alkalinity is negligible (see Fig.3.6). I determine the alkalinity of the solutions evaluating two method of calculation of the equivalence point (EP2) which corresponds to ($[HCO_3^-]$):

(i) *Dynamic equivalence point titration (DET)*: The titration mode is adequate for all standard titrations. The reagent (HCl) is added in variable volume steps. The volume increments vary as function of the slope of the curve. The optimal volume for dosing is determined from the measured value alterations of the previous dosing.

(ii) *Monotonic equivalence point titration (MET)*: The titration mode is adequate for slow titrations or slow response electrodes. The reagent (HCl) is added in constant volume steps. Measured value acceptance drift is controlled by equilibrium titration or after a waiting time.

Better precision and accuracy were obtained using a dilution factor of 2 instead of 7. The results also show that the mode DET provides more accurate (~15%) and precise (< 5 %) alkalinity values than the method MET (5.61% precision and 28.76% accuracy) for a dilution of 2 (1 mL of sample diluted with 1mL of MilliQ water) (Table 3.4). The *appendix A* includes the results of each method for dilution 2, 7 and no dilution.

Table 3.4. Alkalinity and pH measurement following the two method (MET and DET) to determine the equivalence point (EP2). The reference value of Volvic® for alkalinity is 1.21 mmol/L and pH is 7. (a) Results of alkalinity measurements and (b) results of pH measurements.

(a)

Alkalinity measurement	V_s *(ml)*	V_{MQ} *(ml)*	n	Equivalence method	Alk_{avg} *(mmol/L)*	σ	Precision %	Accuracy %
No sample dilution	2.0	0.0	10	DET	1.32	0.04	3.02	9.46
No sample dilution	2.0	0.0	10	MET	1.17	0.24	20.49	-3.22
Dilution 2	1.0	1.0	10	DET	1.39	0.06	4.65	15.21
Dilution 2	1.0	1.0	10	MET	1.56	0.09	5.61	28.76
Dilution 7	0.3	1.7	10	DET	1.64	0.13	7.79	35.87

(b)

pH measurement	V_s *(ml)*	V_{MQ} *(ml)*	n	Equivalence method	pH	σ	Precision %	Accuracy %
No sample dilution	2.0	0.0	10	DET	7.13	0.12	1.75	1.86
Dilution 2	1.0	1.0	10	DET	6.81	0.10	1.41	-2.72
Dilution 7	0.3	1.7	10	DET	6.05	0.16	2.66	-13.59

The measure of the solution pH can be done as part of the alkalinity measurement in using the first value of pH recorded during the titration before the addition of HCl. This is possible to do when the solution has a value around 7 which was the case for the injected solution employed on serpentinization experiments. The development of this techniques has two advantages: (1) this avoid requilibration of the sample with the atmosphere because it provides a fast preparation of the sample (2) it only require 1 mL of fluid sample, that save 2 mL of fluid for analysis of cations and anions. However, diluting the sample with milliQ water could slightly acidify the sample because the milliQ water has a pH of 5.5. The results show that the accuracy of the pH for a dilution 2 is less than 3%. However, the experiments under CO_2-rich solutions have an initial pH of ~3 and diluting with a pH 5.5 will induce not accurate measure of the pH. So, the pH on the carbonation experiments was done first using 1 mL without diluting the sample and then, another extra 1 mL was used for alkalinity measurements. This only let 1mL of reacted fluid for cations analysis.

Alkalinity and pH protocol

The fluid samples were titrated using the mode *Dynamic equivalence point titration (DET)*. Measurements were performed less than 5 minutes after the fluid sample was collected to minimize equilibration with the atmosphere. The preparation of the fluid sample consists on adding 1 mL of sample and 1 mL of MilliQ water in a vessel with a stirrer. The

reagent 0.01 M HCl is added in variable volume steps. After the measurement, the pH electrode is rinsed with MilliQ water and dry with a tissue. The limited volume sample collected on the experiments does not allow making three measurements of the sample in order to determine the precision of each individual analysis. Thus, the evaluation of the precision and accuracy of each measure is done by three measurements performed on Volvic® water after the measurement of the sample. However, one precaution should be taken because the gel on the membrane of the pH electrode keep holding the H^+ after an acid titration. In consequence, the pH measured would be more acid than expected. To avoid this problem, the pH electrode is rinsed with MilliQ and then is introduced for a while in the solution of pH 7 for 2-3 min until the pH becomes stable and then it's possible to start the alkalinity measurement.

2.2 Cations and anions

Spectrometry ICP-MS and ICP-OES

The *cation* concentrations of the collected fluids were analysed using Inductively Coupled Plasma Mass Spectrometry (ICP-MS) and Inductively Coupled Plasma Optical Emission Spectrometry (ICP-OES). The combination of both techniques provides a good characterization of the reacted fluid solutions.

(i) *ICP-MS* was used for metals (Ni, Cr and Co) analysis. The samples were analysed using an Agilent 7700x quadrupole ICP-MS at the AETE-ISO ("Analyses des Eléments en Trace dans l'Environnement et ISOtopes") platform from the OREME observatory (University of Montpellier). A volume of 0.1 ml of fluid sample is diluted into 9.65 ml of 2% nitric acid (Merck suprapur, dilution factor ≈ 100). The addition of 0.1 mL of an In-enriched solution (1 ppb) into the sample, is used as an internal standard to monitor the instrumental drift during analytical time. The ICP-MS provide lower detection limits for metal analysis compared to the ICP-OES which is very adequate for the fluid experimental samples which contains low concentrations in metals and trace elements (>0.001 ppb).

(ii) *ICP-OES* was used for major elements (Si, Mg, Fe, Na, K and Ca) and metals (Mn, Zn and Cu) analysis. The fluid samples have a very concentrated matrix (0.5 M NaCl) which requires high dilutions factor for ICP-MS analysis. However, the ICP-OES is adequate for concentrated matrix and doesn't require high sample dilution. The samples were analysed using an ICAP OES 7400 Thermo Scientific at the AETE-ISO ("Analyses des Eléments en Trace dans l'Environnement et ISOtopes") platform from the OREME observatory (University of Montpellier) after a dilution of 50 in acidified MilliQ water (2% HNO3) and Bismuth (1 ppb) was used as an internal standard.

The SLRS-5 and SLRS-6 standard were used in both ICP-MS and ICP-OES analysis to certify the precision and accuracy of measurements. The results are in good agreement with the expected values for SLRS-5 (Yeghicheyan et al., 2013) and SLRS-6 (National Research Council Canada, NRC). The reproducibility was better than 5% for all elements except for K, Cr, Co, Zn and Ni that was better than 15%. The accuracy was better than 5% for all elements except for Co, Ni, Cu and Zn that was better than 15% (Table 3.5). The *annexe A* shows the measured values for SLRS-5 and SLRS-6 for all the ICP-MS and ICP-OES analysis performed.

Ion chromatography: sulphates and chlorine

The *anion* concentrations (SO_4^{2-} and Cl^-) of the collected fluids was analysed using ion chromatography Dionex ICS-100 (Hydrosciences Montpellier). Samples were analysed after dilution of 500 with MilliQ water. The reproducibility and accuracy of measurements were assessed using IAPSO (Summerhayes and Thorpe, 1996) seawater standards. The reproducibility was better than 2% and the accuracy better than 2 % for both elements (Table 3.5).

Table 3.5. Reproducibility and accuracy of analysed fluids determined using SLRS-5 and IAPSO as reference standards. (Ref.) determines the reference values for SLRS-5 after Yeghicheyan et al (2013), SLRS-6 after NRC and IAPSO (Summerhayes and Thorpe, 1996). Appendix A shows the values of the standard measured.

	Standard	n	Instrument	Ref.	Avg.	Reproducibility %	Accuracy %
				ppb	*ppb*		
Si	SLRS-5	11	ICP-OES	1922.00	1907.15	4.69	-1.21
Mg	SLRS-5	11	ICP-OES	2518.00	2591.95	4.78	2.94
Mn	SLRS-5	11	ICP-OES	4.20	4.20	5.21	1.55
Fe	SLRS-5	11	ICP-OES	91.40	94.59	3.60	3.49
Ca	SLRS-5	10	ICP-OES	10320.00	10587.13	4.11	2.59
Na	SLRS-5	11	ICP-OES	5461.00	5198.12	5.51	-4.81
K	SLRS-5	11	ICP-OES	859.00	848.41	8.39	-1.23
Cr	SLRS-5	23	ICP-MS	0.22	0.22	9.22	0.99
Co	SLRS-5	23	ICP-MS	0.06	0.05	13.04	-13.53
Ni	SLRS-5	23	ICP-MS	0.48	0.44	12.28	-8.19
Cu	SLRS-5	10	ICP-OES	17.50	18.89	4.14	7.94
Zn	SLRS-5	7	ICP-OES	0.99	0.90	7.61	-9.41
Mg	SLRS-6	12	ICP-OES	2137.00	2072.00	6.83	-3.04
Mn	SLRS-6	8	ICP-OES	2.12	2.10	3.51	1.20
Fe	SLRS-6	12	ICP-OES	84.50	82.90	2.35	-1.85
Ca	SLRS-6	12	ICP-OES	8770.00	8642.00	0.85	-1.46
Na	SLRS-6	4	ICP-OES	2770.00	2634.40	1.62	-4.89
K	SLRS-6	12	ICP-OES	8770.00	8650.60	1.09	-1.36
Co	SLRS-6	6	ICP-MS	0.05	0.10	11.20	10.68
Ni	SLRS-6	6	ICP-MS	0.62	0.60	19.12	-4.12
Cu	SLRS-6	8	ICP-OES	24.00	25.10	3.22	4.61
Zn	SLRS-6	8	ICP-OES	1.76	1.70	6.20	-0.78

	Standard	n	Instrument	Ref.	Avg.	Reproducibility %	Accuracy %
				ppm	*ppm*		
SO_4	IAPSO	4	Dionex ICS-100	2775.2	2796.0	0.9	0.3
Cl	IAPSO	4	Dionex ICS-100	19354	19728.7	1.71	1.94

3. Characterization of rock mineralogy

The rock mineralogy of the samples was determined combining different analytical methods. The analyses were determined on powder or polish section. Below I describe the protocol to prepare the samples for the analysis and the analytical methods employed. After the experiments, all the samples were dried under vacuum for 12 hours at room temperature (25°C). The vacuum removes the injected fluid that remains on the pores and avoids post-experiment fluid-rock reaction (see more information on *appendix A*).

3.1 Sample preparation protocol

San Carlos olivine powder samples

The powder samples were prepared following two procedures after the experiments: polish section or powder.

(i) Polish section

A specific protocol was developed to make polish sections from the olivine powder samples (Fig.3.8). The powder was impregnated in an Epoxy resin AR2020® to consolidate the olivine grains to then cut the sample parallel to the flow injection. First, two holes were drilled one at the inlet and outlet of the sample. The sample was placed in a pressure vessel filled with the Epoxy resin. Vacuum was applied (for 30 min) on the vessel and then a pressure of 200-250 MPa was applied to ensure the resin penetrates into the all the porosity. Then the sample was sawn longitudinally (i.e. parallel to the fluid injection) and polished.

(ii) Powder

After the experiments the capsules were opened. The inlet and outlet plugs were removed with a clamp screws. Most of the powder was then collected mechanically in hitting the capsule and the remaining powder sticked to the walls of the capsule was recuperated with an awl. *Note:* The awl could alter the surface of the grains so powder was recuperated in separate tubes and used exclusively for chemical analysis.

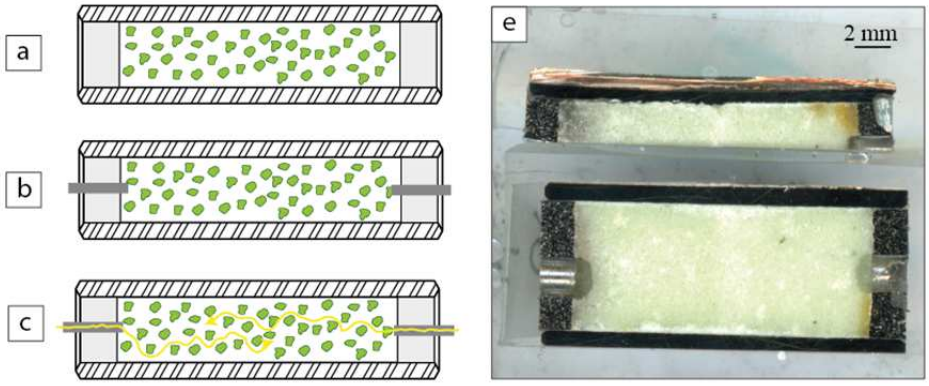

Fig.3.8. Procedure developed to make polish sections on the steel capsules after the experiments for SEM analysis. (a) Olivine grains compressed inside the capsule (b) Two holes are drilled at the inlet and outlet of the sample (c) the capsule with the two holes is introduced into a vacuum vessel filled with resin Epoxy AR 2020. The vacuum allows the resin to penetrate inside the capsule and impregnates the grains. Then the capsule is cut parallel to the fluid direction. (e) Detail of the steel capsule after resin impregnation.

Fractured cores of peridotite

After experiments, the fractured rock samples were analyzed first by X-ray microtomography (XMT) with a resolution of 2.2 µm to obtain a 3D-view of the microstructure of the reacted sample without destroying the sample (see section 3.3). Second, the reacted cores were impregnate in Epoxy resin AR2020® to consolidate the secondary newly phases formed. In order to get a cross section of the progress of the reaction from the inlet to the outlet, four sections of ~4 mm of length were cut perpendicular to the fracture with a separation of 0.5 mm, and then they were polished to get 4 polished section of each reacted core. The samples were renamed from A (inlet) to D (outlet).

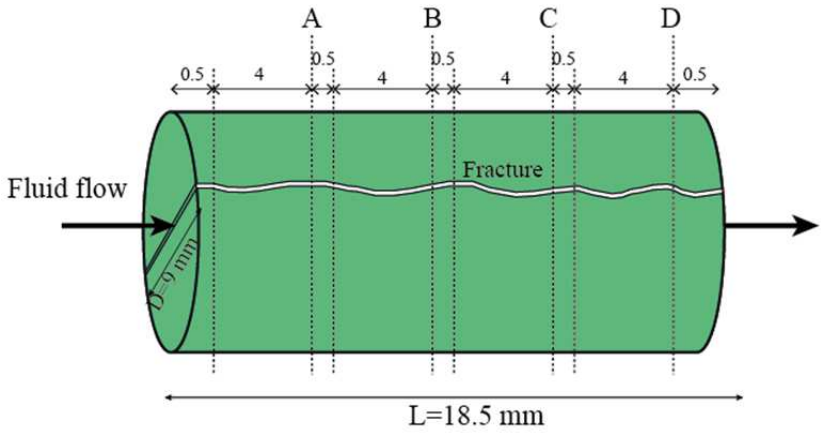

Fig.3.9. Fractured core cut on 4 sections from (A to D). The values are in mm.

3.2 Analytical techniques

Scanning Electron Microscopy (SEM-EDS)

The olivine and peridotite samples were observed by SEM-EDS images on polished section or powder before and after the experiments. This technique allows to observe the grain surface and perform semi quantitative chemistry analysis (using the energy dispersive spectroscopy (EDS)). The analyses were performed at Service de Microscopie Électronique et Analytique (MEA), University of Montpellier, France. SEM images were acquired using a FEI Quanta FEG 200 Scanning Electron Microscope with an acceleration voltage of 15kV and chamber pressure of 0.38 torr.

Thermal Gravimetric Analysis (TGA)

Volatile rich minerals were identified by TGA using a SDT Q600 V20.9. The analyses were performed on powder at the IEEM (Montpellier, France). The minimal amount of sample required for this analysis is 10 mg. The technique allows identifying minerals by the loss of weight when the sample is heated. The loss of weight at a specific temperature corresponds to the temperature of breakdown of a specific mineral (i.e., loss of structural water). Analyses were performed by increasing the temperature from 33 °C to 1200 °C at 2 $°C.min^{-1}$ under Argon (Ar) atmosphere. Since artefacts could be reproduced by buoyancy effects (gain in apparent weight), the resulted curve was corrected by performing an automatic blank curve subtraction. The curves were also corrected using a trend curve to correct the noise.

Electron Probe Micro-Analyser (EPMA)

The major element composition of primary and reacted minerals was determined by Electron Probe Micro-Analyser (EPMA) at the Service Microsonde Sud (University of Montpellier), using a CAMECA SX100 equipped with five wavelength-dispersive X-ray spectrometers (WDS). Analyses were done with 20 kV accelerating potential, 10 nA beam current and 30 s counting times for all elements measured after carbon metallization of the sample surface. Natural minerals and synthetic oxides are used as standards to calibrate the eletronic probe.

Optical Cathodoluminescence (CL)

The petrology of the samples was identified on the polished sections using a cold-cathode CITL 8200 Mk5-1 Optical Cathodoluminescence (CL) Microscope Stage coupled to an Olympus BX41 optical microscope (at Geosciences Montpellier, University of Montpellier), operating at 15 kV and 250 μA. Optical cathodoluminescence is designed to study the luminescence characteristics of minerals irradiated by an electron beam. This method is very adequate to the identification of carbonate phases in the reacted samples of this study.

RAMAN spectroscopy

RAMAN spectroscopy Renishaw Invia was performed at Charles Coulomb Laboratory, University of Montpellier on fractured peridotite samples. RAMAN analysis were made using a laser with a wavelength of 633 nm and a power of 2 mW, coupled with an open microscope equipped with a 50 objective (Leica N Plan). The spectral region investigated was from 100 to 1700 cm^{-1} and from 3650 to 3730 cm^{-1}.

3.3 X-ray microtomography

The microstructural characterization of the experimental samples before and/or after the experiments was performed using X-ray microtomography (XCT, European Synchrotron Radiation Facility (ESRF) at Grenoble (France). XCT images were acquired with a 2.2 μm resolution for fractured peridotite samples and 0.65 μm for powder samples hosted in small titanum capsule on the ID19 beamline (ESRF).

3.3.1 X-ray microtomography overview

X-ray microtomography (XMT) is a radiographic imaging technique that can produce 3D images of a specimen internal structure. The tomography is a non-destructive technique, so the properties of the specimen could be preserved for other future analysis. The technique is based on the absorption of light as it passes through a material for what is a logarithmic function of the absorptivity of the material, and the distance through which the light must

travel (Eq.3.14 and Eq.3.15). The XMT provides a 3D map of X-ray absorption of a specimen.The XMT provides a 3D map of X-ray absorption of a specimen.

The X-ray microtomography at ESRF uses synchrotron radiation. The high brilliance of synchrotron radiation results in a clear superiority in terms of achievable spatial resolution and no signal-to-noise ratio (e.g., Cnudde et al., 2013; Baruchel et al, 2006). The high flux allows one to resolve very subtle variations in absorptivity and therefore internal structure. Synchrotron radiation results from the bending of a high-energy electron beam due to a magnetic field. Electromagnestic waves are emitted when a charged particle is submitted to acceleration. In a circular accelerator such as synchrotron electrons are deviated by magnetic fields. This deviation is due to a radial force which attracts the electrons towards the centre. X-ray spectrum is reached when the energy of the electrons is high enough (i.e., GeV).

Synchrotron X-ray imaging can penetrate deeper into matter and the small wavelengths permit the study of tiny features (e.g., pore space and mineral boundaries). The achievable voxel size is limited by the sample size. This makes it often necessary to take small sub-samples typically 5–10 mm. Sample positioning and sample stability has to be considered. Tomographic reconstruction requires a rigid sample which does not move during the scan.

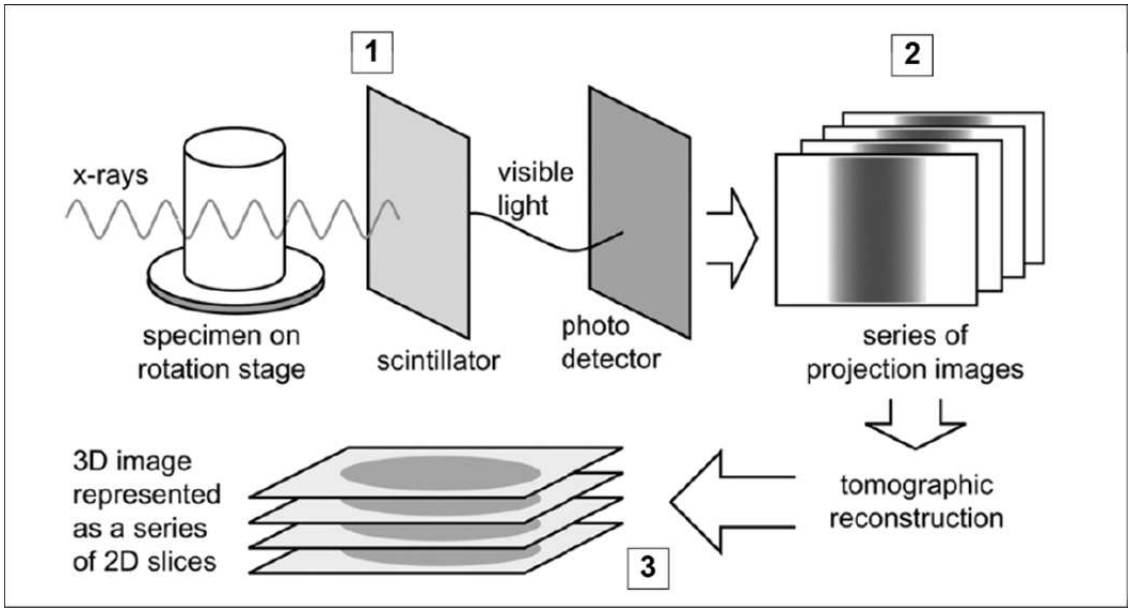

Fig.3.10. Schematic illustration of X-ray acquisition and image reconstruction processes. The series of X-Ray absorbed projection 2D images are acquired and mathematically reconstructed to produce a 3D volume of XR absorption (Landis and Keane, 2010).

The acquisition of the 3D images is typically displayed as a series of 2D images. 2D X-ray absorption images are recorded as the specimen is rotated about a single axis. This setup achieves a better mechanical stability which is required at high resolutions. Fig.3.10 shows the steps during the acquisition of a 3D image: (1) The X-rays energy through the specimen is converted on visible light by the scintillator placed on the camera CDD, (2) Then, the photodetectors placed on the camera CDD produce a 2D projection digital image, (3) using mathematical principles of tomography, this series of images are tomographic reconstructed to produce a three-dimensional digital image where each voxel (volume element or 3D pixel) represents the X-ray absorption (τ) at that point.

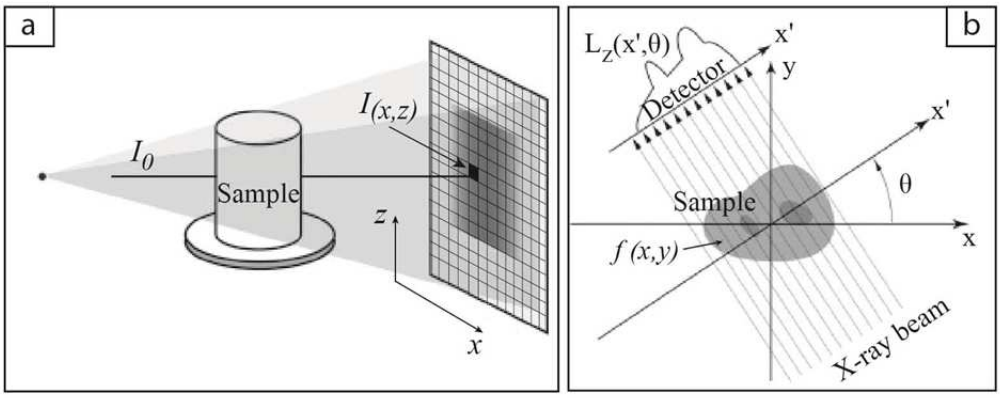

Fig.3.11. Illustration of the incident X-ray intensities when pass through the object redrawn from Landis and Keane, 2010. (a) Illustrate cone beam acquisition configuration. In this configuration, complete 2D projections can be acquired in a single step. The acquired intensity I (x,z) is modelled as a line integral of X-ray absorption along the ray path. Total absorption along the path is calculated through measurements of both I0 and I. (b) Illustration of X-ray absorption model used for tomographic reconstruction. In the x,y plane (normal to the axis of rotation) the object is represented by a spatial function of, f (x,y). Any set of X-rays passing through the object projects an absorption $L_z(x',\theta)$ on and axis x'.

Fig.3.11 shows the X-ray intensities through the sample, in which I_0 is the intensity of the beam and I is the intensity once it had passed the specimen. The X-ray intensities I and I_0 can be determined through the acquisition of the X-ray beam. The X-ray intensity (I), measured at a point (x,z), can be related to the incident X-ray intensity, I_0 (x,z), by:

$$I(x,z) = I_0\ (x,z)e^{-\tau} \qquad \text{(Eq.3.14)}$$

In which τ is the total X-ray absorption along the ray path, and can be represented as a line integral of absorptivity along the path defined by coordinates x and z. Assuming the incident and transmitted X-ray energy are measured quantities, the X-ray absorption (τ) is calculated:

$$\tau = ln(\frac{I_0}{I}) \quad \text{(Eq.3.15)}$$

Because the X-ray detector may have a baseline charge independent of the light striking it, a baseline image of a dark field is typically taken and subtracted from the incident and transmitted images. Hence, the absorption at a particular pixel located at position (x,z) is calculated by:

$$\tau = \ln(\frac{I_0 - I_d}{I - I_d}) \quad \text{(Eq.3.16)}$$

in which I_d is the dark field intensity at that point. For a typical tomographic scan, hundreds of such 2D images are produced each one representing a projection of the object at a different angle.

Tomographic reconstruction is a computationally intensive process. An inverse problem must solve the spatial function of x-ray absorption *f* (x,y) which is determined from a series of projection functions. The inverse model is solved using the Radon's transform. The 3D images acquired in this thesis were reconstructed using pyHST (Mirone et al., 2014). Once the images were reconstructed different post-processing techniques is required for visualization and computation.

3.3.2 Protocol on imaging processing

Image pre-processing on olivine powder experiments

The images acquired on the experiment done with compressed olivine powder in titanium capsules (*chapter IV*) required a special pre-processing before making any calculations and visualization. A pre-processing is made in the 2D images: (i) vertical scan overlap correction, (ii) brightness inhomogeneity correction, and (iii) registration of the

image were done in order to settle the same coordinates of the scanned zone before and after the experiments. This pre-processing was done in collaboration with Pavel Smal (ex-Post-doc Abyss ITN) and Olivier Rodriguez (Voxaya).

Vertical Overlap correction

The field of view (FOV) of the object plane is restricted by the focal depth. In our case to achieve the resolution of 0.65µm in the olivine powder experiments the FOV was 1.4 mm. We make two consecutive scans with a common zone of 0.3 mm at the end of the first scan and the beginning of the second scan (Fig.3.12). To correct this common zone a *Normalize correlation metric* was applied. The normalize correlation metric computes the correlation between pixels in the common zone of the scan 1 and the common of the scan 2. Pixel values are taken from the scan 1 image; their positions are mapped to the scan 2 image and result in general in non-grid position on it. The values at this non-grid position of the scan 2 are interpolated using an interpolator. The correlation is normalized by the autocorrelations of both scans images. When the image is corrected a single image is generated after the two scans acquired.

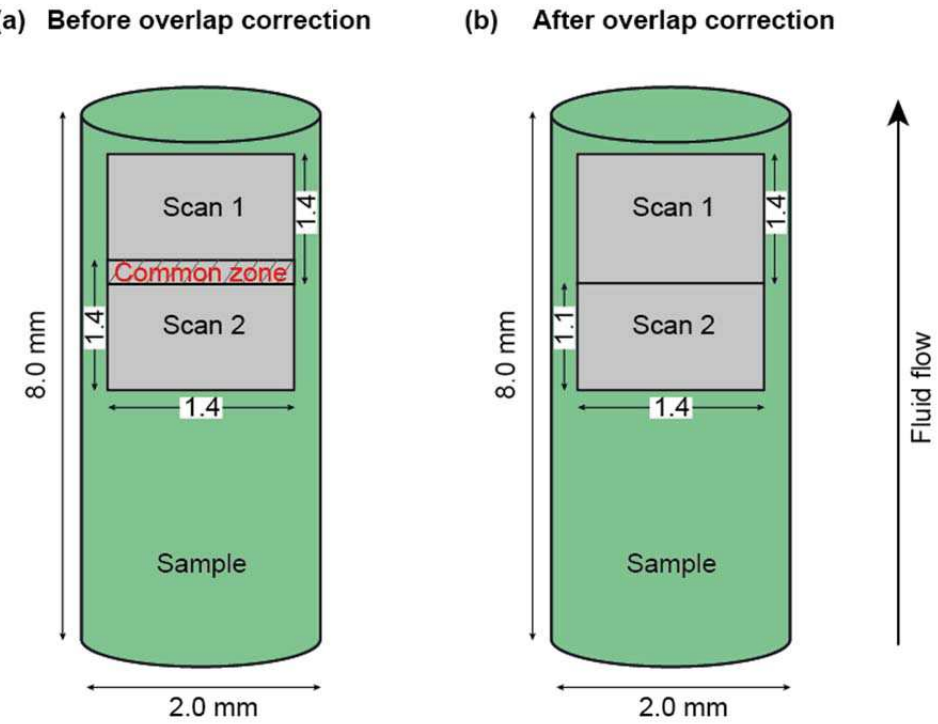

Fig.3.12. Overlap correction. (a) Two consecutive scans of 1.4 mm were acquired on the sample with a common zone of 0.3 mm (in red in the image). The scans were acquired at the outlet of the sample.

(b) After the Normalize correlation metric was applied the common zone was deleted on the scan 2 and the two scans were joined representing a scanned zone of 2.5 mm length. The design is not at scale and the lengths are in mm.

Brightness inhomogeneity correction

The images acquired by X-ray microtomography had brightness inhomogeneity caused by artefacts during the image acquisition (Fig.3.13). This issue makes the image segmentation difficult. To correct this issue a N4 algorithm was applied. The N4 algorithm is ITK (Insight Segmentation and Registration Toolkit) implementation of N3 algorithm (Noparametric Nonuniform intensity Normalization) developed by Sled et al (1998). The algorithim makes little assumptions about the data in order to estimate the bias-field (intensity inhomogeneity) it assumes that the bias field is smooth and smooths the image histogram. The bias field is estimated iteratively by computing the expected value of each voxel given the histogram of the volume after deconvolution with a Gaussian Wiener filter and smoothing the difference to the current volume in logarithmic space. The algorithm was applied to the both scan images (before and after) in order to get the same level of grey in both images (Fig.3.13).

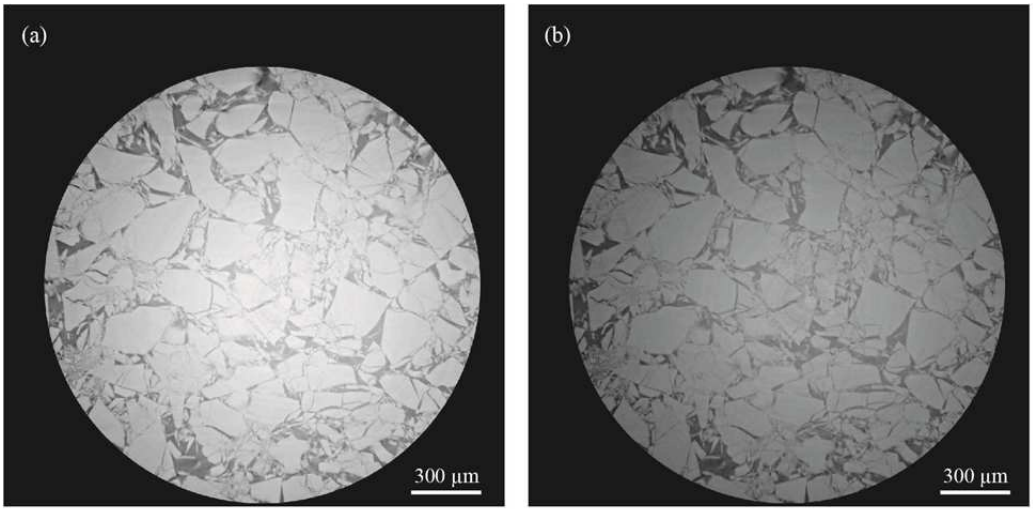

Fig.3.13. (a) Image before brightness inhomogeneity correction. The centre has a gradually increase on brightness which disturbs the values during segmentation (b) Result of the brightness inhomogeneity correction. The corrected image has a homogenous brightness.

Registration

The scans taken before and after the experiment are usually acquired in different coordinates. In order to compare the two scans is necessary both scans have the same coordinates. Registration aims to find coordinate transform that brings two images in the same coordinate. The Landmark Registration requires user defined input: two sets of corresponding landmark points, one from Fixed Image, and one from Moving Image. Based on these landmarks the initial transformation is estimated and further turned by gradient methods. The method was done applying the algorithm developed by Umeyama (1990). The final refinement of the result of registration was implemented using a sequence of gradient fixed step descent alternating with conjugate descent and followed by gradient descent line search (fastest gradient descent). Then, the two scans have a common zone (Fig.3.14a) that is the region of interest used for segmentation and further processing. This method allows superposes the grains before and after the experiments and identify dissolution, precipitation and movement (Fig.3.14b).

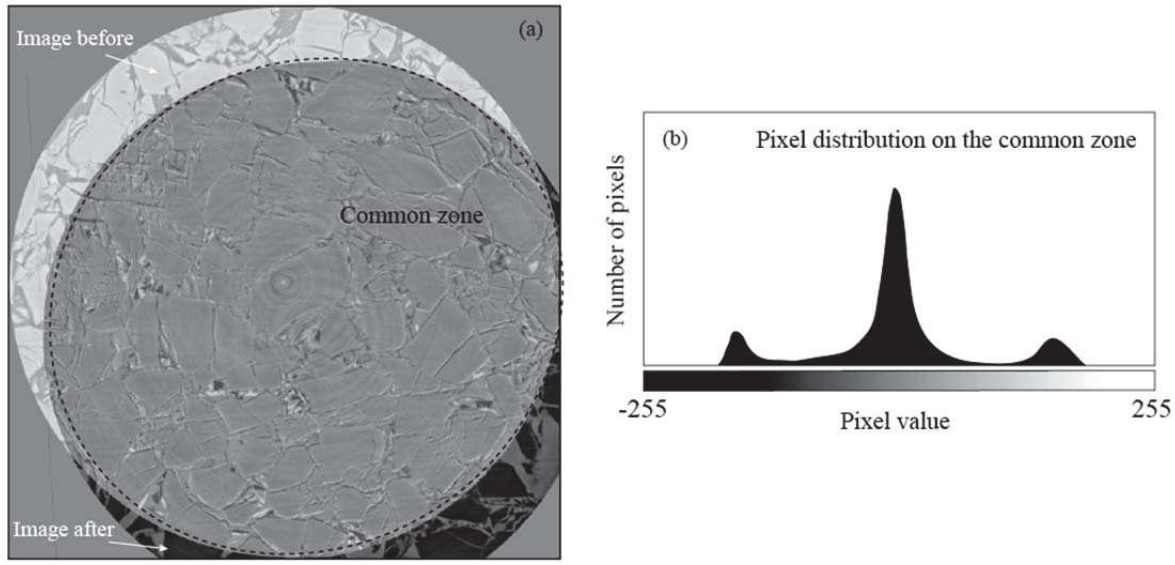

Fig.3.14. Illustration of the difference between the images before and after once registration is corrected (the grains have same coordinates). (a) The difference between the image before and image after leads to a common zone. (b) Histogram of the common zone. The two images show similar matrix pixel values.

3.3.3 Image visualization

The visualization of the images was done in 2D combining Image J, Voxilon and Paraview codes and the 3D visualization was performed using Avizo® software (Fig.3.15).

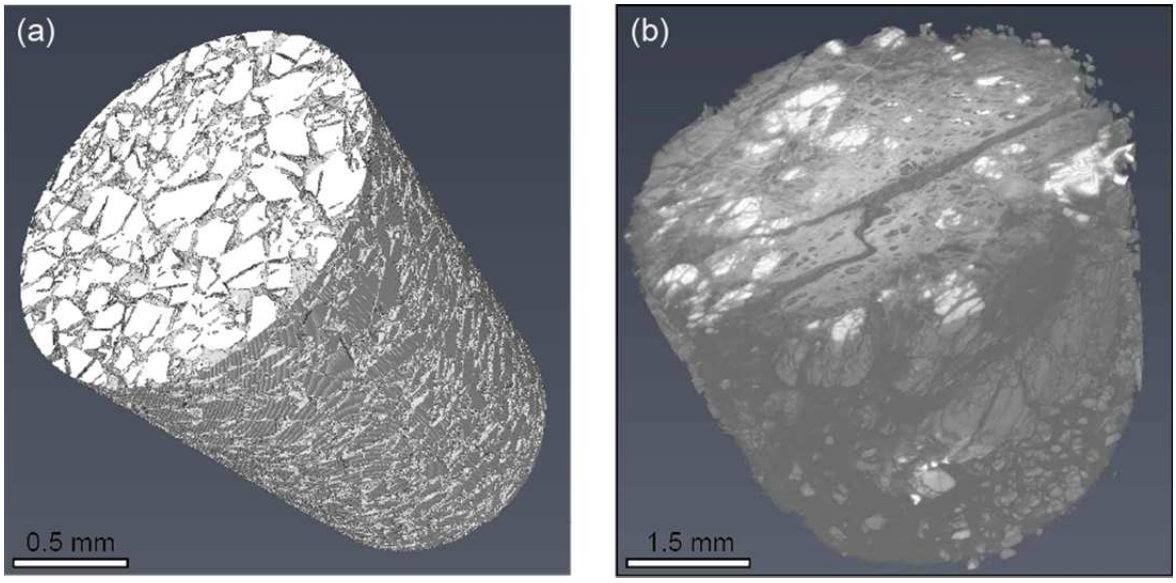

Fig.3.15. Visualization of the acquired 3D image of the reacted samples using Avizo® software. (a) Experimental sample of serpentinization experiments using a Ti-capsule (chapter IV) and (b) fractured peridotite image after carbonation experiments (*chapter V*).

3.3.4 Segmentation

After the acquisition, reconstruction and pre-processing; the 3D image is ready to be segmented. The segmentation is a process that separates the different phases that constitute the specimen. More precisely, image segmentation is the process of assigning a label (threshold) to every pixel in an image such that pixels with the same label share certain visual characteristics. The usefulness of a thresholding procedure is however greatly influenced by the presence of noise in the data.

In our samples, there are two main domains, the pore space and the matrix (Fig.3.16). The matrix it's mainly formed by one mineral, olivine, in the case of olivine powder experiments and several minerals, olivine + serpentine + pyroxenes + spinel + carbonates for fractured peridotite experiments. The segmentation of the images is based on grey value thresholding (Cnudde and Boone, 2013). Each mineral phase has a different absorption

coefficient, so then they will have different level of grey. Likewise, each mineral phase will have a grey value thresholding (Baveye, 2010). Nevertheless, when analyzing reconstructed volumes of similar objects, this error is a constant thus making comparison of these similar objects possible (Cnudde and Bonne, 2013). This error is calculated by the mean of three segmentation of the evaluated image. Two methods of segmentation (Fig.3.16) were evaluated on the images by: i) Simple thresholding and ii) Hysteresis thresholding. The simple form of thresholding simply compares each pixel intensity with a reference (threshold) value. Any pixel value above the reference value will be set as foreground.

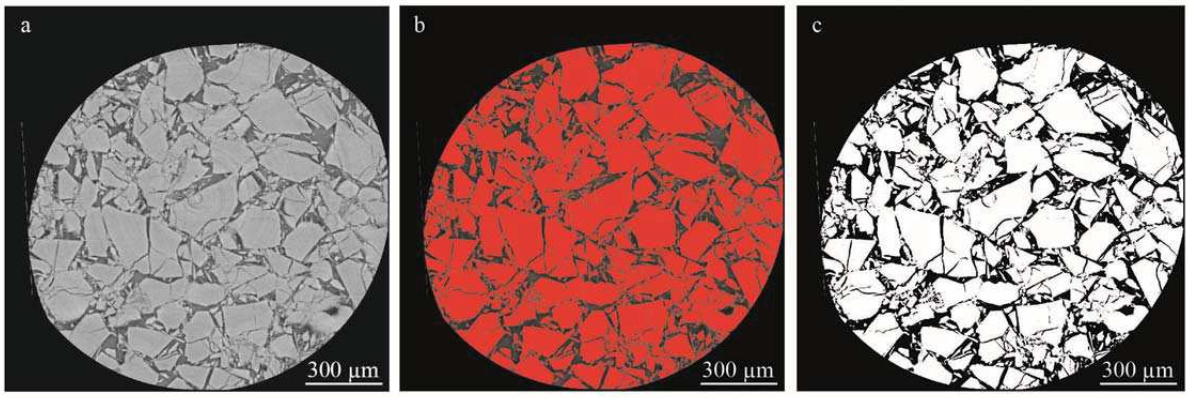

Fig.3.16. Procedure to segment XR tomography images. (a) Original image acquired for olivine powder experiments at 0.65 µm of spatial resolution. (b) The operator chooses the matrix threshold based on their grey value. (c) Image segmented; matrix is in white and pore is in black.

i) Single thresholding

This segmentation method was done using *Image J* code. I employed the default method on auto thresholding based on IsoData algorithm or also known as *iterative intermeans* (Ridler and Calvard, 1978). The procedure divides the image into object and background by taking an initial threshold (single value), and then the averages of the pixels at or below the threshold and pixels above are computed (Fig.3.17a). The averages of those two values are computed, the threshold is incremented and the process is repeated until the threshold is larger than the composite average.

i) Hysteresis thresholding

This segmentation method was done using Voxilon code from Voxaya®. The hysteresis thresholding uses a criterion that combines the pixel value in an image and the

value of neighboring pixels to decide if a pixel belongs to background or foreground (Fig.3.17b). The criterion of hysteresis thresholding consists in two separated thresholds τ_1 and τ_2 (Vera et al., 2011; Smal et al., 2018).

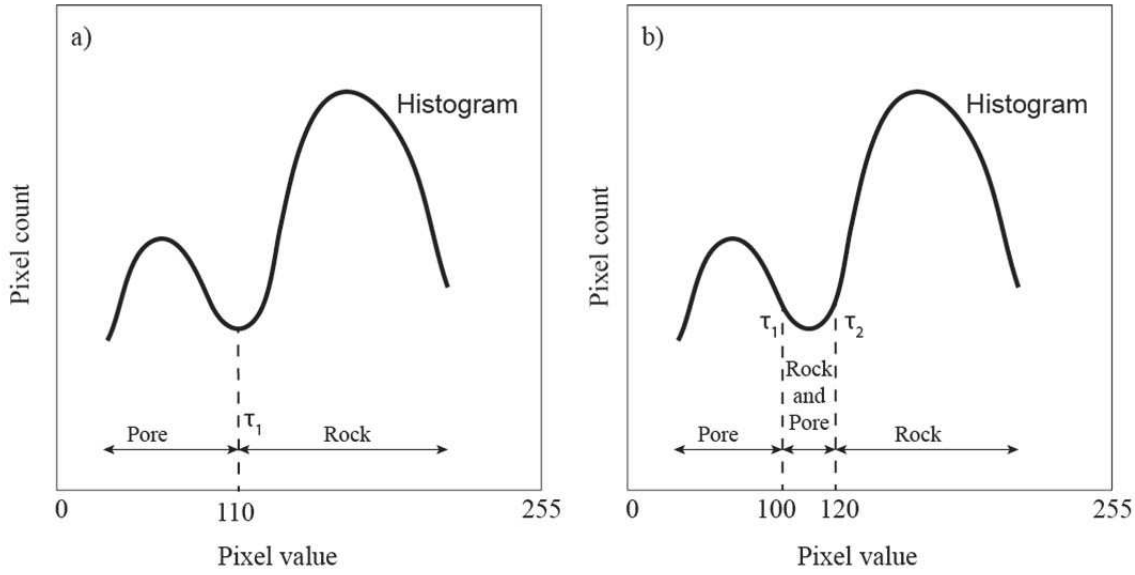

Fig.3.17. (a) Segmentation by single thresholding, the τ_1 value defines the limit between void and solid phaes. (b) Segmentation by hysteresis. The values τ_1 and τ_2 define the initial void and solid phases.

3.3.4 Image computation

Porosity

The porosity is computed after image segmentation. The total porosity φ of the sample is simply the ratio of the pore space to the total number of voxels. The local porosity φ_z can also be calculated for each slice along the flow axis (Noiriel, 2009).

$$\varphi = \frac{N_{voxel\,(pore\,space)}}{N_{\,voxel\,(total)}}\; x\; 100 \qquad \text{(Eq.3.17)}$$

where φ is the porosity in %, $N_{voxel\ (pore\ space)}$ is the number of voxels of the pore space and $N_{voxel\ (total)}$ are the number of voxel of the pore space and the matrix.

Geometric surface area

The surface area is an important parameter, because the mineral-fluid interface partially controls the kinetic behaviour in many geological systems. Thus, the characterization of the surface changes result from dissolution or precipitation. The geometric surface area (m^2) of the porous medium is defined as the number of pore-mineral pixels N_{pix} multiplied by the pixel surface area (S_{pix}=0.65 × 0.65 μm^2).

$$S_g = N_{pix} \; x \; S_{pix} \qquad \text{(Eq.3.18)}$$

Intensity profiles

The measurement of the pixel intensity (reported on a grey scale) in the acquired image between two points allows to have an estimation of the changes of phases (minerals and/or voids). This was performed on the reacted cores of fractured peridotite between two points, each point was located on eachside of the fracture. This method allow me to identify the dissolution front on the experiments with the changes of the pixel intensity to light-grey on the unreacted zone to dark grey on the reacted zone.

4. Geochemical modelling

Owing to issues of complexity and the time scales involved, it is often not possible to conduct sufficiently realistic laboratory experiments to observe the long-term behavior of most geochemical systems. Geochemical models can be used, however, to both interpret and predict processes that may take place over time scales that are not directly achievable in experiments. Thus, they are a valuable predictive tool that can be used to bridge the gap between laboratory experiments and the long-term behavior of geochemical systems. In this thesis different geochemical code has been used as support for interpreting the reactive percolation experiments.

4.1 Geochemical modeling overview

A geochemical model is a theoretical construct used to predict certain properties of water containing dissolved electrolytes. It can help to identify geochemical processes that regulate the concentration of dissolved constituents and may help quantify the effects of temperature, speciation, sorption and solubility on the concentration of dissolved constituents.

All geochemical models are based upon principles of mass conservation (mass balance accounting). Mass is neither created nor destroyed in the system, but transferred between solid, aqueous and gaseous phases. Geochemical models can incorporate transport processes in the simulations however in this thesis I don't consider the transport processes. Here I used ***geochemical reaction models***, also called *batch models*.

Conceptual formulation of geochemical reaction models and numerical solution procedure

The conceptual formulation of a geochemical reaction models is based upon analogy with a stirred tank reactor where the distribution of chemically reactive species is calculated for an aqueous solution. There are *geochemical equilibirum models*, based on the assumption of thermodynamic equilibrium reached in a relative short time. The chemical equilibrium is the state in which both reactants and products are present in concentration which has no further tendency to change with time. There are *Geochemical kinetics models*, which include time factor. There are three different types of geochemical models: (i) *speciation-solubility models*, these models evaluate concentration/activities of chemical species existing in a solution in equilibrium with solids and/or gases of a known composition (ii) *reaction-paths models*, attempts to predict the resulting composition of a system when a fluid with a given chemical composition reacts with a particular mineral or mineral assemblage. At each step in the calculation, the aqueous speciation is calculated and secondary minerals are dissolved or precipitated in order to maintain chemical equilibrium(iii) *inverse (mass balance) models,* attempts to determine reactions that have happened between interaction of a already known chemical solution and mineral composition. In this thesis speciation-solubility and reaction paths models were used.

In all geochemical models, the reactions that describe the aqueous compositions must be defined in terms of a set of *basic components*. A basic component (e.g., Ca_{total}) is the chemical formula unit used to describe a system (Zhu and Anderson, 2002). The basic components are the minimum set of fundamental or basic species (e.g., H_2O, H^+, OH^-, Ca^{2+}, Mg^{2+}…) that are required to describe all the aqueous species (e.g., $MgOH^-$) present in the aqueous solutions. Thus, all aqueous species can be assembled from combinations of the basic species. The total species concentration in solution is defined to equal to the concentration sum of all the aqueous species in solution for each basic species. For example, the total carbonate system is described in terms of basic species (H_2O, H^+ and CO_3^{2-}) and the relevant aqueous species would be (H_2O, H^+, OH^-, CO_3^{-2}, HCO^- and H_2CO_3). The carbonate (CO_3^{2-}) concentration would then be equal to the concentration sum of CO_3^{-2}, HCO^- and H_2CO_3.

The conservation of total species concentration in solution is determined by the chemical equilibrium. The chemical equilibrium calculation is solved in terms of:

(1) Gibb's free energy minimization (G). A system that has a composition, temperature and pressure constant and find the chemical equilibrium will evolve in order to minimize their energy; $\Delta G^0 = \Delta H^0 - T\Delta S^0$, where ΔH^0 is the entalphy change and ΔS^0 is the entropy change and T the temperature.

(2) Law of mass action equations involving equilibrium constants. The equilibrium constant (K) expresses the relationship between the amounts of products and reactants present at equilibrium in a reversible chemical reaction at a given temperature.
Considering a chemical reaction:
aA + bB = cC + dD
The equilibrium constant is:

$$K = \frac{\{C\}^c \{D\}^d}{\{A\}^a \{B\}^b} \qquad \text{(Eq.3.19)}$$

K is the equilibrium constant (which depends on temperature). The curly brackets ({}) represents the activities for each species. In chemical thermodynamics it is more convenient

to work with the logarithm of K in base 10, thus, log K= c log {C} + d log {D} – a log {A} – b log {B}

The relation link between the equilibrium constant K and the Gibbs free energy change is:

$$\Delta G^0 = -RTlnK \quad \text{(Eq.3.20)}$$

where ΔG^0 is the Gibbs free energy, R is the gas constant in J.mol^{-1}K^{-1}, T is the temperature in Kelvin (K), thus the equation can be rearranged to log K:

$$\log K = -\frac{\Delta G^0}{2.303 \cdot RT} \quad \text{(Eq.3.21)}$$

The temperature dependence of the ΔG^0 and log K is related after the Van't Hoff equation, the complete temperature dependence of the log K is determined by the enthalpy change ΔH^0 alone.

$$\log K = \log K_0 + \frac{\Delta H^0}{2.303\, R}\left(\frac{1}{T_0} - \frac{1}{T}\right) \quad \text{(Eq.3.22)}$$

where K_0 is the equilibirum constant determined to a standard temperature (T_0) and K is the equilibirum constant and temperature respectively for an arbitrary temperature (T).

The geochemical codes used in this thesis (EQ3/6, phreeqC and GWB) resolve the chemical equilibrium involving equilibrium constants. The mathematical formulation results in a system of non-linear algebraic equations that must be solved using a numerical method. The three codes use the iterative Newton-Raphson technique to solve the equation system.

Speciation-solubility models

Speciation-solubility models calculate the distribution and concentration of dissolved species between ions and aqueous complexes and saturation indexes for different minerals. The *speciation* part consists in the calculation of the distribution and concentration of the

dissolved species in solution. The activity (a_i) is the thermodynamic concentration or the fraction of total concentration which participates in geochemical reactions. It is calculated as a product of activity coefficient (γ_i) and concentration (m_i):

$$a_i = \gamma_i \cdot m_i \quad \text{(Eq.3.23)}$$

The activity coefficients in reality are complex functions of the composition of the aqueous solution. In electrolyte solutions, the activity coefficients are influenced mainly by electrical interactions. Most of their behaviors can be correlated in terms of the ionic strength (I) defined by:

$$I = I/2 \sum m_i z_i^2 \quad \text{(Eq.3.24)}$$

where m_i is concentration and z_i is the charge of ion i.

The ionic strength is a measure of the charge of a solution (i.e., saline solutions have higher ionic strength). The activity coefficients are calculated using Debye-Hückel equation for ionic strength I<0.1, Davies equation I<0.5, and Pitzer's equation for very high ionic strength. However, Pitzer's parameters are limited in terms of the components that can be treated. The B-dot equation is the extended Debye-Hückel equation adequate for electrically charged species.

The Debye-Hückel equation (Debye and Hückel, 1923) is:

$$\log\gamma_i = -Az_i^2 \frac{\sqrt{I}}{1+B_a\sqrt{I}} \quad \text{(Eq.3.25)}$$

where γ_i is the activity coefficient of ion i, z_i is the ion charge, A, B are temperature-dependent constant, and a is parameter corresponding to the size of the ion.

The Davies equation (Davies (1962)) is:

$$\log \gamma_i = -A_{\gamma,10}\, z_i^2 \left(\frac{\sqrt{I}}{1+\sqrt{I}} + 0.2I\right) \quad \text{(Eq.3.26)}$$

where A is temperature-dependent constant 0.2 and sometimes also is taken as 0.3. The Davies equation is the simple extended Debye-Hückel equation. The activity coefficient is given in terms of the base ten logarithm, instead of the natural logarithm. The Debye-Hückel Aγ parameter bears the additional label "10" to ensure consistency with this. Note that it expresses all dependence on the solution composition through the ionic strength. The Davies equation is normally only used for temperatures close to 25°C.

The B-dot equation of Helgeson (1969) is:

$$\log \gamma i = \frac{A\gamma_{,10}\, z_i^2 \sqrt{I}}{1+\dot{a}_i\, B\gamma\sqrt{I}} + \dot{B}I \qquad \text{(Eq.3.27)}$$

where, $\dot{a}_i$ is the hard core diameter of the species, $B\gamma$ is the Debye-Hückel B parameter, $A\gamma$ is a constant parameter, $\dot{B}$ is the characteristic B-dot parameter, Zi is the electrical charge, I is the ionic strength. The B-dot equation is the extended Debye –Hückel equation. These equations differ in that the Davies equation because they incorporate a coefficient in place of which depends on the electrical charge of the species in question. The B-dot equation it's adequate for electrically charged species and span a wide range of temperature (up to 300°C).

The *solubility* part calculate the degree of saturation of the solution with respect to a given mineral, this is calculated after the saturation index (*SI*):

$$SI = \log \frac{IAP}{K_{sp}} \qquad \text{(Eq.3.28)}$$

where IAP is the ion activity product, for example for the gypsum is IAP= $[Ca^{2+}]$ $[SO_4^{2-}]$ and K_{sp} is the solubility product which determines the equilibrium constant for dissolution/precipitation of a mineral. SI=0 indicates the solution is in equilibrium with respect to a given mineral. If SI>0, solution is supersaturated and mineral should precipitate, and if SI<0, solution is under saturated and mineral should dissolve (if the mineral is present in solid phase in contact with the solution). The saturation index indicates the direction of the reaction but doesn't provide any information about the rate of the reaction.

Reaction-path models

The reaction-path models are used to predict the evolution of a reaction system (Wolery and Daveler, 1992). In this case, initial water chemistry and initial minerals are known and are not in equilibrium and the aim is to predict the water chemistry and mineral assemblage when the system reaches equilibrium. The concept of the model is:

Initial water + reacting phases = predicted water + products

As the overall reaction progresses, the composition of the aqueous solution changes (including *pH*, *Eh*, etc) and the solution may become saturated with new minerals. The model stipulate that the reacting mineral phases dissolve when SI<0 and also mineral phases precipitate when their SI values are higher than 0.

The data base is the core of the geochemical models (see section 4.3). It encompasses the thermodynamic properties of the species (basis, aqueous, minerals and gases) that will be included in the simulations. The creation of data bases requires the calculation of the standard molal thermodynamic properties of reactions among minerals, gases, and aqueous species as a function of temperature and pressure of equilibrium constant, activity coefficients etc. Differences of thermodynamic data bases attribute to differences on the parameters for temperature correction and activity equations. The employment of two different data bases to resolve the same geochemical issue could result in large uncertainties.

4.2 Geochemical modelling codes

EQ3/6 v.8

EQ3/6 v.8 is a software package originated in the middle 1970s (Wolery, 1978). It was originally developed at Northwestern University to model seawater-basalt interactions in mid-ocean ridge hydrothermal systems. The software performs geochemical modelling computations encompassing fluid mineral interactions and/or solution-mineral-equilibria in aqueous systems (Wolery and Jarek, 2003). The basic purpose of EQ3/6 is to make two kinds of calculations (speciation-solubility and reaction path modelling) pertaining to aqueous

solutions and aqueous systems (Table.3.6). Activity coefficients for aqueous species were calculated using the B-dot equation (Helgeson et al., 1981). EQ3/6 was the principal code used in this thesis to calculate speciation and reaction path calculations but additional codes such as phreeqC (describe below) was eventually used to corroborate calculations.

PhreeqC

PhreeqC v.3 is a computer program developed by Parkhurst and Appelo (1999) designed to perform a variety of aqueous geochemical calculation including speciation-solubility and reaction path (Table 3.6). Originally is a batch reaction model, but one-dimensional transport calculations with a wide range of physical and chemical processes was included. PhreeqC v.3 has an innovation on the code that accurate description of the molar volumes of aqueous species and the fugacity coefficients of gases at high pressures and temperatures (Appelo et al. 2014). The modifications reduce the number of fitting parameters, while maintaining or even extending the range of temperature and pressure over which molar volumes can be accurately estimated. Diagrams can be performed coupling phreeqC to phreePlot and AquaChem codes (Table 3.6).

The Geochemist's Workbench (GWB)

GWB v.12 is an integrated geochemical modelling package originally developed at the University of Illinois (Bethke et al., 1994). The code is used for balancing chemical reactions, calculating stability diagrams and equilibrium state of solutions, reaction path calculations and modelling reactive transport in 1D and 2D dimensions (Table 3.6). GWB was used in this thesis to calculate stability diagrams.

Table.3.6. Description of the capabilities of the geochemical codes used in this thesis

	EQ3/6	PhreeqC	GWB
Code Version	**8.0**	**3**	**12**
Simulation features			
Speciation-solubility modelling	x	x	x
Reaction path modelling	x	x	x
Inverse modelling		x	
Mixing processes	x	x	x
Kinetics	x	x	x
Geochemical Modelling Features			
Aqueous complexation	x	x	x
Isotope fractionation		x	x
Precipitation/dissolution mass balancing	x	x	x
Gas exchange mass balancing	x	x	x
Redox reaction calculations	x	x	x
Ion-exchange	x	x	x
Adsorption processes	x		x
Surface complexation		x	x
Ability to fix species activity (e.g., pH)	x	x	x
solid solutions	x	x	
Species activity calculation features			
Davies model	x	x	x
Debye-Hückel model	x	x	x
B-dot equation (extended Debye-Hückel model)	x	x	x
Pitzer aqueous model	x	x	x
Transport capability			
1D		x	x
2D			x
Diagrams			
stability diagrams		x*	x
temperature-activity		x*	x
temperature-fugacity		x*	x
xy plots		x*	x
Ternary		x**	x
Piper		x**	x
Durov		x**	x
Stiff diagrams		x**	x

** coupled with phreePlot code*

*** coupled with AquaChem code*

4.3 Geochemical data base

Thermodynamic databases are critical for modelling geochemical processes during fluid-rock interactions. The earliest thermodynamic databases were published in the late 1960's (e.g., Robie and Waldbaum, 1968; Helgeson, 1969, 1978). During this thesis EQ3/6, PhreeqC and GWB were simultaneously employed to perform geochemical calculations. The common data base available in three codes is the LLNL (Thermo.com V8 R6.230) which operates until 0.858 MPa and then extrapolates the equilibrium constants until 2.5 MPa. This issue could induce errors in the equilibriums constants of aqueous species and minerals. To solve this problem a new thermodynamic data base was generated in this thesis.

The new data base was created using SUPCRT92 (Johnson et al., 1992) in collaboration with Wolfgang Bach and Christian Hansen (University of Bremen). It operates in a temperature range of (0-300°C) at constant pressure of 25 MPa. The new data base include new aqueous species as $CaHSiO_3^{+,}$ $HFeO_2(aq)$, FeO^+, $H_2O_2(aq)$,HCl(aq), KOH(aq), $MgHSiO_3^+$, NiO(aq), NiO_2^-, $NiOH^+$ and $HNiO_2^-$. The data base also includes olivine (Fo90) ($Mg_{1.8}$ $Fe_{0.2}$ SiO_4) among the solid species. It includes all minerals and inorganic aqueous species in the SUPCRT92 data base for the system Mg-Ca-Fe-Si-Na-Cl-O-H. SUPCRT92 incorporates thermodynamic data from Helgeson et al. (1978) for minerals, and Shock and Helgeson (1988) and Shock et al. (1989, 1997) for dissolved inorganic aqueous species. This data base was employed for speciation and reaction path modelling. *Appendix A* contains the equilibrium constants (log K) of aqueous species, minerals and gases of the data base.

Also two other data bases were eventually employed: (i) modify data base of LLNL at 50 MPa and (0-400°C) by Klein and Bach (2013) written in EQ3/6 language format. (ii) LLNL data base was employed on PhreeqC simulations and GWB activity diagram calculations. The data base includes temperature dependence of activity-coefficient constant and Van't Hoff or analytical expressions for equilibrium constants (Eq.3.22).

4.4 Geochemical codes to generate data bases

SUPCRT92

SUPCRT92 is a widely used software package for calculating the standard molal thermodynamic properties; (ΔG_f^0), (ΔH_f^0) and S^0; of minerals, gases, and aqueous species and reactions at given temperature (*T*) and pressure (*P*). The code can operate over a wide range if T (0-1000°C) and P (1-500 bars) (Johnson et al., 1992). The standard thermodynamic properties are calculated using: i) the equations of state for H_2O developed by Levet Segenrs et al (1983) and (Haar et al., 1984), ii) the H_2O dielectric formulation given by Johnson and Norton (1991), and iii) the revised HKF equation of state for aqueous solute species presented by Tanger and Helgeson (1988) and Shock et al (1992).

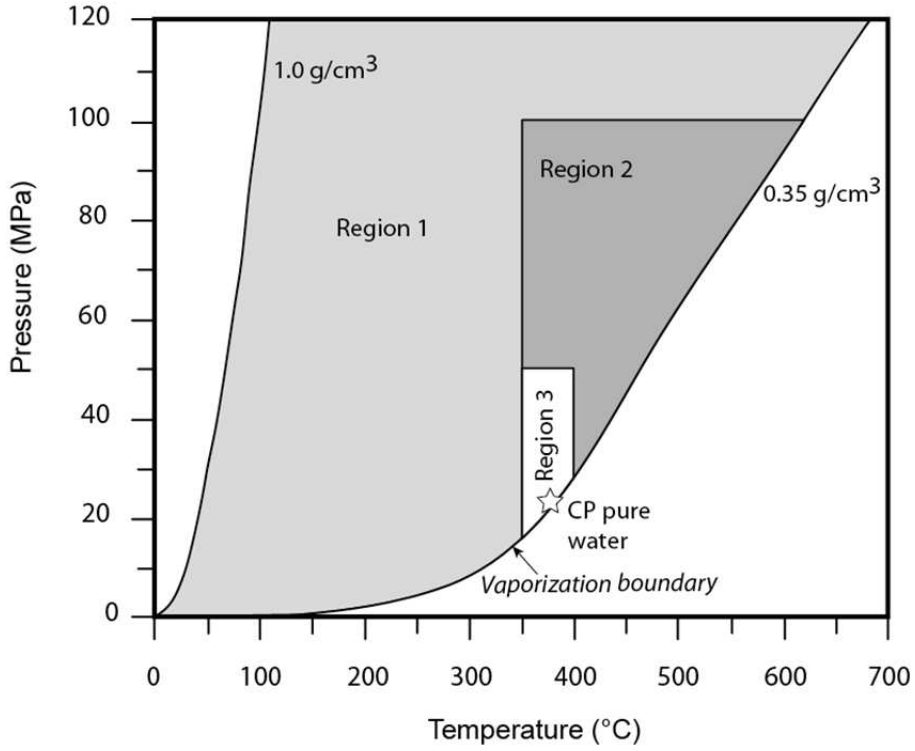

Fig.3.18. Range of P-T conditions for which standard molal thermodynamic properties of aqueous species can be calculated using SUPCRT92. Standard molal themodynamic properties for mineral, gases aqueous species could be generated for P-T Region 1 and 2 but not for Region 3 is not possible to be calculated (Redraw from Johnson et al., 1992). No data could be generated in the white region.

However, calculations can be performed only along the liquid side of the H_2O vaporization boundary and in the single-phase regions of fluid H_2O. Figure 3.18 shows the 3

regions where is possible to calculate the apparent standard molal Gibbs free energy of formation. The conflicted region 3 is localized between 350 and 400°C isotherms, 50 MPa isobar, 0.35g/cm^3 isochore, and vaporization boundary. In this region the uncertainties on the molal Gibb free energy of formation are sufficiently large to inhibit calculation for all the aqueous species and charged species. SUPCRT92 only calculates the log K for neutral species above the vaporization boundary and in the region 3.

4.5 Description of the geochemical modelisations

Modelling the seawater composition at high temperature

The precipitation of anhydrite and carbonates from the natural seawater in the reactor pipelines at the experimental temperature (190°C) produced the interruption of the fluid injection. This issue led to re-calculate the chemical composition of an artificial seawater in order to avoid mineral precipitation in the next suite of experiments. I simulated the chemical composition of seawater at 200°C using the *reaction path modelling* of EQ3/6. This model was firstly designed for experiments run at 190°C.

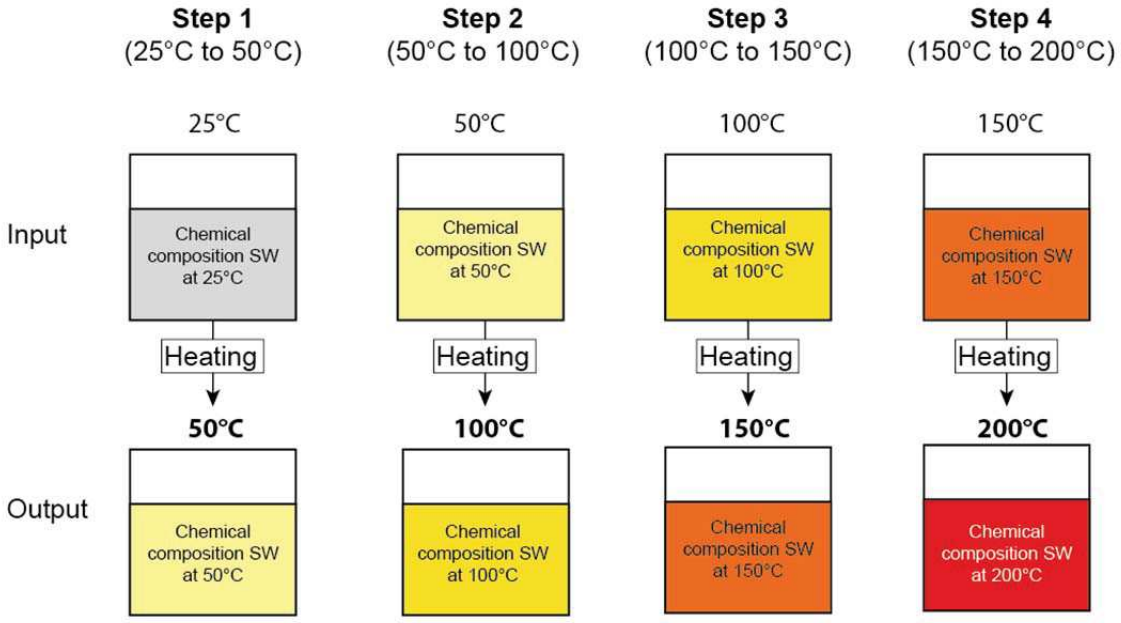

Fig. 3.19. Description of the reaction path model using EQ3/6 to calculate the chemical composition of SW (seawater) at 200°C.The chemical composition comprises the concentration of all basic species in solution and the pH.

The model was done at a temperature (200°C) higher than the experiment (190°C) in order to avoid any precipitation from the fluid in the heating coil. Then, due to teflon deformation constrains at 190°C the temperature of the experiment was decreased to 170°C. We still kept the chemical composition of seawater calculated at 200°C to produce the starting experimental fluids in experiment run at 170°C. The reference composition of seawater at 25°C was the one from Millero et al. (2008). The model consists in heating progressively the seawater from 25°C until 200°C in steps of 50°C. The output chemical composition of seawater at each step is reheated 50°C more in the next simulation (Fig.3.19). I assumed equilibrium on all steps and balance the electrical charge with Na^+. All calculations were performed using the database of thermodynamic parameters for 25 MPa generated for this thesis (section 4.3 and *appendix A*).

Modelling the pH of the fluids at the experimental temperature

Calculations to estimate in situ pH of the fluids were performed using EQ3/6 following the method of McCollom et al (2016) using a *speciation-solubility model*:

(1) Fluid speciation was calculated at 25°C using the fluid composition and pH measured at room temperature, and adjusting for charge balance with Na^+.

(2) The total dissolved Na^+ value calculated at 25°C was used with the ion measured concentrations to calculate the fluid speciation at 170°C adjusting for charge balance with H^+ in order to determine the pH in situ at 170°C.

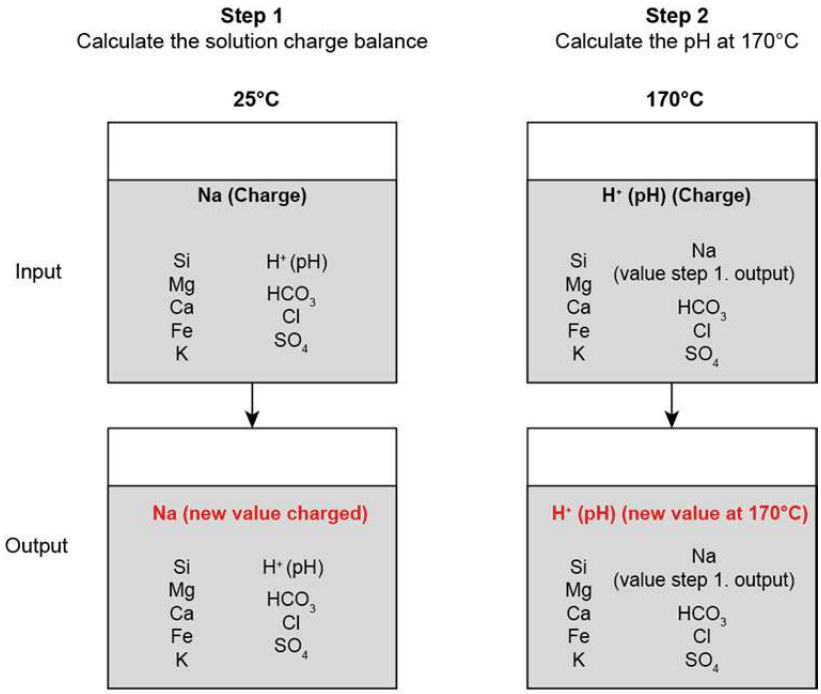

Fig.3.20 Description of the two steps to calculate the pH at 170°C. The input of the model comprises the concentration of the basic species of the outlet fluids measured with ICP-MS, ICP-OES, titration or ion chromatography. In the output results, the concentration of basic species doesn't change as only speciation-solubility were calculated, whereas the Na concentration (step 1) and pH (step 2) has change because they were settle to charge balance the solution.

Modelling the total dissolved inorganic carbon (DIC)

The total dissolved inorganic carbon (DIC) of the fluids at 25°C was estimated using EQ3/6 using a *speciation-solubility model*. Fluid speciation was calculated at 25°C using the fluid composition, the alkalinity and pH measured at 25°C adjusting for charge balance with Na^+ content. The output model provides the speciation of all the carbon species in the fluid at 25°C. The DIC corresponds to the sum of all the carbon species in solution.

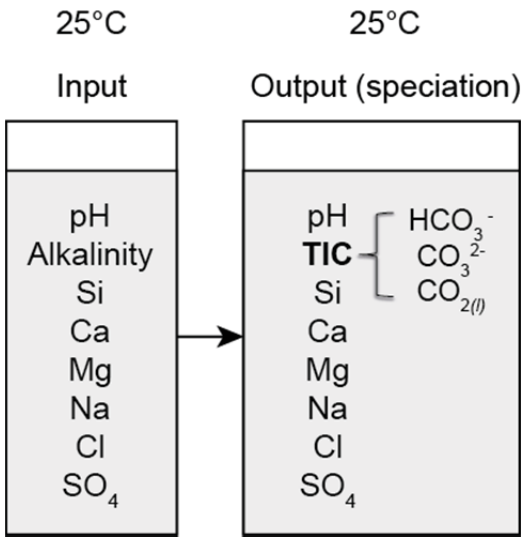

Fig. 3.21. Determination of the total inorganic carbon (TIC) at 25°C after a solubility-speciation model. The input at 25°C corresponds to the concentration of basic species in outlet fluids measured with ICP-MS, ICP-OES, titration or ion chromatography. The alkalinity corresponds to the measured value of HCO_3 after acidimetric titration. The outlet of the model is the speciation of the species in solution. The TIC is calculated after the sum of all carbon species.

Chapter IV

Experimental study of the effects of solute transport on reaction paths during incipient serpentinization

1. Introduction

This chapter describes the impact of flow rate on serpentinization reaction paths for conditions relevant of the oceanic peridotite sub-seafloor during the initial stages of its hydrothermal alteration. Reactive percolation experiments were performed by the percolation of seawater into porous compressed olivine powder cores at constant flow rates (Q).

The first part of the chapter focuses on the effects of flow rate on serpentinization reaction paths. Four reactive percolation experiments were performed by the injection of artificial seawater into porous compressed olivine powder cores at constant flow rates Q: 0.24, 0.48, 1.14 and 5.21 $mL.h^{-1}$. The experimental approach use steel capsules of D=9 mm and L=20 mm which provides enough material (3 g) for rock chemical analysis. The distribution of fluid velocities in the samples was the dominant transport parameter that changes from one experiment to the other. The local Peclet number (Pe) is directly controlled by the fluid velocity; which determines the transport mechanism (advection (Pe>1) or/and diffusion (Pe<1)) dominated at the pore-scale. The experiments were run in a range of Péclet number from 0.02 to 4.

The second part of this chapter focuses on the development of a protocol to study the chemical and physical changes that undergo the ultramafic rock during percolation of natural seawater at fast fluid velocities (Péclet number of 6). X-ray µ-tomography of high resolution (0.65 µm) was performed before and after the experiments at the ESRF (European Synchrotron Radiation Facility, Grenoble, France). The X-Ray µ-tomography provides a 3D virtual model of the experimental sample without destroying it. The experimental approach uses small titanium capsules of D=2 mm and L=20 mm which provides low absorption for X-ray and so access into the olivine samples.

The combination of both studies provides new insights of the role of solute transport during the earliest stages of alteration of the mantle basement, when seawater-derived hydrothermal fluids penetrate and interact with the sub-seafloor mantle basement.

2. Experimental study of the effects of solute transport on reaction paths during incipient serpentinization

S. Escario[*1], M. Godard[1], P. Gouze[1], R. Leprovost[1]

[1] Géosciences Montpellier, CNRS, Univ. Montpellier, 34095 Montpellier, France
(Corresponding author : *Sofia.Escario@gm.univ-montp2.fr)

Note: This section is based on the article: Escario., S., Godard, M., Gouze, P., Leprovost, R., 2018. Experimental study of the effects of solute transport on reaction paths during incipient serpentinization. Accepted in Lithos, Special Volume "ABYSS"

Lithos xxx (2018) xxx–xxx

Contents lists available at ScienceDirect

Lithos

journal homepage: www.elsevier.com/locate/lithos

Experimental study of the effects of solute transport on reaction paths during incipient serpentinization

S. Escario *, M. Godard, P. Gouze, R. Leprovost

Géosciences Montpellier, CNRS, Univ. Montpellier, 34095 Montpellier, France

ARTICLE INFO

Article history:
Received 22 May 2018
Received in revised form 17 September 2018
Accepted 17 September 2018
Available online xxxx

Keywords:
Serpentinization
Reactive-percolation experiments
Solute transport
Kinetics
pH
Fluid composition
Reaction paths

ABSTRACT

This paper presents the results of 4 reactive percolation experiments set up for investigating the impact of flow rate on serpentinization reaction paths for conditions relevant of the oceanic peridotite sub-seafloor during the initial stages of its hydrothermal alteration. The experiments consisted in injecting artificial seawater into porous compressed olivine powder cores at constant flow rates *Q*: 0.24, 0.48, 1.14 and 5.21 mL·h^{-1}. The experiments were conducted at constant temperature (170 °C) and pressure (25 MPa) and lasted 11 to 28 days. At the end of the experiments, the outlet fluids composition displayed similar compositions, buffered by the formation of serpentine ($aMg^{2+}/a(H^+)^2 = 9.7–10$; $aSiO_2 = -3.9$ to -5.2; $pH_{\text{in situ}} = 6.1$). These values were achieved in a few to up to 300 h for the high flow rate experiment suggesting that they corresponded to a steady-state regime of mass transfer which depended on flow rate. Differences in the composition of fluid versus time and in the structure of reacted samples during and after the four reactive percolation experiments suggested also various incipient serpentinization reaction paths. The low *Q* experiments produced SiO_2(aq) enriched outlet fluids and nodular aggregates were identified covering the reacted olivine surfaces. During high *Q* experiments, fibrous filaments of proto-serpentine were formed on the olivine surfaces and the fluids progressively achieved steady state compositions similar to the other experiments. These results together with those of previously published reactive percolation experiments lead us to propose two end-member reaction paths for incipient serpentinization of olivine-dominated permeable rocks infiltrated by seawater derived hydrothermal fluids: (1) a transport-controlled reaction path occurring in diffusion dominated zones is characterized by transient brucite precipitation, which produces Mg trapping and Si release in solution, followed by serpentine precipitation and (2) a kinetics-controlled reaction path occurring in advection dominated zones where transport conditions are favorable to Mg leaching and where serpentine precipitates first. The occurrence of these two end-member reaction paths is determined locally by the composition of the fluid, which varies along flow paths. Thus, both reaction paths can coexist in the sample depending on the local pore geometry. Our study shows that the interplay between fluid transport and reaction kinetics controls the chemical fluxes between the mineral surface and the bulk solution, and the incipient serpentinization reaction paths. In natural systems, the scale and distribution of these reaction domains will depend on the complex structure of the ultramafic basement. Our results suggest that the precipitation of serpentine and silica rich phases will be favored in fluid focusing zones such as faults and fractures, whilst formation of brucite will preferentially occur as part of pervasive background serpentinization.

1. Introduction

Serpentinization is ubiquitous where mantle peridotites are exposed at mid-ocean ridges along magma-starved segments and tectonic windows (e.g., reviews of Mével (2003) and Evans et al. (2013)). It is a low temperature (<350 °C) hydrothermal process resulting in the formation of hydrous minerals (serpentine, brucite, …) after olivine, a Mg-Fe-rich mineral that composes >70% of the shallow oceanic mantle (other phases being pyroxenes and minor spinel) (Bodinier and Godard (2003). Reaction for the serpentinization of the oceanic mantle is often summed up as follows:

$$3\ Mg_{1.8}Fe_{0.2}SiO_4\ (Olivine) + 4.1\ H_2O \rightarrow 1.5\ Mg_3Si_2O_5(OH)_4\ (Serpentine) + 0.9\ Mg(OH)_2\ (Brucite) + 0.2\ Fe_3O_4\ (Magnetite) + 0.2\ H_2(aq) \quad (R1)$$

Oceanic serpentinization is associated to redox reactions and hydrogen production (e.g. Bach et al., 2006; Evans, 2008; Oufi et al., 2002) as

* Corresponding author.
E-mail address: Sofia.Escario@gm.univ-montp2.fr (S. Escario).

https://doi.org/10.1016/j.lithos.2018.09.020
0024-4937/

well as to carbonate formation and carbon reduction reactions when CO_2 is present (e.g., Früh-Green et al., 2004). This suite of reactions can modify the rheological (e.g., Escartín et al., 2001), geophysical (e.g., Maffione et al., 2014) and chemical (e.g., Paulick et al., 2006) properties of the oceanic mantle lithosphere. It is also an important vector of energy and chemical exchanges between the ocean and the deep lithosphere at ridges through the development of mantle hosted hydrothermal vents characterized by their unique fluid chemistry rich in H_2, CH_4 and abiotic hydrocarbons (e.g., Charlou et al., 2013).

Thermodynamic studies show that mantle minerals, olivine and pyroxene, are unstable below 450 °C and 5 kbar, and therefore highly reactive when water is present (e.g., Klein and Garrido, 2011; O'Hanley, 1996; Palandri and Reed, 2004). They indicate also that the olivine hydration reaction is exothermic (MacDonald and Fyfe, 1985) and some authors suggested that it might drive hydrothermal circulation in the oceanic ultramafic basements (e.g., Lowell and Rona, 2002). Nevertheless, the predicted range of pressures and temperatures over which serpentinization can occur is too large to accurately constrain models of hydrothermal alteration of the cooling mantle lithosphere, as it covers the full range over which these processes can take place. For these reasons, since the pioneering works of Martin and Fyfe (1970), numerous experimental studies have been devoted to understanding and constraining the chemical mechanisms driving olivine hydration and serpentinization in oceanic environments.

Experimental studies on serpentinization have been realized mostly using batch approaches with the aim of achieving equilibrium and fluid-rock reaction completion: autoclave reactors (e.g., Malvoisin et al., 2012; Marcaillou et al., 2011; Ogasawara et al., 2013; Okamoto et al., 2011) and hydrothermal gold cells (e.g., Allen and Seyfried, 2003; Berndt et al., 1996; Janecky and Seyfried, 1986; Klein and McCollom, 2013; McCollom et al., 2016; Seyfried et al., 2007; Seyfried and Dibble, 1980) at water/rock mass ratio larger than one, synthetic fluid inclusions used as micro-reactor (Lamadrid et al., 2017) and diamond-anvil cells (e.g., Andreani et al., 2013; Pens et al., 2016). In order to achieve the maximum degree of reaction over time scales consistent with laboratory studies, these experimental studies were often realized using fine grained mineral powders and/or with pure water, which provide the maximum reactive surface areas versus mineral volume ratios (e.g., Malvoisin et al., 2012; Martin and Fyfe, 1970) and the highest H_2O activity (e.g., Lamadrid et al., 2017). These experiments have demonstrated the first order dependence of the kinetics of serpentinization and associated reactions on temperature: serpentinization efficiency is the highest between 250 °C and 310 °C (e.g., Martin and Fyfe, 1970; Wegner and Ernst, 1983) whilst carbonate formation after olivine is the fastest at 185 °C (e.g., Gerdemann et al., 2007; O'Connor et al., 2001; O'Connor et al., 2005). They also pointed to the need to take into account the structural and compositional heterogeneities of the mantle basement and variations of fluid chemistry to model natural systems (e.g., Malvoisin and Brunet, 2014; Janecky and Seyfried, 1986).

The composition of the hydrothermal fluids flowing into the mantle basement at mid-oceanic ridges is expected to have highly variable compositions revealing their different sources from alkaline Mg-rich seawater derived fluids to more acidic *Al*- and Si-rich fluids produced by interactions with pyroxene-bearing peridotite and neighbouring basalts or gabbros (e.g., Douville et al., 2002; Seyfried et al., 2013). Laboratory experiments and thermodynamic computations show that the composition of these fluids will strongly affect serpentinization kinetics and reaction paths (e.g., Allen and Seyfried, 2003; Janecky and Seyfried, 1986; Klein et al., 2013; McCollom and Bach, 2009). Serpentinization is much faster in high pH alkaline conditions (Lafay et al., 2012; Pens et al., 2016) than experiments run under neutral conditions (e.g., Malvoisin et al., 2012; Martin and Fyfe, 1970; Ogasawara et al., 2013; Okamoto et al., 2011; Seyfried et al., 2007) although rates of olivine dissolution decrease with increasing pH (Chen and Brantley, 2000; Giammar et al., 2005; Hänchen et al., 2006; Pokrovsky and Schott, 2000a; Prigiobbe et al., 2009; Rosso and Rimstidt, 2000; Rimstidt et al., 2012). Also olivine serpentinization kinetics is enhanced in presence of alkaline *Al*-rich fluids (Andreani et al., 2013; Pens et al., 2016). Furthermore, high Mg and/or Si activities in fluids determine serpentinization reaction paths by favoring or hindering the precipitation of brucite (Janecky and Seyfried, 1986; Ogasawara et al., 2013; Syverson et al., 2017; Tutolo et al., 2018) or silica-rich hydrous minerals such as talc (e.g., Evans, 2004) rather than serpentine precipitation. The development of such various intermediate reactions and secondary mineral assemblages can in turn modify the micro-scale structure of serpentinizing ultramafic basement and therefore the accessibility of the fluid to the mineral interfaces, which is a critical parameter for chemical reactions to occur.

Peridotites have low permeability (e.g., 10^{-21}–10^{-17} m^2 (Hatakeyama et al., 2017, Hirose and Hayman, 2008)) whilst serpentinization tends to clog efficiently flow paths by producing low density minerals (e.g., hydrous minerals and carbonates) at the expense of high density olivine. Nevertheless, the extensive hydrothermal alteration of the mantle lithosphere indicates that efficient mechanisms favor fluid flow into the serpentinizing mantle basement at mid-ocean ridges (e.g., Rouméjon et al., 2015; Schroeder et al., 2002). Flow paths into the mantle lithosphere probably combine localized flow along high permeability km-scale fractured zones (e.g., Farough et al., 2016; Hirose and Hayman, 2008) and pervasive fluid influx into serpentinizing rocks (e.g., Emmanuel and Berkowitz, 2006), which permeability is assumed to be maintained by the continuous formation of cracks down to the mineral scale through tectonic, thermal or/and reaction-induced stresses (e.g., Boudier et al., 2005; Kelemen and Hirth, 2012; Rouméjon et al., 2015; Rudge et al., 2010). Flow paths into the mantle lithosphere are thus governed by multi-scale heterogeneities in the rock structure (porosity, connectivity, tortuosity), and this implies that solute transport to and from reactive mineral surfaces and its effects on fluid-rock reaction pathways and kinetics will depend on these structural heterogeneities. Two complementary experimental approaches have been developed to study the interplay between chemical reactions and solute transport in peridotites during serpentinization and associated reactions. The first approach was designed to investigate the effect of diffuse transport (no fluid flow): it consisted in long duration (up to 300 days) batch experiments during which low porosity peridotites (Klein et al., 2015) and sintered olivine analogues (Malvoisin and Brunet, 2014) were reacted with water at optimal temperature and pressure for serpentinization. Serpentine and brucite were produced as predicted by thermodynamic models but, in both cases, the serpentinization kinetics were lower than reported for powder experiments (~0.01%/day compared to ~1–2%/day e.g., Marcaillou et al. (2011) on peridotite powder of 1 μm grain size) as a result of the limited olivine surface area accessible to water in porous samples. The second approach aimed at investigating the coupling and feedback effects between flow, transport and mineralogical reactions as fluids were injected into porous (Luhmann et al., 2017) and fractured (Farough et al., 2016) peridotites and in sintered olivine-rich analogues (Andreani et al., 2009; Godard et al., 2013; Peuble et al., 2015a, 2015b). Reactive percolation experiments were run over shorter durations compared to the first approach (maximum 36 days). They showed the strong effect of pore geometry and fluid flow variability triggering the development of local chemical heterogeneities, named chemical micro-environments by Steefel and Maher (2009). The flow heterogeneity which corresponds to several orders of magnitude in the local flow velocity have been identified as a critical parameter that control the nature and the efficiency of hydration processes (Godard et al., 2013) and of carbonate formation (Andreani et al., 2009; Peuble et al., 2015a, 2015b). These studies gave a first insight into the complex coupling between flow, solute transport and kinetics of dissolution and precipitation reactions at the scale of samples of few cubic centimeters (e.g. Godard et al., 2013; Luhmann et al., 2017).

Following this experimental approach, we present in this article the results of reactive percolation experiments designed to investigate the role of solute transport during the earliest stages of alteration of the mantle basement, when seawater-derived hydrothermal fluids

Please cite this article as: Escario, S., et al., Experimental study of the effects of solute transport on reaction paths during incipient serpentinization, Lithos (2018), https://doi.org/10.1016/j.lithos.2018.09.020

penetrate and interact with the sub-seafloor mantle basement. The experiments were conducted by injecting artificial seawater at four different flow rates through cores made of compressed olivine powder. The composition of the injected artificial seawater was calculated in order to model that of seawater heated up when flowing along high permeability fracture zones. Olivine was chosen as starting material to limit the effects of mineralogical heterogeneities on serpentinization reaction paths. Experiments were performed using high porosity and permeability cores in order to avoid clogging of pore network due to serpentinization reactions and thus to minimize the change of the rate of solute renewal at fluid-mineral interfaces along flow paths during experiments. The objectives of this study are to better understand the coupling between fluid flow, solute transport and chemical processes during fluid-rock interactions, its effects on the mechanisms that control outlet fluid chemistry and chemical reaction path from the pore- to the sample-scale, and their role for the serpentinization of the oceanic mantle lithosphere.

2. Experimental and analytical methods

2.1. Experimental setup

Reactive percolation experiments were carried out using the Icare Lab 3 flow-through system (Géosciences Montpellier, France) (Fig. 1). This experimental bench allows investigating water-rock interactions in confined permeable cylindrical samples of 9 mm diameter *(D)* and 20 mm length *(L)*. It includes an automatic system of fluid injection with three computer-controlled hydraulic pumps of 35 mL volume that allows maintaining a constant flow rate (Q) ($10^{-6} \leq Q \leq 2$ mL·min^{-1}) and a heated confinement cell that holds the sample at constant temperature (T) (<400 °C) (Fig. 1). The experiment pressure (P) (< 40 MPa) is controlled by a back pressure system with a hydraulic pump of 100 mL volume (Fig. 1). During experiments, the difference of fluid pressure between the inlet and outlet of the sample ($0.003 < \Delta P \leq 40$ MPa) is monitored using a differential pressure sensor Rosemount 3051 (accuracy of 0.003 MPa) coupled with two high resolution pressure sensors Keller PA-33 X (accuracy of 0.035 MPa). Experimental fluid samples of volume 3 mL are collected using a pressurized computer-controlled syringe. Pump motion, valves and fluid sampling are operated by an in-house LabView-based software.

The four reactive-percolation experiments consisted in injecting artificial seawater (ASW) into compressed San Carlos olivine powders at different constant flow rates (Q): SC1-LQ, SC2-MQ, SC3-HQ and SC4-VHQ were performed at low ($Q = 0.24$ mL·h^{-1}), medium ($Q = 0.48$ mL·h^{-1}), high ($Q = 1.14$ mL·h^{-1}) and very high ($Q = 5.21$ mL·h^{-1}) flow rate respectively. The four experiments were performed at the same temperature ($T = 170$ °C) and pressure ($P = 25$ MPa) conditions. The permeability k of the samples (in m^2) was calculated using Darcy's law assuming laminar flow conditions:

$$k = -\frac{\mu L Q}{S \Delta P} \quad (1)$$

with Q the injection rate (in m^3/s), μ the dynamic fluid viscosity (0.197×10^{-3} Pa. s at 170 °C and 25 MPa for a salinity of 0.5 mol/kg (Kestin et al., 1981), and L and S the sample length (in m) and cross sectional area (in m^2) respectively. The changes in ΔP are measured continuously during the experiment. Experimental conditions and sample characteristics are summarized in Table 1.

2.2. Sample preparation

2.2.1. Olivine samples

The olivine samples are powdered San Carlos olivine compressed into a 20 mm length, 7 mm internal diameter steel tubes (Fig. 2). The composition of San Carlos olivine is Fo91 (Appendix A, Supplementary Material). Powders were obtained by grounding olivine grains of few millimeters (typically 5 mm). The grains were optically selected under a binocular microscope to eliminate those with microphases or inclusions. Then, the grains were grounded in an agate mortar, sieved and ultrasonicated three times in MilliQ water. The 100–150 μm olivine grain fractions was selected for the experiments (Fig. 2a) and introduced into the stainless steel (316 L) tubes by successive layers of ~2 mm. Each layer was compressed, using a hydraulic press, at 4.13 MPa. The process was repeated until the capsule was completely filled (Fig. 2b-c). Then, two cylindrical stainless steel (316 L) frit plugs of 2 mm thickness were emplaced on each end of the tube to seal the

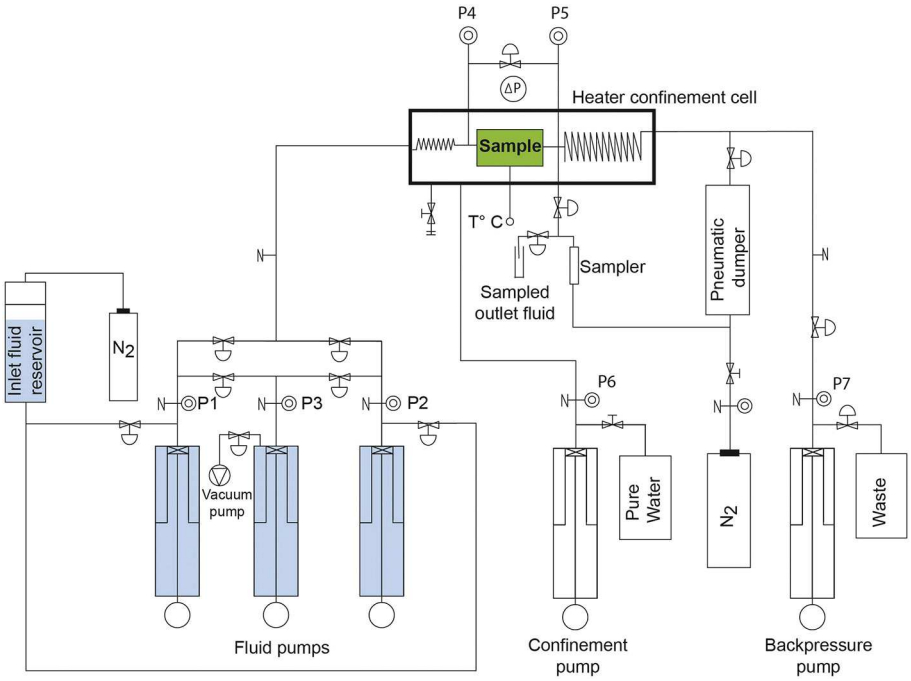

Fig. 1. Schematic diagram of the experimental flow through setup (Icare Lab 3).

Please cite this article as: Escario, S., et al., Experimental study of the effects of solute transport on reaction paths during incipient serpentinization, Lithos (2018), https://doi.org/10.1016/j.lithos.2018.09.020

Table 1
Experimental parameters of experiments SC1-LQ (low flow rate), SC2-MQ (medium flow rate), SC3-HQ (high flow rate) and SC4-VHQ (very high flow rate). The experiments were run at 170 °C and 25 MPa using artificial seawater (ASW) as injected solution.

Experiment	Flow rate	Residence time	Duration	Olivine sample	Sample diameter	Sample length	Grain size	Initial weight	Initial porosity	Peclet number	Mean fluid velocity	Permeability avg.
	$(Q = ml/h)$	(min)	$(hours)$		(mm)	(mm)	(μm)	(g)	$(\%)$		$(v = m/s)$	$(k = m^2)$
SC1-LQ	0.24	158	354	SC1	7.09	16.00	150–100	1.71 ± 0.01	19.3	0.2	8.8×10^{-6}	$5.7 \times 10^{-15} \pm 1.2 \times 10^{-15}$
SC2-MQ	0.48	77	668	SC2	7.11	15.50	150–100	1.76 ± 0.01	14.9	0.5	2.3×10^{-5}	$3.5 \times 10^{-15} \pm 2.9 \times 10^{-15}$
SC3-HQ	1.14	34	263	SC3	7.13	16.02	150–100	1.77 ± 0.01	17.4	0.9	4.6×10^{-5}	$3.3 \times 10^{-15} \pm 1.1 \times 10^{-15}$
SC4-VHQ	5.21	7	617	SC4	7.09	15.85	150–100	1.70 ± 0.01	18.8	4.0	2.0×10^{-4}	$3.7 \times 10^{-15} \pm 1.5 \times 10^{-15}$

olivine powder into the capsule. The characteristics of samples SC1, SC2, SC3 and SC4 used for experiments SC1-LQ, SC2-MQ, SC3-HQ and SC4-VHQ respectively are reported in Table 1.

2.2.2. Artificial seawater

Artificial seawater (ASW) was prepared to simulate the composition of natural seawater progressively heated at 170 °C and depleted in Mg- and Ca-rich carbonates and sulfates while penetrating the oceanic lithosphere. The ASW composition, reported in Table 2, was calculated using the EQ3/6 geochemical modelling software (EQ3/6 v.8.0,Wolery and Jarek, 2003) assuming seawater (Millero et al., 2008) was heated up to 200 °C by 50 °C steps. It was calculated up to 200 °C, i.e. slightly higher than the experimental temperature (170 °C), in order to ensure that no mineral precipitation would take place in the heated confinement cell. The ASW was made before each experiment by dissolving pure salts $MgCl_2.6H_2O$ (Merck), KCl (Prolabo Analar Normapur), $NaHCO_3$ (Panreac), NaCl (Prolabo Analar Normapur), Na_2SO_4 (Prolabo Normapur), and $CaCl_2$ (Sigma-Aldrich) into MilliQ water. The composition of injected ASW was systematically measured together with that of outlet fluids following the protocol described thereafter; it varied little from one experiment to the other. It should be noted that traces of Fe (0.90–12.86 μmol/L) were measured in the "blank solution" when pumping the ASW through the bypass before injection. The source of Fe is probably a minor alteration of the stainless steel material used for the pumps and the circuit.

The pH value of the solution was measured with a Metrohm Titrino 848 with LL Micro glass electrode, was 7.56 at room temperature (25 °C). The pH of the solution at 170 °C, calculated using EQ3/6, was 5.8. The conductivity, measured using a conductivity meter WTW LF340 with a sensor Tetracon WTW 325 was 43.5 mS/cm.

2.3. Mineralogical characterization

The mineralogy of samples was characterized after experiments using scanning electron microscopy (SEM) coupled with energy dispersive spectroscopy (EDS) and thermogravimetric analyses (TGA).

Before analyses, the reacted olivine samples were dried under vacuum for 12 h at room temperature (25 °C) to remove the fluid that remained in pores and to avoid post-experiment fluid-rock reactions. For samples SC1, SC3 and SC4, the reacted powdered samples were recovered after sawing off one of the frit plugs. Sample SC2 was prepared as a polished section using the approach of Peuble et al. (2015a, 2015b); this technique didn't allow recovering powder samples for TGA analyses.

SEM-EDS was used for grain surface characterization and semi-quantitative chemical analyses. Analyses were performed using a FEI Quanta FEG 200 Scanning Electron Microscope (University of Montpellier, France), with an acceleration voltage of 15 kV and chamber pressure of 0.38 Torr. TGA analyses were used for identifying volatile rich minerals by the loss of weight when the sample is heated. Analyses were performed by increasing the temperature from 33 °C to 1200 °C at 2 °C.min^{-1} rate under Argon atmosphere using a SDT Q600 V20.9 (IEEM, Montpellier). The curves were calibrated by performing an automatic blank curve subtraction in order to avoid measurement artefacts such as apparent gain of weight produced by buoyancy effects.

2.4. Fluid analyses

Experimental fluid samples were collected on average every day. Each fluid sample represents the integrated concentrations of the outlet fluids over the time required for 3 mL to flow through the percolated

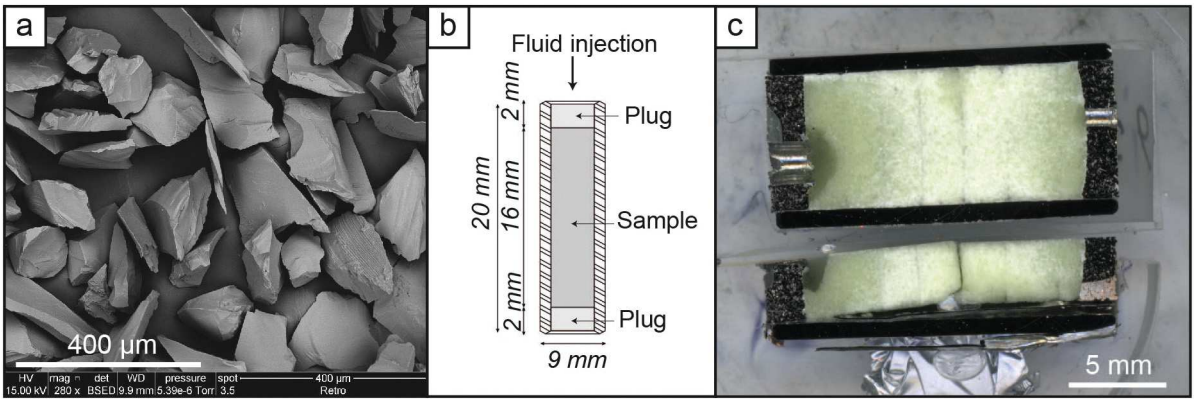

Fig. 2. (a) SEM image of starting material: ultrasonically cleaned San Carlos olivine powder. (b) Schematic diagram of sample capsule. Olivine powder is introduced in the cylindrical steel capsule (20 mm × 9 mm), which is then closed on both ends by two steel frit plugs. (c) Unreacted sample cut longitudinally. Alternating dark to light green layers are related to the filling of the steel capsule. (For interpretation of the references to colour in this figure legend, the reader is referred to the web version of this article.)

Please cite this article as: Escario, S., et al., Experimental study of the effects of solute transport on reaction paths during incipient serpentinization, Lithos (2018), https://doi.org/10.1016/j.lithos.2018.09.020

Table 2
Theoretical chemical composition of the starting fluid at 200 °C calculated after EQ3/6.

Element	mg/L	mmol/L
Mg	1083	44.6
Ca	128	3.2
K	340	8.7
Na	9163	398.6
Cl	16,468	464.5
SO4	1799	18.7
HCO3	47	0.8

samples: the last 12.5 h, 6.25 h, 2.63 h and 0.58 h before sampling time for experiments SC1-LQ, SC2-MQ, SC3-HQ and SC4-VHQ respectively (Appendix B. Table B.1 to B.4).

Alkalinity and pH were measured using a Methrom Titrino 848. Measurements were performed <5 min after the fluid sample was collected to minimize equilibration with the atmosphere. The pH was measured using 2 mL samples at 1:2 dilution in MilliQ water using a Metrohm LL Micro glass electrode. The alkalinity (HCO_3^-) was measured at 25 °C on the same fluid sample by acid titration with 0.01 M HCl. The reagent was added to the fluid sample in variable volume steps to a pH endpoint of 4.5. (HCO_3^-) was assumed to be equal to total alkalinity (Bischoff and Seyfried, 1978). The reproducibility and accuracy of alkalinity measurements were assessed using repeated measurements of Volvic® water. They were better than 5% and 15%, respectively. The pH accuracy was better than 3%. Values are reported in supplementary material (Appendix C).

SO_4^{-2} was analyzed using a Dionex ICS-100. Water samples were analyzed after a dilution of 500 with MilliQ water. The reproducibility and accuracy of measurements were assessed using IAPSO (seawater sample) (Summerhayes and Thorpe, 1996) and was better than 1% and 1% respectively (supplementary material, Appendix C).

Si, Fe, Mg, Ca and Na were analyzed using a Thermo Scientific ICAP 7400 ICP-OES (Géosciences Montpellier) after a dilution of 50 in acidified MilliQ water (2% HNO_3). The reproducibility and accuracy of measurements were assessed using SLRS-5 (River water sample) (NRC-CNRC) certified standard and was better than 10% and 5% respectively (supplementary material, Appendix C).

Speciation and saturation calculations of the experimental fluids were calculated using the EQ3/6 geochemical software (Wolery and Jarek, 2003). Calculations to estimate in situ pH and silica activity were performed using EQ3/6 following the method of Mccollom et al. (2016): first, fluid speciation was calculated at 25 °C using the fluid composition and pH measured at room temperature adjusting for charge balance with Na^+, then, the total dissolved Na^+ calculated at 25 °C was used with other measured concentrations to calculate the fluid speciation at 170 °C adjusting for charge balance with H^+ in order to determine the in situ pH.

All calculations were performed using a data base of thermodynamic parameters for 25 MPa. The data base was generated using SUPCRT92 (Johnson et al., 1992). It includes all minerals and inorganic aqueous species in the SUPCRT92 data base for the system Mg-Ca-Fe-Si-Na-Cl-O-H. SUPCRT92 incorporates thermodynamic data from Helgeson et al. (1978) for minerals, and Shock and Helgeson (1988) and Shock et al. (1989, 1997) for dissolved inorganic aqueous species. Activity coefficients for aqueous species were calculated using the B-dot equation (Helgeson et al., 1981).

3. Results

3.1. Characteristics of the reacted samples: permeability and mineralogy

Permeability stayed constant during the four experiments (Table 1). Experimental samples had high porosities (14.9–19.3%) at the start of the experiments. The lack of permeability variations indicates that changes in mineralogy during the experiments were not large enough in volume to block porosity and flow paths.

At the end of the four experiments, the reacted samples generally preserved the initial green colour of olivine, with locally white patches (Fig. 3), suggesting that changes in the mineralogy of the samples were minor. They show however dark brown patches at the inlet and outlet of the capsule and black spots peppered throughout the samples indicating possible precipitation of oxides. Trace Fe concentrations in injected fluids may have favored oxide precipitation at the sample inlet. At the micro-scale, mineral alteration features become more noticeable. Mineral deposits were identified by SEM-EDS on olivine surfaces in the four reacted samples (Fig. 4). Olivine appears covered by 2 to 3 μm patches of fluffy light grey deposits bounded by dark grey lines (Fig. 4b). At the nano-scale, these fluffy deposits present different textures in the four reacted samples (Fig. 4c-f).

Sample SC1-LQ (lowest flow rate experiment) shows small (<50 nm) nodular aggregates localized along the primitive discontinuities of the olivine grains (Fig. 4c). These textures are similar to that described by Lafay et al. (2012) and Ogasawara et al. (2013) as incipient chrysotile. Sample SC2-MQ (medium flow rate experiment) displays also nodular deposits but slightly bigger than in Sample SC1-LQ (Fig. 4d). Similar nodular textures were described by Andreani et al. (2009) as proto-serpentine. Silica-rich zones were also observed (Fig. 5). They have a characteristic length of approximately 10 μm and SEM-EDS analyses indicate low Mg/Si ratio (~ 0.3) compared to olivine (Mg/Si = 1.8). A few calcite grains were also identified at the sample inlet. Sample SC3-HQ (high flow rate experiment) shows an assemblage of fibrous filaments (Fig. 4e). In some places, filaments follow a preferential orientation; they have textures similar to those described by Lafay et al. (2012) as indicating incipient stages of chrysotile formation. Elsewhere, filaments are randomly oriented forming honeycomb textures similar to those described by Luhmann et al. (2017) and interpreted by these authors as secondary mineralization features. Because of the nature of the samples (powder), we could not determine a possible relation between the texture and the flow direction. Sample SC4-VHQ (highest flow rate experiment) also displays fibrous filaments on olivine surfaces (Fig. 4f). These fibrous filaments have textures similar to those observed in Sample SC3-HQ but they are less prominent (smaller and less abundant).

TGA analysis indicates minor changes in the composition of samples during experiments with a total weight loss of <1% for analyzed samples SC1-LQ, SC3-HQ and SC4-VHQ (Fig. 6). All samples show a steady decrease in mass with increasing temperature up to 1000 °C in relation to progressive dehydration of the rock samples. Weight loss increases for decreasing flow rates suggesting that secondary phases were more abundant when flow rate was slower. Small steps in the weight loss curves can be used to identify these secondary phases (Földvári, 2011). The first step at 100 °C indicates the loss of molecular water. A second step is observed between 600 °C and 700 °C in all samples (Fig. 6). It is particularly marked in Sample SC1-LQ (− 0.92 wt%) where it occurs between 580 °C and 723 °C. It overlaps the expected range of temperature for the dehydration of serpentine (550–750 °C, Godard et al., 2013; Földvári, 2011; Lafay et al., 2012; Viti, 2010). This second step occurs at higher temperature and becomes progressively less pronounced as flow rate increases in samples SC3-HQ (− 0.76 wt %, 638 °C) and SC4-VHQ (− 0.61 wt%, 653 °C. Very small variations in the weight loss curves are observed around 330 °C for Sample SC1-LQ and around 340 °C for Sample SC4-VHQ. It could relate to the presence of small amounts of neoformed brucite which dehydration temperature ranges between 350 and 450 °C (Földvári, 2011).

3.2. Fluid chemistry of the outlet fluids

Outlet fluids have high pH and low alkalinity compared to inlet fluids (Fig. 7; Appendix B. Tables B.1 to B.4). The increase in pH indicates dissolution of silicates (here olivine) (Gislason and Oelkers, 2003; Seyfried et al., 2007) and the decrease in alkalinity suggests carbonate trapping

Please cite this article as: Escario, S., et al., Experimental study of the effects of solute transport on reaction paths during incipient serpentinization, Lithos (2018), https://doi.org/10.1016/j.lithos.2018.09.020

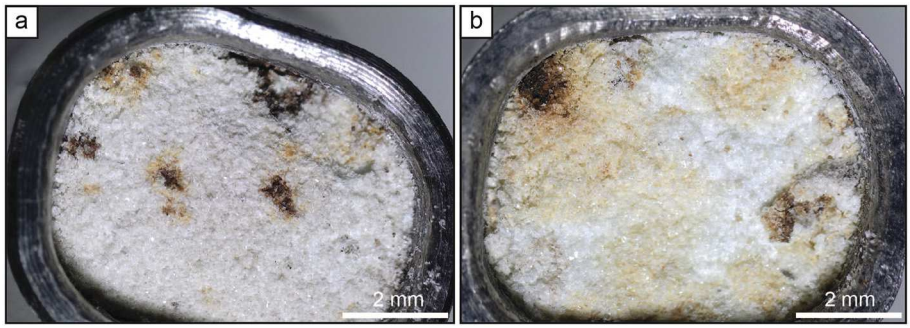

Fig. 3. Binocular photo of the (a) inlet and (b) outlet of sample SC1-LQ.

and/or changes in the carbonate speciation. Outlet fluids display similar in situ pH values from one experiment to the other (~6.1) suggesting that the outlet fluids are buffered by the same mineral assemblage. These pH values calculated at 170 °C indicate that, similar to inlet fluids (in situ pH_{ASW} ~ 5.8), all outlet fluids are slightly alkaline (higher that neutral pH at 170 °C = 5.68 (Bandura and Lvov, 2006) calculated at

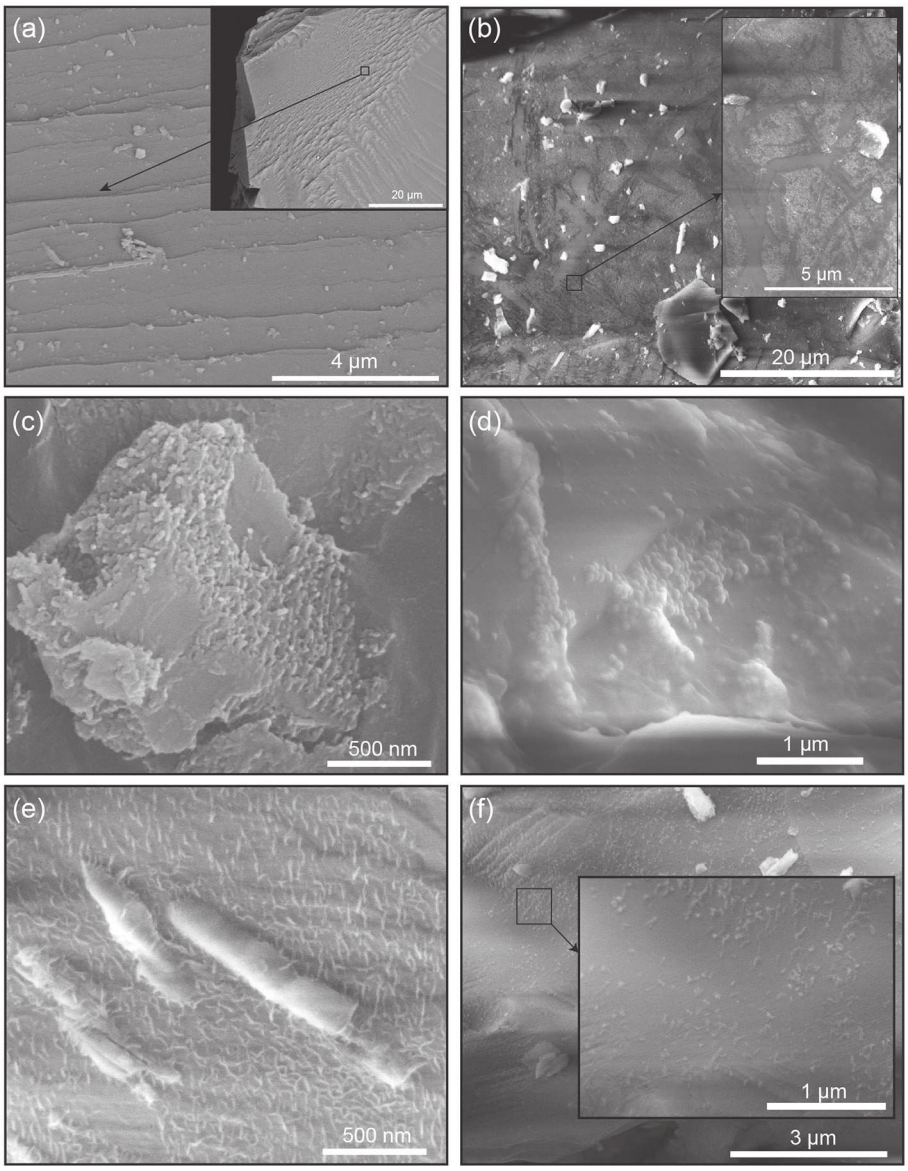

Fig. 4. SEM images of the surface of unreacted and reacted olivine grains. (a) The surface of unreacted olivine grains is rough and uneven: grains were mechanically cracked, mainly along crystallographic planes, during sample preparation (powdering, compression on olivine layers during capsule filling) and nano olivine grains are typically observed on these surfaces. (b) Reacted olivine surfaces are covered by 2–3 µm large patches of a fluffy light grey deposit bounded by dark grey lines (Sample SC3-HQ). Small undissolved olivine grains (white) are observed on the surface and are sometimes covered by these deposits. At nano-scale, the fluffy deposit has different textures in the three reacted samples: (c-d) Nodular aggregates developed on the reacted olivine surface in sample SC1-LQ and SC2-MQ respectively. (e-f) Assemblage of fibrous filaments evolved in sample SC3-HQ and SC4-VHQ respectively.

Please cite this article as: Escario, S., et al., Experimental study of the effects of solute transport on reaction paths during incipient serpentinization, Lithos (2018), https://doi.org/10.1016/j.lithos.2018.09.020

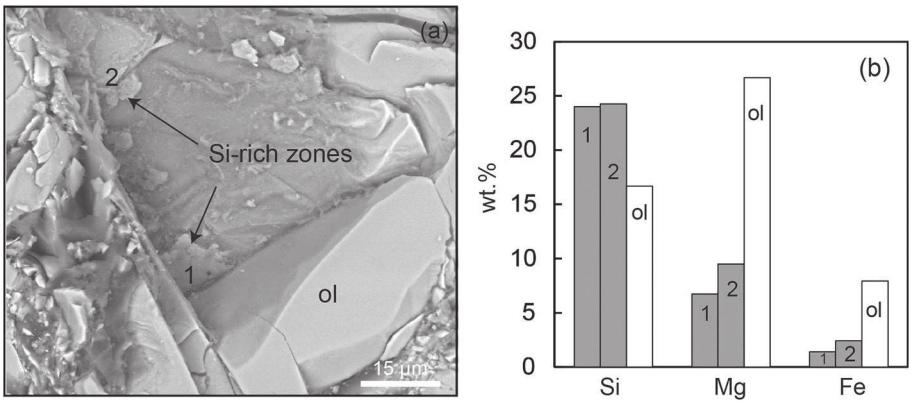

Fig. 5. SEM images of Sample SC2-MQ. (a) Silica rich zones, 1 and 2, were identify by SEM-EDS. (b) SEM-EDS analysis (in wt%) on the silica rich zones and olivine (ol).

25 MPa). In contrast to pH, carbonate alkalinity displays a broad range of values from one experiment to the other. Carbonate alkalinity of outlet fluids is overall low during experiments SC1-LQ (27.5–30.5 mg/L) and SC2-MQ (27.5–33.0 mg/L). It displays highly scattered values (29.9–47.0 mg/L) during experiment SC3-HQ but no significant trends. In contrast, carbonate alkalinity of outlet fluids during experiment SC4-VHQ increases with time (27.5–37.2 mg/L); it increases also with increasing pH, as expected for a solution close to neutral pH becoming more alkaline (Zeebe and Wolf-Gladrow, 2001).

The outlet fluid composition in the cations dominant in olivine (Si, Mg, Fe) and in ASW (Mg, Ca) varies with time and from one experiment to the other (Fig. 8, Appendix B. Tables B.1 to B.4) indicating differences in the extent and kinetics of dissolution and precipitation reactions. Low Q (SC1-LQ and SC2-MQ) and high Q (SC3-HQ and SC4-VHQ) experiments show distinct time series. Experiments SC1-LQ and SC2-MQ are characterized by a sharp and selective increase in Si in the outlet fluids (up to 0.24 mmol/L) followed by a sharp decrease during the early stages of the experiments ($\langle 200h$). Mg, Ca and Fe outlet fluid concentrations are relatively constant during these experiments except for an increase in Mg (up to 41.5 mmol/L) and Ca (up to 3.4 mmol/L) between 90 and 112 h during experiment SC1-LQ. In contrast, experiments SC3-HQ and SC4-VHQ are characterized by a steady decrease in Si concentrations in the outlet fluids with time. Overall, Mg, Fe and Ca concentrations decrease with time in the outlet fluids during experiment SC3-HQ. During experiment SC4-VHQ, Mg, and Ca concentrations are more variable but the overall trend is apparent steady state whilst Fe shows a strong increase in composition during the first 400 h of the experiment (up to 45.1 µmol/L).

Sharp increases in all cation concentrations in outlet fluids are commonly observed during the early stages of reactive-percolation experiments using sintered and compressed mineral powders (e.g., Andreani et al., 2009; Godard et al., 2013; Peuble et al., 2015a). These enrichments are attributed to the fast dissolution of the small mineral fragments (characterized by their large reactive surface area) produced during compression of the µm-olivine grains. Such trends are not observed in this set of experiments. The selective Si enrichment observed during

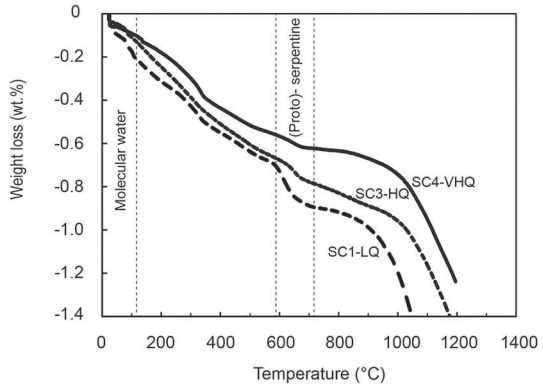

Fig. 6. Thermogravimetric analysis of Samples SC1-LQ, SC3-HQ and SC4-VHQ.

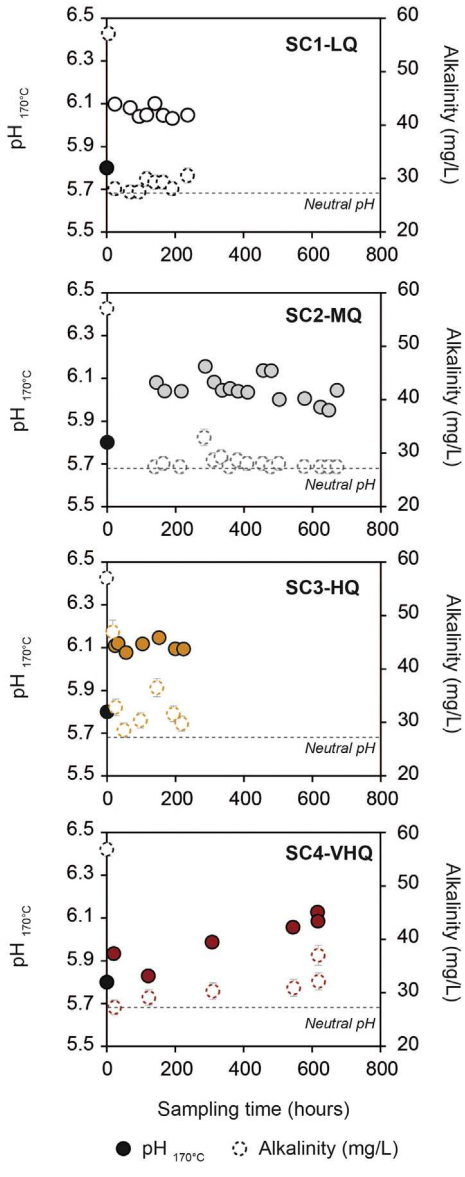

Fig. 7. pH calculated at 170 °C and alkalinity measured at 25 °C of the outlet fluids for SC1-LQ, SC2-MQ, SC3-HQ and SC4-VHQ.

Please cite this article as: Escario, S., et al., Experimental study of the effects of solute transport on reaction paths during incipient serpentinization, Lithos (2018), https://doi.org/10.1016/j.lithos.2018.09.020

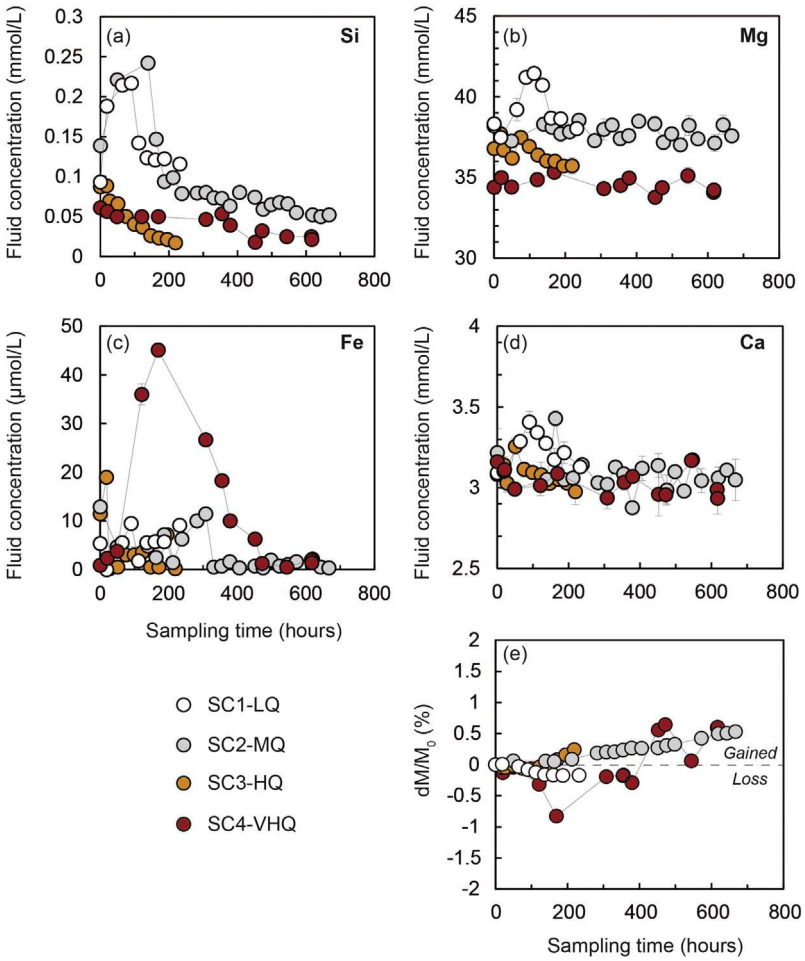

Fig. 8. (a-d) Si, Mg, Fe and Ca concentrations (mg/L) of the outlet fluids as a function of time of sampling (h) for experiments SC1-LQ, SC2-MQ, SC3-HQ and SC4-VHQ. (e) Total mass changes in the reacting samples with time on a volatile-free basis. Mass balances ($M_{inlet} - M_{outlet}$) were calculated using fluid time series assuming all cations occurred as oxides. Positive values indicate that samples gained mass during experiments (mineral trapping). Negative values indicates cationic loss compared to the initial sample mass, but does not preclude an actual increase in the mass of the samples during experiments as H_2O and CO_2 trapping associated to the formation of hydrous phases and carbonates are not taken into account in these calculations.

the early stages of experiments SC1-LQ and SC2-MQ suggests that preferential dissolution of smaller grains did occur but that the kinetics of the processes controlling Mg-trapping were faster compared to those controlling Si-trapping in these experiments. The absence of such transient cationic enrichments in the early stages of experiments SC3-HQ and SC4-VQ suggests an alternate coupling mechanism between dissolution/precipitation kinetics and transport at high flow rates.

As illustrated on Fig. 8, the mass of Si, Mg, Fe and Ca oxides lost and/or gained calculated using fluid time series can provide a first estimate (on a volatile-free basis) of the mass changes in the reacting samples (e.g., Godard et al., 2013). Mass balances are calculated assuming that fluid concentrations at the sampling time are representative of the outlet fluid composition between sampling. The four experiments record variations in the total mass of reacted samples but these changes are small. Sample SC1-LQ shows a progressive decrease in mass with time down to 0.16 wt% relative to its initial mass whilst samples SC2-MQ and SC3-HQ indicate an increase in mass of up to 0.50 wt% relative to its initial mass for experiment SC2-MQ (the longest duration). The overall trend is difficult to evaluate for sample SC4-VHQ: the strong scatter in the calculated mass trends indicates that the assumption that analyzed fluid compositions are representative of the average composition of fluids between sampling is undoubtedly not correct for experiment SC4-VHQ. Nevertheless, we note that similar to sample SC2-MQ, sample SC4-VHQ shows the largest change in mass. Experiment SC4-VHQ was the second longest experiment suggesting that, to the first order, the total mass of dissolved and precipitated minerals at the end of experiments is proportional to their duration (Fig. 8).

In an attempt to constrain the precipitation and dissolution processes that control the sample mass variations, we calculated the saturation indexes in the outlet fluids using the EQ3/6 geochemical software using the 25 MPa thermodynamic database generated for this study. The saturation index Ω is defined as

$$\Omega = \frac{IAP}{K} \tag{2}$$

where *IAP* is the ion activity product, and *K* is the equilibrium constant. When log (Ω) is negative for a given mineral, the solution is under-saturated and can potentially dissolve this mineral. When it is positive, the solution is saturated and this mineral has the potential to precipitate, provided nucleation occurs and kinetics are favorable.

As illustrated on Fig. 9, olivine is under-saturated in the four experiments and is thus expected to dissolve. It should be noted that olivine saturation indexes are overall the lowest for high flow rate experiments, SC3-HQ and SC4-VHQ, suggesting that disequilibrium toward olivine is more efficiently maintained during these experiments compared to the others. Outlet fluids are saturated for serpentine (chrysotile) and hematite, indicating chemical conditions favorable for their precipitation. Magnetite saturation indexes oscillate around zero whilst brucite saturation indexes are slightly negative (close to zero) in the four

Please cite this article as: Escario, S., et al., Experimental study of the effects of solute transport on reaction paths during incipient serpentinization, Lithos (2018), https://doi.org/10.1016/j.lithos.2018.09.020

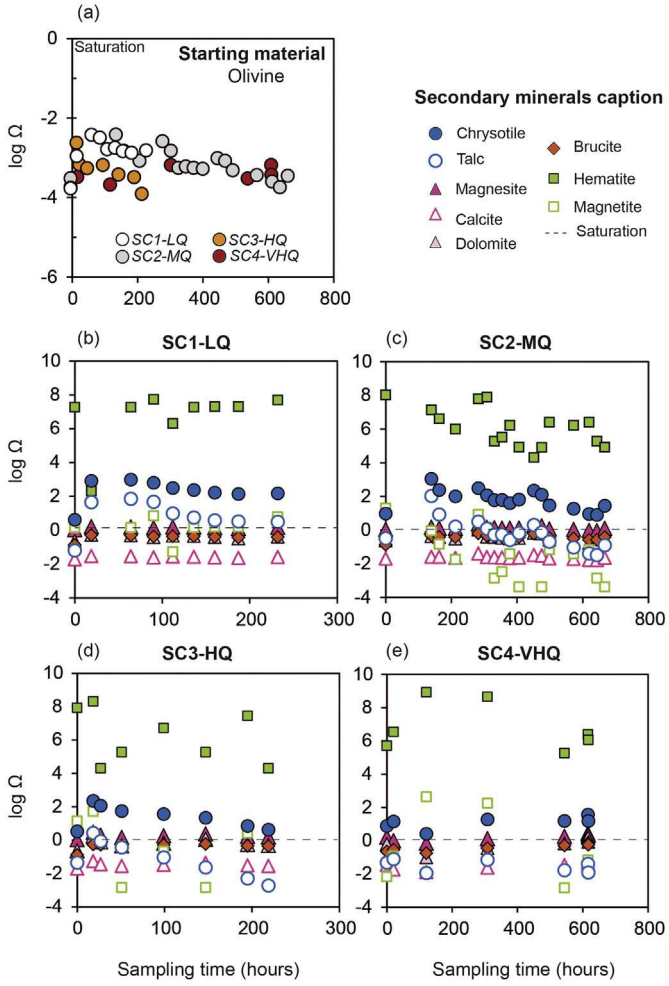

Fig. 9. Saturation index (Ω) for outlet fluids during experiments SC1-LQ, SC2-MQ, SC3-HQ and SC4-VHQ. Saturation indexes were calculated at 170 °C and 25 MPa using EQ3/6 (Wolery and Jarek, 2003). (a) Saturation index of the primary mineral (olivine) versus sampling time; (b-e) Saturation index calculated for chrysotile, talc, magnesite, calcite, dolomite, brucite, hematite and magnetite for each experiment.

experiments. At the calculated pH conditions, outlet fluids are slightly too Fe- and Mg-poor to be systematically saturated relative to magnetite and brucite respectively; we cannot preclude however that percolating fluids did not reach locally saturation for these minerals, in particular in the vicinity of dissolving olivines. Talc saturation indexes in outlet fluids are positive for experiment SC1-LQ, they decrease with time (from positive to negative) during experiments SC2-MQ and SC3-HQ, and are negative for experiment SC4-VHQ. This suggests that the processes controlling silica activity in our experiment is, at least in part, related to flow rate. This may imply a relation to transport properties and/or to the actual water/rock ratio. Thermodynamic modelling using the EQ3/6 code were run at experimental conditions assuming equilibrium to test the effect of effective water / rock ratio on the secondary mineralogy (Appendix G. Fig.G1). Results indicate that brucite precipitates preferentially for low water/rock ratios. Consequently, we infer that its formation would be favored in low flow experiments; this would in turn explain the slightly higher Si activity in the outlet fluids for these experiments (Fig. 8a). Saturation indexes of carbonates are slightly negative (calcite) or close to zero (magnesite and dolomite) for all experiments except for huntite ($Mg_3Ca(CO_3)_4$). Huntite saturation indexes range between 125 and 127 for all experiments (Appendix D. Table D). It is worth to note that, in the field, the precipitation of huntite is also typically associated to low temperature hydrothermal alteration of ultramafic basements (e.g., Stanger and Neal, 1994).

4. Discussion

4.1. Flow rate and fluid-rock reaction paths

Post-experiment characterization shows minor changes in the overall composition and structure of reacted sample suggesting that serpentinization kinetics was slow compared to the duration of the experiments. Nevertheless, outlet fluid composition time series (Fig. 9) and the occurrence of serpentine-type minerals and minor carbonates coating the olivine surface (Fig. 4) indicate that fluid-rock reactions occurred. All measured inlet and outlet fluid compositions plot in the domain of stability of serpentine in the $Mg^{2+}/(H^+)^2$ versus SiO_2 activity diagram (Fig. 10). This denotes that 1) the fluid is undersaturated with respect to olivine and 2) the neoformed serpentine is buffering the composition of fluids throughout the experiments. This implies that serpentine precipitation occurs close to equilibrium. Furthermore one observes that the composition of outlet fluids tends toward similar $aMg^{2+}/a(H^+)^2$ values ranging from 9.7 to 10 suggesting that a steady-state regime of mass transfer is achieved and controls the pH and the Mg activity. This steady-state is achieved in a few hours for all experiments except for experiment SC4-VHQ (Table B.4 (Appendix B); Fig. 10a-b) for which it is achieved after 300 h. This is a first indication that the flow rate is a controlling parameter of the effective fluid-mineral mass transfer rate.

Additionally, we observe two trends in the evolution of SiO_2 activity. Outlet fluid time series of low Q experiments SC1-LQ and SC2-MQ show first an increase in SiO_2 activity then a decrease associated with a constant $aMg^{2+}/(H^+)^2$. At the opposite high Q experiments SC3-HQ and SC4-VHQ are characterized by a decrease of the SiO_2 activity which starts since the beginning for the experiment with the highest value of Q. These distinct behaviors suggest the development of different reaction paths and thus the predominance of different mass transfer mechanisms.

Secondary phases were too few and too small to be analyzed, which precluded evaluating precisely the amount of dissolved and precipitated phases using the fluid-time series. The reactions for the lowest values of Q and for the highest values of Q were thus determined on the basis of (1) our observations of the reacted samples and fluid time series which suggest olivine dissolution and precipitation of oxides, serpentine-type hydrous phases and minor carbonates and (2) the following assumptions for the composition of the precipitated phases: (i) serpentine, and brucite when present, do not incorporate Fe. (ii) The neoformed oxide is magnetite. (iii) All carbonates have the composition of huntite.

Magnetite was hypothesized to be the Fe-bearing secondary phase for these calculations, as it is the main oxide formed during serpentinization in natural conditions (e.g., Bach et al., 2004). Reactions written assuming that the Fe-bearing secondary phase is hematite (oxidizing conditions) are overall similar to those described thereafter (Appendix E). It should be noted also that several studies of experimental serpentinization (e.g., Godard et al., 2013; Marcaillou et al., 2011) and oceanic serpentinites (e.g., Andreani et al., 2013) indicate that incipient serpentinization can produce Fe-bearing serpentines. Unfortunately it was not possible to characterize the chemical composition of the neoformed proto-serpentine aggregates in our experiments because they were too small (<1 μm). Thus, hypotheses (i) and (ii) may lead to overestimating the fraction of secondary oxides (up to 13%).

The first type of serpentinization reaction results in Mg trapping and/or release of Si (Fig. 11a) and produces serpentine-type minerals having nodular textures (Fig. 4c-d). This reaction characterizing the low Q experiments SC1-LQ and SC2-MQ can be written as:

$$15\,Mg_{1.8}Fe_{0.2}SiO_4\,(olivine) + 25H_2O + MgOH^+{}_{(aq)} \rightarrow 4\,Mg_3Si_2O_5(OH)_4\,(serpentine) + 16\,Mg(OH)_2\,(brucite) + Fe_3O_4\,(magnetite) + 7\,SiO_{2(aq)} + H_{2(g)} + H^+ \quad (R2)$$

Please cite this article as: Escario, S., et al., Experimental study of the effects of solute transport on reaction paths during incipient serpentinization, Lithos (2018), https://doi.org/10.1016/j.lithos.2018.09.020

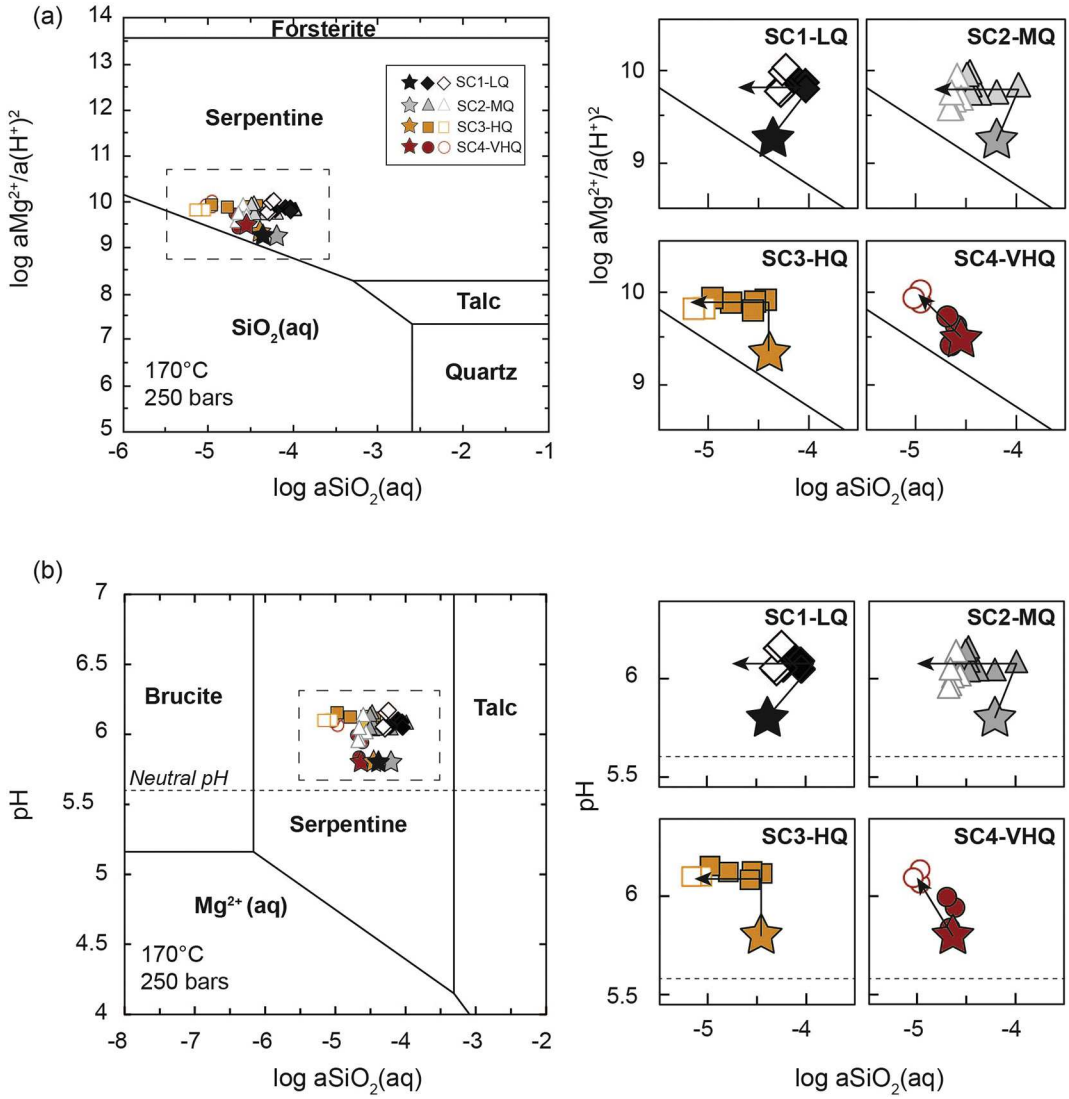

Fig. 10. (a-b) Activity-activity diagrams illustrating equilibrium for the MgO-SiO_2-H_2O-NaCl system at 170 °C and 250 bars calculated using GWB (Bethke, 1996). The filled stars represent the initial fluid (ASW) for each individual experiment. The filled symbols indicate beginning of the experiment (160 h first hours for SC1-LQ, 400 h first hours for SC2-MQ, 150 h first hours for SC3-HQ, and 309 h first hours for SC4-VHQ). The open symbols indicate the end of the experiment (145 h last hours for SC1-LQ, 261 h last hours for SC2-MQ, 72 h last hours for SC3-HQ and 309 h for SC4-VHQ). (a) All fluid samples denote increase in $a Mg^{2+}/a(H^+)^2$ compared to the initial fluid solutions. SC1-LQ and SC2-MQ shows increase in the $aSiO_2$ (aq) compared to the ASW on the first hours to then decrease the activity during the last hours. SC3-HQ and SC4-VHQ shows decrease in $aSiO_2$ (aq) for all fluid samples compared to the ASW. (b) All fluid samples denote an increase on pH.

Concomitant Si enrichment in fluids with Mg trapping has been observed by Godard et al. (2013) during reactive percolation experiments with injection of artificial seawater into olivine cores at low flow rates. Increase in Si concentrations in fluids were also documented during closed-system serpentinization experiments (batch reactors, gold cell hydrothermal equipment) when reacting artificial seawater with olivine (Allen and Seyfried, 2003; Berndt et al., 1996; Klein et al., 2013) and with peridotite (Allen and Seyfried, 2003; Janecky and Seyfried, 1986; Klein et al., 2015; Seyfried et al., 2007; Seyfried and Dibble, 1980). When pyroxene was present in the primary mineral assemblage, selective increase in SiO_2(aq) was ascribed to pyroxene dissolution (e.g., Klein et al., 2015) but Si enrichment in fluids was documented also when only olivine was present (e.g., Mccollom et al. (2016) in seawater and Okamoto et al. (2011) in pure water). It is worth noticing that all these experimental studies indicate that increase in Si concentrations occur essentially during the earliest stages of serpentinization.

The second type of serpentinization reaction favors Si-trapping and release of Mg in the fluid, while produces filament-type proto-serpentine (Fig. 4e-f). It characterizes experiment SC4-VHQ (Fig. 11d):

$$15\ Mg1.8Fe0.2SiO4\ (olivine) + 18H2O + 2SiO2(aq) + 1.5H + \rightarrow 8.5\ Mg3Si2O5(OH)4\ (serpentine) + 1.5\ MgOH + (aq) + Fe3O4\ (magnetite) + H2(g) \quad (R3)$$

The textures of the secondary products are comparable to those reported by Luhmann et al. (2017) for reactive percolation experiments during which artificial seawater and Si-rich artificial seawater were injected into pyroxene-bearing dunite cores. Flow injection rates during the Luhmann et al. (2017) experiments are similar to experiment SC3-HQ. The variations in outlet concentrations in Si and Mg for the Si-rich artificial seawater experiments of Luhmann et al. (2017) are remarkably similar to those of experiment SC4-VHQ suggesting a control of inlet fluid compositions on the reactivity of the fluid-rock system, in addition to transport.

Serpentinization reaction paths (R2) and (R3) indicate strong feedbacks between mineral reactions and fluid compositions, and

Please cite this article as: Escario, S., et al., Experimental study of the effects of solute transport on reaction paths during incipient serpentinization, Lithos (2018), https://doi.org/10.1016/j.lithos.2018.09.020

emphasize the importance of pH variations during serpentinization reactions as previously noted by Janecky and Seyfried (1986). The first type of serpentinization reaction traps Mg and decreases pH (R2) whereas the second traps Si and increases pH (R3) as observed in the course of the low *Q* and the high *Q* experiments respectively. Carbonate formation will increase or hamper these trends as it releases protons in the solution and will decrease both pH and alkalinity:

$$CaOH^{+}_{(aq)} + 3\,MgOH^{+}_{(aq)} + 4\,CO_{2(aq)} \rightarrow CaMg_3(CO_3)_4\ (Huntite) + 4H^{+} \quad (R4)$$

However, it must be noted that the first volume of fluid sampled at the outlet systematically display higher pH values compared to those of the inlet fluid for SC1-LQ, SC2-MQ and SC3-HQ. This indicates that the mechanism(s) governing proton trapping predominate(s) in the early stages of these experiments.

These divergences in chemical trends from one experiment to the other as well as the comparison to other experiments performed for similar conditions suggest that reaction paths and kinetics during incipient serpentinization are, at least partially, controlled by solute transport. The dimensionless Péclet number (*Pe*) is often used for evaluating whether advection or diffusion is the dominant transport mechanism for chemical species in a porous media (e.g., Steefel and Maher, 2009). We calculated the values of *Pe* corresponding to the four reactive percolation experiments as:

$$Pe = \frac{v\lambda}{d} \quad (3)$$

with *v* the mean fluid velocity, *d* the diffusion coefficient and λ the characteristic length at which the process is considered. The mean fluid velocity (m/s) was defined here as the velocity distribution of the fluid in the void space, and calculated as $v = Q/\varphi S$ with *Q* the flow rate (m^3/s), φ the porosity and *S* the cross-section of the sample (m^2). The characteristic length λ was set to be that of the average pore size calculated from SEM images, i.e. 10^{-4} m. Diffusion was set to $5 \times 10^{-9}\ m^2.s^{-1}$ (Philibert, 2005). The calculated *Pe* values and mean velocity *v* values are reported in Table 1. By definition, transport is advective for $Pe >> 1$ and diffusive if $Pe << 1$. As expected, the calculated Pe-numbers increase with *Q* from experiment SC1-LQ ($Pe = 0.2$) to experiment SC4-VHQ ($Pe = 4$). However, these values fall into the range [0.1, 10] in which both diffusion and advection are active mechanisms of solute transport. Yet these values indicate that in average advection is about 20 times more effective for experiment SC4-VHQ than for experiment SC1-LQ. Though, the distribution of the *Pe* values at pore scale does cover a very large spectrum that inherits from the distribution of the fluid velocity that typically covers several orders of magnitude in such porous media (see for examples Gjetvaj et al., 2015 and Siena et al., 2015).

Yet, for this range of *Pe* values, the relation between the type of reaction and the transport regime (from diffusive-dominant to advective-dominant) it not straightforward as illustrated in Fig. 11. In the following section, we will discuss the possible coupling and/or feedback effects between the kinetics of olivine dissolution, the mechanisms driving secondary mineral precipitation and the hydrodynamical renewal of the solutes at the mineral interface.

4.2. Kinetics- versus transport-controlled fluid-rock reaction path scenarios

In order to interpret the chemical trends observed during the olivine-seawater reactive percolation experiments, the mechanisms driving fluid-rock reactions are often described as a four-steps process (Morse and Arvidson, 2002; Ruiz-Agudo et al., 2014): (1) flow and transport of chemical species to the olivine surface, (2) dissolution of olivine, (3) transport of secondary chemical products to the locus of precipitation and (4) precipitation of secondary minerals. Each step is favored or hindered by different hydrodynamic and chemical processes.

Step (1) and (3) are directly related to the structural and hydrodynamic properties of the reacting porous media. First, the surface of minerals accessible to fluids, or the reactive surface area, is structurally restricted in porous media, in particular when compared to uncompressed powdered samples from which most of the thermodynamic and kinetics data available in the literature are measured, thus resulting in an overestimate of the serpentinization rate when applied directly to model natural systems (e.g., Malvoisin and Brunet, 2014). The permeability and the distribution of the fluid velocities, two parameters related to the pore structure variability, are also identified as controlling the transport of solutes to and from the surface of minerals during serpentinization (Farough et al., 2016; Godard et al., 2013; Luhmann

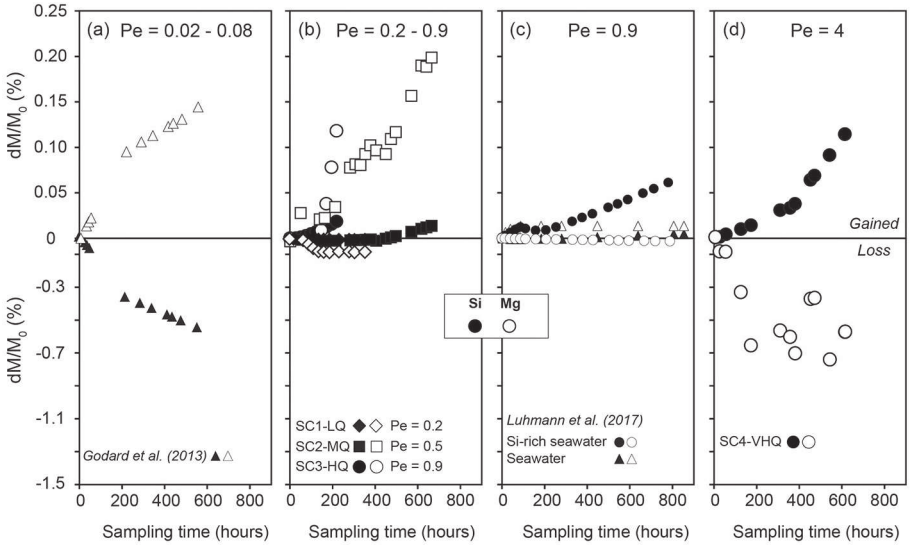

Fig. 11. (a-d) Mass of Silica (Si) and Magnesium (Mg) loss and/or gained compared to the initial mass by the four reacted samples versus sampling time. Solid symbols indicate Si and open symbols indicate Mg. (a) Low Peclet numbers ($Pe = 0.02$–0.08): Results of Godard et al. (2013) run at similar conditions of temperature (190 °C) and fluid composition (seawater) and initial sample conditions (olivine). The Peclet number was determined for a pore length of 50 μm. (b) Peclet number between 0.2 and 0.5: Results of experiment SC1-LQ ($Pe = 0.2$), SC2-MQ ($Pe = 0.5$) and SC3-HQ ($Pe = 0.9$). (c) Peclet number between 0.2 and 0.9: Results of Luhmann et al. (2017) run at similar conditions as the present experiments. Triangles shows experiments run under artificial seawater at 150 °C. Circles shows experiments run under Si-rich seawater at 200 °C. The range of Peclet number was determined for a pore length of 20 μm ($Pe = 0.2$) and 100 μm ($Pe = 0.9$). (d) High Peclet number ($Pe >> 1$): Results of experiment SC4-VHQ ($Pe = 4.0$).

Please cite this article as: Escario, S., et al., Experimental study of the effects of solute transport on reaction paths during incipient serpentinization, Lithos (2018), https://doi.org/10.1016/j.lithos.2018.09.020

et al., 2017). Permeability is controlled mainly by the flow path tortuosity and the overall connectivity of the pore network. Permeability can be noticeably altered depending on the volume and the localization of the dissolution and precipitation reactions, specifically for low porosity systems close to the percolation threshold as evidenced in carbonate dissolution/precipitation experiments for instance (e.g. Luquot and Gouze, 2009). Indeed, fast decrease of permeability was measured during serpentinization experiments of low porosity of the initial material (e.g., Andreani et al., 2009). Conversely, the four experimental samples used in this study displayed similar high initial porosity and permeability values and no noticeable changes of permeability was measured during experiments indicating that alteration of the connected pore structure resulting from fluid-rock reactions were negligible (Table 1).

Conversely, for a well-connected network of pores, the pressure gradient along the flow paths is almost constant. Thus the average (laminar) velocity along a given flow path is linearly proportional to the macroscopic flow rate and scales locally as the square of the pore diameter. Furthermore the velocity profile across a given section of a given flow path is parabolic (Poiseuille flow). This means that the thickness of the layer, at the surface of the mineral, for which the transport is dominantly diffusive (i.e. low value of the local *Pe* number) depends on the local hydraulic diameter and on the macroscopic flow rate (Fig. 12). The diffusion-dominated zones (diffusive layers and dead-ends) in which the mixing of the solutes is maximum, such increasing the probability of reaction compared to advection-dominated zone, control the (relative) localization of the reactions, i.e. steps 2 and 4.

These considerations imply that 1) large variability of the diffusion-dominated zone is expected in heterogeneous porous media, 2) the fraction of diffusion-dominated zones increases at low flow rate and 3) a redistribution of the diffusion-dominated zones can be triggered by the dissolution-precipitation processes while inducing negligible changes in the sample permeability. Furthermore these dissolution-precipitation processes can create dead-ends where the fluid is quasi-immobile. These mechanisms have been observed in the course of experimental dissolution of sedimentary rocks (e.g., Gouze and Luquot, 2011; Noiriel et al., 2007). In the case of the four experiments discussed here, the distribution of fluid velocities is the dominant transport parameter that changes from one experiment to the other. Accordingly, the difference between the results for these experiments must be investigated in terms of local changes induced by the different the flow regimes.

The mechanisms of dissolution (Step 2) and precipitation (Step 4) have been thoroughly investigated for ultramafic water-rock systems (e.g., reviews of Oelkers (2001) and Crundwell (2014), Rimstidt et al., 2012 and references therein). These studies showed the role of pH in controlling olivine dissolution kinetics: in acid solutions, olivine dissolution rate is fast and proportional to the activity of protons whilst, in alkaline solutions, olivine dissolution rates are pH-independent. The transition from one mode to the other is for pH values around 6 at 25 °C (Crundwell, 2014). These studies also stressed the inhibiting effects of the fluid silica activity and carbonate contents on olivine dissolution and the importance of the chemical processes occurring at the mineral surface (adsorption and desorption, protonation) during dissolution. They showed that the precipitation of secondary hydrous phases, carbonates and oxides and their kinetics were controlled by the thermodynamic and chemical parameters (e.g., P, T, pH, ionic strength, speciation as summarized by saturation indexes) whilst investigating the role of nucleation and surface processes. For instance, fast or slow precipitation kinetics determine whether a mineral thermodynamically stable according to activity diagrams and saturation indexes can be present or not (e.g., Bénézeth et al., 2011) and the formation of hydrated surface precursor complexes will facilitate the formation of hydrous species such as brucite (e.g., Pokrovsky and Schott, 2004). Most of studies on the kinetics of mineral dissolution and precipitation were realized at temperatures below 100 °C, nevertheless the rate-controlling mechanisms of these reactions are well understood (Pokrovsky and Schott, 2000a, 2000b; review in Crundwell, 2014 and Ruiz-Agudo et al., 2014) and we posit that the conceptual models based on these studies could be used as a starting point to interpret the results of our four reactive percolation experiments.

We postulate first that the possible intermediate reaction paths for olivine serpentinization are controlled by the coupling between olivine dissolution, assumed to be dominantly controlled by proton activity at the fluid-mineral interface, and serpentine precipitation, which buffers the fluid composition (including pH, see Fig. 10). Flow and transport processes determine the *reaction domains* in which these interactions occur. As illustrated in Fig. 12, two end-member scenarios are proposed to summarize the interplay between these mechanisms. They are governed by the development of diffusive boundary layers at the fluid / mineral interface and by chemical gradients within these diffusive layers. As mentioned earlier, the thickness of diffusive layers is inversely proportional to the local value of *Pe* and, consequently, chemical gradients are directly correlated to local fluid velocity.

The first scenario, hereafter referred to as a *transport-controlled scenario* (Fig. 12a), characterizes low fluid velocity domains, where diffusive layers can grow and occupy significant pore volume. These diffusion-dominated "reaction domains" represent zones where mixing can occur and which are therefore favorable to chemical reactions (e.g., Luquot and Gouze, 2009). In these domains, fluid compositions will be controlled by that of dissolved olivine at the mineral surface and progressively equilibrate with the composition imposed by advecting fluids at the outer boundary of the diffusive domain. Chemical and charge gradients across the diffusive domain drive ionic (cation, anions) and proton exchanges respectively between the olivine surface and advecting fluids. Protons adsorption at the mineral surface induces the dissolution of olivine and the detachment of SiO_4^{4-} and Mg^{2+}. $MgOH^+$(aq) is formed by the hydration of Mg^{2+} and adds up $MgOH^+$(aq) of incoming fluids. Hydration of SiO_4^{4-} increases pH, which favors the precipitation of brucite after $MgOH^+$(aq) in the diffusion-dominated "reaction domain". The early enrichments in $SiO_{2\,(aq)}$ and pH increase of the outlet fluids, which represent the advecting fluids in this model, implies that serpentine precipitation rates are slow compared to brucite precipitation rates as well as to the rate of proton and silica exchanges between the diffusion-dominated "reaction domain" and advecting fluids. As reaction progresses, a steady state will be reached: pH will stabilize and/or decrease slightly (Figs. 7, 10) as a result of the formation of brucite which, in turn, will favor serpentine formation, eventually after brucite (Reaction R3; Godard et al., 2013; Tutolo et al., 2018). The second end-member scenario, here referred to as the *kinetics-controlled scenario* (Fig. 12b), is associated to high fluid velocity zones, where the fast renewal of fluid at the mineral surface limits the development of the diffusive layer. The "reaction domain" then covers the full porous network and the mineral/fluid interface is namely undistinguishable from the outer diffusive layer boundary. In this advection-dominated "reaction domain", spreading will favor efficient transport of protons and chemical species while limiting their interactions in fluids and thus hinder chemical reactions. The sharp chemical gradient between olivine surface and advecting fluids favors high olivine dissolution kinetics and efficient detachment of SiO_4^{4-} and Mg^{2+}. The progressive increase in pH (Fig. 7) indicates that rates of olivine dissolution and hydration of SiO_4^{4-} are faster than the transport of hydrated species, $SiO_{2(aq)}$ and $MgOH^+$(aq), out of the reactive zone. The belated stabilization of pH and evidence of silica trapping in fluid time series suggest a transient stage for the formation of serpentine, during which a silica rich layer could form at the fluid-mineral interface (e.g., Andreani et al., 2009; Daval et al., 2011; Pokrovsky and Schott, 2000a) until conditions favorable for serpentine precipitation are reached in the porous network. After 300 h, saturation relative to serpentine is achieved, serpentine (Spt) precipitates and consumes silica in excess. The serpentinization reaction then controls the mineral assemblage and the fluid composition following reaction path (R3).

These two end-members scenarios are not mutually exclusive at the scale of the studied samples: both diffusion and advection are effective

Please cite this article as: Escario, S., et al., Experimental study of the effects of solute transport on reaction paths during incipient serpentinization, Lithos (2018), https://doi.org/10.1016/j.lithos.2018.09.020

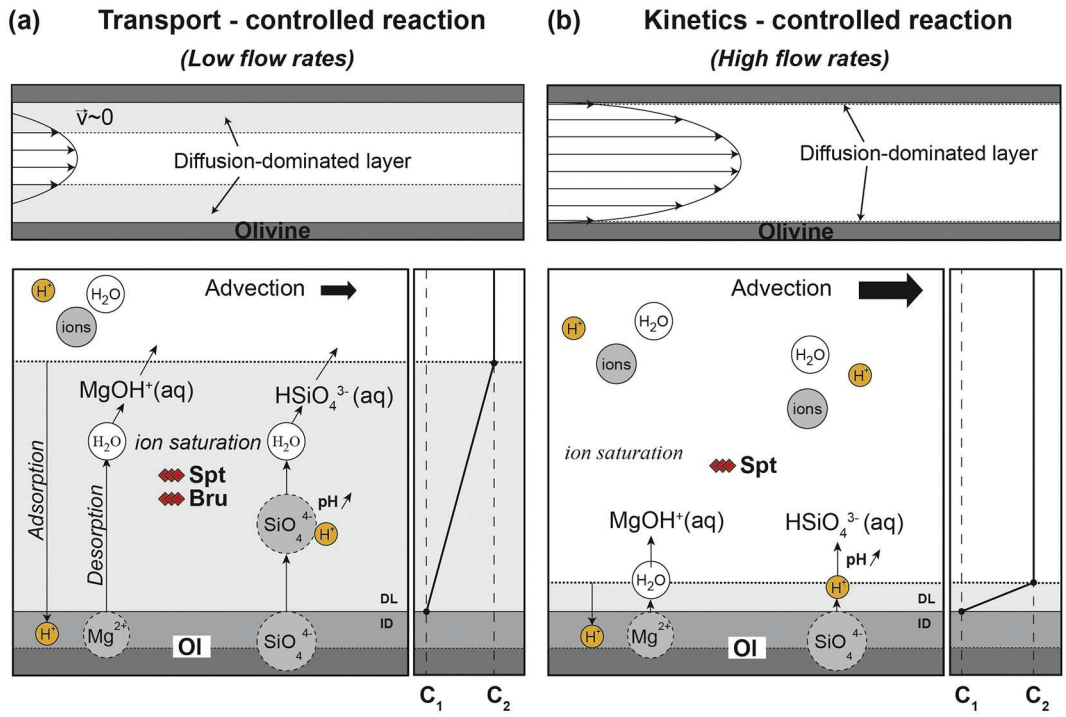

Fig. 12. End-members scenarios for incipient serpentinization at (a) low and (b) high flow rates. The distribution of the fluid velocity (v) in pores and flow paths determines the development of a diffusive boundary layer (DL) where $v \rightarrow 0$ at the mineral/fluid interface. The DL is large at low Q and is minimal for high Q (a-b). The surface of the olivine (Ol) is constituted of an ion detachment layer (ID) where fluid-rock reactions occur. The fluid is composed of water molecules (H_2O) (white circles), ions (grey circles) and protons (H^+) (yellow circles). The composition of the fluid at the outer boundary of the diffusive layer is that of the advected flow (C_2). When different from C_1, the composition of fluid in equilibrium with olivine, this difference in composition creates a chemical and electrical potential gradient in DL. The thickness of DL determines whether chemical and potential gradients will be low or high, which in turn will determine the mechanisms taking place in this layer (a) Transport controlled reaction paths are associated to low fluid velocity zones, which favors the development of diffusive layers and low chemical gradients between the olivine surface and advecting fluids. Proton transport toward the olivine surface is driven by the differences in electric charges between the dissolving olivine surface and advecting fluids. Protons adsorption at the mineral surface induces the stoichiometric dissolution of olivine, the detachment of SiO_4^{4-} and Mg^{2+} and the formation of $HSiO_4^{3-}$(aq) and $MgOH^+$(aq) respectively. The formation of $HSiO_4^{3-}$(aq) increases pH locally. The generation of $MgOH^+$(aq) coupled to the pH increase favors the saturation of brucite (Bru) and its precipitation together with serpentine (Spt) in the diffuse layer. (b) Kinetics controlled reaction are associated to high fluid velocity zones. The fast renewal of fluid at the mineral surface limits the thickness of the diffusive layer and produces sharp chemical gradients. Spreading limits the effects of fluid rock reactions at the mineral interface and favors the transport of $HSiO_4^{3-}$(aq) and $MgOH^+$(aq) out of the reactive zone. Serpentine (Spt) precipitates when super-saturation is reached in fluids flowing through the porous network. (For interpretation of the references to colour in this figure legend, the reader is referred to the web version of this article.)

mechanisms even if the macroscopic value of *Pe* is different from one experiment to the other.

The chemical mechanisms driving serpentinization reactions in the two end-member scenarios proposed here are similar to the scenarios proposed by Crundwell (2014); Lafay et al. (2012); Godard et al. (2013); Tutolo et al. (2018) for olivine dissolution and serpentinization in alkaline fluids and for serpentinization after brucite for the former (transport-controlled scenario), and to that proposed by Crundwell (2014); Seyfried and Dibble (1980); Allen and Seyfried (2003) for olivine dissolution in acidic fluids and serpentinization after Si-rich fluids for the latter (kinetics-controlled scenario). Transport controls local chemical fluxes and therefore the fluid compositions at the scale of the "reaction domain". In other words, these models suggest that local fluid composition is the main parameter governing reaction paths during our experiments. It noteworthy that pH in inlet and outlet fluids is slightly alkaline for all the experiments, suggesting that the transition from "alkaline" to "acidic" reaction paths occur most likely for pH(170 °C) around 6, that is within the alkaline domain for our experiments (neutral pH(170 °C) = 5.6). Interestingly, it is the same pH value as that suggested by Crundwell (2014) for reactions at 25 °C, suggesting that proton activity only (independently from temperature) would govern the change of kinetics for olivine dissolution.

Whatever the reaction paths, all experiments are characterized by a continuous decrease in Si compared to Mg (Figs. 8 and 10) and thus a continuous decrease in Si/Mg ratio (Appendix H Fig.H1). This variation could point to a decrease in the reactive surface areas over time. This process will produce a diminution of reaction rates that will ultimately end the reactions. This implies that the creation of new reactive surface area, via mechanisms such as fracturing (e.g., Kelemen and Hirth, 2012), is required to sustain these reactions over time.

4.3. New insights on serpentinization of oceanic mantle lithosphere

Serpentinization of the oceanic mantle is generally pictured as a single step reaction of hydration of mantle minerals, producing serpentine, magnetite, hydrogen, and minor brucite (e.g., Reaction R1) and/or silica rich fluids, when the alteration of mantle pyroxene is also taken into account (e.g., Beard et al., 2009; Klein et al., 2013; McCollom and Bach, 2009). However, petrological and magnetic studies of serpentinized oceanic mantle basement (e.g., Bach et al., 2006; Oufi et al., 2002) and fluid measurements at ultramafic hosted vents (e.g., Donval et al., 1997; Kelley et al., 2001; Schmidt et al., 2011; Seyfried et al., 2015; Seyfried et al., 2011) provide evidence that serpentinization is a multistage process along mid-ocean ridges. Furthermore, detailed geochemical studies of the fluid time series sampled at ultramafic hosted vents along slow spread ridges show that these fluids sample a single source and therefore the measured variations in fluid compositions are ascribed to the development of different serpentinization reaction paths in the mantle basement (e.g., Bach et al., 2004; Bach et al., 2006; McCollom and Bach, 2009; Seyfried et al., 2015; Syverson et al., 2017; Tutolo et al., 2018). The mantle lithosphere exposed along slow spread oceanic centers is highly heterogeneous with intrusions of large gabbroic bodies (e.g., Cannat et al., 1997; Früh-Green et al., 2003) and/or locally overlain by thin basaltic crust (e.g., Cannat et al., 2006; Escartin

Please cite this article as: Escario, S., et al., Experimental study of the effects of solute transport on reaction paths during incipient serpentinization, Lithos (2018), https://doi.org/10.1016/j.lithos.2018.09.020

et al., 2017). The variability of observed serpentinization reaction paths is thus commonly ascribed to changes in the composition of serpentinizing hydrothermal fluids resulting from interactions with these different lithologies along flow paths (e.g., Andreani et al., 2014; Bach et al., 2004). Our experiments suggest that some of these observed chemical variations might be intrinsic to incipient serpentinization of olivine-rich rocks infiltrated by Mg-bearing seawater derived hydrothermal fluids, thus providing new insights on several questions critical to understand serpentinization processes in the sub-seafloor ultramafic basement.

4.3.1. Origin and fate of silica rich fluids during sub-seafloor serpentinization

Olivine hydration reactions predict the formation of brucite together with that of serpentine, yet brucite remains a minor component in serpentinized oceanic peridotites, observed dominantly in the least serpentinized peridotites (e.g., Bach et al., 2004). Based on petrological observations and compositional considerations, it was proposed that oceanic serpentinization occurred as a two-step reaction sequence with first the formation of Fe-bearing serpentine and brucite after olivine followed by a reaction of silicification of brucite (e.g. Bach et al., 2006) written as (assuming brucite does contain Fe):

$$57\ Mg_{0.75}Fe_{0.25}(OH)_2 + 30\ SiO_2(aq) \rightarrow 15\ Mg_{2.85}Fe_{0.15}Si_2O_5(OH)_4 + 23\ H_2O + 4\ Fe_3O_4 + 4H_2 \quad (R5)$$

The source of aqueous silica driving brucite silicification in the sub-seafloor mantle basement is inferred to be the alteration of the peridotite-forming pyroxenes (e.g., Bach et al., 2006; Beard et al., 2009; Frost et al., 2013), and of the pyroxene and plagioclase from neighbouring gabbroic intrusions (e.g., Bach et al., 2004; Boschi et al., 2006, 2008; Seyfried et al., 2015). Batch serpentinization experiments support this hypothesis as brucite is systematically lacking when pyroxene-bearing peridotites are altered (e.g., Klein et al., 2015) whilst it is often observed when olivine is altered (e.g., Malvoisin and Brunet, 2014).Yet, paradoxically, brucite is not described as being part of the secondary mineral assemblages produced after olivine hydration when Mg-rich fluids are used (e.g., Janecky and Seyfried, 1986; Seyfried et al., 2007; Seyfried and Dibble, 1980) except for the synthetic fluid inclusions experiments of Lamadrid et al. (2017). Another puzzling observation is the selective increase in silica activity in the early stages of batch serpentinization experiments using Mg-rich fluids (e.g., Klein et al., 2015; Seyfried et al., 2007). Reactive percolation experiments simulating interactions between olivine and Mg-rich seawater derived hydrothermal fluids show similar trends when injection flow rates are low ($Pe < 1$) (Godard et al., 2013 and this study). Similar to batch studies, reactive percolation outlet fluids record strong increases in silica activity, up to three times the composition of inlet fluids in our experiment. These ranges of variation are too similar to silica enrichments relative to seawater observed in the ultramafic-hosted hydrothermal vents (e.g., Lost City Hydrothermal Vent fluids (Seyfried et al., 2015)). Our results indicate that fast Mg-trapping and early yet transient brucite formation can be an efficient mechanism for increasing silica activity in hydrothermal fluids during incipient serpentinization. The development of these compositional trends is limited to diffusion dominated domains infiltrated by Mg-rich fluids nevertheless these conditions are analogous to low porosity mantle peridotites being infiltrated by seawater-derived fluids. These processes are however most likely short-lived in natural systems similar to what observed in batch experiments: the local increase in silica activity and the stabilization or decrease of pH produced by brucite precipitation will in turn favor serpentine precipitation as well as the extensive consumption of brucite. Minor brucite observed in poorly serpentinized peridotites is most likely preserved because of the slow kinetics of brucite silicification reactions (Tutolo et al., 2018) or incomplete reactions due to low fluid renewal (see below). Also, as serpentinization reactions progress, Mg-activity should decrease in hydrothermal fluids in diffusion-dominated systems and serpentinization reaction paths tend toward those predicted assuming influx of pure water (e.g., R1) provided that minimal permeability is maintained.

Along oceanic spreading centres, high flow zones are often characterized by silica-rich lithologies, which are attributed to interaction with fluids having high silica activity (e.g., Bonnemains et al., 2017; Escartin et al., 2017; Karson et al., 2006; Paulick et al., 2006). Our results show that serpentinization reaction paths in advection-dominated domains favors leaching of Mg and precipitation of silica rich phases. The silica-rich phase is serpentine in our experiments but these results suggest a possible contribution of serpentinization reactions in enhancing silica trapping reactions along in the most permeable zones in the serpentinizing mantle (fractures, fault zones) at mid-ocean ridges.

4.3.2. Changes of volume for transport-controlled and kinetics-controlled reaction paths

The oceanic mantle lithosphere exposed along slow spreading ridges is commonly envisioned a multi-permeable media: oceanic detachment faults and fractures are the highly permeable zones allowing seawater derived fluids to penetrate deeply into the cooling mantle lithosphere (e.g., de Martin et al., 2007; Emmanuel and Berkowitz, 2006; Farough et al., 2016; Lowell, 2013; McCaig et al., 2007) while, at a smaller scale (cm- and below), the development of veins (e.g., Andreani et al., 2007), mesh networks and microcracks (e.g., Rouméjon et al., 2015) reveals the pervasive infiltration of fluids into the peridotite basement through an interplay between regional stress, thermal cracking and dissolution-precipitation reactions (e.g., Boudier et al., 2005; Plümper et al., 2012). Both advection and diffusion are expected to drive solute transport in the low permeability serpentinizing peridotites, with advection being most likely predominant in the mesh structure and veins, whilst diffusion should prevail along mineral boundaries and microcracks (Malvoisin and Brunet, 2014).

The two end member reaction paths shown by reactive-percolation experiments are expected to yield different local changes in the structure and permeability of the serpentinizing mantle rocks, through the precipitation of low density serpentine +/− brucite at the expense of olivine (Table F.1, Appendix F). Transport controlled reaction paths will produce a lesser volume increase in diffusion-dominated domains (30% according to reaction R2) than kinetics controlled reaction paths in advection-dominated domains (42% according to reaction R3); however both predict lesser volume variations than the commonly used serpentinization relationship (43%- reaction R1). As a result, advection-dominated domains will be clogged more efficiently than diffusion-dominated domains even though olivine dissolution is more efficient (see text for Fig. 12 model). It is worth noting that the accumulation of stress due to fast precipitation localized in narrow zones such as olivine dissolution etch pits is considered as a possible mechanism for cracking and maintaining permeability in serpentinites (dissolution driven cracking; Plümper et al., 2012; Røyne and Jamtveit, 2015). The coupling of kinetics controlled serpentinization reaction paths and dissolution driven cracking could provide an efficient mechanism favoring continuous and pervasive flux of fluids from fault zones into the mantle peridotite basement. In contrast, in diffusion dominated domains, fluid renewal will most likely be controlled by permeability changes resulting from brucite and serpentine precipitation. These processes should in turn, reduce serpentinization reactions thus providing a mechanism for preservation of relict primary minerals often observed in abyssal peridotites (e.g., Hellebrand et al., 2002; Bach et al., 2004; Godard et al., 2008; D'errico et al., 2016).

5. Summary and conclusions

Serpentinization of ultramafic rocks at ridges occurs upon cooling of the oceanic lithosphere if seawater is available. To study the effect of solute transport during incipient stages of serpentinization, four reactive-percolation experiments were performed at different constant flow

Please cite this article as: Escario, S., et al., Experimental study of the effects of solute transport on reaction paths during incipient serpentinization, Lithos (2018), https://doi.org/10.1016/j.lithos.2018.09.020

rates. The experiments consisted in injecting artificial seawater into compressed San Carlos olivine powders at 170 °C and 25 MPa.

Proto-serpentine was formed in the four experiments but different trends were observed for low and high flow rates. Low flow rate experiments showed the precipitation of nodular aggregates on the reacted surface, a strong increase of silica concentration of the outlet fluid relative to magnesium and a slightly decrease of pH. Conversely, high flow rate experiments emphasized the precipitation of fibrous filaments, a strong increase of the magnesium concentration of the outlet fluid compared to silica and a slight increase of pH.

Flow and transport processes, here covering a range of 0.02 to 4 in term of Peclet number, appears to determine the length and time scale of the reaction domains where fluid-rock interactions takes place. Diffusive boundary layers, whose thickness is inversely proportional to local fluid velocities, develop at the fluid/mineral interface and control by chemical gradients in the vicinity of the reactive surfaces. Porous media contain zones of low fluid velocity where the diffusive layers can occupy a significant fraction of the pore volume and zones of fast velocities with reduced diffusive layer. For a given pore structure, the fraction of diffusion-controlled zones increases as the sample scale flow rate decreases. Accordingly, two end-member scenarios are proposed to describe incipient serpentinization reaction paths during reactive percolation experiments. These two scenarios depend on the efficiency of diffusion-controlled renewing of solutes at the mineral reactive surface:

1) Transport-controlled scenario occurs at low flow rate. In this case, the large amount of diffusion zones controls the exchanges between the mineral and the bulk fluid and furthermore allows efficient mixing of the reactants and products. The dissolution of olivine produces hydration of SiO_4^{4-} which increases pH and favors the precipitation of brucite after the Mg detached from olivine and the $MgOH^+(aq)$ of incoming fluids. Eventually, serpentine will precipitate at the expense of brucite. This process could explain, in part, the absence of brucite in most oceanic hydrothermal systems.

2) Kinetics-controlled scenario occurs at high flow rates: the renewing of the reactants and products at the reaction surface is efficiently produced by advection. The sharp chemical gradients between the olivine surface and the bulk fluid trigger high olivine dissolution rate. However, the evidences of silica trapping and magnesium released suggest a transient stage for the formation of serpentine during which a silica rich layer could form at the fluid-mineral interface until conditions favorable for serpentine precipitation are reached in the porous network.

The development of compositional trends (e.g. Si-rich fluids or Mg-rich fluids) is strongly dependent on local flow rates at the scale of the fluid-mineral interface. The two scenarios described in this study can be related to processes occurring in ultramafic hosted hydrothermal systems along mid-ocean ridges: 1) the diffusion-dominated scenario is analogous to low porosity confined zones (i.e. along mineral boundaries and microcracks) where seawater-derived fluids infiltrate mantle peridotites. The local increase of pH resulting from olivine dissolution and the slow renewal of fluid in the pore leads to ion saturation and precipitation of brucite, then serpentine. 2) Advection-dominated scenario is analogous to highly permeable zones (i.e. oceanic detachment faults and fractures). High amounts of serpentine precipitate in this zone, which in turn clog flow paths more efficiently than diffusion-dominated domains.

Both these serpentinization reaction paths are observed in natural systems and commonly ascribed to changes in the composition of serpentinizing hydrothermal fluids resulting from interactions with different lithologies along flow paths. Our results suggest also a control of flow infiltration rate on the development of these different serpentinization reactions paths.

Acknowledgments

We thank Benjamin Tutolo, Andrew Luhmann and Marco Scambelluri (Lithos Editor) for their constructive comments that significantly improved the manuscript. We also thank C. Nevado and D. Delmas for the preparation of the polished sections, F. Fernandez for analytical assistance during SEM-EDS analyses and R. Freydier, C. Douchet and L. Causse for analytical assistance during ICP-OES analyses at the AETE-ISO ("Analyses des Eléments en Trace dans l'Environnement et ISOtopes") platform from the OREME observatory (University of Montpellier). Finally, we would like to thank Christian Hansen and Wolfgang Bach for their help in building the thermodynamic database that was used for the Eq3/6 simulations of our experiments. The research leading to these results has received funding from the People Programme (Marie Curie Actions) of the European Union's Seventh Framework Programme FP7/2007-2013/ under REA Grant Agreement 608001.

Appendix A-H. Supplementary data

Supplementary data to this article can be found online at https://doi.org/10.1016/j.lithos.2018.09.020.

References

Allen, D.E., Seyfried, W.E., 2003. Compositional controls on vent fluids from ultramafic-hosted hydrothermal systems at mid-ocean ridges: an experimental study at 400°C, 500 bars. Geochim. Cosmochim. Acta 67, 1531–1542. https://doi.org/10.1016/S0016-7037(02)01173-0.

Andreani, M., Daniel, I., 2013. Aluminium speeds up the hydrothermal alternation of olivine. Am. Mineral. 98, 1738–1744.

Andreani, M., Daniel, I., Pollet-Villard, M., 2013. Aluminium speeds up the hydrothermal alternation of olivine. Am. Mineral. 98, 1738–1744.

Andreani, M., Mével, C., Boullier, A.M., Escartín, J., 2007. Dynamic control on serpentine crystallization in veins: Constraints on hydration processes in oceanic peridotites. Geochem. Geophys. Geosyst. 8. https://doi.org/10.1029/2006GC001373.

Andreani, M., Luquot, L., Gouze, P., Godard, M., Gibert, B., 2009. Experimental study of carbon sequestration reactions controlled by the percolation of CO_2-rich brine through peridotites. Environ. Sci. Technol. 43, 1226–1231.

Andreani, M., Escartin, J., Delacour, A., Ildefonse, B., Godard, M., Dyment, J., Fallick, A., Fouquet, Y., 2014. Tectonic structure, lithology, and hydrothermal signature of the Rainbow massif (Mid-Atlantic Ridge 36°14'N). Geochem. Geophys. Geosyst. 18, 1541–1576. https://doi.org/10.1002/2014GC005684.

Bach, W., Garrido, C.J., Paulick, H., Harvey, J., Rosner, M., 2004. Seawater-peridotite interactions: first insights from ODP Leg 209, MAR 15°N. Geochem. Geophys. Geosyst. 5. https://doi.org/10.1029/2004GC000744.

Bach, W., Paulick, H., Garrido, C.J., Ildefonse, B., Meurer, W.P., Humphris, S.E., 2006. Unraveling the Sequence of Serpentinization Reactions: Petrography, Mineral Chemistry , and Petrophysics of Serpentinites From MAR 15°N (ODP Leg 209 , Site 1274). 33, pp. 4–7. https://doi.org/10.1029/2006GL025681.

Bandura, A.V., Lvov, S.N., 2006. The Ionization constant of water over wide ranges of temperature and density. J. Phys. Chem. Ref. Data 35, 15–30. https://doi.org/10.1063/1.1928231.

Beard, J.S., Frost, B.R., Fryer, P., McCaig, A., Searle, R., Ildefonse, B., Zinin, P., Sharma, S.K., 2009. Onset and progression of serpentinization and magnetite formation in Olivine-rich troctolite from IODP hole U1309D. J. Petrol. 50, 387–403. https://doi.org/10.1093/petrology/egp004.

Bénézeth, P., Saldi, G.D., Dandurand, J.L., Schott, J., 2011. Experimental determination of the solubility product of magnesite at 50 to 200°C. Chem. Geol. 286, 21–31. https://doi.org/10.1016/j.chemgeo.2011.04.016.

Berndt, M.E., Allen, D.E., Seyfried, W.E., 1996. Reduction of CO_2 during serpentinization of olivine at 300°C and 500 bar. Geology 24, 351–354. https://doi.org/10.1130/0091-7613(1996)024<0351.

Bethke, C.M., 1996. Geochemical Reaction Modeling. Oxford University Press, New York 397 p.

Bischoff, J.L., Seyfried, W.E., 1978. Hydrothermal Chemistry of seawater from 25° to 350°C. Am. J. Sci. 278, 838–860.

Bodinier, J., Godard, M., 2003. Orogenic, ophiolitic, and abyssal peridotites. Treatise on Geochemistry. Elsevier, pp. 1–73 https://doi.org/10.1016/B0-08-043751-6/02004-1.

Bonnemains, D., Escartin, J., Mevel, M., Andreani, M., Verlaguet, A., 2017. Pervasive silicification and hanging wall overplating along the 13°20'N oceanic detachment fault (Mid-Atlantic Ridge). Geochem. Geophys. Geosyst., 1–26 https://doi.org/10.1002/2016GC006679.

Boschi, C., Früh-Green, G.L., Delacour, A., Karson, J.A., Kelley, D.S., 2006. Mass transfer and fluid flow during detachment faulting and development of an oceanic core complex, Atlantis Massif (MAR 30°N). Geochem. Geophys. Geosyst. 7. https://doi.org/10.1029/2005GC001074.

Boschi, C., Dini, A., Früh-Green, G.L., Kelley, D.S., 2008. Isotopic and element exchange during serpentinization and metasomatism at the Atlantis Massif (MAR 30°N): Insights from B and Sr isotope data. Geochim. Cosmochim. Acta 72, 1801–1823. https://doi.org/10.1016/j.gca.2008.01.013.

Boudier, F., Nicolas, A., Mainprice, D., 2005. Does anisotropy of thermal contraction control hydrothermal circulation at the moho level below fast spreading oceanic ridges? Int. Geol. Rev. 47, 101–112. https://doi.org/10.2747/0020-6814.47.1.101.

Cannat, M., Lagabrielle, Y., Bougault, H., Casey, J.F., de Coutures, N., Dmitriev, L., Fouquet, Y., 1997. Ultramafic and gabbroic exposures at the Mid-Atlantic Ridge: geological mapping in the 15°N region. Tectonophysics 279, 193–213.

Cannat, M., Sauter, D., Mendel, V., Ruellan, E., Okino, K., Escartin, J., Combier, V., Baala, M., 2006. Modes of seafloor generation at a melt-poor ultraslow-spreading ridge. Geology 34, 605–608. https://doi.org/10.1130/G22486.1.

Charlou, J.L., Donval, J.P., Konn, C., Ondréas, H., Fouquet, Y., Jean-Baptiste, P., Fourré, E., 2013. High production and fluxes of H_2 and CH_4 and evidence of abiotic hydrocarbon synthesis by serpentinization in ultramafic-hosted hydrothermal systems on the mid-Atlantic ridge. Divers. Hydrothermal Syst. Slow Spreading Ocean Ridges, 265–296 https://doi.org/10.1029/2008GM000752.

Chen, Y., Brantley, S.L., 2000. Dissolution of forsteritic olivine at 65°C and 2 < pH < 5. Chem. Geol. 165, 267–281. https://doi.org/10.1016/S0009-2541(99)00177-1.

Crundwell, F.K., 2014. The mechanism of dissolution of minerals in acidic and alkaline solutions: Part II Application of a new theory to silicates, aluminosilicates and quartz. Hydrometallurgy 149, 265–275. https://doi.org/10.1016/j.hydromet.2014.07.003.

Daval, D., Sissmann, O., Menguy, N., Saldi, G.D., Guyot, F., Martinez, I., Corvisier, J., Garcia, B., Machouk, I., Knauss, K.G., Hellmann, R., 2011. Influence of amorphous silica layer formation on the dissolution rate of olivine at 90°C and elevated pCO_2. Chem. Geol. 284, 193–209. https://doi.org/10.1016/j.chemgeo.2011.02.021.

Donval, J.P., Charlou, J.L., Douville, E., Knoery, J., Fouquet, Y., Ponzevera, E., Jean-Baptiste, P., Stievenard, M., German, C., 1997. High H_2 and CH_4 content in hydrothermal fluids from rainbow site newly sampled at 36°14' on the AMAR segment, Mid-Atlantic Ridge (diving Flores cruise, July 1997). Comparison with other sites. EOS Trans. Am. Geophys. Union 78, 832.

Douville, E., Charlou, J.L., Oelkers, E.H., Bienvenu, P., Jove Colon, C.F., Donval, J.P., Fouquet, Y., Prieur, D., Appriou, P., 2002. The rainbow vent fluids (36°14'N, MAR): the influence of ultramafic rocks and phase separation on trace metal content in Mid-Atlantic Ridge hydrothermal fluids. Chem. Geol. 184, 37–48. https://doi.org/10.1016/S0009-2541(01)00351-5.

Emmanuel, S., Berkowitz, B., 2006. Suppression and stimulation of seafloor hydrothermal convection by exothermic mineral hydration. Earth Planet. Sci. Lett. 243, 657–668. https://doi.org/10.1016/j.epsl.2006.01.028.

Escartín, J., Hirth, G., Evans, B., 2001. Strength of slightly serpentinized peridotites: Implications for the tectonics of oceanic lithosphere. Geology 29, 1023–1026. https://doi.org/10.1130/0091-7613(2001)029<1023:SOSSPI>2.0.CO.

Evans, B.W., 2004. The serpentinite multisystem revisited : Chrysotile is metastable. Int. Geol. Rev. 46, 479–506.

Evans, B.W., 2008. Control of the products of serpentinization by the Fe^{2+} Mg_{-1} exchange potential of olivine and orthopyroxene. J. Petrol. 49, 1873–1887. https://doi.org/10.1093/petrology/egn050.

Evans, B.W., Hattori, K., Baronnet, A., 2013. Serpentinite: what, why, where? Elements 9, 99–106. https://doi.org/10.2113/gselements.9.2.99.

Farough, A., Moore, D.E., Lockner, D.A., Lowell, R.P., 2016. Evolution of fracture permeability of ultramafic rocks undergoing serpentinization at hydrothermal conditions: an experimental study. Geochem. Geophys. Geosyst. 17, 44–55. https://doi.org/10.1002/2015GC005973.

Földvári, M., 2011. Handbook of Thermogravimetric System of Minerals and its Use in Geological Practice (Geological Institute of Hungary).

Frost, B.R., Evans, K.A., Swapp, S.M., Beard, J.S., Mothersole, F.E., 2013. The process of serpentinization in dunite from New Caledonia. Lithos 178, 24–39. https://doi.org/10.1016/j.lithos.2013.02.002.

Früh-Green, G.L., Kelley, D.S., Bernasconi, S.M., Karson, J.A., Ludwig, K.A., Butterfield, D.A., Boschi, C., Proskurowski, G., 2003. 30,000 Years of Hydrothermal Vent Field. Science 301, 495–498 (80-.).

Früh-Green, G.L., Connolly, J.A.D., Plas, A., Kelley, D.S., Grobéty, B., 2004. Serpentinization of oceanic peridotites: Implications for geochemical cycles and biological activity. Geophys. Monogr. Ser. 144, 119–136. https://doi.org/10.1029/144GM08.

Gerdemann, S.J., O'Connor, W.K., Dahlin, D.C., Penner, L.R., Rush, H., 2007. Ex situ aqueous mineral carbonation. Environ. Sci. Technol. 41, 2587–2593. https://doi.org/10.1021/es0619253.

Giammar, D.E., Bruant, R.G., Peters, C.A., 2005. Forsterite dissolution and magnesite precipitation at conditions relevant for deep saline aquifer storage and sequestration of carbon dioxide. Chem. Geol. 217, 257–276. https://doi.org/10.1016/j.chemgeo.2004.12.013.

Gislason, S.R., Oelkers, E.H., 2003. Mechanism, rates, and consequences of basaltic glass dissolution: II. An experimental study of the dissolution rates of basaltic glass as a function of pH and temperature. Geochim. Cosmochim. Acta 67, 3817–3832. https://doi.org/10.1016/S0016-7037(03)00176-5.

Gjetvaj, F., Russian, A., Gouze, P., Dentz, M., 2015. Dual control of flow field heterogeneity and immobile porosity on non-Fickian transport in Berea sandstone. Water Resour. Res. 51, 8273–8293. https://doi.org/10.1002/ 2015WR017645.

Godard, M., Lagabrielle, Y., Alard, O., Harvey, J., 2008. Geochemistry of the highly depleted peridotites drilled at ODP Sites 1272 and 1274 (Fifteen-twenty Fracture Zone, Mid-Atlantic Ridge): Implications for mantle dynamics beneath a slow spreading ridge. Earth Planet. Sci. Lett. 267, 410–425. https://doi.org/10.1016/j.epsl.2007.11.058.

Godard, M., Luquot, L., Andreani, M., Gouze, P., 2013. Incipient hydration of mantle lithosphere at ridges: a reactive-percolation experiment. Earth Planet. Sci. Lett. 371–372, 92–102. https://doi.org/10.1016/j.epsl.2013.03.052.

Gouze, P., Luquot, L., 2011. X-ray microtomography characterization of porosity, permeability and reactive surface changes during dissolution. J. Contam. Hydrol. 120–121, 44–55. https://doi.org/10.1016/j.jconhyd.2010.07.004.

Hänchen, M., Prigiobbe, V., Storti, G., Seward, T.M., Mazzotti, M., 2006. Dissolution kinetics of fosteritic olivine at 90-150 °C including effects of the presence of CO_2. Geochim. Cosmochim. Acta 70, 4403–4416. https://doi.org/10.1016/j.gca.2006.06.1560.

Hatakeyama, K., Katayama, I., Hirauchi, K., Michibayashi, K., 2017. Mantle hydration along outer-rise faults inferred from serpentinite permeability. Sci. Rep. 7, 13870. https://doi.org/10.1038/s41598-017-14309-9.

Helgeson, H.C., Delany, J.M., Nesbitt, H.W., Bird, D.K., 1978. Summary and critique of the thermodynamic properties of rock-forming minerals. Am. J. Sci. 278-A, 229.

Helgeson, H.C., Kirkham, D.H., Flowers, G.C., 1981. Theoretical prediction of the thermodynamic behavior of aqueous electrolytes at high pressures and temperatures. Calculation of activity coefficients, osmotic coefficients, and apparent molal and standard and relative partial molal properties to 600°C and 5 kbar. Am. J. Sci. 281, 1249–1516.

Hellebrand, E., Snow, J., Hoppe, P., Hofmann, A., 2002. Garnet-field melting and late-stage refertilization in "residual" abyssal peridotites from the Central Indian Ridge. J. Petrol. 43, 2305–2338.

Hirose, T., Hayman, N.W., 2008. Structure, permeability, and strength of a fault zone in the footwall of an oceanic core complex, the Central Dome of the Atlantis Massif, Mid-Atlantic Ridge, 30°N. J. Struct. Geol. 30, 1060–1071. https://doi.org/10.1016/j.jsg.2008.04.009.

Janecky, D.R., Seyfried, W.E., 1986. Hydrothermal Serpentinization of peridotite within the oceanic-Crust: Experimental investigations of mineralogy and major element chemistry. Geochim. Cosmochim. Acta 50, 1357–1378. https://doi.org/10.1016/0016-7037(86)90311-X.

Johnson, J.W., Oelkers, E.H., Helgeson, H.C., 1992. SUPCRT92: a software package for calculating the standard molal thermodynamic properties of minerals, gases, aqueous species, and reactions from 1 bar to 5000 bar and 0 to 1000°C. Comput. Geosci. 18, 899–947.

Karson, J.A., Früh-Green, G.L., Kelley, D.S., Williams, E.A., Yoerger, D.R., Jakuba, M., 2006. Detachment shear zone of the Atlantis Massif core complex, Mid-Atlantic Ridge, 30°N. Geochemistry, Geophys. Geosystems 7. https://doi.org/10.1029/2005GC001109.

Kelemen, P.B., Hirth, G., 2012. Reaction-driven cracking during retrograde metamorphism: Olivine hydration and carbonation. Earth Planet. Sci. Lett. 345–348, 81–89. https://doi.org/10.1016/j.epsl.2012.06.018.

Kelley, D.S., Karson, J.A., Blackman, D.K., Fruh-Green, G.L., Butterfield, D.A., Lilley, M.D., Olson, E.J., Schrenk, M.O., Roe, K.K., Lebon, G.T., Rivizzigno, P., 2001. An off-axis hydrothermal vent field near the Mid-Atlantic Ridge at 30° N. Nature 412, 145–149.

Kestin, J., Khalifa, E., Correira, R., 1981. Tables of the dynamic and kinematic viscosity of aqueous KCl Solutions in the temperature range 25–150°C and the pressure range 0.1-35 MPa. Data 10, 57–70.

Klein, F., Garrido, C.J., 2011. Thermodynamic constraints on mineral carbonation of serpentinized peridotite. Lithos 126, 147–160. https://doi.org/10.1016/j.lithos.2011.07.020.

Klein, F., Bach, W., McCollom, T.M., 2013. Compositional controls on hydrogen generation during serpentinization of ultramafic rocks. Lithos 178, 55–69. https://doi.org/10.1016/j.lithos.2013.03.008.

Klein, F., Grozeva, N.G., Seewald, J.S., McCollom, T.M., Humphris, S.E., Moskowitz, B., Berquo, T.S., Kahl, W.A., 2015. Fluids in the Crust. Experimental constraints on fluid-rock reactions during incipient serpentinization of harzburgite. Am. Mineral. 100, 991–1002. https://doi.org/10.2138/am-2015-5112.

Klein, F., McCollom, T., 2013. From serpentinization to carbonation: New insights from a CO_2 injection experiment. EPSL 379, 137–145. https://doi.org/10.1016/j.epsl.2013.08.017.

Lafay, R., Montes-Hernandez, G., Janots, E., Chiriac, R., Findling, N., Toche, F., 2012. Mineral replacement rate of olivine by chrysotile and brucite under high alkaline conditions. J. Cryst. Growth 347, 62–72. https://doi.org/10.1016/j.jcrysgro.2012.02.040.

Lamadrid, H.M., Rimstidt, J.D., Schwarzenbach, E.M., Klein, F., Ulrich, S., Dolocan, A., Bodnar, R.J., 2017. Effect of water activity on rates of serpentinization of olivine. Nat. Commun. 8, 1–9. https://doi.org/10.1038/ncomms16107.

Lowell, R.P., 2013. Hydrothermal Circulation at Slow Spreading Ridges: Analysis of Heat sources and Heat transfer Processes. Divers. Hydrothermal Syst. Slow Spreading Ocean Ridges, 11–26 https://doi.org/10.1029/2008GM000758.

Lowell, R.P., Rona, P.A., 2002. Seafloor hydrothermal systems driven by the serpentinization of peridotite. Geophys. Res. Lett. 29, 0–3. https://doi.org/10.1029/2001GL014411.

Luhmann, A., Tutolo, B., Bagley, B., Mildner, D.F.R., Scheuermann, P.P., Feinberg, J.M., Ignatyev, K., Seyfried, W.E., 2017. Chemical and physical changes during seawater flow through intact dunite cores: an experimental study at 150–200°C. Geochim. Cosmochim. Acta 214, 86–114. https://doi.org/10.1016/j.gca.2017.07.020.

Luquot, L., Gouze, P., 2009. Experimental determination of porosity and permeability changes induced by injection of CO_2 into carbonate rocks. Chem. Geol. 265, 148–159. https://doi.org/10.1016/j.chemgeo.2009.03.028.

MacDonald, A.H., Fyfe, W.S., 1985. Rate of serpentinization in seafloor environments. Tetonophysics 116, 123–135.

Maffione, M., Morris, A., Plümper, O., Van Hinsbergen, D., 2014. Magnetic properties of variably serpentinized peridotites and their implication for the evolution of oceanic core complexes. Geochem. Geophys. Geosyst. 15, 923–944. https://doi.org/10.1002/2013GC004993.

Malvoisin, B., Brunet, F., 2014. Water diffusion-transport in a synthetic dunite: Consequences for oceanic peridotite serpentinization. Earth Planet. Sci. Lett. 403, 263–272. https://doi.org/10.1016/j.epsl.2014.07.004.

Malvoisin, B., Brunet, F., Carlut, J., Rouméjon, S., Cannat, M., 2012. Serpentinization of oceanic peridotites: 2. Kinetics and processes of San Carlos olivine hydrothermal alteration. J. Geophys. Res. Solid Earth 117, 1–13. https://doi.org/10.1029/2011JB008842.

Please cite this article as: Escario, S., et al., Experimental study of the effects of solute transport on reaction paths during incipient serpentinization, Lithos (2018), https://doi.org/10.1016/j.lithos.2018.09.020

Marcaillou, C., Muñoz, M., Vidal, O., Parra, T., Harfouche, M., 2011. Mineralogical evidence for H_2 degassing during serpentinization at 300°C and 300bar. Earth Planet. Sci. Lett. 303, 281–290. https://doi.org/10.1016/j.epsl.2011.01.006.

Martin, B., Fyfe, W.S., 1970. Some experimental and theoretical observations on the kinetics of hydration reactions with particular reference to serpentinization. Chem. Geol. 6, 185–202.

de Martin, B.J., Reves-Sohn, R.A., Canales, J.P., Humphris, S.E., 2007. Kinematics and geometry of active detachment faulting beneath the Trans-Atlantic geotraverse (TAG) hydrothermal field on the Mid-Atlantic Ridge. Geology 35, 711–714. https://doi.org/10.1130/G23718A.1.

McCaig, A.M., Cliff, R.A., Escartin, J., Fallick, A.E., MacLeod, C.J., 2007. Oceanic detachment faults focus very large volumes of black smoker fluids. Geology 35, 935–938. https://doi.org/10.1130/G23657A.1.

McCollom, T.M., Bach, W., 2009. Thermodynamic constraints on hydrogen generation during serpentinization of ultramafic rocks. Geochim. Cosmochim. Acta 73, 856–875. https://doi.org/10.1016/j.gca.2008.10.032.

Mccollom, T.M., Klein, F., Robbins, M., Moskowitz, B., Jo, N., Berquo, T.S., Bach, W., Templeton, A., 2016. Temperature trends for reaction rates, hydrogen generation, and partitioning of iron during experimental serpentinization of olivine. Geochem. Cosmochim. Acta 181, 175–200. https://doi.org/10.1016/j.gca.2016.03.002.

Mével, C., 2003. Serpentinization of abyssal peridotites at mid-ocean ridges. Compt. Rendus Geosci. 335, 825–852. https://doi.org/10.1016/j.crte.2003.08.006.

Millero, F.J., Feistel, R., Wright, D.G., McDougall, T.J., 2008. The composition of standard seawater and the definition of the reference-composition salinity scale. Deep Sea Res. Part I Oceanogr. Res. Pap. 55, 50–72. https://doi.org/10.1016/j.dsr.2007.10.001.

Morse, J.W., Arvidson, R.S., 2002. The dissolution kinetics of major sedimentary carbonate minerals. Earth-Sci. Rev. 58, 51–84.

Noiriel, C., Madé, B., Gouze, P., 2007. Impact of coating development on the hydraulic and transport properties in argillaceous limestone fracture. Water Resour. Res. 43. https://doi.org/10.1029/2006WR005379.

O'Connor, W.K., Dahlin, D.C., Nilsen, D.N., Rush, G.E., Walters, R.P., Turner, P.C., 2001. Carbon dioxide sequestration by direct mineral carbonation: results from recent studies and current status. 1st Annu. DOE Carbon Sequestration Conf. Washington, D.C. 11.

O'Connor, W., Dahlin, D., Rush, G., Gerdemann, S., Penner, L.R., Nilsen, D., 2005. Aqueous Mineral Carbonation. National Energy Technology Laboratory, Albany Research Center, Office of Fossil Energy, US DOE.

Oelkers, E.H., 2001. An experimental study of forsterite dissolution rates as a function of temperature and aqueous Mg and Si concentrations. Chem. Geol. 175, 485–494. https://doi.org/10.1016/S0009-2541(00)00352-1.

Ogasawara, Y., Okamoto, A., Hirano, N., Tsuchiya, N., 2013. Coupled reactions and silica diffusion during serpentinization. Geochim. Cosmochim. Acta 119, 212–230. https://doi.org/10.1016/j.gca.2013.06.001.

O'Hanley, D.S., 1996. Serpentinites. Oxford University Press.

Okamoto, A., Ogasawara, Y., Ogawa, Y., Tsuchiya, N., 2011. Progress of hydration reactions in olivine-H_2O and orthopyroxenite-H_2O systems at 250°C and vapor-saturated pressure. Chem. Geol. 289, 245–255. https://doi.org/10.1016/j.chemgeo.2011.08.007.

Oufi, O., Cannat, M., Horen, H., 2002. Magnetic properties of variably serpentinized abyssal peridotites. J. Geophys. Res. 107, 2095. https://doi.org/10.1029/2001JB000549.

Palandri, J.L., Reed, M.H., 2004. Geochemical models of metasomatism in ultramafic systems: Serpentinization, rodingitization, and seafloor carbonate chimney precipitation. Geochim. Cosmochim. Acta 68, 1115–1133. https://doi.org/10.1016/j.gca.2003.08.006.

Paulick, H., Bach, W., Godard, M., De Hoog, J.C.M., Suhr, G., Harvey, J., 2006. Geochemistry of abyssal peridotites (Mid-Atlantic Ridge, 15°20′N, ODP Leg 209): Implications for fluid/rock interaction in slow spreading environments. Chem. Geol. 234, 179–210. https://doi.org/10.1016/j.chemgeo.2006.04.011.

Pens, M., Andreani, M., Daniel, I., Perrillat, J.P., Cardon, H., 2016. Contrasted effect of aluminum on the serpentinization rate of olivine and orthopyroxene under hydrothermal conditions. Chem. Geol. 441, 256–264. https://doi.org/10.1016/j.chemgeo.2016.08.007.

Peuble, S., Andreani, M., Godard, M., Gouze, P., Barou, F., Van de Moortele, B., Mainprice, D., Reynard, B., 2015a. Carbonate mineralization in percolated olivine aggregates : linking effects of crystallographic orientation and fluid flow. Am. Mineral. 100, 474–482.

Peuble, S., Godard, M., Luquot, L., Andreani, M., Martinez, I., Gouze, P., 2015b. CO_2 geological storage in olivine rich basaltic aquifers: New insights from reactive-percolation experiments. Appl. Geochem. 52, 174–190. https://doi.org/10.1016/j.apgeochem.2014.11.024.

Philibert, J., 2005. One and a half Century of Diffusion: Fick, Einstein, before and beyond. Diffus. Fundam. 4, 1–19.

Plümper, O., Røyne, A., Magrasó, A., Jamtveit, B., 2012. The interface-scale mechanism of reaction-induced fracturing during serpentinization. Geology 40, 1103–1106. https://doi.org/10.1130/G33390.1.

Pokrovsky, O.S., Schott, J., 2000a. Kinetics and mechanism of forsterite dissolution at 25°C and pH from 1 to 12. Geochim. Cosmochim. Acta 64, 3313–3325. https://doi.org/10.1016/S0016-7037(00)00434-8.

Pokrovsky, O.S., Schott, J., 2000b. Forsterite surface composition in aqueous solutions: a combined potentiometric, electrokinetic, and spectroscopic approach. Geochim. Cosmochim. Acta 64, 3299–3312. https://doi.org/10.1016/S0016-7037(00)00435-X.

Pokrovsky, O.S., Schott, J., 2004. Experimental study of brucite dissolution and precipitation in aqueous solutions: Surface speciation and chemical affinity control. Geochim.Cosmochim. Acta 68, 31–45. https://doi.org/10.1016/S0016-7037(03)00238-2.

Prigiobbe, V., Costa, G., Baciocchi, R., Hänchen, M., Mazzotti, M., 2009. The effect of CO_2 and salinity on olivine dissolution kinetics at 120°C. Chem. Eng. Sci. 64, 3510–3515. https://doi.org/10.1016/j.ces.2009.04.035.

Rimstidt, J.D., Brantley, S.L., Olsen, A.A., 2012. Systematic review of forsterite dissolution rate data. Geochim. Cosmochim. Acta 99, 159–178. https://doi.org/10.1016/j.gca.2012.09.019.

Rosso, J.J., Rimstidt, D.J., 2000. A high resolution study of forsterite dissolution rates. Geochim. Cosmochim. Acta 64, 797–811. https://doi.org/10.1016/S0016-7037(99)00354-3.

Rouméjon, S., Cannat, M., Agrinier, P., Godard, M., Andreani, M., 2015. Serpentinization and Fluid pathways in tectonically exhumed peridotites from the southwest indian ridge (62–65°E). J. Petrol. 56, 703–734. https://doi.org/10.1093/petrology/egv014.

Røyne, A., Jamtveit, B., 2015. Pore-scale controls on reaction-driven fracturing. Rev. Mineral. Geochem. 80, 25–44. https://doi.org/10.2138/rmg.2015.80.02.

Rudge, J.F., Kelemen, P.B., Spiegelman, M., 2010. A simple model of reaction-induced cracking applied to serpentinization and carbonation of peridotite. Earth Planet. Sci. Lett. 291, 215–227. https://doi.org/10.1016/j.epsl.2010.01.016.

Ruiz-Agudo, E., Putnis, C.V., Putnis, A., 2014. Coupled dissolution and precipitation at mineral – fluid interfaces. Chem. Geol. 383, 132–146. https://doi.org/10.1016/j.chemgeo.2014.06.007.

Schmidt, K., Garbe-Schönberg, D., Koschinsky, A., Strauss, H., Jost, C.L., Klevenz, V., Königer, P., 2011. Fluid elemental and stable isotope composition of the Nibelungen hydrothermal field (8°18′S, Mid-Atlantic Ridge): Constraints on fluid-rock interaction in heterogeneous lithosphere. Chem. Geol. 280, 1–18. https://doi.org/10.1016/j.chemgeo.2010.07.008.

Schroeder, T., John, B., Frost, B.R., 2002. Geologic implications of seawater circulation through peridotite exposed at slow-spreading mid-ocean ridges. Geology 30, 367–370. https://doi.org/10.1130/0091-7613(2002)030<0367:GIOSCT>2.0.CO;2.

Seyfried, W.E., Dibble, W.E., 1980. Seawater-peridotite interaction at 300°C and 500 bars : implications for the origin of oceanic serpentinites. Geochim. Cosmochim. Acta 44, 309–321.

Seyfried, W.E., Foustoukos, D.I., Fu, Q., 2007. Redox evolution and mass transfer during serpentinization: an experimental and theoretical study at 200°C, 500 bar with implications for ultramafic-hosted hydrothermal systems at Mid-Ocean Ridges. Geochim. Cosmochim. Acta 71, 3872–3886. https://doi.org/10.1016/j.gca.2007.05.015.

Seyfried, W.E., Pester, N.J., Ding, K., Rough, M., 2011. Vent fluid chemistry of the Rainbow hydrothermal system (36°N, MAR): phase equilibria and in situ pH controls on subseafloor alteration processes. Geochim. Cosmochim. Acta 75, 1574–1593. https://doi.org/10.1016/j.gca.2011.01.001.

Seyfried, W.E., Pester, N., Fu, Q., 2013. Phase equilibria controls on the chemistry of vent fluids from hydrothermal systems on slow spreading ridges: reactivity of plagioclase and olivine solid solutions and the pH-silica connection. Divers. Hydrothermal Syst. Slow Spreading Ocean Ridges, 297–320 https://doi.org/10.1029/2009GM000854.

Seyfried, W.E., Pester, N.J., Tutolo, B.M., Ding, K., 2015. The lost City hydrothermal system: Constraints imposed by vent fluid chemistry and reaction path models on subseafloor heat and mass transfer processes. Geochim. Cosmochim. Acta 163, 59–79. https://doi.org/10.1016/j.gca.2015.04.040.

Shock, E.L., Helgeson, H.C., 1988. Calculation of the thermodynamic and transport properties of aqueous species at high pressures and temperatures: Correlation algorithms for ionic species and equation of state predictions to 5 kb and 1000°C. Geochim. Cosmochim. Acta 52, 2009–2036. https://doi.org/10.1016/0016-7037(88)90181-0.

Shock, E.L., Helgeson, H.C., Sverjensky, D.A., 1989. Calculation of the thermodynamic and transport properties of aqueous species at high pressures and temperatures: Standard partial molal properties of inorganic neutral species. Geochim. Cosmochim. Acta 53, 2157–2183. https://doi.org/10.1016/0016-7037(89)90341-4.

Shock, E.L., Sassani, D.C., Willis, M., Sverjensky, D.A., 1997. Inorganic species in geologic fluids: Correlations among standard molal thermodynamic properties of aqueous ions and hydroxide complexes. Geochim. Cosmochim. Acta 61, 907–950. https://doi.org/10.1016/S0016-7037(96)00339-0.

Siena, M., Hyman, J.D., Riva, M., Guadagnini, A., Winter, C.J., Smolarkiewic, P.K., Gouze, P., Sadhukhan, S., Inzoli, F., Guedon, G., Colombo, E., 2015. Direct numerical simulation of fully saturated flow in natural porous media at the pore scale: a comparison of three computational systems. Comput. Geosci. 19, 423–437. https://doi.org/10.1007/s10596-015-9486-7.

Stanger, G., Neal, C., 1994. The occurrence and chemistry of huntite from Oman. Chem. Geol. 112, 247–254. https://doi.org/10.1016/0009-2541(94)90027-2.

Steefel, C.I., Maher, K., 2009. Fluid-rock interaction: a reactive transport approach. Rev. Mineral. Geochem. 70, 485–532. https://doi.org/10.2138/rmg.2009.70.11.

Summerhayes, C.P., Thorpe, S.A., 1996. Oceanography: An Illustrated Guide. Manson Publishing Co. via Oxford University Press, Oxford.

Syverson, D.D., Tutolo, B.M., Borrok, D.M., Seyfried, W.E., 2017. Serpentinization of olivine at 300°C and 500 bars: an experimental study examining the role of silica on the reaction path and oxidation state of iron. Chem. Geol. 475, 122–134. https://doi.org/10.1016/j.chemgeo.2017.11.006.

Tutolo, B.M., Luhmann, A.J., Tosca, N.J., Seyfried, W.E., 2018. Serpentinization as a reactive transport process: the brucite silicification reaction. Earth Planet. Sci. Lett. 1, 1–13. https://doi.org/10.1016/j.epsl.2017.12.029.

Viti, C., 2010. Serpentine minerals discrimination by thermal analysis. Am. Mineral. 95, 631–638. https://doi.org/10.2138/am.2010.3366.

Wegner, W., Ernst, W., 1983. Experimentally determined hydration and dehydration reaction rates in the system MgO-SiO_2-H_2O. Am. J. Sci. 283–A, 151–180.

Wolery, T., Jarek, R.L., 2003. Software User's Manual EQ3/6, Version 8.0. Sandia National Laboratories, Albuquerque, New Mexico.

Zeebe, R.E., Wolf-Gladrow, D., 2001. CO_2 in Seawater: Equilibrium, Kinetics, Isotopes. Elsevier Oceanography series, New York.

Please cite this article as: Escario, S., et al., Experimental study of the effects of solute transport on reaction paths during incipient serpentinization, Lithos (2018), https://doi.org/10.1016/j.lithos.2018.09.020

The first part of this chapter (*section 2*) had demonstrated an effect of solute transport (advection vs diffusion) on the chemical changes of the fluid and the initial rock during the serpentinization reaction which in turn controls the serpentinization reaction paths.

However, the effects of solute transport on the physical changes of the ultramafic rock are not very well constrained. It is so that the second part of this chapter (*section 3*) focuses on the study of the physical and chemical changes that undergo the ultramafic rocks during percolation of natural seawater at advection dominated conditions (Péclet number of 6). New experiments were performed at 25 MPa as the experiments of *section 2*. However, the temperature was increased to 190°C this provides an increase on the kinetics of the serpentinization reactions.

A specific experimental protocol has been developed to monitor the physical and chemical change that triggers the rock during interaction with seawater in dominated advection-conditions. X-Ray microtomography of high resolution performed at the ESRF (European Synchrotron Radiation Facility, Grenoble, France) was used to analyze the reacted samples before and after the experiments. In this case a special capsule filled with San Carlos olivine was used in the experiments. The capsules were small (D=2 mm and L=20 mm) and made in titanium. The small size of the capsules allows reaching a high image resolution (0.65 μm) and the titanium material provides low absorption for X-ray and so access of X-ray into the olivine samples.

3. The study of the effect of solute transport on serpentinization through X-ray μ-tomography

3.1 Introduction

The present section describes the micro-structural changes that undergo olivine-rocks by assessing the effects of *advection dominated transport*. High-quality resolution 3D observations at the ESRF (European Synchrotron Radiation Facility, Grenoble, France) were performed on hydrothermally altered olivine samples in order to detect: (a) physical changes in the samples (e.g., porosity, surface area and grain size) and (b) dissolution and precipitation process resulting from water-rock interactions. A special protocol has been developed to track the onset of the reactions. The olivine samples were analysed before and after the reactive percolation experiments. In order to realize the percolation experiments the olivine powder was enclosed in thin titanium capsule (with low absorption for X-ray) specially designed for the ESRF analyses. The titanium capsule can hold a sample of size 8 mm length (*L*) x 2 mm diameter (*D*). The titanium capsule has a total length (L) of 20 mm (see *Chapter III*) and can be installed into the confining cell of ICARE 3. The Ti-capsule required a minimum thickness to manufacture (~0.3 mm) and this thickness is too thick to allow <0.2 μm resolution imaging (0.16 μm) of the olivine samples, thus 0.65 μm was the resolution used in this experiments.

3.2 Methodology

3.2.1 Reactive percolation experiments

Two reactive percolation experiments were performed using the Icare lab 3 (Géosciences Montpellier) (see *chapter III.* section 1.1). Natural seawater (*appendix B*. Table B.10) with pCO_2=0.1 MPa was percolated into small titanium capsules filled with San Carlos olivine grains of 150-200 μm size. The chemical composition of San Carlos olivine is described on *chapter III*. Table.3.2. The capsules are enclosed in a Teflon sleeve to ensure the radial containment pressure during the experiment. The containment pressure in the sample is controlled by a hydraulic pump filled with pure water. Thus, the pure water is at a higher

pressure with a pressure 25 MPa compared to the pressure applied into the Teflon sleeve (20 Mpa) see *chapter III*. Section 1.1. The sample is screwed into the heated containment cell of the ICARE 3 and is therefore ready to be percolated by a fluid. Two FFKM O-rings ensure the watertight of the sample assemblage. The experiments were run during 7 and 15 days at 190°C and 20 MPa. The experimental conditions are reported in table 4.1.

Table 4.1. Experimental conditions. Q denotes flow rate, D inner diameter, L length of the sample, $M_{initial}$ and M_{final} the mass of olivine sample, φ is the porosity, Pe is the Péclet number and N° is the number of the sample.

	Time	Q	D	L	Grain size	$M_{initial}$	M_{final}	φ	φ	*Pe*	N°
Experiment	*hours*	*ml/h*	*mm*	*mm*	*µm*	*mg*	*mg*	%	%		
SC1	173.3	0.06	1.7	8	150-200	50.3 ± 0.1	47.3 ± 0.1	17.4 ± 0.02	22.32 ± 0.05	1	3
SC2	334.7	0.3	1.7	8	150-200	49.5 ± 0.1	49.1 ± 0.2	18.7 ± 0.04	19.36 ± 0.08	6	4

(-) not determined

The Péclet number was estimated after: $Pe = \frac{v \cdot L}{D}$ where v is the mean velocity of the fluid in $m.s^{-1}$, $v = Q/S \cdot \varphi$. D the diffusion coefficient in $m^2.s^{-1}$ and L the local pore length in m. The Péclet number was determined for a pore length of 150 µm. Experiment SC2 shows a Péclet of 6 compared to SC1 that shows a Péclet number of 1.

3.2.2 Sample preparation

The titanium capsule use in this study has an outer dimeter of D=2 mm and inner diameter of 1.7 mm and total length of L=20 mm in order to fit in the percolation reactor ICARE 3 (Fig.4.1). 8 mm of the capsule corresponds to the olivine sample. The olivine powder was introduced in the capsules by layers; ~1 mm filling a length of 8 mm in the capsule. Each olivine layer was compressed at room temperature applying pressure of ~5 MPa using an *Enerpac*® hydraulic press. A hydraulic piston of 1.6 mm of diameter was used to compress the powder. The capsule was closed by two permeable plugs of 3 mm at each end of the sample and made on titanium to avoid galvanic problems (Fig.4.1b). The sample was weighed on a balance. First, the empty capsule and the two plugs were measured on a balance. Second, the capsule filled with olivine powder was weighted on a balance. The mass of the sample results in the subtraction of the capsule filled with olivine powder and the mass

of empty capsule. The error of the measured mass was estimated after measuring 3 times a standard weight of 1 g. The total porosity of the samples was estimated according to:

$$\varphi_{total} = \frac{V_{voids}}{V_{total}} = \left(1 - \frac{\rho_{measured}}{\rho_{theoretical}}\right) x\ 100 \qquad \text{(Eq.4.1)}$$

where $\rho_{measured}$ is the ratio between the dry olivine sample and the total volume of the sample in g/cm^3. $\rho_{theoretical}$ is the theoretical density of the olivine 3.3 g/cm^3 (Abramson, 1997).

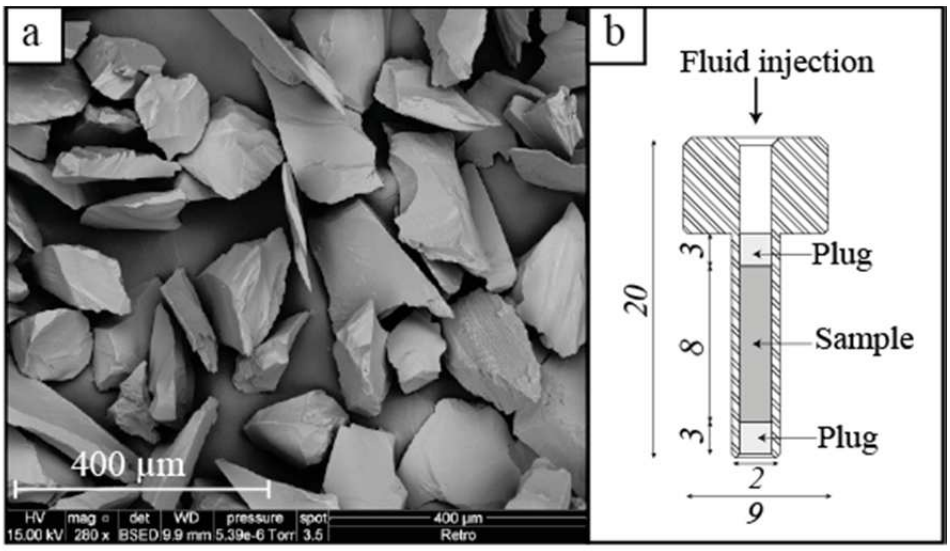

Fig.4.1. Olivine powder samples. (a) SEM image of the unreacted San Carlos Olivine powder filling the capsules. (b) Sketch of the titanium capsule use in the reactive percolation experiments.

3.2.3 Fluid analysis

Alkalinity and pH were measured using a Methrom Titrino 848 according to the protocol described on *chapter III* section 2.1. The reproducibility and accuracy of alkalinity measurements were assessed using repeated measurements of Volvic® water. They were better than 5 % and 10 %, respectively. The pH accuracy was better than 5%. The reproducibility and accuracy of the measurements is reported on *appendix B*. Table B.11.

SO_4^{-2} and Cl^- were analyzed using a Dionex ICS-100. Water samples were analyzed after a dilution of 500 with MilliQ water. The reproducibility and accuracy of measurements were assessed using IAPSO (seawater sample) (Summerhayes and Thorpe., 1996) was better than 2% and 5%, respectively (*appendix B*. Table B.11).

Si, Fe, Mg, Ca and Na were analysed using and ICP-MS Agilent 7700x quadrupole (Géosciences Montpellier) after a dilution of 100 in acidified MilliQ water (2% HNO_3). The reproducibility and accuracy of measurements were assessed using SLRS-5 (River water sample) (NRC-CNRC) certified standard and was better than 5 % and 10 % (a*ppendix B.* Table B.11).

3.2.4 X-Ray microtomography protocol

Image acquisition

The samples were scanned before and after the experiments at the ESRF with a resolution of 0.65 µm and energy of 55 KeV. The high energy was required to allow electrons to get into the sample. The outlet of the samples was scanned because they were easier to identify in the window field of view (FOV) because the plug of the sample acts as a landmark. Two consecutive scans with a length of 1.4 mm were acquired in the samples (Fig.4.2). The first scan (ROI-1) was acquired from the edge of the titanium plug towards the inside of the olivine sample (Fig.4.2). The second scan (ROI-2) overlaps a common zone (0.3 mm) of the first scan. The total length scanned is 2.5 mm which represents 34% of the total volume of the capsule.

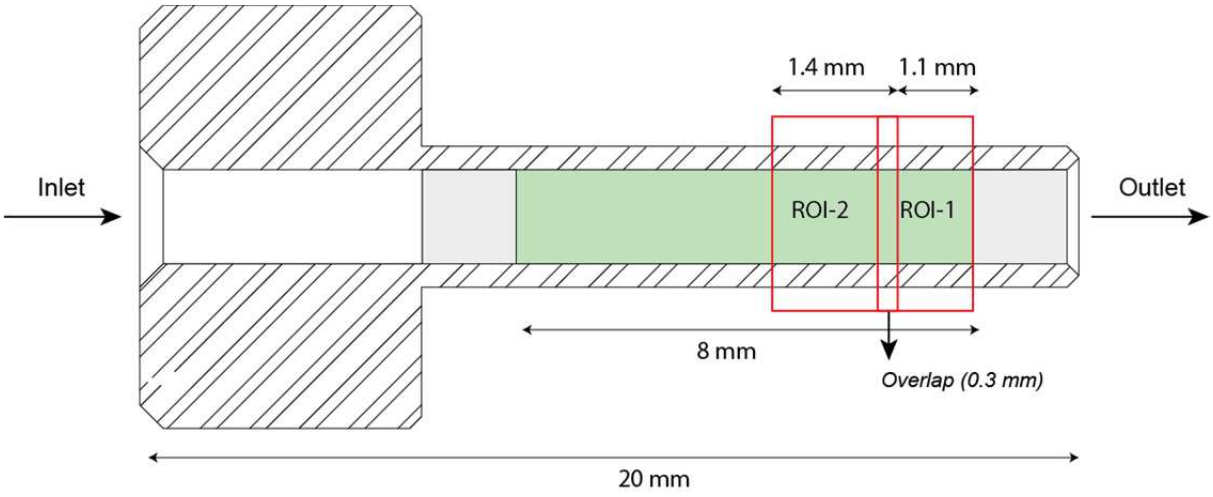

Fig.4.2. Sketch of the titanium capsule use in the experiment. The dimensions are in mm.

Image processing and computation

A post-processing was applied on images before visualization and calculation: (1) a deletion of the common zone (vertical overlap correction), (2) a correction of the brightness inhomogeneity for each 2D-images, (3) a registration, in order to get the same spatial coordinates of the grains before and after the images (see *chapter III.* Section 3.3 Methodology for additional information).

The images were segmented after post-processing. The voxels belonging to the pore space were distinguished from those belonging to the solid matrix. The segmentation was done using the method of "*region growing*" available in Voxilon code from Voxaya® (see *Chapter III.* Section 3.2.3). After segmentation, the total porosity (ϕ) of the samples was calculated assuming the total porosity of the sample is simply the ratio between the number of voxels belonging to the pore space over the total number of voxels (Eq.4.5) (Noiriel, 2009). Grain size distribution and surface area were calculated using Voxilon code.

$$\% \phi = N_{\text{voxel (pore space)}} / N_{\text{voxel (Total sample)}} \quad \text{(Eq. 4.5)}$$

Method to estimate the precipitation and dissolution degree after the experiments

The dissolution and precipitation degree was calculated from the subtraction of the segmented images before and after the experiments (Fig.4.3). Different pixel values were given for the porous and matrix in the image segmented before and after the experiments. The pixel value was changed using the voxilon code. The segmented image before the experiments has a pixel value of 150 for matrix and 250 for pores (Fig.4.3a). The segmented image after the experiments has a pixel value of 50 for matrix and 150 for pores (Fig.4.3b).

The resulted images after the subtraction have a new pixel value (Fig.4.3c). Dissolution process is recorded by a pixel value of 0 (Dissolution (0) = Matrix $_{\text{before}}$ (150) – Pore $_{\text{after}}$ (150)), whereas precipitation processes is recorded by a pixel value of 200 (Precipitation (200) = Pore $_{\text{before}}$ (250) – Matrix $_{\text{after}}$ (50). Lack of modification is represented

by a pixel value of 100; (No changes (100) = Matrix $_{before}$ (150) – Matrix $_{after}$ (50) and/or No changes (100) = Pore $_{before}$ (250) – Pore $_{after}$ (150).

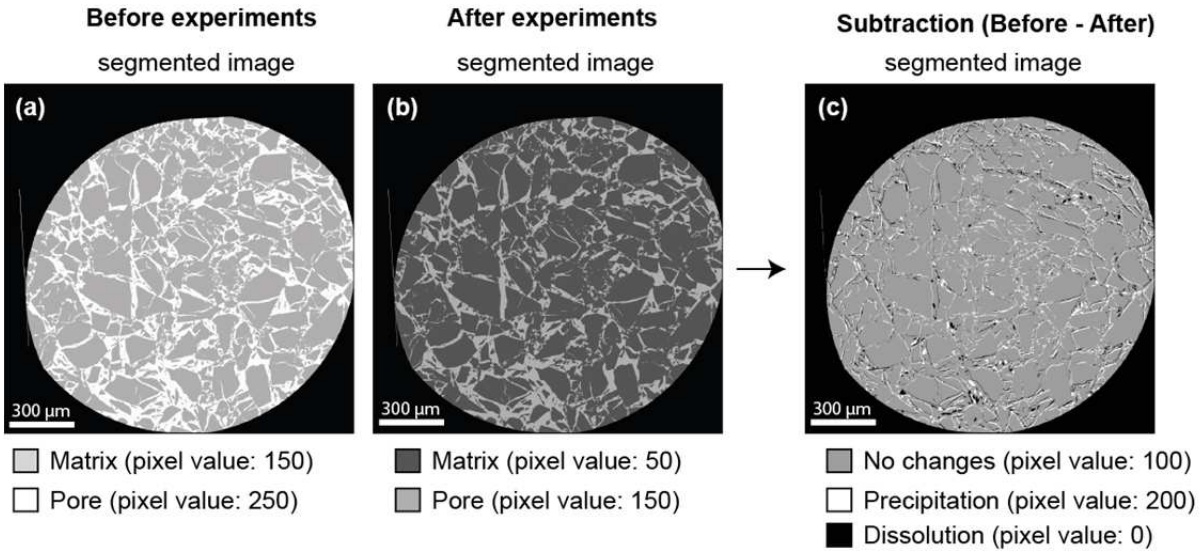

Fig.4.3. Method to estimate the precipitation and dissolution after the experiments. (a) Image before experiments segmented. (b) Image after experiments segmented. (c) Result from the subtraction the image before and after.

3.3 Results

3.3.1 Hydraulic conditions

Fluid leak

During the experiment, the Teflon sleeve and the FFKM O-ring were deformed due to the experimental temperature (190°C). This produces the mixing of the containment fluid (pure water) with the outlet fluids at the outlet of the samples. The mixing produces the dilution of the samples and their pollution. The fluid leak was identified by the decrease of the volume of the containment pump during the experiment (Fig.4.16). The fluid volume decreases with an almost constant rate on experiment SC2 from 65.000 mm^3 to 15.000 mm^3 (Fig.4.4). At 15.000 mm^3 the volume was manually refilled to continue the experiments from 58.000 mm^3 at 110 h and 80.000 mm^3 at 160 h.

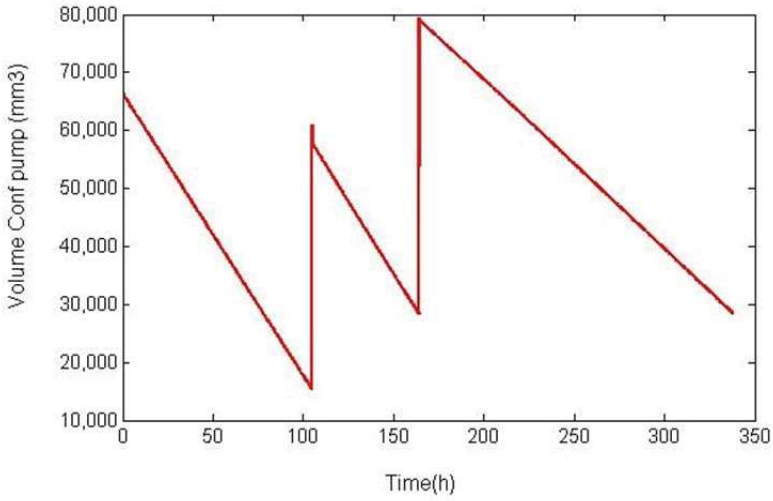

Fig.4.4. Volume of the containment pumps variating during the experiment time on experiment SC2. The negative slope of the curve corresponds to the fluid leak and the peaks the refilling of the pump.

The rate of the fluid leak was estimated after the slope of the containment volume curve on figure 4.16. The fluid leak was constant on experiment SC1 with a flow rate of 0.7 ml/h; this represents 128% of the initial flow rate (0.06 ml/h). In the other hand, the experiment SC2 presents a fluid leak of 0.06 ml/h which represents a 20% of the initial flow rate (0.3 ml/h). Thus, due to experimental issues encountered on experiment SC1 only the experiment SC2 was post processed in this thesis.

The chemistry of the outlet fluids of experiment SC2 was corrected according to the following equations 4.6 and 4.7 assuming: (1) the chemistry of the containment fluid was constant (pure water) and (2) the fluid leak was constant.

$$[C_i]_{corrected} = (1-\alpha)\cdot[C_i]_{Outlet\ fluid} + \alpha\cdot[C_i]_{leak} \quad \text{(Eq.4.6)}$$

$$\alpha = \frac{Q_{leak}}{Q_{total}} = \frac{Q_{leak}}{Q_{leak}+Q_{injected}} \quad \text{(Eq.4.7)}$$

where $[C_i]_{corrected}$ is the corrected concentration of the specie i in the fluid in mg/L, $[C_i]_{Outlet\ fluid}$ is the concentration of the specie i in the outlet fluid in mg/L, $[C_i]_{leak}$ is the concentration of the specie i in the containment fluid in mg/L. α is the dilution factor. Q_{leak} is the flow rate of the leak in ml/h and $Q_{injected}$ is the flow rate of the injected fluid in the experiment in ml/h.

Change on the chemistry of the injected solution

During the experiment, the composition of natural seawater at 25°C changes during its heating at 190°C. In consequence, secondary phases precipitate in the heating coil and stop the fluid injection after 15 days of experiment SC2 (Fig.4.5). Thus, the initial solution injected was no longer constant during the experiment. A precipitate was clogging the pipelines and avoids the injection of fluid. Anhydrite was identified using an optical microscope. Saturation index of the outlet fluids indicates saturation within anhydrite (SI>0) but also within carbonates (magnesite and calcite) (SI>0). The precipitation of anhydrite during the experiments led to not use natural seawater in future experiments and decreases of SO_4 and Ca content in next experiments.

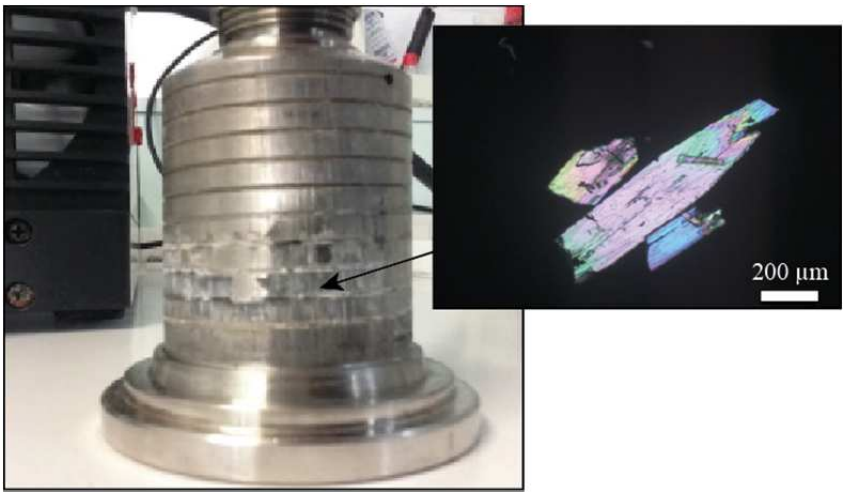

Fig.4.5. Anhydrite precipitated in the heating coil.

Permeability changes

Permeability stayed constant during the experiment SC2 (Fig.4.6). The strong variations at the beginning and the end of the experiments correspond to the noise from the pressure sensor likely due to precipitation of the secondary phases and/or the fluid leak.

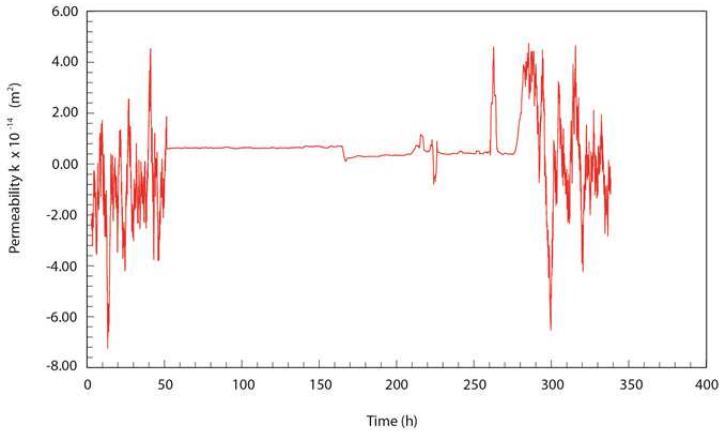

Fig.4.6. Permeability changes of experiment SC2.

3.3.2 Changes on the aqueous solutions

Outlet fluids composition showed variations in all elements that appeared coupled to Na content variations, and their respective concentrations are lower compared to the concentrations of the inlet fluid. Na is considered to behave as a conservative element in our experimental conditions. The dilution of the outlet fluids with the containment fluid likely produced the dilution of the outlet fluids. In order to correct the effect of chemical variations not related to the fluid-rock interaction, the values were normalized to the concentration of Na+ in the inlet fluid.

The overall chemistry of the aqueous solutions increases in the first hours for Si, Mg and Fe (Fig.4.7 and *appendix B*, table B.12). Si, Mg and Fe were enriched in the outlet fluids suggesting dissolution of the olivine powder. However oscillations during all the experiment were produced (Fig.4.7). Ca and SO_4 decreases since the beginning of the experiment. However enrichment in the outlet fluid at SO_4 at 46 h was produced. This suggests dissolution of previous anhydrite minerals precipitated in the heating coil. The pH of the outlet fluids remains almost constant and alkalinity decreases since the beginning of the experiments (Fig.4.7).

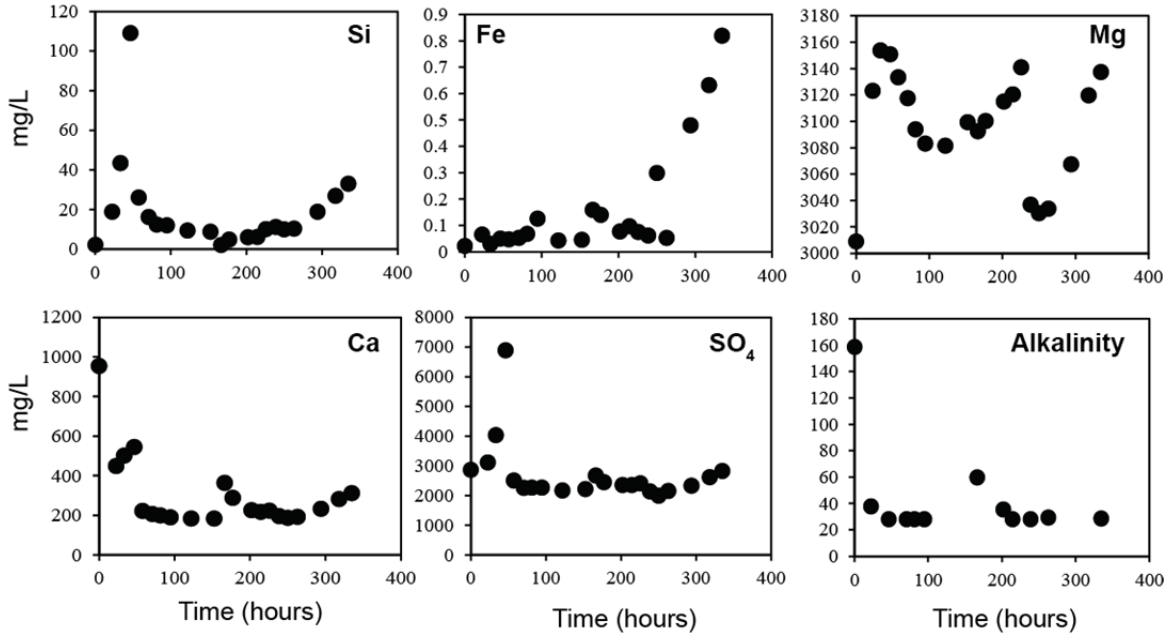

Fig.4.7. Chemistry of the outlet fluid normalized within Na^+. Note: The uncertainty on compositions is smaller than the size of symbols

3.3.3 Grain size distribution

Grain size distribution was calculated after the segmented images before and after the experiments. The images acquired before the experiments shows a substantial decrease of the grain size from the initial 150-200 µm used to 0-25 µm (Table 4.2). The decrease of the grain size is related to the technique used to fill the capsules. The mechanical compression applied on the grains generates the breakage of the grains into smaller sizes.

The small grain fraction (0-25 µm) increases of around 40% in both scans compared to the initial grain size (150-200 µm). After the experiments, the inner zone in the capsule (ROI-2) shows a decrease on the grain size distribution rather than the small increase observed on the outer zone (ROI-1) (Fig.4.20).

Table 4.2. Grain size distribution calculated before and after the experiments of the scans ROI-1 and ROI-2.

		Grain size %				
		0-25 µm	25-50 µm	50-75 µm	75-150 µm	150-200 µm
ROI-1	Before	45.8	24.8	14.1	13.4	1.4
	After	37.4	23.0	14.9	18.5	3.7
ROI-2	Before	40.4	23.9	14.8	16.8	2.7
	After	73.5	17.8	5.5	2.9	0.2

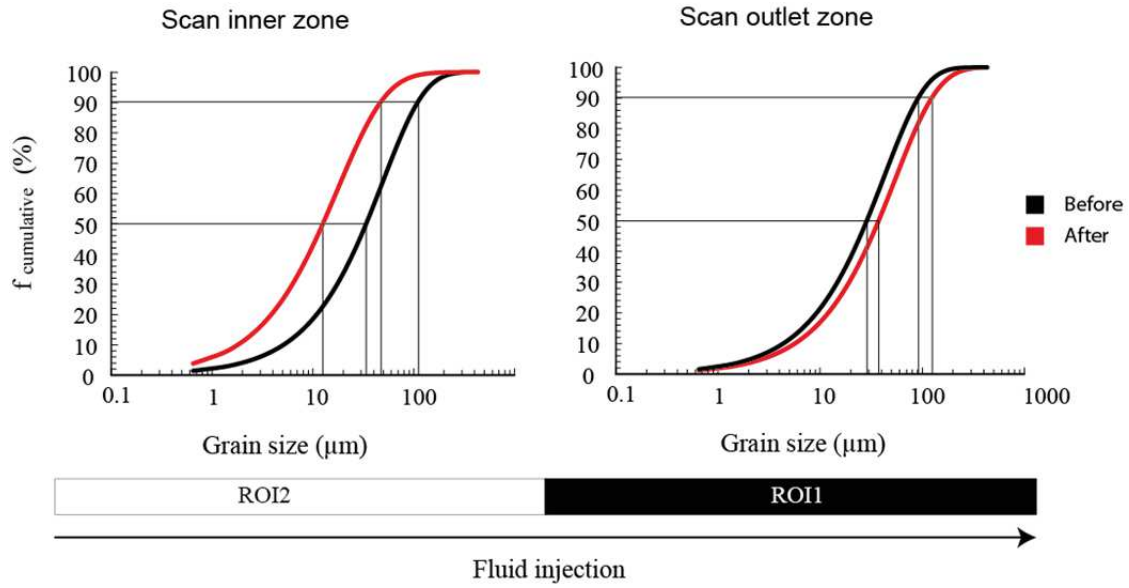

Fig.4.8. Grain size distribution computed before and after the experiments for the scan (ROI-1) and (ROI-2).

The small grains preferentially fill big pores (Fig.4.8). After the experiments, the small grains that were accumulated in the big pores disappears (i.e., are dissolved or moved) or are re-accumulated on other zones of the pore space (Fig.4.8).

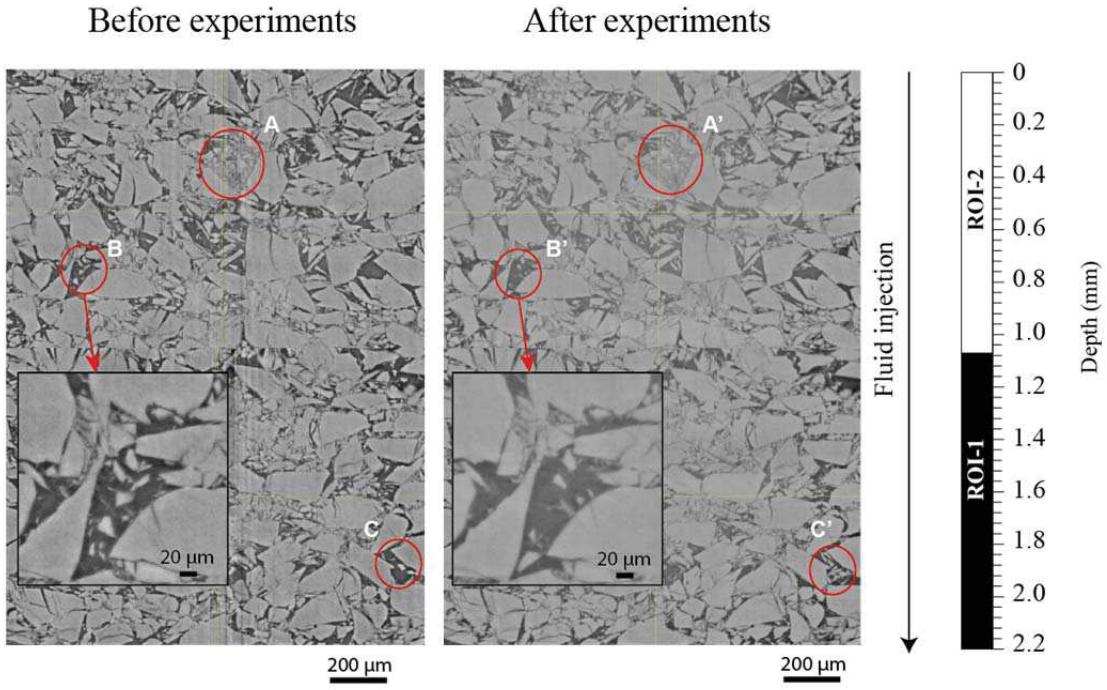

Fig.4.9. Vertical image of the scan ROI-1 and ROI-2. The image shows the presence of small grains accumulated in big pores before experiments (A-A') and the grain movement after the experiments (B-B') and (C-C').

3.3.4 Evaluation of the dissolution and precipitation process after the experiments

After the experiments, dissolution and precipitation process were estimated in the inner zone (ROI-2) and the outlet zone (ROI-1) of the sample (Table 4.3). The protocol followed was described in section 3.2.4. The total percentage of dissolution and precipitation was calculated from the number of pixel that corresponds to dissolution or precipitation over the total number of pixels in the scan. Thus, in the inner zone dissolution dominates with 8.4% over 5.7 % of precipitation. However, in the outlet zone precipitation dominates with 10.5% over 5.5% of dissolution. The subtracted images reveals the precipitation (white colour, pixel value 250) dominated in confined zones (i.e., grain fissures or small pores) and replacing the grain boundaries (Fig.4.10). Distinctively, dissolution (dark colour, pixel value of 0) is located preferentially on big pores at the grain boundaries (Fig.4.10). However, after the experiments a remarkable grain movement occurs. Small rounded grains appear (white) and disappears (dark) in the subtracted image (Fig.4.10c). This method is not able to make

the difference between the small grain movement and the precipitation and/or dissolution. Thus, it produced an over or under-estimation of the overall control process in the sample.

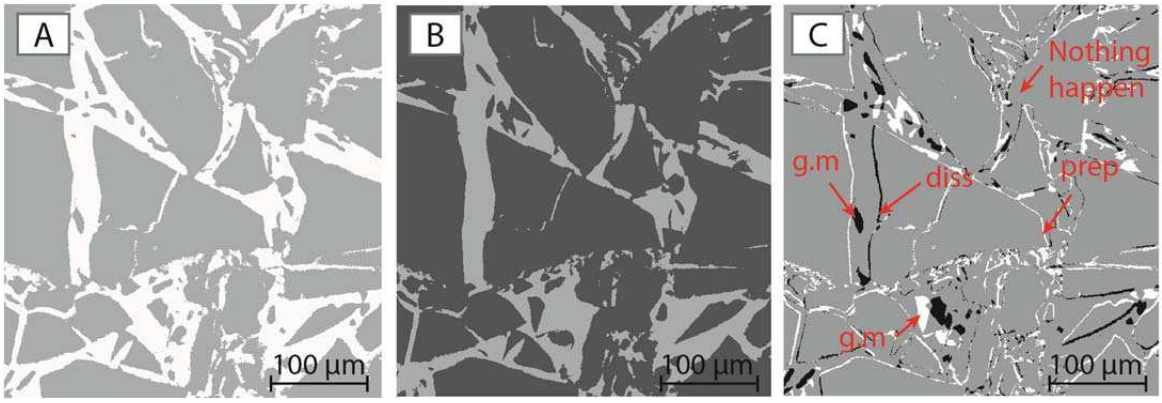

Fig.4.10. Method to estimate dissolution, precipitation and grain movement. (a) Segmentation image before experiments. (b) Segmentation after experiments. (c) Result of the subtraction of the image before and after. g.m: grain movement (Black and white) diss: dissolution (Black) prep: precipitation (White). Nothing happen: Grey.

After the experiments, the total dissolved volume was estimated in the overall sample. I make this calculation from the mass loss calculated by weight using a balance after the experiments ($M_{dissolved}$= 0.4±0.01 mg), $V_{dissolved} = M_{dissolved} / \rho_{olivine}$. The volume dissolved ($V_{dissolved}$) was 133 μm^3 which represents <<1% of the sample volume. Thus, is very difficult to identify dissolution process after the experiments. However, this method provides a visual localization of the dissolution-precipitation processes.

3.3.5 Sample microstructure changes: Porosity and geometric surface area

The porosity was estimated before and after the experiments in the inner zone (ROI-2) and the outlet zone (ROI-1) of the sample. The porosity is calculated as the number of pixels that corresponds to voids (pore) over the total number of pixel of each scan (Eq.4.5). The porosity is the average of 3 segmentations performs with different threshold values. This method provides estimate an error which is the standard deviation of the three porosity values. The porosity shows an increase in the inner zone of the sample (scan ROI-2) from 21.28 ± 0.01 (%) to 24.02 ± 0.01 (%) and a decrease towards the outlet of the sample (scan ROI-1) from 25.40 ± 0.02 (%) to 20.46 ± 0.02 (%) (Table.4.3). The overall porosity of the sample was calculated after the measure of the weight of the sample before and after the

experiment. The porosity shows an overall increase from 18.71 ± 0.1 to 19.36 ± 0.1 %. The difference between the value calculated after the weight and the micro-tomography images is related: (1) to the small volume scanned only 34% of the total volume of the sample and (2) overestimation due to the choice of the threshold values during segmentation.

Table.4.3. Porosity, geometric surface area and quantification of the dissolution and precipitation process calculated on both scans before and after the experiments.

Z (mm)	**ROI-1** outlet zone 0-1.1		**ROI-2** inner zone 1.1-2.5	
	Before	After	Before	After
Porosity (φ) %	25.40 ± 0.02	20.46 ± 0.02	21.28 ± 0.01	24.02 ± 0.01
Surface area (S_g) mm^2	327 ± 0.6	240 ± 0.6	270 ± 0.6	234 ± 0.6
Dissolution %		5.5		8.4
Precipitation %		10.5		5.7

Porosity profiles in depth were performed in both segmented scans before and after the experiments (Fig.4.11). The profiles were performed applying a Z-profile algorithm in the whole scan segmented using image J. The Z-profile provides the number of pixel for matrix and pore (i.e., void) for each slide of the block. The porosity is estimated by: $\phi = Pixel_{void} / Total_{pixel}$. The total pixel number is the sum of the pixel that corresponds to matrix plus the pixel that corresponds to void. The increment of porosity was calculated: ($\Delta\phi = \phi_{before} - \phi_{after}$). A positive value corresponds to a decrease of porosity and a negative value an increase of porosity. The $\Delta\phi$ was negative on the whole scan ROI-2 (inner zone) indicating an increase of the porosity with depth and $\Delta\phi$ was positive for scan ROI-1 (outlet zone) indicating adecrease of the porosity with depth.

The average intensity of each scans (ROI-1 and ROI-2) acquired before and after the experiments shows almost constant intensity pixel values with depth (Fig.4.11). This indicates that the algorithm applied to correct the brightness inhomogeneity successfully correct the brightness for each individual scan. However, both scans (ROI-1 and ROI-2) still have difference in the average intensity between them. This issue is more emphasize in the images acquired after the experiments especially on the scan ROI-1 (Fig.4.11 red line). As the segmentation depends on the intensity values of the image, a huge difference between average intensity values for either scans can over or under estimate the calculations performed in segmented images. Thus, this questions the confidence that we have in the

results for the scan ROI-1. We suggest that the average intensity of ROI-1 after the experiments could be corrected by subtracting the differences of average intensity between ROI-1 and ROI-2 at 1.1 mm depth; Average intensity ROI-1 $_{\text{after (corrected) (at x mm)}}$ = Average intensity ROI-1 $_{\text{after (at x mm)}}$ – (Average intensity ROI-1 $_{\text{after (at 1.1 mm)}}$ - Average intensity ROI-2 $_{\text{after (at 1.1 mm)}}$).

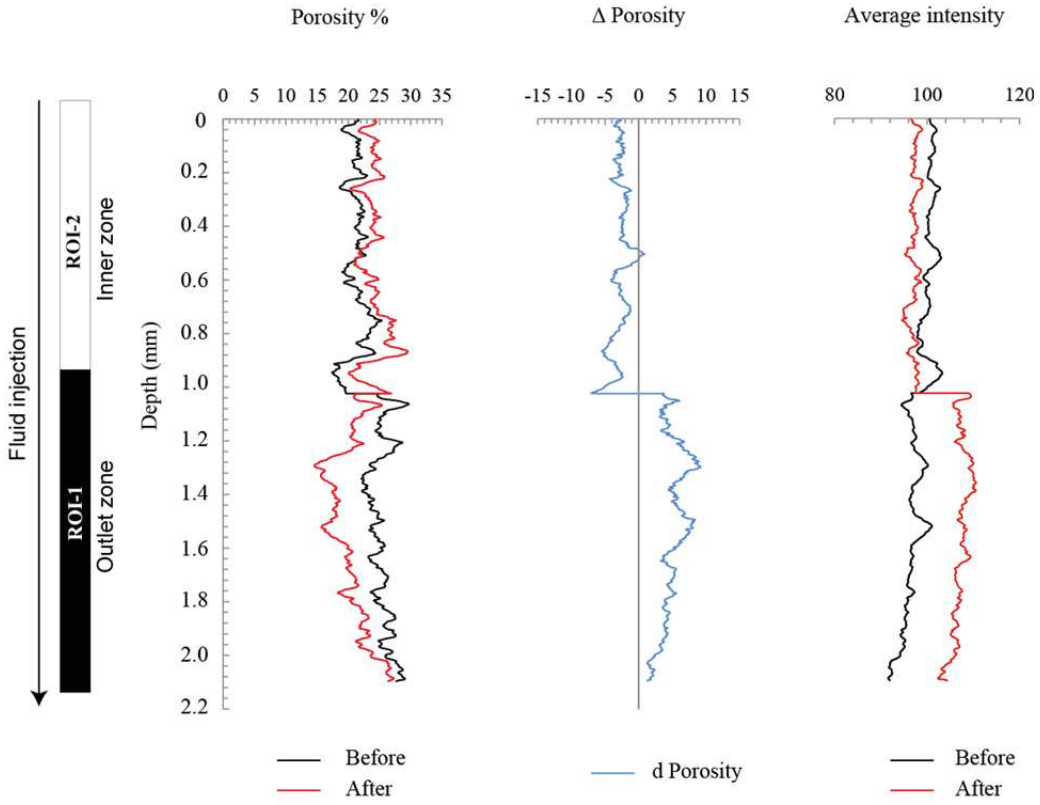

Fig.4.11. Porosity was estimated from 0 to 2.2 mm. Scan (ROI-2) from 0 to 1 mm and scan (ROI-1) from 1 to 2.2 mm. The average intensity corresponds to the grey images no segmented.

The geometric surface area (S_g) was calculated on the segmented images using the numed code (Table 4.3). The geometric surface area is calculated from the segmented grain observed in 3D images as the number of pore-mineral edge pixels N_{pix} multiplied by the pixel surface area (S_{pix}=0.65 × 0.65 μm^2). The geometric surface area is calculated as the average of 3 segmentations performs with different threshold values. This method provides an estimate of the error which is the standard deviation of the three geometric surface area values. The geometric surface area decreases in both scans (ROI-1 and ROI-2) after the experiments. The inner zone (ROI-2) shows a decrease from 270 ± 0.6 mm^2 to 234 ± 0.6 mm^2; and the outlet zone (ROI-1) shows a decrease from 327 ± 0.6 mm^2 to 240 ± 0.6 mm^2.

3.4 Discussion and conclusions

Reactive percolation experiments allow studying reactive processes in olivine rich rocks in a context where no macroscopic differential stress is applied (Godard et al., 2013). The experiment reported in this study allowed to identify and solved several technical challenges in the laboratory and for scanning.

High-quality multi-resolution 3D observations of hydrothermally altered olivine samples require building specific samples holders adaptable for synchrotron imaging and reactive percolation experiments. To achieve a resolution of 0.65 µm samples holders need to have a small size (D=2 mm and L=20 mm) and be made on titanium material to get a low absorption for X-ray and thus x-ray access into the sample.

The identification of secondary phases precipitated in the heating coil and pipelines suggest an evolution of the natural seawater when is heated to 190°C due to the retrograde solubility of anhydrite with temperature (Blounot and Dickson, 1969). This produces the stop of the fluid injection and the early end of the experiments.

The compression of olivine grains when they are introduced in the capsules generates a high reduction of the initial grain size of around ~80%. The increase of the small grain fraction suggests the olivine surface roughness increase and thus the surface area (e.g., Hodson, 2006, Steefel et al., 2015). This suggests that the small grains increase the reactivity of the overall sample. However, the injection of the fluid in the sample produces the displacement of the non-cohesive small grains that accumulate filling big pores. The accumulation of small grains with high surface area can enhance the locally the dissolution-precipitation processes

The method used here to estimate the dissolution and precipitation of the sample provides a visual estimation of the local dissolution or precipitation occur in the sample but could over- or under-estimate calculations on non-cohesive porous samples due to the mechanical displacement of small grains. However, it would be interesting to apply this method on cohesive samples that will not sustain grain movements.

The result of this experiment shows that the injection of very high fluid velocity into olivine non-cohesive samples produces an increase of the overall dissolution of the samples. However, the nature of the porous media leads to the development of local microenvironments far from the injection point where precipitation dominates. This suggests that a prolonged reaction time could clog the fluid path at the end of the samples and jeopardize the continuity of the percolation of the fluid in the sample.

Chapter V

Experimental study of carbonation into fractured peridotites

Ultramafic rocks or *peridotites* have the potential to efficiently trap CO_2 as carbonate minerals (e.g., Kelemen and Matter, 2008). They contain olivine and pyroxenes that are particularly rich in divalent cations (e.g. Mg^{2+}, Ca^{2+}, Fe^{2+}). When those primary minerals are dissolved by a CO_2-bearing fluid, the divalent cations are released into this fluid and react with the $CO_{2(aq)}$ to form carbonates. Several studies on carbonation of ultramafic rocks have shown that carbonation depends on a series of physico-chemical parameters such as temperature, fluid composition and mineral reactive surface area (e.g., Daval et al., 2010; Gerdermann et al, 2007; Harrison et al, 2015; Kelemen et al., 2011; O'Connor et al., 2014). The transport of fluid within the host rock is still a parameter poorly studied (e.g., Andreani et al., 2009; Peuble et al., 2015). However, fluid transport plays a major role in the in-situ carbonation of CO_2 in natural ultramafic reservoir, notably by controlling the supply of reagents at the fluid-rock interface and the chemical equilibrium conditions in the system. Thus, in situ carbonation of peridotites required that CO_2-rich fluids have an on-going access to fresh sources of host rock primary minerals. Nevertheless, ultramafic rocks are dense, fully crystallized, having allow porosity and permeability that can limit the fluid flow. The presence of a fracture network in peridotite reservoirs provides preferential fluid paths, where fluids can access mineral reactive surface areas and promote fluid-rock interaction. Until now, very little studies have been performed on fractured reservoirs of peridotite (Farough et al., 2016) mainly focalized on the evolution of the fracture permeability during serpentinization reactions rather than during carbonation. This chapter provides the first insights on the dissolution-precipitation processes that occurred on artificial fractured serpentinized peridotites by assessing the effects of dissolved CO_2 on the reactions under open conditions.

The results of this study are described in the paper presented below being prepared for submission to *International Journal of Greenhouse Gas Control*

1. Introduction

Geological carbon storage is one of the methods envisaged today for mitigating increasing CO_2 concentrations in the Earth's atmosphere; it consists in injecting CO_2 into geological reservoirs (e.g., Goff and Lackner, 1998; Matter and Kelemen, 2009; Oelkers et al., 2008). In geological reservoirs, CO_2 is trapped by physical and chemical mechanisms, which can result in long-term and secure storage (a process hereafter referred to as CO_2 mineralization and carbonation). Ultramafic (peridotite) and mafic (basalts) rocks have the highest potential among geologically common rock types to trap CO_2 as carbonates because they contain silicate minerals (e.g., olivine, pyroxenes and serpentine) that are particularly rich in divalent cations (Ca^{+2}, Mg^{+2} and Fe^{+2}) (Garcia et al., 2010; Kelemen et al., 2011; Xu et al., 2004). Mineral trapping occurs in a series of reactions. First, dissolution of CO_2 acidifies the water (R1). CO_2 solubility decreases with increasing temperature and ionic strength of the water, and increases with increasing pressure (Duan et al., 2003). Dissolution of CO_2 in water produces a weak carbonic acid (H_2CO_3) that will dissociate into bicarbonate (HCO_3^-) and carbonate (CO_3^{2-}) ions (R1) (Bénézeth et al., 2013). Then, bicarbonate and carbonate ions combine with calcium, magnesium and iron ions that come from the dissolution of primary silicate minerals, to form solid carbonates (R2 and R3).

$$CO_{2(aq)} + H_2O = H_2CO_3 = HCO_3^- + H^+ = CO_3^{2-} + 2H^+ \quad \text{(R1)}$$

$$(Ca,Mg,Fe)^{2+} + HCO_3^- = (Ca,Mg,Fe)CO_3 + H^+ \quad \text{(R2)}$$

$$(Ca,Mg,Fe)^{2+} + CO_3^{2-} = (Ca, Mg,Fe)CO_3 \quad \text{(R3)}$$

CO_2 mineralization in ultramafic and mafic rocks occurs as a part of a complex suite of fluid–rock reactions involving silicate dissolution and precipitation of carbonates, hydrous phases, and minor phases (e.g., oxides) that may in turn modify flow paths and the hydrodynamic properties of the reacted rocks. Laboratory experiments are a good way to determine the reaction pathways in these highly reactive fluid–rock systems. Over the last decade, extensive experimental work has provide insights of chemical processes controlling the dissolution of silicate minerals (e.g., Chen and Brantley, 2000; Daval et al., 2011; Hänchen et al., 2006; Pokrovsky and Schott, 2000; Prigiobbe et al., 2009) and associated precipitation of carbonates (e.g., Giammar et al., 2005; Saldi et al., 2012). These studies

provide better understanding on the effects of pH, concentration of dissolved CO_2, temperature, fluid composition and reactive surface areas on carbonation reactions.

Most of the experimental studies have been performed on monomineral (porous media or sintered material) which provides simplicity of the system and effective access of fluid to reactive surface area (e.g., Andreani et al., 2009; Daval et al., 2011; Peuble et al., 2015; Luhmann et al., 2017a) but only a few carbonation experiments have been performed on coherent ultramafic rock material (peridotite) (e.g., Grozeva et al., 2017; Hövelmann et al., 2011; Hövelman et al., 2012; Klein and McCollom, 2013; Lacinska et al., 2017; Van Noort et al., 2013). Unlike porous media material, peridotites are dense, crystalline rocks, having low porosity and permeability (Macdonald and Fyfe, 1985). In situ carbonation of peridotites needs that CO_2 has an on-going access to fresh sources of host rock minerals, as progressive carbonation depends on the ability to maintain a high concentration of divalent metal ions within the fluid (Matter and Kelemen, 2011). In addition, the presence of a fracture network in a peridotite reservoir provides preferential fluid path where fluids can access mineral reactive surface area (Farough et al., 2016). However the chemical changes, rock microstructure evolution and hydrodynamic feedbacks that produce the interaction of CO_2-rich fluid through fractured reservoirs of peridotite are still limited. This study focuses on the dissolution-precipitation processes that occurred on artificial fractured serpentinized peridotites by assessing the effects of dissolved CO_2 on the reactions under open conditions.

2. Experimental and analytical methods

2.1 Reactive percolation experiments

Four reactive-percolation experiments were performed at the same temperature (T = 170°C) and pressure (P = 25 MPa) conditions. NaCl (0.5 M) - CO_2 enriched in solution was injected into fractured cores of serpentinized peridotites of 9 mm diameter (D) and 18 mm length (L) during 6 to 11 days. In the following FP1-HC, FP2-HC, FP3-HC denote the experiments performed with high concentration of CO_2 (1 mol.L^{-1}) in solution and FP4-LC denote the experiment with low concentration of CO_2 (0.1 mol.L^{-1}) in solution. Experimental conditions are summarized in Table.5.1. The reactive percolation experiments were carried out using Icare Lab 3 flow-through system (Géosciences Montpellier, France). It includes an

automatic system of fluid injection with three computer-controlled hydraulic pumps that allow maintaining a constant flow rate ($10^{-6} \leq Q \leq 2$ mL.min^{-1}) and a heated confinement cell that hold the sample at constant temperature (T<400°C). The experiment pressure (P) < 40 MPa is controlled by a back pressure system. During the experiments, the difference of fluid pressure between the inlet and outlet of the sample ($0.003 < \Delta P \leq 40$ MPa) is monitored during the experiments using a differential pressure sensor Rosemount 3051 (accuracy of 0.003 MPa) coupled with two high resolution pressure sensors Keller PA-33 X (accuracy of 0.035 MPa). 3 mL of reacted fluid were collected using a pressurized computer-controlled syringe. Pumps motion, valves and fluid sampling are operated by a LabView-based software.

Table 5.1. Experimental conditions of the carbonation experiments.

Exp.	Sample	XCO_2	pCO_2	Duration		Flow rate	pH	Core diameter (d)	Core length (L)	Initial weight
		M	*MPa*	*(days)*	*(hours)*	*(Q=ml/h)*	*(t=0)*	*(mm)*	*(mm)*	*(g)*
FP1-HC	FP1	1	20	7.3	175	6	3.38	8.95	19.96	3.32
FP2-HC	FP2	1	20	5.6	134	6	3.38	8.91	20.09	3.30
FP3-HC	FP3	1	20	6.9	165	2.4	3.38	8.88	19.54	3.30
FP4-LC	FP4	0.1	10	10.7	257	6	3.88	8.92	19.74	3.30

2.2 Fluid and rock samples preparation

Fluid solution

Saline-CO_2 enriched solution was made by dissolving 0.5 M of NaCl (Prolabo Analar Normapur) into MilliQ water (18 M.Ω cm) at room temperature (T=25°C) and under atmospheric pressure. Thereafter, to reproduce CO_2 injection conditions, an industrial-grade pure CO_2(g) was added to the saline solution under 25 MPa of pressure and T=25°C below 1.24 mol/L, which is the solubility (S) of CO_2 at the experimental conditions (Duan et al., 2003), in order to ensure completely dissolution of CO_2(g) into the NaCl solution. 1 mol/L of CO_2 was added to the saline solution for experiments FP1-HC, FP2-HC and FP3-HC, and 0.1 mol/L of CO_2 was added for experiment FP4-HC.

Initial rock sample and core preparation

A serpentinized harzburgite (sample 99OL15) from the Oman ophiolite was used for these experiments (a*ppendix C*.Fig.C.1). The sample is composed of serpentine (dominantly lizardite, Mg#= 90), olivine (Fo_{90}), orthopyroxene ($Wo_3En_{88}Fs_9$), clinopyroxene ($Wo_{49}En_{47}Fs_4$), carbonate (calcite), spinel and magnetite; minerals were identified after optical microscope. The bulk composition of the initial rock was determined by X-Ray fluorescence (XRF) at Geolabs (Canada) and is reported on table C.1 (*appendix C*) and the major element composition of primary mineral and reacted minerals was determined on samples by EPMA at the Service Microsonde Sud (University of Montpellier).

Samples were cored from hand specimens to form cylinders with 9 mm diameter (*D*) and 20 mm length (*L*) parallel to the foliation direction. After coring, both ends of the core were sawn in order to remove the roughness and thus lead both sides polished. Approximately 1 mm of samples was removed at each end of the core. The fractures were generated following the indirect tensile test or Brazilian test, (Claesson et al., 2002). The Brazilian test is a common method for determining the tensile strength of rock. It calculates the principle tensile stress, in particular at the rock core centre where cracks start. Pressure was applied on the generatrix of the cylindrical cores with an *Enerpac*® hydraulic press. Pressure was applied until the first cracks appear, in order to avoid that the core to split into two pieces and to maintain a small fissure all along the core. The advantage of this method is that the core maintains the rough surfaces of the walls fracture analogous to natural systems, it also provides more surface area for chemical reactions than samples prepared by saw cutting.

2.3 Monitoring changes in permeability and fracture aperture

Changes on fracture permeability *k(t)* during the experiments were calculated following the method of Garcia-Rios (2015). Fracture permeability was calculated from the pressure difference $\Delta P(t)$ measured between the inlet and the outlet of the sample and combining Darcy's law (Eq.5.1) with a cubic law for flow through two parallel plates (Eq.5.2) (Witherspoon et al.,1980).

$$k = \frac{\mu \cdot L \cdot Q}{S \cdot \Delta P} \quad \text{(Eq.5.1)}$$

$$Q = \frac{a_h^3 . \Delta P \cdot d}{12 \cdot \mu \cdot L} \quad \text{(Eq.5.2)}$$

where μ is the dynamic viscosity of the solution (0.197 x 10^{-3} Pa.s at 150°C and 25 MPa for a salinity of 0.5 mol/kg, Kestin et al. (1981)), L is the length of the sample in the flow direction (m), Q is the volumetric flow rate (m^3/s), S is the sample cross section (m^2), ΔP is the measured pressure difference (Pa) and d is the width of the fracture (here is the diameter of the sample) (m). The values of Q, S, d are summarized on table 5.1 and the figure 5.1 illustrates the core parameters.

Combining the equations (Eq.5.1) and (Eq.5.2), the hydraulic aperture a_h of the fracture was determined from:

$$a_h(t) = \sqrt[3]{\frac{12 \cdot \mu \cdot L \cdot Q}{\Delta P(t) \cdot d}} \quad \text{(Eq.5.3)}$$

and fracture permeability from:

$$k(t) = \frac{a_h^2(t)}{12} \quad \text{(Eq.5.4)}$$

2.4 Rock characterization

Before analyses, the reacted rock samples were dried under vacuum for 12 hours at room temperature (25°C) to remove the fluid that remained in pores and to avoid post-experiment fluid-rock reactions.

The microstructure of samples was characterized after experiments using X-ray microtomography (XCT, European Synchrotron Radiation Facility (ESRF), Grenoble, France), Scanning Electron Microscope (SEM, coupled with energy dispersive spectroscopy (EDS) service de Microscopie Électronique et Analytique (MEA), University of Montpellier,

France). XCT images were acquired with a 2.2 µm resolution and energy of 100 KeV on the ID19 beamline (ESRF) and 3D images were reconstructed using pyHST (Mirone et al., 2014) then processed for computation using ImageJ and visualization using Avizo® and Voxilon® softwares. The diameter scanned was 5.6 mm since the centre of the sample to achieve the resolution of 2.2 µm.

Then, the reacted cores were impregnated with Epoxy resin AR2020® to consolidate the secondary formed newly phases. Four sections of ~4 mm of length were cut perpendicular to the fracture with a separation of 0.5 mm, and then they were polished to get 4 polished section of each reacted core (Fig.5.1). This provides a cross section of the progress of the reaction from the inlet to the outlet. The samples were renamed from A to D, with section A for the inlet and D for the outlet (*appendix C*. Fig.C.2-5). This method to cut the samples is not completely precise as is user dependent. A posteriori comparison of the polish sections and the x-ray images provides a more precise estimation of the position (i.e., depth) of the sections relative to the inlet of the samples for experiments FP2-HC, FP3-HC and FP4-LC (*appendix C*. Fig.C.6-7).

SEM images of the reacted samples were acquired using a FEI Quanta FEG 200 Scanning Electron Microscope with an acceleration voltage of 15kV and chamber pressure of 0.38 torr.

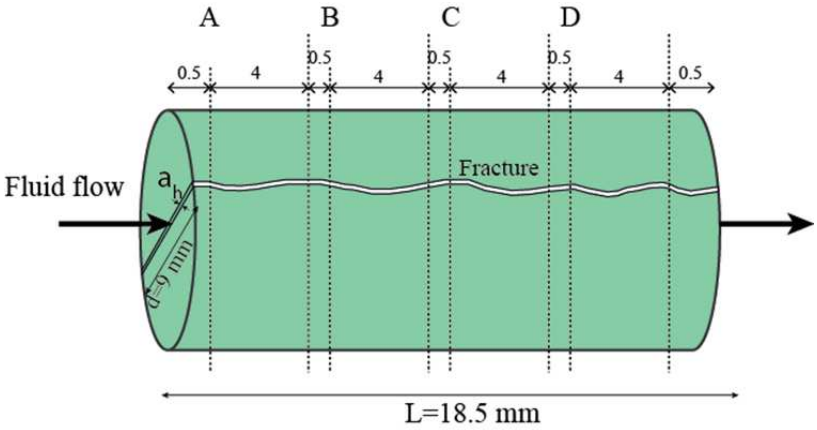

Fig.5.1. Fractured core cut on 4 sections from (A to D). The values are in mm. (a_h) is the fracture aperture, d and L are the diameter and length respectively of the sample.

The minerals were identified by cathodoluminescence using a cold-cathode CITL 8200 Mk5-1 Optical Cathodoluminescence (CL) Microscope Stage coupled to an Olympus BX41 optical microscope (Geosciences Montpellier, University of Montpellier), operating at

15 kV and 250 µA and by RAMAN spectroscopy using a Renishaw Invia (at Charles Coulomb Laboratory, University of Montpellier). RAMAN analysis were made using a laser with a wavelength of 633 nm and a power of 2 mW, coupled with an open microscope equipped with a x50 objective (Leica N Plan). Acquisition time was 10 sec and the spectral region investigated range from 100 to 1700 cm^{-1}.

The major element composition of primary mineral and reacted minerals was determined on samples 99OL15, FP2-B and FP4-B by Electron Probe Micro-Analyser (EPMA) at the Service Microsonde Sud (University of Montpellier), using a CAMECA SX100 equipped with five wavelength-dispersive X-ray spectrometers (WDS). Analyses were done with 20 kV accelerating potential, 10 nA beam current and 30 s counting times for all elements measured. Chemical composition of the pristine minerals of the sample OL15 is reported in *appendix C*. Table.C.2.

2.5 Fluid characterization

Alkalinity and pH were measured using a Methrom Titrino 848. Measurements were performed in less than 5 minutes after the fluid sample was collected to minimize equilibration with the atmosphere. The pH was measured using 2 mL samples at 1:2 dilution in MilliQ water using a Metrohm LL Micro glass electrode. The alkalinity (HCO_3^-) was measured at 25°C on the same fluid sample by acid titration with 0.01M HCl. The reagent was added to the fluid sample in variable volume steps to a pH endpoint of 4.5. HCO_3^- was assumed to be equal to total alkalinity (Bischoff and Seyfried, 1978). The reproducibility and accuracy of alkalinity and pH measurements were assessed using repeated measurements of Volvic® water. They were better than 5 % and 15 %, respectively for alkalinity and 2% and 3%, respectively for pH (see a*ppendix C.* Table C.15).

Si, Fe, Mg, Ca, Na, Mn, Cu and Zn were analysed using ICP-OES Thermo Scientific ICAP 7400 (Géosciences Montpellier) after a dilution of 50 in acidified MilliQ water (2% HNO_3). The reproducibility and accuracy of measurements were assessed using SLRS-5 and SLRS-6 (River water sample) (NRC-CNRC) certified standard and was better than 10 % and 15 % respectively (see *appendix C.* Table C.15).

Ni, Cr and Co were analysed using ICP-MS using Agilent 7700x quadrupole (Géosciences Montpellier) after a dilution of 100 in acidified MilliQ water (2% HNO_3). The reproducibility and accuracy of measurements were assessed using SLRS-5 (River water sample) (NRC-CNRC) and SLRS-6 certified standard and was better than 15 % and 10 % respectively (see *appendix C.* Table C.15).

The initial pH of the solutions was calculated using EQ3/6 code to be 3.33 at 170°C and 25 MPa for the experiments with FP1, FP2 and FP3 and 3.83 for FP4, (Wolery and Jared, 2003). Speciation and saturation calculations of the experimental fluids were calculated using EQ3/6 (Wolery and Jared, 2003). Calculations to estimate in situ pH and silica activity were performed using EQ3/6 following the method of McCollom et al. (2016). The calculations were determined in two steps. First, fluid speciation were calculated at 25°C using the measured fluid composition and the pH measured at room temperature adjusting for charge balance with Na^+. Second, the total dissolved Na^+ calculated at 25°C was used with other measured concentrations to establish the fluid speciation at 170°C in adjusting the H^+ content to balance the electrical charge. .

The total dissolved inorganic carbon (DIC) of the fluids at 25°C was estimated using EQ3/6 using a speciation-solubility model. Fluid speciation was calculated at 25°C using the fluid composition, the alkalinity and pH measured at 25°C adjusting for charge balance the Na^+ content. The output model provides the speciation of all the carbon species in the fluid at 25°C. The total dissolved inorganic carbon (DIC) corresponds to the sum of all the carbon species in solution.

The sampling of the fluid sample from the reactor tubes into the sampling tubes triggers a depressurization of the fluid from 25 MPa to an atmospheric pressure which produce the degassing (loss) of carbon in the fluid. We estimate the total concentration of CO_2 (XCO_2) loss by degassing is constant for all the samples. The total XCO_2 loss is estimated using the samples collected circulating through the by-pass of the reactor which represents the initial composition of the fluid injected at the temperature and pressure chosen for the experiment. The total concentration of CO_2 loss is calculated by:

$$XCO_{2(degassing)} = DIC_{Theoretical} - DIC_{25°C} \quad \text{(Eq. 5.5)}$$

where $DIC_{Theoretical}$ corresponds to the theoretical concentration of total inorganic carbon injected in the solution at 25°C (1 mol/L for experiments FP1-HC, FP2-HC, FP3-HC and 0.1 mol/L for experiment FP4-LC), $DIC_{25°C}$ corresponds to the concentration of total inorganic carbon once the sample is collected at ambient pressure and is calculated after geochemical modelling (EQ3/6, Wolery and Jared, 2003) at 25°C following the procedure describe above.

Thus, the concentration of CO_2 loss by degassing is 0.95 mol/L for high CO_2 experiment and 0.08 mol/L for low CO_2 experiments which represent a loss of 95% and 80% from the initial injected concentration respectively. 1.24 mol/L is the solubility of CO_2 in 0.5M NaCl solution at 170°C and 25MPa and 0.05 mol/L is the solubility of CO_2 in 0.5M NaCl solution at 25°C and 0.1MPa (1atm) (Duan et al., 2003). Thus, the degassing of CO_2 is produced instantaneously since the fluid sample is collected at 25°C and 0.1MPa until the dissolved CO_2 content reach the solubility value of 0.05 mol/L of CO_2 at 25°C and 0.1MPa.

All calculations were performed using a data base of thermodynamic parameters for 25 MPa. The data base was generated using SUPCRT92 (Johnson et al, 1992), includes all minerals and inorganic aqueous species in the SUPCRT92 data base for the system Mg-Ca-Fe-Si-Na-Cl-O-H. SUPCRT92 incorporates thermodynamic data from Helgeson et al. (1978) for minerals, and Shock and Helgeson (1988) and Shock et al. (1989, 1997) for dissolved inorganic aqueous species. Activity coefficients for aqueous species are calculated using the B-dot equation (Helgeson et al, 1981).

3. Results

3.1 Fracture aperture and permeability changes

The fracture aperture (a_h) and fracture permeability $k(t)$ were calculated in the four percolation experiments according to Eq.(5.3) and Eq.(5.4) respectively, from the measured values of $\Delta P(t)$ through time. Table 5.2 summarize the aperture length of the samples and the permeability for each experiment. The fracture aperture value represents the average of the fracture aperture of the whole sample calculated by the ΔP. The samples show different initial fracture aperture. This suggests a control of the heterogeneity of the rock when the fracture was made using the same conditions for all the samples.

Table 5.2. Permeability and fracture aperture of the samples during the experiments

Experiment	Time *hours*	Flow rate (Q) *ml/h*	Core length (L) *mm*	Core diameter (d) *mm*	Initial fracture aperture (a_h) *µm*	Final fracture aperture (a_h) *µm*	Initial permeability (k) *m2*	Final permeability (k) *m2*
FP1-HC	175	6	19.96	8.95	9.9	4.2	0.8 (±0.01) x10^{-11}	0.14 (±0.01) x10^{-11}
FP2-HC	134	6	20.09	8.91	13.5	8.9	1.5 (±0.01) x 10^{-11}	0.67 (±0.01) x10^{-11}
FP3-HC	165	2.4	19.54	8.88	2.7	1.5	6.1 (±0.01) x10^{-13}	1.82 (±0.01) x10^{-13}
FP4-LC	257	6	19.74	8.92	9.3	4.8	0.7 (±0.01) x10^{-11}	0.18 (±0.01) x10^{-11}

The initial permeability is different for each sample because samples have different initial fracture aperture (Table 5.2). Nevertheless, fracture permeability decreases over time in the four experiments (Fig.5.2). Experiments with the highest concentration of $CO_{2(g)}$ (FP1-HC and FP2-HC) records a higher decrease of permeability with time compared to the lowest concentration of $CO_{2(g)}$ FP4-LC (Table 5.2 and Fig.5.2). Experiment FP1-HC records a stage of no-fluid injection of 9 hours and the permeability trend remains unchanged after this period (Fig.5.2). Sample FP3-HC shows also a longer period of 53 hours of no-fluid injection and the permeability decrease faster during this period. The permeability results shows that permeability decrease much faster with time for FP3-HC run with a low injection rate (Q=2.4 ml/h) than the other 3 experiments run with a faster injection rate (Q=6 ml/h).

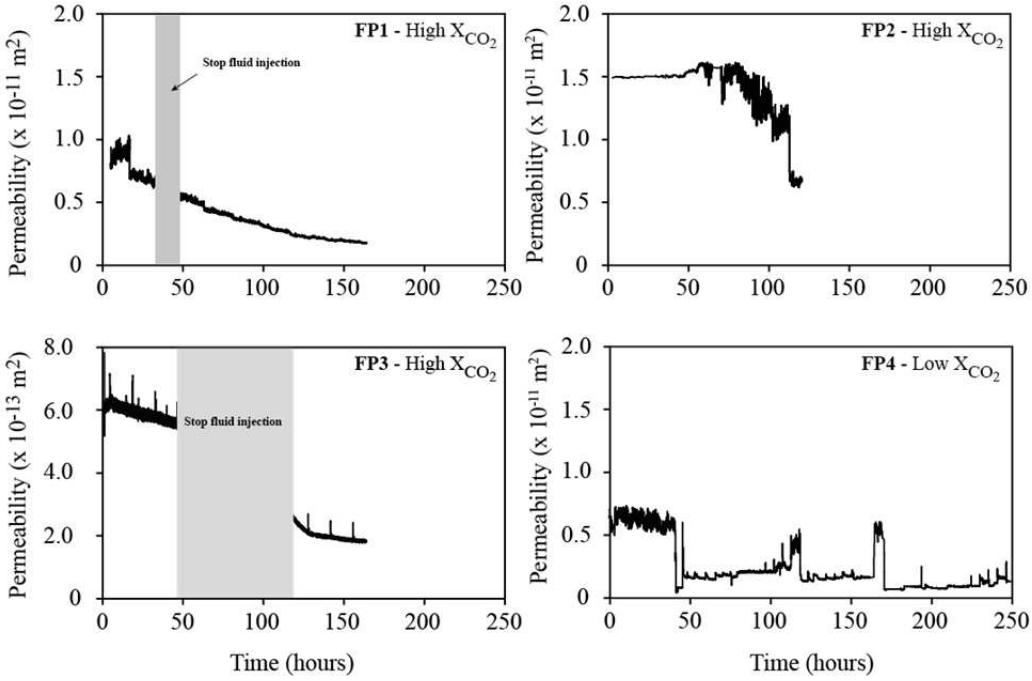

Fig.5.2. Monitoring the permeability changes during experiments FP1-HC, FP2-HC, FP3-HC and FP4-LC.

3.2 Micro-texture of the reacted samples

After the experiments, XR-tomography images reveal the development of a reacted zone along the fracture in all samples. The reacted zone is characterized by two reaction fronts with similar length on each side of the fracture (Fig.5.3). This is highlighted by a grey-dark colour near to the fracture compared to the grey colour far from the fracture. Mineral phases and pore spaces are represented by different grey-scale values, with darker colours being lower density (pores; pixel value=0) and lighter colours being higher density minerals (pixel value=255). Lizardite has a value of ~120, olivine and pyroxenes ~200 and spinel ~240 on the present images.

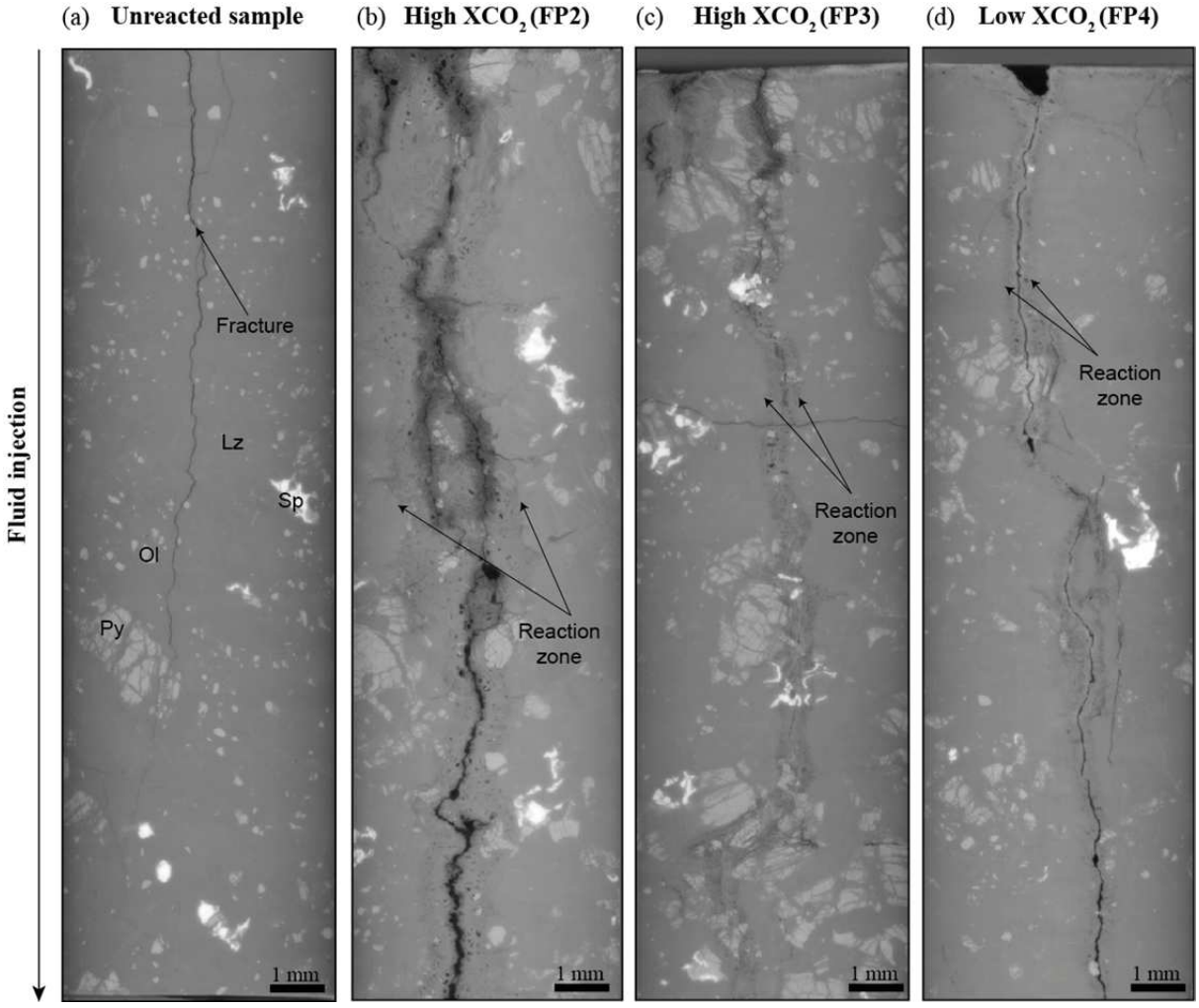

Fig.5.3. X-ray microtomography acquired with a resolution of 2.2 µm. (a) unreacted fractured sample used here to compare the images post-experiment. The unreacted sample contains lizardite (Lz) as major mineral and small grains of olivine (Ol), big grains of pyroxene (Py) and minor reflective

spinel. (b-d) Reacted samples run under low XCO_2 and high XCO_2 experiments. All samples show strong dissolution on the inlet compared to the outlet and the development of a dissolution front at both sides of the fracture with a colour slightly darker. (b) Experimental sample of experiment FP2 (High XCO_2) run during 134h. (c) Experimental sample of experiment FP3 (high XCO_2) run during 165h and low flow rate (Q). (d) Experimental sample of experiment FP4 (high XCO_2) run during 257h.

Figure 5.4 and Fig. 5.5 shows four sections of the XMT images from the inlet to the outlet acquired on samples of experiments FP2-HC and FP4-HC respectively. Grey values intensity profiles were performed on the images perpendicular to the fracture in order to identify changes on the porosity from the unreacted zones to the adjacent zones to the fracture. In experiment FP2-HC, the profiles show an increase on the grey value as approaching the fracture interpreted as evidence of strong dissolution. In experiment FP4-LC, the zone adjacent to the fracture shows lower degree of dissolution compared to the sample FP2-HC. However, a light band develops parallel and next to the fracture. The light band is only remarkable in the inlet compared to the outlet of the sample.

During the generation of the main fracture parallel to the core length, secondary fractures were generated associated to the main fracture. FP1-HC shows only one single fracture (*appendix C.* Fig C.2). FP2-HC shows a complex fracture network; a main fracture and associated parallel secondary fracture all along the core length (Fig.5.4 and *appendix C.* Fig.C.3). FP3-HC shows a single fracture along the whole core but the inlet of the core shows secondary fractures perpendicular to the main fracture (a*ppendix C.* Fig C.4 and 7). FP4-LC has a single fracture but as sample FP3-HC, the inlet of the core presents secondary fractures perpendicular to the main fracture (Fig.5.5 and *appendix C.* Fig.C.5 and Fig.C.8). The tomography images revealed that the associated fractures were in some cases pre-existing carbonate veins that dissolved during the injection of CO_2-solutions (Fig.5.5). But in other cases as in FP2-HC they were mechanically formed under pressure. XMT images show the dissolution fronts were produced also at both sides of the associated fractures (Fig.5.4 and Fig.5.5). This produces an apparent increase of the overall dissolved zone.

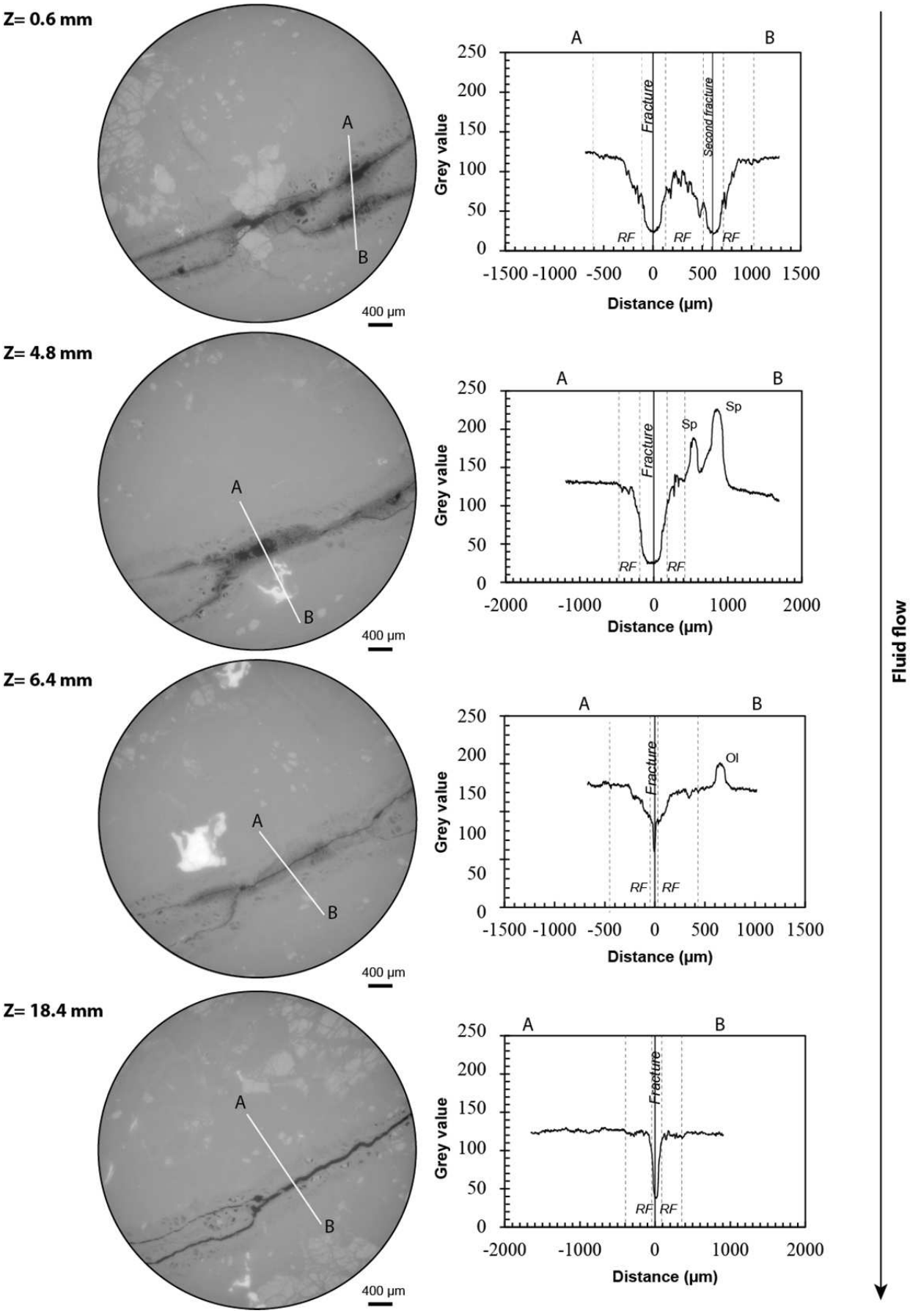

Fig.5.4. Grey value intensity profiles on sample FP2-HC (high CO_2-rich solutions and high Q).

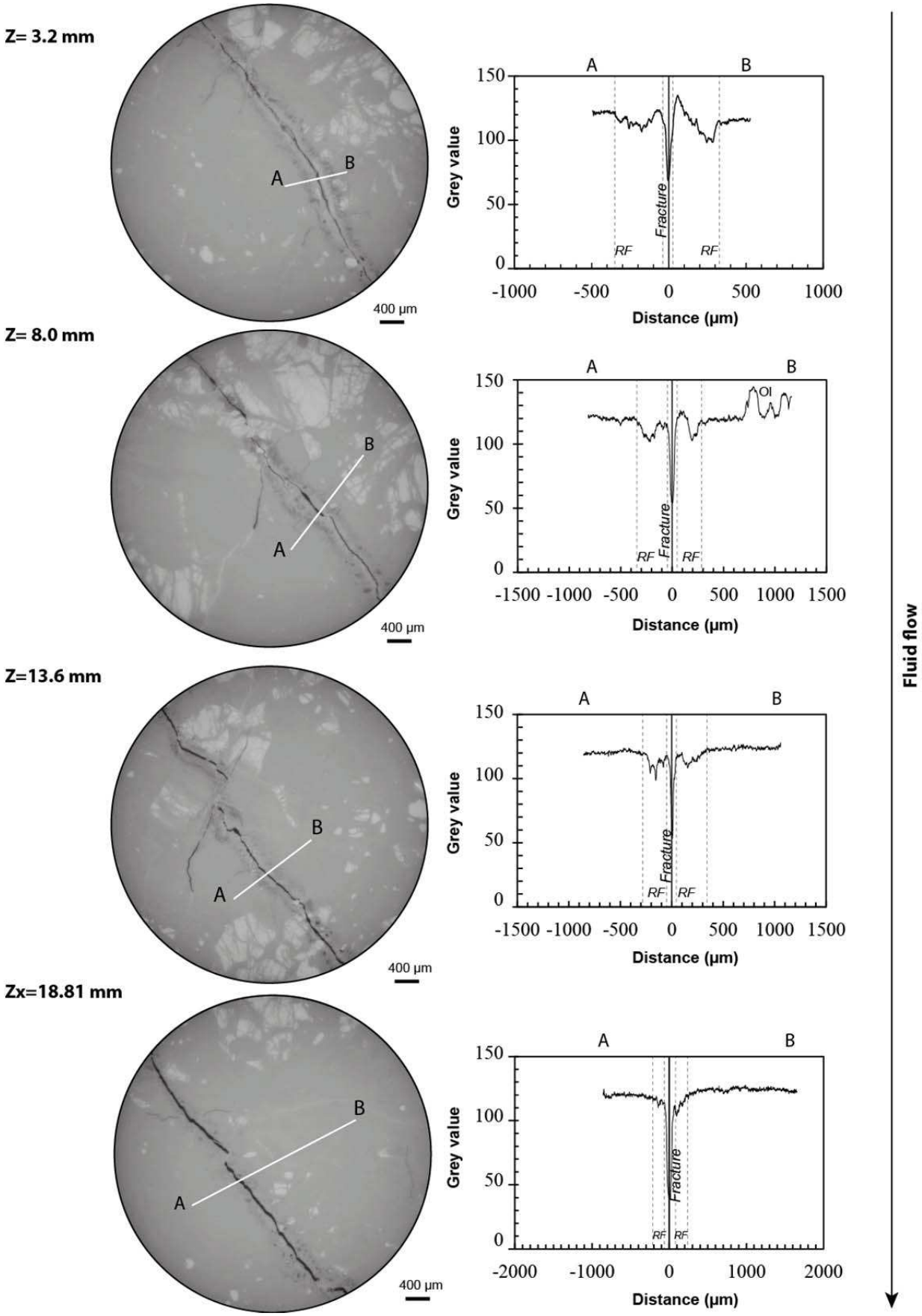

Fig.5.5. Grey value intensity profiles on sample FP4-LC (Low CO_2-rich solution and high Q).

Dissolution front length

The length of the dissolution front was measured after the X-ray microtomography images of experiments FP2-HC, FP3-HC and FP4-LC. The measurements were performed on X-ray 2D sections that correspond to the cut polished section A, B, C and D (*appendix C*. Fig.C.6-8). The measurements were performed on both reaction fronts (3 measurements on each front, a total of 6 measurements) and perpendicular to the fracture direction with a separation of 1.8 mm between each other. The results of the measurements are reported on *appendix C*. Table C.3. The dissolution front was thicker on the inlet (section A) of the samples and progressively becomes thinner towards the outlet (section D) of the samples (e.g., FP2-HC in section A, 640 ± 95 μm and section D, 520 ± 40 μm). Experiment run with the same XCO_2 (FP2-HC and FP3-HC) but at different flow rate, shows an overall dissolution front thicker for the experiment run at high *Q* (FP2-HC) compared to low *Q* (FP3-HC). Therefore, experiments run with the same *Q* but different XCO_2 (FP2-HC and FP4-LC), shows an overall dissolution front thicker for the experiment run with XCO_2 (FP2-HC) compared to low XCO_2 (FP4-LC).

The fracture aperture and the dissolved front were measured after the experiments in the X-ray images at different depth than polished sections to get more extended information. The measurements were performed on the X-ray images of experiments FP2-HC (Fig.5.4), FP3-HC (*appendix C*. Fig.C.9) and FP4-LC (Fig.5.5). The measurements were performed on both reaction fronts (5 measurements on each front, a total of 10 measurements) and perpendicular to the fracture direction with a separation of 0.5 mm between each other. The results of the measurements are reported on *appendix C*. Table C.5. FP2-HC shows a final fracture aperture of 19 ± 5.6 μm at Z=0.6 mm and 56 ± 12.6 μm at Z=18.4 mm. FP3-HC shows a final fracture aperture of 7.2 ± 1.6 μm at Z= 3 mm and 7.0 ± 1.0 μm at 18.3 mm. FP4-LC shows a final fracture aperture of 11.9 ± 2.2 μm at Z= 3.2 mm and 38.5 ± 7.5 μm at Z=18.8 mm.

Dissolution front textural characteristics

Textural changes occur on the reacted zone in all the samples (Fig.5.6). The pristine minerals (e.g., olivine) show dissolution along the grain boundaries (Fig.5.6a-e). Voids were

generated which indicates completely dissolution of the pristine minerals (Fig.5.6a-e). The dissolved grains show saw-toothed textures (Fig.5.6e and *appendix C*. Fig.C.11a). Adjacent zones to the fracture were strongly dissolved when the concentration of CO_2 in solution was high. They were characterized by preferential dissolution of olivine and pyroxene (Fig.5.6a). Lizardite was the most resistant mineral but shows incipient dissolution (Fig.5.6a,c). Dissolution takes place between grain boundaries (Fig.5.6c). Numerous dissolution patterns penetrate the original olivine and pyroxene grains resulting in saw-toothed appearance (Fig.5.6.e).

The lowest degree of dissolution are recorded in zones further to the fracture for samples reacted with high XCO_2 and in the entire reaction front for the samples reacted with low XCO_2 (Fig.5.6a and Fig.5.6b). Dissolution surfaces around the grain boundary of olivine and pyroxenes and lizardite were slightly dissolved (Fig.5.6d). Polygonal cracks patterns appear on a white precipitated that covers the inlet of the reacted sample FP4-LC (Fig.5.6f). The cracks are slightly filled by a laminar mineral that was not possible to identify by SEM-EDS analysis due to the small size.

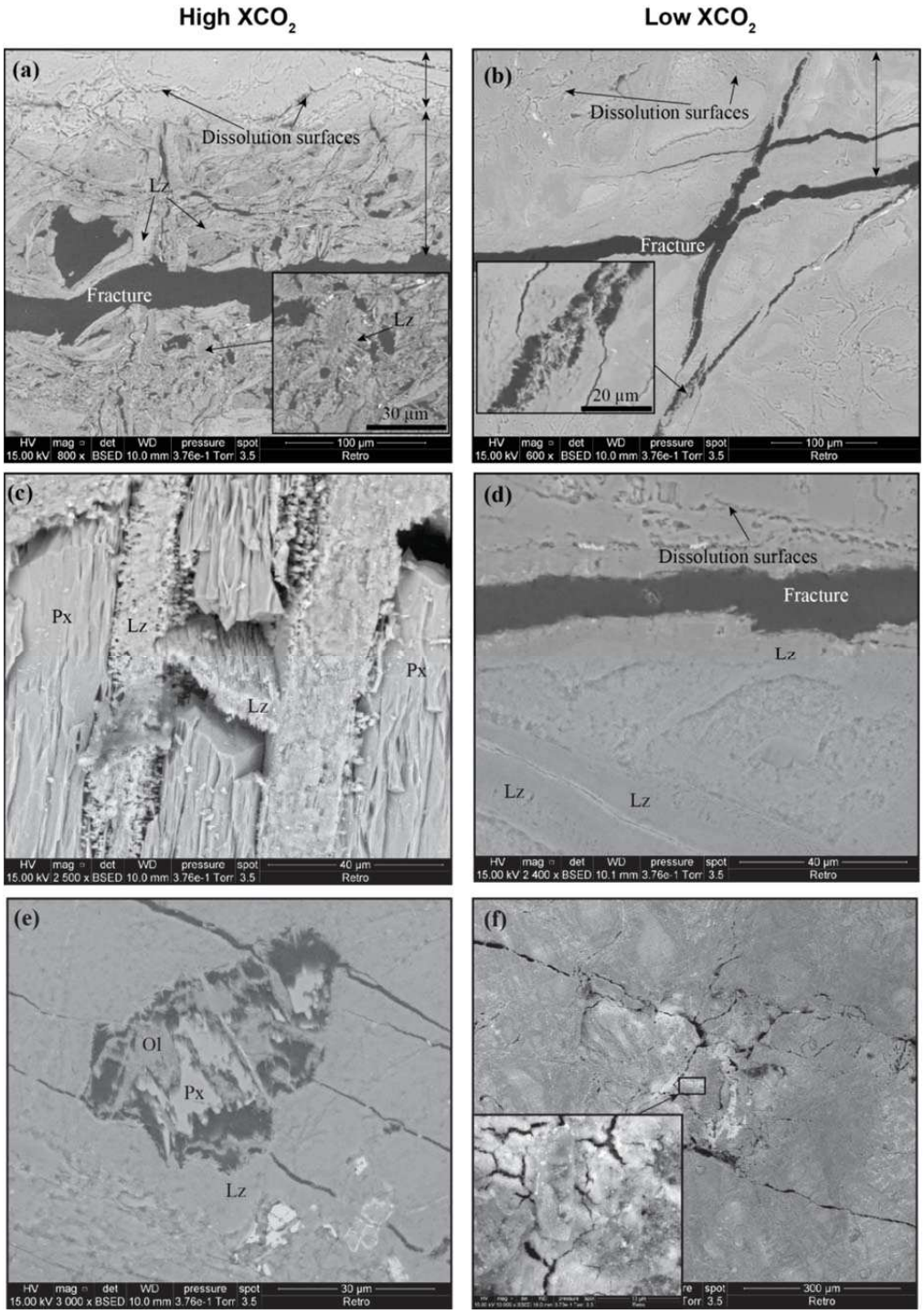

Fig.5.6. SEM images reveals textural changes of the reaction samples for (a) high XCO_2 experiments; samples FP2-HC (section B) and (b) low XCO_2 experiments; sample FP4-HC (section B). (c) Inlet surface of the reacted sample FP2 show dissolved pyroxene grains surrounded by a low altered lizardite mesh. (d) Sample FP2-HC (section B) shows the development of dissolution surfaces around the grains boundaries and low degree of alteration of lizardite. (e) Dissolved olivine and pyroxene grain on sample FP2-HC (section B). (f) Polygonal cracks patterns developed in the surface of a precipitate in the inlet of the sample FP4-HC (section B).

Fracture volume

Estimating the volume of the fracture in the entire sample was complicated because: (1) the fracture grey values were not always the same at all depth in the core (Fig 5.4 and Fig 5.5) and (2) the zone of high degree of dissolution in the reaction front has pixel grey values sometimes similar to the pixel grey values of the fracture. Therefore applying the same threshold on the entire core to segment the fracture induces an overestimation and sub estimation of the fracture volume. Thus, a first estimation of the fracture volume was performed in the first 2.5 mm from the inlet of the sample. The volume segmented analysed was 62 mm^3 which represents a ~13% of the total volume scanned (Table 5.3).

The fracture volume was estimated on samples with a fracture aperture larger than the pixel resolution (2.2 μm); FP2-HC and FP4-LC. Sample FP2-HC shows a fracture volume at the inlet of the sample of 0.9 mm^3 compared to 0.5 mm^3 on sample FP4-LC for a sample length of 2.5 mm from the inlet of the sample and core diameter of 5.6 mm. This is related to the larger fracture aperture on sample FP2-HC than FP4-LC (Table 5.2). However, it should be interesting to estimate the fracture volume in the entire sample and further work testing different algorithm of segmentation should be done.

Table 5.3. Fracture volume estimated on samples FP2-HC and FP4-LC. The total sample volume represents the volume of (*d*=9 mm x *L*=20 mm) and the total sample scanned volume represents the volume scanned at the ESRF of (*d*=5.6 mm x *L*=20 mm). The fracture volume at the inlet represents a volume of (*d*=5.6 mm x *L*= 2.5 mm).

	Total sample volume	Total sample scanned volume	Section selected (inlet) volume	Fracture volume (inlet)
Experiment	mm^3	mm^3	mm^3	mm^3
FP2-HC	1252.00	494.57	61.96	0.89
FP4-LC	1230.19	485.95	61.25	0.45

3.3 Colour changes on the reacted samples

After the experiments, all the reacted samples show a reddish colour on both sides of the core (inlet and outlet) compared to the characteristic green of the initial samples (Fig.5.7). The inlet shows strong red colour compared to the lighter-red at the outlet. Small voids where found on the inlet of the samples, indicating dissolved minerals. The voids were more abundant on samples reacted with high CO_2-rich solutions compared to low CO_2-rich solutions.

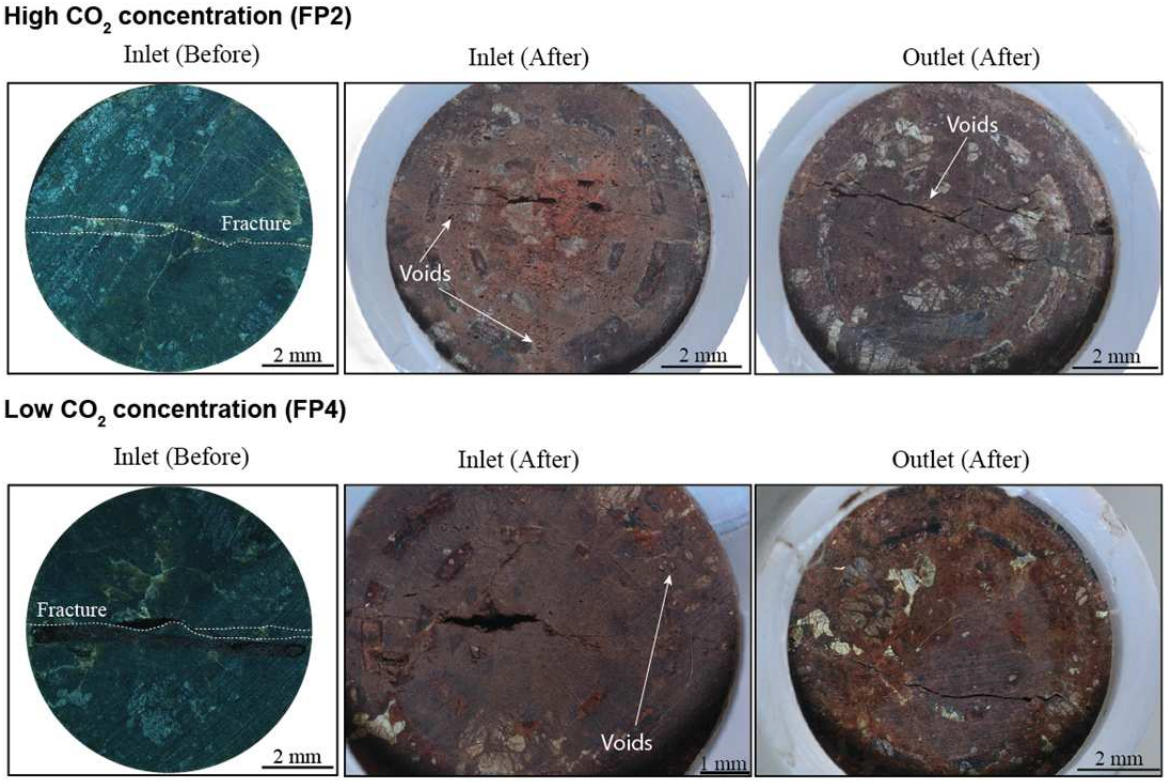

Fig.5.7. Reacted samples FP2 (High $XCO_2(g)$) and FP4 (Low $XCO_2(g)$).

The polished sections (A to D) of all the reacted samples exposed a coloured zone at both sides of the fracture. The colour in this zone changes from the characteristic green of the initial peridotite to a reddish-brownish colour (Fig.5.7). Three consecutive zones were distinguished on the coloured reacted zone during observation of the reacted samples with binocular lens (Fig.5.8). They have difference on the red colour intensity. In the following, zone 1, zone 2 and zone 3 define the three reacted zones, where zone 3 is adjacent to the fracture and zone 1 is adjacent to the unreacted zone named zone 0. The reacted zone 2 is located between the reacted zone 1 and 3. The zone 1 and 2 appears on high and low CO_2-

rich solutions. However, the zone 3 only appears when the concentration of CO_2 in solution was high. The ***zone 1*** is characterized by a light brown colour and is the biggest one which is presented along the whole core sample on the reacted samples. The ***zone 2*** is characterized by a reddish dark colour and is the thinnest one which disappears as approaches the outlet of the sample on section D. The ***zone 3*** is characterized by a light pink colour.

High CO_2(g) concentration (FP2)

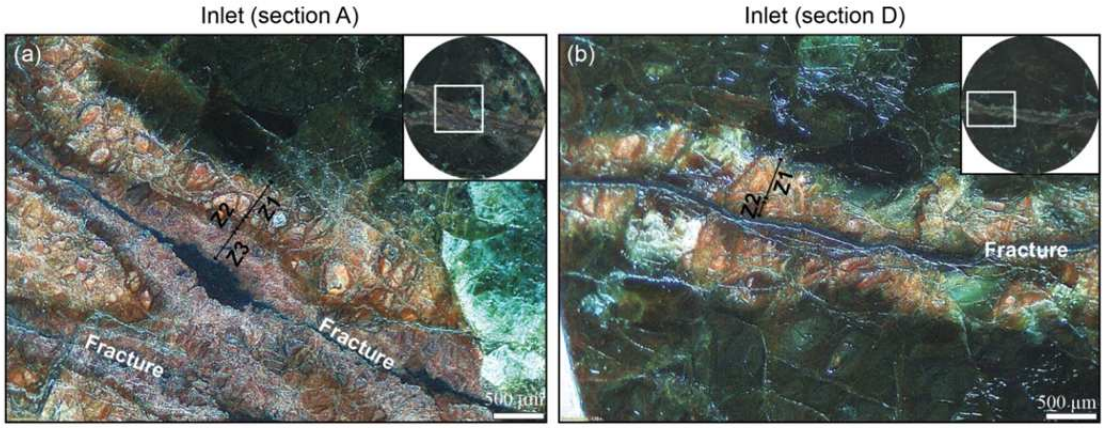

High CO_2(g) concentration (FP3)

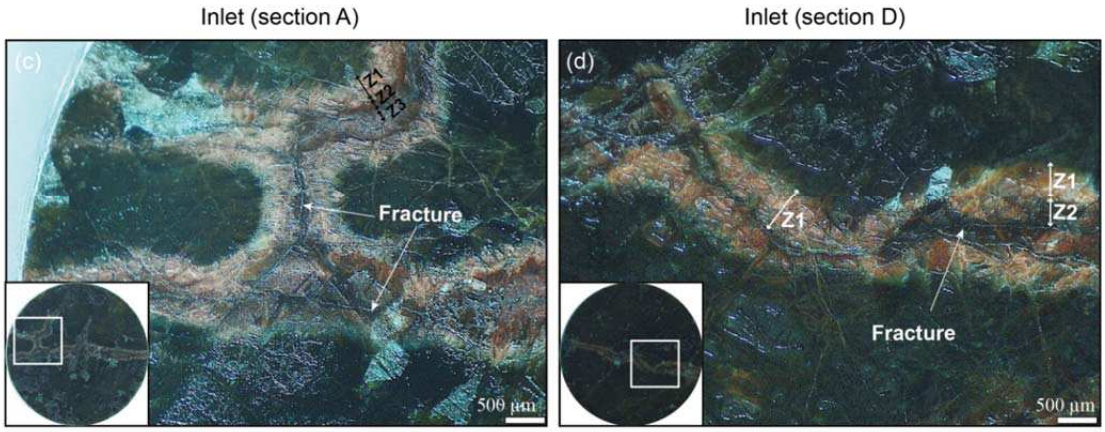

Low CO_2(g) concentration (FP4)

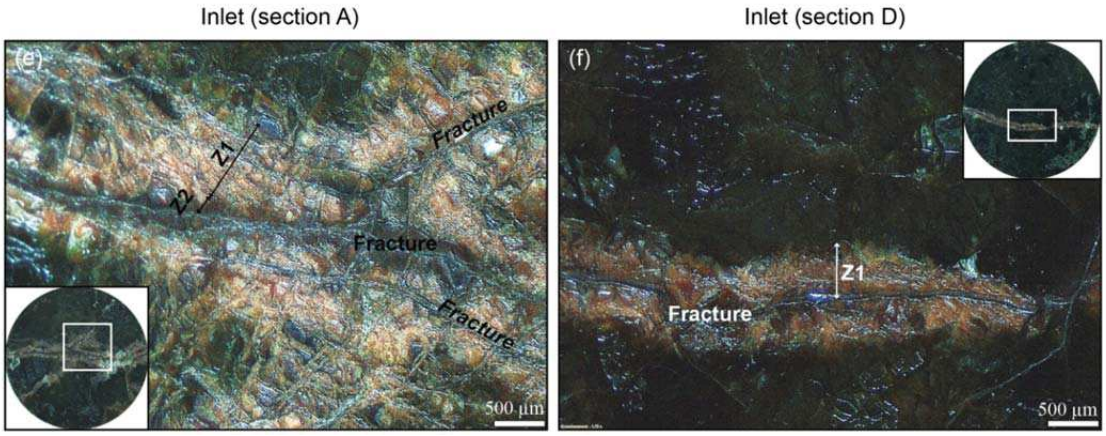

Fig.5.8. Discoloration of the peridotite matrix in the zone adjacent to the fracture (reaction zone). Z1 denotes to zone 1, Z2 to zone 2 and Z3 to zone 3. (a) Inlet of the sample FP2-HC shows the development of a 3 coloured zones on the reaction zone. (b) Outlet of the sample FP2-HC shows the development of the zone 1 and 2. (c) Inlet of the sample FP3-HC shows the development of a 3 coloured zones on the reaction zone. (d) Outlet of the sample FP2-HC shows the development of the zone 1 and 2. (e) Inlet of the sample FP4-LC shows the development of zone 1 and 2. (f) Outlet of the sample FP4-LC shows the development of the zone 1.

The length of the coloured reaction front was measured regarding to the fracture in the four polished sections (A to D). The length represents the distance of the distal boundary of each colour zone from the fracture. Thus, three types of length measurements were performed. X1 corresponds to the entire reaction front, X2 corresponds to the distal boundary of the zone 2 and X3 corresponds to the distal boundary of the zone 3 (Fig.5.9). Each measurement was performed on both reaction fronts (3 measurements on each front) and perpendicular to the fracture direction with a separation of ~2.6 mm each other (see table C.5 *appendix C*). Sample FP2-HC and FP3-HC have several fracture branches (*appendix C*. Fig.C.3 and Fig.C.4). When the fracture exhibits several branches, the measurements (n=6, i.e. 3 measurements on both side) was performed on reaction fronts along the branches that are not superimposed with another reaction front from another branch.

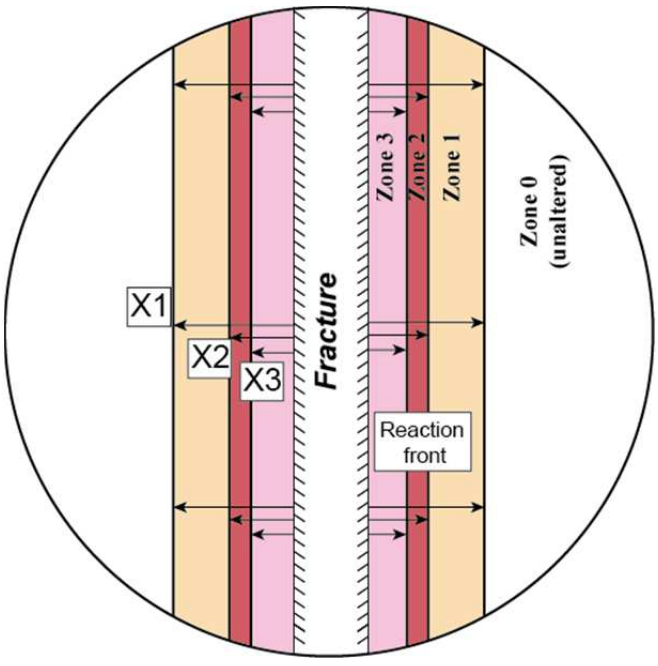

Fig.5.9. Illustration of the methodology followed to measure the length of the coloured zones. The circle represents the polish section with a diameter of ~9 mm.

All reacted samples show the coloured reaction front is thicker on the inlet and progressively thinner towards the outlet. Reacted samples with high CO2 concentration (FP1-HC and FP2-HC) show the largest reaction front (X1) compared to sample FP4-LC reacted with low XCO_2 in solution. However sample FP3-HC, run at low Q and with a long period (53 h) of no fluid injection, shows the smallest reaction front compared to the other experiments (*appendix C*. Table C.5).

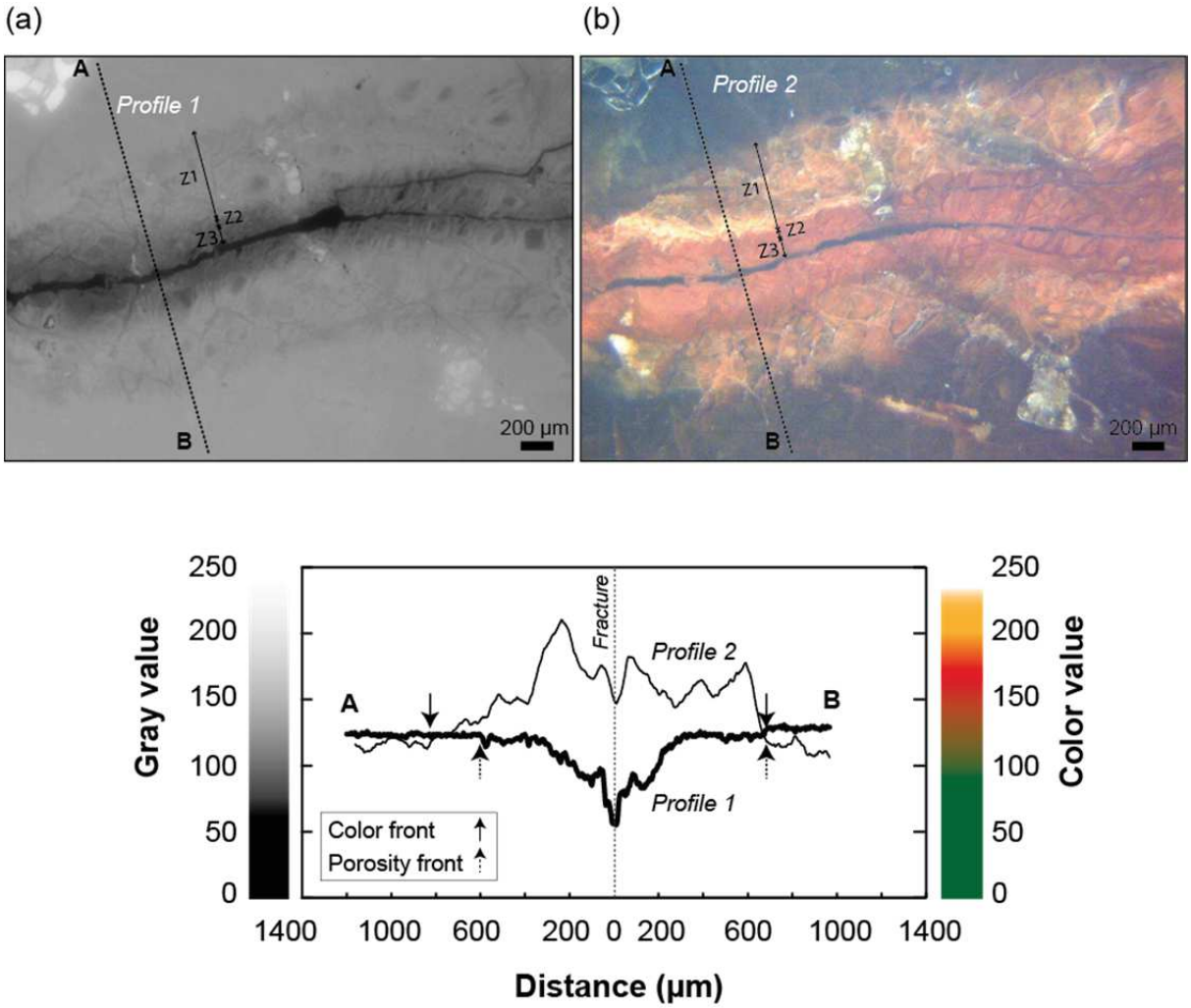

Fig.5.10. Superposition of the coloured reacted zone and the dissolution zone. Z1 denotes to zone 1, Z2 to zone 2 and Z3 to zone 3. (a) XMT image of the sample FP2-HC. The image shows the dissolution of the reacted zone. (b) Binocular lens image of the reacted zone of the sample FP2-HC. The superposition of the intensity profile 1 (dissolution zone) and the intensity profile 2 (coloured zone) reveals that both reacted zones have similar length and chemical and dissolution processes are related each other.

The dissolution and coloured reacted zones have almost similar length. Thus, each coloured zone corresponds to a different degree of dissolution. The *zone 1* is characterized by a light reddish colour and has a lower degree of dissolution compared to the adjacent zones to the fracture (*zone 2 and 3*) which have an intense reddish colour and high degree of dissolution. This suggests that the length of dissolution and the coloration (chemical process) are related each other (Fig.5.10).

3.4 Mineralogy and chemical characterization of the reacted zones

3.4.1 Mineralogy

At the end of the four experiments, the reacted samples highlight a coloured zone at both sides of the fracture, suggesting that changes in the mineralogy of the samples took place. The secondary minerals precipitated on the samples were carbonates, Ni-oxides, hematite and amorphous silica (Table 5.4). The mineralogy varies for each coloured zone in the samples.

Carbonates

Secondary carbonates were revealed by cathodoluminescence imaging. However, primary carbonates were also already present in the starting serpentinized peridotite (Fig.5.11a). For high XCO_2 experiments (FP1-HC), the reacted samples show the presence of strong density of carbonates (Fig.5.11b-c). Carbonates were preferentially concentrated further from the fracture (zone 1) around grain boundaries and following the lizardite mesh. The outlet of the sample present more carbonates rather than the inlet (Fig.5.11c). Surprisingly, reacted rock from low XCO_2 experiment (FP4-LC) reveals the development of the zone 1, but only with minor carbonates inside (Fig.5.11d).

Table 5.4. Mineralogy of unreacted sample (OL15) and each reacted zone for each polished section (A to D) of the reacted samples. The minerals were identified with Raman, SEM-EDS, Cathodoluminiscense or EPMA. The reacted sample FP3-HC and section C for all samples was not analysed.

	Unreacted	High XCO_2						Low XCO_2	
		High Q						High Q	
Sample:	**OL15**	**FP1-HC**			**FP2-HC**			**FP4-LC**	
	Zone 0	**Zone 1**	**Zone 2**	**Zone 3**	**Zone 1**	**Zone 2**	**Zone 3**	**Zone 1**	**Zone 2**
Section A									
Raman		Magnesite	Magnesite	Magnesite					
SEM-EDS		(Fe-Ni)-oxide (Fe) - Magnesite Amorphous silica	(Fe-Ni)-Magnesite	(Fe-Ni) Magnesite Calcite Amorphous silica					
Cathodo.		Carbonates			Carbonates			Carbonates	
EPMA	Olivine Orthopyroxene Clinopyroxene Serpentine Calcite Magnetite Spinel								
Section B									
Raman					Hematite	Hematite Ni-oxide	Hematite	Hematite	Hematite
SEM-EDS								Magnesite (Ca-Mg) carbonate	Ni-oxide
Cathodo.									
EPMA						Ni-lizardite	Ni-lizardite		Ni-lizardite
Section C									
(-)									
Section D									
Raman									
SEM-EDS									
Cathodo.		Carbonates			Carbonates			Carbonates	
EPMA									

i) Magnesite

Magnesite was present on all the reacted zones on high XCO_2 experiments. However, magnesite crystals exhibit differences on the chemical composition in relation to the position with respect to the fracture (Fig.5.12). The ***zone 1*** reveals the presence of Fe-rich magnesite precipitation on the rims of the partially dissolved olivine (Fig.5.12a). The ***zone 2*** is characterized by the precipitation of (Fe-Ni)-rich magnesite on the rims of the void resulting from the dissolution of an olivine and following the boundary of the core (Fig.5.12b). The ***zone 3***, next to the fracture, shows the presence of (Fe-Ni)-rich magnesite on the rims of the voids and filling the boundary between two grains of lizardite (Fig.5.12c).

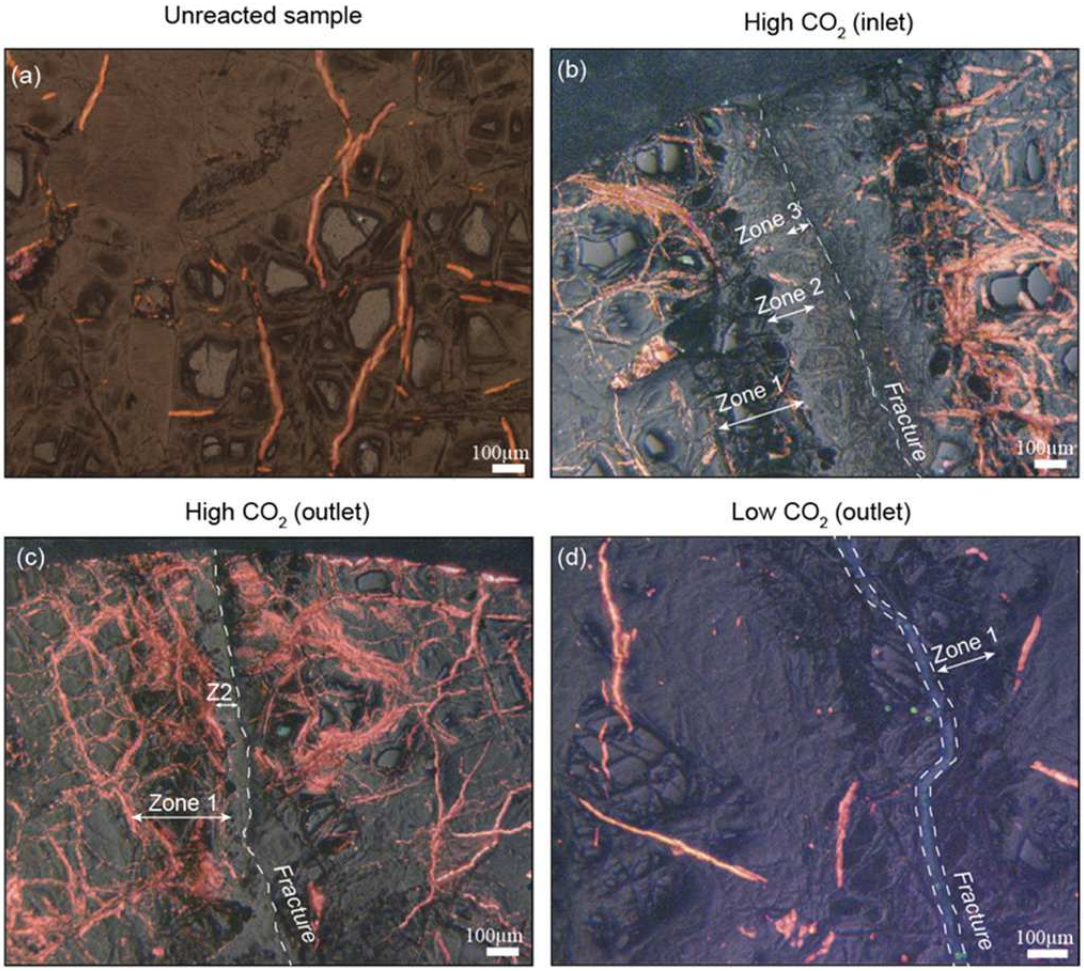

Fig.5.11. Cathodoluminescense analyses were acquired on unreacted and reacted samples. (a) Thin section of unreacted sample. (b) Inlet of the sample FP2-HC (section A) reacted under high XCO_2 and high Q (c) Outlet of the sample FP2-HC (section D) reacted under high XCO_2 and high Q. (d) Outlet of the sample FP4-LC (section D) reacted under low XCO_2 and high Q.

ii) Calcite

Calcite was also present following the rims of the dissolved olivine in high XCO_2 experiments in the zone 3 (Fig.5.12c). Dissolved grains of olivine were typically surrounded by continuous replacement rims composed by Ca-rich phases (see *appendix C*. Fig.C.10b). Hence, it appears that the replacement of olivine by magnesite was much more extensive than the replacement by calcite in high XCO_2 experiments.

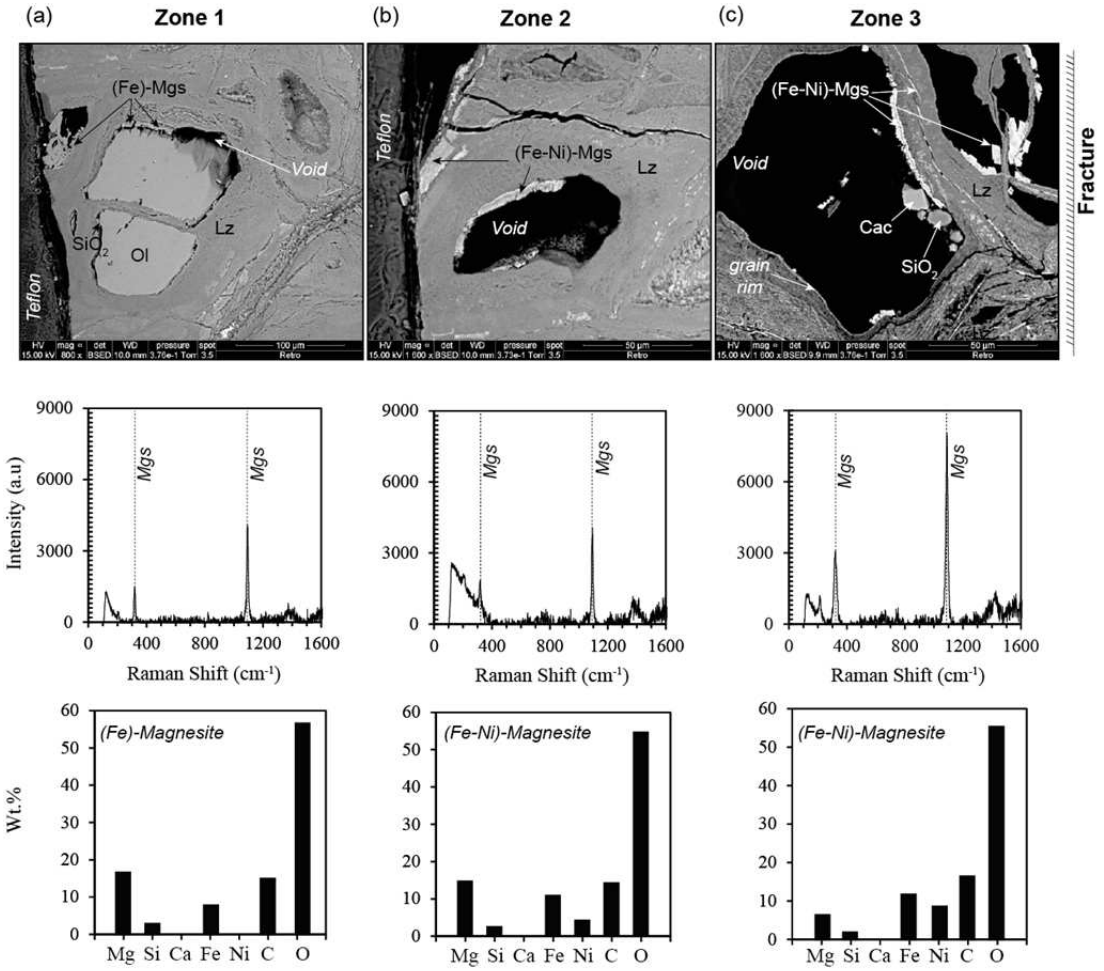

Fig.5.12. Mineralogy of the reacted zones of sample FP1 (section A) (high XCO_2).Mgs denotes magnesite, Cac denotes calcite and SiO_2 amorphous silica. (a) Zone 1 shows the precipitation of Fe-rich magnesite confirmed by Raman spectra and SEM-EDS and the presence of amorphous silica (see EDS spectrum values 47 and 51 in appendix C. Table C.8) (b) Zone 2 shows the precipitation of (Fe-Ni)-rich magnesite on the rims of the relict dissolved olivine. Raman spectra confirm the precipitation of magnesite and SEM-EDS analysis the presence of Ni and Fe in their structure (see EDS spectrum values 52,53 in appendix C. Table C.8) (c) Zone 3 shows the precipitation of calcite with minor Fe and Mg, (Fe-Ni)-rich magnesite (mgs) and amorphous silica on the rims of the dissolved olivine. Raman spectra confirm the precipitation of magnesite and SEM-EDS analysis the presence of Fe and Ni on the structure (see EDS spectrum values 23, 24, 22, 25 in appendix C. Table C.8).

iii) Dolomite

(Ca-Mg)-carbonates and (Mg)-carbonates were present during low XCO_2 experiments (Fig.5.13b). We interpret that (Ca-Mg) carbonate could be dolomite based on the EDS analysis (see *appendix C*. Table C.8). They were present on the ***zone 1*** and they present

minor content of nickel and iron in their chemical composition. The ***zone 2***, adjacent to the fracture is characterized by a strong presence of nickel oxides and absence of carbonates (Fig.5.13c).

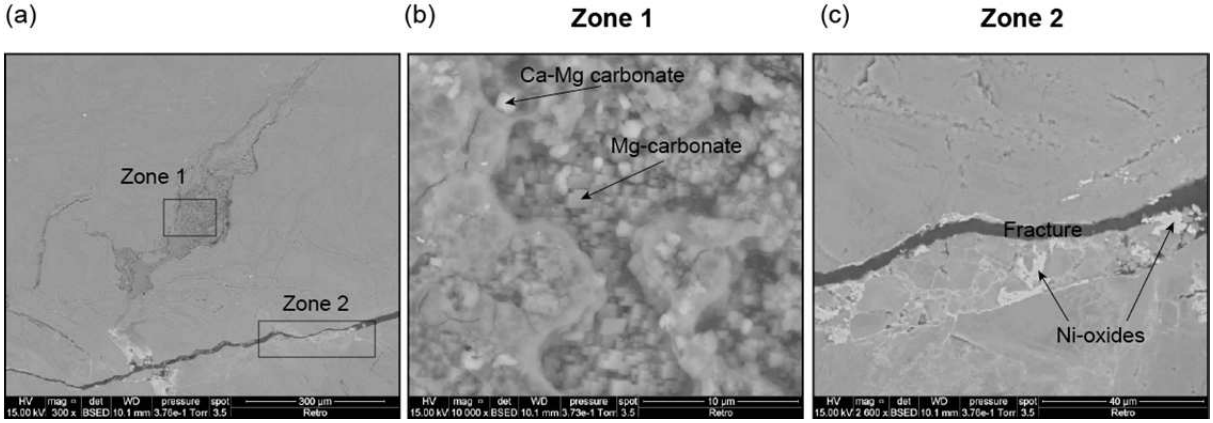

Fig.5.13. Mineralogy of the reacted zones in sample FP4 (section B) (low XCO_2). (a) Overall SEM image of the zone 1 and 2. (b) The zone 1 is characterized by the presence of (Ca-Mg)-carbonate and Mg-carbonate, both with minor presence of Nickel (see EDS spectra 18 and 16, respectively on appendix C. Table C.8) and (c) the zone 2 is characterized by the presence of Ni-oxides (see spectra 15 on appendix C. Table C.8).

Oxides

The zone 2 and 3, adjacent to the fracture, were characterized by strong presence of shinny phases with sizes less than < 1µm (Fig.5.14). SEM-EDS confirm the presence of Fe-oxides (Fig.5.14). However, minor presence of Fe-oxides were noticed on the zone 1 compared to zones 2 and 3 adjacent to the fracture.

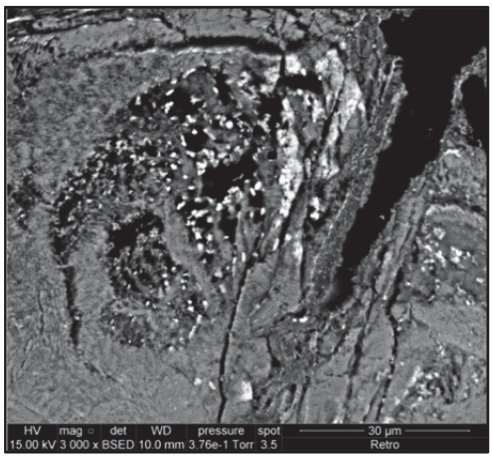

Fig.5.14. SEM-EDS image of the reacted zone 3 of sample FP1-HC (section A) (High XCO_2). The white spots indicate the presence of Fe-oxides and the dark colour the voids generated by dissolution (EDS spectrum values 87 on appendix C. Table.C.8).

Hematite (Fe_2O_3) and magnetite (Fe_3O_4) were present covering the lizardite surface on all the experiments (Fig.5.15). This suggests that the reddish colour of the reacted zones could be related to the presence of these oxides. However, different intensity was observed on the magnetite and hematite Raman spectra between the zones. The most characteristic feature of the hematite spectrum is the scattering peak at 1320 cm^{-1} and at 667 cm^{-1} for magnetite (de Faria et al., 1997).

The ***zone 1***, the furthest form the fracture, reveals the presence of magnetite and hematite on the surface of lizardite of samples FP2-HC (section B) and FP4-LC (section B). Similar intensity was encountered on the spectra of both minerals. Both samples show the preservation of two peaks of lizardite at 384 cm^{-1} and 230 cm^{-1}. In the ***zone 2*** the reacted sample FP4-LC (section B) shows the presence of magnetite and hematite but magnetite shows strong intensity compared to hematite, 5989 and 2394 (a.u) respectively. Two peaks of lizardite were preserved at 384 cm^{-1} and 230 cm^{-1}. The sample FP2-HC (section B) shows a peak at 1061 cm^{-1} suggesting the possible presence of NiO which has a peak at 1090 cm^{-1} (Zhou et al., 2014).The ***zone 3*** was only present on sample FP2-HC (section B). This zone is adjacent to the fracture and the most affected by dissolution. Hematite and magnetite shows similar intensity peaks, 8075 and 8365 (a.u.) respectively. Only one peak of the pristine lizardite at 230 cm^{-1} was preserved.

Amorphous silica

Amorphous silica was associated to the magnesite in the rims of the partially dissolved olivine in the zone 1 and 3 of the experiments run with high XCO_2 (Fig.4.12a and c). The zone 3 is strongly altered and most of the grains were completely dissolved but they preserve their initial shape. In most cases they were defined by continuous light thin rims probably amorphous silica as was already identified on similar carbonation experiments (e.g., Hövelmann et al (2012)) (see *appendix C*. Fig.C.10d).

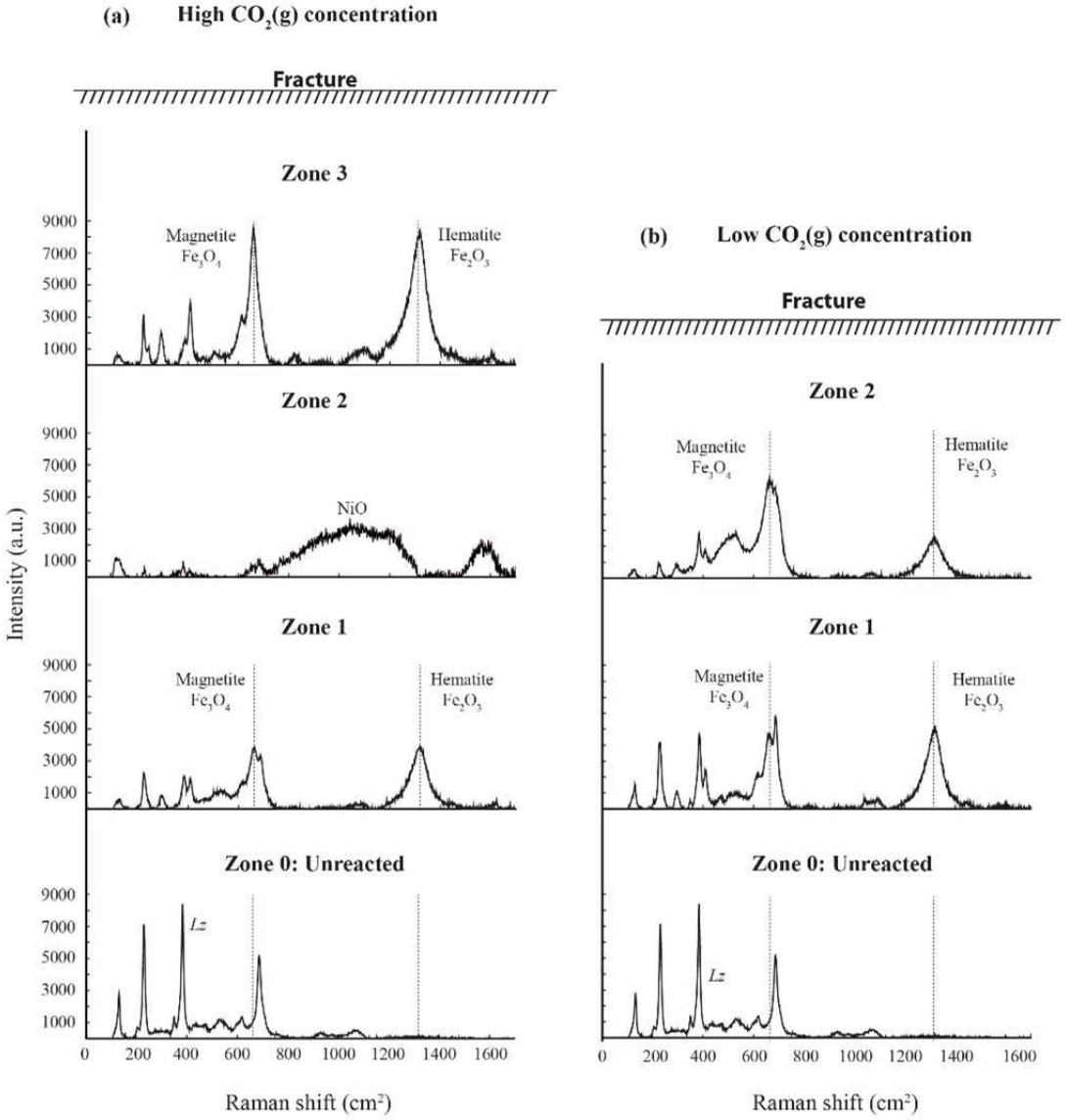

Fig.5.15. Raman spectra acquired on the lizardite surface of the unreacted zone and reacted zones (1 to 3) for FP2-HC, section B and FP4-LC, section B samples. The surface of lizardite was covered by hematite and magnesite oxides.

3.4.2 Majors elements distribution in the lizardite

Chemical microprobe profiles (EPMA) were performed on the lizardite from the unreacted zone to the fracture (Fig.5.16). No major changes were encountered on the concentration of SiO_2 and MgO on the three zones of the reaction front. However, FeO, NiO and MnO show distinct behaviour. FeO concentration was strongly variable on the three zones on high XCO_2 experiments. FeO variates from 8 wt.% on the unreacted zone to 4.67 – 8.67 wt.% on the zone 1, 5.95 – 10.09 wt.% on the zone 2 and 5.26 – 10.27 wt.% on the zone 3. Low XCO_2 experiments shows a depletion trend from 9.03 wt.% on the unreacted zone to 5.65 wt.% on the zone 1 and an small enrichment of 7.72 wt.% on the zone 2. NiO was strongly enriched on the reacted samples for both set of experiments. This result suggests the precipitation of serpentine enriched in nickel. The zone 2 was specially enriched from 0.26 wt.% on the unreacted zone to 2.55 wt.% and 4.71 wt.% for high XCO_2 and low XCO_2 respectively. Further, MnO was systematically depleted on the lizardite as approaching the fracture. The zone 3 was specially depleted under high XCO_2-rich solutions.

3.4.3 Ni as tracer of the fluid-rock reaction

High XCO_2 experiments show the precipitation of (Ni-Fe) magnesite and enrichment of Ni in the lizardite (Fig. 5.12 and Fig.5.16). The main source of nickel in these experiments comes from the injected solution. The presence of CO_2 in the fluid at the 1 M and 0.1 M produces the corrosion of the reactor pipelines which enriches the injected solutions in strong concentrations of nickel (~30 mg/L) (Fig.5.17). The nickel is trapped in zones adjacent to the fracture (i.e., zone 2 and 3) and absence in zones further to the fracture (i.e., zone 1). This suggests that the mobilization of Mg and Fe is faster than the mobilization of Ni, suggesting that the nickel is trapped in the zones of strong dissolution. However, experiments with low XCO_2 in solution presents absence of Ni-rich carbonates and only precipitation of Ni-oxides and strong enrichment of Ni in the lizardite in the zones adjacent to the fracture.

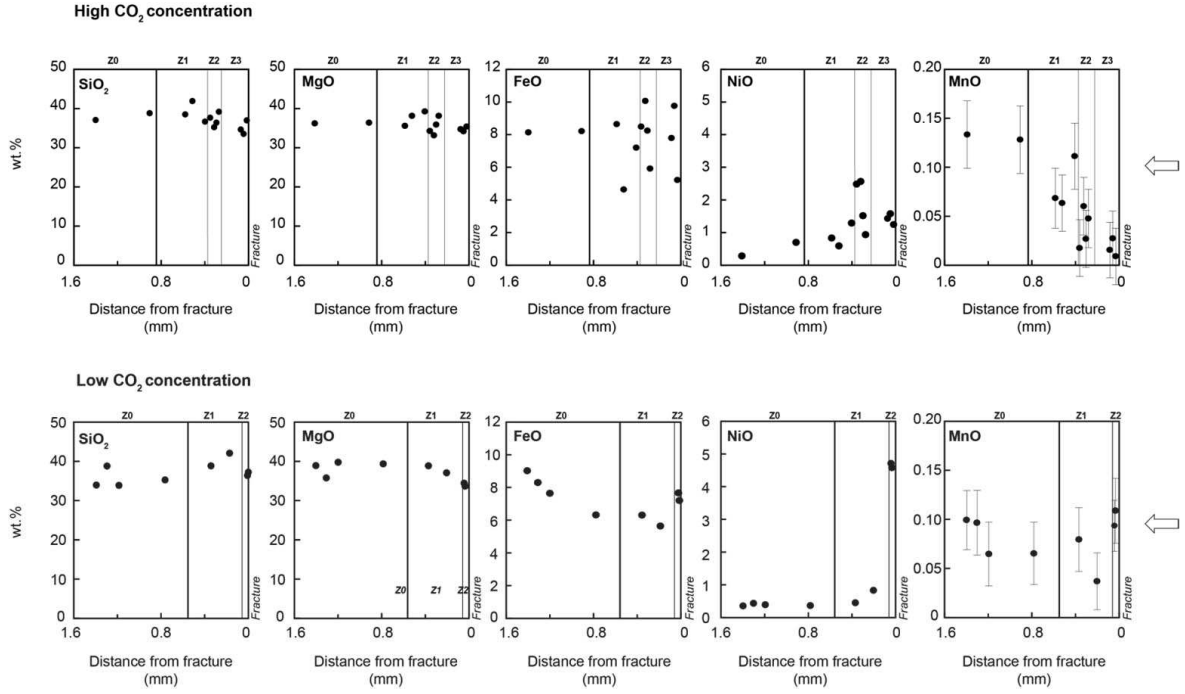

Fig.5.16. Chemical microprobe analysis of lizardite of samples FP2-HC (section B) and FP4-LC (section B) (see appendix C. Table C.11 and Table C.13 for chemical analysis data.

3.5 Chemistry of the aqueous solutions

The composition of the reacted fluid is different compared to the initial fluid (e.g. DIC, pH, cation and anion content).

Total dissolved inorganic carbon (DIC) decreased steadily from the beginning of the experiments suggesting carbon trapping probably occurred (Fig.5.17). Experiments at high XCO_2 shows a decrease on the initial DIC from 1800 mg/L to 1302 mg/L (FP1-HC), 1271 mg/L (FP2-HC) and 1468 mg/L (FP3-HC). Low XCO_2 experiment (FP4-LC) records a decrease from 900 mg/L to 682 mg/L, slightly lower than experiments at high XCO_2.

The pH of the outlet fluids remained roughly constant during the experiments after a strong increase on the fluids during incipient hours (Fig.5.13). High XCO_2 experiments reach a constant value after 50h (FP1-HC), 30h (FP2-HC) and 17h (FP3-HC) and low XCO_2 after 30h (FP4-LC). High XCO_2 experiments show an increase from 3.3 to 4.8 for FP1-HC, 4.9 for FP2-HC and 4.8 for FP3-HC. The FP3-HC shows a slightly decrease on the pH to a value of 4.14 during the period of no fluid injection. Low XCO_2 experiment (FP4-LC) shows an increase from 3.8 to 5.2 slightly higher than high XCO_2 experiments. The increase of pH is attributed to silicate precipitation (Gislason and Oelkers, 2003). This suggests that dissolution of silicates was occuring throughout the experiments

The outlet fluids were systematically enriched in Si, Mg, Fe and Ca compared to the injected NaCl solution indicating dissolution of the primary rock minerals (olivine and pyroxenes) (Fig.5.17). The chemistry of the outlet fluids remained roughly constant during the experiments after a strong increase on the fluids during early hours. Reacted fluids from high XCO_2 experiments (FP1-HC, FP2-HC and FP3-HC) shows higher enrichment of Si, Mg, Fe and Ca compared to the one from low XCO_2 (FP4-LC). The three replicates (FP1-HC, FP2-HC and FP3-HC) show variable chemical concentration among each other. This could be related to differences on the mineral proportions in the core samples. However, is important to remark that experiment FP3-HC shows a flow rate (Q) relatively low compared to the other experiments and also period of no flow injection between 51 to 90 h. During this time interval the fluid records an increase on the concentration of Fe and Ca but a decrease on the Si and Mg concentration (see *appendix C*. Table C.16-23 for fluid chemistry analysis).

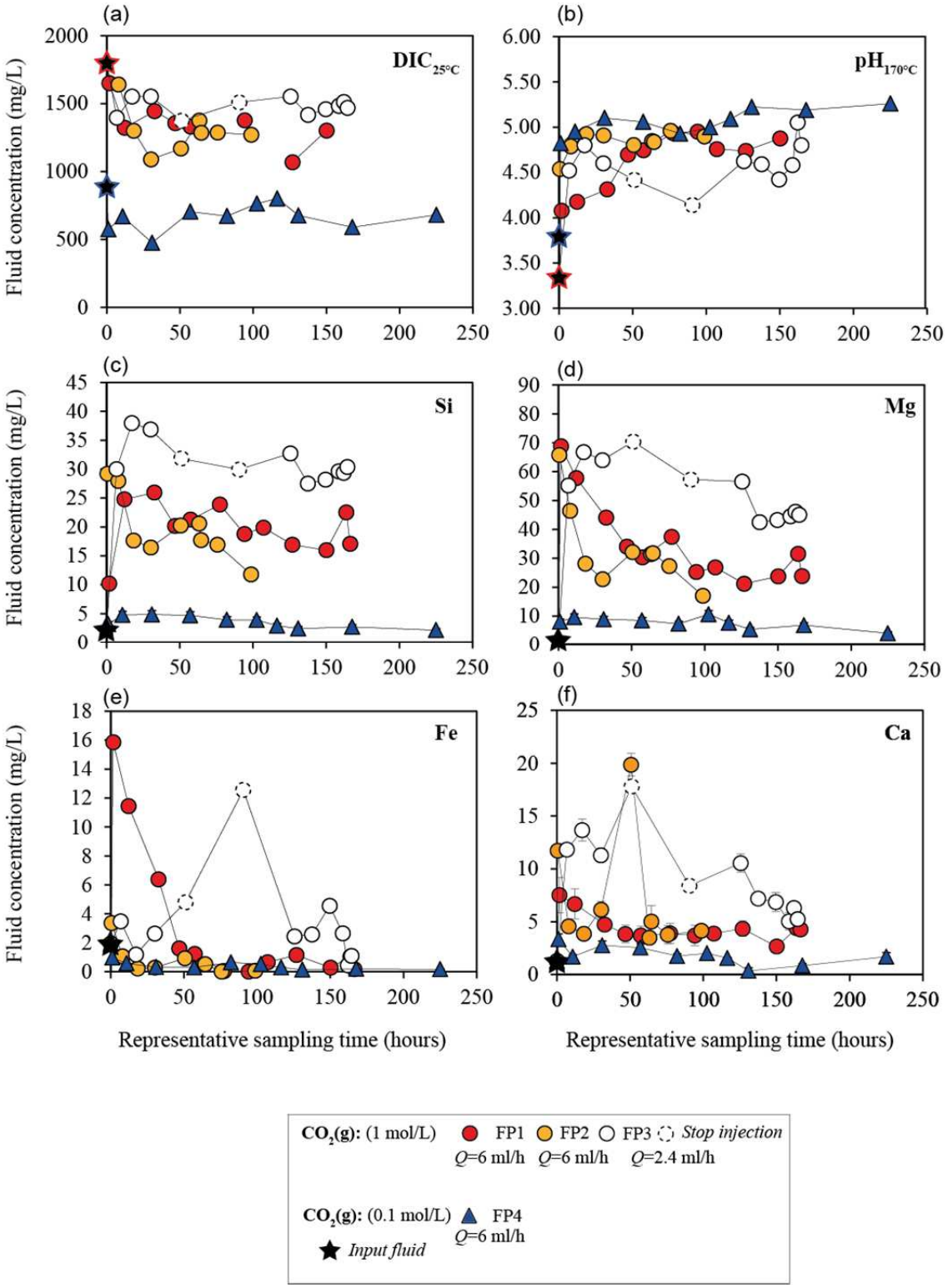

Fig.5.17. Chemistry of the outlet fluids of experiments FP1, FP2, FP3 and FP4. (a) Total dissolved inorganic carbon (DIC) calculated at 25°C. (b) pH calculated at 170°C and 25 MPa). (c-f) Si, Mg, Fe and Ca concentrations on the fluids. The representative sampling time is the time at which half of the volume of analysed fluid was sample.

The metals Cu, Zn, Ni, Cr and Mn in the outlet fluids remained nearly constant during the experiments after a strong increase on the fluids during the first hours (Fig.5.18). Zn was slightly concentrated in the outlet fluids of low XCO_2 (FP4) compared high XCO_2 (FP1 and FP2). However, FP3-HC shows strong enrichment (18.3 mg/L) during the period of no fluid injection. Ni was greatly enriched in the initial solution (ASW) (30 mg/L) probably due to the corrosion of the pipelines by the acidic injected solution. The concentration of Ni in the outlet fluids was slightly lower than the input solution. FP3-HC shows strong depletion (14.2 mg/L) during the period of no fluid injection. Mn was more enrich in the outlet fluids during high XCO_2 experiments compared to low XCO_2 experiments.

In an attempt to constrain the precipitation and dissolution processes that control the sample mass variations, the saturation indexes were calculated in the outlet fluids using the EQ3/6 geochemical software using the 25MPa thermodynamic database generated for this study. As illustrated on Fig.5.19, olivine, chrysotile, enstatite and diopside were under-saturated in the four experiments and were thus expected to dissolve. It should be noted that olivine, chrysotile and enstatite saturation indexes were overall the lowest for low XCO_2 experiments, suggesting that disequilibrium towards this minerals are more efficiently maintained for low CO_2 concentrations in the fluids compared to high CO_2 concentrations. All the final solutions were found to be supersaturated (SI>0) with respect to huntite (high XCO_2: SI= ~124 and low XCO_2: SI= 121) and hematite (SI= 7.8) under experimental conditions. In addition, all solutions were slightly above saturation with respect to magnetite and slightly below saturation with respect to magnesite, calcite and quartz. Nepouite ($Ni_3Si_2O_5(OH)_4$) was slightly above saturation for experiments FP1-HC and FP2-HC from 58 h and 15h respectively until the end of the experiment (see *appendix C.* Table C.24-27*)* for saturation index data).

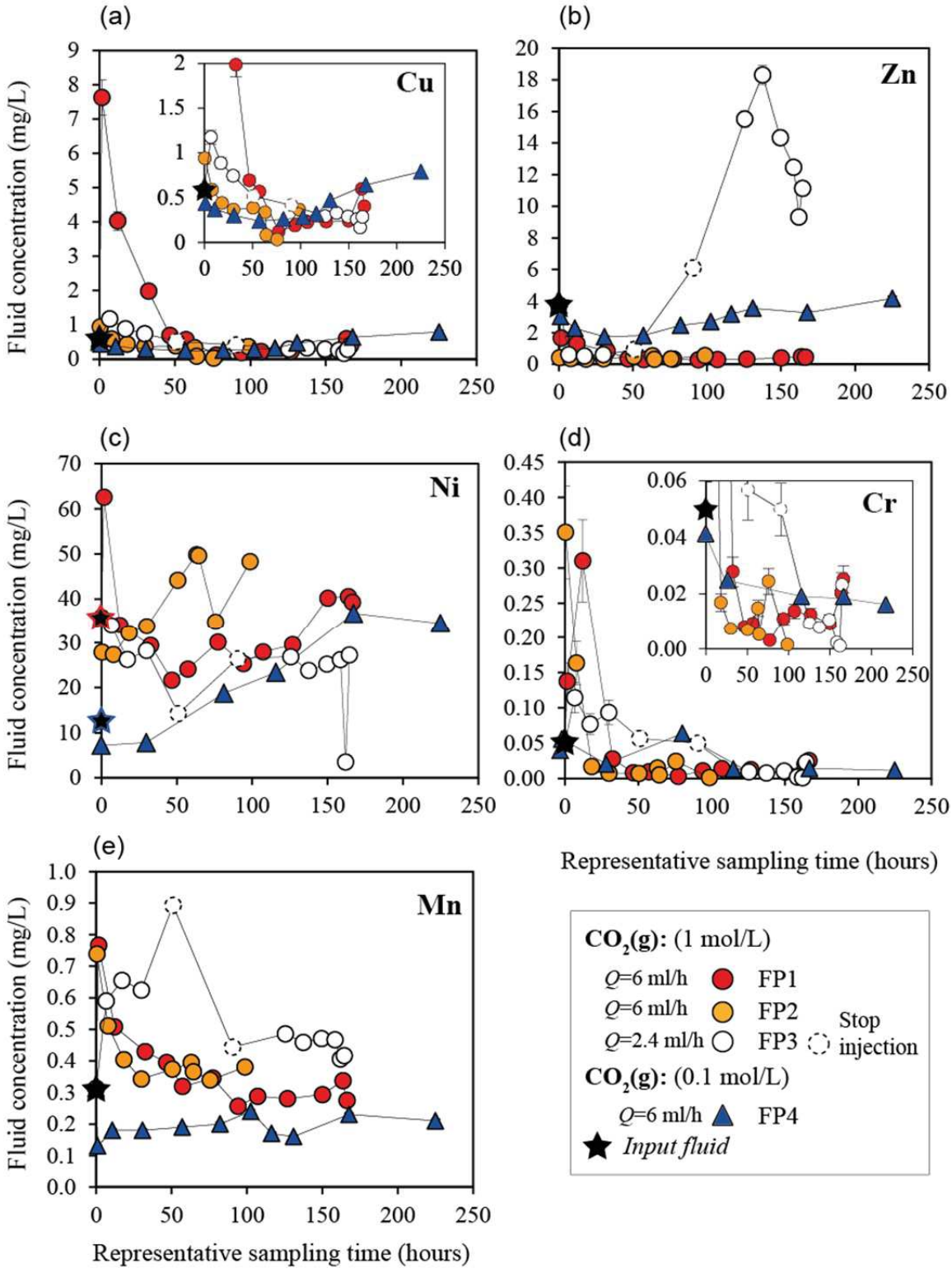

Fig.5.18. Chemistry of the outlet fluids of experiments FP1, FP2, FP3 and FP4. (a-e) Cu, Zn, Ni, Cr and Mn concentration on the fluids. The representative sampling time is the time at which half of the volume of analysed fluid was sample.

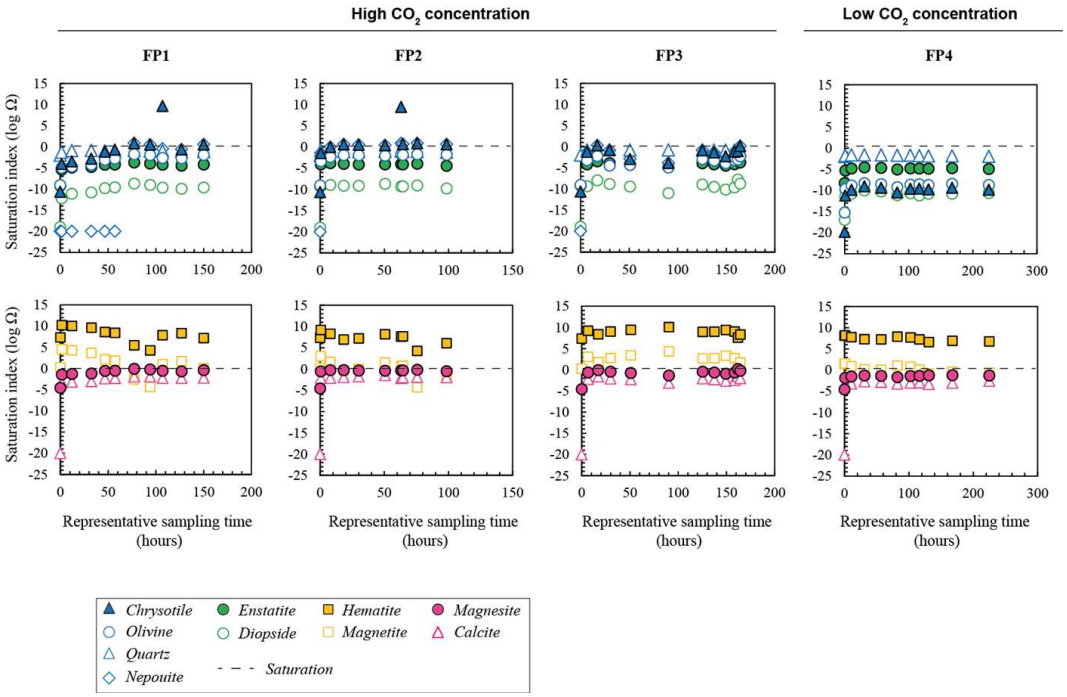

Fig.5.19. Saturation index of the outlet fluids of experiments FP1, FP2, FP3 and FP4. The representative sampling time is the time at which half of the volume of analysed fluid was sample.

4. Discussion

4.1 Chemical and mineralogical budget

Geochemical and spectroscopic analyses revealed the high reactivity of serpentinized peridotite fractured cores percolated by high CO_2-saline fluids (Fig.5.3 and Fig.5.6). All the outlet fluids sampled during the percolation experiments are enriched in Si-Mg-Fe-Ca but depleted in dissolved carbon relative to inlet fluids (Fig.5.17). Changes in Si-Ca-Mg-Fe concentrations between the inlet and the outlet fluids indicate that several chemical reactions occurred within the peridotite during CO_2-rich fluids transfer and suggest mass changes of the reacted samples.

An estimation of the total mass change of the sample was obtained by calculating the amount of cation oxides lost and/or gained on a volatile free basis (Fig.5.20). More than 99% of the total mass of ultramafic minerals can be described using Si, Fe, Mg and Ca written as oxides. The calculations were realized by comparing the composition of injected CO_2-rich solution to those of the outlet fluids, assuming that the sampled fluids were representative of the average composition of the reacted fluids between each sampling. The residual oxides were then normalized to 100% to represent the mass gained/lost, with respect to the initial mass of the samples. This approach provides a first estimate of the mass gained/lost by the reacting samples ($\Delta M(t)$) (e.g., Godard et al., 2013; Peuble et al., 2015):

$$\Delta M(t) = \sum_{i=1}^{n} m_i\ (t) \qquad \text{(Eq.5.6)}$$

$$m_i\ (t) = \int_0^t \left(c_{i,in} - c_{i,out}\ (t) \right) \cdot Q(t) \cdot dt \qquad \text{(Eq.5.7)}$$

where $c_{i,in}$ and $c_{i,out}$ represent the concentrations of the oxide in g/L in the injected and the outlet fluids respectively, Q the injection rate in L/h and m_i the total mass of the oxide in g trapped ($m_i > 0$) or released ($m_i < 0$) from the sample at the time t.

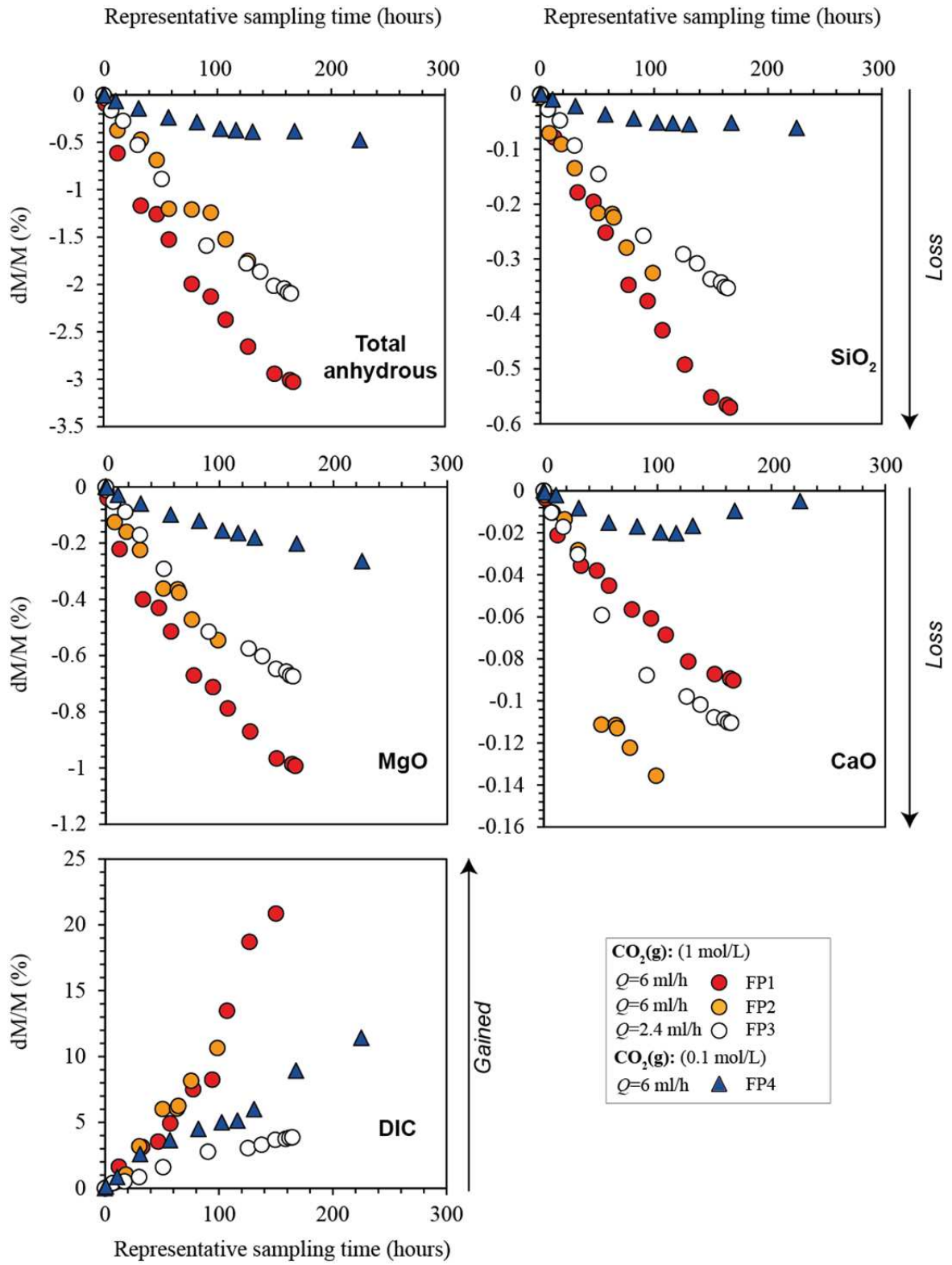

Fig.5.20. Mass changes lost and/or gained compared to the initial mass versus representative sampling time for samples of high XCO_2 experiments (FP1-HC, FP2-HC, FP3-HC) and low XCO_2 experiments (FP4-LC). The representative sampling time is the time at which half of the volume of analysed fluid was sampled.

Primary minerals dissolution

After the experiments all the reacted samples shows an overall weight loss relative to the initial mass of the percolated samples (Fig.5.20). The mass loss was preferentially dominated by SiO_2 and MgO for all the experiments. This indicates that the silicate minerals initially present in the samples (e.g., olivine, pyroxenes and serpentine) were dissolved. Evidences of silicate dissolution were observed in the dissolution front for all the samples (Fig.5.3 and Fig.5.6). This suggests that the fluid-rock interactions are mainly controlled by the dissolution of silicates in the serpentinized peridotite. The calculated total mass loss and the textural evidences of the reacted rock sample (e.g., FP1-HC - 3.03 wt.% at the end of 166 h and FP4-LC – 0.46 wt.% at the end of 256 h), suggest that the degree of dissolution of the rock was higher during experiments with a fluid with higher CO_2 concentration. The dissolution of $CO_{2(g)}$ into the fluid produces the acidification of the fluid according to the reaction (R1) (Zeebe and Wolf-Gladrow, 2001). High dissolved CO_2 concentration in solution produces a stronger drop of the fluid pH compared to low-XCO_2 fluid, which in turn promotes a faster dissolution of silicates present initially in the rock samples (e.g., Daval et al., 2013; Hänchen et al., 2008; Klein and McCollom, 2013; Prigiobbe et al., 2009).

The mass of other oxides varies with the concentration of dissolved CO_2 in the fluid. Therefore, CaO shows enrichment in the reacted fluid (Fig.5.17) which reflects the dissolution of clinopyroxenes and/or carbonates veins initially present in the peridotite. FeO increases in the outlet fluids (Fig.5.17), suggesting that the dissolution of silicate minerals (e.g., olivine, pyroxene) and the magnetite initially present in the samples. The carbon content in the rock samples increases with time for all the experiments which suggests that carbonate precipitation occured. Furthermore, experiments run with high flow rate and high concentration of CO_2 shows the highest mass of carbonates precipitated in the samples based on mass balance calculations (Fig.5.20).

The strong dissolution of the minerals initially present in the peridotite is probably underestimated in the samples due to the precipitation of secondary phases trapping part of the divalent cations released in the fluid such as magnesium in the magnesite and dolomite, calcium in the calcite and dolomite and iron in the hematite (Fig.5.14 and Fig.5.15).

Carbonate precipitation

Several types of secondary carbonates precipitated during these set of fluid-rock experiments. Magnesite was the principal carbonate precipitated on high XCO_2 experiments and (Ca-Mg)-carbonates were found mostly on low XCO_2 experiments. Minor calcite also precipitated during interaction of the serpentinized peridotite with a high XCO_2 fluid. Cathodoluminescense images reveal that the density of carbonates is higher in the reacted zone 1 (next to the unreacted rock) and carbonates are located along the lizardite mesh (Fig.5.11). This suggests that the reacted fluid is saturated with respect to the carbonates during its path from the fracture to the unreacted peridotite. Therefore carbonates precipitation would imply an increase of the pH of the fluid and an increase of the concentration of dissolved Mg and Ca.

Calcite and dolomite has been documented as the dominant carbonate minerals in natural systems (e.g., Andreani et al., 2009; Alt and Shanks, 1998; Früh-Green et al., 2004; Müntener and Manatschal, 2006; Nöel et al., 2018). However, magnesite was the main mineral precipitated in this study compared to minor calcite and dolomite (Fig.5.12). The low Ca concentration in solution and in the initial rock sample (serpentinized harzburgite) could be one of the reasons explaining this discrepancy (*appendix C*. Table C.1). This is in good agreement with the observation of Gablina et al. (2006) which suggest that the formation of magnesite in oceanic settings is therefore likely limited to domains of Ca-poor ultramafic rocks, such as dunite or fully serpentinized peridotite. In addition, experimental studies demonstrate that the increase of the ionic strength of the solution produces an increase on the rate of magnesite precipitation (e.g., Eikeland et al., 2015; O'Connor et al., 2001; Sayles and Fyfe, 1973). Thus, saline environments enhance magnesite reaction rates through decreasing the activity of water and thus facilitating the dehydration of the Mg^{2+} ion. Magnesite is a mineral very difficult to precipitate experimentally (Bénézeth et al., 2011).

Therefore, the low Ca concentration in the initial fluid and rock and the high ionic strength of the initial solution could be the key parameters that control the magnesite precipitation in these experiments. The difference of the mineralogy of the carbonates precipitated could be explained by the relative activity of Ca and Mg in the aqueous solution. The outlet fluids of all the experiments show a decrease of the log aCa^{+2}/aMg^{+2} ratio and an increase of pH relative to the initial solution (Fig.5.21). Higher concentrations of CO_2 in

solution records the lowest log aCa^{+2}/aMg^{+2} ratios (Fig.5.21). This is due to the strong dissolution of the olivine and orthopyroxene resulting in the strong increase of the aMg^{+2} in the outlet fluids compared to minor dissolution of clinopyroxenes and carbonate veins that produces low aCa^{+2} in the fluids. Thus, the high enrichment of the Mg concentration in the fluids relative to Ca produces a decrease on the Ca/Mg ratios. Thereby, low Ca/Mg ratios of the fluid allow the precipitation of magnesite (Fig.5.21).

The outlet fluids of all the experiments were slightly enriched of Ca compared to the initial solution (Fig.5.17). Mass balance calculations show a depletion of CaO in the rock (Fig.5.20) especially more pronounced for solutions with high concentrations of dissolved CO_2. The concentration of Ca in the reacted fluids slightly increases due to dissolution of primary calcite veins and/or clinopyroxenes. This increase of Ca concentration is enough to raise the activity of calcium in the reacted solution that helps to expand the stability field of magnesite, dolomite and calcite towards acidic pH (i.e., the left) (Fig.5.21). Thus, the outlet fluids approach the stability field of magnesite and dolomite (±calcite) through the increase in their pH (Fig.5.21).

The occurrence of carbonate rims over olivine and orthopyroxene suggests that carbonate minerals replaced these primary silicates via dissolution-precipitation reactions, such as:

$$Mg_2SiO_2 + 2CO_{2(aq)} = 2MgCO_3 + SiO_{2(aq)} \quad \text{(R4)}$$

olivine *magnesite*

$$Mg_2(SiO_3)_2 + 2CO_{2(aq)} = 2MgCO_3 + 2SiO_{2(aq)} \quad \text{(R5)}$$

orthopyroxene *magnesite*

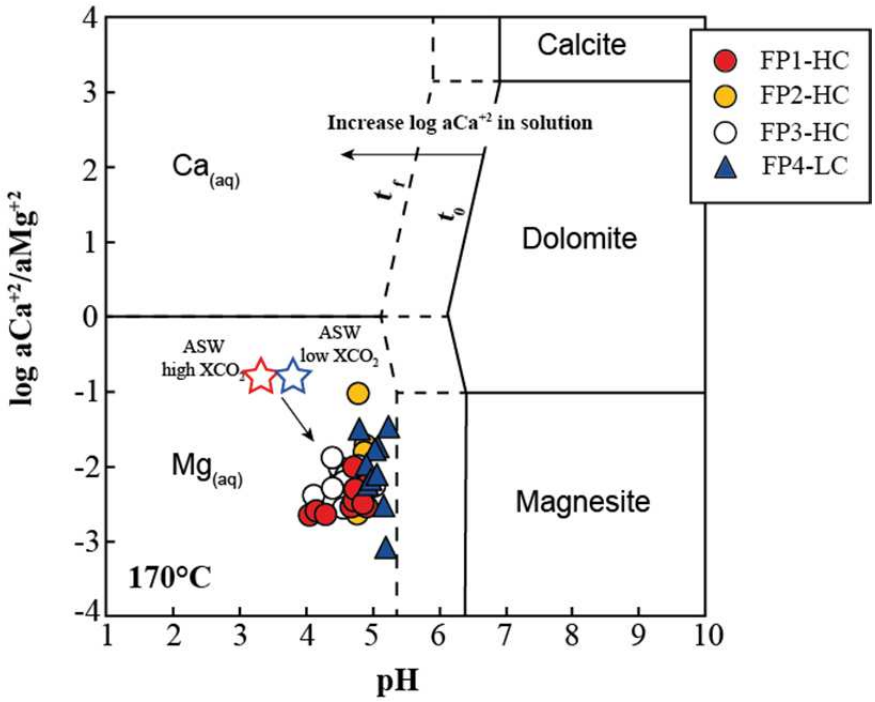

Fig.5.21. Activity-activity diagram of the system CaO-MgO-CO_2-NaCl-H_2O calculated after GWB (Bethke et al., 2006). The star in red and blue corresponds to the initial solution of high XCO_2 and low XCO_2 experiments respectively. The stability field of the carbonate minerals at the initial of the experiments log aCa^{+2}=-5.5) is represented by a continuous line (t_0). Experiments at high XCO_2 records increase on the log aCa^{+2} (FP1 (-5.5 to -4.7), FP2 (-5.5 to -4.3), FP3 (-5.5 to -4.3)) and low XCO_2 experiment from -5.5 to -4.2. The dashed lines (t_f) correspond to the stability field boundary of carbonates for a log aCa^{2+} in solution of -4.

A secondary calcium carbonate enriched in Fe and Mg was found close to a magnesite crystal along the rim of a void produced by the dissolution of a primary silicate, such as olivine, that interacted with a high-CO_2 fluid (Fig.5.12). No accurate Raman analysis could be done in this grain as they have strong fluorescence. However, EDS analysis reveals high content of Ca compared to Mg and Fe and suggest precipitation of calcite (see *appendix C*. Table C.8, spectra 23). Nevertheless, dolomite could not be neglected. Dolomite was the major carbonate precipitated on experiments with low concentrations of CO_2 in solution. The precipitation of Ca-carbonates could be explained also by the relative activity of Mg and Ca in solution. The precipitation of Ca-carbonates next to magnesite rims of dissolved grains suggests that the early precipitation of magnesite depleted locally the concentration of magnesium (i.e., decrease aMg^{2+}) in the fluid and thus the log aCa^{2+}/aMg^{2+} ratio of the fluid increased towards the stability field of calcite and dolomite (Fig.5.21).

The precipitation of dolomite could be described by the reaction R6:

$$Mg_2SiO_4 + 4CO_{2(aq)} + 2Ca^{2+} + 2H_2O = 2CaMg(CO_3)_2 + SiO_{2(aq)} + 4H^+ \quad (R6)$$

olivine *dolomite*

The carbonation of olivine requires two moles less of $CO_{2(aq)}$ to precipitate magnesite compared dolomite according to (R4 and R5) and (R6).

The increase of $SiO_{2(aq)}$ concentration in solution by the carbonation of olivine and orthopyroxene (R4 and R5) could explain the precipitation of amorphous silicate grains encountered associated to the rims of magnesite on experiments with high concentrations of CO_2 in the fluid (Fig.5.12). The local increase of the $aSiO_{2(aq)}$ displaced the fluids towards the equilibrium field of quartz (Fig.5.22).

Silicate precipitation

Carbonation of peridotites is sometimes associated to the formation of Si-rich layers at the interfaces between the dissolving Mg-silicates and the precipitated carbonates (e.g., Béarat et al., 2006; Chizmeshya et al., 2007; Andreani et al., 2009; Daval et al., 2011; Daval et al., 2010; Hövelmann et al., 2012; Ulrich et al., 2014) and/or the precipitation of sparsely disseminated amorphous silica-enriched phases (Peuble et al., 2015). The formation of silica-rich phase on the rims of the dissolved grains suggest that incipient dissolution of olivine may quickly supersaturate the fluid at the mineral fluid interface with respect to amorphous silica, which then precipitated close to the olivine surface. The saturation with respect to amorphous silica suggests that the diffusion of released Si from the interfacial solution into the bulk solution is slower than the supply of new Si from the dissolving olivine resulting in a concentration gradient close to the solid surface (Ruiz-Agudo, 2014). In addition, the speciation calculation suggests that the outlet fluids were close to saturation with respect to quartz, especially on experiments involving high CO_2-rich solutions favouring the potential development of this rims layers (*appendix C*.Table C.24-27).

Fig.5.22 shows the stability diagram of the system MgO-SiO_2-NaCl. All outlet fluids plot in the stability diagram of the aqueous silica, however fluids shows an increase of the

activity of SiO_2 and Mg approaching them towards the stability field of quartz (Fig.5.22a-b). The outlet fluids show an increase of their pH during the progression of the experiments due to the silicates dissolution (fig.5.17b). The increase on the pH modifies the stability field of silicate minerals (talc, serpentine and forsterite) towards low activity of magnesium in solution. The outlet fluids are then closer to the boundaries of silicate minerals (quartz, talc and serpentine). Reacted fluids from high XCO_2 experiments are closer to the quartz boundary compare to low XCO_2 experiments. This could explain the precipitation of silica grains on the samples that interact with a high CO_2 fluid.

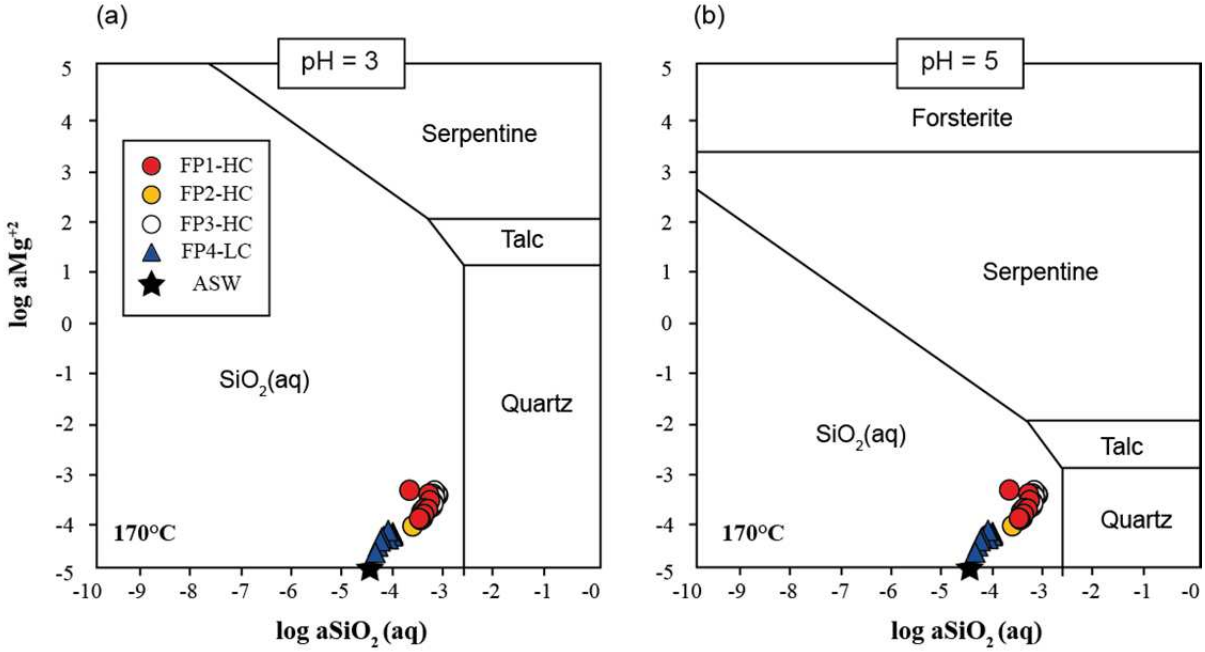

Fig.5.22. Activity-activity diagrams of the system $MgO\text{-}SiO_2\text{-}NaCl\text{-}H_2O$ calculated after GWB (Bethke et al., 2006). (a) Diagram calculated at pH=3. (b) Diagram calculated at pH=5.

Speciation calculations show that the reacted fluids were close to saturation with respect to chrysotile and nepounite (Ni-rich serpentine) on experiments with high XCO_2 in solution. Despite the fact that thoses phases (Mg-rich phases) were not clearly identified, acicular phases, that could be potentially serpentine minerals, were found filling neo-formed polygonal cracks on the inlet surface of sample FP4-LC in experiments with low concentration of CO_2 in the fluid (Fig.5.6 and *appendix C*. Fig.C.8). The formation of secondary Mg-silicates is of particular relevance for in situ CO_2 mineral sequestration because it would limit the potential amount of carbonate formation (King et al., 2010). Early studies demonstrate that the precipitation of Mg-silicates further away from the dissolution sites may clog fluid pathways and reduce rock permeability (Andreani et al., 2009). In the

present experiments carbonation reaction was effectively maintained during all the experiment time and records only small diminution on permeability (Fig.5.2). This suggests that Mg and Si were continuously mobilized further away from the dissolution sites and thus avoided an early termination of the carbonation reaction.

Experiment FP3-HC run at low Q and with a period on no fluid injection shows a decrease on the permeability rate faster than the other experiments (Fig.5.2). In contrast this experiment shows the lowest carbonation rate (Table 5.4). This suggests that the decrease in permeability could be related to the precipitation of other mineral phases such as silicate minerals that could effectively reduce the permeability.

Oxides precipitation

During all the experiments, the colour of peridotite material evolved from dark green to reddish colour. As mentioned previously, Raman analysis demonstrated that the reaction front was covered by Fe-oxides, (magnetite and hematite) (Fig.5.15). Hematite is characterized by a brown to reddish brown colour and has been identified in numerous experiments of peridotite alteration under seawater (e.g., Hövelmann et al., 2011; Godard et al., 2013). Ongoing fluid-rock reactions on serpentinized peridotites may lead to primary magnetite destruction and transformation into secondary hematite (Bach et al., 2004). The presence of hematite-magnetite suggests that the systems evolved from reducing (magnetite) to more oxidative conditions (hematite) (e.g., Evans et al., 2008, 2009). The discoloration of the reaction front through a reddish colour could be associated to the formation of hematite on the reaction front. Dissolution-reprecipitation process is the most likely mechanism for colour change in the samples (e.g., Van Noort et al., 2012). The colour change provides an opportunity to monitor the reaction front migration.

4.2 Chemical and hydrodynamic parameters that controls the carbonation rate

Previous fluid-rock interaction studies have demonstrated that chemical and hydrodynamics play a key role on the carbonation rate (e.g., Andreani et al., 2009; Peuble et al., 2015). In this study, the carbon trapped into the peridotite core shows with a positive

correlation with time on the four experiments, suggesting the carbonation rate was constant during each experiment (Fig.5.20). The total mass of carbonate trapped as a function of time in each experiment was fit by a linear regression and the rate of carbonation was taken as the slope of the regression line in the figure 5.20 (DIC).

Table 5.4. Estimation of the carbonation rate in experiments FP1-HC, FP2-HC, FP3, HC and FP4-LC and Péclet number (Eq.5.8). The residence time (RT) was calculated as: RT=Volume sample / Q. (FP1 and FP2) denotes the common carbonation rate for both experiments run under the same conditions (XCO_2 and *Q*).

	Carbonation rate	XCO_2	Residence time	Flow rate (*Q*)	Flow rate (*Q*)	a_h (initial)	*d*	V_{darcy}	Pe
	wt.% / h	*mol/L*	*min*	*ml/h*	*m3/s*	*m*	*m*	*m/s*	
FP1-HC	**0.12 ± 0.01**	1	12.6	6	1.66×10^{-9}	9.90×10^{-6}	8.95×10^{-3}	1.88×10^{-2}	37
FP2-HC	**0.10 ± 0.02**	1	12.5	6	1.66×10^{-9}	1.35×10^{-5}	8.91×10^{-3}	1.39×10^{-2}	37
FP3-HC	**0.02 ± 0.01**	1	30.2	2.4	6.66×10^{-10}	2.70×10^{-6}	8.88×10^{-3}	2.78×10^{-2}	15
FP4-LC	**0.05 ± 0.01**	0.1	12.3	6	1.66×10^{-9}	9.30×10^{-6}	8.92×10^{-3}	2.01×10^{-2}	37
FP1 and FP2	**0.11 ± 0.08**	1		6					37

Effect of the concentration of CO_2 on the carbonation rate

The results of this study put in light the effect of the concentration of dissolved CO_2 on the carbonation rate. High concentration of CO_2 in solution shows carbonation of peridotite 2.4 times faster than low XCO_2 solutions for a similar injected flow rate (Table.5.4 and Fig.5.23a). The CO_2-rich solutions provide H^+ in the fluid after the reaction (R1) (e.g., Zeebe and Wolf-Gladrow, 2001). Thus, when the concentration of CO_2 is higher, then the concentration of H^+ increased higher too. The presence of H^+ (acidic solution) in the fluid enhances effectively the dissolution of the silicate minerals initially present in the rock (e.g., Chen and Brantley, 2000; Hänchen et al., 2008; Hänchen et al., 2006; Pokrovsky and Schott, 2000; Prigiobbe et al., 2009). Hence, an increase in the concentration of CO_2 will favour the dissolution of the rock that enriches the solution in divalent cations (Mg^{2+}, Ca^{2+}, Fe^{2+}) (Fig.5.3 and Fig.5.6). In addition, the dissolution of peridotite triggers the increase of pH by silicate precipitation (Gislason and Oelkers, 2003). Therefore, the presence of divalent cations in solution and the increase of pH of the fluid favour carbonate saturation and thus, consequently the precipitation of carbonate minerals.

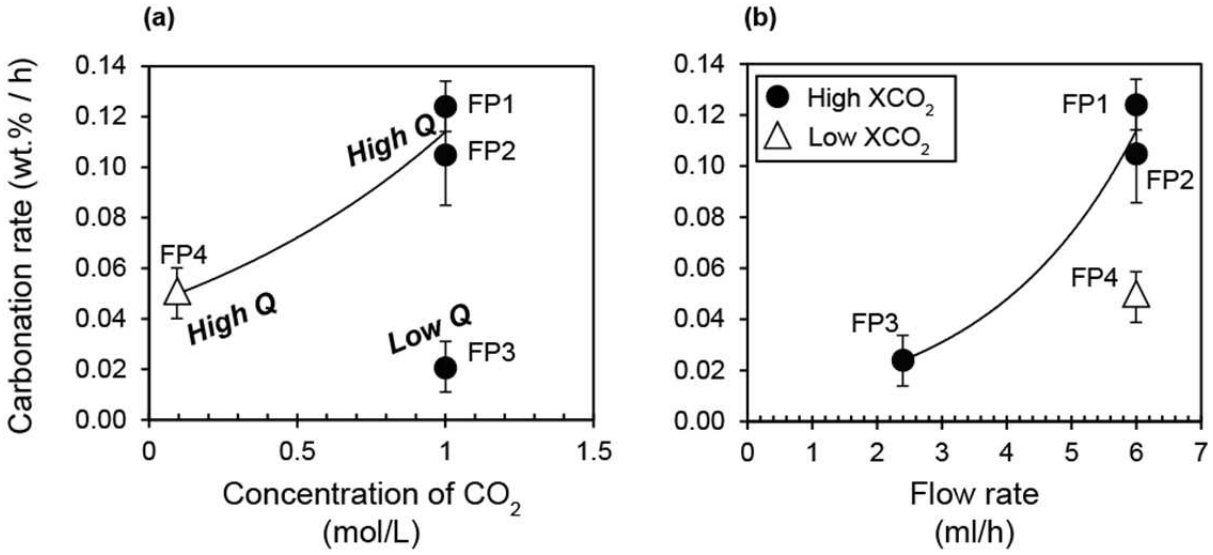

Fig.5.23. (a) Carbonation rate (wt.% /h) vs the concentration of CO_2 in solution and (b) carbonation rate (wt.% / h) vs the flow rate. The curve denotes an exponential regression curve.

Effect of the flow rate on the carbonation rate

The flow rate shows an effect on the carbonation rate. The carbonation rate was 6 times faster for experiments run with the same concentration of CO_2 in solution but with high flow rate (Q=6 ml/h) rather than low flow rates (Q=2.4 ml/h for FP3 experiment) (Table 5.4 and Fig.5.22b). This suggests that the rate of solute supply in the sample controls the carbonation rate. This is consistent with the observation of Peuble et al. (2014) on carbonation experiments performed on San Carlos olivine aggregates, which determines that carbonation rates are higher when higher flow rates are injected. High flow rates (Q) produce efficient fluid renewal on the samples that maintains the fluid-rock system at disequilibrium. This results in a higher degree of silicates dissolution which provides more cations for carbonation reactions.

The dimensionless Péclet number (Pe) is often used for evaluating whether advection ($Pe > 1$) or diffusion ($Pe < 1$) is the dominant transport mechanism for chemical species in a porous and fractured media (e.g., Steefel and Maher, 2009). The Pe values corresponding to the four reactive percolation experiments were calculated as:

$$Pe = \frac{v \cdot a_h}{D} \qquad \text{(Eq.5.8)}$$

where with v the mean fluid velocity in m/s, D the diffusion coefficient 5.10^{-9} $m^2.s^{-1}$ (Philibert, 2005) and a_h the initial fracture aperture estimated with (Eq.5.3) which is the characteristic length at which the process is considered. The fluid velocity in m/s was defined here as the velocity distribution of the fluid in the fracture space, and calculated as $v = Q/S$ with Q the flow rate in m^3/s, and S the cross-section of the sample in m^2 and calculated as $S = a_h \cdot d$, where a_h is the initial fracture aperture and d is the diameter of the core in m.

The calculated *Pe* values and fluid velocity v values are reported in Table 5.4. By definition, transport is advective for *Pe* >> 1 and diffusive if *Pe* << 1. As expected, the calculated *Pe*-numbers increase with Q for experiment FP1-HC, FP2-HC and FP4-LC (*Pe*=37) and decrease with Q for experiment FP3-HC (*Pe*= 15). All experiments show advection domination conditions. High Péclet numbers (*Pe*= 37) shows higher carbonation rates than low Péclet numbers (*Pe*=15) independently of the concentration of CO_2 dissolved in the fluid (Table 5.4). This suggests that advection conditions triggers efficient transport of protons and chemical species in solution. Thus, the sharp chemical gradient between mineral surface and advecting fluids favors relatively fast olivine dissolution kinetics and efficient detachment of divalent cations from the mineral surface into the fluid. The dissolution of peridotite results in the increase of pH of the fluid (Fig. 5.17) which enhance the carbonate saturation.

Therefore, this study has demonstrated that both the concentration of CO_2 dissolved in solution and the injected flow rates are key parameters that control the carbonation rate during hydrothermal alteration of ultramafic rocks.

4.3 Reaction front migration

Fluid penetration

Peridotite minerals dissolution and subsequent carbonates and iron oxides precipitation can occur only when primary minerals surface are accessible by a hydrous fluid containing enough H^+. Olivine and pyroxenes were preferentially dissolved compared to lizardite on high and low XCO_2 experiments (Fig.5.6). This was also observed during experimental carbonation of partially serpentinized peridotites (e.g., Hövelmann et al., 2011;

Lacinska et al., 2017; Van Noort et al., 2013). The preferential dissolution of olivine may be related to the different crystal structures between olivine and lizardite. The isolated Si-tetrahedra in olivine promotes faster dissolution than the polymerised Si-tetrahedra in serpentine (e.g., Klein and Hurlbut, 1993). In addition, olivine is a mineral stable at higher temperature and is thermodynamically less stable than serpentine under the conditions applied on these experiments. Studies of Daval et al (2013) demonstrate that lizardite dissolution rates are orders of magnitude lower than those of olivine and pyroxenes for T=27 to 90°C and pH of 2.5 to 6.7.

The dissolution of olivine resulted in the development of secondary porosity that provided additional pathways for fluid ingress (Fig.5.3) (e.g., Van Noort et al., 2013). These pathways may have become interconnected, helping the progressive dissolution of rock components. In addition, observations in reacted sample show that the contact between two lizardite sheets were preferentially dissolved (Fig.5.6c and *appendix C*. Fig.C.10b).

This study revealed that the infiltration of fluids into the serpentinized peridotite produced the dissolution of olivine grains but also the precipitation of carbonate on the rims of the dissolved grains (Fig.5.12). Similar observation was point out by Nöel et al (2018) on natural peridotite samples of the Oman Ophiolite. Thus, figure 5.24 explain the mechanism for fluid infiltration into the serpentinized peridotite: (1) fluid follow serpentine mesh/sheets and reach the olivine and/or pyroxene surface (Fig.5.24), (2) Olivine and/or pyroxene grain boundary are preferentially dissolved into the fluid compared to lizardite which is dissolved in a lesser extent, which result in the formation of an empty space between the olivine/pyroxene and the lizardite (Fig. 5.24), (3) Olivine and/or pyroxene are fully dissolved leading behind them a void that conserve the negative shape of the dissolved mineral. Carbonate saturation is produced in the voids leading to carbonate replacing the rims of dissolved mineral grains.

Length and velocity of the reaction front

The velocity of the reaction front provides an estimation of the reaction kinetics. The velocity of the reaction front was calculated on the dissolution front and the coloured reaction front. The velocity is the ratio between the length of the measured reaction and the

experiment time ($V_{fr} = X_{reaction\ front}/t$); X is the length of the reaction front in µm and t is the duration of the experiment in hours.

Discoloration of the reacted samples provides an opportunity to identify and monitor the length of the reaction coloured zones. The calculated lengths of each reacted zone were measured on 4 polished sections (A, B, C, D) using binocular images (Fig.5.25 and *appendix C*. Table C.5). The level of grey in the X-ray images provides an opportunity to identify and monitor the length of the dissolved zone, which is a porosity front (*appendix C*. Table C.3).

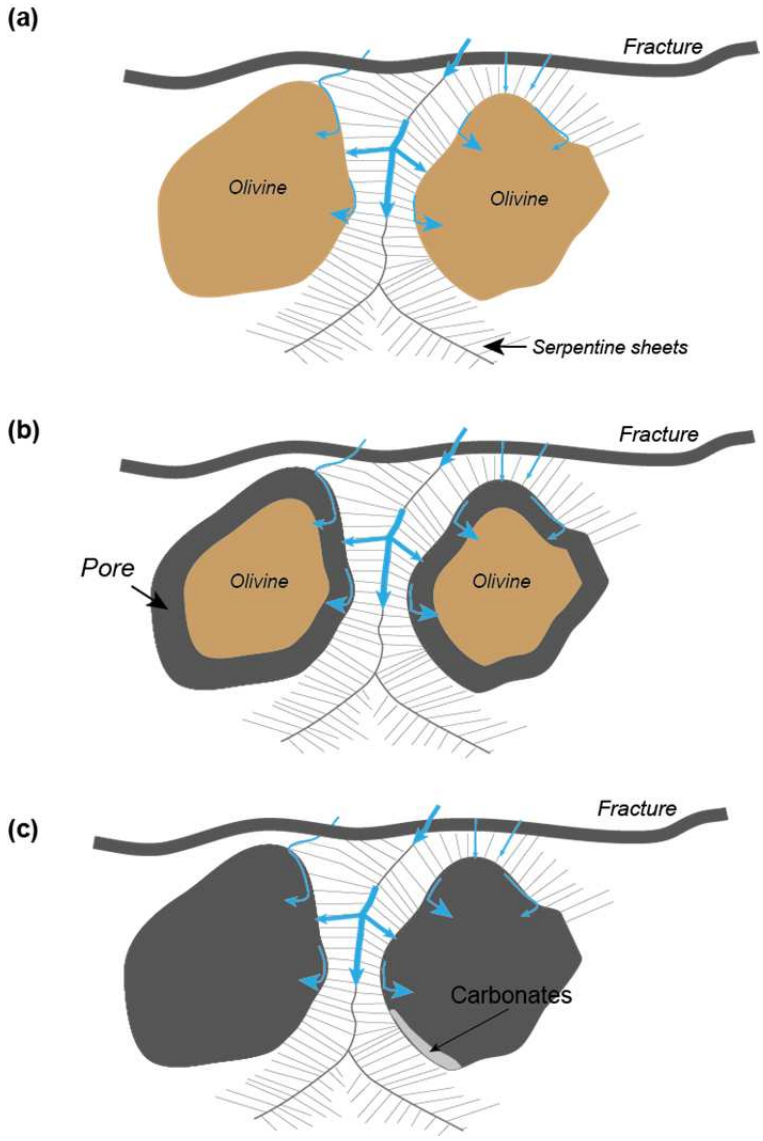

Fig.5.24. Mechanism proposed of olivine (+ pyroxene) dissolution in serpentinized peridotites. (a) Fluid infiltrates the serpentine network and grain boundaries. (b) Olivine (+ pyroxene) dissolution and formation of voids that creates secondary porosity and serves as fluid paths. (c) Grain completely dissolved and partial replacement by carbonates.

Coloured reaction front

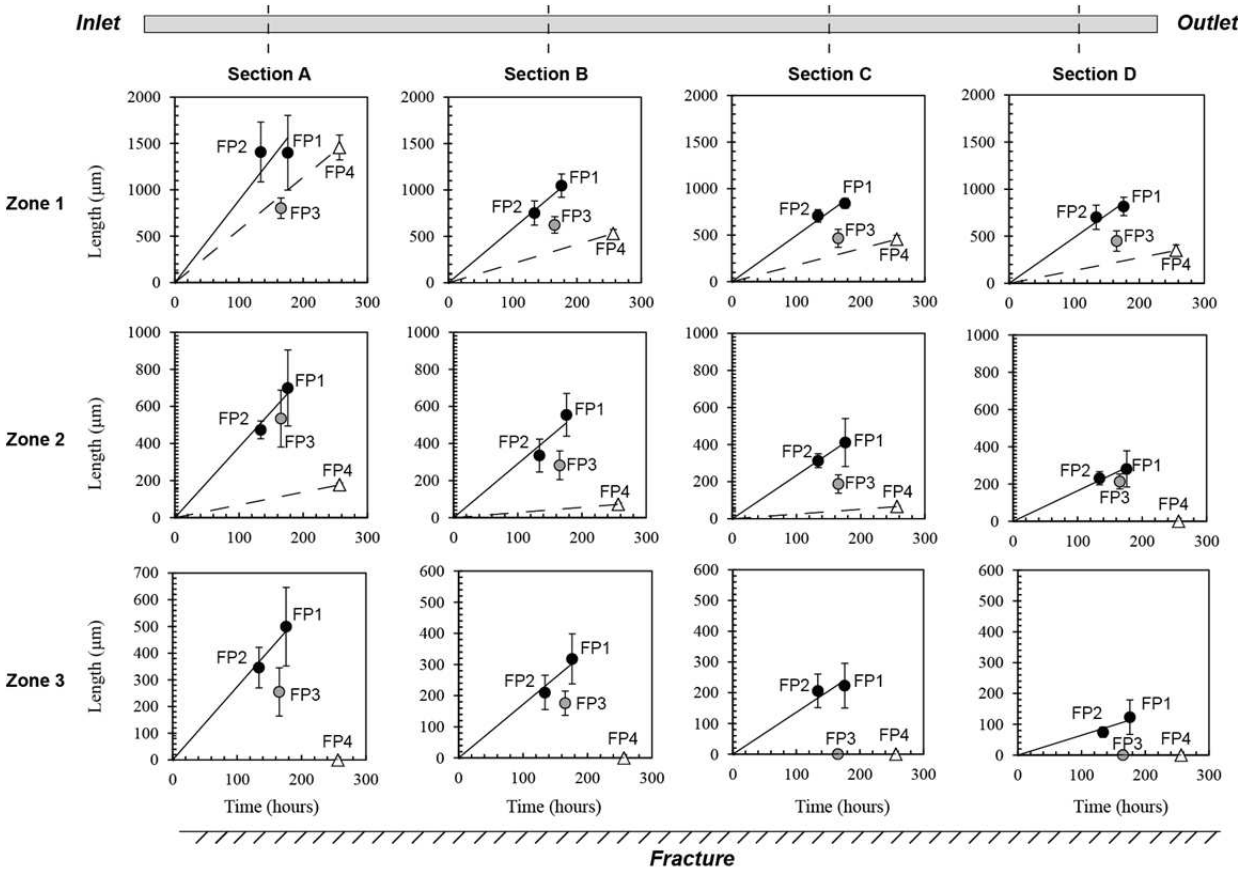

Fig.5.25. Coloured reaction front migration for all the reacted samples (FP1-HC, FP2-HC, FP3-HC and FP4-LC). The section A to D represents the distribution of the reaction front in the polished section from the inlet to the outlet of the samples. The zone 1 represents the furthest zone to the fracture, zone 2 the middle zone and the zone 3 the adjacent zone to the fracture. The solid line corresponds to the regression curve (order 1) for high XCO_2 experiments (FP1-HC and FP2-HC) and the dashed line correspond to the regression curve (order 1) for low XCO_2 experiment FP4-LC.

We identify differences on the length of the coloured reaction front: (1) between experiments, (2) on each experiment along the core from the inlet to the outlet and (3) on each zone. Experiments involving high XCO_2 concentration in solution shows wider reaction fronts in the rock compared to the one with low XCO_2 concentrations. All experiments show that the mean length of the front is wider at the inlet (section A) and become thinner towards the outlet of the samples (section D) (Fig.5.25). This suggests that the injected fluid loses its reactivity as it approaches the outlet of the sample (i.e., fluid and rock should be closer to equilibrium).

The length of reacted front in similar experiments FP1-HC and FP2-HC (similar XCO_2 in the fluid and similar flow rate) display a positive correlation with time for all zones (Fig.5.25). This suggests that the heterogeneity between samples (e.g., fracture topology and mineralogy distribution) is negligible compared to the effect of dissolved CO_2 concentration during peridotite alteration.

The overall positive correlation FP1-HC and FP2-HC experiments allow us to estimate a single velocity trend for high XCO_2 – high Q experiments from a linear regression (*appendix C*. Table C.6). The velocity of the coloured reaction front is faster when the concentration of CO_2 in solution is high (Fig.5.26). The velocity of the reaction front decreases from the inlet to the outlet of the samples in all the reacted zones (Fig.5.26). The coloured reaction front is faster in the zones further to the fracture rather the zones more closely to the fracture. For example at the inlet of the samples FP1 and FP2, the zone further from the fracture (zone 1) shows a velocity of 8.9 ± 3.3 μm/h compared to the zone adjacent to the fracture, zone 2 (3.8 ± 1.2 μm/h) and zone 3 (2.7 ± 0.9 μm/h). The velocity of the reaction front at the inlet of the samples in the zone 1 decrease 1.5 times when the concentration in the fluid is decreased 10 times from 1 mol/L to 0.1 mol/L (Fig.5.26). The sample FP3-HC injected with high concentration of CO_2 but with a flow rate 2.5 slower than FP1-HC and FP2-HC (Table 5.1) shows a progression of the reaction front 1.8 slower at the inlet of the samples compared to high flow rates.

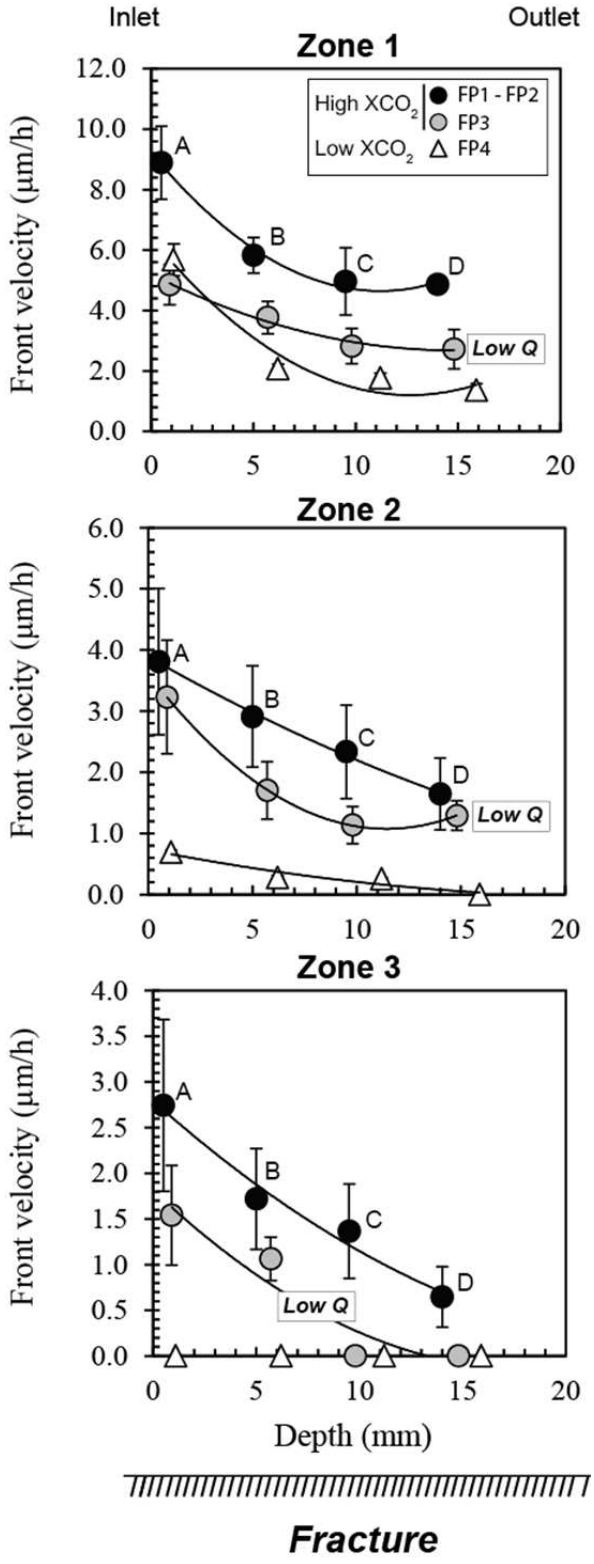

Fig.5.26. Velocity of coloured reaction front in the zones 1, 2 and 3 measured in the polish sections for high (FP1-HC, FP2-HC and FP3-HC) and low (FP4-HC) XCO_2 experiments. The depth represents the position of the polish section relative to the inlet of the samples and calculated after XMT images. The curve represents a polygonal regression (order 2).

Comparison between coloured, dissolution and nickel front velocity

All experiments show that the velocity of the reaction fronts decreases from the inlet towards the outlet of the samples (Fig.5.27 and Table 5.5). The dissolution front is slightly faster than the zone 2 and slightly lower than the zone 1 in all the experiments (Fig.5.26 and Fig.5.27).Therefore, the dissolution front doesn't have the same length as the coloured front. This differences between the coloured and dissolution front could be due because (1) the resolution of the X-ray microtomography images is too big (2.2 µm) than the possible microporosity generated in the zone 1 and is not able to identified it in the images, (2) the discoloration is due to diffusion process before dissolution of the samples and (3) the coloured images are not completely cut perpendicular to the fracture and could have small angle with respect the x-ray microtomography images, this issue can sub estimate the dissolution length measurements.

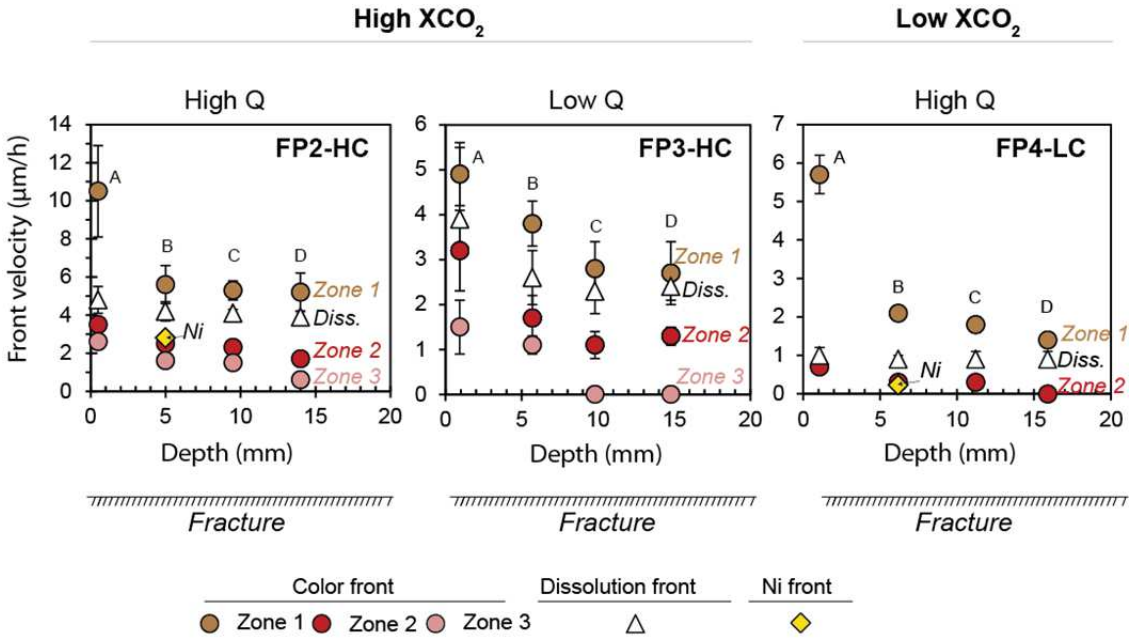

Fig.5.27. Sumarize of the dissolved (porosity), coloured and nickel reaction front velocity in the samples FP2-HC, FP3-HC and FP4-LC. (Diss.) denotes the dissolution front velocity. The dissolution front velocity was calculated in the XMT images that corresponds to the polished sections A, B, C and D respectively (appendix C. Fig.C.6-8). The coloured reaction front in the zones 1, 2 and 3 was calculated in the polished sections A, B, C and D (appendix C. Fig.C.2-4)

The velocity of nickel incorporation in the lizardite is the same as the velocity of the zone 2 in experiment FP2-HQ and FP4-LC. The zone 2 and zone 3 shows the highest degree of dissolution in the samples (Fig.5.10). Thus, the nickel could be considered as a tracer of the zones with the highest degree of dissolution. The newly formed magnesite incorporates nickel in the zones 2 and 3 but not in the zone 1 (Fig.5.14). This also supports the idea that the nickel is incorporated in the zones of highly dissolution.

Table 5.5. Sumarize of the dissolved (porosity), coloured and nickel reaction front velocity.

Reaction front velocity: High CO_2 and High Q

Experiment FP1-HC						
Physico-chemical parameters		**Color and Mineralogy**			**Chemical tracer**	**Porosity**
Analytical technique		Binocular lens + Raman + SEM-EDS			EPMA	XMT
Paramaters Observed secondary minerals		**Brown Carbonate + Hematite**	**Intense red Hematite**	**Pink Hematite**	**Ni-Lizardite**	**Grey value**
	Core depth	Zone 1	Zone 2	Zone 3		
	mm	µm/h	µm/h	µm/h	µm/h	µm/h
Section A	0.5	7.9 ± 2.3	4.0 ± 1.2	2.8 ± 0.8		
Section B	5.0	5.9 ± 0.7	3.1 ± 0.7	1.8 ± 0.5		
Section C	9.5	4.8 ± 0.3	2.3 ± 0.7	1.3 ± 0.4		
Section D	14.0	4.6 ± 0.6	1.6 ± 0.6	0.7 ± 0.3		

Experiment FP2-HC						
Physico-chemical parameters		**Color and Mineralogy**			**Chemical tracer**	**Porosity**
Analytical technique		Binocular lens + Raman + SEM-EDS			EPMA	XMT
Paramaters Observed secondary minerals		**Brown Carbonate + Hematite**	**Intense red Hematite**	**Pink Hematite**	**Ni-Lizardite**	**Grey value**
	Core depth	Zone 1	Zone 2	Zone 3		
	mm	µm/h	µm/h	µm/h	µm/h	µm/h
Section A	0.5	10.5 ± 2.4	3.5 ± 0.3	2.6 ± 0.4		4.8 ± 0.7
Section B	5.0	5.6 ± 1.0	2.5 ± 0.5	1.6 ± 0.3	2.8 ± 0.1	4.2 ± 0.5
Section C	9.5	5.3 ± 0.5	2.3 ± 0.2	1.5 ± 0.3		4.1 ± 0.2
Section D	14.0	5.2 ± 1.0	1.7 ± 0.2	0.6 ± 0.1		3.9 ± 0.3

Reaction front velocity: High CO_2 and Low Q

Experiment FP3-HC						
Physico-chemical parameters		**Color and Mineralogy**			**Chemical tracer**	**Porosity**
Analytical technique		Binocular lens + Raman + SEM-EDS			EPMA	XMT
Paramaters Observed secondary minerals		**Brown Carbonate + Hematite**	**Intense red Hematite**	**Pink Hematite**	**Ni-Lizardite**	**Grey value**
	Core depth	Zone 1	Zone 2	Zone 3		
	mm	µm/h	µm/h	µm/h	µm/h	µm/h
Section A	0.9	4.9 ± 0.7	3.2 ± 0.9	1.5 ± 0.6		3.9 ± 1.6
Section B	5.7	3.8 ± 0.5	1.7 ± 0.5	1.1 ± 0.2		2.6 ± 0.6
Section C	9.8	2.8 ± 0.6	1.1 ± 0.3	(-)		2.3 ± 0.5
Section D	14.8	2.7 ± 0.7	1.3 ± 0.2	(-)		2.4 ± 0.3

Reaction front velocity: Low CO_2 and High Q

Experiment FP4-LC						
Physico-chemical parameters		**Color and Mineralogy**			**Chemical tracer**	**Porosity**
Analytical technique		Binocular lens + Raman + SEM-EDS			EPMA	XMT
Paramaters Observed secondary minerals		**Brown Carbonate + Hematite**	**Intense red Hematite + Ni-alloys**		**Ni-Lizardite**	**Grey value**
	Core depth	Zone 1	Zone 2	Zone 3		
	mm	µm/h	µm/h	µm/h	µm/h	µm/h
Section A	1.1	5.7 ± 0.5	0.7 ± 0.04	(-)		1.0 ± 0.2
Section B	6.2	2.1 ± 0.2	0.3 ± 0.03	(-)	0.23 ± 0.1	0.9 ± 0.1
Section C	11.2	1.8 ± 0.2	0.3 ± 0.01	(-)		0.9 ± 0.2
Section D	15.9	1.4 ± 0.2	(-)	(-)		0.9 ± 0.2

4.4 Implications of CO_2 geological storage

Geological carbon storage is one of the methods envisaged today for mitigating increasing CO_2 concentration in the Earth's atmosphere (e.g., Kelemen and Matter, 2008; Oelkers et al., 2008). Natural analogs of in situ mineral carbon sequestration in ultramafic bodies present potential alternatives to CO_2 storage (Beinlich et al., 2012; Hansen et al., 2005; Kelemen et al., 2011). Mineral carbonations of ultramafic rocks provide an environmentally safe and permanent solution for CO_2 sequestration (e.g., Pronost et al., 2011). This investigation offers a preliminary basis for the assessment of the carbonation potential of fractured serpentinized peridotite systems that have been flushed with CO_2-rich saline solutions.

This study reveals that the carbonation of peridotite under high dissolved CO_2 concentration (1 mol/L, i.e., pCO_2=20 MPa) shows carbonation rate 2.4 times faster than solutions with 10 times less concentrated in dissolved CO_2 (0.1 mol/L, i.e., pCO_2=10 MPa). This observation agrees with previous studies that determine that CO_2 uptake increases with the dissolved concentration of CO_2 (e.g., O'Connor et al., 2004). High XCO_2 in solution provides strong concentrations of H^+ that promotes olivine dissolution and the precipitation of carbonates is induced by cationic supersaturation conditions mainly provide by olivine dissolution (Kelemen et al., 2011). High concentration of CO_2 in the fluids modifies also the hydrodynamic properties of the rock (porosity). It generates strong primary rock dissolution in the region adjacent to the fracture that leads to an increase in the porosity of the rock. This has a positive feedback on the CO_2-storage especially when it is close to the injection point because it increases the porosity and if the porosity is connected, the permeability of the rock increase and thus helps to maintain the fluid flow.

Carbonation rate was lower during the low flow rate experiment with high XCO_2 in the fluid (FP3-HC) compared to high flow rate experiment with high XCO_2 in the fluid (FP3-HC). This agrees with the observation of Peuble et al (2015) that shows that the increase of the flow rate enhances the carbonation rate. This suggests that an efficient renewal of the fluid in the rock increase the carbonation process. In addition, carbonates are localized in the zone further to the fracture and far from the injection point. However, this observation could also limit long-term carbonation on industrial scale because carbonation reactions could be a

self-limiting process in zones far from the injection well. Carbonate minerals precipitate on the pore space this fact could clog the fluid paths (Hövelmann et al., 2012) decreasing permeability and jeopardizing the effectiveness of the carbonation reaction. This implies that repeated hydro fracturing at depth may become necessary to exploit the full carbonation potential of the reservoir (e.g., Kelemen and Matter, 2008).

5. Summary and conclusions

Interaction between a circulating CO_2-bearing fluid (0.1-1M) at 170°C and 25 MPa into a fractured serpentinized peridotite led to the formation of a reddish reaction front along the fracture characterized by (1) higher porosity degree compared to the unreacted rock, (2) primary minerals that exhibit evidences of dissolution (e.g. voids, etch pits and saw-toothed appearance), and (3) secondary mineral formation, such as hematite, carbonates, Si-rich phase (i.e., amorphous silica) and Fe-Ni oxides. The reaction front is thicker in the inlet part of the samples compared to the outlet part. The reacted fluid show higher concentration of element (Si, Ca, Mg, Fe) in response to primary mineral dissolution.

Both degree of dissolution and secondary mineral precipitation are more elevated when the fluid contain a higher concentration of dissolved CO_2. The mineral assemblage that precipitates is different: (i) Samples interacted with high concentrations of dissolved CO_2 are characterized by the presence of Fe-magnesite (+Ni in the zones adjacent to the fracture), hematite and amorphous silica. Low concentrations of dissolved CO_2 in the fluids are characterized by the presence of magnesite with eventual content on Ca, hematite and (Ni-Fe) oxides on zones adjacent to the fracture. All experiments show an enrichment of Ni in the primitive lizardite in the zones adjacent to the fracture. The zones adjacent to the fracture present a high degree of dissolution and high content of Ni compared to the zones further from the fracture that present less degree of dissolution but high content of carbonates. The presence of nickel in the fluid can be used as a tracer of the progression of the reaction front (1) indicates the higher zones of dissolution and (2) delimit the boundary where there is more presence of carbonates.

Magnesite was the main carbonate precipitated under high concentration of CO_2 in the fluid. This suggests that the Mg/Ca ratios in the outlet fluid are effectively maintained to

saturate with magnesite. However, very few studies have reported magnesite in oceanic peridotites (Gablina et al., 2006), suggesting that it is rare in subseafloor environments or has yet to be sampled. Klein and Garrido (2011) suggest magnesite may form during reaction with clinopyroxene-poor ultramafic rocks such as dunite or completely serpentinized peridotite that has lost of its Ca to solution. In addition, our initial rocks were partially serpentinized and present very small veins of pre-existing carbonates (calcite), suggesting a potential source of Ca in solution when they are dissolved by the interaction with CO_2-rich solutions. Even so, the strong dissolution of olivine provides high concentration of Mg in solution which induces an increase on Mg/Ca ratios and a local increase on pH favouring magnesite saturation. Only Ca-carbonates precipitate in experiments with low concentration of CO_2 in solution which generates low degree of dissolution in the rock and lower Mg/Ca ratios.

Olivine and pyroxenes were preferentially dissolved compared to lizardite under high and low concentrations of dissolved CO_2. Dissolution of olivine and pyroxene can decrease the olivine surface area which can reduce the effective alteration of the peridotite. Experimental observations show that grain boundaries provided by lizardite mesh were preferentially dissolved. This suggests that the dissolution of the microstructure of serpentinized peridotites can outweigh the effect of the decrease in olivine surface area and sustain the peridotite alteration. The migration of the reaction front was faster in the inlet of the samples and lower as approaching the outlet. This suggests the fluid re-equilibrates with the peridotite decreasing progressively their dissolution reactivity. However, the density of carbonates was bigger at the outlet of the samples with high CO_2 concentration in solution, this suggest that the fluid as migrate to the outlet of the sample increase their saturation with carbonates.

This investigation provides a preliminary basis for the assessment of the peridotite carbonation potential in fractured reservoirs. Carbonation rate was lower at low flow rate even if at high concentrations of dissolved CO_2, which suggest efficient renewal of CO2 into the samples. However, carbonation of serpentinized peridotite under high dissolved CO_2 concentration (1 mol/L, i.e., pCO_2=20 MPa) shows carbonation rate 2.4 times faster than solutions with 10 times less concentrated in dissolved CO_2 (0.1 mol/L, i.e., pCO_2=10 MPa). This study demonstrate that controlling the dissolved CO_2 concentrations and the flow rate would allow enhancing/limiting the efficiency of in situ carbonation.

Chapter VI

Conclusions and Perspectives

Seawater-ultramafic rock interaction in regions of high heat flow triggers a complex of chemical reactions that modifies the composition of both the seawater and the rock. This chemical reactions give rise the so-called *serpentinization* and *carbonation* process; the later when $CO_{2(aq)}$ is present in the fluid. Both reactions have special interest on H_2 production, CO_2 storage and development of life. The feedback effects between chemical reactions and physical changes in the rock can modify reaction paths and hydrodynamic properties of the rock that in turn affect the reaction paths and effectiveness of the processes.

This thesis examined the effect of reactive transport in incipient serpentinization and carbonation reactions occurring in ultramafic-influenced hydrothermal systems. Two suite of percolation experiments were performed simulating the percolation of artificial seawater and saline CO_2 rich solutions into ultramafic rocks at conditions relevant during the initial stages of its hydrothermal alteration (170-190°C and 25 MPa). The experiments were performed using a flow-through reactor (Icare-3 bench) that can attain temperatures (<400°C) and pressures (<40 MPa) similar to ocean floor hydrothermal systems. The first suite of experiments evaluates the effect of solute transport in *serpentinization* reaction paths on porous ultramafic material and the second suite of experiments evaluates the *carbonation reaction* processes on serpentinized peridotites mechanically fractured.

The effect of solute transport in incipient serpentinization reaction paths

In this thesis, I put in light the effect of the local mean fluid velocity on the reaction path during serpentinization process. Four reactive percolation experiments were performed at constant flow rate. The distribution of fluid velocities in the samples was the dominant transport parameter that changes from one experiment to the other. The mean fluid velocity relates the flow rate (Q) with the surface (S) and porosity (φ) of the sample via: $v=Q/S*\varphi$. The local Péclet number (Pe) is directly controlled by the local mean fluid velocity; which determines the transport mechanism (advection or/and diffusion) dominated at the pore-scale. Advection dominates at fast fluid velocities and diffusion at slow fluid velocities.

The results of this study show that the development of different compositional trends (e.g. Si-rich fluids or Mg-rich fluids) was strongly dependant on local mean fluid velocity in

the reaction domains. The mean fluid velocity controls the thickness of the diffusive boundary layers in the reaction domains and the interplay between transport and reaction kinetics controls the chemical fluxes between the fluid-mineral interface and the bulk solution in the diffusive boundary layers. Therefore, chemical fluxes will control the local fluid composition and the serpentinization reaction path. The difference in the outlet fluid composition between experiments has served to develop two end-member scenarios depending on the renewing of solutes at the mineral reactive surface:

(1) *Transport-controlled scenario* occurs at low flow rate. They are characterized by large diffusion zones (Pe<1) where efficient mixing of the reactants and products takes place. In these zones the detachment of olivine Si-tetrahedra and consequently hydration produces an increase on the local pH that favors the precipitation of brucite after the Mg detached from olivine and the aqueous Mg from the incoming fluids. The progression of the reaction with time produces an increase of the local $aSiO_{2(aq)}$ in the diffusion zone that destabilized the brucite and serpentine precipitates probably after brucite silicification.

(2) *Kinetics-controlled scenario* occurs at high flow rate. Advection transport dominates (Pe>1) at the pore scale and efficiently renews reactants and products at the reaction surface. The fast renewal of reactants and products in the sample produces high chemical gradients between the mineral surface and the bulk fluid enhancing high olivine dissolution rates. Surprisingly, $SiO_{2(aq)}$ was deficient in the outlet fluid rather than Mg, this evidences SiO_2 is effectively trapped in the samples, probably as silica-rich layers as was already postulated on olivine dissolution experiments (e.g., Daval et al., 2013). In addition, the results show that serpentine was effectively trapped in kinetics controlled scenarios.

For a given pore structure, the fraction of diffusion-controlled zones increases as the sample scale flow rate decreases. This suggests that transport-controlled and kinetics-controlled scenarios coexist in porous samples for intermediate flow rates.

This study can be applied to ultramafic hosted hydrothermal systems along the mid-ocean ridges. Low porosity zones such as mineral boundaries and micro-cracks are mainly dominated by diffusion transport. Here, transport-controlled scenarios can be applied. The local increase of pH of the hydrothermal fluid resulted from olivine dissolution and the slow renewal of fluid in the pore leads to ion saturation and precipitation of brucite, followed by

serpentine. However, highly permeable zones (for example oceanic detachment faults and fractures) are controlled by advection transport; here kinetics-controlled scenarios can be applied. High amounts of serpentine precipitate in this zone, which in turn clog flow paths more efficiently compared to diffusion-dominated domains.

This study has demonstrated that a control of flow infiltration rate at the pore-scale can controls the local fluid compositions and the development of different reaction paths at the sample-scale. These new supporting data will allow numerical models to better simulate serpentinization reactions from the pore-scale to the sample-scale and calls into question the size of the rig. Analytical techniques such as X-ray microtomography of high resolution can be considered as powerful tools to monitor the physical changes at the pore-scale. This thesis had provided advances in this area through the use of special small titanium capsules for X-ray analysis but further development of the protocol is still necessary to better process the resulting data

The effect of solute transport and dissolved CO_2 concentration in carbonation of fractured serpentinized peridotite reservoirs

This thesis has brought for the first time new insights of the process that triggers the percolation of CO_2-rich fluids into fractured serpentinized peridotite reservoirs at the lab-scale.

The results of the experiments show that interaction between a circulating CO_2-bearing fluids and a fractured serpentinized peridotite led to the formation of a reddish reaction front along the fracture. The reaction front is characterized by: (1) holes that indicate an increase in the porosity and result from strong dissolution in this zone and (2) secondary mineral formation. Monitoring the reaction front length had provided information about the kinetics of the dissolution and precipitation reactions at different CO_2 concentrations and flow injection rates.

The migration of the reaction front was faster in the inlet of the samples and slower towards the outlet. This suggests that the fluid re-equilibrates with the peridotite, decreasing progressively its ability to dissolve. However, the density of carbonates was bigger at the outlet of the samples compared to the inlet. This suggests that the fluid had migrated to the

outlet of the sample and increases its saturation with respect to carbonates. Magnesite was the main carbonate precipitated under high concentration of CO_2 in the fluid, whereas (Ca-Mg) carbonate was the main carbonate precipitated under low concentration of CO_2 in the fluid. This suggests that the Mg/Ca ratios in the outlet fluid are effectively maintained to saturate with magnesite under high CO_2 concentration in the fluid.

Carbonation rate was lower at low flow rate (Q=2.4 ml/h) than at high flow rates (Q=6 ml/h), even if the solution contains high concentrations of dissolved CO_2. An efficient renewal of the fluid in the rock is required to increase the carbonation process. On the other hand, carbonation of serpentinized peridotite under high dissolved CO_2 concentration (1 mol/L, i.e., pCO_2=20 MPa) shows carbonation rate 2.4 times faster than solutions with 10 times less concentrated in dissolved CO_2 (0.1 mol/L, i.e., pCO_2=10 MPa). High concentration of CO_2 in the fluids generates strong primary rock dissolution in the region adjacent to the fracture. This observation favours the industrial scale injection of CO_2 into peridotite as it will tend to increase porosity and permeability near the injection well. However, carbonation reactions could be a self-limiting process in zones far from the injection well, as carbonates are effectively trapped in the pore space and clogs fluid path. The control of the concentration of dissolved $CO_{2(g)}$ and the fluid flow rate can enhance/limit the efficiency of CO_2-storage in these non-conventional reservoirs.

This study has demonstrated that a control of flow infiltration rate and the concentration of CO_2 control the carbonation potential of serpentinized peridotite in fracture reservoirs. These new supporting data provides new insights for the study of: (1) natural carbonation systems, such as litsvenites (fuchsite-quartz-carbonate assemblage produced by alteration of ultramafic rocks) collected from the Hole BT1B from the Oman Drilling Project that exhibit some similar features (i.e. reddish coloration, dissolution holes and secondary Si-phases and carbonates) compared to our experimental reacted rock and (2) potential consideration of fractured reservoirs of serpentinized peridotite for CO_2-storage.

Future research directions

❖ *Serpentinization experiments*

It should be interesting to check if the two end-member scenarios proposed for incipient serpentinization reaction paths are maintained for longer reaction times. Reactive percolation experiments should be done in experimental duration more than one month. However the experimental challenges that entails longer reactive percolation experiments and the slow reaction kinetics at the conditions here used (T=170°C, P=25MPa, seawater), suggest that it would be convenient to use a chemical catalyst such as aluminium or alkaline solutions to accelerate the reaction.

The flow rate controls the olivine dissolution and serpentine precipitation, i.e., very high flow rates produces high degree of olivine dissolution but also produces more precipitation of serpentine. It should be interesting to test this effect on other silicate minerals that have the potential to serpentinize (e.g., pyroxenes).

The method developed to estimate dissolution and/or precipitation after X-ray imaging before and after the experiments is very promising to use with cohesive samples such as natural rock or sintered aggregates with no displacement of small grains into the samples.

❖ *Carbonation experiments*

It should be interesting to test the effect of the fluid composition on carbonation reaction paths: *(i)* Experiments under solutions rich in NaOH or $NaHCO_3$ could be used to accelerate carbonation and check the extent of the reaction during short experimental time. *(ii)* Also it should be interesting to test the effect of the ion strength of the solution (i.e., water activity). Experiments with pure water could be performed in order to achieve higher water activity. *(iii)* Ca-rich solutions could be also very interesting to test the effect of the Ca/Mg ratios in the fluid on the composition of the precipitated carbonates during the carbonation reaction.

Finally, it should be interesting to test the effect of the fracture roughness on the carbonation reactions. Several experiments could be performed on saw cores of peridotite. It should be also interesting to test the reactivity of peridotite fractures reservoirs with a developed fracture network. Several experiments could be performed under the same experimental conditions but in changing the fracture network (i.e. number of fractures in the sample). However, after the challenges that entail mechanical fracturing, sawing the samples could be a solution even if the fracture roughness is lost.

References

A

Abramson, E.H., Brown, M., Slutsky, L.J., Zaug, J., 1997. The elastic constants of San Carlos olivine to 12 GPa. J. Geophys. Res. 102, 12252–12263. doi:10.1029/97JB00682

Allen, D.E., Seyfried, W.E., 2004. Serpentinization and heat generation: Constraints from Lost City and Rainbow hydrothermal systems. Geochim. Cosmochim. Acta 68, 1347–1354. doi:10.1016/j.gca.2003.09.003

Allen, D.E., Seyfried, W.E., 2003. Compositional controls on vent fluids from ultramafic-hosted hydrothermal systems at mid-ocean ridges: An experimental study at 400°C, 500 bars. Geochim. Cosmochim. Acta 67, 1531–1542. doi:10.1016/S0016-7037(02)01173-0

Alt, J.C., 1995. Subseafloor processes in Mid-Ocean ridge hydrothermal systems. Geophys. Monogr. 91, 85–114. doi:10.1017/CBO9781107415324.004

Alt, J.C., Shanks, W., 1998. Sulfur in serpentinized oceanic peridotites: Serpentinization processes and microbial sulfate reduction. J. Geophys. Res. 103, 9917–9929. doi:10.1029/98JB00576

Andreani, M., Daniel, I., 2013a. Aluminium speeds up the hydrothermal alternation of olivine. Am. Mineral. 98, 1738–1744.

Andreani, M., Muñoz, M., Marcaillou, C., Delacour, A., 2013b. μXANES study of iron redox state in serpentine during oceanic serpentinization. Lithos 178, 70–83. doi:10.1016/j.lithos.2013.04.008

Andreani, M., Escartin, J., Delacour, A., Ildefonse, B., Godard, M., Dyment, J., Fallick, A., Fouquet, Y., 2014. Tectonic structure, lithology, and hydrothermal signature of the Rainbowmassif (Mid-Atlantic Ridge 36°14'N). Geochemistry Geophys. Geosystems 18, 1541–1576. doi:10.1002/2014GC005684.Key

Andreani, M., Luquot, L., Gouze, P., Godard, M., Gibert, B., 2009. Experimental Study of Carbon Sequestration Reactions Controlled by the Percolation of CO_2-Rich Brine through Peridotites. Environ. Sci. Technol. 43, 1226–1231.

Andreani, M., Mével, C., Boullier, A.M., Escartín, J., 2007. Dynamic control on serpentine crystallization in veins: Constraints on hydration processes in oceanic peridotites. Geochemistry, Geophys. Geosystems 8. doi:10.1029/2006GC001373

Angiboust, S., Wolf, S., Burov, E., Agard, P., Yamato, P., 2012. Effect of fluid circulation on subduction interface tectonic processes : Insights from thermo-mechanical numerical modelling. Earth Planet. Sci. Lett. 357–358, 238–248. doi:10.1016/j.epsl.2012.09.012

Appelo, C.A.J., Parkhurst, D.L., Post, V.E.A., 2014. Equations for calculating hydrogeochemical reactions of minerals and gases such as CO_2 at high pressures and temperatures. Geochim. Cosmochim. Acta 125, 49–67. doi:10.1016/j.gca.2013.10.003

Awad, A., Koster Van Groos, A.F., Guggenheim, S., 2000. Forsteritic olivine: Effect of crystallographic direction on dissolution kinetics. Geochim. Cosmochim. Acta 64, 1765–1772. doi:10.1016/S0016-7037(99)00442-

B

Bach, W., Garrido, C.J., Paulick, H., Harvey, J., Rosner, M., 2004. Seawater-peridotite interactions: First insights from ODP Leg 209, MAR 15°N. Geochemistry, Geophys. Geosystems 5. doi:10.1029/2004GC000744

Bach, W., Klein, F., 2009. The petrology of seafloor rodingites: Insights from geochemical reaction path modeling. Lithos 112, 103–117. doi:10.1016/j.lithos.2008.10.022

Bach, W., Paulick, H., Garrido, C.J., Ildefonse, B., Meurer, W.P., Humphris, S.E., 2006. Unraveling the sequence of serpentinization reactions : petrography , mineral chemistry , and petrophysics of serpentinites from MAR 15 ° N (ODP Leg 209 , Site 1274) 33, 4–7. doi:10.1029/2006GL025681

Baker, E., German, C., Ederfield, H., 1995. Seafloor Hydrothermal Systems: Physical, Chemical, Biological, and Geological Interactions. Geophys. Monogr. 91, 47–71.

Bales, R.C., Morgan, J.J., 1985. Dissolution kinetics of chrysotile at pH 7 to 10. Geochim. Cosmochim. Acta 49, 2281–2288. doi:10.1016/0016-7037(85)90228-5

Bandura, A. V., Lvov, S.N., 2006. The Ionization Constant of Water over Wide Ranges of Temperature and Density. J. Phys. Chem. Ref. Data 35, 15–30. doi:10.1063/1.1928231

Bard, A., Faulkner, L., 1980. Electrochemical Methods: Fundamentals and Applications. JohnWiley and Sons, New York.

Barnes, I., Oneil, J.R., Trescases, J.J., 1978. Present Day Serpentinization in New-Caledonia, Oman and Yugoslavia. Geochim. Cosmochim. Acta 42, 144–145. doi:10.1016/0016-7037(78)90225-9

Barnes, I., O'Neil, J., 1969. The Relationship between Fluids in Some Fresh Alpine-Type Ultramafks and Possible Modern Serpentinization, Western United States. Geol. Soc. Am. Bull. 80, 1947–1960.

Baruchel, J., Buffiére, J., Cloetens, P., DiMiciel, M., Ferrie, E., Ludwig, W., 2006. Advances in synchrotron radiation microtomography. ScrMater 55.

Baveye, P.., Laba, M., Otten, W., Bouckaert, L., Dello Sterpaio, P., Goswami, R.., Grinev, D., Houston, A., Hu, Y., Liu, J., Mooney, S., Pajor, R., Sleutel, S., Tarquis, A., Wang, W., Wei, Q., Sezgin, M., 2010. Observer-dependent variability of the thresholding step in the quantitative analysis of soil images and X-ray microtomography data. Geoderma.

Bear, J., 1972. Dynamics of Fluids in Porous Media, Dover.

Bearat, H., McKelvy, M.J., Chizmeshya, A.V.G., Gormley, D., Nunez, R., Carpenter, R.W., Squires, K., Wolf, G.H., 2006. Carbon sequestration via asueous olivine mineral carbonation: role of passivating layer formation. Environ. Sci. Technol. 40, 4802–4808.

Beard, J.S., Frost, B.R., Fryer, P., McCaig, A., Searle, R., Ildefonse, B., Zinin, P., Sharma, S.K., 2009. Onset and progression of serpentinization and magnetite formation in Olivine-rich troctolite from IODP hole U1309D. J. Petrol. 50, 387–403. doi:10.1093/petrology/egp004

Békri, S., Thovert, J., Adler, P., 1997. Dissolution and deposition in fractures. Eng. Geol. 48, 283–308.

Bénézeth, P., Saldi, G.D., Dandurand, J.L., Schott, J., 2011. Experimental determination of the solubility product of magnesite at 50 to 200°C. Chem. Geol. 286, 21–31. doi:10.1016/j.chemgeo.2011.04.016

Bénézeth, P., Stefánsson, A., Quentin, G., Schott, J., 2013. Mineral Solubility and Aqueous Speciation Under Hydrothermal Conditions to 300 °C – The Carbonate System as an Example. Rev. Mineral. Geochemistry 76, 81–133.

Berndt, M.E., Allen, D.E., Seyfried, W.E., 1996. Reduction of CO_2 during serpentinization of olivine at 300°C and 500bar. Geology 24, 351–354. doi:10.1130/0091-7613(1996)024<0351

Berman, R.., Engi, M., Greenwood, H.J., Brown, T.H., 1986. Derivation of internally-consistent thermodynamic data by the technique of mathematical programming : A review with application to the system MgO-SiO2-H2O. J. Petrol. 27, 1331–1364.

Bethke, C., 2008. Geochemical and Biogeochemical Reaction Modeling, second. Ed. Cambridge Univ. Press, New York.

Bethke, C.M., 1994. The Geochemist's WorkbenchTM, version 2.0.A User's Guide to Rxn, Act2, React, and Gtplot. Hydrogeology Program, University of Illinois.

Birle, J., Gibbs, G., Moore, P., Smith, J.V., 1968. Crystal structures of natural olivines (Mg0.9Fe0.1)2SiO4 from Minas Gerais, Brazil. Am. Mineral. 53, 807–824.

Bischoff, J.L., Seyfried, W.E., 1978. Hydrothermal Chemistry of seawater from 25° to 350°C. Am. J. Sci. 278, 838–860.

Blum, A., Lasaga, A., 1988. Role of surface speciation in the low-temperature dissolution of minerals. Nature 331.

Blount, C.W., Dickson, F.W., 1969. The solubility of anhydrite (CaSO4) in NaCl-H_2O from 100 to 450 ° C and 1 to 1000 bars. Geochim. Cosmochim. Acta 33, 227–245. doi:10.1016/0016-7037(69)90140-9

Bodinier, J.., Godard, M., 2003. Orogenic, Ophiolitic, and Abyssal Peridotites, in: Treatise on Geochemistry. Elsevier, pp. 1–73. doi:10.1016/B0-08-043751-6/02004-1

Bonnemains.D, Escartin.J, Mevel.M, Andreani.M, Verlaguet.A, 2017. Pervasive silicification and hanging wall overplating along the 13°20'N oceanic detachment fault (Mid-Atlantic Ridge). Geochemistry, Geophys. Geosystems 1–26. doi:10.1002/2016GC006679

Boschi, C., Dini, A., Früh-Green, G.L., Kelley, D.S., 2008. Isotopic and element exchange during serpentinization and metasomatism at the Atlantis Massif (MAR 30°N): Insights from B and Sr isotope data. Geochim. Cosmochim. Acta 72, 1801–1823. doi:10.1016/j.gca.2008.01.013

Boudier, F., Nicolas, A., Mainprice, D., 2005. Does Anisotropy of Thermal Contraction Control Hydrothermal Circulation at the Moho Level below Fast Spreading Oceanic Ridges? Int. Geol. Rev. 47, 101–112. doi:10.2747/0020-6814.47.1.101

Brantley, S., Mellott, N., 2000. Surface area and porosity of primary silicate minerals. Am. Mineral. 85, 1767–1783.

Brazelton, W.J., Nelson, B., Schrenk, M.O., Christner, B.C., State, L., 2012. Metagenomic evidence for H2 oxidation and H2 production by serpentinite-hosted subsurface microbial communities. Front. Microbiol. 2. doi:10.3389/fmicb.2011.00268

Butterfield, D.A., McDuff, R.E., Mottl, M.J., Lilley, M.D., Lupton, J.E., Massoth, G.J., 1994. Gradients in the Composition of Hydrothermal Fluids From the Endeavor Segment Vent Field - Phase-Separation and Brine Loss. J. Geophys. Res. Earth 99, 9561–9583. doi:10.1029/93jb03132

C

Cannat, M., Fontaine, F., Escartín, J., 2010. Serpentinization and Associated Hydrogen and Methane Fluxes at Slow Spreading Ridges. Divers. Hydrothermal Syst. Slow Spreading Ocean Ridges 241–264. doi:10.1029/2008GM000760

Carman, P., 1937. Fluid flow through granular beds. Trans. Inst. Chem 15, 150–166.

Charlou, J.L., Donval, J.P., Douville, E., Jean-Baptiste, P., Radford-Knoery, J., Fouquet, Y., Dapoigny, A., Stievenard, M., 2000. Compared geochemical signatures and the evolution of Menez Gwen (35°50N) and Lucky Strike (37°17N) hydrothermal fluids, south of the Azores Triple Junction on the Mid-Atlantic Ridge. Chem. Geol. 171, 49–75. doi:10.1016/S0009-2541(00)00244-8

Charlou, J.L., Donval, J.P., Fouquet, Y., Jean-Baptiste, P., Holm, N., 2002. Geochemistry of high H2 and CH4 vent fluids issuing from ultramafic rocks at the Rainbow hydrothermal field (36°14′N,MAR). Chem. Geol. 191, 345–359. doi:10.1016/S0009-2541(02)00134-1

Charlou, J.L., Donval, J.P., Jean-Baptiste, P., Dapoigny, A., Rona, P.A., 1996. Gases and helium isotopes in high temperature solutions sampled before and after ODP Leg 158 drilling at TAG hydrothermal field (26°N, MAR). Geophys. Res. Lett. 23, 3491–3494. doi:10.1029/96GL02141

Charlou, J.L., Donval, J.P., Konn, C., Ondréas, H., Fouquet, Y., Jean-Baptiste, P., Fourré, E., 2013. High Production and Fluxes of H_2 and CH_4 and Evidence of Abiotic Hydrocarbon Synthesis by Serpentinization in Ultramafic-Hosted Hydrothermal Systems on the Mid-Atlantic Ridge. Divers. Hydrothermal Syst. Slow Spreading Ocean Ridges 265–296. doi:10.1029/2008GM000752

Charlou, J.L., Donval, J.P., Jean-Baptiste, P., Dapoigny, A., Rona, P.A., 1996. Gases and helium isotopes in high temperature solutions sampled before and after ODP Leg 158 drilling at TAG hydrothermal field (26°N, MAR). Geophys. Res. Lett. 23, 3491–3494. doi:10.1029/96GL02141

Chen, Y., Brantley, S., 1998. Diopside and anthophyllite dissolution at 25° and 90 °C and acid pH. Chem. Geol. 147, 233–248.

Chen, Y., Brantley, S.L., 2000. Dissolution of forsteritic olivine at 65°C and 2<pH<5. Chem. Geol. 165, 267–281. doi:10.1016/S0009-2541(99)00177-1

Chetverikov, D., Kropatsch, W., 1993. Computer Analysis of Images and Patterns, Springer-V. ed. Springer-Verlang.

Chiba, H., Masuda, H., Lee, S.Y., Fujioka, K., 2001. Chemistry of hydrothermal fluids at the TAG active mound, MAR 26. Geophys. Res. Lett. 28, 2919–2922. doi:10.1029/2000GL012645

Chizmeshya, A.V.G., McKelvy, M.J., Squires, K., Carpenter, R.W., Béarat, H., 2007. A novel approach to mineral carbonation: Enhancing carbonation while avoiding mineral pretreatment process cost. Arizona State Univ. Dep.

Chou, L., Wollast, R., 1985. Steady-state kinetics and dissolution mechanisims of albite. Am. J. Sci. 285, 963–993.

Claesson, J., Bohloli, B., 2002. Brazilian test: Stress field and tensile strength of anisotropic rocks using an analytical solution. Int. J. Rock Mech. Min. Sci. 39, 991–1004. doi:10.1016/S1365-1609(02)00099-0

Cnudde, V., Boone, M.N., 2013. Earth-Science Reviews High-resolution X-ray computed tomography in geosciences : A review of the current technology and applications. Earth Sci. Rev. 123, 1–17. doi:10.1016/j.earscirev.2013.04.003

Cole, D., Ohmoto, H., Jacobs, G.K., 1992. Isotopic exchange in mineral-fluid systems : III. Rates and mechanisms of oxygen isotope exchange in the system granite±H2O±NaCl ±KCl at hydrothermal conditions. Geochemica Cosmochim. Acta 56, 445–466.

Coleman, R.G., 1971. Petrologic and Geophysical Nature of Serpentinites. Geol. Soc. Am. 82, 897–918. doi:10.1130/0016-7606(1971)82

Crundwell, F.K., 2014a. The mechanism of dissolution of forsterite, olivine and minerals of the orthosilicate group. Hydrometallurgy 150, 68–82. doi:10.1016/j.hydromet.2014.09.006

Crundwell, F.K., 2014b. The mechanism of dissolution of minerals in acidic and alkaline solutions: Part II Application of a new theory to silicates, aluminosilicates and quartz. Hydrometallurgy 149, 265–275. doi:10.1016/j.hydromet.2014.07.003

D

Darcy H. P. G., 1856. Les Fontaines Publiques de la Ville de Dijon (The Public Fountains of the City of Dijon), Dalmont. Paris.

Daval, D., Sissmann, O., Menguy, N., Saldi, G.D., Guyot, F., Martinez, I., Corvisier, J., Garcia, B., Machouk, I., Knauss, K.G., Hellmann, R., 2011. Influence of amorphous silica layer formation on the dissolution rate of olivine at 90°C and elevated pCO_2. Chem. Geol. 284, 193–209. doi:10.1016/j.chemgeo.2011.02.021

Daval, D., Sissman, O., Corvisier, J., Garcia, B., Martinez, I., Guyot, F., Hellmann, R., 2010. The effect of silica coatings on the weathering rates of wollastonite ($CaSiO_3$) and forsterite (Mg_2SiO_4): an apparent paradox ? The effect of silica coatings on the weathering rates of wollastonite. Water-Rock Interact. P. Birkle, 713–716.

Davies, C., 1962. Ion Association. London, Butterworths 37–53.

Debye, P., Hückel, E., 1923. The theory of electrolytes. I. Lowering of freezing point and related phenomena. Phys. Zeitschrift 24, 185–206.

de Marsily, G., 1986. Quantitative Hydrogeology-Groundwater Hydrology for Engineers. Academic Press, New-York.

Deschamps, F., Godard, M., Guillot, S., Hattori, K., 2013. Geochemistry of subduction zone serpentinites: A review. Lithos 178, 96–127. doi:10.1016/j.lithos.2013.05.019

Douville, E., Charlou, J.L., Oelkers, E.H., Bienvenu, P., Jove Colon, C.F., Donval, J.P., Fouquet, Y., Prieur, D., Appriou, P., 2002. The Rainbow vent fluids (36°14°N, MAR): The influence of ultramafic rocks and phase separation on trace metal content in Mid-Atlantic Ridge hydrothermal fluids. Chem. Geol. 184, 37–48. doi:10.1016/S0009-2541(01)00351-5

Duan, Z., Sun, R., 2003. An improved model calculating CO_2 solubility in pure water and aqueous NaCl solutions from 273 to 5333 K and from 0 to 2000 bar. Chem Geol 193, 257–271.

Dyment, J., Arkani-hamed, J., Ghods, A., 1997. Contribution of serpentinized ultramafics to marine magnetic anomalies at slow and intermediate spreading centres : insights from the shape of the anomalies. Geophys. J. Int. 129, 691–701.

E

Edmond, J., Measures, C., McDuff, R., Chan, L., Collier, R., Grant, B., 1979. Ridge crest hydrothermal activity and the balances of the major and minor elements in the ocean. Earth Planet. Sci. Lett. 46, 1–18.

Eggleton, R.., 1986. The relation between crystal structure and silicate weathering rates. Rates Chem. Weather. Rocks Miner. 2.

Elderfield, H., Schultz, A., 1996. Mid-Ocean Ridge Hydrothermal Fluxes and the Chemical Composition of the Ocean. Annu. Rev. Earth Planet. Sci. 24, 191–224. doi:10.1146/annurev.earth.24.1.191

Emmanuel, S., Berkowitz, B., 2006. Suppression and stimulation of seafloor hydrothermal convection by exothermic mineral hydration. Earth Planet. Sci. Lett. 243, 657–668. doi:10.1016/j.epsl.2006.01.028

Escartin, J., Hirth, G., Evans, B., 1997. Nondilatant brittle deformation of serpentinites : Implications for Mohr-Coulomb theory and the strength of faults. J. Geophys. Res. 102, 2897–2913.

Escartín, J., Hirth, G., Evans, B., 2001. Strength of slightly serpentinized peridotites: Implications for the tectonics of oceanic lithosphere. Geology 29, 1023–1026. doi:10.1130/0091-7613(2001)029<1023:SOSSPI>2.0.CO

Evans, B.W., 2008. Control of the products of serpentinization by the Fe2+ Mg-1 exchange potential of olivine and orthopyroxene. J. Petrol. 49, 1873–1887. doi:10.1093/petrology/egn050

Evans, B.W., 2004. The Serpentinite Multisystem Revisited : Chrysotile Is Metastable. Int. Geol. Rev. 46, 479–506.

Evans, B.W., Hattori, K., Baronnet, A., 2013. Serpentinite: What, why, where? Elements 9, 99–106. doi:10.2113/gselements.9.2.99

Evans, B.W., Johannes, W., Oterdoom, H., Trommsdorf, V., 1976. Stability of chrysotile and antigorite in the serpentine multisystem. Schweiz. Miner. Petrogr. Mitt 56, 79–93.

F

Farough, A., Lowell, R.P., Bodnar, R.J., Caddick, M.J., Hole, J.A., Rimstidt, J.D., 2015. An experimental study on characterization of physical properties of ultramafic rocks and controls on evolution of fracture permeability during serpentinization at hydrothermal conditions.

Farough, A., Moore, D.E., Lockner, D.A., Lowell, R.P., 2016. Evolution of fracture permeability of ultramafic rocks undergoing serpentinization at hydrothermal conditions: An experimental study. Geochemistry Geophys. Geosystems 17, 44–55. doi:10.1002/2015GC005973.

Földvári, M., 2011. Handbook of thermogravimetric system of minerals and its use in geological practice. Geological Institute of Hungary.

Foustoukos, D., Seyfried, W.E.J., 2004. Hydrocarbons in Hydrothermal Vent Fluids: The Role of Chromium-Bearing Catalysts. Science (80). 304. doi:10.1126/science.1096033

Frost, B.R., 1985. On the stability of sulfides, oxides, and native metals in serpentinite. J. Petrol. 26, 31–63. doi:10.1093/petrology/26.1.31

Frost, B.R., Beard, J.S., 2007. On Silica Activity and Serpentinization. J. Petrol. 48, 1931–1368. doi:10.1093/petrology/egm021

Früh-Green, G.L., Connolly, J.A.D., Plas, A., Kelley, D.S., Grobéty, B., 2004. Serpentinization of oceanic peridotites: Implications for geochemical cycles and biological activity. Geophys. Monogr. Ser. 144, 119–136. doi:10.1029/144GM08

Früh-Green, G.L., Kelley, D.S., Bernasconi, S.M., Karson, J.A, Ludwig, K.A, Butterfield, D.A, Boschi, C., Proskurowski, G., 2003. 30,000 Years of Hydrothermal Vent Field. Science (80). 301, 495–498.

Früh-green, G.L., Weissert, H., Bernoulli, D., 1990. A multiple fluid history recorded in Alpine ophiolites. J. Geol. Soc. London. 147, 959–970.

Fryer, P., 2002. Recent Studies of Serpentinite Occurrences in the Oceans : Mantle-Ocean Interactions in the Plate Tectonic Cycle 62, 257–302.

G

Gablina, F., Semkova, T., Stepanova, T., Gor'kova, N., 2006. Diagenetic alterations of copper sulfides in modern ore-bearing sediments of the Logatchev-1 hydrothermal field (Mid-Atlantic Ridge 14°450 N). Lithol. Miner. Resour 41, 27–44.

Garcia, B., Beaumont, V., Perfetti, E., Rouchon, V., Blanchet, D., Oger, P., Dromart, G., Huc, A.Y., Haeseler, F., 2010. Experiments and geochemical modelling of CO_2 sequestration by olivine: Potential, quantification. Appl. Geochemistry 25, 1383–1396. doi:10.1016/j.apgeochem.2010.06.009

Gerdemann, S.J., O'Connor, W.K., Dahlin, D.C., Penner, L.R., Rush, H., 2007. Ex situ aqueous mineral carbonation. Environ. Sci. Technol. 41, 2587–2593. doi:10.1021/es0619253

German, C.R., Seyfried, W.E., 2014. Hydrothermal Processes, 2nd ed, The Oceans and Marine Geochemistry. Elsevier Ltd. doi:10.1016/B978-0-08-095975-7.00607-0

German, C., Baker, E., Mevel, C., Tamaki, K., 1998. Hydrothermal activity along the Southwest Indian Ridge. Nature 395, 490–492.

German, C.R., Lin, J., 2004. The Thermal Structure of the Oceanic Crust , Ridge-Spreading and Hydrothermal Circulation : How Well Do We Understand Their Inter-Connections ? 1–18.

Ghanbarian, B., Hunt, A.G., Ewing, R.P., Sahimi, M., 2013. Tortuosity in Porous Media: A Critical Review. Soil Sci. Soc. Am. J. 77, 1461. doi:10.2136/sssaj2012.0435

Giammar, D.E., Bruant, R.G., Peters, C.A., 2005. Forsterite dissolution and magnesite precipitation at conditions relevant for deep saline aquifer storage and sequestration of carbon dioxide. Chem. Geol. 217, 257–276. doi:10.1016/j.chemgeo.2004.12.013

Gislason, S.R., Oelkers, E.H., 2003a. Mechanism, rates, and consequences of basaltic glass dissolution: II. An experimental study of the dissolution rates of basaltic glass as a function of pH and temperature. Geochim. Cosmochim. Acta 67, 3817–3832. doi:10.1016/S0016-7037(03)00176-5

Gislason, S.R., Oelkers, E.H., 2003b. Mechanism, rates, and consequences of basaltic glass dissolution: II. An experimental study of the dissolution rates of basaltic glass as a function of pH and temperature. Geochim. Cosmochim. Acta 67, 3817–3832. doi:10.1016/S0016-7037(00)00176-5

Godard, M., Luquot, L., Andreani, M., Gouze, P., 2013. Incipient hydration of mantle lithosphere at ridges: A reactive-percolation experiment. Earth Planet. Sci. Lett. 371–372, 92–102. doi:10.1016/j.epsl.2013.03.052

Goff, F., Lackner, K.., 1998. Carbon dioxide sequestering using ultramafic rocks. Environ. Geosci. 5, 89–101.

Golubev, S. V, T, O.S.P., Schott, J., 2005. Experimental determination of the effect of dissolved CO2 on the dissolution kinetics of Mg and Ca silicates at 25°C. Chem. Geol. 217, 227–238. doi:10.1016/j.chemgeo.2004.12.011

Gouze, P., Luquot, L., 2011. X-ray microtomography characterization of porosity, permeability and reactive surface changes during dissolution. J. Contam. Hydrol. 120–121, 44–55. doi:10.1016/j.jconhyd.2010.07.004

Grozeva, N.G., Klein, F., Seewald, J.S., Sylva, S.P., 2017. Experimental study of carbonate formation in oceanic peridotite. Geochim. Cosmochim. Acta 199, 264–286. doi:10.1016/j.gca.2016.10.052

Gudbrandsson, S., Wolff-Boenisch, D., Gislason, S.R., Oelkers, E.H., 2011. An experimental study of crystalline basalt dissolution from 2<pH<11 and temperatures from 5 to 75°C. Geochim. Cosmochim. Acta 75, 5496–5509. doi:10.1016/j.gca.2011.06.035

Guyon, E., Hulin, J.., Petit, L., 2001. Hydrodynamique Physique. EDP/CNRS.

Guyot, F., Daval, D., Dupraz, S., Martinez, I., Ménez, B., Sissman, O., 2011. CO_2 geological storage: The environmental mineralogy perspective. Comptes Rendus Geosci. 343, 246–259. doi:10.1016/j.crte.2010.12.007

Gvirtzman, H., Gorelick, S.M., 1991. Dispersion and advection in unsaturated porous media enhanced by anion exclusion. Nature 352, 793–795. doi:doi:10.1038/352793a0

H

Haar, L., Gallagher, J.., Kell, G.., 1984. NBS/NRC steam tables: thermodynamic and transport properties and computer programs for vapor and liquid states of water in SI units.

Hänchen, M., Prigiobbe, V., Storti, G., Seward, T.M., Mazzotti, M., 2006. Dissolution kinetics of fosteritic olivine at 90-150 °C including effects of the presence of CO_2. Geochim. Cosmochim. Acta 70, 4403–4416. doi:10.1016/j.gca.2006.06.1560

Harrison, A.L., Dipple, G.M., Power, I.M., Mayer, K.U., 2015. Influence of surface passivation and water content on mineral reactions in unsaturated porous media: Implications for brucite carbonation and CO2 sequestration. Geochim. Cosmochim. Acta 148, 477–495. doi:10.1016/j.gca.2014.10.020

Helgeson, H., 1969. Thermodynamics of hydrothermal systems at elevated temperatures and pressures. Am. J. Sci. 26, 729–804.

Helgeson, H.C., Delany, J.M., Nesbitt, H.W., Bird, D.K., 1978. Summary and Critique of the Thermodynamic Properties of Rock-Forming Minerals., American Journal of Science.

Helgeson, H.C., Kirkham, D.H., Flowers, G.C., 1981. Theoretical prediction of the thermodynamic behavior of aqueous electrolytes at high pressures and temperatures. IV. Calculation of activity coefficients, osmotic coefficients, and apparent molal and standard and relative partial molal properties to 600. Am. J. Sci. 281, 1249–1516.

Hellmann, R., Wirth, R., Daval, D., Barnes, J.P., Penisson, J.M., Tisserand, D., Epicier, T., Florin, B., Hervig, R.L., 2012. Unifying natural and laboratory chemical weathering with interfacial dissolution-reprecipitation: A study based on the nanometer-scale chemistry of fluid-silicate interfaces. Chem. Geol. 294–295, 203–216. doi:10.1016/j.chemgeo.2011.12.002

Hem, J.., 1985. Study and interpretation of the chemical characteristics of natural water. U.S. Geological Survey Water-Supply Paper.

Hill, C., Root, T., 1977. Introduction to chemical engineering kinetics and reactor design, Second. ed. wiley.

Hirose, T., Hayman, N.W., 2008. Structure, permeability, and strength of a fault zone in the footwall of an oceanic core complex, the Central Dome of the Atlantis Massif, Mid-Atlantic Ridge, 30°N. J. Struct. Geol. 30, 1060–1071. doi:10.1016/j.jsg.2008.04.009

Hodson, M., 2006. Does reactive surface area depend on grain size? Results from pH 3, 25 °C far-from-equilibrium flow-through dissolution experiments on anorthite and biotite. Geochemica Cosmochim. Acta 70, 1677–1667

Horen, H., Zamora, M., Dubuisson, G., 1996. Seismic waves velocities and anisotropy in serpentinized peridotites from Xigaze ophiolite : Abundance of serpentine in slow spreading ridge . Geophys. Res. Lett. 23, 9–12.

Horita, J., Berndt, M.E., 1999. Abiogenic Methane Formation and Isotopic Fractionation Under Hydrothermal Conditions. Science (80). 285, 1055–1057. doi:10.1126/science.285.5430.1055

Hövelmann, J., Austrheim, H., Beinlich, A., Anne Munz, I., 2011. Experimental study of the carbonation of partially serpentinized and weathered peridotites. Geochim. Cosmochim. Acta 75, 6760–6779. doi:10.1016/j.gca.2011.08.032

Hövelmann, J., Austrheim, H., Jamtveit, B., 2012. Microstructure and porosity evolution during experimental carbonation of a natural peridotite. Chem. Geol. 334, 254–265. doi:10.1016/j.chemgeo.2012.10.025

Huang, R., Lin, C.T., Sun, W., Ding, X., Zhan, W., Zhu, J., 2017. The production of iron oxide during peridotite serpentinization: Influence of pyroxene. Geosci. Front. 8, 1311–1321. doi:10.1016/j.gsf.2017.01.001

Huang, R.F., Sun, W.D., Ding, X., Liu, J.Z., Peng, S.B., 2015. Olivine versus peridotite during serpentinization: Gas formation. Sci. China Earth Sci. 58, 2165–2174. doi:10.1007/s11430-015-5222-3

Huitt, J.., 1956. Fluid flow in simulated fractures. Am. Inst. Chem. Eng 2, 259–264.

Humphris, S.E., Klein, F., 2018. Progress in Deciphering the Controls on the Geochemistry of Fluids in Seafloor Hydrothermal Systems. Ann. Rev. Mar. Sci. 10, annurev-marine-121916-063233. doi:10.1146/annurev-marine-121916-063233

Humphris, S.E., Thompson, G., 1978. Hydrothermal alteration of oceanic basalts by seawater. Geochemica Cosmochim. Acta 42, 107–125.

I - J

Iyer, K., Austrheim, H., John, T., Jamtveit, B., 2008. Serpentinization of the oceanic lithosphere and some geochemical consequences: Constraints from the Leka Ophiolite Complex, Norway. Chem. Geol. 249, 66–90. doi:10.1016/j.chemgeo.2007.12.005

Janecky, D.R., Seyfried, W.E., 1986. Hydrothermal Serpentinization of Peridotite within the Oceanic-Crust. Experimental Investigations of Mineralogy and Major Element Chemistry. Geochim. Cosmochim. Acta 50, 1357–1378. doi:Doi 10.1016/0016-7037(86)90311-X

Jarrard, R.D., Abrams, L.J., Pockalny, R., Larson, R.L., 2003. Physical properties of upper oceanic crust : Ocean Drilling Program Hole 801C and the waning of hydrothermal circulation. J. Geophys. Res. 108. doi:10.1029/2001JB001727

Johnson, J.W., Norton, D., 1991. Critical phenomena in hydrothermal systems: State, thermodynamic, electrostatic, and transport properties of H_2O in the critical region. Am. J. Sci. 291, 541–648.

Johnson, J.W., Oelkers, E.H., Helgeson, H.C., 1992. SUPCRT92: A software package for calculating the standard molal thermodynamic properties of minerals, gases, aqueous species, and reactions from 1 bar to 5000 bar and 0 to 1000°C. Comput. Geosci. 18, 899–947.

Jones, L.C., Rosenbauer, R., Goldsmith, J.I., Oze, C., 2010. Carbonate control of H_2 and CH_4 production in serpentinization systems at elevated P-Ts. Geophys. Res. Lett. 37, 1–6. doi:10.1029/2010GL043769

K

Kaszuba, J., Yardley, B., Andreani, M., 2013. Experimental Perspectives of Mineral Dissolution and Precipitation due to Carbon Dioxide-Water-Rock Interactions. Rev. Mineral. Geochemistry 77, 153–188. doi:10.2138/rmg.2013.77.5

Kelemen, P.B., Hirth, G., 2012. Reaction-driven cracking during retrograde metamorphism: Olivine hydration and carbonation. Earth Planet. Sci. Lett. 345–348, 81–89. doi:10.1016/j.epsl.2012.06.018
Kelemen, P.B., Matter, J., 2008. In situ carbonation of peridotite for CO2 storage. Proc. Natl. Acad. Sci. 105, 17295–17300. doi:10.1073/pnas.0805794105

Kelemen, P.B., Matter, J., Streit, E.E., Rudge, J.F., Curry, W.B., Blusztajn, J., 2011. Rates and Mechanisms of Mineral Carbonation in Peridotite: Natural Processes and Recipes for Enhanced, in situ CO2 Capture and Storage. Annu. Rev. Earth Planet. Sci 39, 545–76. doi:10.1146/annurev-earth-092010-152509

Kelley, D.S., Karson, J.A., Blackman, D.K., Fruh-Green, G.L., Butterfield, D.A., Lilley, M.D., Olson, E.J., Schrenk, M.O., Roe, K.K., Lebon, G.T., Rivizzigno, P., 2001. An off-axis hydrothermal vent field near the Mid-Atlantic Ridge at 30° N. Nature 412, 145–149.

Kelley, D.S., Karson, J.A., Früh-green, G.L., Dana, R., Shank, T.M., Butterfield, D.A., Hayes, J.M., Schrenk, M.O., Olson, E.J., Proskurowski, G., Jakuba, M., Bradley, A., Larson, B., Ludwig, K., Glickson, D., Buckman, K., Bradley, A.S., Brazelton, W.J., Roe, K., Elend, M.J., Delacour, A., Bernasconi, S.M., Lilley, M.D., Baross, J.A., Summons, R.E., Kelley, D.S., Karson, J.A., Früh-green, G.L., Hayes, J.M., Schrenk, M.O., Olson, E.J., Proskurowski, G., Jakuba, M., Bradley, A., Larson, B., Ludwig, K., Glickson, D., Buckman, K., Bradley,

A.S., Brazelton, W.J., Roe, K., 2005. A serpentine-Hosted Ecosystem: The Lost City Hydrothermal Field. Science (80-.). 307.

Kestin, J., Khalifa, E., Correira, R.., 1981. Tables of the Dynamic and Kinematic Viscosity of Aqueous KCl Solutions in the Temperature Range 25-150°C and the Pressure Range 0.1-35 MPa. J. Phys. Chem. Ref. Data 10, 57–70.

King, H.E., Plümper, O., Putnis, A., 2010. Effect of Secondary Phase Formation on the Carbonation of Olivine 44, 6503–6509.

Klein, C., Hurlbut, C., 1993. Manual of mineralogy, wiley. New-York.

Klein, F., Bach, W., Humphris, S.E., Kahl, W.A., Moskowitz, B., 2014. Magnetite in seafloor serpentinite-Some like it hot. Geology 42, 135–138. doi:10.1130/G35068.1

Klein, F., Bach, W., Jöns, N., McCollom, T., Moskowitz, B., Berquó, T., 2009. Iron partitioning and hydrogen generation during serpentinization of abyssal peridotites from 15°N on the Mid-Atlantic Ridge. Geochim. Cosmochim. Acta 73, 6868–6893. doi:10.1016/j.gca.2009.08.021

Klein, F., Bach, W., McCollom, T.M., 2013a. Compositional controls on hydrogen generation during serpentinization of ultramafic rocks. Lithos 178, 55–69. doi:10.1016/j.lithos.2013.03.008

Klein, F., Bach, W., McCollom, T.M., 2013b. Compositional controls on hydrogen generation during serpentinization of ultramafic rocks. Lithos 178, 55–69. doi:10.1016/j.lithos.2013.03.008

Klein, F., Garrido, C.J., 2011. Thermodynamic constraints on mineral carbonation of serpentinized peridotite. Lithos 126, 147–160. doi:10.1016/j.lithos.2011.07.020

Klein, F., Grozeva, N.G., Seewald, J.S., McCollom, T.M., Humphris, S.E., Moskowitz, B., Berqu, T.S., Kahl, W.A., 2015a. Fluids in the Crust. Experimental constraints on fluid-rock reactions during incipient serpentinization of harzburgite. Am. Mineral. 100, 991–1002. doi:10.2138/am-2015-5112

Klein, F., Grozeva, N.G., Seewald, J.S., McCollom, T.M., Humphris, S.E., Moskowitz, B., Berquó, T.S., Kahl, W.A., 2015b. Fluids in the Crust. Experimental constraints on fluid-rock reactions during incipient serpentinization of harzburgite. Am. Mineral. 100, 991–1002. doi:10.2138/am-2015-5112

Klein, F., McCollom, T.M., 2013. From serpentinization to carbonation: New insights from a CO2 injection experiment. Earth Planet. Sci. Lett. 379, 137–145. doi:10.1016/j.epsl.2013.08.017

Knauss, K., Nguyen, S., Weed, H., 1993. Diopside dissolution kinetics as a function of pH, CO2, temperature, and time. Geochemica Cosmochim. Acta 57, 285–294.

Kodolanyi, J., Pettke, T., Spandler, C., Kamber, B.S., Gme, K., 2012. Geochemistry of Ocean Floor and Fore-arc Serpentinites : Constraints on the Ultramafic Input to Subduction Zones. J. Petrol. 53, 235–270. doi:10.1093/petrology/egr058

Krevor, S.C.M., Lackner, K.S., 2011. Enhancing serpentine dissolution kinetics for mineral carbon dioxide sequestration. Int. J. Greenh. Gas Control 5, 1073–1080. doi:10.1016/j.ijggc.2011.01.006

L

Lacinska, A.M., Styles, M.T., Bateman, K., Hall, M., Brown, P.D., 2017. An Experimental Study of the Carbonation of Serpentinite and Partially Serpentinised Peridotites. Front. Earth Sci. 5. doi:10.3389/feart.2017.00037

Lafay, R., Montes-hernandez, G., Janots, E., Chiriac, R., Findling, N., Toche, F., 2012a. Mineral replacement rate of olivine by chrysotile and brucite under high alkaline conditions. J. Cryst. Growth 347, 62–72. doi:10.1016/j.jcrysgro.2012.02.040

Lafay, R., Montes-Hernandez, G., Janots, E., Chiriac, R., Findling, N., Toche, F., 2014. Simultaneous precipitation of magnesite and lizardite from hydrothermal alteration of olivine under high-carbonate alkalinity. Chem. Geol. 368, 63–75. doi:10.1016/j.chemgeo.2014.01.008

Lafay, R., Montes-Hernandez, G., Janots, E., Chiriac, R., Findling, N., Toche, F., 2012b. Mineral replacement rate of olivine by chrysotile and brucite under high alkaline conditions. J. Cryst. Growth 347, 62–72. doi:10.1016/j.jcrysgro.2012.02.040

Lamadrid, H.M., Rimstidt, J.D., Schwarzenbach, E.M., Klein, F., Ulrich, S., Dolocan, A., Bodnar, R.J., 2017. Effect of water activity on rates of serpentinization of olivine. Nat. Commun. 8, 1–9. doi:10.1038/ncomms16107

Landis, E.N., Keane, D.T., 2010. Tutorial review X-ray microtomography 1. doi:10.1016/j.matchar.2010.09.012

Laurent, R., 1980. Regimes of Serpentinization and Rodingitization in Quebec Appalachian Ophiolites. Arch. Des Sci. 33, 311–320.

Lechat, K., Lemieux, J.M., Molson, J., Beaudoin, G., Hébert, R., 2016. Field evidence of CO_2 sequestration by mineral carbonation in ultramafic milling wastes, Thetford Mines, Canada. Int. J. Greenh. Gas Control 47, 110–121. doi:10.1016/j.ijggc.2016.01.036

Levet Segenrs, J.M.., Kamgar-Parsi, B., Balfour, F.., Sengers, J.., 1983. Thermodynamic properties of steam in the critical region. J. Phys. Chem. Ref. Data 12, 1–28.

Lowell, R.P., Rona, P.A., 2002. Seafloor hydrothermal systems driven by the serpentinization of peridotite. Geophys. Res. Lett. 29, 0–3. doi:10.1029/2001GL014411

Luhmann, A., Tutolo, B., Bagley, B., Mildner, D.F.R., Scheuermann, P.P., Feinberg, J.M., Ignatyev, K., Seyfried, W.E., 2017a. Chemical and physical changes during seawater flow

through intact dunite cores: An experimental study at 150–200 °C. Geochim. Cosmochim. Acta 214, 86–114. doi:10.1016/j.gca.2017.07.020

Luhmann, A., Tutolo, B., Bagley, B., Mildner, D.F.R., Seyfried, W.E., Saar, M.O., 2017b. Permeability, porosity and mineral surface are changes in balsalt cores induced by reactive transport of CO_2-rich brine. Water Resour. Res. 53, 1908–1927. doi:10.1002/2016WR019216.

Luquot, L., Gouze, P., 2009. Experimental determination of porosity and permeability changes induced by injection of CO_2 into carbonate rocks. Chem. Geol. 265, 148–159. doi:10.1016/j.chemgeo.2009.03.028

M

Macdonald, A.H., Fyfe, W.S., 1985. Rate of serpentinization in seafloor environments. Tenonophysics 116, 123–135.

Maffione, M., Morris, A., Plumper, O., Van Hinsbergen, D., 2014. Magnetic properties of variably serpentinized peridotites and their implication for the evolution of oceanic core complexes. Geochemistry Geophys. Geosystems 15, 923–944. doi:10.1002/2013GC004993.

Malvoisin, B., Brunet, F., 2014. Water diffusion-transport in a synthetic dunite: Consequences for oceanic peridotite serpentinization. Earth Planet. Sci. Lett. 403, 263–272. doi:10.1016/j.epsl.2014.07.004

Malvoisin, B., Brunet, F., Carlut, J., Rouméjon, S., Cannat, M., 2012a. Serpentinization of oceanic peridotites: 2. Kinetics and processes of San Carlos olivine hydrothermal alteration. J. Geophys. Res. Solid Earth 117, 1–13. doi:10.1029/2011JB008842

Malvoisin, B., Carlut, J., Brunet, F., 2012b. Serpentinization of oceanic peridotites: 1. A high-sensitivity method to monitor magnetite production in hydrothermal experiments. J. Geophys. Res. Solid Earth 117, 1–10. doi:10.1029/2011JB008612

Manning, C.E., 2004. The chemistry of subduction-zone fluids. Earth Planet. Sci. Lett. 223, 1–16. doi:10.1016/j.epsl.2004.04.030

Marcaillou, C., Muñoz, M., Vidal, O., Parra, T., Harfouche, M., 2011a. Mineralogical evidence for H_2 degassing during serpentinization at 300°C/300bar. Earth Planet. Sci. Lett. 303, 281–290. doi:10.1016/j.epsl.2011.01.006

Marcaillou, C., Muñoz, M., Vidal, O., Parra, T., Harfouche, M., 2011b. Mineralogical evidence for H2 degassing during serpentinization at 300 °C/300 bar. Earth Planet. Sci. Lett. 303, 281–290. doi:10.1016/j.epsl.2011.01.006

Martin, B., Fyfe, W.S., 1970. Some experimental and theoretical observations on the kinetics of hydration reactions with particular reference to serpentinization. Chem. Geol. 6, 185–202.

Matter, J.M., Kelemen, P.B., 2009. Permanent storage of carbon dioxide in geological reservoirs by mineral carbonation. Nat. Geosci. 2, 837–841. doi:10.1038/ngeo683

Mayhew, L.E., Ellison, E.T., McCollom, T.M., Trainor, T.P., Templeton, A.S., 2013. Hydrogen generation from low-temperature water-rock reactions. Nat. Geosci 6, 478–484. doi:10.1038/ngeo1825

McCollom, T.M., Bach, W., 2009. Thermodynamic constraints on hydrogen generation during serpentinization of ultramafic rocks. Geochim. Cosmochim. Acta 73, 856–875. doi:10.1016/j.gca.2008.10.032

McCollom, T.M., Klein, F., Robbins, M., Moskowitz, B., Berquó, T.S., Jöns, N., Bach, W., Templeton, A., 2016. Temperature trends for reaction rates, hydrogen generation, and partitioning of iron during experimental serpentinization of olivine. Geochim. Cosmochim. Acta 181, 175–200. doi:10.1016/j.gca.2016.03.002

Mccollom, T.M., Klein, F., Robbins, M., Moskowitz, B., Jo, N., Berquo, T.S., Bach, W., Templeton, A., 2016. Temperature trends for reaction rates , hydrogen generation , and partitioning of iron during experimental serpentinization of olivine. Geochemica Cosmochim. Acta 181, 175–200. doi:10.1016/j.gca.2016.03.002

Mccollom, T.M., Seewald, J.S., 2006. Carbon isotope composition of organic compounds produced by abiotic synthesis under hydrothermal conditions. Earth Planet. Sci. Lett. 243, 74–84. doi:10.1016/j.epsl.2006.01.027

McCollom, T.M., Seewald, J.S., 2001. A reassessment of the potential for reduction of dissolved CO2 to hydrocarbons during serpentinization of olivine. Geochim. Cosmochim. Acta 65, 3769–3778. doi:10.1016/S0016-7037(01)00655-X

Mével, C., 2003. Serpentinization of abyssal peridotites at mid-ocean ridges. Comptes Rendus Geosci. 335, 825–852. doi:10.1016/j.crte.2003.08.006

Miller, D.J., Christensen, N.I., 1997. Seismic velocities of lower crustal and upper mantle rocks from the slow-spreading mid-atlantic ridge,south of the kane transform zone (MARK). Proc. Ocean Drill. Program, Sci. Results 153.

Miller, H.M., Matter, M., Kelemen, P., Ellison, E.T., Conrad, M.E., Fierer, N., Ruchala, T., Tominaga, M., Templeton, A.S., 2016. Modern water / rock reactions in Oman hyperalkaline peridotite aquifers and implications for microbial habitability 179, 217–241. doi:10.1016/j.gca.2016.01.033

Millero, F.J., Feistel, R., Wright, D.G., McDougall, T.J., 2008. The composition of Standard Seawater and the definition of the Reference-Composition Salinity Scale. Deep Sea Res. Part I Oceanogr. Res. Pap. 55, 50–72. doi:10.1016/j.dsr.2007.10.001

Monnin, C., Chavagnac, V., Boulart, C., Ménez, B., Gérard, M., Gérard, E., Pisapia, C., Quéméneur, M., 2014. Fluid chemistry of the low temperature hyperalkaline hydrothermal system of Prony Bay (New Caledonia). Biogeosciences 2, 5687–5706. doi:10.5194/bg-11-5687-2014

Moody, J.B., 1976. Serpentinization: a review. Lithos 9, 125–138. doi:10.1016/0024-4937(76)90030-X

Morel, F.M., Hering, J.G., 1993. Principles and Applications of Aquatic Chemistry. New York: John Wiley and Sons.

Morrison, S.., 1980. Electrochemistry at semiconductor and oxidized metal electrodes, Plenum Pre. ed.

Morse, J.W., Arvidson, R.., 2002. The dissolution kinetics of major sedimentray carbonate minerals. Earth-Science Rev. 58, 51–84.

Mottl, M.J., 1983. Metabasalts, axial hot springs, and the structure of hydrothermal systems at mid-ocean ridges. Geol. Soc. Am. Bull. 94, 161–180. doi:10.1130/0016-7606(1983)94<161

Müntener, O., Manatschal, G., 2006. High degrees of melt extraction recorded by spinel harzburgite of the Newfoundland margin: The role of inheritance and consequences for the evolution of the southern North Atlantic. Earth Planet. Sci. Lett 252, 437–452.

N

Neal, C., Stanger, G., 1985. Past and Present Serpentinisation of Ultramafic Rocks: An Example from the Semail Ophiolite Nappe of Northern Oman, in: The Chem. of Weathering. Reidel Publishing Company, Dordrecht, Holland, pp. 249–275.

Nicolas, A., Boudier, F., 2003. Where ophiolites come from and what they tell us. Geol. Soc. Am. 373.

Nicolas, A., Boudier, F., Ildefonse, B., Ball, E., 2000. Accretion of Oman and United Arab Emirates ophiolite – Discussion of a new structural map. Mar. Geophys. Res. 21, 147–179.

Noel, J., Godard, M., Oliot, E., Martinez, I., Morgan, W., Boudier, F., Rodriguez, O., Chaduteau, C., Escario, S., Gouze, P., 2018. Evidence of polygenetic carbon trapping in the Oman Ophiolite: petro-structural, geochemical, and carbon and oxygen isotope study of the Wadi Dima harzburgite-hosted carbonates (Wadi Tayin massif, Sultanate of Oman). In press. Lithos.

Noiriel, C., Gouze, P., Bernard, D., 2004. Investigation of porosity and permeability effects from microstructure changes during limestone dissolution. Geophys Res Lett 31.

Noiriel, C., Luquot, L., Mad, B., Raimbault, L., Gouze, P., van der Lee, J., 2009. Changes in reactive surface area during limestone dissolution: An experimental and modelling study. Chem. Geol. 262, 353–363. doi:10.1016/j.chemgeo.2009.01.032

Noiriel, C., Madé, B., Gouze, P., 2007. Impact of coating development on the hydraulic and transport properties in argillaceous limestone fracture. Water Resour. Res. 43. doi:10.1029/2006WR005379

Normand, C., Williams-Jones, A.E., Martin, R.F., Vali, H., 2002. Hydrothermal alteration of olivine in a flow-through autoclave: Nucleation and growth of serpentine phases. Am. Mineral. 87, 1699–1709. doi:10.1016/S0169-1317(02)00087-X

O

O'Connor, W., Dahlin, D., Rush, G., Gerdemann, S., Nilsen, D., 2004. Final Report: Aqueous Mineral Carbonation. DOE/ARC-TR-04-002. Office of Process Development. Albany Research Center, Office of Fossil Energy, US DOE, Albany, OR.

O'Connor, W., Dahlin, D., Rush, G., Gerdemann, S., Penner, L.R., Nilsen, D., 2005. Aqueous Mineral Carbonation. Natl. Energy Technol. Lab. Albany Res. Center, Off. Foss. Energy, US DOE.

O'Connor, W.K., Dahlin, D.C., Nilsen, D.N., Rush, G.E., Walters, R.P., Turner, P.C., 2001. Carbon Dioxide Sequestration by Direct Mineral Carbonation: Results from Recent Studies and Current Status. 1st Annu. DOE Carbon Sequestration Conf. Washington, D.C. 11.

O'Hanley, D.S., 1996. Serpentinites. Oxford University Press.

O'Neil, J.., Taylor, H.., 1967. The oxygen isotope and cation exchange chemistry of feldspars. Am. Mineral. 52, 1414–1437.

Oelkers, E.H., 2001a. An experimental study of forsterite dissolution rates as a function of temperature and aqueous Mg and Si concentrations. Chem. Geol. 175, 485–494. doi:10.1016/S0009-2541(00)00352-1

Oelkers, E.H., Benezeth, P., Pokrovski, G.S., 2009. Thermodynamic Databases for Water-Rock Interaction. Rev. Mineral. Geochemistry 70, 1–46. doi:10.2138/rmg.2009.70.1

Oelkers, E.H., Gislason, S.R., Matter, J., 2008. Mineral Carbonation of CO_2. Elements 4, 333–338. doi:10.2113/gselements.4.5.333

Ogasawara, Y., Okamoto, A., Hirano, N., Tsuchiya, N., 2013. Coupled reactions and silica diffusion during serpentinization. Geochim. Cosmochim. Acta 119, 212–230. doi:10.1016/j.gca.2013.06.001

Okamoto, A., Ogasawara, Y., Ogawa, Y., Tsuchiya, N., 2011. Progress of hydration reactions in olivine-H2O and orthopyroxenite-H2O systems at 250°C and vapor-saturated pressure. Chem. Geol. 289, 245–255. doi:10.1016/j.chemgeo.2011.08.007

Oufi, O., Cannat, M., Horen, H., 2002. Magnetic properties of variably serpentinized abyssal peridotites. J. Geophys. Res. 107, 2095. doi:10.1029/2001JB000549

P

Palandri, J.L., Reed, M.H., 2004. Geochemical models of metasomatism in ultramafic systems: Serpentinization, rodingitization, and sea floor carbonate chimney precipitation. Geochim. Cosmochim. Acta 68, 1115–1133. doi:10.1016/j.gca.2003.08.006

Palciaukas, V., Domenico, P., 1976. Solution chemistry, mass transfert, and the approach to chemical equilibriumin porous carbonate rocks and sediments. Geol. Soc. Am. 87, 207–214.

Pankow, J.F., 1991. Aquatic Chemistry Concepts. MI: Lewis Publishers, Chelsea.

Parkhurst, B.D.L., Appelo, C. a J., 1999. User's Guide To PHREEQC (version 2) — a Computer Program for Speciation, and Inverse Geochemical Calculations. Exch. Organ. Behav. Teach. J. D, 326. doi:Rep. 99-4259

Paulick, H., Bach, W., Godard, M., De Hoog, J.C.M., Suhr, G., Harvey, J., 2006. Geochemistry of abyssal peridotites (Mid-Atlantic Ridge, 15°20′N, ODP Leg 209): Implications for fluid/rock interaction in slow spreading environments. Chem. Geol. 234, 179–210. doi:10.1016/j.chemgeo.2006.04.011

Paukert, A., 2014. Mineral Carbonation in Mantle Peridotite of the Samail Ophiolite , Oman : Implications for permanent geological carbon dioxide capture and storage. Thesis manuscript.

Pens, M., Andreani, M., Daniel, I., Perrillat, J.P., Cardon, H., 2016. Contrasted effect of aluminum on the serpentinization rate of olivine and orthopyroxene under hydrothermal conditions. Chem. Geol. 441, 256–264. doi:10.1016/j.chemgeo.2016.08.007

Peuble, S., 2014. Caracterization experimentale des processus d'hydratation et de carbonatation des roches basiques et ultrabasiques.

Peuble, S., Andreani, M., Godard, M., Gouze, P., Barou, F., Van de Moortele, B., Mainprice, D., Reynard, B., 2015a. Carbonate mineralization in percolated olivine aggregates : Linking effects of crystallographic orientation and fluid flow. Am. Mineral. 100, 474–482.

Peuble, S., Godard, M., Luquot, L., Andreani, M., Martinez, I., Gouze, P., 2015b. CO_2 geological storage in olivine rich basaltic aquifers: New insights from reactive-percolation experiments. Appl. Geochemistry 52, 174–190. doi:10.1016/j.apgeochem.2014.11.024

Philibert, J., 2005. One and a Half Century of Diffusion: Fick, Einstein, Before and Beyond. Diffus. Fundam. 4, 1–19.

Plümper, O., Røyne, A., Magrasó, A., Jamtveit, B., 2012. The interface-scale mechanism of reaction-induced fracturing during serpentinization. Geology 40, 1103–1106. doi:10.1130/G33390.1

Pokrovsky, O., Golubev, S., Schott, J., Castillo, A., 2009. Calcite, dolomite and magnesite dissolution kinetics in aqueous solutions at acid to circumneutral pH, 25 to 150°C and 1 to 55 atm pCO2: New constraints on CO2 sequestration in sedimentary basins. Chem. Geol. 265, 20–32.

Pokrovsky, O.S., Schott, J., 2004. Experimental study of brucite dissolution and precipitation in aqueous solutions: Surface speciation and chemical affinity control. Geochim. Cosmochim. Acta 68, 31–45. doi:10.1016/S0016-7037(03)00238-2

Pokrovsky, O.S., Schott, J., 2000a. Kinetics and mechanism of forsterite dissolution at 25°C and pH from 1 to 12. Geochim. Cosmochim. Acta 64, 3313–3325. doi:10.1016/S0016-7037(00)00434-8

Pokrovsky, O.S., Schott, J., 2000b. Forsterite surface composition in aqueous solutions: A combined potentiometric, electrokinetic, and spectroscopic approach. Geochim. Cosmochim. Acta 64, 3299–3312. doi:10.1016/S0016-7037(00)00435-X

Prigiobbe, V., Costa, G., Baciocchi, R., Hänchen, M., Mazzotti, M., 2009. The effect of CO_2 and salinity on olivine dissolution kinetics at 120°C. Chem. Eng. Sci. 64, 3510–3515. doi:10.1016/j.ces.2009.04.035

Proskurowski, G., Lilley, M.D., Kelley, D.S., Olson, E.J., 2006. Low temperature volatile production at the Lost City Hydrothermal Field , evidence from a hydrogen stable isotope geothermometer. Chem. Geol. 229, 331–343. doi:10.1016/j.chemgeo.2005.11.005

Proskurowski, G., Lilley, M.D., Seewald, J.S., Früh-green, G.L., Olson, E.J., Lupton, J.E., Sylva, S.P., Kelley, D.S., 2008. Abiogenic Hydrocarbon Production at Lost City Hydrothermal Field. Science (80). 319.

R

Ridler, T., Calvard, S., 1978. Picture thresholding using an iterative selection method. IEEE Trans. Syst. Man Cybern 8, 630–632. doi: 10.1109/TSMC.1978.4310039

Rimstidt, J.D., Brantley, S.L., Olsen, A. a., 2012a. Systematic review of forsterite dissolution rate data. Geochim. Cosmochim. Acta 99, 159–178. doi:10.1016/j.gca.2012.09.019

Rimstidt, J.D., Brantley, S.L., Olsen, A.A., 2012b. Systematic review of forsterite dissolution rate data. Geochim. Cosmochim. Acta 99, 159–178. doi:10.1016/j.gca.2012.09.019

Rimstidt, J.D., Dove, M., 1986. Mineral / solution reaction rates in a mixed flow reactor : Wollastonite hydrolysis. Geochemica Cosmochim. Acta 50, 2509–2516.

Robie, R.A., Aldbaum, D.R., 1968. Thermodynamic properties of minerals and related sustances. U. S. G. S. BUN.

Rosso, J.J., Rimstidt, D.J., 2000. A high resolution study of forsterite dissolution rates. Geochim. Cosmochim. Acta 64, 797–811. doi:10.1016/S0016-7037(99)00354-3

Rouméjon, S., Cannat, M., Agrinier, P., Godard, M., Andreani, M., 2015. Serpentinization and Fluid Pathways in Tectonically Exhumed Peridotites from the Southwest Indian Ridge (62–65°E). J. Petrol. 56, 703–734. doi:10.1093/petrology/egv014

Rudge, J.F., Kelemen, P.B., Spiegelman, M., 2010. A simple model of reaction-induced cracking applied to serpentinization and carbonation of peridotite. Earth Planet. Sci. Lett. 291, 215–227. doi:10.1016/j.epsl.2010.01.016

Ruiz-agudo, E., Putnis, C. V, Putnis, A., 2014. Coupled dissolution and precipitation at mineral fluid interfaces. Chem. Geol. 383, 132–146. doi:10.1016/j.chemgeo.2014.06.007

S

Saldi, G.D., Schott, J., Pokrovsky, O.S., Gautier, Q., Oelkers, E.H., 2012. An experimental study of magnesite precipitation rates at neutral to alkaline conditions and 100-200°C as a function of pH, aqueous solution composition and chemical affinity. Geochim. Cosmochim. Acta 83, 93–109. doi:10.1016/j.gca.2011.12.005

Sayles, F.., Fyfe, W.., 1973. The crystallization of magnesite from aqueous solution. Geochemica Cosmochim. Acta 37, 87–99.

Schmidt, K., Garbe-Schönberg, D., Koschinsky, A., Strauss, H., Jost, C.L., Klevenz, V., Königer, P., 2011. Fluid elemental and stable isotope composition of the Nibelungen hydrothermal field (8°18'S, Mid-Atlantic Ridge): Constraints on fluid-rock interaction in heterogeneous lithosphere. Chem. Geol. 280, 1–18. doi:10.1016/j.chemgeo.2010.07.008

Schmidt, K., Koschinsky, A., Garbe-schönberg, D., 2007. Geochemistry of hydrothermal fluids from the ultramafic-hosted Logatchev hydrothermal field , 15 ° N on the Mid-Atlantic Ridge : Temporal and spatial investigation 242, 1–21. doi:10.1016/j.chemgeo.2007.01.023

Schroeder, T., John, B., Frost, B.R., 2002. Geologic implications of seawater circulation through peridotite exposed at slow-spreading mid-ocean ridges. Geology 30, 367–370. doi:10.1130/0091-7613(2002)030<0367:GIOSCT>2.0.CO;2

Seifritz, W., 1990. CO_2 Disposal by Means of Silicates. Nature 345. doi:http://dx.doi.org/10.1038/345486b0

Seyfried, W.., Dibble, W.., 1980. Seawater-peridotite interaction at 300 ° C and 500 bars : implications for the origin of oceanic serpentinites. Geochemica Cosmochim. Acta 44, 309–321.

Seyfried, W.E., 1987. Experimantal and theoretical constrains on hydrothermal alteration processes at mid-ocean ridges.Ann.Rev.Earth Planet Sci,15:317-35

Seyfried, W.E., Foustoukos, D.I., Fu, Q., 2007. Redox evolution and mass transfer during serpentinization: An experimental and theoretical study at 200°C, 500 bar with implications for ultramafic-hosted hydrothermal systems at Mid-Ocean Ridges. Geochim. Cosmochim. Acta 71, 3872–3886. doi:10.1016/j.gca.2007.05.015

Seyfried, W.E., Pester, N., Fu, Q., 2013. Phase Equilibria Controls on the Chemistry of Vent Fluids from Hydrothermal Systems on Slow Spreading Ridges: Reactivity Of Plagioclase and Olivine Solid Solutions and the pH-Silica Connection. Divers. Hydrothermal Syst. Slow Spreading Ocean Ridges 297–320. doi:10.1029/2009GM000854

Seyfried, W.E., Pester, N.J., Ding, K., Rough, M., 2011. Vent fluid chemistry of the Rainbow hydrothermal system (36°N, MAR): Phase equilibria and in situ pH controls on subseafloor alteration processes. Geochim. Cosmochim. Acta 75, 1574–1593. doi:10.1016/j.gca.2011.01.001

Seyfried, W.E., Pester, N.J., Tutolo, B.M., Ding, K., 2015. The Lost City hydrothermal system: Constraints imposed by vent fluid chemistry and reaction path models on subseafloor heat and mass transfer processes. Geochim. Cosmochim. Acta 163, 59–79. doi:10.1016/j.gca.2015.04.040

Seyfried, W.E., Seewald, J.S., Berndt, M.E., Ding, K., Foustoukos, D.I., 2003. Chemistry of hydrothermal vent fluids from the Main Endeavour Field, northern Juan de Fuca Ridge: Geochemical controls in the aftermath of June 1999 seismic events. J. Geophys. Res. Solid Earth 108, 1–23. doi:10.1029/2002JB001957

Shervais, J.W., Kolesar, P., Andreasen, K., 2005. A Field and Chemical Study of Serpentinization-Stonyford, California: Chemical Flux and Mass Balance. Int. Geol. Rev. 47, 1–23. doi:10.2747/0020-6814.47.1.1

Shock, E.L., Helgeson, H.C., 1988. Calculation of the thermodynamic and transport properties of aqueous species at high pressures and temperatures: Correlation algorithms for ionic species and equation of state predictions to 5 kb and 1000°C. Geochim. Cosmochim. Acta 52, 2009–2036. doi:10.1016/0016-7037(88)90181-0

Shock, E.L., Helgeson, H.C., Sverjensky, D.A., 1989. Calculation of the thermodynamic and transport properties of aqueous species at high pressures and temperatures: Standard partial molal properties of inorganic neutral species. Geochim. Cosmochim. Acta 53, 2157–2183. doi:10.1016/0016-7037(89)90341-4

Shock, E.L., Oelkers, E.H., Johnson, J.., Sverjensky, D.A., Helgeson, H.C., 1992. Calculation of the thermodynamic properties of aqueous species at high pressures and temperatures: Effective electrostatic radio, dissociation constants and standard partial molal properties to 1000°C and 5 kbar. J. Chem. Soc. Faraday Trans. 88, 803–826.

Shock, E.L., Sassani, D.C., Willis, M., Sverjensky, D.A., 1997. Inorganic species in geologic fluids: Correlations among standard molal thermodynamic properties of aqueous ions and hydroxide complexes. Geochim. Cosmochim. Acta 61, 907–950. doi:10.1016/S0016-7037(96)00339-0

Smal, P., Gouze, P., Rodriguez, O., 2018. An automatic segmentation algorithm for retrieving sub-resolution porosity from X-ray tomography images. Journal of Petroleum Science and Engineering. DOI: 10.1016/j.petrol.2018.02.062

Stamoudi, C., 2002. Processus de serpentinisation des péridotites de Hess-Deep (leg 147, site 895) et de la zone MARK (leg 153, site 920): approche chimique et minéralogique. Univ. Pierre Marie Curie 372. Thesis manuscript.

Stanger, G., Neal, C., 1994. The occurrence and chemistry of huntite from Oman. Chem. Geol. 112, 247–254. doi:10.1016/0009-2541(94)90027-2

Steefel, C.I., Maher, K., 2009. Fluid-rock interaction: A reactive transport approach. Rev. Mineral. geochemistry 70, 485–532. doi:10.2138/rmg.2009.70.11

Stumm, W., Morgan, J., 1996. Aquatic Chemistry. John Wiley & Sons Inc, New York, NY.

Summerhayes, C.P., Thorpe, S.A., 1996. Oceanography: An illustrated guide. Manson Publishing Co. via Oxford University Press, Oxford.

Syverson, D.D., Tutolo, B.M., Borrok, D.M., Seyfried, W.E., 2017a. Serpentinization of olivine at 300 °C and 500 bars: An experimental study examining the role of silica on the reaction path and oxidation state of iron. Chem. Geol. 475, 122–134. doi:10.1016/j.chemgeo.2017.11.006

Syverson, D.D., Tutolo, B.M., Borrok, D.M., Seyfried, W.E., 2017b. Serpentinization of olivine at 300 °C and 500 bars: An experimental study examining the role of silica on the reaction path and oxidation state of iron. Chem. Geol. 475, 122–134. doi:10.1016/j.chemgeo.2017.11.006

T

Tanger, J.., Helgeson, H.., 1988. Calculation of the thermodynamic and transport properties of aqueous species at high pressures and temperatures: Revised equations of state for the standard partial molal properties of ions and electrolytes. Am. J. Sci. 288, 19–98.

Thomassin, J.., Goni, J., Baillif, P., Touray, J.., Jaurand, M.., 1977. An XPS study of the dissolution kinetics of chrysotile in 0. I N oxalic acid at different temperatures. Phys. Chem. Miner. 1, 385–398.

Tivey, M., 2007. Generation of Seafloor Hydrothermal Vent Fluids and Associated Mineral Deposits. Oceanography 20, 50–65. doi:10.5670/oceanog.2007.80

Tutolo, B.M., Luhmann, A.J., Tosca, N.J., Seyfried, W.E.J., 2018. Serpentinization as a reactive transport process: The brucite silicification reaction. Earth Planet. Sci. Lett. 1, 1–13. doi:10.1016/j.epsl.2017.12.029

U

Ulrich, M., 2010. Péridotites et serpentinites du complexe ophiolitique de la Nouvelle-Calédonie. Université de Nouvelle Caldedonie. tel-00509848.

V

Van Noort, R., Spiers, C.J., Drury, M.R., Kandianis, M.T., 2013. Peridotite dissolution and carbonation rates at fracture surfaces under conditions relevant for in situ mineralization of CO_2. Geochim. Cosmochim. Acta 106, 1–24. doi:10.1016/j.gca.2012.12.001

Vera, S., Perez, F., Lara, L., Gonzalez, M., 2011. A threshold with hystereris, The insight Journal.

Viti, C., 2010. Serpentine minerals discrimination by thermal analysis. Am. Mineral. 95, 631–638. doi:10.2138/am.2010.3366

Von Damm, K.L., Lilley, M.D., Shanks, I.C., Brockington, M., Bray, A.M., O'Grady, K.M., Olson, E., Graham, A., Proskurowski, G., 2003. Extraordinary phase separation and segregation in vent fluids from the southern East Pacific Rise. Earth Planet. Sci. Lett. 206, 365–378. doi:10.1016/S0012-821X(02)01081-6

Von damm, K., 2005. Evolution of the hydrothermal system at the East Pacific Rise 9°50'N: Geochemical evidence for changes in the upper oceanic crust, in Mid-Ocean Ridges: Hydrothermal Interactions Between the Lithosphere and Oceans. Geophys. Monogr. Ser. 148, 285–304.

W

Wegner, W.., Ernst, W.., 1983. Experimentally determined hydration and dehydration reaction rates in the system MgO-SiO_2-H_2O. Am. J. Sci. 283–A, 151–180.

White, A.., Brantley, S.L., 1995. Chemical Weathering Rates of Silicate Minerals, Mineralogical Society of America. Washington, D.C.

Wicks, F.J., Whittaker, E.J.W., 1975. A reappraisal of the structures of the serpentine minerals. Can. Mineral. 13, 227–243.

Wirth, K.R., Bird, J.M., 1992. Chronology of ophiolite crystallization, detachment, and emplacement: Evidence from the Brooks Range, Alaska. Geology 20, 75–78.

Witherspoon, P.., Wang, J.S.., Iwai, K., Gale, 1980. Validity of cubic law for fluid flow in a deformable rock fracture. Water Resour. Res. 16, 1016–1024.

Wolery, T., Jarek, R.L., 2003. Software user's manual EQ3/6, Version 8.0, Sandia National Laboratories, Albuquerque, New Mexico.

Wolery, T., Daveler, S., 1992. EQ6, A computer program for geochemical aqueous speciation-solubility calculations: theoretical manual, user's guide and related documentation (Version 7.0). UCRL-MA-110662-PT-IV, Lawrence Livermore Natl. Lab. Livermore, Calif. 338.

Wolff-Boenisch, D., Wenau, S., Gislason, S.R., Oelkers, E.H., 2011. Dissolution of basalts and peridotite in seawater, in the presence of ligands, and CO_2: Implications for mineral sequestration of carbon dioxide. Geochim. Cosmochim. Acta 75, 5510–5525. doi:10.1016/j.gca.2011.07.004

X – Y - Z

Xu, T., Apps, J.A., Pruess, K., 2004. Numerical simulation of CO_2 disposal by mineral trapping in deep aquifers. Appl. Clay Sci. 19, 917–936. doi:10.1016/j.apgeochem.2003.11.003

Yeghicheyan, D., Bossy, C., Coz, M.., Douchet, C., Granier, G., Heimburger, A., Lacan, F., Lanzanova, A., Rousseau, T., Seidel, J.L., 2013. A compilation of Silicon, Rare Earth Element and twenty-one other Trace Element concentrations in the Natural River Water Reference Material SLRS-5 (NRC-CNRC). Geostand. Geoanalytical Res.

Zeebe, R.E., Wolf-Gladrow, D., 2001. CO_2 in seawater: Equilibrium, Kinetics, Isotopes. Elsevier Oceanography series, New York.

Zhu, Anderson, G., 2002. Environmental Applications of Geochemical Modelling. Cambridge University Press, New York, Melbourne.

Appendix A

Methodology

A.1 Estimation CO_2- pump volume

For each peridotite fractured experiments is possible to fix a volume of $CO_{2\ (g)}$ to fill the CO_2 pumps. This volume is calculated after the [$CO_{2\ (g)}$] imposed for each experiment. First, it is necessary to calculate the solubility of CO_2 under the experimental conditions of pressure, temperature and salinity in order to be in monophasic conditions, choosing a [CO_2] less than the solubility of CO_2. We use the similar approximation of Peuble (2014).

Calculation of CO_2 solubility

The solubility mCO_2 is calculated through the equation of state of Duan et al (2006). The equation is available for temperature (T < 260°C), a pressure between 0 and 200 MPa and salinity (NaCl) between 0 and 4.5 mol.kg^{-1}.

$$\ln m_{CO2} = ln_{\gamma_{CO_2}} \varphi_{CO2}\, P - \frac{\mu_{CO2}^{l(0)}}{RT} - 2\,\lambda_{CO2-NaCl}\left(m_{Na} + m_k + 2m_{Ca} + 2m_{Mg}\right) - \zeta_{CO2-Na-Cl}\; m_{cl}\left(m_{Na} + m_k + m_{Ca} + m_{Mg}\right) + 0.07 m_{SO4} \qquad \text{(Eq. A.1)}$$

where γ_{CO2} is the mole fraction of CO_2 in vapor phase, φ_{CO2} is the fugacity coefficient of CO_2. $\mu_{CO2}^{l(0)}$ is the standard chemical potential of CO_2 in liquid phase, $\lambda_{CO2-NaCl}$ is the interaction parameter between CO_2 and Na^+, $\zeta_{CO2-Na-Cl}$ is the interaction parameter between CO_2 and Na^+, Cl^-, m is the molality of components dissolved in water.

The parameters of the equation above are computed after Duan et al. (1992a; 1992b). I detail the equations to calculate each parameter.

Mole fraction of CO_2 in vapor phase (γ_{CO2})

$$\gamma_{CO2} = \frac{P - P_{H2O}}{P} \qquad \text{(Eq. A.2)}$$

Where P is the total pressure in bar and P_{H2O} is the water pressure calculated after Duan et al (2003).

$$P_{H2O} = \left(\frac{P_{c\,H2O} \cdot T}{T_{c\,H2O}}\right) \cdot (1 + b_1(-t)^{1.9} + b_2 t + b_3 t^2 + b_4 t^3 + b_5 t^4) \quad \text{(Eq. A.3)}$$

where T is the temperature fixed for the experiment in K, T_{cH2O} is the water critical temperature ($T_{c\ H2O}$ = 647.29 K), P_{cH2O} is water critical pressure (P_{cH2O} = 22.085 MPa), coefficients b1 and b4 are fixed by Duan et al (2003) reported in table A.1.1.

t is calculated after $t = \frac{T - T_{c\,H2O}}{T_{c\,H2O}}$

Table A.1.1 *Parameters of equations Eq.A.3, Eq.A.4 and Eq.A.5*

Parameters	*b*
b_1	-38.64084
b_2	5.89484
b_3	59.87652
b_4	26.65463
b_5	10.6371

Parameters	*a*
a_1	8.99E-02
a_2	-4.95E-01
a_3	4.78E-02
a_4	1.04E-02
a_5	-2.83E-02
a_6	9.50E-02
a_7	5.21E-04
a_8	-2.94E-04
a_9	-1.77E-03
a_{10}	-2.51E-05
a_{11}	8.93E-05
a_{12}	7.89E-05
a_{13}	-1.67E-02
a_{14}	1.40E+00
a_{15}	2.96E-02

Fugacity coefficient of CO_2 (φ_{CO2})

CO_2 fugacity coefficient is calculated after Duan et al (1992a; 1992b)

$$ln\varphi_{CO2(P,T)} = Z - 1 - lnZ + \frac{a_1 + \frac{a_2}{T_r^2} + \frac{a_3}{T_r^3}}{V_r} + \frac{a_4 + \frac{a_5}{T_r^2} + \frac{a_6}{T_r^3}}{2V_r^2} + \frac{a_7 + \frac{a_8}{T_r^2} + \frac{a_9}{T_r^3}}{4V_r^4} + \frac{a_{10} + \frac{a_{11}}{T_r^2} + \frac{a_{12}}{T_r^3}}{5V_r^5} + \frac{a_{13}}{2T_r^3\, a_{15}} \left(a_{14} + 1 - \left(a_{14} + 1 + \frac{a_{15}}{V_r^2}\right) e^{\frac{-a_{15}}{V_r^2}}\right) \quad \text{(Eq.A.4)}$$

where parameters a_1 to a_{15} are reported on table A.1. T_r is the reduce temperature of CO_2 calculated after $T_r = \frac{T}{T_{c\,CO2}}$ (T_{cH2O} = 304.128 K), P_r is the reduce pressure of CO_2 after $P_r = \frac{P}{P_{c\,CO2}}$

($P_{c\,CO2}$ = 7.37 MPa).

Z is the coefficient on equation A.4 and is calculated after $Z = \frac{P_r\, v_r}{T_r}$ where v_r is the reduce volume of CO_2 and its calculated finding all the solution of the equation here below (A.5) when $\frac{P_r\, v_r}{T_r}$ =0

$$\frac{P_r\, v_r}{T_r} = 1 + \frac{a_1 + \frac{a_2}{T_r^2} + \frac{a_3}{T_r^3}}{V_r} + \frac{a_4 + \frac{a_5}{T_r^2} + \frac{a_6}{T_r^3}}{V_r^2} + \frac{a_7 + \frac{a_8}{T_r^2} + \frac{a_9}{T_r^3}}{V_r^4} + \frac{a_{10} + \frac{a_{11}}{T_r^2} + \frac{a_{12}}{T_r^3}}{V_r^5} + \frac{a_{13}}{2T_r^3\, v_r^2}\left(a_{14} + \frac{a_{15}}{V_r^2}\right) e^{\frac{-a_{15}}{V_r^2}} \quad \text{(Eq.A.5)}$$

Standard chemical potential of μCO_2 and interaction parameter $\lambda_{CO2-NaCl}$, $\zeta_{CO2-Na-Cl}$

The CO_2 ($\mu^{l(0)}_{CO2}$)/RT , λ (CO_2-NaCl) and ζ (CO_2-Na-Cl) of the equation Eq.A.1 are also called $Par(T,P)$. They are calculated after the equation (Eq.A.6) and combining the parameters reported on the table A.1.2 for each parameter.

$$Par(T,P) = c_1 + c_2 T + \frac{c_3}{T} + c_4 T^2 + \frac{c_5}{(630-T)} + c_6 P + c_7 P ln T + \frac{c_8 P}{T} + \frac{c_9 P}{(630-T)} + \frac{c_{10} P^2}{(630-T)^2} + c_{11} T ln P \quad \text{(Eq.A.6)}$$

Table A.1.2. *Parameters (c) to calculate* ($\mu_{CO2}^{1(0)}$)/RT , λ (CO2-NaCl) and ζ (CO2-Na-Cl) using equation A.6

Par (T,P)	μ_{CO2} / RT	$\lambda_{CO2\text{-}Na}$	$\zeta_{CO2\text{-}Na\text{-}Cl}$
c_1	2.89E+01	-4.11E-01	3.36E-04
c_2	-3.55E-02	6.08E-04	-1.98E-05
c_3	-4.77E+03	9.75E+01	(-)
c_4	1.03E-05	(-)	(-)
c_5	3.38E+01	(-)	(-)
c_6	9.04E-03	(-)	(-)
c_7	-1.15E-03	(-)	(-)
c_8	-3.07E-01	-2.38E-02	2.12E-03
c_9	-9.07E-02	1.71E-02	-5.25E-03
c_{10}	9.33E-04	(-)	(-)
c_{11}	(-)	1.41E-05	(-)

Estimation CO_2 (g) volume

The volume of CO_2 (g) required to fill the reactor CO_2-pump for a concentration of CO_2 (g) fixed for each experiment is calculated after the ideal gas law

$$PV = nRT \quad \text{(Eq.A.7)}$$

where *P* is the pressure in MPa, *V* is the volume in L, n is the concentration of the gas in moles, *R* is the constant of ideal gas law and *T* is the temperature in kelvin (K).

To ensure the solubility of $CO_{2(g)}$ in the water the concentration of [$CO_{2(g)}$] (in mol/L) in the experiment have to be less than the solubility of $CO_{2(g)}$ at the experimental conditions of T, P and salinity.

$$V_{co2(g)} = \frac{n_{CO2\ pump} \cdot R \cdot T_{filled}}{P_{filled}} \quad \text{(Eq.A.8)}$$

where $n_{CO2\ pump}$ is the number of moles in the pump, is calculated after $n_{CO2\ pump} = \frac{n_{CO2} \cdot V_{pump}}{V_{fluid}}$ in L, n_{CO2} is the number of moles of the fixed [CO_2] in 1 L of V_{fluid}, V_{pump} is the volume of the CO_2-pump which is 35 mL.

R is the ideal gas constant in 8.314 kPa.L.mol^{-1}.K^{-1}, T_{filled} is the temperature one the CO_2 (g) is filled on the reactor CO_2-pump (T_{filled} = 293 K) and P_{filled} is the pressure of the CO_2-bottle required to fill the CO_2-pump (normally is fixed on 3 MPa).

A.2 Fluid standard measured values SLRS-5, SLRS-6 and IAPSO

SLRS-5

						Si	Mg	Mn	Fe	Ca	Na	K
						ppb	*ppb*	*ppb*	*ppb*	*ppb*	*ppb*	*ppb*
Date:	**Instrument**	**Standard**	**Acidity**	**Dilution**	**n**							
02/12/2014	ICP-MS	SLRS-5	2% HNO_3	1.05	1	2059.10	2636.99	3.97	96.57	11309.15	5262.24	887.35
02/12/2014	ICP-MS	SLRS-5	2% HNO3	1.69	2	1422.90	1873.04	2.79	67.67	7825.46	3715.81	601.11
02/12/2014	ICP-MS	SLRS-5	2% HNO3	1.05	3	2055.40	2727.33	3.95	98.43	11434.97	5432.23	889.20
02/12/2014	ICP-MS	SLRS-5	2% HNO3	1.7	4	1497.00	1971.96	2.88	71.96	8399.49	3944.06	634.07
06/07/2015	ICP-MS	SLRS-5	2% HNO3	1.01	5	2041.60	2770.23	4.33	96.81	10488.44	5153.18	880.44
06/07/2015	ICP-MS	SLRS-5	2% HNO3	1.05	6	1978.20	2738.21	4.28	95.67	10342.04	5016.59	858.01
06/07/2015	ICP-MS	SLRS-5	2% HNO3	1.05	7	2059.90	2753.04	4.39	95.03	10795.36	5045.68	898.38
06/07/2015	ICP-MS	SLRS-5	2% HNO3	1.01	8	2145.10	2791.77	4.55	97.21	10787.24	5154.13	891.96
07/07/2015	ICP-MS	SLRS-5	2% HNO3	1.05	9	1934.20	2604.63	4.24	91.76	10089.15	4828.12	823.52
07/07/2015	ICP-MS	SLRS-5	2% HNO3	1.05	10	2072.50	2774.43	4.35	95.33	10752.31	5133.12	887.10
30/11/2015	ICP-MS	SLRS-5	2% HNO3	1.01	11	1878.50	2491.19	3.75	96.08	10437.74	5079.22	831.90
30/11/2015	ICP-MS	SLRS-5	2% HNO3	1.05	12	1835.00	2440.34	3.75	95.92	10285.23	5006.95	839.62
30/11/2015	ICP-MS	SLRS-5	2% HNO3	1.05	13	1978.50	2524.99	3.89	96.35	10916.39	5110.01	887.62
30/11/2015	ICP-MS	SLRS-5	2% HNO3	1.05	14	1984.50	2494.33	3.83	94.63	10919.24	5042.63	879.26
09/03/2016	ICP-MS	SLRS-5	2% HNO3	1.01	15	1902.80	2580.84	4.00	101.15	10635.78	5250.25	864.41
09/03/2016	ICP-MS	SLRS-5	2% HNO3	1.05	16	1891.80	2528.22	3.98	100.00	10603.13	5154.23	852.87
09/03/2016	ICP-MS	SLRS-5	2% HNO3	1.05	17	1923.50	2573.33	4.00	100.20	10728.84	5263.27	871.07
09/03/2016	ICP-MS	SLRS-5	2% HNO3	1.05	18	2169.10	2932.53	4.30	109.00	11879.04	6072.52	969.95
04/04/2017	ICP-MS	SLRS-5	2% HNO3	1.05	19	2043.12	2738.53	4.58	105.46	11616.96	5828.66	931.89
04/04/2017	ICP-MS	SLRS-5	2% HNO3	1.05	20	2140.48	2877.94	4.70	109.34	12467.31	6062.15	1030.24
22/06/2017	ICP-MS	SLRS-5	2% HNO3	1.03	21	2162.33	2305.63	3.82	86.22	9490.51		817.90
22/06/2017	ICP-MS	SLRS-5	2% HNO3	1.05	22	2469.40	2614.78	4.19	94.88	10889.20		943.36
22/06/2017	ICP-MS	SLRS-5	2% HNO3	1.04	23	2504.12	2610.24	4.19	93.90	10986.96		957.05
					Avg.	2006.48	2580.63	4.03	95.20	10612.17	5127.75	866.45
					σ	238.25	254.50	0.46	9.52	1003.18	558.73	93.08

						Si	Mg	Mn	Fe	Ca	Na	K
						ppb	*ppb*	*ppb*	*ppb*	*ppb*	*ppb*	*ppb*
Date:	**Instrument**	**Standard**	**Acidity**	**Dilution**	**n**							
04/06/2017	ICP-OES	SLRS-5	2% HNO_3	1.04	1	2206.51	2340.90	15.16	147.68	11768.45	-4456.13	909.87
04/06/2017	ICP-OES	SLRS-5	2% HNO3	1.04	2	1965.34	2761.90	4.43	98.95	11242.82	5425.79	874.23
04/06/2017	ICP-OES	SLRS-5	2% HNO3	1.04	3	2010.09	2737.78	4.51	97.96	10930.74	5504.51	995.53
04/06/2017	ICP-OES	SLRS-5	2% HNO3	1.03	4	2020.09	2651.57	4.64	97.74	10775.72	5279.95	892.40
20/06/2017	ICP-OES	SLRS-5	2% HNO3	1.039	5	1991.52	2735.63	4.43	98.71	11023.74	5502.60	857.18
05/07/2017	ICP-OES	SLRS-5	2% HNO3	1.044	6	1800.20	2440.80	4.05	90.36	10192.88	4928.28	771.41
05/07/2017	ICP-OES	SLRS-5	2% HNO3	1.0312	7	1832.10	2392.70	4.00	88.52	9922.21	4574.65	722.02
05/07/2017	ICP-OES	SLRS-5	2% HNO3	1.0443	8	1975.80	2537.50	4.42	95.19	10499.50	4914.12	810.03
05/07/2017	ICP-OES	SLRS-5	2% HNO3	1.033	9	1906.90	2508.80	4.11	93.14	9999.82	5168.92	820.12
05/07/2017	ICP-OES	SLRS-5	2% HNO3	1.0436	10	1862.54	2656.77	4.19	94.18	10885.65	5238.70	885.29
05/07/2017	ICP-OES	SLRS-5	2% HNO3	1.0442	11	1834.71	2674.91	4.09	93.71	10868.85	5304.84	831.94
05/07/2017	ICP-OES	SLRS-5	2% HNO3	1.044	12	1779.38	2556.72	4.05	92.05	10553.11	5336.98	872.31
					Avg.	1932.10	2583.00	5.17	99.02	10721.96	4393.60	853.53
					σ	121.11	141.79	3.15	15.68	528.41	2800.29	70.17

						Cr	Co	Ni	Cu	Zn
						ppb	*ppb*	*ppb*	*ppb*	*ppb*
Date:	**Instrument**	**Standard**	**Acidity**	**Dilution**	**n**					
02/12/2014	ICP-MS	SLRS-5	2% HNO_3	1.05	1	0.22	0.05	0.42	16.28	0.51
02/12/2014	ICP-MS	SLRS-5	2% HNO3	1.69	2	0.19	0.03	0.30	11.49	0.76
02/12/2014	ICP-MS	SLRS-5	2% HNO3	1.05	3	0.22	0.05	0.39	16.12	0.50
02/12/2014	ICP-MS	SLRS-5	2% HNO3	1.7	4	0.19	0.03	0.31	11.80	0.81
06/07/2015	ICP-MS	SLRS-5	2% HNO3	1.01	5	0.22	0.05	0.48	18.10	1.26
06/07/2015	ICP-MS	SLRS-5	2% HNO3	1.05	6	0.24	0.05	0.46	17.22	0.93
06/07/2015	ICP-MS	SLRS-5	2% HNO3	1.05	7	0.23	0.05	0.52	16.20	0.95
06/07/2015	ICP-MS	SLRS-5	2% HNO3	1.01	8	0.21	0.05	0.48	18.56	1.01
07/07/2015	ICP-MS	SLRS-5	2% HNO3	1.05	9	0.23	0.05	0.44	16.75	0.64
07/07/2015	ICP-MS	SLRS-5	2% HNO3	1.05	10	0.22	0.05	0.50	17.11	0.66
30/11/2015	ICP-MS	SLRS-5	2% HNO3	1.01	11	0.19	0.05	0.43	15.83	1.39
30/11/2015	ICP-MS	SLRS-5	2% HNO3	1.05	12	0.20	0.05	0.42	15.32	4.83
30/11/2015	ICP-MS	SLRS-5	2% HNO3	1.05	13	0.20	0.05	0.41	14.82	4.88
30/11/2015	ICP-MS	SLRS-5	2% HNO3	1.05	14	0.19	0.05	0.42	14.48	4.77
09/03/2016	ICP-MS	SLRS-5	2% HNO3	1.01	15	0.21	0.05	0.47	17.35	1.44
09/03/2016	ICP-MS	SLRS-5	2% HNO3	1.05	16	0.22	0.05	0.43	16.64	1.58
09/03/2016	ICP-MS	SLRS-5	2% HNO3	1.05	17	0.23	0.05	0.43	16.45	1.60
09/03/2016	ICP-MS	SLRS-5	2% HNO3	1.05	18	0.24	0.05	0.49	17.62	1.68
04/04/2017	ICP-MS	SLRS-5	2% HNO3	1.05	19	0.26	0.06	0.48	18.71	0.84
04/04/2017	ICP-MS	SLRS-5	2% HNO3	1.05	20	0.25	0.06	0.51	18.04	0.89
22/06/2017	ICP-MS	SLRS-5	2% HNO3	1.03	21	0.21	0.05	0.42	16.77	0.95
22/06/2017	ICP-MS	SLRS-5	2% HNO3	1.05	22	0.23	0.05	0.41	17.29	0.87
22/06/2017	ICP-MS	SLRS-5	2% HNO3	1.04	23	0.24	0.05	0.44	17.12	0.73
					Avg.	0.22	0.05	0.44	16.35	1.50
					σ	0.02	0.01	0.05	1.83	1.36

						Cu	Zn
						ppb	*ppb*
Date:	**Instrument**	**Standard**	**Acidity**	**Dilution**	**n**		
04/06/2017	ICP-OES	SLRS-5	2% HNO_3	1.04	1	117.61	18.06
04/06/2017	ICP-OES	SLRS-5	2% HNO3	1.04	2	19.03	0.88
04/06/2017	ICP-OES	SLRS-5	2% HNO3	1.04	3	19.77	0.92
04/06/2017	ICP-OES	SLRS-5	2% HNO3	1.03	4	18.75	0.80
20/06/2017	ICP-OES	SLRS-5	2% HNO3	1.039	5	18.68	0.98
05/07/2017	ICP-OES	SLRS-5	2% HNO3	1.044	6	18.02	0.78
05/07/2017	ICP-OES	SLRS-5	2% HNO3	1.0312	7	17.37	0.49
05/07/2017	ICP-OES	SLRS-5	2% HNO3	1.0443	8	19.24	0.69
05/07/2017	ICP-OES	SLRS-5	2% HNO3	1.033	9	18.31	0.53
05/07/2017	ICP-OES	SLRS-5	2% HNO3	1.0436	10	19.22	0.82
05/07/2017	ICP-OES	SLRS-5	2% HNO3	1.0442	11	19.80	0.96
05/07/2017	ICP-OES	SLRS-5	2% HNO3	1.044	12	19.38	0.94
					Avg.	27.10	2.24
					σ	28.51	4.98

SLRS-6

						Si	Mg	Mn	Fe	Ca	Na	K
						ppb	*ppb*	*ppb*	*ppb*	*ppb*	*ppb*	*ppb*
Date:	**Instrument**	**Standard**	**Acidity**	**Dilution**	**n**							
26/10/2016	ICP-MS	SLRS-6	1% HNO3	1.01	1	2031.10	2012.37		79.63	8503.96		613.70
26/10/2016	ICP-MS	SLRS-6	1% HNO3	1.01	2	2159.70	1836.09		83.05	8709.14		630.99
26/10/2016	ICP-MS	SLRS-6	1% HNO3	1.01	3	2265.60	1837.40		81.53	8719.04		633.12
29/11/2016	ICP-MS	SLRS-6	1% HNO3	1.01	4	1449.50	2007.46	2.11	81.72	8576.50		630.58
29/11/2016	ICP-MS	SLRS-6	1% HNO3	1.01	5	2088.70	2015.95	2.11	83.35	8683.57		655.94
05/12/2016	ICP-MS	SLRS-6	1% HNO3	1.01	6	2214.90	2045.11		82.33	8657.15		603.43
31/01/2017	ICP-MS	SLRS-6	1% HNO3	1.01	7	2057.50	2098.64	2.09	82.97	8701.65		613.96
31/01/2017	ICP-MS	SLRS-6	1% HNO3	1.01	8	2162.50	2108.90	2.07	81.14	8579.26		611.72
09/02/2017	ICP-MS	SLRS-6	2% HNO3	1.01	9	2148.10	2051.70		83.86	8882.33		563.59
04/04/2017	ICP-MS	SLRS-6	2% HNO3	1.01	10	2383.22	2419.00	2.35	95.47	9767.02	3126.89	729.74
04/04/2017	ICP-MS	SLRS-6	2% HNO3	1.01	11	2993.73	3013.14	2.74	109.96	12003.16	3933.01	911.64
22/06/2017	ICP-MS	SLRS-6	2% HNO3	1.01	12	2162.33	2305.63	3.82	86.22	9490.51		817.90
22/06/2017	ICP-MS	SLRS-6	2% HNO3	1.01	13	2975.36	2374.76	2.18	89.24	9342.57		765.49
06/07/2017	ICP-MS	SLRS-6	2% HNO3	1.01	14	2702.42	2244.52	2.11	84.19	8693.76		407.99
					Avg.	2271.05	2169.33	2.40	86.05	9093.54	3529.95	656.41
					σ	400.26	300.55	0.57	7.96	920.83	570.02	120.61

						Si	Mg	Mn	Fe	Ca	Na	K
						ppb	*ppb*	*ppb*	*ppb*	*ppb*	*ppb*	*ppb*
Date:	**Instrument**	**Standard**	**Acidity**	**Dilution**	**n**							
08/03/2017	ICP-OES	SLRS-6	2% HNO_3	1.01	1	2236.80	2261.16	2.23	87.05	8988.60	2688.50	649.36
08/03/2017	ICP-OES	SLRS-6	2% HNO3	1.01	2	2273.01	2207.33	2.23	87.72	8782.96	2645.35	645.58
08/03/2017	ICP-OES	SLRS-6	2% HNO3	1.01	3	2234.46	2206.74	2.27	87.31	8647.93	2683.23	648.09
04/07/2017	ICP-OES	SLRS-6	2% HNO3	1.01	4	2152.70	2219.58	2.11	84.79	8793.56	2656.89	618.77
04/07/2017	ICP-OES	SLRS-6	2% HNO3	1.010	5	2183.87	2257.65	2.26	83.83	8744.62	2600.96	650.39
04/07/2017	ICP-OES	SLRS-6	2% HNO3	1.01	6	2182.72	2217.88	2.13	83.60	8491.20	2596.67	688.33
					Avg.	2210.59	2228.39	2.21	85.71	8741.48	2645.27	650.09
					σ	44.71	24.62	0.07	1.86	165.47	39.42	22.22

						Cr	Co	Ni	Cu	Zn
						ppb	*ppb*	*ppb*	*ppb*	*ppb*
Date:	**Instrument**	**Standard**	**Acidity**	**Dilution**	**n**					
26/10/2016	ICP-MS	SLRS-6	1% HNO3	1.01	1					
26/10/2016	ICP-MS	SLRS-6	1% HNO3	1.01	2					
26/10/2016	ICP-MS	SLRS-6	1% HNO3	1.01	3					
29/11/2016	ICP-MS	SLRS-6	1% HNO3	1.01	4	0.24	0.05		23.99	1.58
29/11/2016	ICP-MS	SLRS-6	1% HNO3	1.01	5	0.25	0.06	0.59	24.51	1.82
05/12/2016	ICP-MS	SLRS-6	1% HNO3	1.01	6					
31/01/2017	ICP-MS	SLRS-6	1% HNO3	1.01	7	0.24	0.05	0.58	24.77	1.80
31/01/2017	ICP-MS	SLRS-6	1% HNO3	1.01	8	0.24	0.05	0.58	24.57	1.76
09/02/2017	ICP-MS	SLRS-6	2% HNO3	1.01	9				25.33	
04/04/2017	ICP-MS	SLRS-6	2% HNO3	1.01	10	0.28	0.06	0.64	27.65	2.22
04/04/2017	ICP-MS	SLRS-6	2% HNO3	1.01	11	0.32	0.07	0.72	30.49	2.42
22/06/2017	ICP-MS	SLRS-6	2% HNO3	1.01	12	0.21	0.05	0.42	16.77	0.95
22/06/2017	ICP-MS	SLRS-6	2% HNO3	1.01	13	0.25	0.05	0.56	26.00	2.12
06/07/2017	ICP-MS	SLRS-6	2% HNO3	1.01	14	0.26	0.06	0.62	28.15	1.97
					Avg.	0.26	0.06	0.59	25.22	1.85
					σ	0.04	0.01	0.09	3.61	0.42

						Cu	Zn
						ppb	*ppb*
Date:	**Instrument**	**Standard**	**Acidity**	**Dilution**	**n**		
08/03/2017	ICP-OES	SLRS-6	2% HNO_3	1.01	1	26.91	1.96
08/03/2017	ICP-OES	SLRS-6	2% HNO3	1.01	2	26.16	1.99
08/03/2017	ICP-OES	SLRS-6	2% HNO3	1.01	3	26.14	1.91
04/07/2017	ICP-OES	SLRS-6	2% HNO3	1.01	4	26.01	1.61
04/07/2017	ICP-OES	SLRS-6	2% HNO3	1.010	5	25.91	1.76
04/07/2017	ICP-OES	SLRS-6	2% HNO3	1.01	6	24.94	1.73
					Avg.	26.01	1.83
					σ	0.63	0.15

IAPSO

						Si	Mg	Mn	Fe	Ca	Na	K
						ppb	*ppb*	*ppb*	*ppb*	*ppb*	*ppb*	*ppb*
Date:	**Instrument**	**Standard**	**Acidity**	**Dilution**	**n**							
29/11/2016	ICP-MS	IAPSO	1% HNO3	94.40	1.00	22996.18	1235745.01			472359.67		395282.30
31/01/2017	ICP-MS	IAPSO	1% HNO3	62.80	2.00	9784.14	1275142.63	3.32	24.59	463787.69		380387.20
31/01/2017	ICP-MS	IAPSO	1% HNO3	62.80	3.00	5203.95	1283274.14	3.18	18.19	470557.78		383312.29
31/01/2017	ICP-MS	IAPSO	1% HNO3	64.80	4.00	17088.77	1352804.86	3.11	23.67	479330.29		406015.16
09/02/2017	ICP-MS	IAPSO	1% HNO3	68.30	5.00	1219.94	1659447.03		39.86	614397.08		438480.83
09/02/2017	ICP-MS	IAPSO	1% HNO3	63.00	6.00	1297.34	1782561.02		39.67	650810.53		462539.88
09/02/2017	ICP-MS	IAPSO	1% HNO3	72.90	7.00	773.98	1743837.17		44.26	640199.85		456988.71
04/04/2017	ICP-MS	IAPSO	2% HNO3	38.60	8.00	1421.86	1767794.26	1.77	23.43	620817.25	15521681.08	547694.34
04/04/2017	ICP-MS	IAPSO	2% HNO3	39.70	9.00	883.36	1732012.48	1.28	19.22	624108.59	15044228.28	555967.21
22/06/2017	ICP-MS	IAPSO	2% HNO3	112.00	10.00	11473.66	1362884.74	27.01	12.75	452273.31		440978.82
22/06/2017	ICP-MS	IAPSO	2% HNO3	108.40	11.00	1966.34	1470540.18	8.22	0.00	493064.63		485578.62
					Avg.	6737.23	1515094.86	6.84	24.56	543791.52	15282954.68	450293.22
					σ	7658.01	222812.55	9.18	13.60	83717.94	337610.11	60564.16

						Si	Mg	Mn	Fe	Ca	Na	K
						ppb	*ppb*	*ppb*	*ppb*	*ppb*	*ppb*	*ppb*
Date:	**Instrument**	**Standard**	**Acidity**	**Dilution**	**n**							
08/03/2017	ICP-OES	IAPSO	2% HNO_3	63.13	1.00	52673.21	65538193.55	128.39	-1593.86	23147024.68	534294805.74	22700306.44
08/03/2017	ICP-OES	IAPSO	2% HNO3	62.96	2.00	54725.54	72081103.32	86.68	-15.20	25748705.89	588755094.43	24924197.67
08/03/2017	ICP-OES	IAPSO	2% HNO3	62.96	3.00	58135.69	68193266.75	52.42	759.04	24189642.39	552588973.34	23670436.07
20/06/2017	ICP-OES	IAPSO	2% HNO3	51.80	4.00	51528.89	54206292.50	-163.75	-44.80	21339555.30	558172292.00	21543972.90
04/06/2017	ICP-OES	IAPSO	2% HNO3	51.80	5.00	1029.35	1094221.40	2.64	24.69	416239.51	10836958.60	441135.75
05/07/2017	ICP-OES	IAPSO	2% HNO3	56.87	6.00	913.86	992306.30	0.57	-18.87	386897.73	9484252.19	397158.35
					Avg.	36501.09	43684230.64	17.83	-148.17	15871344.25	375688729.38	15612867.86
					σ	27612.51	33561567.31	101.64	773.05	12068318.53	283679271.03	11821457.88

						Cr	Co	Ni	Cu	Zn
						ppb	*ppb*	*ppb*	*ppb*	*ppb*
Date:	**Instrument**	**Standard**	**Acidity**	**Dilution**	**n**					
29/11/2016	ICP-MS	IAPSO	1% HNO3	94.40	1.00	33.26			0.80	60.78
31/01/2017	ICP-MS	IAPSO	1% HNO3	62.80	2.00	2.78	0.40	19.79	0.00	66.45
31/01/2017	ICP-MS	IAPSO	1% HNO3	62.80	3.00	2.79	0.45	19.89	1.25	67.94
31/01/2017	ICP-MS	IAPSO	1% HNO3	64.80	4.00	3.10	0.38	19.70	-1.84	67.26
09/02/2017	ICP-MS	IAPSO	1% HNO3	68.30	5.00				1.04	
09/02/2017	ICP-MS	IAPSO	1% HNO3	63.00	6.00				1.44	
09/02/2017	ICP-MS	IAPSO	1% HNO3	72.90	7.00				1.51	
04/04/2017	ICP-MS	IAPSO	2% HNO3	38.60	8.00	2.45	0.10	0.24	1.15	88.63
04/04/2017	ICP-MS	IAPSO	2% HNO3	39.70	9.00	1.92	0.10	0.00	0.98	87.52
22/06/2017	ICP-MS	IAPSO	2% HNO3	112.00	10.00	5.57	0.35	2.91		88.33
22/06/2017	ICP-MS	IAPSO	2% HNO3	108.40	11.00	3.09	0.00	1.32		83.94
					Avg.	3.26	0.25	9.12	0.70	76.35
					σ	1.61	0.18	10.03	1.05	11.77

						Cu	Zn
						ppb	*ppb*
Date:	**Instrument**	**Standard**	**Acidity**	**Dilution**	**n**		
08/03/2017	ICP-OES	IAPSO	2% HNO_3	63.13	1.00	0.91	4806.77
08/03/2017	ICP-OES	IAPSO	2% HNO3	62.96	2.00	1.37	4741.61
08/03/2017	ICP-OES	IAPSO	2% HNO3	62.96	3.00	1.24	4758.99
20/06/2017	ICP-OES	IAPSO	2% HNO3	51.80	4.00	204.71	3876.78
04/06/2017	ICP-OES	IAPSO	2% HNO3	51.80	5.00	14.48	81.16
05/07/2017	ICP-OES	IAPSO	2% HNO3	56.87	6.00	44.64	52.37
					Avg.	44.56	3052.95
					σ	80.25	2338.88

					Na	Cl	SO_4
					ppm	*ppm*	*ppm*
Date:	**Instrument**	**Standard**	**Dilution**	**n**			
19/01/2017	DIONEX	IAPSO	543.29	1.00	11486.20	19800.30	2796.40
06/02/2017	DIONEX	IAPSO	545.07	2.00	11028.12	20116.55	2790.38
06/02/2017	DIONEX	IAPSO	541.12	3.00	10628.49	19513.71	2754.80
06/02/2017	DIONEX	IAPSO	548.02	4.00	10837.66	19555.89	2803.17
				Avg.	10995.12	19746.61	2786.19
				σ	365.81	277.10	21.57

A.3 Alkalinity results method MET and DET

Table. A.3.1 Alkalinity and pH results for 2 ml of Volvic® not diluted.(Avg.) denotes average and σ standard deviation

No sample dilution V_s (ml)= 2 V_{MQ} (ml) =0

Date	n	V_s *(ml)*	V_{MQ} *(ml)*	Equivalence point method	Alk *(mmol/L)*	pH	V_{HCl} *(ml)*	Slope %
13/04/2015	1	2	0	DET	1.32	7.1	0.261	97.0
13/04/2015	2	2	0	DET	1.37	7.3	0.274	97.0
13/04/2015	3	2	0	DET	1.34	7.4	0.268	97.0
13/04/2015	4	2	0	DET	1.37	7.0	0.274	97.0
13/04/2015	5	2	0	DET	1.33	6.9	0.267	97.0
13/04/2015	6	2	0	DET	1.27	7.1	0.254	97.0
13/04/2015	7	2	0	DET	1.29	7.1	0.258	97.0
13/04/2015	8	2	0	DET	1.38	7.1	0.276	97.0
13/04/2015	9	2	0	DET	1.29	7.2	0.258	97.0
13/04/2015	10	2	0	DET	1.29	7.1	0.257	97.0
				Avg.	1.32	7.13		
				σ	0.04	0.12		

Date	n	V_s *(ml)*	V_{MQ} *(ml)*	Equivalence point method	Alk *(mmol/L)*	pH	V_{HCl} *(ml)*	Slope %
13/04/2015	1	2	0	MET	1.34	7.0	0.268	97.0
13/04/2015	2	2	0	MET	1.23	7.3	0.245	97.0
13/04/2015	3	2	0	MET	1.32	7.4	0.265	97.0
13/04/2015	4	2	0	MET	1.30	7.4	0.259	97.0
13/04/2015	5	2	0	MET	1.41	6.8	0.282	97.0
13/04/2015	6	2	0	MET	0.88	7.3	0.175	97.0
13/04/2015	7	2	0	MET	0.63	6.6	0.126	97.0
13/04/2015	8	2	0	MET	1.28	7.1	0.257	97.0
13/04/2015	9	2	0	MET	1.14	7.0	0.228	97.0
13/04/2015	10	2	0	MET	1.18	7.1	0.237	97.0
				Avg.	1.17	7.09		
				σ	0.24	0.28		

Table.A.3.2 Alkalinity and pH results for a Volvic® diluted with MilliQ water (dilution 2). 1ml Volvic® with 1ml MilliQ water. .(Avg.) denotes average and σ standard deviation

Sample dilution 2 V_s (ml)=1 V_{MQ}(ml)=1

Date	n	V_s *(ml)*	V_{MQ} *(ml)*	Equivalence point method	Alk *(mmol/L)*	pH	V_{HCl} *(ml)*	Slope %
15/04/2015	1	1	1	DET	1.40	6.9	0.140	97.0
15/04/2015	2	1	1	DET	1.32	6.8	0.132	97.0
15/04/2015	3	1	1	DET	1.40	6.7	0.140	97.0
15/04/2015	4	1	1	DET	1.34	6.7	0.134	97.0
15/04/2015	5	1	1	DET	1.46	6.8	0.146	97.0
15/04/2015	6	1	1	DET	1.54	7.0	0.154	97.0
15/04/2015	7	1	1	DET	1.37	6.8	0.137	97.0
15/04/2015	8	1	1	DET	1.36	6.8	0.136	97.0
15/04/2015	9	1	1	DET	1.40	6.9	0.140	97.0
15/04/2015	10	1	1	DET	1.35	6.7	0.135	97.0
				Avg.	1.39	6.81		
				σ	0.06	0.10		

Date	n	V_s *(ml)*	V_{MQ} *(ml)*	Equivalence point method	Alk *(mmol/L)*	pH	V_{HCl} *(ml)*	Slope %
15/04/2015	1	1	1	MET	1.40	5.7	0.140	96.8
15/04/2015	2	1	1	MET	1.56	5.8	0.156	96.8
15/04/2015	3	1	1	MET	1.73	5.6	0.173	96.8
15/04/2015	4	1	1	MET	1.57	5.7	0.158	96.8
15/04/2015	5	1	1	MET	1.45	5.7	0.145	96.8
15/04/2015	6	1	1	MET	1.59	5.7	0.159	96.8
15/04/2015	7	1	1	MET	1.55	5.7	0.155	96.8
15/04/2015	8	1	1	MET	1.57	5.8	0.157	96.8
15/04/2015	9	1	1	MET	1.59	5.8	0.159	96.8
15/04/2015	10	1	1	MET	1.57	5.7	0.157	96.8
				Avg.	1.56	5.71		
				σ	0.09	0.06		

Table.A.3.3 Alkalinity and pH results for a Volvic® diluted with MilliQ water (dilution 7). 0.3 ml Volvic® with 1.7 ml MilliQ. .(Avg.) denotes average and σ standard deviation

Sample dilution 7 V_s(ml)=0.3 V_{MQ}(ml)=1

Date	n	V_s *(ml)*	V_{MQ} *(ml)*	Equivalence point method	Alk *(mmol/L)*	pH	V_{HCl} *(ml)*	Slope %
17/04/2015	1	0.3	1.7	DET	1.52	6.2	0.046	97.0
17/04/2015	2	0.3	1.7	DET	1.60	6.1	0.048	97.0
17/04/2015	3	0.3	1.7	DET	1.78	6.1	0.054	97.0
17/04/2015	4	0.3	1.7	DET	1.67	6.1	0.050	97.0
17/04/2015	5	0.3	1.7	DET	1.55	6.0	0.046	97.0
17/04/2015	6	0.3	1.7	DET	1.68	6.1	0.051	97.0
17/04/2015	7	0.3	1.7	DET	1.93	6.1	0.058	97.0
17/04/2015	8	0.3	1.7	DET	1.53	5.8	0.046	97.0
17/04/2015	9	0.3	1.7	DET	1.58	5.7	0.047	97.0
17/04/2015	10	0.3	1.7	DET	1.60	6.2	0.048	97.0
				Avg.	1.64	6.05		
				σ	0.13	0.16		

A.4 Protocol to dry the reacted samples after experiments

The samples after the experiments could retain the injected solution on their pores. It is necessary to dry them to avoid post precipitation. I estimate the time required to dry the sample at room temperature (25°C). To make this estimation, I use a steel capsule filled with olivine powder and I submerged in water during 24 hours. Then I measured the sample weight until the weight was stable following two methods: (i) drying at 25°C and (ii) drying under vacuum.

The results reported on the Fig. A.4.1 shows after 3 hours under vacuum the sample reaches the initial dry weight faster than drying the sample just at room temperature (25°C. However, I leave between 12 to 24 hours the samples under vacuum in order to ensure the sample was completely dried.

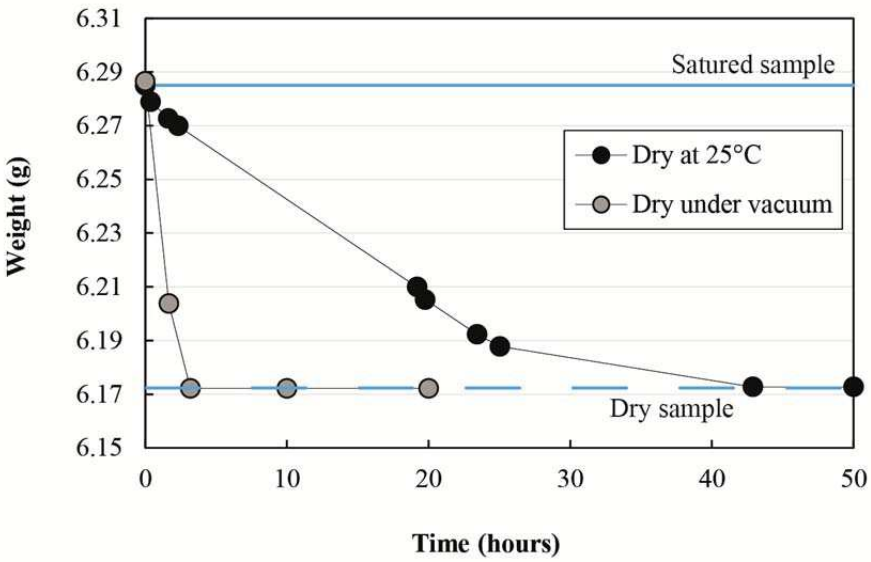

Fig.A.4.1. Time estimation to dry the samples of powder olivine experiments using two approaches i) dry at 25°C and ii) dry under vacuum.

A.5 Data bases

Data base 250 bars generated after SUPCRT92

Table A.5.1. Aqueous species on data base at 250 bars computed after SUPCRT92

Aqueous species	Log K *1°C*	Log K *25°C*	Log K *50°C*	Log K *100°C*	Log K *150°C*	Log K *200°C*	Log K *250°C*	Log K *300°C*
Al(OH)2+	12.704	10.973	8.885	6.983	5.113	3.614	2.356	1.242
AlOH++	5.824	4.991	3.985	3.068	2.164	1.438	0.826	0.283
CO2(aq)	-6.434	-6.229	-6.154	-6.264	-6.582	-7.037	-7.608	-8.325
CO3--	10.478	10.199	10.005	9.960	10.073	10.326	10.705	11.246
CaCO3(aq)	7.397	6.906	6.365	5.901	5.447	5.053	4.647	4.139
CaOH+	13.509	12.569	11.437	10.396	9.352	8.497	7.755	7.067
CaCl+	0.390	0.319	0.119	-0.185	-0.638	-1.159	-1.761	-2.494
CaCl2(aq)	0.545	0.709	0.699	0.474	-0.018	-0.700	-1.580	-2.752
CaHCO3+	-1.159	-0.974	-0.928	-1.068	-1.429	-1.940	-2.586	-3.407
CaHSiO3+	9.124	8.735	8.161	7.603	7.053	6.621	6.261	5.921
CaSO4(aq)	-2.007	-2.072	-2.232	-2.469	-2.840	-3.313	-3.938	-4.831
FeCl+	0.181	0.184	0.062	-0.174	-0.558	-1.021	-1.572	-2.258
FeCl++	-1.475	-1.493	-1.623	-1.853	-2.218	-2.659	-3.186	-3.850
FeOH+	10.038	9.262	8.319	7.455	6.603	5.923	5.355	4.856
FeOH++	2.835	2.179	1.409	0.727	0.075	-0.435	-0.860	-1.239
FeO(aq)	22.114	20.353	18.263	16.382	14.551	13.106	11.913	10.872
HFeO2-	31.193	29.089	26.575	24.311	22.136	20.481	19.212	18.266
HFeO2(aq)	14.229	12.052	9.642	7.641	5.866	4.600	3.641	2.847
FeO+	6.818	5.553	4.145	2.963	1.894	1.108	0.487	-0.049
Fe(OH)4-	23.477	21.277	18.683	16.318	13.957	12.040	10.432	9.061
FeCl2(aq)	9.655	8.232	6.317	4.360	2.172	0.160	-1.792	-3.848
H2S(aq)	-7.324	-6.924	-6.587	-6.417	-6.409	-6.563	-6.854	-7.309
H2O2(aq)	19.593	18.138	16.410	14.854	13.351	12.187	11.259	10.495
HAlO2(aq)	2.801	3.031	3.189	3.224	3.142	2.972	2.741	2.448
HCl(aq)	0.394	0.710	0.894	0.868	0.615	0.196	-0.355	-1.053
HO2-	31.659	29.692	27.457	25.542	23.809	22.593	21.770	21.295
HSO4-	-1.620	-1.888	-2.356	-2.922	-3.639	-4.369	-5.134	-5.990
HSiO3-	10.115	9.717	9.261	8.937	8.768	8.798	8.987	9.333
KCl(aq)	2.879	2.584	2.188	1.781	1.312	0.859	0.383	-0.179
KHSO4(aq)	2.174	1.626	0.713	-0.359	-1.688	-3.015	-4.387	-5.915
KSO4-	-0.845	-0.861	-0.979	-1.179	-1.491	-1.864	-2.317	-2.908
KOH(aq)	15.392	14.385	13.266	12.335	11.514	10.946	10.546	10.257
LiCl(aq)	1.598	1.560	1.433	1.238	0.943	0.595	0.175	-0.372
MgCO3(aq)	7.640	7.259	6.847	6.509	6.194	5.920	5.617	5.197
MgSO4(aq)	-2.123	-2.190	-2.357	-2.593	-2.952	-3.408	-4.015	-4.896

MgCl+	0.127	0.157	0.064	-0.143	-0.494	-0.924	-1.442	-2.096
MgOH+	12.653	11.705	10.525	9.422	8.315	7.419	6.668	6.010
MgHCO3+	-1.037	-1.009	-1.135	-1.393	-1.808	-2.301	-2.876	-3.579
MgHSiO3+	8.797	8.483	7.989	7.509	7.047	6.699	6.420	6.156
NaAlO2(aq)	2.801	3.031	3.189	3.224	3.142	2.972	2.741	2.448
NaCl(aq)	0.868	0.809	0.680	0.505	0.257	-0.031	-0.380	-0.847
NaHSiO3(aq)	7.966	7.924	7.822	7.757	7.766	7.845	7.957	8.058
NaSO4-	-0.971	-0.897	-0.923	-1.048	-1.289	-1.606	-2.012	-2.558
NaOH(aq)	15.033	14.147	13.155	12.327	11.598	11.095	10.738	10.475
NiCl+	1.066	1.016	0.850	0.591	0.204	-0.246	-0.772	-1.427
NiO(aq)	23.203	20.653	17.586	14.784	12.017	9.808	7.975	6.389
NiO2--	46.971	43.890	40.281	37.095	34.113	31.933	30.370	29.363
NiOH+	11.605	10.763	9.697	8.681	7.637	6.771	6.028	5.364
HNiO2-	32.803	30.866	28.485	26.282	24.108	22.407	21.066	20.032
OH-	14.781	13.898	12.942	12.173	11.544	11.183	11.039	11.118
SO2(aq)	40.815	36.293	30.606	25.147	19.458	14.649	10.426	6.516
B(OH)4-	9.349	9.110	8.914	8.809	8.791	8.868	9.039	9.341
NaB(OH)4(aq)	9.086	8.894	8.635	8.411	8.229	8.125	8.071	8.041
B2O(OH)5-	10.062	9.574	9.090	8.790	8.681	8.775	9.017	9.392
B3O3(OH)4-	7.067	7.155	7.296	7.509	7.852	8.260	8.726	9.264
B4O5(OH)4--	15.683	15.752	15.990	16.425	17.151	18.035	19.065	20.299
B(OH)3Cl-	0.968	0.867	0.727	0.623	0.566	0.562	0.581	0.591
Al(OH)4-	25.677	22.927	19.657	16.704	13.823	11.557	9.719	8.203
Al(OH)3(aq)	19.459	17.117	14.300	11.749	9.257	7.281	5.637	4.193
AlSO4+	-2.922	-3.059	-3.656	-4.599	-5.969	-7.473	-9.131	-11.090
NaAl(OH)4(aq)	25.968	23.010	19.498	16.324	13.210	10.724	8.646	6.813

Table. A.5.2. Minerals on data base at 250 bars generated after SUPCRT92

Minerals	**Log K** *1°C*	**Log K** *25°C*	**Log K** *50°C*	**Log K** *100°C*	**Log K** *150°C*	**Log K** *200°C*	**Log K** *250°C*	**Log K** *300°C*
Forsterite	31.535	28.268	24.285	20.669	17.153	14.388	12.105	10.091
Fayalite	21.974	19.533	16.519	13.757	11.046	8.887	7.072	5.429
Ol (90)	31.268	28.020	24.058	20.458	16.953	14.196	11.917	9.905
Antigorite	544.975	489.420	421.039	359.541	300.836	255.496	218.257	184.689
Chrysotile	35.437	31.857	27.467	23.521	19.751	16.838	14.446	12.298
Dolomite	3.656	2.748	1.536	0.292	-1.137	-2.522	-3.965	-5.625
Magnesite	3.074	2.400	1.533	0.680	-0.249	-1.102	-1.947	-2.876
Calcite	2.370	1.979	1.445	0.881	0.211	-0.455	-1.161	-1.981
Mg-Brucite	18.058	16.340	14.306	12.490	10.739	9.373	8.255	7.289
Fe-Brucite	14.223	12.850	11.216	9.747	8.318	7.187	6.248	5.418
Magnetite	14.085	10.763	6.755	3.098	-0.540	-3.524	-6.134	-8.596
Hematite	2.304	0.322	-2.077	-4.270	-6.465	-8.291	-9.922	-11.506
Graphite	67.449	61.269	53.785	46.870	39.960	34.397	29.771	25.783

Anhydrite	-3.565	-3.831	-4.338	-4.998	-5.902	-6.898	-8.029	-9.410
Chalcedony (SiO2)	-3.820	-3.441	-3.069	-2.752	-2.432	-2.166	-1.945	-1.779
Diopside (cpx)	23.913	21.640	18.768	16.133	13.571	11.557	9.877	8.338
Enstatite (orp)	13.041	11.665	9.941	8.368	6.845	5.657	4.677	3.796
Spinel	44.019	37.913	30.542	23.800	17.115	11.718	7.147	3.060

Table A.5.3. Gases on data base at 250 bars generated after SUPCRT92

Gases	**Log K** *1°C*	**Log K** *25°C*	**Log K** *50°C*	**Log K** *100°C*	**Log K** *150°C*	**Log K** *200°C*	**Log K** *250°C*	**Log K** *300°C*
CO(g)	41.697	37.215	31.766	26.707	21.622	17.498	14.037	11.011
CO2(g)	-7.700	-7.842	-8.082	-8.380	-8.777	-9.202	-9.671	-10.227
H2(g)	45.858	41.474	36.230	31.460	26.789	23.126	20.181	17.767
H2O(g)	2.183	1.507	0.715	0.014	-0.647	-1.142	-1.517	-1.803
H2S(g)	-8.159	-8.065	-8.011	-8.027	-8.125	-8.297	-8.547	-8.914
N2(g)	-3.129	-3.331	-3.456	-3.460	-3.348	-3.155	-2.906	-2.604
SO2(g)	41.251	36.298	30.162	24.358	18.399	13.439	9.142	5.214

Appendix B

Serpentinization experiments

2. Experimental study of the effects of solute transport on reaction paths during incipient serpentinization

Chemical composition of starting material

Table.B.1. Chemical composition of the initial olivine composition. The mineral composition was determined by electron probe micro-analyzer EPMA (Géosciences Montpellier).

(wt%)	Initial mineral composition
	Olivine
	n=3
SiO_2	41.62 ± 0.04
Al_2O_3	0.02 ± 0.01
FeO	8.63 ± 0.04
MgO	48.79 ± 0.01
MnO	0.11 ± 0.02
CaO	0.08 ± 0.002
Na_2O	< 0.01
K_2O	< 0.01
NiO	0.37 ± 0.01
Cr_2O_3	0.04 ± 0.01
TiO_2	0.02 ± 0.01
Total	99.69 ± 0.02

Outlet fluid composition

Table B.2. Composition of the injected seawater (ASW) and outlet fluids for the experiment 1 (low flow rate). Fluid concentrations are in mg/L. The time of sampling is indicated in hours (h) after the beginning of the experiment. Outlet fluids composition is measured by ICP-OES with a dilution of 50 for Si, Fe, Mg and Ca. Cations are normalized to injected ASW Na content (9163 mg/L). SO4 is measured with Ion chromatography DIONEX with a dilution of 500 and HCO3 is measured by titration with Methrom titrino with a dilution of 2.Note: the composition of each fluid represents the composition of the fluid integrated over the time interval needed to fill the sampling tool (3 mL). Experiment 1 needs 12.5 h to fill 3 ml.The uncertainty on the fluid composition (noted σ) is in mg/L, it takes into account the variability due to analythical uncertainty.

Experiment 1 - (SC1-LQ)

Sampling time (h)	$pH_{25°C}$		$pH_{170°C}$	HCO_3		Si		Fe		Mg		Ca		SO_4	
		σ		*mg/L*	σ	*mg/L*	σ	*mg/L*	σ	*mg/L*	σ	*mg/L*	σ	*mg/L*	σ
ASW	7.56	0.11	5.80	57.05	1.27	2.62	0.04	0.30	0.03	931.35	8.38	123.92	1.23	1688.50	35.38
19	6.26	0.09	6.10	28.07	1.31	5.28	0.07	<0.001	<0.001	910.89	11.84	124.33	1.23	1629.79	35.19
64	6.28	0.08	6.08	27.46	1.28	6.02	0.07	0.31	0.02	952.74	17.15	131.71	1.58	1642.29	35.46
90	6.22	0.05	6.04	27.46	1.28	6.09	0.08	0.53	0.03	1001.40	7.01	136.54	2.59	1690.80	36.51
112	6.18	0.03	6.05	29.90	1.39	3.99	0.05	0.10	0.002	1007.46	7.05	133.94	1.07	1638.41	35.37
136	6.20	0.06	6.10	29.29	1.36	3.47	0.08	0.31	0.04	989.68	6.93	131.25	1.58	1724.00	37.22
160	6.15	0.02	6.05	29.29	1.36	3.39	0.08	0.32	0.03	939.91	10.34	127.21	2.80	1734.57	37.45
187	6.14	0.12	6.03	28.07	1.31	3.43	0.09	0.32	0.03	938.91	4.69	128.92	2.71	1677.49	36.22
232	6.14	0.03	6.05	30.51	1.42	3.25	0.06	0.51	0.02	924.19	5.55	125.43	1.38	1662.56	35.90

(-) not analysed

Table B.3. Composition of the injected seawater (ASW) and outlet fluids for the experiment 2 (Medium flow rate). Fluid concentrations are in mg/L. The time of sampling is indicated in hours (h) after the beginning of the experiment. Outlet fluids composition is measured by ICP-OES with a dilution of 50 for Si, Fe, Mg and Ca. Cations are normalized to injected ASW Na content (9163 mg/L). SO4 is measured with Ion chromatography DIONEX with a dilution of 500 and HCO3 is measured by titration with Methrom titrino with a dilution of 2.Note: the composition of each fluid represents the composition of the fluid integrated over the time interval needed to fill the sampling tool (3 mL). Experiment 2 needs 6.25 h to fill 3 ml. The uncertainty on the fluid composition (noted σ) is in mg/L, it takes into account the variability due to analythical uncertainty.

Experiment 2 - (SC2-MQ)

Sampling time (h)	$pH_{25°C}$		$pH_{170°C}$	HCO_3		Si		Fe		Mg		Ca		SO_4	
		σ		*mg/L*	σ	*mg/L*	σ	*mg/L*	σ	*mg/L*	σ	*mg/L*	σ	*mg/L*	σ
ASW	7.56	0.11	5.80	57.05	1.27	3.90	0.03	0.72	0.03	928.24	12.73	128.95	5.94	1692.70	32.36
49	(-)	(-)	(-)	(-)	(-)	6.21	0.05	0.26	0.02	905.59	6.85	119.90	0.47	1870.10	33.66
139	6.25	0.04	6.08	27.46	1.28	6.80	0.11	0.27	0.01	930.95	10.47	122.29	1.76	1790.00	32.22
163	6.15	0.06	6.04	28.07	1.31	4.12	0.01	0.14	0.03	926.09	5.99	137.41	1.95	1727.50	31.09
187	(-)	(-)	(-)	(-)	(-)	2.63	0.09	0.40	0.03	916.32	12.37	122.23	0.78	1798.80	32.38
212	6.14	0.14	6.04	27.46	1.28	2.77	0.09	0.08	0.03	919.46	8.38	122.65	3.23	1808.40	32.54
238	(-)	(-)	(-)	(-)	(-)	2.21	0.03	0.35	0.01	936.85	9.16	125.95	1.44	1750.00	31.50
282	6.33	0.04	6.15	32.95	1.53	2.23	0.03	0.56	0.01	906.03	5.04	121.48	0.69	1776.30	31.97
308	6.28	0.26	6.08	28.68	1.33	2.25	0.05	0.64	0.01	923.12	15.88	121.07	0.71	1822.40	32.80
331	6.13	0.12	6.04	29.29	1.36	2.06	0.09	0.03	0.03	929.56	4.13	125.37	0.25	1753.30	31.55
354	6.16	0.07	6.05	27.46	1.28	2.04	0.02	0.04	0.04	909.30	10.76	123.67	1.20	1796.80	32.35
378	6.12	0.04	6.04	28.68	1.33	1.77	0.07	0.09	0.01	913.76	5.56	115.29	0.71	1802.40	32.44
406	6.16	0.07	6.03	28.07	1.31	2.25	0.07	0.02	0.01	935.49	5.97	125.06	3.00	1801.50	32.44
451	6.36	0.11	6.14	28.07	1.31	2.08	0.05	0.04	0.01	931.38	11.52	125.76	3.00	1813.20	32.63
475	6.35	0.10	6.13	27.46	1.28	1.66	0.06	0.02	0.01	903.58	11.58	119.66	3.72	1782.10	32.08
498	6.08	0.03	6.00	28.07	1.31	1.82	0.07	0.11	0.01	916.44	5.33	124.20	1.44	1787.90	32.18
523	6.11	0.03	(-)	(-)	(-)	1.90	0.02	0.04	0.01	899.84	4.17	119.41	1.04	1838.60	33.10
547	6.08	0.07	(-)	(-)	(-)	1.85	0.01	0.06	0.04	928.91	14.74	127.13	1.15	1787.10	32.17
572	6.07	0.10	6.00	27.50	1.28	1.54	0.05	0.09	0.01	908.87	4.55	121.97	2.96	1787.40	32.17
619	5.99	0.03	5.96	27.46	1.28	1.46	0.02	0.12	0.02	902.68	12.67	122.67	2.73	1808.60	32.56
643	5.98	0.02	5.95	27.46	1.28	1.40	0.08	0.03	0.03	930.03	14.26	124.62	1.03	1748.60	31.48
667	6.14	0.03	6.04	27.46	1.28	1.46	0.02	0.02	0.03	913.35	6.16	122.17	5.14	1852.40	33.34

(-) not analysed

Table.B.4. Composition of the injected artificial seawater (ASW) and outlet fluids for the experiment 3 (High flow rate). Fluid concentrations are in mg/L. The sampling time is indicated in hours (h) after the beginning of the experiment. Outlet fluid composition is measured by ICP-OES with a dilution of 50 for Si, Fe, Mg and Ca. Cations are normalized to injected ASW Na content (9163 mg/L). SO4 is measured with Ion chromatography DIONEX with a dilution of 500 and HCO3 is measured by titration with Methrom titrino with a dilution of 2. Note: the composition of each fluid represents the composition of the fluid integrated over the time interval needed to fill the sampling tool (3 mL). Experiment 3 needs 2.63 h to fill 3 ml. The uncertainty on the fluid composition (noted σ) is in mg/L, it takes into account the variability due to analytical uncertainty.

Experiment 3 - (SC3-HQ)

Sampling time (h)	$pH_{25°C}$		$pH_{170°C}$	HCO_3		Si		Fe		Mg		Ca		SO_4	
		σ		*mg/L*	σ	*mg/L*	σ	*mg/L*	σ	*mg/L*	σ	*mg/L*	σ	*mg/L*	σ
ASW	7.56	0.11	5.80	57.05	1.27	2.45	0.08	0.64	0.04	894.05	24.29	123.51	3.41	1721.41	33.15
18	6.13	0.03	6.11	46.98	2.18	2.48	0.06	1.06	0.01	916.42	10.08	125.90	1.26	1464.00	26.37
27	6.20	0.03	6.12	32.95	1.53	1.95	0.06	0.01	0.02	892.10	11.60	121.36	2.18	1763.39	31.76
51	6.16	0.05	6.08	28.68	1.33	1.85	0.03	0.03	0.01	879.78	7.04	130.48	1.96	1798.79	32.40
75	(-)	(-)	(-)	(-)	(-)	1.41	0.04	0.17	0.04	910.96	9.11	124.79	1.87	1841.14	33.16
99	6.23	0.07	6.12	30.51	1.42	1.13	0.04	0.17	0.00	897.44	4.49	124.00	1.49	1842.95	33.20
123	(-)	(-)	(-)	(-)	(-)	1.03	0.06	0.20	0.03	884.48	10.61	123.47	3.09	1832.27	33.00
147	6.20	0.02	6.15	36.61	1.70	0.73	0.05	0.03	0.02	875.58	6.13	121.32	1.21	1806.67	32.54
171	(-)	(-)	(-)	(-)	(-)	0.65	0.06	0.03	0.01	875.17	1.75	122.31	1.47	1665.93	30.01
195	6.16	0.06	6.09	31.73	1.48	0.60	0.07	0.40	0.03	868.02	9.55	121.36	1.33	1831.80	33.00
219	6.16	0.03	6.09	29.90	1.39	0.48	0.05	0.01	0.02	868.11	12.15	119.24	3.22	1867.42	33.64

(-) not analysed

Table.B.5. Composition of the injected artificial seawater (ASW) and outlet fluids for the experiment 4 (very high flow rate). Fluid concentrations are in mg/L. The sampling time is indicated in hours (h) after the beginning of the experiment. Outlet fluid composition is measured by ICP-OES with a dilution of 50 for Si, Fe, Mg and Ca. Cations are normalized to injected ASW Na content (9163 mg/L). SO4 is measured with Ion chromatography DIONEX with a dilution of 500 and HCO3 is measured by titration with Methrom titrino with a dilution of 2. Note: the composition of each fluid represents the composition of the fluid integrated over the time interval needed to fill the sampling tool (3 mL). Experiment 4 needs 0.58 h to fill 3 ml. The uncertainty on the fluid composition (noted σ) is in mg/L, it takes into account the variability due to analytical uncertainty.

Experiment 4 - (SC4-VHQ)

Sampling time (h)	$pH_{25°C}$		$pH_{170°C}$	HCO_3		Si		Fe		Mg		Ca	
		σ		*mg/L*	σ	*mg/L*	σ	*mg/L*	σ	*mg/L*	σ	*mg/L*	σ
ASW	7.56	0.11	5.80	57.05	1.27	1.71	0.02	0.05	0.007	836.08	8.90	126.68	3.44
20	6.07	0.08	5.93	27.46	1.37	1.58	0.05	0.13	0.015	850.30	8.40	124.70	3.30
49	(-)	(-)	(-)	(-)	(-)	1.40	0.05	0.21	0.003	836.20	9.20	119.90	0.70
121	5.98	0.08	5.83	29.29	1.46	1.40	0.04	2.01	0.120	847.40	11.00	120.80	2.50
169	(-)	(-)	(-)	(-)	(-)	1.40	0.04	2.52	0.082	858.50	7.30	123.70	3.20
308	6.18	0.09	5.99	30.51	1.53	1.30	0.04	1.49	0.064	833.90	6.00	117.70	2.70
355	(-)	(-)	(-)	(-)	(-)	1.50	0.04	1.02	0.024	838.80	8.00	121.60	2.00
379	(-)	(-)	(-)	(-)	(-)	1.10	0.04	0.56	0.027	849.80	9.30	123.00	0.50
452	(-)	(-)	(-)	(-)	(-)	0.50	0.08	0.35	0.038	821.00	9.90	118.60	5.40
472	(-)	(-)	(-)	(-)	(-)	0.90	0.03	0.07	0.025	835.20	4.80	118.50	2.30
544	6.25	0.09	6.06	31.12	1.56	0.70	0.05	0.03	0.015	853.40	12.10	127.00	0.80
616	6.30	0.09	6.13	37.22	1.86	0.70	0.05	0.11	0.024	828.30	3.90	119.80	1.60
617	6.28	0.09	6.08	32.34	1.62	0.60	0.01	0.08	0.008	831.80	8.10	117.60	3.90

(-) not analysed

Table.B.6. Accuracy and Reproducibility of analysed fluids

	Standard	n	Ref.	Avg.	Reproducibility %	Accuracy %
			ppb	*ppb*		
Si	SLRS-5	11	1922.0	1907.1	4.7	-0.8
Fe	SLRS-5	11	91.4	94.6	3.7	3.5
Mg	SLRS-5	10	2518.0	2591.9	4.8	2.9
Ca	SLRS-5	10	10320.0	10587.1	4.1	2.6
Na	SLRS-5	11	5461.0	5198.1	5.5	-4.8
			ppm	*ppm*		
SO_4	IAPSO	4	2775.2	2786.2	0.8	0.4
			mmol.l^{-1}	*mmol.l^{-1}*		
Alkalinity	VOLVIC ®	11	1.2	1.4	4.7	15.2
pH	VOLVIC ®	10	7.0	6.8	1.4	-2.7

Saturation index of the outlet fluids

Table. B.7. Saturation index (log Ω) of the inlet and outlet fluids of SC1-LQ, SC2-MQ, SC3-HQ and SC4-VHQ

Experiment 1 (SC1-LQ)

Time	**Olivine**	**Chrysotile**	**Talc**	**Magnesite**	**Calcite**	**Brucite**	**Hematite**	**Magnetite**	**Dolomite**	**Huntite**
hours	$Mg_{1.8}Fe_{0.2}SiO_4$	$Mg_3Si_2O_5(OH)_4$	$Mg_3Si_4O_{10}(OH)_2$	$MgCO_3$	$CaCO_3$	$Mg(OH)_2$	Fe_2O_3	Fe_3O_4	$CaMg(CO_3)_2$	$CaMg_3(CO_3)_4$
ASW	-3.75	0.62	-1.19	0.04	-1.72	-0.87	7.27	0.16	-0.64	125.78
19	-2.90	2.90	1.70	0.20	-1.50	-0.30	2.30	(-)	-0.30	126.50
64	-2.40	2.99	1.90	0.20	-1.54	-0.31	7.27	0.15	-0.30	126.43
90	-2.47	2.80	1.70	0.14	-1.60	-0.37	7.73	0.85	-0.42	126.21
112	-2.77	2.49	1.00	0.19	-1.56	-0.35	6.31	-1.27	-0.33	126.40
136	-2.70	2.40	0.70	0.20	-1.60	-0.40	7.30	0.16	-0.30	126.40
160	-2.81	2.22	0.60	0.15	-1.60	-0.40	7.30	0.20	-0.41	126.23
187	-2.90	2.14	0.50	0.11	-1.64	-0.42	7.30	0.20	-0.49	126.07
232	-2.80	2.20	0.50	0.20	-1.60	-0.40	7.70	0.80	-0.40	126.30

(-) Phases with affinities less than -10 kcal

Experiment 2 (SC2-MQ)

Time	**Olivine**	**Chrysotile**	**Talc**	**Magnesite**	**Calcite**	**Brucite**	**Hematite**	**Magnetite**	**Dolomite**	**Huntite**
hours	$Mg_{1.8}Fe_{0.2}SiO_4$	$Mg_3Si_2O_5(OH)_4$	$Mg_3Si_4O_{10}(OH)_2$	$MgCO_3$	$CaCO_3$	$Mg(OH)_2$	Fe_2O_3	Fe_3O_4	$CaMg(CO_3)_2$	$CaMg_3(CO_3)_4$
ASW	-3.50	0.98	-0.49	0.04	-1.70	-0.90	8.03	1.30	-0.60	125.80
139	-2.40	3.00	2.00	0.20	-1.60	-0.30	7.10	-0.03	-0.40	126.30
163	-2.81	2.38	0.90	0.12	-1.58	-0.40	6.61	-0.84	-0.41	126.17
212	-3.06	2.00	0.20	0.11	-1.65	-0.42	6.01	-1.74	-0.50	126.05
282	-2.57	2.49	0.50	0.37	-1.38	-0.19	7.79	0.94	0.03	127.10
308	-2.81	2.07	0.10	0.16	-1.60	-0.33	7.90	0.16	-0.39	126.28
331	-3.20	1.78	-0.30	0.15	-1.60	-0.40	5.27	-2.84	-0.41	126.22
354	-3.20	1.79	-0.30	0.12	-1.62	-0.39	5.52	-2.47	-0.46	126.13
378	-3.20	1.60	-0.60	0.10	-1.70	-0.40	6.20	-1.41	-0.50	126.10
406	-3.30	1.80	-0.20	0.10	-1.60	-0.40	4.90	-3.37	-0.50	126.10
451	-3.00	2.30	0.30	0.30	-1.50	-0.20	4.30	-4.28	-0.20	126.70
475	-3.10	2.10	-0.13	0.30	-1.50	-0.20	4.90	-3.38	-0.20	126.60
498	-3.30	1.47	-0.69	0.07	-1.68	-0.47	6.40	-1.15	-0.57	125.91
572	-3.40	1.28	-1.03	0.05	-1.71	-0.49	6.23	-1.41	-0.62	125.81
619	-3.60	0.96	-1.39	-0.03	-1.77	-0.58	6.40	-1.15	-0.76	125.52
643	-3.70	0.91	-1.48	-0.03	-1.78	-0.58	5.27	-2.84	-0.78	125.50
667	-3.40	1.45	-0.90	0.11	-1.64	-0.41	4.92	-3.37	-0.49	126.06

Experiment 3 (SC3-HQ)

Time	**Olivine**	**Chrysotile**	**Talc**	**Magnesite**	**Calcite**	**Brucite**	**Hematite**	**Magnetite**	**Dolomite**	**Huntite**
hours	$Mg_{1.8}Fe_{0.2}SiO_4$	$Mg_3Si_2O_5(OH)_4$	$Mg_3Si_4O_{10}(OH)_2$	$MgCO_3$	$CaCO_3$	$Mg(OH)_2$	Fe_2O_3	Fe_3O_4	$CaMg(CO_3)_2$	$CaMg_3(CO_3)_4$
ASW	-3.74	0.53	-1.35	0.03	-1.71	-0.88	7.93	1.15	-0.64	125.75
18	-2.60	2.35	0.43	0.47	-1.27	-0.25	8.31	1.72	0.24	127.52
27	-3.15	2.07	-0.06	0.29	-1.45	-0.28	4.31	-4.28	-0.12	126.81
51	-3.25	1.75	-0.43	0.16	-1.55	-0.37	5.27	-2.84	-0.35	126.30
99	-3.17	1.57	-1.04	0.25	-1.49	-0.29	6.72	-0.67	-0.19	126.65
147	-3.41	1.30	-1.64	0.40	-1.36	-0.24	5.27	-2.85	0.00	127.10
195	-3.47	0.80	-2.30	0.20	-1.51	-0.35	7.45	0.43	-0.30	126.50
219	-3.90	0.60	-2.72	0.20	-1.55	-0.35	4.31	-4.28	-0.30	126.40

Experiment 4 (SC4-VHQ)

Time	**Olivine**	**Chrysotile**	**Talc**	**Magnesite**	**Calcite**	**Brucite**	**Hematite**	**Magnetite**	**Dolomite**	**Huntite**
hours	$Mg_{1.8}Fe_{0.2}SiO_4$	$Mg_3Si_2O_5(OH)_4$	$Mg_3Si_4O_{10}(OH)_2$	$MgCO_3$	$CaCO_3$	$Mg(OH)_2$	Fe_2O_3	Fe_3O_4	$CaMg(CO_3)_2$	$CaMg_3(CO_3)_4$
0	-3.72	0.88	-1.32	0.22	-1.46	-0.66	126.56	-2.17	-0.21	126.56
20	-3.50	1.20	-1.10	0.00	-1.73	-0.54	125.64	-0.93	-0.69	125.64
121	-3.70	0.40	-1.90	-0.20	-1.90	-0.75	125.02	2.64	-1.01	125.02
308	-3.20	1.30	-1.20	0.10	-1.62	-0.45	126.14	2.25	-0.45	126.14
544	-3.50	1.20	-1.80	0.30	-1.47	-0.30	126.69	-2.84	-0.17	126.69
616	-3.20	1.60	-1.40	0.40	-1.30	-0.17	127.40	-1.17	0.18	127.40
617	-3.40	1.20	-1.90	0.30	-1.43	-0.25	126.88	-1.65	-0.08	126.88

Mineral reactions

Table.B.8. Mineral reactions proposed in oxidized conditions using hematite as reactant Fe-oxide.

Reaction mechanism 1: Kinetics controlled reaction

$$10\ Mg_{1.8}Fe^{+2}_{0.2}SiO_4 + 15\ H_2O + MgOH^+(aq) = 4\ Mg_3Si_2O_5(OH)_4 + 7\ Mg(OH)_2 + (Fe^{3+})_2O_3 + 2\ SiO_2(aq) + 1.5\ H_2(g) + H^+$$

Reaction mechanism 2: Transport controlled reaction

$$10\ Mg_{1.8}Fe^{+2}_{0.2}SiO_4 + 12\ H_2O + SiO_2(aq) + 1.5\ H^+ = 5.5\ Mg_3Si_2O_5(OH)_4 + 1.5\ MgOH^+(aq) + (Fe^{3+})_2O_3 + H_2(g)$$

Mass and volume changes of secondary phases

Table.B.9. Mass and volume changes of secondary phases associated to type of serpentinization reaction (R2), (R3) and (R4)

(R1) $3\ Mg_{1.8}Fe_{0.2}SiO_4$ (*Olivine*) + 4.1 $H_2O \rightarrow$ 1.5 Mg3Si2O5(OH)4 (Serpentine) + + 0.9 Mg(OH)2 (Brucite) + 0.2 Fe3O4 (Magnetite) + 0.2 H2(aq)

(R2) $15\ Mg_{1.8}Fe_{0.2}SiO_4$ (olivine) + $25H_2O$ + $MgOH^+(aq) \rightarrow$ $4\ Mg_3Si_2O_5(OH)_4$ (serpentine) + 16 $Mg(OH)_2$ (brucite)+ Fe_3O_4 (magnetite)+ 7 $SiO_2(aq)$ + $H_2(g)$ + H^+

(R3) $15\ Mg_{1.8}Fe_{0.2}SiO_4$ (olivine) + $18H_2O$ + $2SiO_2(aq)$ + 1.5 $H^+ \rightarrow$ 8.5 $Mg_3Si_2O_5(OH)_4$ (serpentine) + 1.5 $MgOH^+(aq)$ + Fe_3O_4 (magnetite) + $H_2(g)$

(R4) $CaOH^+(aq)$ + 3 $MgOH^+(aq)$ + 4 $CO_2(aq) \rightarrow CaMg_3(CO3)_4$ (Huntite)+ 4 H^+

				Volume changes			Mass changes		
		Density	Ref.	R1	Low Q experiments (R2 and R4)	High Q experiments (R3 and R4)	R1	Low Q experiments (R2 and R4)	High Q experiments (R3 and R4)
		g/cm3		*cm3*	*cm 3*	*cm 3*	*g*	*g*	*g*
Olivine	$Mg_{1.8}Fe_{0.2}SiO_4$	*3.3*	*Christensen, 2004*	134	668	668	441	2205	2205
Serpentine	$Mg_3Si_2O_5(OH)_4$	2.6	*Christensen, 2004*	160	426	906	416	1108	2356
Brucite	$Mg(OH)_2$	2.4	*Christensen, 2004*	22	394	0	52	933	0
Magnetite	Fe_3O_4	5.0	*Christensen, 2004*	9	45	45	46	232	232
Huntite	$CaMg_3(CO_3)_4$	2.7	*Hollingbery and Hull, 2010*		131	131		353	353

3. The study of the effect of very high flow rates on serpentinization through X-ray μ-tomography

Table.B.10. Chemical composition of natural seawater (Villafrance sur-mer) at 25°C

	Natural seawater Villafrance sur Mer	
	mg/L	σ
Li	0.2	0.002
B	7.0	0.044
Na	17860.0	305.7
Mg	2138.2	33.9
Si	1.0	0.2
K	641.0	9.5
Ca	752.9	8.1
Ti	0.024	0.002
Fe	0.327	0.013
Ni	0.002	0.004
Cu	0.008	0.011
Zn	0.011	0.015
Sr	9.5	0.04
Cl	21160.2	1058.0
SO_4	2913.0	145.7
HCO_3	163.5	8.2
pH	7.72	0.386

Table.B.11. Reproducibility and accuracy of the fluid measurements.

	Standard	n	Instrument	Ref.	Avg.	Reproducibility %	Accuracy %
				ppb	*ppb*		
Si	SLRS-5	6	ICP-MS	1922.00	2038.6	3.6	6.1
Mg	SLRS-5	6	ICP-MS	2518.00	2738.7	2.5	8.8
Fe	SLRS-5	6	ICP-MS	91.40	95.3	2.0	4.3
Ca	SLRS-5	6	ICP-MS	10320.00	10542.4	2.7	2.2
Na	SLRS-5	6	ICP-MS	5461.00	5055.1	2.5	-7.4
K	SLRS-5	6	ICP-MS	859.00	873.2	3.2	1.7

	Standard	n	Instrument	Ref.	Avg.	Reproducibility %	Accuracy %
				ppm	*ppm*		
SO_4	IAPSO	2	Dionex ICS-100	2775.2	2796.0	0.2	0.2
Cl	IAPSO	2	Dionex ICS-100	19354	19728.7	1.1	3.1

	Standard	n	Instrument	Ref.	Avg.	Reproducibility %	Accuracy %
				mol/L	*mol/L*		
Alkalinity	Volvic	5	Methrom Titrino	1.2	1.3	4.5	7.4
pH	Volvic	5	Methrom Titrino	7	6.7	3.9	-4.3

Table.B.12. Composition of the outlet fluids of experiment SC2. The composition are corrected regarding to the leak produced during the experiment and the the compositions are normalize with Na.

Experiment SC2

Sample name	Sampling time (h)	pH		Si		Fe		Mg		Ca		K		Na		SO_4		Cl		Alkalinity	
			σ	*mg/L*	σ	*mg/L*	σ	*mg/L*	σ	*mg/L*	σ	*mg/L*	σ	*mg/L*	σ	*mg/L*	σ	*mg/L*	σ	*mg/L*	σ
NSW (input)		6.10	0.17	2.2	0.1	0.02	0.01	3009.0	63.1	954.0	28.9	850.1	17.1	23419.8	489.0	2863.1	20.0	21614.7	60.2	158.6	7.9
Leak		(-)	(-)	0.0	0.0	0.02	0.01	1.2	0.1	1.6	0.0	0.5	0.0	10.2	0.5	(-)	(-)	(-)	(-)	(-)	(-)
1	23	6.15	0.17	18.9	2.8	0.07	0.011	3123.1	44.6	449.1	12.8	448.3	7.6	2849.9	48.7	3109.0	58.1	22841.8	262.7	37.8	1.9
2	33	(-)	(-)	43.4	5.7	0.03	0.003	3153.8	6.1	501.6	4.4	456.1	2.8	1238.5	2.4	4036.3	75.5	21450.3	246.7	(-)	(-)
3	46	6.52	0.18	109.1	2.2	0.05	0.001	3150.9	18.0	545.0	0.2	493.2	5.7	510.3	2.0	6890.6	128.9	20917.7	240.6	28.1	1.4
4	57	(-)	(-)	26.1	2.0	0.05	0.003	3133.4	39.4	222.5	2.3	448.5	5.9	3907.3	70.4	2501.8	46.8	23001.0	264.5	(-)	(-)
5	71	5.95	0.16	16.2	1.1	0.05	0.002	3117.5	52.5	206.8	1.2	446.4	5.1	5386.1	94.0	2255.6	42.2	21700.8	249.6	28.1	1.4
6	81	6.13	0.17	12.4	1.6	0.07	0.016	3093.9	65.1	199.3	5.1	445.7	8.8	5735.0	126.1	2266.6	42.4	21666.3	249.2	28.1	1.4
7	95	5.72	0.16	12.0	0.7	0.13	0.002	3083.1	26.9	189.2	2.0	444.5	3.1	5767.4	17.8	2263.0	42.3	21820.7	250.9	28.1	1.4
8	122	(-)	(-)	9.4	0.7	0.04	0.002	3081.6	36.3	183.8	2.4	445.7	5.9	5699.4	74.8	2169.5	40.6	21402.1	246.1	(-)	(-)
9	152	(-)	(-)	8.8	1.4	0.05	0.004	3099.4	88.9	183.1	5.2	448.9	13.1	5679.4	149.8	2218.2	41.5	21461.6	246.8	(-)	(-)
10	166	6.20	0.17	2.1	0.4	0.16	0.080	3092.6	22.0	363.8	4.1	444.4	4.0	9698.8	62.0	2672.7	50.0	22674.4	260.8	59.8	3.0
11	177	(-)	(-)	4.8	1.0	0.14	0.023	3100.2	40.0	288.0	3.1	443.2	6.7	8982.3	141.7	2447.2	45.8	21901.7	251.9	(-)	(-)
12	202	6.18	0.17	6.0	0.9	0.08	0.003	3115.0	31.2	225.1	1.6	442.2	4.0	8257.6	62.3	2353.3	44.0	22509.7	258.9	35.4	1.8
13	214	5.87	0.16	6.1	0.6	0.10	0.002	3120.4	51.2	217.3	3.3	446.2	4.2	5564.2	57.9	2352.9	44.0	21753.9	250.2	28.1	1.4
14	226	(-)	(-)	10.1	1.1	0.08	0.074	3140.9	43.3	223.1	3.9	446.2	6.2	6719.7	111.9	2409.5	45.1	22382.2	257.4	(-)	(-)
15	239	5.87	0.16	11.2	1.3	0.06	0.010	3037.0	67.5	195.9	4.3	424.1	8.0	6389.4	191.8	2135.9	39.9	20381.5	234.4	28.1	1.4
16	250	(-)	(-)	10.0	0.6	0.30	0.007	3030.4	24.2	187.9	1.5	422.6	1.1	9189.1	24.4	1991.6	37.2	19739.4	227.0	(-)	(-)
17	263	5.77	0.16	10.3	0.5	0.05	0.001	3033.9	27.1	191.6	2.2	423.3	3.2	8598.3	45.9	2152.8	40.3	20382.8	234.4	29.3	1.5
18	294	(-)	(-)	18.8	0.7	0.48	0.011	3067.5	51.4	232.8	3.2	427.2	9.5	5462.3	105.2	2332.2	43.6	20664.2	237.6	(-)	(-)
19	318	(-)	(-)	26.9	1.3	0.63	0.044	3119.8	20.1	281.7	2.6	423.4	3.0	3817.6	37.8	2617.2	48.9	21166.0	243.4	(-)	(-)
20	335	5.79	0.16	33.0	8.0	0.82	0.013	3137.4	46.7	312.6	5.6	430.8	5.9	3067.6	54.3	2825.2	52.8	21015.2	241.7	28.7	1.4

(-) Not determined

Appendix C

Carbonation experiments

Characterization of the initial rock sample

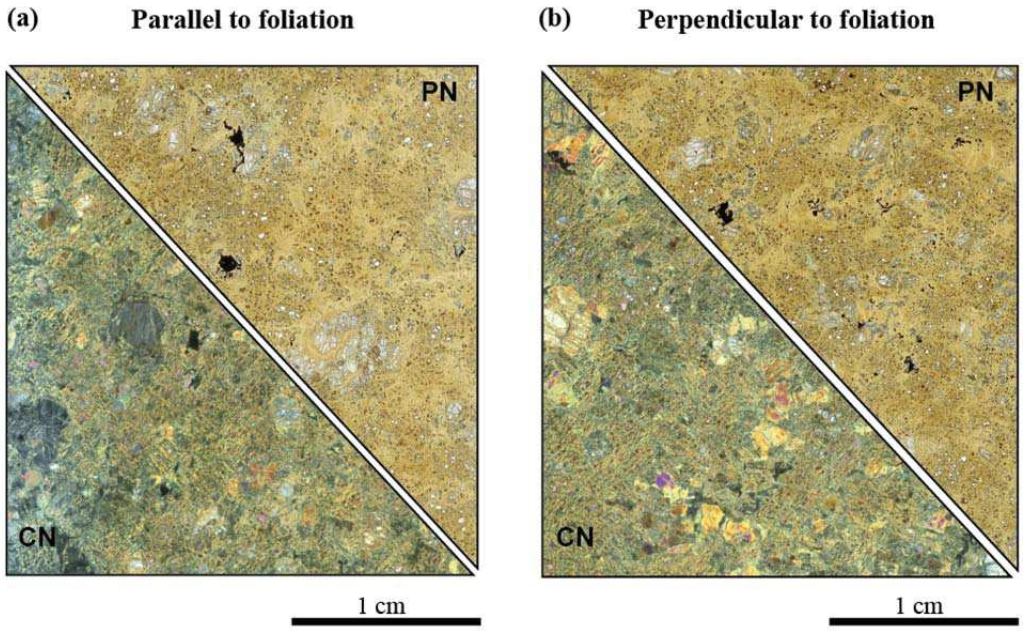

Fig.C.1. Thin section of the unreacted serpentinized peridotite sample (99OL15) used on carbonation experiments.(a) Thin section is parallel to the foliation and (b) Thin section is perpendicular to the foliation. PN corresponds to parallel nicols and CN crossed nicols.

Table.C.1. Chemical composition of the sample 99OL15 determine by XRF (X-Ray fluorescence) at Geolabs (Canada).

Oxide	wt%	Element	ppm
SiO_2	38.14	Co	101
Al_2O_3	0.84	Cu	<14
Fe_2O_3	7.49	Ni	2088
MnO	0.11	Pb	<12
MgO	37.61	Sr	<8
CaO	1.08	V	44
Na_2O	<0.02	Zn	43
K_2O	0.01	Zr	<10
TiO_2	0.01		
P_2O_5	<0.002		
Cr_2O_3	0.34		
BaO	<0.004		
Total	99.26		
Nitrogen 105	0.84		
Total LOI 1000	13.65		

Table.C.2. Chemical composition of the pristine minerals determine by EPMA at the University of Montpellier (France)

	Olivine		**Orthopyroxene**		**Clinopyroxene**		**Cr-Spinel**		**Lizardite**		**Magnetite**		**Ca-Carbonate**	
n analysis	4		4		2		3		3		1		2	
	wt.%	σ	wt.%	σ	wt.%	σ	wt.%	σ	wt.%	σ	wt.%	σ	wt.%	σ
SiO_2	40.80	0.20	55.79	0.26	52.43	0.03	0.10	0.02	38.45	1.51	0.24	0.03	0.05	0.03
TiO_2	0.01	0.01	0.02	0.01	0.08	0.00	0.05	0.02	0.00	0.00	0.00	0.00	0.02	0.01
Al_2O_3	0.00	0.00	2.59	0.23	3.02	0.18	31.32	0.81	0.81	0.68	0.00	0.00	0.02	0.03
FeO^T	9.13	0.12	5.95	0.09	2.22	0.04	17.93	0.14	7.34	0.54	90.20	0.78	0.20	0.02
MnO	0.13	0.01	0.15	0.01	0.08	0.01	0.25	0.03	0.17	0.07	0.08	0.04	0.00	0.00
MgO	49.03	0.18	32.94	0.47	16.54	0.14	14.01	0.11	36.20	2.09	0.12	0.03	0.00	0.00
CaO	0.01	0.00	1.50	0.73	24.31	0.05	0.01	0.01	0.06	0.02	0.00	0.02	54.84	7.67
Na_2O	0.01	0.01	0.02	0.01	0.11	0.04	0.03	0.02	0.03	0.02	0.04	0.07	0.02	0.01
K_2O	0.00	0.00	0.00	0.00	0.00	0.00	0.00	0.00	0.00	0.00	0.01	0.02	0.00	0.00
NiO	0.42	0.02	0.09	0.03	0.05	0.03	0.16	0.01	0.16	0.13	0.05	0.04	0.02	0.01
Cr_2O_3	0.00	0.00	0.72	0.08	1.11	0.11	36.31	0.65	0.39	0.34	0.01	0.03	0.00	0.00
Total	99.55	0.56	99.76	1.92	99.96	0.63	100.18	1.82	83.62	5.41	90.75	1.05	55.18	7.78
Mg#	90.5	0.1							89.8	0.5				
Wo			2.9	1.4	49.4	0.2								
En			88.2	1.3	47.0	0.1								
Fs			8.9	0.2	3.6	0.0								

Structural formula	
Olivine	$(Mg_{1.80}Fe_{0.19}Ni_{0.01})Si_{1.00}O_4$
Opx	$(Mg_{1.7}Fe_{0.2}Al_{0.1})Si_{2.0}O_6$
Cpx	$(Ca_{1.0}Mg_{0.9}Fe_{0.7}Al_{0.1})Si_{1.9}O_6$
Cr-spinel	$Fe_{0.4}Mg_{0.6}Cr_{0.9}Al_{1.1}O_4$
Lizardite	$(Mg_{2.71}Fe_{0.31})(Si_{1.93}Al_{0.05})O_5(OH)_4$
Magnetite	Fe_3O_4
Calcite	$CaCO_3$

Polish section of the reacted samples

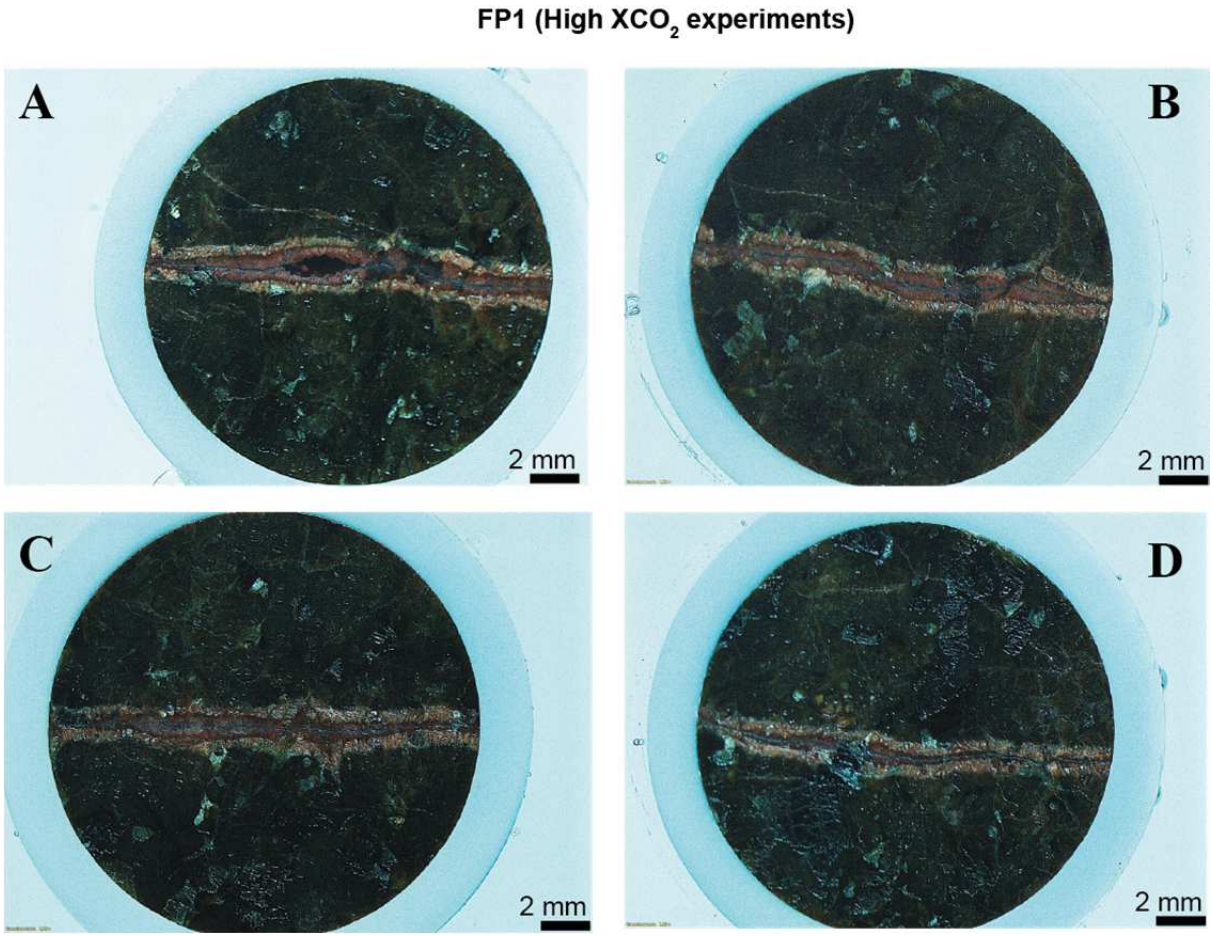

Fig.C.2. Experiment FP1. Fracture perpendicular sections of the peridotite sample from inlet (section A) to the outlet (section D).

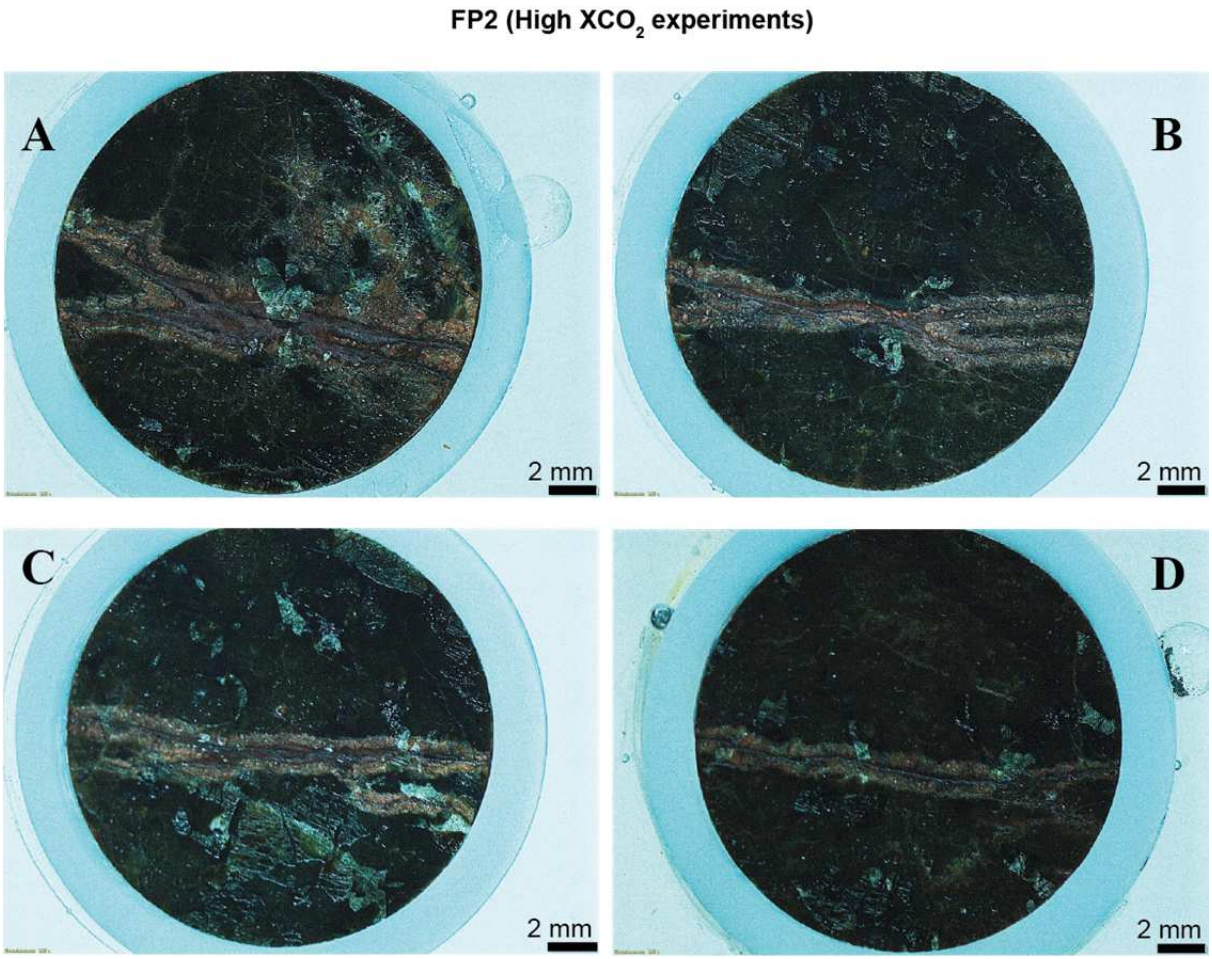

Fig.C.3. Experiment FP2. Fracture perpendicular sections of the peridotite sample from inlet (section A) to the outlet (section D).

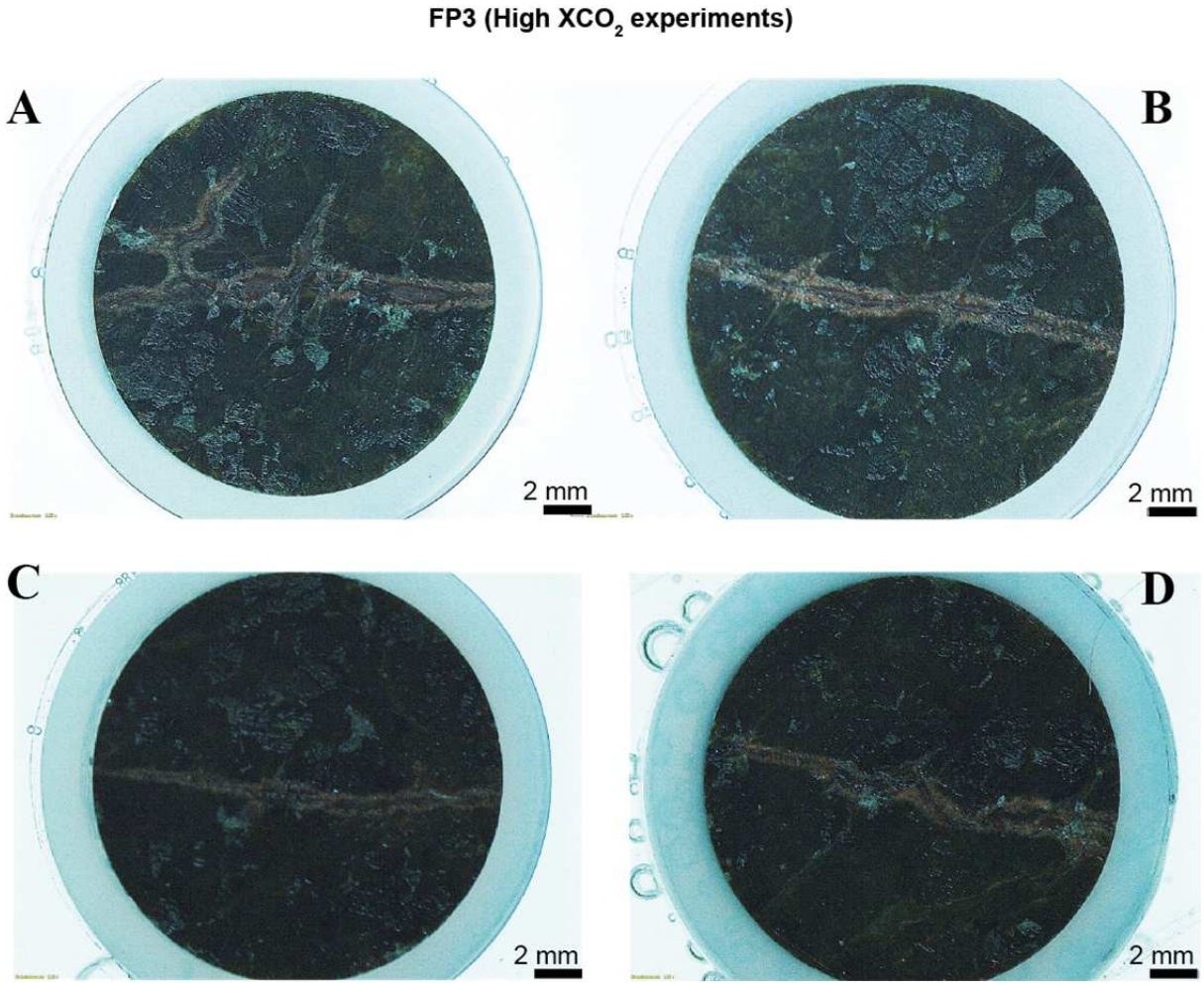

Fig.C.4. Experiment FP3. Fracture perpendicular sections of the peridotite sample from inlet (section A) to the outlet (section D).

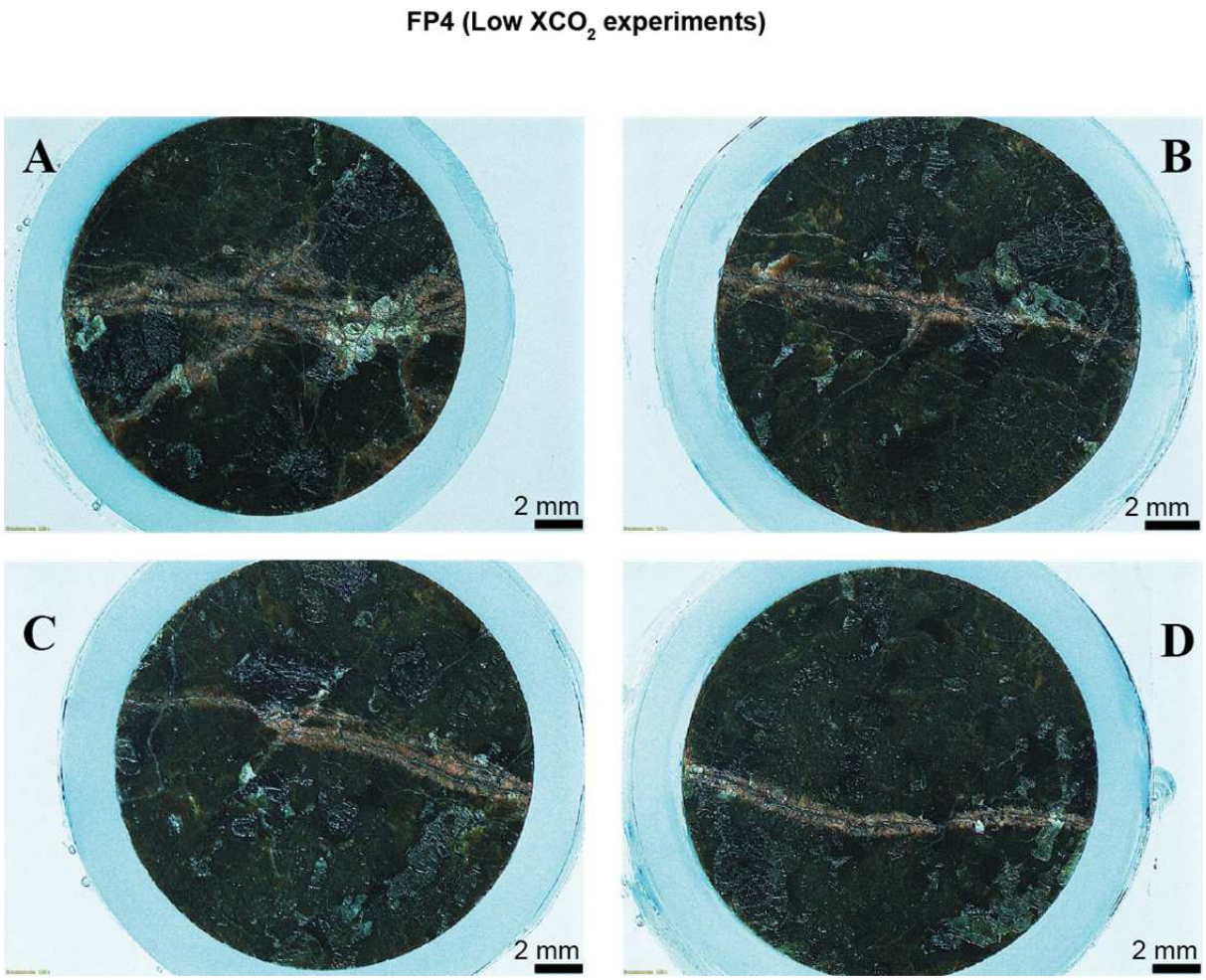

Fig.C.5. Experiment FP4. Fracture perpendicular sections of the peridotite sample from inlet (section A) to the outlet (section D).

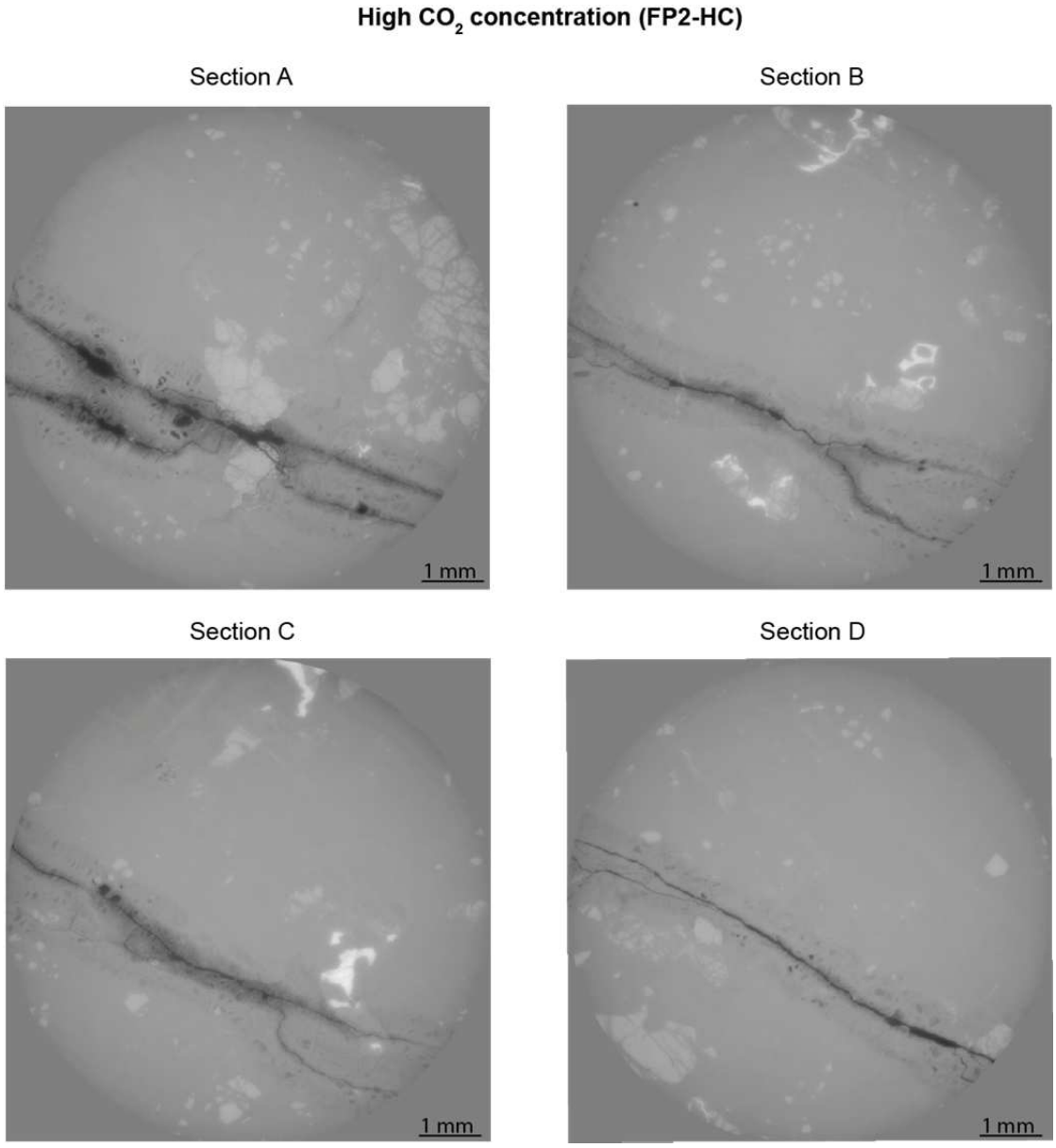

Fig.C.6. 2D XMT sections of the experiments FP2-HC. Section A (Z=0.5 mm), Section B (Z=5 mm), Section C (Z=9.5 mm) and Section D (Z=14 mm).

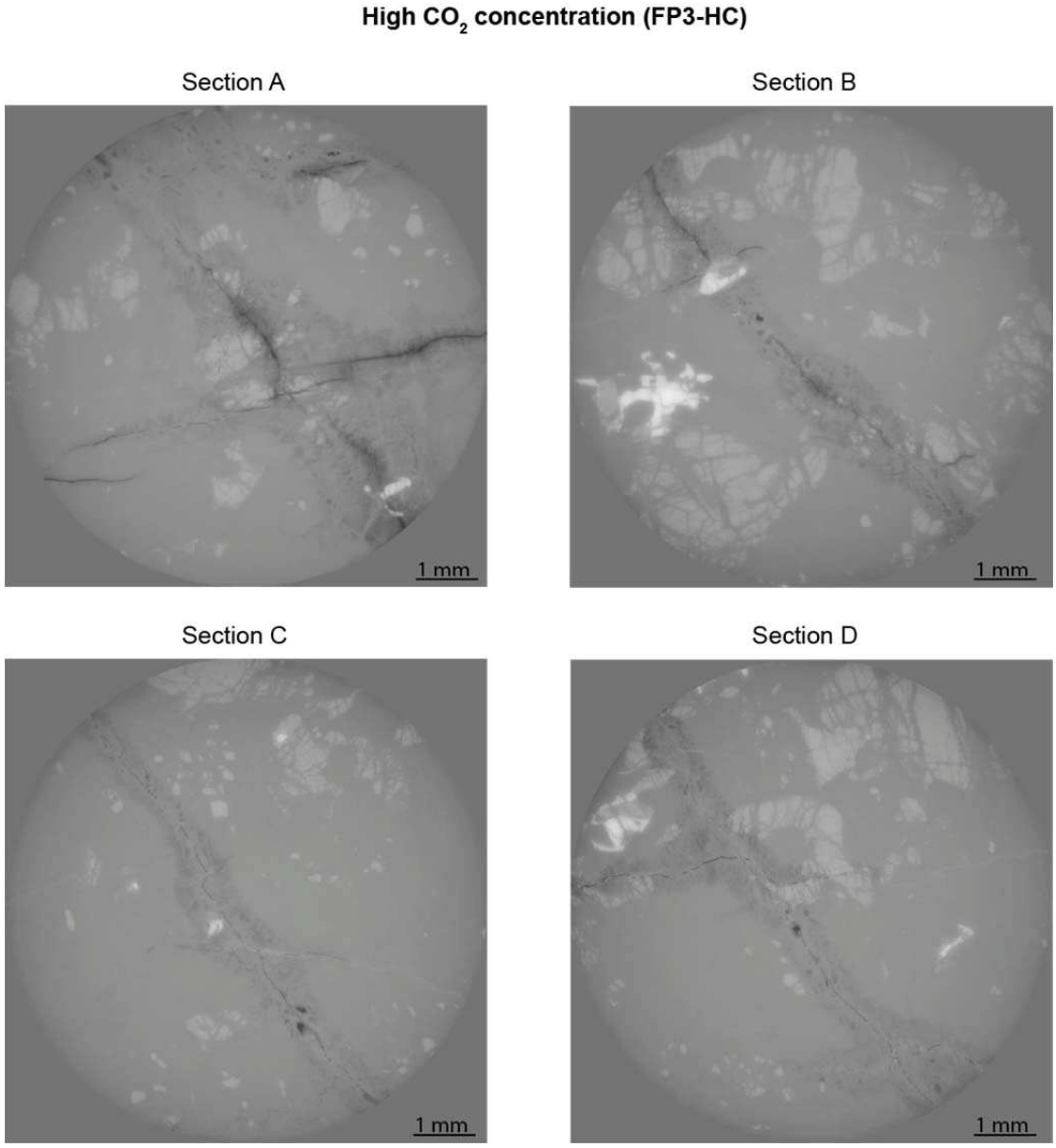

Fig.C.7. 2D XMT sections of the experiments FP3-HC. Section A (Z=0.9 mm), Section B (Z=5.7 mm), Section C (Z=9.8 mm) and Section D (Z=14.8 mm).

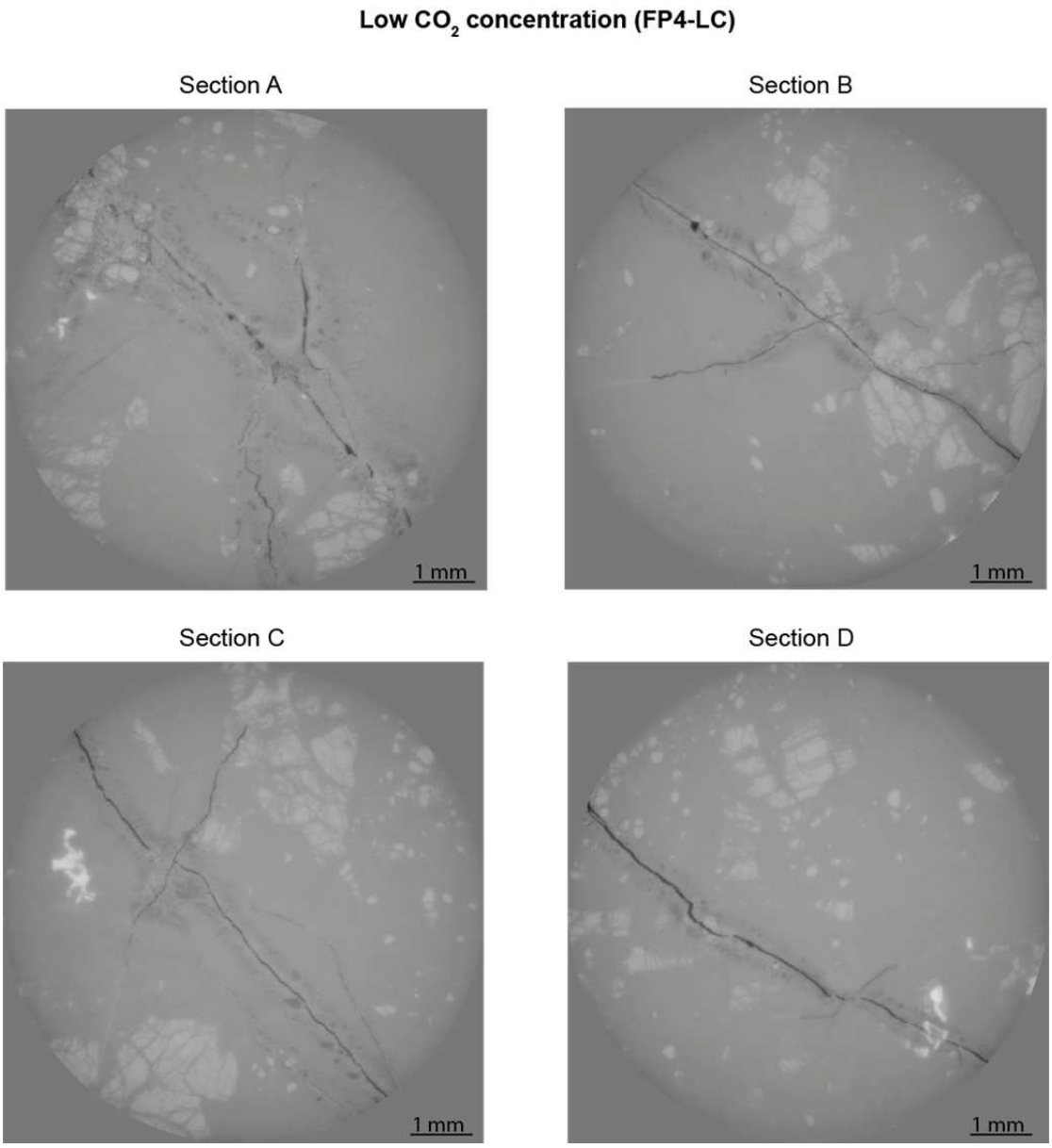

Fig.C.8. 2D XMT sections of the experiments FP4-HC. Section A (Z=1.1mm), Section B (6.2 mm), Section C (11.2 mm) and Section D (15.9 mm).

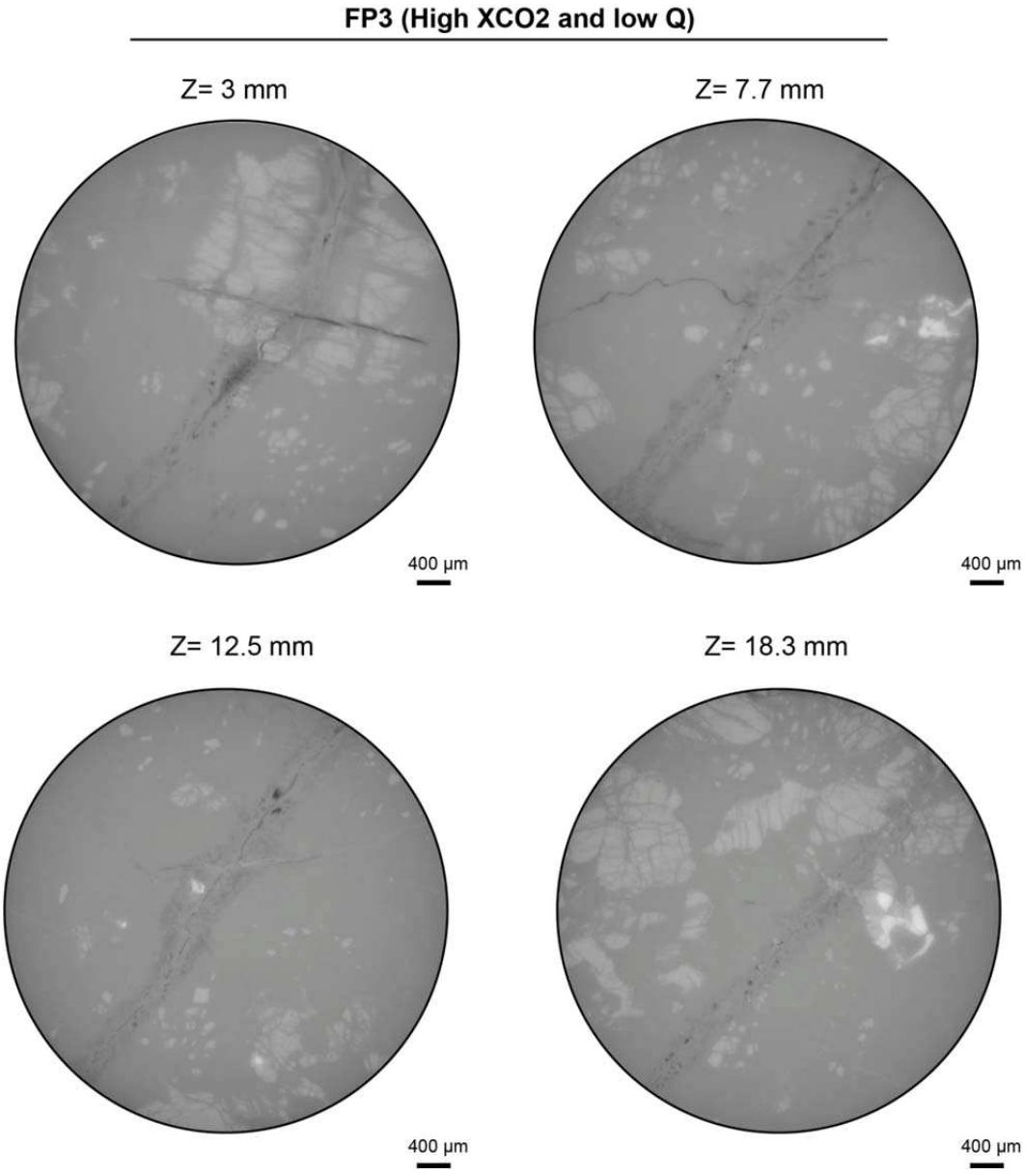

Fig.C.9. 2D XMT sections of the experiments FP3-HC

Dissolved and coloured reaction front length measurements

Dissolved reaction front length measurements after XMT images for polished sections A, B, C and D

Table C.3. Measure length of the dissolved reaction front acquire in XMT images. Measurements were performed: Experiment FP2-HC: Fig.C.6, Experiment FP3-HC: Fig.C.7 and Experiment FP4-LC: Fig.C.8. The dissolution front velocity was calculated by the ratio of the length of the dissolved front and the experimental time.

FP2-HC			***High XCO_2 and High Q***			
			Length		**Dissolution front velocity**	
	Depth		Avg.	σ	Avg.	σ
Section	*mm*	*n*	*µm*	*µm*	*µm/h*	*µm/h*
A	0.5	6	640.3	94.7	4.78	0.71
B	5.0	6	556.5	64.6	4.16	0.48
C	9.5	6	546.0	30.3	4.08	0.23
D	14.0	6	520.8	40.1	3.89	0.30

FP3-HC			***High XCO_2 and Low Q***			
			Length		**Dissolution front velocity**	
	Depth		Avg.	σ	Avg.	σ
Section	*mm*	*n*	*µm*	*µm*	*µm/h*	*µm/h*
A	0.9	6	636.29	268.51	3.85	1.62
B	5.7	6	433.94	100.96	2.62	0.61
C	9.8	6	383.78	83.99	2.32	0.51
D	14.8	6	394.82	49.42	2.39	0.30

FP4-LC			***Low XCO_2 and High Q***			
			Length		**Dissolution front velocity**	
	Depth		Avg.	σ	Avg.	σ
Section	*mm*	*n*	*µm*	*µm*	*µm/h*	*µm/h*
A	1.1	6	545.98	146.90	2.13	0.57
B	6.2	6	329.96	64.61	1.29	0.25
C	11.2	6	306.58	51.92	1.20	0.20
D	15.9	6	289.28	53.24	1.13	0.21

Dissolved reaction front length measurements and fracture aperture after XMT images

Table C.4. Measure length of the dissolved reaction front and final fracture aperture acquired in X-ray images FP2-HC (Fig.5.4), FP3-HC (appendix C. Fig.C.8) and FP4 (Fig.5.5).

	Depth	n	Dissolution front		Final fracture	
	mm		*Avg.*	*σ*	*Avg.*	*σ*
			μm	*μm*	*μm*	*σ*
FP2						
	0.6	10	486.4	78.5	19.6	5.6
	4.8	10	428.3	63.7	12.4	5.0
	6.5	10	389.0	45.2	14.3	5.2
	18.4	10	332.4	21.9	56.0	12.6
FP3						
	3.0	10	277.8	64.2	7.2	1.6
	7.7	10	296.3	69.9	7.3	1.5
	12.5	10	225.4	56.2	6.8	1.7
	18.3	10	196.7	40.6	7.0	1.0
FP4						
	3.2	10	244.7	39.2	11.9	2.2
	8.0	10	228.9	30.8	11.1	2.0
	13.6	10	222.7	54.2	25.5	5.1
	18.8	10	229.9	41.9	38.5	7.5

Distance of the coloured reaction zones regarding to the fracture

Table C.5. Measure of the distance of the coloured reaction zones regarding to the fracture performed on the polish section of experiments FP1, FP2, FP3 and FP4. *X1* corresponds to the distance of the zone 1 regarding to the fracture, *X2* corresponds to the distance of the zone 2 regarding to the fracture and *X3* corresponds to the distance of the zone 3 regarding to the fracture.

	Section A			Section B			Section C			Section D		
	n	Avg. *µm*	σ *µm*	n	Avg. *µm*	σ *µm*	n	Avg. *µm*	σ *µm*	n	Avg. *µm*	σ *µm*
FP1												
X1	6	1399	403	6	1047	125	6	841	54	6	816	98
X2	6	699	205	6	554	115	6	411	129	6	281	97
X3	6	499	147	6	318	80	6	223	73	6	123	56
FP2												
X1	6	1407	322	6	752	131	6	707	67	6	702	129
X2	6	473	48	6	335	89	6	313	37	6	231	35
X3	6	346	76	6	210	55	6	206	55	6	74	16
FP3												
X1	6	802	110	6	623	89	6	466	97	6	450	108
X2	6	534	154	6	281	77	6	213	50	6	188	40
X3	6	255	90	6	176	39	6	0	0	6	0	0
FP4												
X1	6	1457	134	6	532	41	6	456	40	6	350	57
X2	6	177	10	6	72	9	6	66	4	6	0	0
X3	6	0	0	6	0	0	6	0	0	6	0	0

Velocity of each individual coloured reaction zone of the reaction front

Table C.6. Velocity of each individual zone for experiments FP1, FP2, FP3 and FP4. The velocity corresponds to the average length (X) of each zone (Table C.5) divided by the experimental time. Z denotes the depth of the polished section calculated after the XMT images.

Experiment: FP1

	Z(mm)	Zone 1 µm/h	Zone 2 µm/h	Zone 3 µm/h
Section A	0.5	7.9 ± 2.3	4.0 ± 1.2	2.8 ± 0.8
Section B	5.0	5.9 ± 0.7	3.1 ± 0.7	1.8 ± 0.5
Section C	9.5	4.8 ± 0.3	2.3 ± 0.7	1.3 ± 0.4
Section D	14.0	4.6 ± 0.6	1.6 ± 0.6	0.7 ± 0.3

Experiment: FP2

	Z(mm)	Zone 1 µm/h	Zone 2 µm/h	Zone 3 µm/h
Section A	0.5	10.5 ± 2.4	3.5 ± 0.3	2.6 ± 0.4
Section B	5.0	5.6 ± 1.0	2.5 ± 0.5	1.6 ± 0.3
Section C	9.5	5.3 ± 0.5	2.3 ± 0.2	1.5 ± 0.3
Section D	14.0	5.2 ± 1.0	1.7 ± 0.2	0.6 ± 0.1

Experiment: FP3

	Z(mm)	Zone 1 µm/h	Zone 2 µm/h	Zone 3 µm/h
Section A	0.9	4.9 ± 0.7	3.2 ± 0.9	1.5 ± 0.5
Section B	5.7	3.8 ± 0.5	1.7 ± 0.5	1.1 ± 0.2
Section C	9.8	2.8 ± 0.6	1.1 ± 0.3	0.0
Section D	14.8	2.7 ± 0.7	1.3 ± 0.2	0.0

Experiment: FP4

	Z(mm)	Zone 1 µm/h	Zone 2 µm/h	Zone 3 µm/h
Section A	1.1	5.7 ± 0.5	0.7 ± 0.04	0.0
Section B	6.2	2.1 ± 0.2	0.3 ± 0.03	0.0
Section C	11.2	1.8 ± 0.2	0.3 ± 0.01	0.0
Section D	15.9	1.4 ± 0.2	0.0	0.0

Table C.7. Common velocity for FP1 and FP2 calculated after a regression curve (x=0) of Fig.5.23. (Z) denotes the depth of the polished section: (1) Theoretical for FP1-HC and (2) Estimate after the XMT images for FP2-HC, that corresponds with the theoretical depth.

Experiment: FP1 and FP2 (regresion curve)

	Z *mm*	Zone 1 *µm/h*	Zone 2 *µm/h*	Zone 3 *µm/h*
Section A	0.5	8.9 ± 3.3	3.8 ± 1.2	2.7 ± 0.9
Section B	5.0	5.8 ± 1.2	2.9 ± 0.8	1.7 ± 0.6
Section C	9.5	5.0 ± 0.6	2.3 ± 0.8	1.4 ± 0.5
Section D	14.0	4.9 ± 1.1	1.6 ± 0.6	0.6 ± 0.3

Mineralogy and chemical characterization of the reacted samples

Table C.8. SEM-EDS chemical analysis of sample FP1-A and FP4-B

Spectrum	47	51	52	53	87	23	24	22	25	16	18	15
Sample	FP1-A	FP1-A	FP1-A	FP1-A	FP1-A	FP1-A	FP1-A	FP1-A	FP1-A	FP4-B	FP4-B	FP4-B
Localization	Zone 1	Zone 1	Zone 2	Zone 2	Zone 3	Zone 3	Zone 3	Zone 3	Zone 3	Zone 1	Zone 1	Zone 2
Phase	Magnesite	Amorphous silica	Magnesite	Magnesite	(Fe-Ni) oxide	Calcite	Amorphous silica	Magnesite	Magnesite	Magnesite	(Ca-Mg) carbonate	Ni-oxide
	wt.%	wt.%	wt.%	wt.%	wt.%	wt.%	wt.%	wt.%	wt.%	wt.%	wt.%	wt.%
C	14.5	7.47	14.24	14.11	14.67	16.3	11.9	16.27	16.18	(-)	(-)	12.07
O	56.09	56.94	54.61	53.03	54.74	56.46	60.53	55.58	55.68	58.46	59.03	48.08
Mg	17.5	4.38	14.83	11.35	6.73	2.91	2.33	6.24	7.09	32.29	14.77	3.61
Al	0	0	0	0	0.07	0	0	0	0	0.19	0.12	1.99
Si	2.96	29.55	2.61	2.22	5.07	2.11	23.42	2.24	2.21	4.35	8.7	2.72
Cl	0	0.05	0.08	0.08	0.1	0	0	0	0	0	0	1.45
Ca	0.09	0.13	0.14	0.11	0.04	20.77	0.29	0.08	0.1	2.39	15.32	0.08
Ti	0	0	0.05	0.08	0.09	0	0.08	0	0.05	0	0	0
V	0	0.02	0	0	0.01	0.06	0.05	0.03	0.09	0	0	0
Cr	0	0	0.18	0.05	0.08	0	0.04	0.03	0.04	0	0	0.87
Fe	8.2	1.12	11.02	11.92	17.22	1.01	0.84	11.04	12.27	1.29	1.55	3.93
Ni	0.66	0.33	2.23	7.07	1.18	0.37	0.51	8.46	6.28	1.05	0.5	25.01

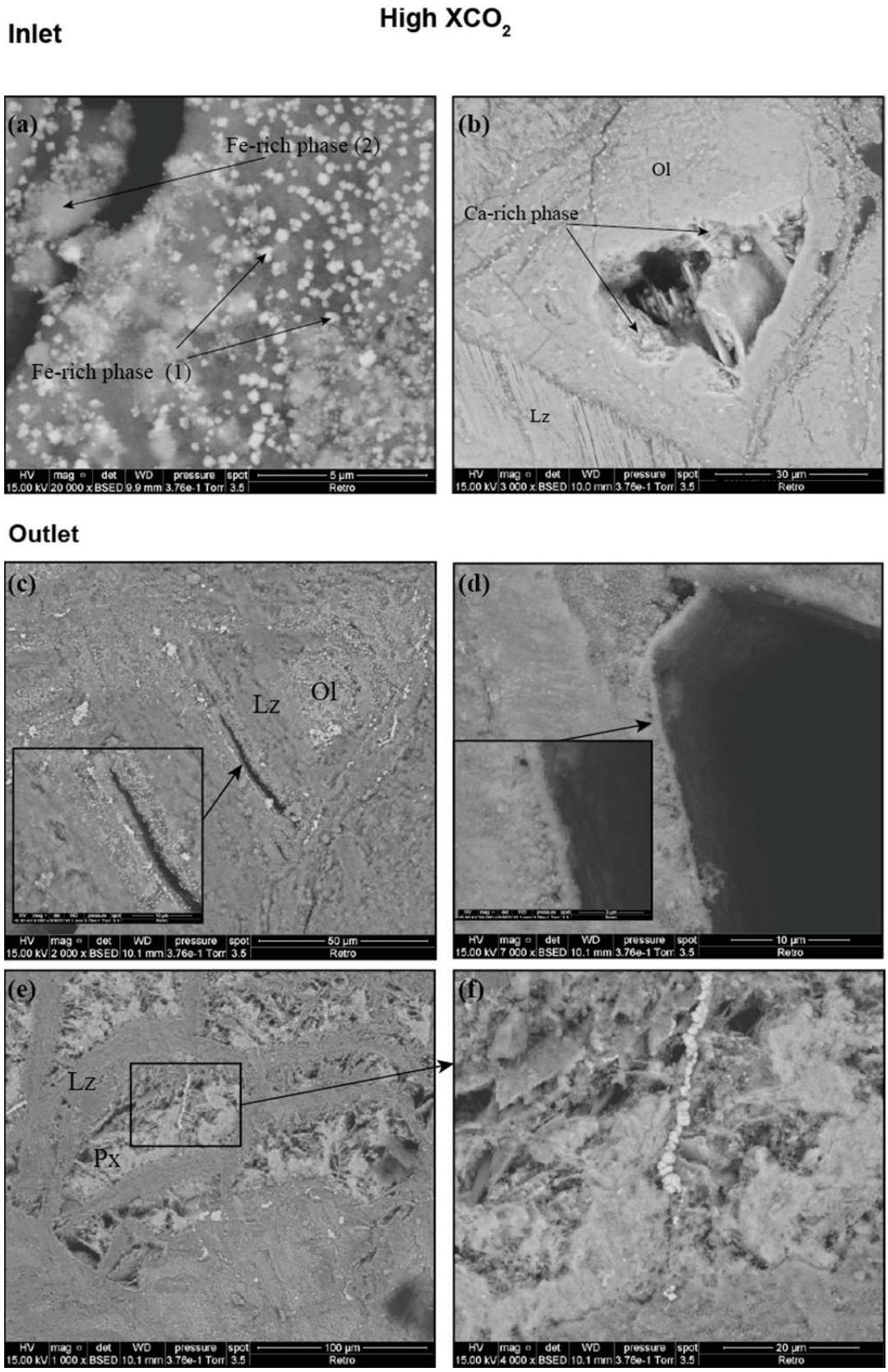

Fig.C.10. Mineralogy of the reacted samples under high CO_2 concentration. The mineralogy characterization corresponds to the sample FP2. Inlet of the samples: (a) Precipitation of two types of Fe-rich phases (1) cubic shapes (see table C.7 appendix C. SEM-EDS spectrum 50) and (2) fluffy

shape (see table C.7.appendix C. SEM-EDS spectrum 46). (b) Ca-rich phase replacing the core of the dissolved olivine. Outlet of the samples: (c) Fe-rich phases covering the olivine and lizardite. (d) Continuous thin rims of a white-lighter phase probably silica on the dissolved grains. (e-f) Fluffy deposit precipitates on the surface of the dissolved pyroxene and the precipitation of a bright nodular phase among the dissolved pyroxene and fluffy deposit.

Table. C.9. SEM-EDS chemical analysis of sample FP2

Spectrum	46	50
Sample	FP2	FP2
Localization	inlet surface	inlet surface
Phase	Fe-rich phase(1)	Fe-rich phase(2)
	wt.%	wt.%
C	2.19	3.03
O	41.43	44.43
Na	0.28	0.26
Mg	17.22	17.72
Al	0.71	0.82
Si	14.71	16.43
P	0	0.09
S	0	0
K	0.03	0.01
Ca	0.02	0.03
Ti	0	0.16
Cr	0.38	0.32
Mn	0.04	0
Fe	22.7	16.64
Sr	0.25	0.07
Zr	0.02	0
Ba	0	0

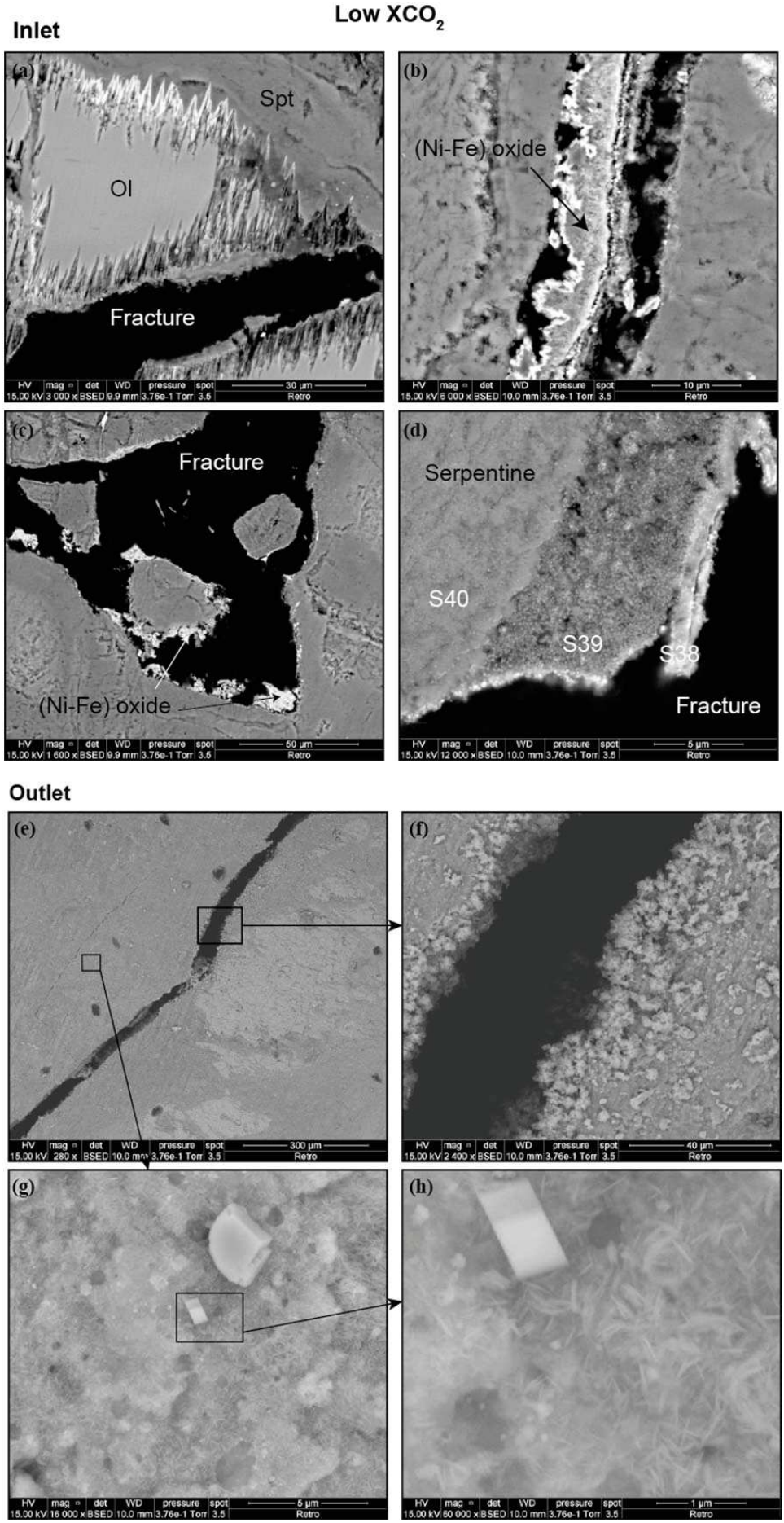
Low XCO_2
Inlet
(a)
Spt
Ol
Fracture
(b)
(Ni-Fe) oxide
(c)
Fracture
(Ni-Fe) oxide
(d)
Serpentine
S40
S39
S38
Fracture
Outlet
(e)
(f)
(g)
(h)

Fig.C.11. Mineralogy of the reacted samples under low CO_2 concentration in solution. The mineralogy characterization corresponds to sample FP4. Inlet of the samples: (a) Dissolved olivine on the zone adjacent to the fracture leading to a saw-toothed texture. (b) Precipitation of Ni-Fe oxide filling secondary fractures (see table C.10 spectrum 19 for EDS chemical analysis).(c) Precipitation of Ni-Fe oxide on the fracture associated to dissolved olivine (see table C.10. spectrum 52 for EDS chemical analysis). (d) Detail of dissolving serpentine adjacent to the fracture progressive enriched in Ni and Fe (see table C.10 spectrum 38, 39, 40).Outlet of the samples: (d) Detail of the adjacent zones of the fracture covered by dark circle spots (inorganic carbon?). (e) Detail of the inner of the fracture filled by a fluffy material. (f-g) Detail of the material covering the surface of the lizardite. The rhombohedral grains and acicular grains were splited all around the lizardite surface. They were very small to be analysed but the rhombohedral shape suggest could be calcite and the acicular grains approaches the shapes of hematite or Mg-silicate minerals.

Table. C.10. SEM-EDS chemical analysis of sample FP4. (Spt) denotes serpentine

Spectrum	19	52	38	39	40
Sample	FP4-A	FP4-A	FP4-A	FP4-A	FP4-A
Localization	Zone 2	Zone 1	Zone 2	Zone 2	Zone 2
Phase	(Fe-Ni) oxide	(Ni) oxide	Spt	Spt	Spt
	wt.%	wt.%	wt.%	wt.%	wt.%
C	11	14.35	21.06	13.21	9.19
O	46.03	52.72	63.83	56.49	53.26
Mg	4.5	7.45	3.35	11.85	17.25
Al	0.17	0.1	0.11	0.12	0.05
Si	2.8	2.91	2.37	9.56	13.64
Cl	0.87	0.04	0.07	0.11	0.16
Ca	0.04	0.34	0.03	0	0
Ti	0	0	0	0	0
V	0	0	0	0	0
Cr	3.48	0.11	0.36	0.03	0.08
Fe	21.45	1.84	5.33	4.82	4.41
Ni	9.64	20.15	3.43	3.74	1.96

Lizardite and Chrysotile major element profiles in FP2-B and FP4-B

Table. C.11. Lizardite major element profiles in FP2-B

Sample	**FP2-B**																											
Phase	Lizardite																											
Point	48 / 1 .		50 / 1 .		51 / 1 .		52 / 1 .		54 / 1 .		55 / 1 .		56 / 1 .		59 / 1 .		57 / 1 .		64 / 1 .		63 / 1 .		61 / 1 .		62 / 1 .		65 / 1 .	
Location	Zone 0				Zone 1						Zone 2								Zone 3						Zone 3		Zone 2	
Dist. (µm)	-1400	σ	-905	σ	-579	σ	-514	σ	-398	σ	-351.40	σ	-314	σ	-294	σ	-270	σ	-70	σ	-44	σ	-15	σ	7.18	σ	268.24	σ
wt.%																												
SiO2	37.12	0.20	38.83	0.21	38.51	0.21	41.92	0.22	36.68	0.20	37.66	0.21	35.24	0.20	36.44	0.20	39.20	0.21	34.67	0.20	33.56	0.19	37.00	0.20	32.32	0.19	37.65	0.21
TiO2	0.00	0.00	0.03	0.02	0.00	0.02	0.01	0.02	0.00	0.00	0.00	0.00	0.00	0.00	0.01	0.02	0.00	-21.89	0.02	0.02	0.00	0.00	0.00	0.00	0.00	0.00	0.00	0.02
Al2O3	0.10	0.02	0.21	0.02	0.10	0.02	0.00	0.02	0.01	0.02	0.04	0.02	0.06	0.02	0.03	0.02	0.00	0.00	0.15	0.02	0.16	0.02	0.21	0.02	0.27	0.02	0.11	0.02
Cr2O3	0.02	0.03	0.00	0.00	0.00	0.00	0.01	0.03	0.00	0.00	0.01	0.03	0.00	0.03	0.00	0.00	0.01	0.03	0.00	0.03	0.00	0.00	0.02	0.03	0.00	0.03	0.02	0.03
FeO	8.17	0.16	8.25	0.16	8.67	0.17	4.67	0.12	7.23	0.15	8.53	0.16	10.09	0.18	8.28	0.16	5.95	0.14	7.83	0.16	9.80	0.18	5.26	0.13	10.27	0.18	5.35	0.13
MnO	0.13	0.03	0.13	0.03	0.07	0.03	0.06	0.03	0.11	0.03	0.02	0.03	0.06	0.03	0.03	0.03	0.05	0.03	0.02	0.03	0.03	0.03	0.01	0.03	0.02	0.03	0.03	0.03
MgO	36.21	0.30	36.36	0.30	35.58	0.30	38.15	0.31	39.25	0.32	34.25	0.30	33.15	0.29	35.88	0.30	38.15	0.31	34.71	0.30	34.19	0.29	35.40	0.30	25.82	0.25	38.08	0.31
CaO	0.03	0.01	0.08	0.02	0.05	0.01	0.02	0.01	0.12	0.02	0.02	0.01	0.02	0.01	0.03	0.01	0.00	0.01	0.02	0.01	0.02	0.01	0.02	0.01	0.01	0.01	0.01	0.01
Na2O	0.00	0.00	0.00	0.03	0.00	0.00	0.03	0.03	0.05	0.04	0.04	0.04	0.03	0.04	0.02	0.03	0.00	0.00	0.02	0.04	0.02	0.04	0.00	0.03	0.03	0.03	0.02	0.03
K2O	0.01	0.01	0.00	0.01	0.00	0.00	0.00	0.01	0.00	0.01	0.00	0.00	0.00	0.00	0.00	0.00	0.00	0.01	0.01	0.01	0.00	0.01	0.01	0.01	0.00	0.01	0.00	0.01
NiO	0.26	0.04	0.68	0.05	0.81	0.06	0.57	0.05	1.27	0.07	2.47	0.09	2.55	0.09	1.49	0.07	0.92	0.06	1.41	0.07	1.56	0.07	1.25	0.07	1.61	0.08	0.99	0.06
Cl	0.63	0.05	0.33	0.04	0.08	0.02	0.04	0.02	0.06	0.02	0.11	0.02	0.13	0.02	0.15	0.03	0.04	0.02	0.13	0.03	0.11	0.02	0.10	0.02	0.07	0.02	0.05	0.02
Total	82.70	0.41	84.90	0.41	83.88	0.41	85.48	0.41	84.77	0.42	83.15	0.41	81.34	0.41	82.36	0.41	84.32	21.90	78.98	0.41	79.43	0.41	79.29	0.39	70.43	0.37	82.32	0.41

Table C.12. Chrysotile major element profiles in FP2-B

Sample	**FP2-B**			
Phase	Chrysotile			
Point	53 / 1 .		58 / 1 .	
Location	Zone 1		Zone 2	
Dist. (µm)	-514	σ	-270	σ
wt.%				
SiO2	39.72	0.21	37.02	0.20
TiO2	0.00	0.02	0.00	0.00
Al2O3	0.24	0.02	0.26	0.02
Cr2O3	0.00	0.00	0.02	0.03
FeO	9.51	0.17	9.31	0.17
MnO	0.06	0.03	0.08	0.03
MgO	32.50	0.28	32.73	0.29
CaO	0.07	0.02	0.04	0.01
Na2O	0.07	0.04	0.07	0.04
K2O	0.01	0.01	0.00	0.00
NiO	3.53	0.11	4.02	0.11
Cl	0.22	0.03	0.16	0.03
Total	85.93	0.42	83.72	0.41

Table C.13. Lizardite major element profiles in FP4-B

Sample	**FP4-B**																							
Phase	Lizardite																							
Point	17 / 1 .		15 / 1 .		14 / 1 .		22 / 1 .		24 / 1 .		25 / 1 .		33 / 1 .		32 / 1 .		34 / 1 .		35 / 1 .		42 / 1 .		40 / 1 .	
Location	Zone 0								Zone 1				Zone 2				Zone 2		Zone 1		Zone 0			
Dist. (µm)	-1400	σ	-1303	σ	-1194	σ	-777	σ	-360	σ	-191	σ	-29	σ	-20	σ	20.54	σ	54.22	σ	621.59	σ	687.17	σ
wt.%																								
SiO2	33.92	0.20	38.77	0.21	33.83	0.20	35.20	0.21	38.78	0.21	42.01	0.22	36.32	0.20	37.19	0.21	36.81	0.20	37.23	0.21	40.14	0.22	41.79	0.22
TiO2	0.00	0.00	0.00	0.00	0.00	0.02	0.02	0.02	0.00	0.02	0.02	0.02	0.00	0.00	0.00	0.00	0.03	0.02	0.00	0.03	0.01	0.02	0.01	0.02
Al2O3	0.00	0.00	0.07	0.02	0.00	0.02	0.01	0.02	0.00	0.00	0.00	0.00	0.00	0.00	0.00	0.00	0.01	0.02	0.05	0.02	0.00	0.00	0.00	-10.12
Cr2O3	0.01	0.03	0.00	0.03	0.00	0.00	0.01	0.03	0.01	0.03	0.03	0.03	0.01	0.03	0.00	0.00	0.00	0.00	0.00	0.00	0.01	0.03	0.01	0.03
FeO	9.03	0.18	8.31	0.16	7.66	0.16	6.33	0.15	6.32	0.14	5.65	0.13	7.68	0.15	7.21	0.15	7.72	0.16	7.05	0.15	4.80	0.12	4.59	0.12
MnO	0.10	0.03	0.10	0.03	0.07	0.03	0.07	0.03	0.08	0.03	0.04	0.03	0.09	0.03	0.11	0.03	0.06	0.03	0.07	0.03	0.07	0.03	0.03	0.03
MgO	39.10	0.33	35.98	0.30	39.96	0.33	39.55	0.33	39.06	0.32	37.26	0.31	34.65	0.30	33.88	0.29	35.73	0.30	35.01	0.30	38.69	0.32	38.95	0.32
CaO	0.08	0.02	0.08	0.02	0.15	0.02	0.05	0.01	0.05	0.01	0.03	0.01	0.01	0.01	0.02	0.01	0.02	0.01	0.03	0.01	0.03	0.01	0.02	0.01
Na2O	0.00	0.00	0.03	0.03	0.01	0.04	0.01	0.04	0.03	0.03	0.02	0.04	0.01	0.04	0.01	0.04	0.00	0.00	0.04	0.04	0.02	0.04	0.03	0.03
K2O	0.00	0.00	0.00	0.01	0.00	0.01	0.00	0.00	0.01	0.01	0.00	0.01	0.00	0.00	0.00	0.01	0.01	0.01	0.00	0.00	0.00	0.00	0.01	0.01
NiO	0.33	0.05	0.40	0.05	0.36	0.05	0.33	0.05	0.42	0.05	0.80	0.06	4.71	0.12	4.58	0.12	1.97	0.08	4.25	0.12	0.36	0.04	0.30	0.04
Cl	0.27	0.03	0.11	0.02	0.16	0.03	0.06	0.02	0.14	0.03	0.08	0.02	0.16	0.03	0.14	0.03	0.13	0.03	0.12	0.02	0.03	0.02	0.04	0.02
Total	82.84	0.43	83.86	0.41	82.21	0.43	81.66	0.42	84.88	0.42	85.95	0.41	83.63	0.42	83.16	0.41	82.48	0.41	83.83	0.42	84.15	0.41	85.77	10.13

Table C.14. Chrysotile major element profiles in FP4-B

Sample	**FP4-B**															
Phase	Chrysotile															
Point	18 / 1 .		12 / 1 .		13 / 1 .		23 / 1 .		31 / 1 .		38 / 1 .		41 / 1 .		43 / 1 .	
Location	Zone 0								Zone 1		Zone 2		Zone 0			
Dist. (µm)	-1400	σ	-1139	σ	-1139	σ	-777	σ	-132	σ	15	σ	687	σ	687	σ
wt.%																
SiO2	37.02	0.20	35.38	0.21	36.00	0.21	39.23	0.21	42.97	0.22	36.27	0.20	35.81	0.20	33.65	0.19
TiO2	0.02	0.02	0.00	0.00	0.00	0.00	0.00	0.00	0.00	0.00	0.00	0.02	0.01	0.02	0.03	0.02
Al2O3	0.37	0.03	0.33	0.03	0.27	0.03	0.19	0.02	0.24	0.02	0.49	0.03	0.44	0.03	0.39	0.03
Cr2O3	0.00	0.00	0.00	0.03	0.00	0.03	0.00	0.00	0.00	0.00	0.00	0.00	0.00	0.00	0.00	0.00
FeO	7.56	0.15	8.53	0.17	7.65	0.16	7.88	0.16	6.15	0.14	10.46	0.18	10.01	0.18	10.68	0.18
MnO	0.09	0.03	0.11	0.03	0.11	0.03	0.17	0.04	0.09	0.03	0.05	0.03	0.17	0.04	0.12	0.03
MgO	37.52	0.31	37.36	0.32	37.54	0.32	36.38	0.30	33.05	0.29	28.55	0.26	35.99	0.30	35.18	0.30
CaO	0.05	0.01	0.09	0.02	0.08	0.02	0.17	0.02	0.04	0.01	0.07	0.02	0.08	0.02	0.06	0.01
Na2O	0.03	0.04	0.03	0.03	0.02	0.03	0.01	0.03	0.07	0.04	0.06	0.04	0.07	0.04	0.03	0.04
K2O	0.00	0.00	0.00	0.01	0.00	0.00	0.00	0.01	0.00	0.00	0.00	0.00	0.01	0.01	0.00	0.00
NiO	0.45	0.05	0.34	0.05	0.58	0.05	0.32	0.04	3.64	0.11	5.60	0.13	0.47	0.05	0.72	0.06
Cl	0.40	0.04	0.74	0.05	0.64	0.05	0.31	0.03	0.22	0.03	0.34	0.04	0.58	0.05	0.68	0.05
Total	83.51	0.41	82.93	0.43	82.91	0.42	84.67	0.41	86.47	0.41	81.90	0.41	83.63	0.42	81.54	0.41

Chemistry of the aqueous solutions

Table C.15. Accuracy and reproducibility of analysed fluids

	Standard	n	Instrument	Ref.	Avg.	Reproducibility %	Accuracy %
				ppb	*ppb*		
Si	SLRS-5	12	ICP-OES	1922.00	1932.10	9.22	17.79
Mg	SLRS-5	12	ICP-OES	2518.00	2583.00	8.05	4.43
Mn	SLRS-5	12	ICP-OES	4.20	5.17	8.22	2.31
Fe	SLRS-5	12	ICP-OES	91.40	99.02	9.54	7.18
Ca	SLRS-5	12	ICP-OES	10320.00	10721.96	9.86	7.46
Na	SLRS-5	12	ICP-OES	5461.00	4393.60	2.78	8.87
K	SLRS-5	12	ICP-OES	859.00	853.53	8.16	8.97
Cr	SLRS-5	5	ICP-MS	0.22	0.24	9.35	9.71
Co	SLRS-5	5	ICP-MS	0.06	0.05	6.53	-2.26
Ni	SLRS-5	5	ICP-MS	0.48	0.45	9.85	-5.29
Cu	SLRS-5	12	ICP-OES	17.50	27.10	3.95	7.83
Zn	SLRS-5	12	ICP-OES	0.99	2.24	20.94	-19.59
Mg	SLRS-6	6	ICP-OES	2137.00	2228.39	1.10	4.28
Mn	SLRS-6	6	ICP-OES	2.12	2.21	3.09	4.01
Fe	SLRS-6	6	ICP-OES	84.50	85.72	2.17	1.44
Ca	SLRS-6	6	ICP-OES	8770.00	8741.48	1.89	-0.33
Na	SLRS-6	6	ICP-OES	2770.00	2645.27	1.49	-4.50
K	SLRS-6	6	ICP-OES	877.00	650.09	3.42	-25.87
Co	SLRS-6	6	ICP-MS	0.05	0.06	10.42	7.82
Ni	SLRS-6	6	ICP-MS	0.62	0.59	15.73	-4.64
Cu	SLRS-6	6	ICP-OES	24.00	26.01	2.43	8.38
Zn	SLRS-6	6	ICP-OES	1.76	1.83	8.20	3.79

	Standard	n	Instrument	Ref.	Avg.	Reproducibility %	Accuracy %
				mol/L	*mol/L*		
Alkalinity	Volvic	10	Methrom Titrino	1.2	1.4	4.7	15.2
pH	Volvic	10	Methrom Titrino	7	6.8	1.4	-2.7

Fluid chemistry of the major elements concentration on the outlet fluids

Table.C.16. Fluid chemistry of the major elements concentration on the outlet fluids of experiment FP1

Experiment FP1

Sample name	Sampling time	pH 25°C		pH 170°C	Alkalinity 25°C		DIC 25°C	Si		Fe		Mg		Ca		Na	
	hours		*σ*		*mg/L*	*σ*	*mg/L*	*mg/L*	*σ*	*mg/L*	*σ*	*mg/L*	*σ*	*mg/L*	*σ*	*mg/L*	*σ*
SW	0.0	5.54	0.28	3.34	416.4	20.8	1803.8	1.93	0.06	1.94	0.03	1.37	0.03	1.27	0.26	12045.2	96.2
1	3.3	5.71	0.29	4.08	533.3	26.7	1651.0	10.23	0.14	15.87	0.06	68.86	0.23	7.52	1.68	12795.7	31.9
2	21.1	5.77	0.29	4.18	467.4	23.4	1322.0	24.80	0.16	11.45	0.05	57.79	0.13	6.69	1.44	12194.7	122.8
3	44.2	5.54	0.28	4.31	350.8	17.5	1445.0	25.97	0.06	6.39	0.01	44.09	0.08	4.74	0.43	11881.9	34.5
4	49.3	5.44	0.27	4.70	274.6	13.7	1356.0	20.18	0.02	1.61	0.02	34.05	0.18	3.84	0.83	12558.3	64.3
5	65.4	5.39	0.27	4.74	245.9	12.3	1331.0	21.29	0.08	1.24	0.01	30.37	0.10	3.71	0.87	12108.0	100.6
6	89.4	5.31	0.27	4.93	(-)	(-)	(-)	23.89	0.20	0.04	0.02	37.47	0.28	3.90	0.96	11869.1	262.0
7	98.9	5.26	0.26	4.95	198.3	9.9	1377.0	18.82	0.12	0.01	0.00	25.29	0.11	3.70	0.97	12337.7	102.7
8	115.4	5.07	0.25	4.76	(-)	(-)	(-)	19.91	0.06	0.66	0.01	26.91	0.09	3.89	0.41	12708.9	206.9
9	138.4	5.33	0.27	4.74	176.3	8.8	1069.0	16.96	0.05	1.15	0.04	21.25	0.07	4.34	0.72	11896.2	75.8
10	161.9	5.40	0.27	4.88	245.3	12.3	1302.0	15.99	0.12	0.29	0.02	23.79	0.08	2.66	0.25	12486.9	23.8
11	165.6	(-)	(-)	(-)	(-)	(-)	(-)	22.55	0.11	1.05	0.01	31.62	0.06	4.40	0.55	11929.8	14.9
12	167.2	(-)	(-)	(-)	(-)	(-)	(-)	17.11	0.15	0.18	0.02	23.89	0.15	4.28	0.40	11698.3	126.2

(-) Not analysed*

Table.C.17. Fluid chemistry of the major elements concentration on the outlet fluids of experiment FP2

Experiment FP2

Sample name	Sampling time	pH 25°C		pH 170°C	Alkalinity 25°C		DIC 25°C	Si		Fe		Mg		Ca		Na	
	hours		*σ*		*mg/L*	*σ*	*mg/L*	*mg/L*	*σ*	*mg/L*	*σ*	*mg/L*	*σ*	*mg/L*	*σ*	*mg/L*	*σ*
SW	0.00	5.54	0.28	3.34	416.4	20.8	1803.8	1.93	0.06	1.94	0.03	1.37	0.03	1.27	0.26	12045.2	96.2
1	1.03	5.75	0.29	4.54	(-)	(-)	(-)	29.23	0.02	3.37	0.08	65.79	0.24	11.74	0.65	10354.2	69.4
2	14.88	5.50	0.28	4.79	369.2	18.5	1640.5	28.00	0.02	1.07	0.01	46.45	0.10	4.57	0.27	10783.6	72.7
3	21.85	5.49	0.27	4.92	287.4	14.4	1300.2	17.68	0.08	0.22	0.03	28.21	0.09	3.87	0.48	10443.5	82.7
4	38.37	5.50	0.27	4.91	245.3	12.3	1090.1	16.47	0.02	0.29	0.01	22.82	0.04	6.15	0.77	10308.4	143.7
5	62.92	5.67	0.28	4.80	351.5	17.6	1169.8	20.27	0.11	0.94	0.02	32.21	0.04	19.87	1.08	10511.1	96.0
6	63.38	5.57	0.28	4.85	350.2	17.5	1376.6	20.62	0.14	0.49	0.02	31.52	0.29	3.49	0.29	10349.0	223.0
7	65.53	5.55	0.28	4.84	316.1	15.8	1286.3	17.74	0.07	0.53	0.02	31.82	0.02	5.03	1.49	9863.0	38.7
8	85.82	5.58	0.28	4.96	333.2	16.7	1287.5	16.95	0.07	0.01	-0.01	27.35	0.07	3.78	0.86	10539.4	126.9
9	111.45	5.47	0.27	4.90	270.9	13.5	1270.6	11.81	0.09	0.08	0.01	17.08	0.05	4.15	0.46	10234.7	88.2

Table.C.18. Fluid chemistry of the major elements concentration on the outlet fluids of experiment FP3

Experiment FP3

Sample name	Sampling time	pH 25°C		pH 170°C	Alkalinity 25°C		DIC 25°C	Si		Fe		Mg		Ca		Na	
	hours		σ		*mg/L*	σ	*mg/L*	*mg/L*	σ	*mg/L*	σ	*mg/L*	σ	*mg/L*	σ	*mg/L*	σ
SW	0.0	5.54	0.28	3.34	416.4	20.8	1803.8	1.93	0.06	1.94	0.03	1.37	0.03	1.27	0.26	12045.2	96.2
1	13.4	5.72	0.29	4.52	457.0	22.9	1396.1	30.02	0.14	3.49	0.09	55.26	0.27	11.83	0.35	10257.0	31.9
2	21.0	5.68	0.28	4.80	477.8	23.9	1552.4	37.99	0.15	1.19	0.03	66.80	0.11	13.67	1.04	10324.1	43.2
3	39.0	5.68	0.28	4.60	477.8	23.9	1552.9	36.89	0.30	2.64	0.00	64.02	0.34	11.30	0.66	10297.1	23.7
4*	63.0	5.65	0.28	4.42	403.3	20.2	1374.9	31.87	0.04	4.80	0.01	70.43	0.43	17.81	0.58	9330.3	94.8
5*	118.0	5.69	0.28	4.14	471.7	23.6	1510.0	29.96	0.14	12.56	0.01	57.28	0.13	8.41	0.45	10320.8	158.7
6	133.0	5.67	0.28	4.62	466.8	23.3	1553.2	32.76	0.14	2.44	0.02	56.61	0.19	10.56	0.88	10966.4	41.0
7	142.0	5.57	0.28	4.59	360.0	18.0	1417.5	27.54	0.09	2.58	0.02	42.55	0.08	7.20	0.13	11503.2	51.8
8	157.0	5.58	0.28	4.42	380.1	19.0	1458.8	28.21	0.09	4.56	0.06	43.28	0.16	6.86	0.90	11432.5	51.5
9	160.0	5.58	0.28	4.58	383.8	19.2	1483.7	29.63	0.05	2.66	0.04	44.56	0.12	5.05	0.83	11257.5	92.1
10	164	5.57	0.28	5.05	386.2	19.3	1513.0	29.40	0.06	0.45	0.04	46.16	0.16	6.30	0.36	11629.7	117.5
11	165	5.58	0.28	4.80	382.0	19.1	1468.4	30.39	0.10	1.09	0.02	45.08	0.10	5.26	0.53	11138.2	54.8

** Stop fluid injection*

Table.C.19. Fluid chemistry of the major elements concentration on the outlet fluids of experiment FP4

Experiment FP4

Sample name	Sampling time	pH 25°C		pH 170°C	Alkalinity 25°C		DIC 25°C	Si		Fe		Mg		Ca		Na	
	hours		σ		*mg/L*	σ	*mg/L*	*mg/L*	σ	*mg/L*	σ	*mg/L*	σ	*mg/L*	σ	*mg/L*	σ
SW	0.0	5.30	0.27	3.83	139.1	7.0	899.8	1.93	0.06	1.94	0.03	1.37	0.03	1.27	0.26	12045.2	96.2
1	2.1	5.27	0.26	4.82	84.2	1.7	575.5	3.21	0.07	0.97	0.04	8.09	0.01	3.34	0.51	10876.1	103.4
2	19.5	5.29	0.26	4.95	101.9	1.2	669.7	4.79	0.02	0.58	0.03	9.65	0.06	1.70	0.18	11554.5	171.9
3	42.2	5.38	0.27	5.10	86.0	1.7	475.7	4.87	0.07	0.32	0.07	8.92	0.04	2.77	0.41	11744.5	104.8
4	72.0	5.27	0.26	5.06	103.1	1.7	704.9	4.72	0.12	0.30	0.02	8.54	0.01	2.55	0.37	11900.9	112.8
5	92.4	5.30	0.26	4.93	104.3	1.7	672.7	3.95	0.05	0.65	0.03	7.38	0.03	1.76	0.22	11795.6	38.6
6	112.8	5.35	0.27	5.00	130.6	4.5	764.2	3.91	0.03	0.52	0.01	10.67	0.02	2.02	0.02	11874.5	88.2
7	120.2	5.33	0.27	5.09	131.8	4.5	801.7	2.94	0.05	0.30	0.02	7.73	0.02	1.57	0.04	11684.6	98.0
8	141.7	5.41	0.27	5.22	129.4	7.1	676.5	2.44	0.07	0.14	0.03	5.47	0.03	0.36	0.29	12072.6	121.6
10	193.8	5.42	0.27	5.19	115.3	3.2	590.2	2.73	0.08	0.20	0.03	6.88	0.03	0.86	0.18	11954.3	79.2
11	256.5	5.53	0.28	5.26	162.3	5.5	681.8	2.16	0.01	0.17	0.03	4.11	0.02	1.70	0.37	11906.0	48.8

Fluid chemistry of the metal concentration on the outlet fluids

Table.C.20. Fluid chemistry of the major elements concentration on the outlet fluids of experiment FP1

Experiment FP1

Sample name	Sampling time	Mn		Cu		Zn		Cr		Ni		Co	
	hours	*mg/L*	*σ*	*mg/L*	*σ*	*mg/L*	*σ*	*mg/L*	*σ*	*mg/L*	*σ*	*mg/L*	*σ*
SW	0.0	0.31	0.01	0.59	0.04	3.75	0.02	0.05	0.010	35.83	0.2	0.13	0.002
1	3.3	0.77	0.02	7.63	0.52	1.66	0.01	0.14	0.004	62.54	0.4	0.10	0.000
2	21.1	0.51	0.01	4.03	0.27	1.30	0.02	0.31	0.008	34.08	0.6	0.06	0.002
3	44.2	0.43	0.01	1.98	0.13	0.83	0.02	0.03	0.002	29.40	0.3	0.05	0.001
4	49.3	0.40	0.01	0.69	0.05	0.35	0.01	0.01	0.001	21.65	0.1	0.04	0.001
5	65.4	0.32	0.01	0.57	0.04	0.30	0.01	0.01	0.001	24.14	0.2	0.03	0.001
6	89.4	0.35	0.01	0.12	0.01	0.32	0.01	0.00	0.000	30.15	0.1	0.02	0.000
7	98.9	0.26	0.01	0.19	0.01	0.28	0.01	0.01	0.000	25.34	0.2	0.03	0.001
8	115.4	0.29	0.01	0.23	0.02	0.31	0.01	0.01	0.000	27.95	0.3	0.02	0.001
9	138.4	0.28	0.01	0.23	0.02	0.32	0.00	0.01	0.000	29.57	0.1	0.03	0.001
10	161.9	0.29	0.01	0.24	0.02	0.40	0.02	0.01	0.001	40.19	0.8	0.03	0.000
11	165.6	0.34	0.01	0.60	0.04	0.48	0.01	0.02	0.001	40.54	0.4	0.03	0.001
12	167.2	0.28	0.01	0.40	0.03	0.44	0.01	0.03	0.004	39.29	0.3	0.03	0.001

Table.C.21. Fluid chemistry of the major elements concentration on the outlet fluids of experiment FP2

Experiment FP2

Sample name	Sampling time	Mn		Cu		Zn		Cr		Ni		Co	
	hours	*mg/L*	*σ*	*mg/L*	*σ*	*mg/L*	*σ*	*mg/L*	*σ*	*mg/L*	*σ*	*mg/L*	*σ*
SW	0.00	0.31	0.00	0.59	0.02	3.75	0.02	0.05	0.010	35.83	0.2	0.13	0.002
1	1.03	0.74	0.00	0.94	0.02	0.42	0.00	0.35	1.353	27.91	0.2	0.05	0.001
2	14.88	0.51	0.01	0.59	0.02	0.35	0.00	0.16	1.136	27.35	0.3	0.05	0.000
3	21.85	0.40	0.00	0.44	0.04	0.32	0.00	0.02	12.439	32.26	0.3	0.04	0.000
4	38.37	0.34	0.00	0.36	0.02	0.35	0.01	0.01	11.577	33.80	0.6	0.03	0.001
5	62.92	0.37	0.00	0.39	0.01	0.49	0.01	0.01	4.261	44.13	0.3	0.03	0.000
6	63.38	0.39	0.00	0.33	0.01	0.53	0.01	0.01	8.318	49.82	0.6	0.03	0.000
7	65.53	0.37	0.00	0.08	0.02	0.32	0.01	0.01	6.613	49.61	0.4	0.03	0.001
8	85.82	0.34	0.00	0.03	0.03	0.35	0.01	0.02	4.762	34.82	0.8	0.05	0.001
9	111.45	0.38	0.00	0.36	0.00	0.55	0.00	0.001	16.053	48.30	0.4	0.01	0.000

Table.C.22. Fluid chemistry of the major elements concentration on the outlet fluids of experiment FP3

Experiment FP3

Sample name	Sampling time	Mn		Cu		Zn		Cr		Ni		Co	
	hours	*mg/L*	*σ*	*mg/L*	*σ*	*mg/L*	*σ*	*mg/L*	*σ*	*mg/L*	*σ*	*mg/L*	*σ*
SW	0.0	0.31	0.00	0.59	0.02	3.75	0.02	0.050	0.010	35.83	0.2	0.13	0.002
1	13.4	0.59	0.00	1.17	0.01	0.62	0.01	0.114	0.002	34.00	0.5	0.03	0.000
2	21.0	0.65	0.00	0.89	0.03	0.53	0.01	0.077	0.004	26.25	0.3	0.03	0.001
3	39.0	0.62	0.01	0.74	0.03	0.61	0.01	0.093	0.004	28.27	0.1	0.03	0.000
4*	63.0	0.89	0.00	0.52	0.03	0.94	0.01	0.057	0.001	14.25	0.1	0.02	0.000
5*	118.0	0.44	0.00	0.42	0.01	6.09	0.07	0.050	0.000	26.45	0.3	0.04	0.001
6	133.0	0.49	0.01	0.29	0.03	15.52	0.07	0.009	0.000	26.85	0.3	0.05	0.001
7	142.0	0.46	0.00	0.33	0.01	18.31	0.07	0.008	0.001	23.78	0.3	0.05	0.001
8	157.0	0.47	0.00	0.29	0.04	14.34	0.02	0.011	0.002	25.21	0.2	0.06	0.002
9	160.0	0.47	0.01	0.26	0.01	12.47	0.07	0.002	0.000	26.21	0.4	0.07	0.000
10	164	0.41	0.00	0.17	0.02	9.32	0.08	0.001	0.000	3.51	0.0	0.01	0.000
11	165	0.42	0.00	0.28	0.03	11.13	0.03	0.023	0.001	27.25	0.2	0.07	0.000

* Stop fluid injection

Table.C.23. Fluid chemistry of the major elements concentration on the outlet fluids of experiment FP4

Experiment FP4

Sample name	Sampling time	Mn		Cu		Zn		Cr		Ni		Co	
	hours	*mg/L*	*σ*	*mg/L*	*σ*	*mg/L*	*σ*	*mg/L*	*σ*	*mg/L*	*σ*	*mg/L*	*σ*
B	0.0	0.31	0.00	0.59	0.02	3.75	0.02	0.04	0.02	12.76	0.24	0.06	0.00
1	2.1	0.13	0.00	0.44	0.02	3.03	0.01	0.06	0.01	7.13	0.09	0.03	0.00
2	19.5	0.18	0.00	0.37	0.03	2.27	0.01	(-)	(-)	(-)	(-)	(-)	(-)
3	42.2	0.18	0.00	0.30	0.02	1.74	0.01	0.02	0.00	7.72	0.04	0.04	0.00
4	72.0	0.19	0.00	0.24	0.03	1.82	0.02	(-)	(-)	(-)	(-)	(-)	(-)
5	92.4	0.20	0.00	0.26	0.01	2.46	0.02	0.07	0.03	18.63	0.21	0.05	0.00
6	112.8	0.24	0.00	0.28	0.03	2.69	0.03	(-)	(-)	(-)	(-)	(-)	(-)
7	120.2	0.17	0.00	0.32	0.02	3.17	0.02	0.02	0.00	23.25	0.20	0.04	0.00
8	141.7	0.16	0.00	0.47	0.04	3.55	0.01	(-)	(-)	(-)	(-)	(-)	(-)
9	193.8	0.23	0.00	0.64	0.01	3.26	0.03	0.02	0.00	36.57	0.25	0.05	0.00
10	256.5	0.21	0.00	0.79	0.04	4.17	0.01	0.01	0.00	34.30	0.51	0.04	0.00

(-) Not analyzed*

Saturation index of the outlet fluids

Table.C.24. Saturation index of the outlet fluids for experiment FP1

Experiment 1 (FP1)

Sampling time	RST	**Chrysotile**	**Olivine**	**Diopside**	**Enstatite**	**Mg-cronstedtite**	**Nepouite**	**Quartz**	**Hematite**	**Magnetite**	**Huntite**	**Magnesite**	**Calcite**	**Dolomite**
hours	*hours*	$Mg_3Si_2O_5(OH)_4$	Mg_2SiO_4	$CaMgSi_2O_6$	$MgSiO_3$	$Mg_2Fe_2SiO_5(OH)_4$	$Ni_3Si_2O_5(OH)_4$	SiO_2	Fe_2O_3	Fe_3O_4	$CaMg_3(CO_3)_4$	$MgCO_3$	$CaCO_3$	$MgCa(CO_3)_2$
0	0	-10.66	-9.07	-19.00	-9.20	(-)	(-)	-1.99	7.33	0.24	108.13	-4.58	(-)	(-)
3	2	-4.06	-4.92	-12.16	-5.40	-1.25	(-)	-1.27	10.20	4.55	119.84	-1.42	-3.28	-3.66
21	12	-3.48	-4.66	-11.12	-4.90	-0.81	(-)	-0.88	10.01	4.26	120.33	-1.30	-3.13	-3.40
44	33	-2.82	-4.23	-10.82	-4.73	-0.88	(-)	-0.86	9.60	3.66	120.88	-1.16	-3.02	-3.14
49	47	-1.14	-3.07	-9.77	-4.24	-0.69	(-)	-0.97	8.60	2.15	123.35	-0.56	-2.36	-1.88
65	57	-0.67	-2.77	-9.61	-4.18	-0.79	(-)	-0.95	8.38	1.83	123.53	-0.52	-2.28	-1.77
89	77	0.85	-1.77	-8.70	-3.70	-2.73	0.89	-0.90	5.45	-2.57	125.20	-0.09	-1.90	-0.95
99	94	0.51	-1.96	-9.04	-3.95	-4.31	0.55	-1.01	4.25	-4.37	124.76	-0.24	-1.90	-1.10
115	107	9.66	-2.62	-9.66	-4.24	-1.41	-0.43	-0.98	7.84	1.01	123.50	-0.55	-2.24	-1.74
138	127	-0.64	-2.71	-9.92	-4.44	-1.28	-0.60	-1.05	8.32	1.73	123.08	-0.69	-2.23	-1.88
162	150	0.53	-1.92	-9.62	-4.17	-1.82	0.57	-1.08	7.16	-0.01	124.01	-0.40	-2.18	-1.53

(-) Phases with affinities less than -10 kcal
**RST: Representative sampling time*

Table.C.25. Saturation index of the outlet fluids for experiment FP2

Experiment 2 (FP2)

Time	RST	**Chrysotile**	**Olivine**	**Diopside**	**Enstatite**	**Mg-cronstedtite**	**Nepouite**	**Quartz**	**Hematite**	**Magnetite**	**Huntite**	**Magnesite**	**Calcite**	**Dolomite**
hours	*hours*	$Mg_3Si_2O_5(OH)_4$	Mg_2SiO_4	$CaMgSi_2O_6$	$MgSiO_3$	$Mg_2Fe_2SiO_5(OH)_4$	$Ni_3Si_2O_5(OH)_4$	SiO_2	Fe_2O_3	Fe_3O_4	$CaMg_3(CO_3)_4$	$MgCO_3$	$CaCO_3$	$MgCa(CO_3)_2$
0	0	-10.66	-9.07	-19.00	-9.20	(-)	(-)	-1.99	7.33	0.24	108.13	-4.58	(-)	(-)
1	1	-1.43	-3.32	-9.28	-4.08	-0.01	-1.40	-0.81	9.17	3.01	123.49	-0.57	-2.19	-1.71
15	8	0.00	-2.36	-8.93	-3.79	-0.23	0.04	-0.83	8.27	1.66	124.51	-0.26	-2.11	-1.32
22	18	0.62	-1.88	-9.12	-3.97	-1.66	0.66	-1.03	6.93	-0.35	124.74	-0.24	-1.92	-1.12
38	30	0.52	-1.93	-9.13	-4.12	-1.71	0.56	-1.06	7.17	0.00	124.55	-0.36	-1.75	-1.07
63	51	0.42	-2.03	-8.68	-4.07	-0.75	0.46	-0.97	8.16	1.49	124.75	-0.39	-1.45	-0.80
63	63	9.45	-1.75	-9.27	-3.99	-1.14	0.89	-0.97	7.61	0.66	124.28	-0.33	-2.12	-1.40
66	65	0.66	-1.85	-9.27	-4.07	-1.17	0.70	-1.03	7.67	0.76	124.39	-0.34	-1.98	-1.27
86	76	0.89	-1.69	-9.05	-3.94	-4.24	0.94	-1.05	4.25	-4.37	124.94	-0.19	-1.87	-1.02
111	99	0.63	-1.81	-9.76	-4.41	-3.27	0.67	-1.21	6.04	-1.68	123.92	-0.50	-1.95	-1.41

(-) Phases with affinities less than -10 kcal
**RST: Representative sampling time*

Table.C.26. Saturation index of the outlet fluids for experiment FP3

Experiment 3 (FP3)

Time	RST	**Chrysotile**	**Olivine**	**Diopside**	**Enstatite**	**Mg-cronstedtite**	**Nepouite**	**Quartz**	**Hematite**	**Magnetite**	**Huntite**	**Magnesite**	**Calcite**	**Dolomite**
hours	*hours*	$Mg_3Si_2O_5(OH)_4$	Mg_2SiO_4	$CaMgSi_2O_6$	$MgSiO_3$	$Mg_2Fe_2SiO_5(OH)_4$	$Ni_3Si_2O_5(OH)_4$	SiO_2	Fe_2O_3	Fe_3O_4	$CaMg_3(CO_3)_4$	$MgCO_3$	$CaCO_3$	$MgCa(CO_3)_2$
0	0	-10.66	-9.07	-19.00	-9.20	(-)	(-)	-1.99	7.33	0.24	108.13	-4.58	(-)	(-)
13	7	-1.26	-3.21	-9.39	-4.18	(-)	-1.22	-0.80	9.20	3.05	123.16	-0.67	-2.21	-1.84
21	17	0.29	-2.21	-7.99	-3.48	0.36	0.32	-0.70	8.36	1.80	125.54	-0.08	-1.61	-0.64
39	30	-0.84	-4.49	-8.87	-3.88	0.13	-0.81	-0.71	8.99	2.74	123.93	-0.46	-2.08	-1.49
63	51	-2.95	-4.34	-9.46	-4.24	-0.15	-2.92	-0.78	9.42	3.38	122.87	-0.76	-2.24	-1.95
118	91	-3.87	-4.95	-11.01	-4.89	-0.83	-3.84	-0.80	10.05	4.33	120.13	-1.38	-3.11	-3.45
133	126	-0.87	-2.96	-8.96	-3.94	0.01	-0.83	-0.76	8.93	2.65	123.92	-0.47	-2.06	-1.48
142	138	-1.38	-3.28	-9.53	-4.20	-0.42	-1.35	-0.84	8.96	2.70	123.12	-0.65	-2.29	-1.91
157	150	-2.30	-3.89	-10.17	-4.50	-0.65	-2.27	-0.83	9.38	3.32	121.85	-0.96	-2.64	-2.56
160	159	-1.24	-3.20	-9.63	-4.16	-0.35	-1.21	-0.81	8.99	2.73	122.97	-0.65	-2.46	-2.07
164	162	-1.06	-3.08	-7.80	-3.32	0.13	-1.04	-0.81	7.57	0.61	126.47	0.19	-1.48	-0.25
165	165	0.13	-2.28	-8.77	-3.75	-0.16	0.17	-0.80	8.29	1.69	124.60	-0.25	-2.03	-1.23

(-) Phases with affinities less than -10 kcal
**RST: Representative sampling time*

Table.C.27. Saturation index of the outlet fluids for experiment FP4

Experiment 4 (FP4)

Time	RST	**Chrysotile**	**Olivine**	**Diopside**	**Enstatite**	**Mg-cronstedtite**	**Nepouite**	**Quartz**	**Hematite**	**Magnetite**	**Huntite**	**Magnesite**	**Calcite**	**Dolomite**
hours	*hours*	$Mg_3Si_2O_5(OH)_4$	Mg_2SiO_4	$CaMgSi_2O_6$	$MgSiO_3$	$Mg_2Fe_2SiO_5(OH)_4$	$Ni_3Si_2O_5(OH)_4$	SiO_2	Fe_2O_3	Fe_3O_4	$CaMg_3(CO_3)_4$	$MgCO_3$	$CaCO_3$	$MgCa(CO_3)_2$
0	0	-19.85	-15.27	-17.02	-8.27	(-)	(-)	-1.99	8.10	1.41	108.15	-4.57	(-)	(-)
2	1	-11.21	-9.67	-11.44	-5.33	-2.64	(-)	-1.77	8.19	1.54	118.66	-1.86	-3.15	-3.96
20	11	-9.88	-8.84	-10.80	-4.83	-2.21	(-)	-1.60	7.78	0.92	119.62	-1.53	-3.18	-3.67
42	31	-9.07	-8.31	-10.01	-4.55	-2.16	(-)	-1.59	7.29	0.18	120.84	-1.28	-2.69	-2.93
72	57	-9.42	-8.53	-10.27	-4.67	-2.45	(-)	-1.61	7.22	0.09	120.48	-1.37	-2.79	-3.12
92	82	-10.51	-9.24	-11.15	-5.07	-2.52	(-)	-1.68	7.87	1.06	119.13	-1.68	-3.21	-3.85
113	103	-9.64	-8.66	-10.67	-4.78	-2.11	(-)	-1.69	7.69	0.79	120.22	-1.38	-3.01	-3.35
120	117	-9.60	-8.56	-11.23	-4.83	-2.61	(-)	-1.81	7.23	0.10	120.41	-1.35	-2.94	-3.24
142	131	-9.78	-8.70	-10.81	-4.86	-3.10	(-)	-1.89	6.58	-0.87	120.31	-1.25	-3.32	-3.53
194	168	-9.40	-8.45	-10.79	-4.75	-2.68	(-)	-1.84	6.89	-0.41	120.70	-1.22	-3.02	-3.20
257	225	-9.86	-8.72	-10.64	-4.94	-3.08	(-)	-1.95	6.76	-0.61	120.89	-1.30	-2.58	-2.84

(-) Phases with affinities less than -10 kcal
**RST: Representative sampling time*

Pump CO_2 parameters

Table.C.28. Parameters (V_{CO2} and P_{filled} CO_2) of each experiment to fill the CO_2 pump for a known pCO_2

Exp.	Sample	XCO_2	pCO_2	$V\ CO_2$	$P_{filled}CO_2$
		M	*MPa*	*(mm^3)*	*MPa*
FP1-HC	FP1	1	20	28420	3
FP2-HC	FP2	1	20	28420	3
FP3-HC	FP3	1	20	28420	3
FP4-LC	FP4	0.1	10	8526	1